WOODHEAD PUBLISHING IN MATERIALS

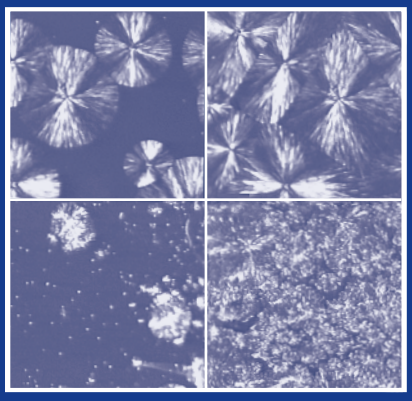

Polymer nanocomposites

Edited by Yiu-Wing Mai and Zhong-Zhen Yu

CRC

WP

Polymer nanocomposites

Related titles:

Lightweight ballistic composites for military and law-enforcement applications
(ISBN-13: 978-1-85573-941-3; ISBN-10: 1-85573-941-0)
Ballistic composites are materials with superior properties being lightweight and durable under environmental conditions (water and chemicals) with high performance (high strength, impact and ballistic resistance, damage tolerance). Lightweight ballistic composites are used in a wide range of lightweight vehicles, watercraft and aircraft armour giving high performance and lightweight protection against bullets and fragments. They also have exceptional insulating properties in high temperature environments. This major new book will be the first of its kind to give a comprehensive review of the current use of lightweight ballistic composites in both military and law-enforcement applications.

Design and manufacture of textile composites
(ISBN-13: 978-1-85573-744-0; ISBN-10: 1-85573-744-2)
This book brings together the design, manufacture and applications of textile composites. The term 'textile composites' is often used to describe a rather narrow range of materials, based on three-dimensional reinforcements produced using specialist equipment. The intention here though is to describe the broad range of polymer composite materials with textile reinforcements, from woven and non-crimp commodity fabrics to 3D textiles. Whilst attention is given to modelling of textile structures, composites manufacturing methods and subsequent component performance, it is substantially a practical book intended to help all those developing new products with textile composites.

Green composites: Polymer composites and the environment
(ISBN-13: 978-1-85573-739-6; ISBN-10: 1-85573-739-6)
There is an increasing movement of scientists and engineers dedicated to minimising the environmental impact of polymer composite production. Life cycle assessment is of paramount importance at every stage of a product's life, from initial synthesis through to final disposal and a sustainable society needs environmentally safe materials and processing methods. With an internationally recognised team of authors, *Green composites* examines polymer composite production and explains how environmental footprints can be diminished at every stage of the life cycle. This book is an essential guide for agricultural crop producers, governmental agricultural departments, automotive companies, composite producers and materials scientists all dedicated to the promotion and practice of eco-friendly materials and production methods.

Details of these and other Woodhead Publishing materials books and journals, as well as materials books from Maney Publishing, can be obtained by:

- visiting our web site at www.woodheadpublishing.com
- contacting Customer Services (e-mail: sales@woodhead-publishing.com; fax: +44 (0) 1223 893694; tel.: +44 (0) 1223 891358 ext. 30; address: Woodhead Publishing Limited, Abington Hall, Abington, Cambridge CB1 6AH, England)

If you would like to receive information on forthcoming titles, please send your address details to: Francis Dodds (address, tel. and fax as above; email: francisd@woodhead-publishing.com). Please confirm which subject areas you are interested in.

Maney currently publishes 16 peer-reviewed materials science and engineering journals. For further information visit www.maney.co.uk/journals.

Polymer nanocomposites

Edited by
Yiu-Wing Mai and Zhong-Zhen Yu

Woodhead Publishing and Maney Publishing
on behalf of
The Institute of Materials, Minerals & Mining

CRC Press
Boca Raton Boston New York Washington, DC

WOODHEAD PUBLISHING LIMITED
Cambridge England

Woodhead Publishing Limited and Maney Publishing Limited on behalf of
The Institute of Materials, Minerals & Mining

Published by Woodhead Publishing Limited, Abington Hall, Abington,
Cambridge CB1 6AH, England
www.woodheadpublishing.com

Published in North America by CRC Press LLC, 6000 Broken Sound Parkway, NW,
Suite 300, Boca Raton, FL 33487, USA

First published 2006, Woodhead Publishing Limited and CRC Press LLC

British Library Cataloguing in Publication Data
A catalogue record for this book is available from the British Library.

Library of Congress Cataloging in Publication Data
A catalog record for this book is available from the Library of Congress.

Woodhead Publishing Limited ISBN-13: 978-1-85573-969-7 (book)
Woodhead Publishing Limited ISBN-10: 1-85573-969-0 (book)
Woodhead Publishing Limited ISBN-13: 978-1-84569-112-7 (e-book)
Woodhead Publishing Limited ISBN-10: 1-84569-112-1 (e-book)
CRC Press ISBN-10: 0-8493-9297-7
CRC Press order number: WP9297

The publishers' policy is to use permanent paper from mills that operate a sustainable forestry policy, and which has been manufactured from pulp which is processed using acid-free and elementary chlorine-free practices. Furthermore, the publishers ensure that the text paper and cover board used have met acceptable environmental accreditation standards.

Project managed by Macfarlane Production Services, Dunstable, Bedfordshire
(macfarl@aol.com)
Typeset by Godiva Publishing Services Ltd, Coventry, West Midlands
Printed by TJ International Limited, Padstow, Cornwall, England

Contents

Contributor contact details

(* = main contact)

Chapter 1
Makoto Kato* and Dr Arimitsu Usuki
41-1 Yokomichi
Nagakute
Nagakute-Cho
Aichi-Gun
Aichi 480-1192
Japan

Tel: +81-561-63-5252
Email: makoto@mosk.tytlabs.co.jp; usuki@mosk.tytlabs.co.jp

Chapter 2
Dr Ole Becker*
Airbus Deutschland GmbH
Cabin Supply Systems – BCEBS
Kreetslag 10
21129 Hamburg
Germany

Email: ole.becker@airbus.com

Professor George Simon
School of Physics & Materials Engineering
Monash University
Melbourne
Victoria 3800
Australia

Email: George.Simon@eng.monash.edu.au

Chapter 3
Dr Suprakas Sinha Ray* and Mosto Bousmina
Department of Chemical Engineering
Laval University
Sainte-Foy
Quebec G1K 7P4
Canada

Tel.: +1 418 656 2131 Ext. 8368
Fax: +1 418 656 5993
Email: suprakas73@yahoo.com; suprakas.sinha-ray.1@ulaval.ca

Chapter 4
Professor Krishnamurthy Jayaraman* and Dr Sharad Kumar
Department of Chemical Engineering and Materials Science
2527 Eng. Bldg
Michigan State University
East Lansing
MI 48824
USA

Tel: 517 355-5138; 517 432-1105
Email: jayarama@egr.msu.edu

Chapter 5
Ding-Ru Yei, Huei-Kuan Fu and Professor Feng-Chih Chang
Institute of Applied Chemistry
National Chiao-Tung University
Hsin-Chu 30050
Taiwan

Tel: 886-3-5727077
Email: changfc@cc.nctu.edu.tw
changfc@mail.nctu.edu.tw

Chapter 6
Professor Tao Tang, Xin Tong, Zhiliu Feng and B Huang
State Key Laboratory of Polymer Physics and Chemistry
Changchun Institute of Applied Chemistry
Chinese Academy of Sciences
Changchun 130022
People's Republic of China

Tel: 0086-0431-5685653
Email: ttang@ns.ciac.jl.cn

Chapter 7
Professor Christian Decker
Département de Photochimie Générale (UMR-CNRS N7525)
Ecole Nationale Supérieure de Chimie de Mulhouse
Université de Haute-Alsace
3, rue Werner
68200 Mulhouse
France

Email: c.decker@uha.fr

Chapter 8
Dr Kenneth E Strawhecker*
Veeco Instruments Inc
112 Robin Hill Road
Santa Barbara
CA 93117
USA

Email: kstrawhecker@veeco.com

Evangelos Manias
Department of Materials Science and Engineering
The Pennsylvania State University
University Park
PA 16801
USA

Chapter 9
Professor Chang-Sik Ha
Department of Polymer Science and Engineering
Pusan National University
Pusan 609-735
Korea

Tel: +82/51-510-2407
Email: csha@pusan.ac.kr

Chapter 10
Marco Zanetti
Dipartimento di Chimica Inorganica Fisica e dei Materiali and Nanostructured Interfaces and Surfaces Centre of Excellence
Università degli Studi di Torino
Via Pietro Giuria, 7
I-10125, Torino
Italy

Email: marco.zanetti@unito.it

Chapter 11
Professor Vittoria Vittoria*, Dr Andrea Sorrentino, Dr Giuliana Gorrasi, Dr Mariarosaria Tortora
Chemical and Food Engineering Department
University of Salerno

via Ponte Don Melillo
I-84084 Fisciano – Salerno
Italy

Tel.: +39 089 96 4114/4019
Fax: +39 089 96 4057
Email: vvittoria@unisa.it
asorrent@unisa.it
ggorrasi@unisa.it
mrtortor@unisa.it

Chapter 12

Professor George Simon* and Abubaker Mohammad
Department of Materials Engineering
Monash University
Melbourne
Victoria 3800
Australia

Email:
George.Simon@eng.monash.edu.au

Chapter 13

Associate Professor Kin Liao*
School of Chemical and Biomedical Engineering,
Nanyang Technological University
50 Nanyang Avenue
Singapore 639798

Email: ASKLiao@ntu.edu.sg

Yu Ren
School of Mechanical and Aerospace Engineering
Nanyang Technological University
50 Nanyang Avenue
Singapore 639798

Tan Xiao
Department of Physics
Shantou University
Shantou 515063
People's Republic of China

Chapter 14

Professor Toru Kuzumaki
Institute of Industrial Science
The University of Tokyo
4-6-1 Komaba
Meguro-ku
Tokyo 153 8505
Japan

Tel: +81 (3) 5452 6302
Fax: +81 (3) 5452 6301
Email: kuzumaki@iis.u-tokyo.ac.jp

Chapter 15

Professor O Ok Park*, Jong Hyeok Park, Tae-Ho Kim
Department of Chemical & Biomolecular Engineering
Korea Advanced Institute of Science and Technology
373-1 Guseong-dong
Yuseong-gu
Daejeon, 305-701
Korea

Tel: +82-42-869-3923
Email: ookpark@kaist.ac.kr

Chapter 16

Dr Xuehong Lu*
School of Materials Science & Engineering
Nanyang Technological University
Nanyang Avenue
Singapore 639798

Email: asxhlu@ntu.edu.sg

Dr Tianxi Liu
Institute of Advanced Materials
Fudan University
220 Handan Road
Shanghai 200433
People's Republic of China

Email: txliu@fudan.edu.cn

Chapter 17
Professor Angel Millan* and
Fernando Palacio
Instituto de Ciencia de Materiales de
Aragón
CSIC-Universidad de Zaragoza
Facultad de Ciencias
c/ Pedro Cerbuna 12
50009 Zaragoza
Spain

Email: amillan@posta.unizar.es

Etienne Snoeck, Virginie Serin and
Pierre Lecante
CEMES-CNRS
29 rue Jeanne Marvig
F-31055 Toulouse Cedex
France

Chapter 18
Dr Chin-lung Chiang
Department of Industrial Safety and
Health
Hung-Kuang University
Sha-Lu
Taiwan, 433
Republic of China

Tel: 886-426318652-2250
Email: dragon@sunrise.hk.edu.tw

Professor Chen-Chi M. Ma*
Department of Chemical Engineering
National Tsing-Hua University
Hsin-Chu
Taiwan, 30043
Republic of China

Email: ccma@che.nthu.edu.tw

Chapter 19
Professor Yuezhong Meng
Institute of Energy & Environmental
Materials
School of Physics & Engineering
Sun Yat-Sen University
Guangzhou 510275
People's Republic of China

Tel/Fax: +8620-84114113
Email: mengyzh@mail.sysu.edu.cn

Chapter 20
Professor Ming Qiu Zhang*
Materials Science Institute
Zhongshan University
Guangzhou 510275
People's Republic of China

Tel/Fax: +86-20-84036576
Email: ceszmq@zsu.edu.cn

Min Zhi Rong
Key Laboratory for Polymeric
Composite and Functional
Materials of Ministry of Education
Zhongshan University
Guangzhou 510275
People's Republic of China

Klaus Friedrich
Institute for Composite Materials
(IVW)
University of Kaiserslautern
D-67663 Kaiserslautern
Germany

Preface

Polymer nanocomposites are commonly defined as the combination of a polymer matrix and additives that have at least one dimension in the nanometer range. The additives can be one-dimensional (examples include nanotubes and fibres), two-dimensional (which include layered minerals like clay), or three-dimensional (including spherical particles). Over the past decade, polymer nanocomposites have attracted considerable interests in both academia and industry, owing to their outstanding mechanical properties like elastic stiffness and strength with only a small amount of the nanoadditives. This is caused by the large surface area to volume ratio of nanoadditives when compared to the micro- and macro-additives. Other superior properties of polymer nanocomposites include barrier resistance, flame retardancy, scratch/wear resistance, as well as optical, magnetic and electrical properties.

This book covers both fundamental and applied research associated with polymer-based nanocomposites, and presents possible directions for further development of high performance nanocomposites. It has two main parts. Part I has 12 chapters which are entirely dedicated to those polymer nanocomposites containing layered silicates (clay) as an additive. Many thermoplastics, thermosets, and elastomers are included, such as polyamide (Chapter 1), polypropylene (Chapter 4), polystyrene (Chapter 5), poly(butylene terephthalate) (Chapter 9), poly(ethyl acrylate) (Chapter 6), epoxy resin (Chapter 2), biodegradable polymers (Chapter 3), water soluble polymers (Chapter 8), acrylate photopolymers (Chapter 7) and rubbers (Chapter 12). In addition to synthesis and structural characterisation of polymer/clay nanocomposites, their unique physical properties like flame retardancy (Chapter 10) and gas/liquid barrier (Chapter 11) properties are also discussed. Furthermore, the crystallisation behaviour of polymer/clay nanocomposites and the significance of chemical compatibility between a polymer and clay in affecting clay dispersion are also considered.

Part II of this book deals with the most recent developments of polymer nanocomposites with other nanoadditives such as carbon nanotubes, graphite, nanoparticles and other inorganic–organic hybrid systems and has eight

chapters. Carbon nanotubes, since their discovery in 1991, have attracted a great deal of attention because of their exceptional elastic modulus, bending strength, aspect ratio, electrical and thermal conductivity, chemical and thermal stability, and adsorbability. Chapters 13 and 14 are concerned with carbon nanotubes as a means of reinforcement. The former is concerned with the mechanical properties and long-term performance of carbon nanotube/epoxy composites; and the latter illustrates the fabrication and potential applications of nanocomposites fabricated by using carbon nanotubes as the fibre and carbon 60 crystals as the matrix. Three chapters are entirely devoted to functional polymer nanocomposites. The design and fabrication of polymer nanocomposites filled with functional nanoparticles for specific functional properties (Chapter 15), the synthesis and characterisation of magnetic polymer nanocomposites (Chapter 17), and the conducting polymer/graphite nanocomposites (Chapter 19) are discussed. The wear characteristics of polymer nanocomposites reinforced with different nanoparticles are studied in Chapter 20. The effect of different surface treatment techniques of nanoparticles on the wear behaviour is investigated. In addition, the latest progress on surface modification of $CaCO_3$ nanoparticles and their polymer nanocomposites in terms of toughening and reinforcement is given in Chapter 16. Phenolic resin/silica nanocomposites synthesised by sol-gel techniques are described in Chapter 18.

We would like to express our sincerest appreciation to all the authors for their valuable contributions and the referees for their critical evaluations of the manuscripts. Our special thanks go to Francis Dodds, Gwen Jones, Melanie Cotterell and Emma Pearce at Woodhead Publishing Limited, as well as Amanda Macfarlane at Macfarlane Production Services for their cooperation, suggestions and advice during the various phases of preparation, organisation and production of the book.

Yiu-Wing Mai
Zhong-Zhen Yu
Sydney, Australia

Part I

Layered silicates

1

Polyamide/clay nanocomposites

M KATO and A USUKI, Toyota Central R&D Labs Inc., Japan

1.1 Introduction

A typical polymer composite is a combination of a polymer and a filler. Because compounding is a technique that can ameliorate the drawbacks of conventional polymers, it has been studied over a long period and its practical applications are well known. Reinforcing materials such as 'short-fiber' are often used for compounding with thermoplastic polymers in order to improve their mechanical or thermal properties. Polyamide (nylon) is a thermoplastic polymer, and glass fiber and carbon fiber are used mainly as reinforcing materials. A filler, typically micron-sized, is incorporated into composite materials to improve their properties. The polymer matrix and the fillers are bonded to each other by weak intermolecular forces, and chemical bonding is rarely involved. If the reinforcing material in the composite could be dispersed on a molecular scale (nanometer level) and interacted with the matrix by chemical bonding, then significant improvements in the mechanical properties of the material or unexpected new properties might be realized. These are the general goals of polymer nanocomposite studies. In order to achieve this purpose, clay minerals (montmorillonite, saponite, hectorite, etc.) have been discussed as candidates for the filler material. A layer of silicate clay mineral is about 1 nm in thickness and consists of platelets of around 100 nm in width, so it represents a filler with a significantly large aspect ratio. For comparison, a glass fiber 13 μm in diameter with a length of 0.3 mm is 4×10^9 times the size of a typical silicate layer. In other words, if the same volumes of glass fiber and silicate were evenly dispersed, there would be a roughly 10^9-fold excess of silicate layers, with an exponentially higher specific surface area available.

A nylon 6-clay hybrid (nanocomposite, NCH: Nylon 6-Clay Hybrid) was originally developed by Usuki and his colleagues and was the first polymer nanocomposite to be used practically. Since 1990 when it was first used, various studies and analyses have been reported. In this chapter, details of the NCH and other nylon-clay nanocomposites will be described.

1.2 Nylon 6-clay hybrid (NCH)

Nylon 6-clay hybrid (NCH) is synthesized by the 'monomer intercalation' method, in which clay is first ion-exchanged using an organic compound in order for the monomer to intercalate into the layers of the clay. The monomers that form the intercalated layer become a polymerized interlayer. The basic concept of the technique is as follows. Nylon 6 is produced by the ring-opening polymerization of ϵ-caprolactam. This can occur in the presence of clay, after ϵ-caprolactam intercalates into a clay gallery so that the silicate layers are dispersed uniformly in the nylon 6 matrix. Usuki and his colleagues found that organophilic clay that had been ion-exchanged with 12-aminododecanoic acid could be swollen by molten ϵ-caprolactam (the basal spacing expanded from 1.7 nm to 3.5 nm) (Usuki, 1993a). ϵ-caprolactam was then polymerized in the clay gallery and the silicate layers were dispersed in nylon 6 to yield a nylon 6-clay hybrid (NCH) (Usuki, 1993b). This is the first example of an industrial clay-based polymer nanocomposite. Figure 1.1 shows a schematic representation of the polymerization.

The modulus of NCH increased to 1.5 times that of nylon 6, the heat distortion temperature increased to 140ºC from 65ºC, and the gas barrier effect was doubled at a low loading (2 wt.%) of clay (Kojima, 1993a).

1.3 Synthesis of nylon 6-clay hybrid (NCH)

1.3.1 Clay organization and monomer swelling (Usuki, 1993a)

If montmorillonite containing sodium ions between its layers is dispersed in water, its silicate layers swell uniformly. If an alkylammonium salt is added to this aqueous mixture, the alkylammonium ions are exchanged with the sodium ions. As a result of this exchange reaction, an organophilic clay forms, in which the alkylammonium ions are intercalated between the layers. Because the silicate layers in the clay are negatively charged, they form ionic bonds with the

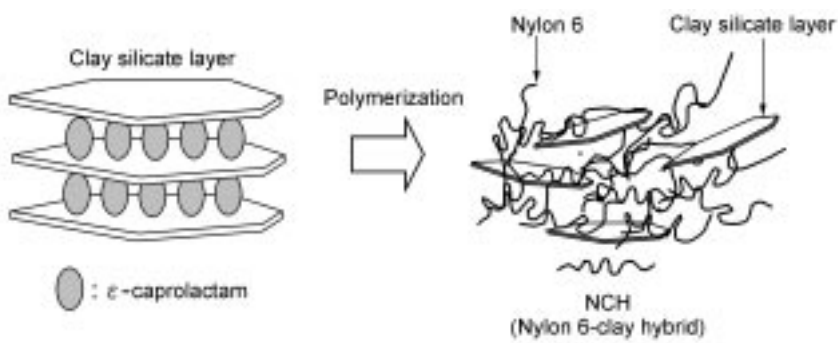

1.1 Schematic diagram of polymerization to NCH.

intercalated alkylammonium ions. By changing the length and type of alkyl chain, the hydrophilic/hydrophobic and other characteristics of this organophilic clay can be adjusted such that surface modification of the clay becomes possible.

A novel compounding technique was developed to synthesize nylon 6 in a clay gallery by modifying the clay surface and intercalating monomers into the gallery. The organophilic material used in this technique must satisfy the following three requirements:

1. It must have an ammonium ion at one end of the chain so that it can interact with clay through ionic bonding.
2. It must have a carboxylic acid group (–COOH) at the other end to react with ϵ-caprolactam, a nylon 6 monomer, for ring opening and polymerization.
3. It must possess intermediate polarity to enable ϵ-caprolactam to intercalate among silicate layers.

It was found that 12-aminododecanoic acid ($H_2N(CH_2)_{11}COOH$) met all of these requirements.

A representative method for making organophilic clay by using 12-aminododecanoic acid and the method of swelling organophilic clay by ϵ-caprolactam will now be described.

Using a homomixer, 300 g of montmorillonite were uniformly dispersed in 9 liters of deionized water at 80ºC. 154 g of 12-aminododecanoic acid and 72 g of concentrated hydrochloric acid were dissolved in 2 liters of deionized water at 80ºC. This solution was mixed with the montmorillonite dispersion and stirred for five minutes. The mixture was filtered to obtain aggregates, which were washed twice with water at 80ºC and freeze-dried. In this way, organophilic clay was obtained in the form of a fine white powder, called '12-Mt'.

12-Mt and ϵ-caprolactam in a weight ratio of 1:4 were mixed thoroughly in a mortar, and then dried and dehydrated for 12 hours in a vacuum desiccator containing phosphorous pentoxide. These specimens were left in a temperature-controlled bath at 100ºC for one hour to be swollen by ϵ-caprolactam. They were then subjected to X-ray diffraction measurements at 25ºC and 100ºC. It was found that two distinct spacings were present at the different temperatures: 3.15 nm (25ºC) and 3.87 nm (100ºC) and that the specimen processed at 100ºC had caprolactam molecules intercalated between the layers.

1.3.2 Synthesizing the nylon-clay nanocomposite (Usuki, 1993b)

A typical synthesis method of NCH containing 5 wt.% of 12-Mt is described below. Amounts of 509 g of ϵ-caprolactam, 29.7 g of 12-Mt (with about 300 g of water), and 66 g of 6-aminocaproic acid were put in a 3 liter separable flask with stirrers, and were degassed using nitrogen. These flasks were then immersed in

an oil bath and stirred at 250ºC with nitrogen gas flow for 6 hours to polymerize the ϵ-caprolactam. Water overflowed the flasks due to distillation halfway through this process. Polymerization was terminated when the load on the stirrers increased to a certain level.

After the flasks were cooled, aggregated polymers were removed from the flasks and pulverized. They were then washed with water at 80ºC three times to remove any monomers and oligomers that remained unreacted. Finally, the aggregates were dried for 12 hours at 80ºC in a vacuum to obtain NCH. In this chapter, the loadings of 12-Mt are expressed in wt.%, and NCHs with different loadings of 12-Mt are called NCH2, NCH5, NCH70 (and so on) for 2, 5 and 70 wt.%, respectively.

1.4 Characterization of NCH

Figure 1.2 shows various X-ray diffraction spectra. With NCH70 and NCH50, a clear peak showing the interlayer distance associated with the d (001) plane of montmorillonite was observed. With NCH30 and NCH15, however, the peak was weak and took the form of a shoulder. With NCH2, NCH5 and NCH8, no peak was observed in the measurement range. The inflection point of each shoulder-shaped feature was defined as the peak of d (001), in order to calculate the interlayer distance. These results are shown in Table 1.1.

Figure 1.3 shows the surfaces of press-molded NCH and NCC products. NCC was a composite material prepared by melting and kneading sodium-type montmorillonite (unorganized type) and nylon 6 using a twin-screw extruder at 250ºC for the purpose of comparing with NCH. The surface of the press-molded NCH product was smooth, whereas many millimeter-scale aggregates of clay minerals were seen on the surface of the press-molded NCC product. Furthermore, many bubbles were observed during the molding of the press-molded NCC product. This was thought to be an effect of water contained in the sodium-type montmorillonite.

Table 1.1 Basal spacing of NCHs

	Content of clay (wt.%)	Basal spacing from XRD
NCH2	1.5	—
NCH5	3.9	—
NCH8	6.8	—
NCH15	13.0	12.1
NCH30	26.2	6.0
NCH50	42.8	4.4
NCH70	59.6	2.6
12-Mt	78.7	1.7
Nylon 6	0	—

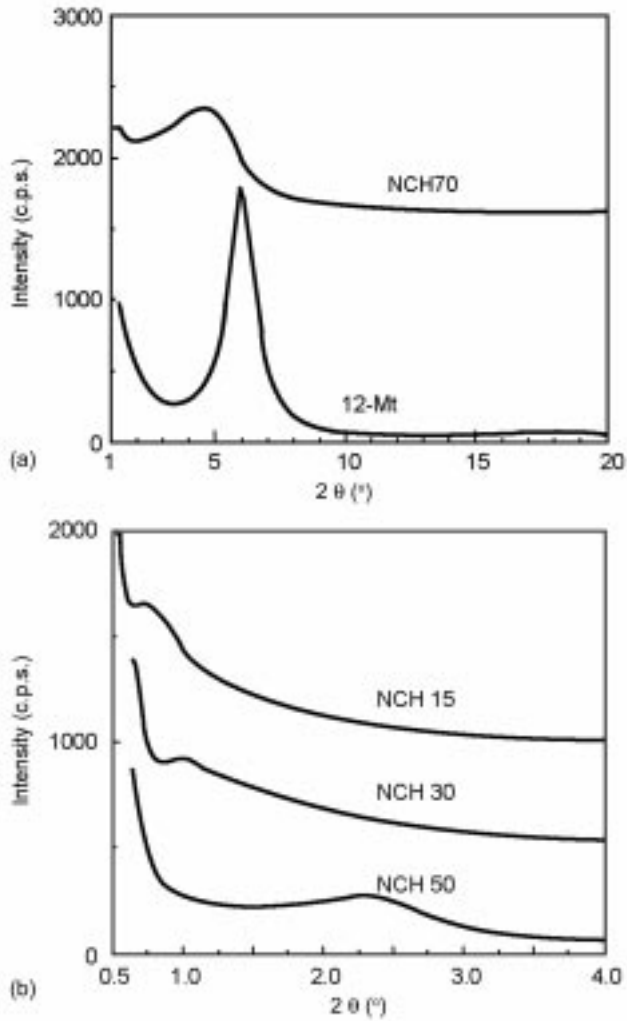

1.2 (a) X-ray diffraction patterns of NCH70 and 12-Mt, (b) X-ray diffraction patterns of NCH15, 30 and 50.

To observe the dispersed state of silicate layers in the NCH more closely, the press-molded NCH product was observed using a TEM at high magnification. The results of this observation are shown in Figure 1.4. As shown in this figure, the cross-sections of the silicate layers have a black, fibrous appearance, and the silicate layers are uniformly dispersed at a molecular level in the nylon 6 matrix. It was found that the interlayer distances in NCH15 and NCH30 measured by X-ray diffraction were nearly equal to those measured by TEM.

The relationship between the interlayer distance *ds* (d-spacing) in the silicate layers and the amount of 12-Mt in the NCH was analyzed as follows. If the ratio

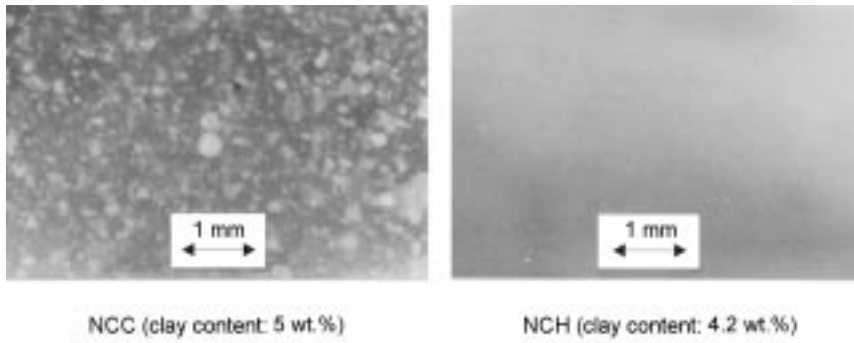

1.3 Surface appearances of NCC and NCH.

of the amount of nylon 6 to the amount of 12-Mt is designated R, then Equation (1.1) holds true:

$$R = \rho n \cdot (ds - t)/\rho c \cdot t \tag{1.1}$$

Here, R is nylon 6/12-Mt (g/g), ρn is the density of nylon 6 (1.14 g/cm^3), ρc is the density of 12-Mt (1.9 g/cm^3), and t is the interlayer distance of 12-Mt (1.72 nm). Substituting the appropriate numerical values in Equation (1.1), Usuki and his colleagues obtained:

$$ds = 2.87R + 1.72 \tag{1.2}$$

Figure 1.5 shows the ds values calculated using Equation (1.2), as well as actual measurements, which are slightly lower than the calculated values. These results show that the silicate layers are dispersed in nylon 6. The fact that the actual measurements differ from the calculated values indicates that nylon exists

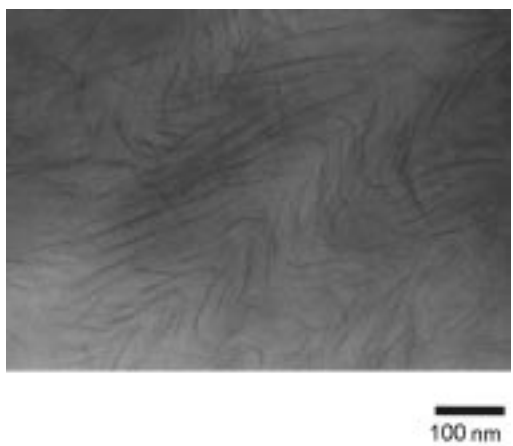

1.4 Transmission electron micrograph of section of NCH (NCH10).

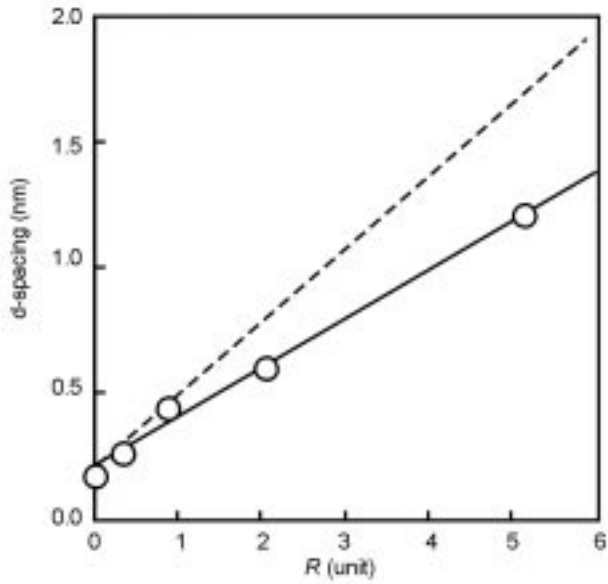

1.5 Relationship between ratio *R* of nylon 6/12-Mt and basal spacings (*ds*). Solid line: observed values, dotted line: calculated from Equation (1.2).

not only inside, but also outside the layers. The quantity *pi*, the ratio of the amount of nylon inside the layers to the total amount of nylon inside and outside the layers can be calculated using Equation (1.3):

$$pi = (d_0 - 1/ds - 1) \times 100 \tag{1.3}$$

In this equation, d_0 is the observed interlayer distance, *ds* is the interlayer distance calculated using Equation (1.2), and the thickness of a silicate layer is taken to be 1.

The *pi* value of NCH15 was 73.0% and that of NCH70 was 97.6%, i.e., the *pi* value increased as the amount of 12-Mt increased. These results show that 12-Mt initiated ϵ-caprolactam polymerization and that most of the nylon was polymerized between the 12-Mt layers.

Table 1.2 shows the results of measurements of the amount of montmorillonite and the amount of $-NH_2$ and –COOH terminal groups in each NCH. Figure 1.6 shows the amount of each terminal group plotted relative to the amount of montmorillonite. With increasing amounts of montmorillonite, the amount of carboxylic acid groups increased almost linearly, while the amount of amino groups remained almost unchanged. In addition, the amount of carboxylic acid groups far exceeded the amount of amino groups in each NCH. This is thought to be because some amino groups at the N-end of the nylon molecules combine with the silicate layers of the montmorillonite to form ammonium ions.

Table 1.2 End group analysis results for NCHs

	Content of clay (wt.%)	C_{NH_2}	C_{COOH}	Mn From C_{COOH} (10^3)
		From end group analysis (10^{-5}eq/g)		
NCH2	1.5	3.85	5.69	17.2
NCH5	3.9	4.86	9.49	10.0
NCH8	6.8	6.70	14.4	6.34
NCH15	13.0	8.04	22.9	3.80
NCH30	26.2	12.6	44.3	1.66
NCH50	42.8	12.1	70.6	0.81
NCH70	59.6	6.64	86.7	0.466
12-Mt	78.7	—	—	(0.216)[a]
Nylon 6	0	5.69	5.41	—

[a] Molecular weight of 12-aminododecanoic acid.

If the montmorillonite content is Wm (wt.%), the amount $C_{NH_3^+}$ (mol/g) of ammonium groups in NCH can be calculated based on the equivalence between the montmorillonite's cation exchange capacity (CEC) and the amount of ammonium groups, as shown in Equation (1.4):

$$C_{NH_3^+} = \mathrm{Wm} \times \mathrm{CEC}/100 \tag{1.4}$$

In this equation, CEC is 1.2×10^{-3} eq/g. The relationships between the amino, carboxylic acid and ammonium groups are defined based on the equivalence between the N- and C-ends of the nylon 6 molecules, as shown in Equation (1.5):

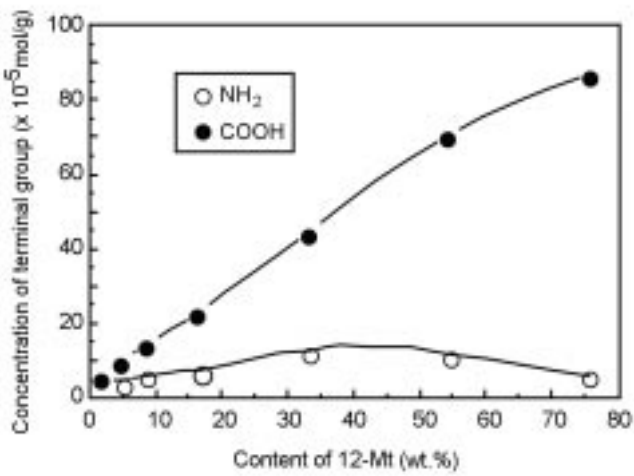

1.6 Relationship between 12-Mt content and end group concentration.

Table 1.3 Calculated number of anion sites of clay and observed values of C_{COOH}-C_{NH_2}

	$C_{NH_3}^+$	C_{COOH}-C_{NH_2} (10^{-5}eq/g)
NCH2	1.79	1.84
NCH5	4.64	4.60
NCH8	8.09	7.69
NCH15	15.5	14.9
NCH30	31.2	31.7
NCH50	50.9	58.5
NCH70	70.9	80.1

$$C_{NH_3^+} + C_{NH_2} = C_{COOH} \tag{1.5}$$

in which C_{NH_2} is the amount (mol/g) of amino groups and C_{COOH} is the amount (mol/g) of carboxylic acid groups. Therefore, Equation (1.6) can be formulated from Equations (1.4) and (1.5) as follows:

$$C_{NH_3^+} = C_{COOH} - C_{NH_2} = Wm \times (1.2 \times 10^{-5}) \tag{1.6}$$

Table 1.3 shows the values calculated using Equation (1.6) and the measured values ($C_{COOH} - C_{NH_2}$). As is apparent from this table, both values are in good agreement. This shows that the N-end of the nylon 6 turns into an ammonium group and that these ammonium ions combine with ions in the montmorillonite layers. The number average molecular weight (Mn) of the nylon 6 is expressed as the inverse of the mole number per gram of nylon 6. The number average molecular weight Mn of nylon 6 in NCH can be calculated based on the amount, C_{COOH}, of carboxylic acid end groups and the montmorillonite content Wm, as shown in Equation (1.7):

$$Mn = 1/\{C_{COOH}[100/(100 - Wm)]\} \tag{1.7}$$

Table 1.2 shows the results of calculations made using this equation.

The molecular weight decreased as the amount of 12-Mt increased. Assuming that the carboxylic acid groups in 12-Mt are the only active sites and that the polymerization reaction progresses without side reactions, the molecular weight Mn can be expressed by Equation (1.8):

$$Mn - 216 = (1/Cm) \times ((1 - f)/f) \times p \tag{1.8}$$

in which Cm is the amount of carboxyl groups in 12-Mt (9.6×10^{-4} mol/g), f is the weight percent of injected 12-Mt, p is the caprolactam conversion rate (%), and 216 is the molecular weight of 12-aminododecanoic acid in g/mol.

Because $(1 - f) \cdot p/f = R$, Equation (1.8) can also be expressed as:

$$Mn = (1.04 \times 10^3) \times R + 216 \tag{1.9}$$

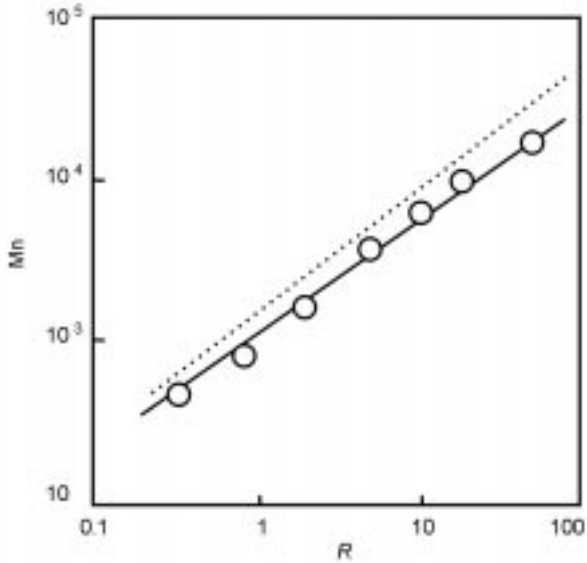

1.7 Relationship between ratio *R* of nylon 6/12-Mt and molecular weight (Mn). Solid line: observed values, dotted line: calculated from Equation (1.9).

Mn values calculated using Equation (1.9) and measured Mn values are shown in Fig. 1.7.

The slope of the line for the measured Mn values is smaller than that of the calculated values. This means that there were active sites (e.g., a small amount of water) other than the carboxylic acid end groups present in the 12-Mt during polymerization.

1.5 Crystal structure of NCH (Kojima, 1995)

1.5.1 Test specimens for crystal structure analysis

The surfaces of NCH and nylon 6 test specimens (thickness: 3 mm each) were scraped around the center to a depth of 0.5 mm. The surfaces of other NCH and nylon 6 test specimens were scraped to a depth of 1 mm. X-ray diffraction photographs of these test specimens were taken using Laue cameras. Specifically, the surfaces and insides of these test specimens were subjected to X-ray diffraction photography in the 'through,' 'edge' and 'end' directions, and the orientations of the crystals were examined.

The X-ray diffraction intensity of these test specimens was also measured in the reflection mode. By scraping their surfaces to specified depths, their X-ray diffraction spectra were measured at each thickness. This process of scraping and spectrum measurement was repeated to obtain X-ray diffraction spectra at each different thickness.

1.5.2 Alignment of silicate layers in NCH

Figure 1.8 shows X-ray diffraction photographs of the surface and the inside of NCH. Figure 1.9 shows X-ray diffraction photographs of nylon 6. 'Through' labels a diffraction photograph taken by introducing the X-rays perpendicular to the molded surface. 'Edge' represents a diffraction photograph taken by introducing the X-rays parallel with the molded surface and perpendicular to the direction of flow on the molded surface. 'End' marks a diffraction photograph taken by introducing the X-rays in the direction of flow on the molded surface. These directions are illustrated in Figs 1.8 and 1.9. In these figures, x and y represent the directions perpendicular and parallel to the surface of the test specimen; y and z represent the directions perpendicular and parallel to the flow of resin.

In the 'end' and 'edge' patterns on the surface of the NCH and inside the NCH, a pair of clear streak diffractions was observed in the horizontal direction (x-direction), showing that the silicate layers were aligned parallel to the molded surface. On the surface of the NCH and inside the NCH, the inside streak of the 'end' pattern became a little wider toward the azimuthal angle. This showed that the alignment of the silicate layers was less orderly inside the NCH than on the surface.

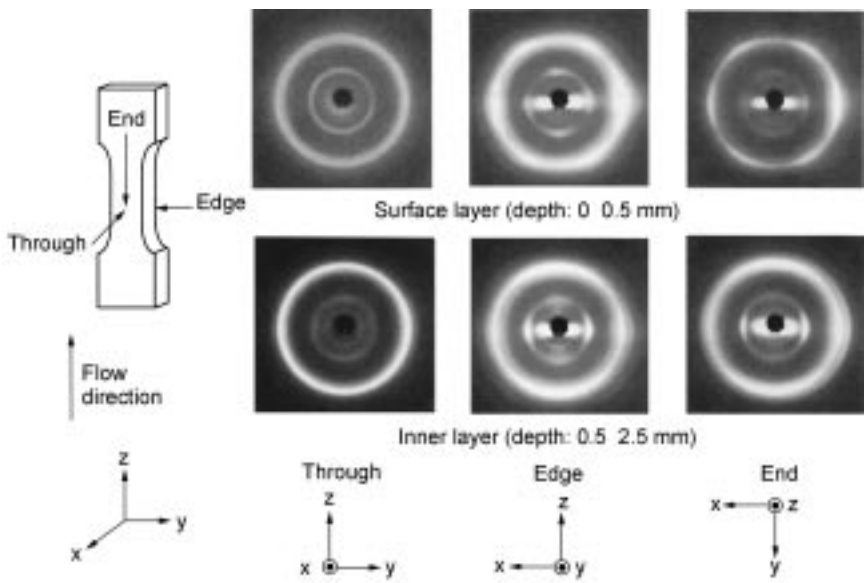

1.8 X-ray diffraction photographs for the surface and interior of an injection-molded NCH bar 3 mm thick. Surface and inner layers correspond to the regions 0–0.5 and 0.5–2.5 mm in depth from the bar surface, respectively. The diffraction photographs are termed through, edge, and end-view patterns when the X-ray beam was incident on the NCH bar along the x-, y-, and z-axes, respectively. These are also defined in the figure.

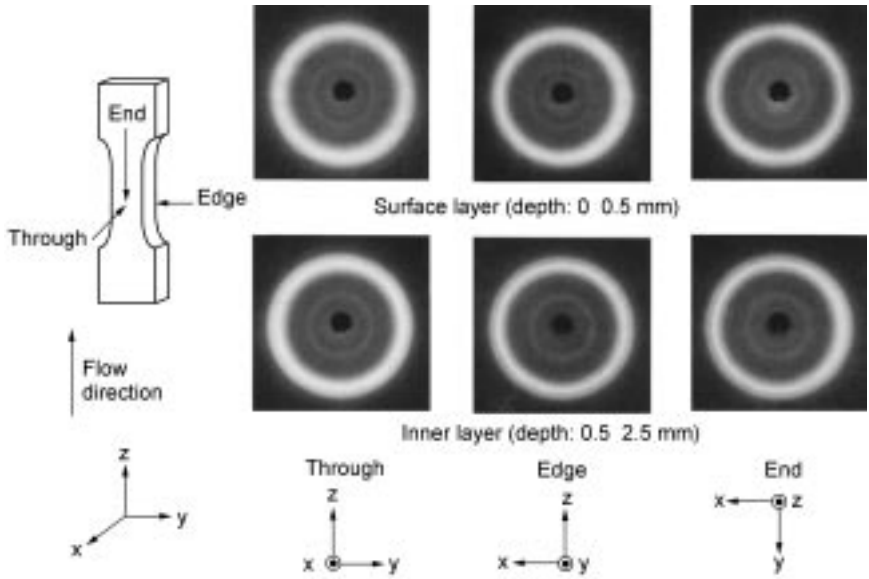

1.9 X-ray diffraction photographs for the surface and interior of an injection-molded nylon 6 bar 3 mm thick. For photography conditions see the legend of Fig. 1.8.

X-ray scattering measurements were made along the x-direction of the 'edge' pattern in the surface layers. The diffraction spectrum obtained from this measurement is shown in Fig. 1.10. The strong scattering peak ($2\theta = 25^{\circ}$) is thought to be associated with the superposition of the γ-type planes (020 and 110) of nylon 6. On the other hand, the curve that appears between $2\theta = 4^{\circ}$ and 10° is thought to be associated with the clearly-visible streak originating from the silicate layers of the montmorillonite. The intense clearly-visible streak in the center of Fig. 1.8 is at $2\theta = 10^{\circ}$, which is at almost the same level as the background. The angle 2θ can be explained based on the hypothesis that the 1 nm silicate layers are aligned parallel with the surface of the molded specimen.

The intensity function $I(q)$ of thin layers (thickness: d) is proportional to their number and projected area in cross-section:

$$I(q) = Nn_e^2[\sin(qd/2)/(qd/2)] \tag{1.10}$$

where q is $4\pi \sin\theta/\lambda$, λ is the X-ray wavelength, N is the number of silicate layers aligned in parallel with the surface of the test specimen in the volume irradiated by the X-ray, and n_e is the number of electrons in the silicate layers.

In Equation (1.10), the scattering intensity is 0, which is calculated by $q = 2\pi/d$. When this scattering intensity corresponds to the critical value, 2θ, we have the following:

$$\theta = \arcsin(\lambda/2d) \tag{1.11}$$

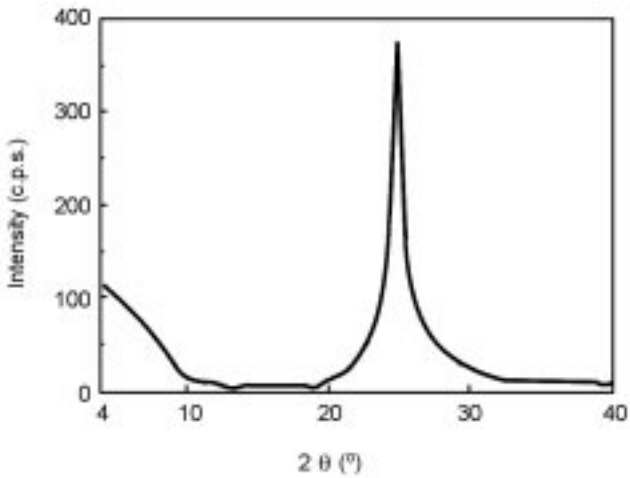

1.10 X-ray diffraction intensity curve along the x-direction for the edge-view patterns of the surface layers in Fig. 1.8.

Substituting 0.1790 nm for λ and 1 nm for d in Equation (1.11), we have $2\theta = 10.3^{\circ}$, which is approximately consistent with the results of this experiment. This shows that silicate layers 1 nm in thickness (single layers) are dispersed.

Equation (1.10) seems to indicate that the streak intensity is proportional to the amount of silicate layers that exist in parallel with the surface of a test specimen. Fig. 1.11 shows the relationship between the intensity $I(4^{\circ})$ at $2\theta = 4^{\circ}$ and the depth from the surface of the NCH test specimen.

The intensity $I(4^{\circ})$ decreases linearly with increasing depth. However, it becomes almost constant between 0.8 mm and 1.2 mm, after which it starts decreasing again. This means that the amount of silicate layers parallel to the surface of a molded specimen decreases continuously in the depth direction. That is, the fluctuations in the alignment of silicate layers in the direction of resin flow increase as the depth increases. It is estimated from the inside 'end' pattern shown in Figure 1.8 that the maximum intensity of this fluctuation is $\pm 15^{\circ}$.

The decreased scattering intensity around the center of molded specimens is thought to be due to disturbances in the alignment caused by silicate layers that are uniaxially aligned along the flow direction.

1.5.3 Alignment of nylon 6 crystals

The other reflection patterns (except for the reflections off the silicate layers) shown in the diffraction photographs in Fig. 1.8 are related directly to γ-type crystals of nylon 6. There have been some previous reports concerning the γ-

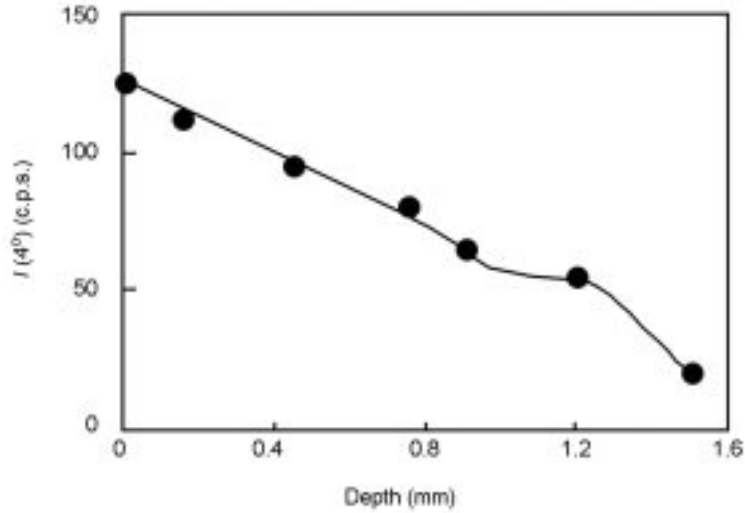

1.11 Scattering intensity, $I(4^{\circ})$, of the streak due to the silicate monolayers parallel to the bar surface at a scattering angle of 4° as a function of depth from the bar surface. The streak is in the x-direction of the edge-view pattern in Fig. 1.8.

type crystal structure of nylon 6, for which Bradbury has determined a set of lattice constants (Bradbury, 1965). Using these lattice constants, unit lattices can be determined correctly with high reliability.

In this study, the following lattice constants were used: a = 0.482 nm, b = 0.782 nm, and c = 1.67 nm (the molecular chain axis is the c-axis). Although these constants are basically for monoclinic systems, they allow for orthorhombic approximation. In Fig. 1.8, arcuate reflections are observed in the 'edge' and 'end' patterns, while a Debye-Scherrer ring is observed in the 'through' pattern. This shows that nylon 6 crystals are aligned to the surface layers of the molded NCH specimen in the inside layers. It is found from the diffraction patterns of the surface layers that nylon 6 crystals are uniaxially aligned in planes, that the hydrogen-bonding surface (020) or the zigzag plane (110) of the carbon skeleton is aligned parallel with the surface, and that the molecular chain axes exist randomly on the surface. On the other hand, the diffraction patterns of the internal layers were different: the pattern in the 'edge' direction differed from that in the 'end' direction. This could be explained by considering that the molecular chain of the nylon 6 was uniaxially aligned to the crystals that were perpendicular to the surface of a molded test specimen or the silicate layers. The following facts support this explanation:

- (002) reflections of $2\theta = 12.3^{\circ}$ were observed in the x-direction.
- (020) and (110) double reflections of $2\theta = 25^{\circ}$ were observed in the z-direction in both 'edge' and 'end' patterns.

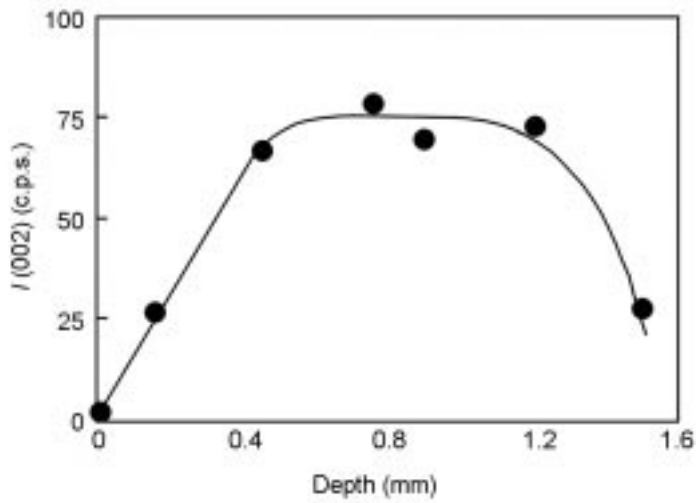

1.12 Peak intensity, *I*(002), of the 002 reflection of γ-nylon 6 as a function of depth from the NCH bar surface when the X-ray beam was incident in the y-direction and the scattering intensity in the x-direction was scanned.

- (020) and (110) double Debye-Scherrer rings and strong (002) reflections were not observed in the 'through' pattern.

Changes in the alignment of nylon 6 crystals were examined relative to their depth from the surface of a molded test specimen. Figure 1.12 shows how the intensity of the (002) reflections changed relative to the depth from the surface of a molded test specimen. The scattering intensity in the x-direction was measured by introducing the X-ray beam in the y-direction. As the depth increased, the intensity increased dramatically. It stopped increasing at 0.5 mm, and remained constant until the depth reached 1.2 mm. After the depth exceeded 1.2 mm, the intensity suddenly dropped around the center of the molded specimen. The change in intensity at 1.2 mm depth was approximately consistent with the observations in the X-ray diffraction photographs of Fig. 1.8. The molecular chain axes of the crystals near the surface of the molded specimen were parallel to the surface. Although they were aligned randomly inside the plane, they changed their orientation toward the direction perpendicular to the surface as the depth increased. Around a depth of 0.5 mm, they were aligned almost perpendicularly. The sudden decrease in the (002) reflections around the center plane was attributed to the uniaxial alignment of the silicate layers along the flow axis of the resin. Around the center plane of the specimen, the silicate layers were parallel to the flow axis. The molecular chain axes of the nylon 6 crystals that were aligned perpendicular to the silicate layers were aligned randomly around the flow axis, causing the intensity of the (002) reflections to decrease.

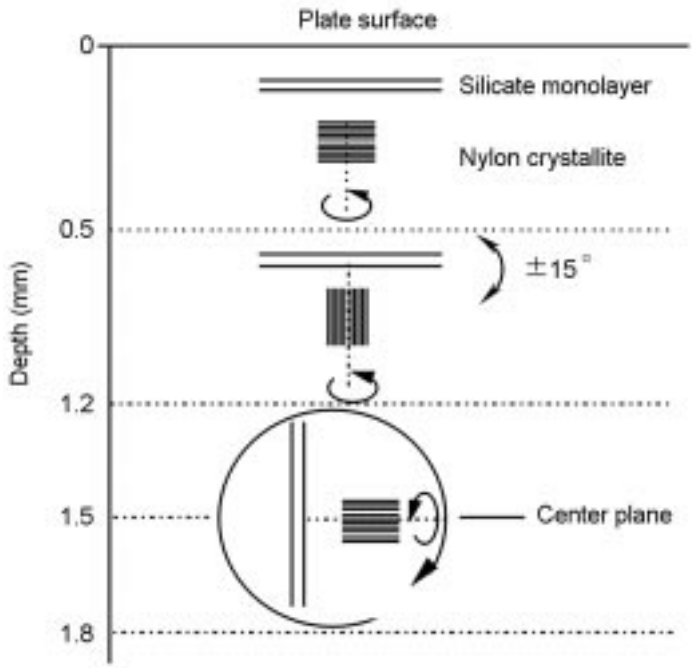

1.13 End-view diagram of the triple-layer structure model for an injection-molded NCH bar 3 mm thick. The flow direction during injection-molding is normal to the plane of the page. Curved arrows with one head indicate random orientation around the axis normal to the plane containing the curve. Arrows with two heads indicate fluctuation.

The above results show that NCH consists of three layers: a surface layer, an intermediate layer, and a central layer. Figure 1.13 shows a schematic representation of this three-layer structure model. In the surface layer, which is located from zero depth (surface) to a depth of 0.5 mm, silicate layers were aligned parallel to the surface, and nylon 6 crystals were uniaxially-aligned along the plane. For example, the (020) or (110) lattice plane was parallel to the plane. On the other hand, the molecular chain axes were aligned randomly inside the plane. In the intermediate layer, from a depth of 0.5 mm to a depth of 1.2 mm, the silicate layers were slightly displaced from the direction parallel to the surface. This displacement was within $\pm 15^{\circ}$, which was considered rather large. Nylon 6 crystals were rotated 90º, and aligned almost perpendicular to the surface or the silicate layers. They were aligned randomly around the vertical plane that was perpendicular to the silicate layers. In the center layer, from a depth of 1.2 mm to a depth of 1.8 mm, silicate layers existed parallel to the flow-axis of the resin. Although the nylon 6 crystals were aligned randomly around the flow axis, the molecular chain axes of each crystal were aligned perpendicular to the silicate layers.

1.6 Properties of NCH (Kojima, 1993a)

1.6.1 Mechanical properties

Table 1.4 shows the mechanical properties of NCH along with those of nylon 6 (1013B, molecular weight: 13,000, Ube Industries, Ltd.) for comparison. As is apparent from Table 1.4, NCH is superior to nylon 6 in terms of strength and elastic modulus. In the case of NCH5 in particular, the tensile strength at 23ºC is 1.5 times higher than that of nylon 6, the flexural strength at 120ºC is twice that of nylon 6, and the flexural modulus at 120ºC is about four times as large as that of nylon 6. However, its impact strength was below that of nylon 6.

The heat distortion temperature of NCH5 increased to 152ºC, i.e., its heat resistance also improved relative to nylon 6. Fig. 1.14 shows heat distortion temperatures versus clay content in wt.%. This figure indicates that the heat distortion temperature is almost at a maximum in NCH5.

The characteristics of the dependency of injection-molded NCH products on layer thickness have been investigated and reported (Uribe-Arocha, 2003). An investigation of 0.5, 0.75, 1.0 and 2.0 mm-thick test specimens revealed that the thicker the product, the lower was the elastic modulus under tension.

1.6.2 Gas barrier characteristics of NCH

Table 1.5 shows a comparison between the gas barrier characteristics of NCH (with 0.74 vol.% of montmorillonite) and those of nylon 6. The hydrogen permeability and water vapor permeability coefficients of NCH containing only 0.74 vol.% of montmorillonite were less than 70% of the corresponding

Table 1.4 Properties of NCH and nylon 6

Properties		Unit	NCH2	NCH5	NCH8	Nylon 6
Tensile strength	23ºC	MPa	76.4	97.2	93.6	68.6
	120ºC		29.7	32.3	31.4	26.6
Elongation	23ºC	%	>100	7.30	2.5	>100
	120ºC		>100	>100	51.6	>100
Tensile modulus	23ºC	GPa	1.43	1.87	2.11	1.11
	120ºC		0.32	0.61	0.72	0.19
Flexural strength	23ºC	MPa	107	143	122	89.3
	120ºC		23.8	32.7	37.4	12.5
Flexural modulus	23ºC	GPa	2.99	4.34	5.32	1.94
	120ºC		0.75	1.16	1.87	0.29
Charpy impact strength (without notch)		kJ/m^2	102	52.5	16.8	>150
Heat distortion temperature		ºC	118	152	153	65

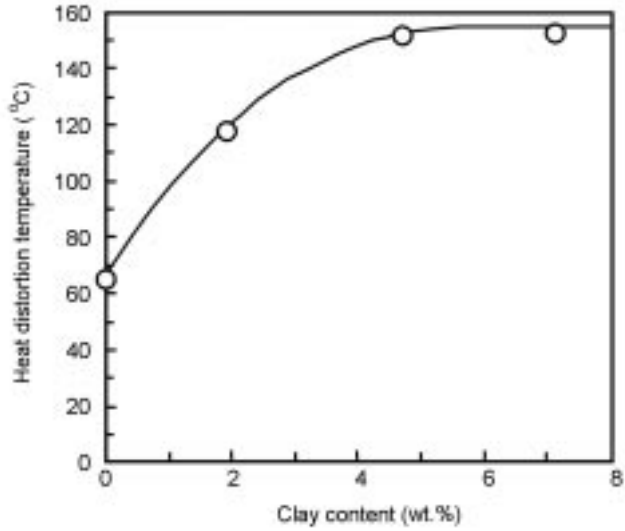

1.14 Dependence of heat distortion temperature on clay content.

coefficients for nylon 6, indicating that NCH had superior gas barrier characteristics.

This gas barrier effect of NCH can be explained by postulating that the added fillers caused the diffusion paths of the gases to meander, forcing the gases to follow complicated, tortuous paths through the material, and hence decreasing the diffusion efficiency.

For gases traveling through NCH, the permeability coefficient of the gas can be analyzed using a geometrical model for dispersed silicate layers. In NCH, the silicate layers are aligned nearly parallel with the film surface. According to Nielsen, the diffusion coefficient D of a liquid or a gas can be calculated using Equation (1.12) if the liquid or gas is in a composite material in which plate particles are in a planar orientation:

$$D = D_0/\{1 + (L/2d)V\} \tag{1.12}$$

Table 1.5 Permeability of NCH and nylon 6

	NCH*	Nylon 6
Permeability of hydrogen $\times 10^{-11}/\text{cm}^3 \cdot (\text{STP}) \cdot \text{cm} \cdot \text{cm}^{-2} \cdot \text{s}^{-1} \cdot \text{cm Hg}^{-1}$	1.79	2.57
Permeability of water vapor $\times 10^{-10}/\text{g} \cdot \text{cm}^{-2} \cdot \text{s}^{-1} \cdot \text{cmHg}^{-1}$	1.78	2.83

* montmorillonite = 0.74 vol.%

where D_0 is the diffusion coefficient in a matrix, L is the size of one side of a plate particle, d is the particle thickness, and V is the volume fraction of particles. Given that L is 100 nm, d is 1 nm, and V is 0.0074, we obtain $D/D_0 = 0.73$. This value is close to the experimental value obtained for hydrogen (0.70), and for water (0.63). This shows that the gas barrier characteristics of NCH should be interpreted as being due to the geometrical detour effect of the silica layers of the montmorillonite.

1.6.3 Flame retardancy (Gilman, 2000; Kashiwagi, 2004)

It is reported that the nylon 6 clay nanocomposite has flame-retardant properties, thought to be due to the formation of a heat-protective layer on the surface of this composite. The analysis of this protective layer revealed that it contained an organophilic layer consisting of about 80% clay and 20% graphite.

1.6.4 Self-passivation (Fong, 2001)

If the nylon 6 clay nanocomposite is processed in an oxygen plasma, a uniform passivation film is formed. It was found that as the polymers were oxidized, highly oblique composites formed, in which the clay concentration increased toward the surface, and that the clay layers in these composites protected the polymer. This indicates that the uniform passivation film may prevent deterioration of the polymers.

1.7 Synthesizing NCH using different types of clay (Usuki, 1995)

Different types of clay other than montmorillonite (e.g., synthetic mica, saponite and hectorite) were used to synthesize nylon 6-clay hybrids. The nanocomposites fabricated by using each of these types of clay were called NCHM, NCHP, and NCHH, respectively.

Silicate layers were uniformly dispersed in NCHM, NCHP, and NCHH at the molecular level, as in NCH. The thickness of the silicate layers was 1 nm in all these nanocomposites, but their widths varied depending on the type of clay used. TEM examination of these materials revealed that the width of silicate layers in the nanocomposites fabricated using montmorillonite and synthetic mica were about 100 nm, and that those in the nanocomposites fabricated using saponite and hectorite were about 50 nm.

Table 1.6 shows the mechanical properties of various nanocomposites. The tensile strengths of nanocomposites at 23ºC and 120ºC decreased in the following order: NCH (montmorillonite) > NCHM (synthetic mica) > NCHP (saponite) $\geq$ NCHH (hectorite). The heat distortion temperatures of the nanocomposites also decreased in the same order: NCH > NCHM > NCHP > NCHH.

Table 1.6 Properties of NCH synthesized using 5 wt.% organic clay

Properties		NCH	NCHM	NCHP	NCHH	Nylon 6
Clay		Montmorillonite	Mica	Saponite	Hectorite	None
Tensile strength	23°C	97.2	93.1	84.7	89.5	68.6
(MPa)	120°C	32.3	30.2	29.0	26.4	26.6
Elongation	23°C	7.3	7.2	>100	>100	>100
(%)						
Tensile modulus	23°C	1.87	2.02	1.59	1.65	1.11
(GPa)	120°C	0.61	0.52	0.29	0.29	0.19
Heat distortion temperature (°C)		152	145	107	93	65
Heat of fusion (J/g)		61.1	57.2	51.5	48.4	70.9
Heat of fusion (J/nylon 6 1 g)		63.6	59.6	53.4	50.4	70.9

To study the differences between the mechanical properties of these nanocomposites, the interface affinity between clay and nylon 6 was analyzed by measuring the NMR of nitrogen at the chain end in nylon 6. Because the concentration of chain-end nitrogens in nylon 6 is extremely low, glycine (H_2NCH_2COOH) and hexamethylene diamine ($H_2N(CH_2)_6NH_2$) were used as model compounds.

Table 1.7 shows the ^{15}N chemical shifts of glycine-organized clays and hexamethylene diamine (HMDA). Because glycine contains ampholyte ions in the neutral state, the chemical shift values of HMDA were used for neutral N.

The ^{15}N chemical shifts of four types of glycine-organized clays were found to lie midway between those of the highly polar glycine hydrochloride (15.6 ppm) and of neutral HMDA (7.0 ppm).

As the chemical shift moves toward lower fields, the electron density decreases, i.e., nitrogen is more positively polarized (δ^+). It is thought that if δ^+ of nitrogen is large, stronger ionic bonding with the negative charge of the silicate layers of the clay can be realized. Nitrogen in montmorillonite (of the

Table 1.7 ^{15}N-NMR chemical shift of model compounds

Compounds	Chemical shift* (ppm)		
$Cl^-NH_3^+CH_2COOH$	15.6	ionized	large
Montmorillonite-$NH_3^+CH_2COOH$	11.2	partially ionized	δ^+ nitrogen atom
Mica-$NH_3^+CH_2COOH$	9.4		
Saponite-$NH_3^+CH_2COOH$	8.4		
Hectorite-$NH_3^+CH_2COOH$	8.3		
HMDA	7.0	neutral	small

*ppm relative to $^{15}NH_4NO_3$

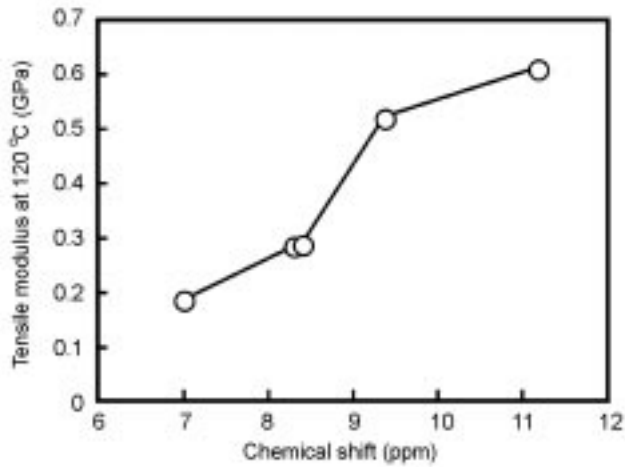

1.15 Relation between ^{15}N-NMR chemical shift of model compounds and tensile modulus at 120ºC of nylon 6-clay nanocomposites.

four types of clay) had the largest δ^+, corresponding to a chemical shift of 11.2 ppm. In the remaining clays, δ^+ decreased in the order: synthetic mica > saponite $\geq$ hectorite.

It was inferred from the foregoing results that of all types of clay, montmorillonite bonded most strongly with nylon 6 and that the bond strength decreased in the order: synthetic mica > saponite $\geq$ hectorite. Figure 1.15 shows the chemical shift of ^{15}N-NMR as an indicator of bond strength versus the flexural modulus at 120ºC as the central characteristic value. As is apparent from this figure, the chemical shift and the flexural modulus are closely correlated.

1.8 Improving the synthesis method of NCH

1.8.1 One-pot synthesis of NCH (Kojima, 1993b)

A 'one-pot' polymerization method has been proposed. Mixing montmorillonite, caprolactam and phosphoric acid simultaneously in a glass receptacle and initiating polymerization can produce NCH quite readily. The dispersion of the clay minerals and the mechanical properties of specimens produced in this way were the same as those of specimens made by the polymerization method described earlier. Successful synthesis of NCH by the one-pot technique indicates that process times can be shortened.

1.8.2 Melt compounding method (Liu, 1999; Cho, 2001)

Besides the polymerization method, a method of directly mixing nylon polymers and organophilic clay using a twin-screw extruder was developed. Although clay

minerals were not dispersed sufficiently using a single-screw extruder (screw speed: 40 rpm, barrel temperature: 240ºC), they could be well dispersed using a twin-screw extruder (screw speed: 180 rpm, barrel temperature: 240ºC). Experimental results and mechanical characteristics have been reported by Toyota CRDL, Allied Signal and the Chinese Academy of Sciences.

1.8.3 Master batch method (Fornes, 2001; Shah, 2004)

To produce composite materials on a commercial basis, the master batch method of diluting materials and mixing them in specified proportions is widely used. A case is known in which this method was used to prepare nylon-clay nanocomposites. When high molecular weight grades (Mn = 29,300) of nylon 6 were used, the level of exfoliation of clay was higher than when low molecular weight grades (Mn = 16,400) were used. Using this technical knowledge, nylon 6 of high molecular weight was mixed with 20.0, 14.0 and 8.25%, respectively, of clay to prepare the master batches. Each master batch of nylon 6 mixed with clay was diluted using nylon 6 of low molecular weight. The mechanical properties of the nylon 6-clay nanocomposites prepared in this way were found to be almost the same as those of nanocomposites produced using the melt compounding method from nylon 6 of high molecular weight by the addition of 6.5, 4.0 and 2.0%, respectively, of clay.

1.8.4 Wet compounding method (Hasegawa, 2003)

The process of organizing clay using ammonium ions has a considerable impact on production cost. In order to omit this expensive process, silicate layers of clay (sodium-type montmorillonite) were uniformly dispersed in a water slurry and mixed with a molten resin. This method is shown schematically in Fig. 1.16. The clay slurry was injected into a twin-screw extruder by a pump, and water was removed under reduced pressure. In this process, a nylon nanocomposite with uniformly dispersed silicate layers was fabricated successfully. This method simplified the clay organization process, allowing nanocomposites to be obtained at low cost. Table 1.8 shows the mechanical properties of this nanocomposite. The heat distortion temperature was somewhat lowered because the bonding between clay and nylon was not ionic bonding.

1.9 Other types of nylon

After it was verified that nylon 6 could be mixed with clay to make nanocomposites with dramatically improved performance characteristics, the same synthesis techniques were applied to other types of nylon resins.

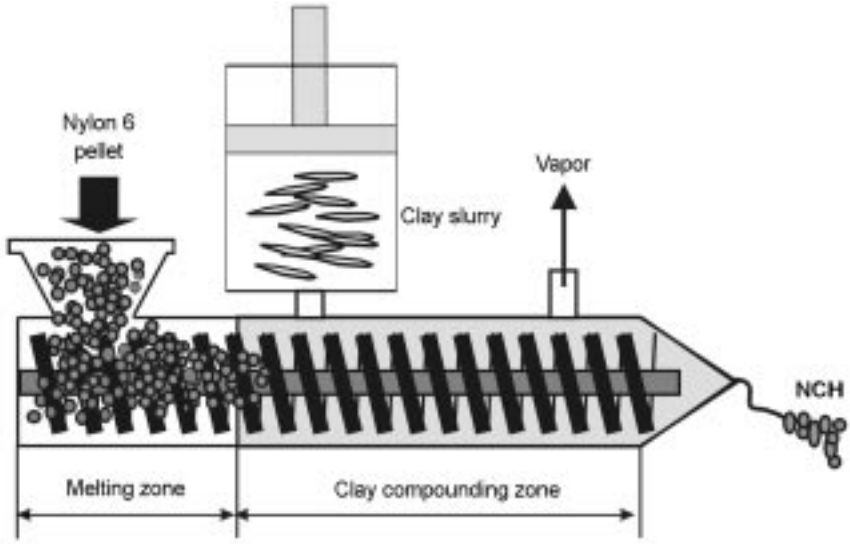

1.16 Schematic depicting the compounding process for preparing nanocomposites using a clay slurry.

1.9.1 Nylon 6,6 (Liu, 2002)

A nylon 6,6-clay nanocomposite was produced using the melt compounding method. Co-intercalated organophilic clay was used as the clay base. Na-montmorillonite was first processed using hexadecyl trimethyl ammonium ions and epoxy resin, then kneaded using a twin-screw extruder to make a clay nanocomposite. The amount of γ phases increased with increasing clay content. This was thought to be due to the strong interactions between the nylon 6,6 chains and the surface of the clay layers.

Table 1.8 Properties of NCH

Specimen	Clay content (%)	Tensile strength (MPa)	Tensile modulus (GPa)	Heat distortion temperature (°C at 18.5 kg/cm)
Nylon 6	0	69	1.1	75
Synthesized NCH	1.9	76	1.43	118
Melt compounding NCH	1.8	82	1.41	135
Clay slurry compounding NCH	1.6	82	1.38	102

1.9.2 Nylon 10,12 (Wu, 2002)

1,10-diaminodecane and 1,10-decanedicarboxylic acid were polycondensed in the presence of an organophilic clay to form a nylon 10,12-clay nanocomposite. X-ray diffraction and TEM observations revealed that the clay layers were exfoliated and uniformly dispersed in nylon 10,12. The speed of crystallization of the nanocomposite was higher than that of nylon 10,12. Furthermore, the tensile strength and the elastic modulus in tension were improved, and the amount of absorbed water was decreased through improvement of the nanocomposite's barrier characteristics.

1.9.3 Nylon 11 (Liu, 2003)

A nylon 11-clay nanocomposite was prepared using the melt compounding method. X-ray diffraction and TEM observations showed that this technique formed an exfoliated nanocomposite at low concentrations of clay (less than 4 wt.%) and that a nanocomposite with both exfoliated and intercalated clay layers was formed at high clay concentrations. TGA, DMA and tensile tests showed that the thermal stability and mechanical properties of the exfoliated nanocomposite were superior to those of the intercalated nanocomposite material (with higher clay content). The superior thermal stability and mechanical properties of the exfoliated nanocomposite were attributed to the organophilic clay being dispersed stably and densely in the nylon 11 matrix.

1.9.4 Nylon 12 (Kim, 2001)

12-aminododecanoic acid (ADA) was polycondensed in the presence of a clay organized with ADA to form a nylon 12-clay nanocomposite.

1.10 Conclusions

A variety of polyamide (nylon) nanocomposites have been developed and many of these now have practical applications. Nylon-clay nanocomposite materials containing small amounts of clay minerals exhibit high performance and robust gas barrier properties and have attracted attention worldwide from major chemical manufacturing companies in this field. There are a number of expected applications:

- resin materials for molding; in particular, automotive components that require enhanced hardness characteristics
- use in thin-film materials; especially, food-packing films
- use in rubber materials that require barrier performance; particularly, hoses for automotive use

- use in resin components for domestic electrical appliances that require flame resistance.

1.11 Future trends

1. Clay (nanoscale clay) can be used for the reinforcement of various resin materials and can replace glass fiber reinforcement materials.
2. The reinforcement mechanism has yet to be clarified, and therefore, industry/government-academia collaborations will help create new materials.

1.12 References

Bradbury E M (1965), 'The structure of the gamma form of polycaproamide (nylon 6)' *Polymer* 6: 465–482.

Cho J W (2001), 'Nylon 6 nanocomposites by melt compounding', *Polymer* 42: 1083–1094.

Fong H (2001), 'Self-passivation of polymer-layered silicate nanocomposites', *Chem. Mater*. 13: 4123–4129.

Fornes T D (2001), 'Nylon 6 nanocomposites: the effect of matrix molecular weight', *Polymer* 42: 9929–9940.

Gilman J W (2000), 'Flammability properties of polymer – Layered-silicate nanocomposites. Polypropylene and polystyrene nanocomposites', *Chem. Mater*. 12 (7): 1866–1873.

Hasegawa N (2003), 'Nylon 6/Na–montmorillonite nanocomposites prepared by compounding Nylon 6 with Na–montmorillonite slurry', *Polymer* 44: 2933–2937.

Kashiwagi T (2004), 'Flame retardant mechanism of polyamide 6-clay nanocomposites', *Polymer* 45: 881–891.

Kim G M (2001), 'Influence of nanofillers on the deformation process in layered silicate/polyamide-12 nanocomposites', *Polymer* 42: 1095–1100.

Kojima Y (1993a), 'Mechanical-properties of nylon 6-clay hybrid' , *J. Mater. Res*. 8: 1185–1189.

Kojima Y (1993b), 'One-pot synthesis of nylon-6 clay hybrid', *J. Polym. Sci. A Polym. Chem*. 31: 1755–1758.

Kojima Y (1995), 'Novel preferred orientation in injection-molded nylon 6-clay hybrid', *J Polym. Sci. B Polym. Phys*. 33: 1039–1045.

Liu L (1999), 'Studies on nylon 6 clay nanocomposites by melt-intercalation process', *J. Appl. Polym. Sci*. 71: 1133–1138.

Liu T (2003), 'Preparation and characterization of nylon 11/organoclay nanocomposites', *Polymer* 44: 3529–3535.

Liu X (2002), 'Polymorphism in polyamide 66/clay nanocomposites', *Polymer* 43: 4967–4972.

Shah R K (2004), 'Nylon 6 nanocomposites prepared by a melt mixing masterbatch process', *Polymer* 45: 2991–3000.

Uribe-Arocha P (2003), 'Effect of sample thickness on the mechanical properties of injection-molded polyamide-6 and polyamide-6 clay nanocomposites', *Polymer* 44: 2441–2446.

Usuki A (1993a), 'Swelling behavior of montmorillonite cation exchanged for ω-amino acids by ϵ-caprolactam', *J. Mat. Res*. 8: 1174–1178.

Usuki A (1993b), 'Synthesis of nylon 6-clay hybrid', *J. Mat. Res*. 8: 1179–1184.

Usuki A (1995), 'Interaction of nylon-6 clay surface and mechanical-properties of nylon-6 clay hybrid', *J. Appl. Polym. Sci*. 55: 119–123.

Wu Z (2002), 'Synthesis and characterization of nylon 1012/clay nanocomposite', *J. Appl. Polym. Sci.* 83: 2403–2410.

2

Epoxy nanocomposites based on layered silicates and other nanostructured fillers

O BECKER and G P SIMON, Monash University, Australia

2.1 Introduction

In the late 1930s Pierre Castan of Switzerland and Sylvian Greenlee from the United States independently synthesized the first bisphenol-A epichlorohydrin-based resin material. A few years later in 1946, the first industrially-produced epoxy resins were introduced to the market. Since then, the use of thermosetting polymers has steadily increased. The wide variety of epoxy resin applications include: coatings, electrical, automotive, marine, aerospace and civil infrastructure as well as tool fabrication and pipes and vessels in the chemical industry. Due to their low density of around 1.3 g/cm^2 and good adhesive and mechanical properties, epoxy resins became a promising material for high performance applications in the transportation industry, usually in the form of composite materials such as fibre composites or in honeycomb structures. In the aerospace industry, epoxy-composite materials can be found in various parts of the body and structure of military and civil aircrafts, with the number of applications on the rise. A recent approach to improve and diversify polymer properties in the aerospace industry is through the dispersion of nanometer-scaled fillers in the polymer matrix.[1] A significant number of academic and industrial projects have investigated the possibility to further improve epoxy resins (and in some cases composites or other binary systems) through the strategy of producing nanocomposites. This chapter reviews the published work on the use of layered silicates and other nanofillers to improve epoxy resin systems.

The term ‘epoxy resin’ refers to both the prepolymer and its cured resin/hardener system. The former is a low molecular weight oligomer that contains one or more epoxy groups per molecule (more than one unit per molecule is required if the resultant material is to be crosslinked). The characteristic group, a three-membered ring known as the epoxy, epoxide, oxirane, glycidyl or ethoxyline group is highly strained and therefore very reactive. Epoxy resins can be cross-linked through a polymerization reaction with a hardener at room temperature or at elevated temperatures (latent reaction). Curing agents used for

room temperature cure are usually aliphatic amines, whilst commonly-used higher temperature, higher performance hardeners are aromatic amines and acid anhydrides. However, an increasing number of specialized curing agents, such as polyfunctional amines, polybasic carboxylic acids, mercaptans and inorganic hardeners are also used. All of these result in different, tailored properties of the final polymer matrix. In general, the higher temperature cured resin systems have improved properties, such as higher glass transition temperatures, strength and stiffness, compared to those cured at room temperature.

Figure 2.1 illustrates the simplified cure reaction of an epoxy resin with an amine hardener.[2] The two different functional groups react during the initial conversion (Reaction I) and form a linear or branched polymer. The addition of the primary amine to an epoxide group leads to the formation of a hydroxyl group and a secondary amine, which continues until the primary amine groups are exhausted. Reaction II illustrates the crosslinking through the addition of secondary amines with epoxy groups, where the macromolecules develop a three-dimensional network. One of the most common side reactions is etherification (Reaction III), where a hydroxyl group reacts with an epoxide group, forming an ether linkage and a further hydroxyl group. The extent to which etherification takes place during cure depends on the structure and chemistry of the resin and hardener, as well as the cure conditions. When the branched structures extend throughout the whole system, the gel point is reached. At this characteristic point, the crosslinked resin does not dissolve in a suitable solvent of the parent resin, although a soluble (sol) fraction may still be extractable. Further, diffusion-controlled cure is required to increase the degree

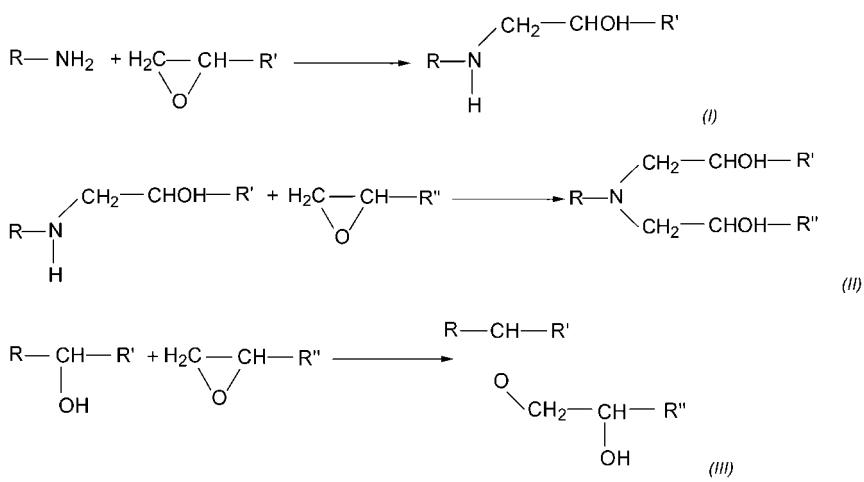

2.1 The three possible main reactions during cure of an epoxy resin with an amine – (*I*) primary amine-epoxy addition, (*II*) secondary amine-epoxy addition, (*III*) etherification[2] (from Chiao, L., (1990) *Macromolecules* 23: 1286).

of crosslinking and to finally produce a structural material with a mechanical modulus of a vitrified or glassy solid material. The point at which the glass transition temperature of the growing network reaches the cure temperature is known as vitrification.

2.2 Epoxy-layered silicate nanocomposites

The use of nanostructured fillers in epoxy systems has gained significant importance in the development of thermosetting composites. One of the more widely studied nanocomposite strategies is the incorporation of layered silicates into the epoxy matrix. In comparison to other nanoparticles to be discussed later in this review, layered silicates belong to a unique group of nanofillers with only one dimension on the nanometer scale. The individual platelets of this filler are slightly below 1 nm in thickness, and the diameter of the platelets varies between 200 and 600 nm, these fillers being distinguished from other nanoscaled additives by their high aspect ratio.

Layered silicate minerals belong to the structural group of swelling phyllosilicates or smectites. This group of minerals consists of periodic stacks of layers, which form tactoids between 0.1 and 1 μm.[3] The crystal lattice of the individual silicate platelets is composed of two tetrahedral silica sheets that are merged at the tip to a central octahedral plane of alumina or silica[4,5]. Due to this repeating structure, these minerals are also often referred to as 2:1 phyllosilicates. Determined by isomorphous substitution of central anions of lower valences in both the tetrahedral and the octahedral plane, the layered silicates have a negative charge on their surfaces. This negative charge is counterbalanced by inorganic cations located in the interlayers or galleries. Further details about the crystallography of layered silicates can be found in the literature.[4,5]

2.2.1 Layered silicate surface modification

The untreated smectite mineral is strongly hydrophilic and hence is not suitable for the absorption of most organic molecules. It is the exchange reaction of the interlayer ions with organophilic ions that modify and tailor the layered silicates for the use as polymer filler. The key parameter for the modification of a layered silicate is its charge density, which determines the concentration of exchangeable ions in the galleries. Studies by Lan *et al.*[6] and Kornmann *et al.*[7] showed that layered silicate minerals with cation exchange capacities (CEC) of 60–100 mol-equivalent/100 g of the mineral (such as montmorillonite and hectorite minerals) gave better exfoliation after modification and cure compared to other clay minerals with higher CEC values. It has been theorized, that the differences in the degree of separation are related to the space available to the epoxy within the ion-populated silicate layers. Further details about the absorption of organics

through cation exchanged layered silicates[8,9] and the particular modification process of layered silicates for epoxy nanocomposite applications[10–17] can be found in the literature.

Another determining factor for the control of organoclay-epoxy interaction during in-situ polymerization is the nature of the interlayer exchanged ion. The number and the structure of these ions determine the initial space available and hence the accessibility of the resin/hardener monomers to the layered silicate galleries. Lan *et al*.[6] varied the alkylammonium ion chain length of the layered silicate modification from 4 to 18 units. Investigation of the d-spacing of the organoclay showed that both the swelling of the clay by the resin before cure and the intercalation during cure were affected by the chain length of the interlayer exchanged ion. A minimum of eight methylene units was required to achieve nanocomposite formation in the final structure. Wang and Pinnavaia[13] showed that the acidity and therefore the ability of the interlayer exchanged ion to act as a catalyser for the cure (and homopolymerization reaction) plays a key role in the nanocomposite formation. In their work it was shown for a series of primary to quaternary octadecylammonium modified layered silicates that the higher Brönsted-acid catalytic effect of the primary and secondary alkylammonium ions gave larger interlayer increases during the cure process. A general overview of the intercalation process before and during cure is provided in Section 2.2.3.

2.2.2 Rheology of epoxy layered silicate network precursors

Whilst layered silicates are a relatively new type of filler to improve the materials performance of crosslinked thermosets, these minerals have been widely used for flow modification of coatings and paints, primarily to induce thixotropic behaviour. Organophilic layered silicates are widely known for their ability to swell in organic fluids and form a thixotropic gel. Mardis[18] related thixotropy to the dispersed silicate platelets forming a three-dimensional network in the fluid via interplate hydrogen bonds of low bond energies. If there are high shear forces during processing, these are able to overcome the secondary bonding forces between platelets and the viscosity of the coating is close to that of a coating without the additive. At rest the bonds reform rapidly, thereby increasing the viscosity of the coating. Pignon *et al*.[19] have investigated this thixotropic behaviour in more detail for a water-laptonite dispersion. This will be further discussed below, in reference to the behaviour of epoxy resins and layered silicates.

The rheological behaviour of organoclay-filled epoxy resins prior to cure can significantly influence the processing of the nanocomposite and therefore the properties of the final material. Becker *et al*.[20,21] investigated the effect of an octadecyl-ammonium modified layered silicate on the viscosity of three epoxy resins with different structures and functionalities (DGEBA, TGAP, TGDDM).

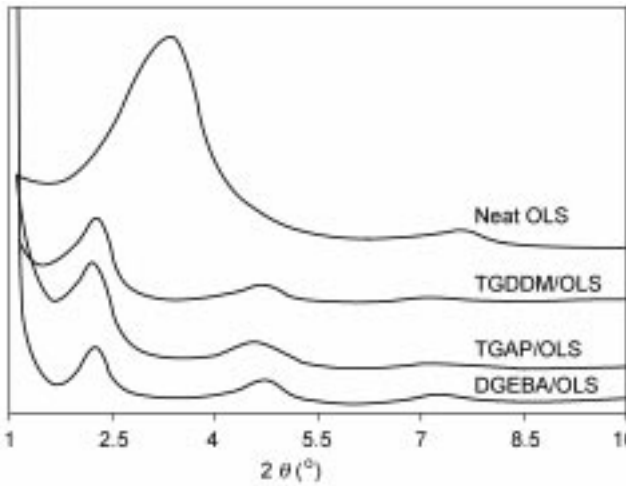

2.2 XRD traces of neat organically modified layered silicate (OLS) and OLS/epoxy resin blends[21] (Figure 6, page 1688, Becker, O., Sopade, P, Bourdonnay, Halley P.J., Simon, G.P (2003) *Polym. Eng. Sci.* 43: 1683).

Steady and dynamic shear rheology tests were conducted at concentrations of 0–12.5% organoclay and temperatures of 40ºC. The results showed very little deviation of the resin/clay blends from Newtonian flow behaviour. Noticeable yield stress was found for layered silicate concentrations of 10% and above, this effect being strongest in the case of the highly viscous, tetrafunctional TGDDM resin. As illustrated in Fig. 2.2, all suspensions investigated in this study showed an increase in the d-spacing of the layered silicate from initially 23 to 39 Å $\pm$ 0.5.

Le Pluart *et al.*[22] investigated the rheological properties of three different organoclays on a DGEBA resin system, as well as a Jeffamine D-2000 hardener before cure. Results showed that the rheological properties of the suspensions strongly depend on the interactions between the monomer and the layered silicate. Those systems which showed significant interactions with a d-space of around 3.4 nm after swelling, formed weak gels, because the clay becomes well separated. When high shear forces are applied these monomer/layered silicate blends behave as high relative viscosity fluids. In contrast, suspensions with low interactions between the monomer and the layered silicates cause gel-like behaviour, but have a much lower viscosity when sheared because of poor monomer-clay interaction (note: strong and weak, in this context, refers to the strength of the gel, not of the monomer-clay interaction). The strength or otherwise of the gels in these studies was experimentally characterized by measurement of shear modulus (G'). The issue is also related to percolation, with weaker interacting systems (stronger gels) having a lower percolation threshold (and thus the particles, a higher effective volume fraction). These high aspect ratio particles are most often seen when the system is broken down. The

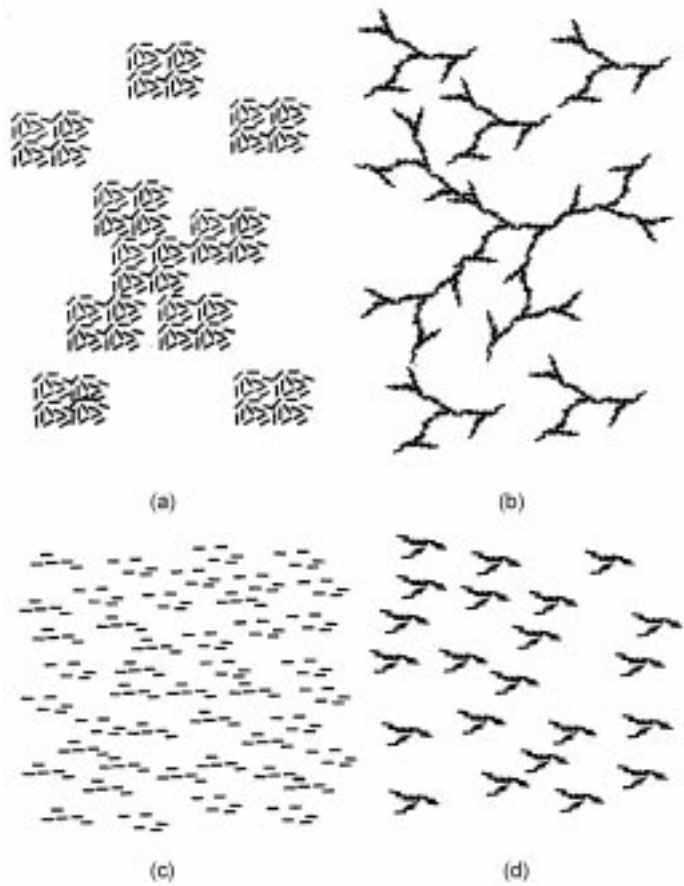

2.3 Structure of nanoclays in epoxy resin with (a) poor clay-epoxy interaction, strong gel, no shear, (b) strong clay-epoxy interaction, weak gel, no shear, (c) poor clay-epoxy interaction, strong gel, shear, (d) strong clay-epoxy interaction, weak gel, shear[22] (Figure 12, page 217, Le Pluart, L., Duchet, J., Sautereau, H., Halley, P., Gerard, J.- F. (2004) *Applied Clay Science* 25: 207).

converse is true of a strongly interacting monomer-clay systems (weak gel) in which the particles are well-dispersed and further broken down by shear. This mode is represented diagrammatically in Fig. 2.3.

2.2.3 Formation and microstructure of epoxy nanocomposites

The synthesis of polymer nanocomposites can be divided into three main classes, i.e. melt intercalation, intercalation of the polymer from solution and in-situ polymerization. Whilst synthesis via melt intercalation is not applicable to thermosetting systems, a few reports were made on the epoxy nanocomposites formation from solution,[23,24] mainly as a way to get intimate mixing or to

achieve higher clay loadings. However, the most common process to synthesize epoxy layered silicate nanocomposites is via the in-situ polymerization, where the clay is pre-intercalated by the epoxy resin and then the resin is caused to react after the addition of a hardener. The basic principle behind the formation of an epoxy nanocomposite is that the resin and hardener monomers are able to enter the galleries between the platelets of the layered silicate tactoids. This is encouraged by appropriate organophilic modification of the layered silicate, where the inorganic cations in the galleries have been exchanged by organophilic cations.

Epoxy layered silicate nanocomposite formation has been widely discussed in the literature and may be summarized as follows: if the nature and polarity of the layered silicate gallery matches that of the resin and hardener monomer, the molecules will move into the layered silicate galleries, a process often referred to as intercalation. During this intercalation, the clay layers are moved slightly apart. This process is limited by a thermodynamic equilibrium between the surface energy of the layered silicate and the polarity of the swelling monomers.[6,7] Curing reaction in the galleries changes this equilibrium and enables further reactive monomers to diffuse into the galleries and further increase the interlayer distance. Since the interlayer reaction competes with the polymerization outside the clay galleries, it is necessary that the silicate modification also act as a catalyst for the interlayer reaction. If the silicate layers are further pushed apart by the incoming material, a 'true' nanocomposite may result, with the individual silicate platelets fully dispersed, exfoliated or delaminated within the polymer matrix. The structure of the final composite material thus depends on various factors, such as the nature of the clay interlayer ion and the polymer, as well as reaction conditions, i.e. reaction temperature and mixing conditions in case of an in-situ polymerized nanocomposite. Figure 2.4 illustrates two examples of transmission electron microscopy (TEM) images taken from highly intercalated or orderly exfoliated epoxy nanocomposites. The general requirements to achieve the formation of epoxy nanocomposites were established by the group of Pinnavaia *et al*.[3] In brief, the nature of the layered silicate and the interlayer exchanged ion, the cure conditions and the resin and hardener chemistry are the key factors controlling the final composite structure.

Recent work by Park and Jana[25] expanded on this process by noting that polymerizing networks may store up elastic energy, which pushes against the interacting clay layers, the mobility of the layers themselves inhibited by the viscosity of the reacting monomer sitting outside the clay layers at any given time. The force balance thus involves the attractive clay-organo-ion adhesion and, importantly, interaction between the organo-ions themselves, and is illustrated in Fig. 2.5. Such a build-up in energy of the cure inside the gallery means that entropy increases to a point that this counterbalances the attractive energies and the clay expands. The rate of build up of this so-called recoil energy is slow in slow curing systems because molecules have longer to relax as

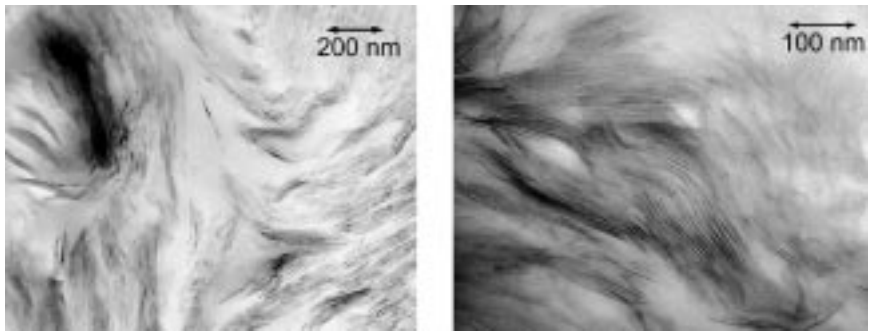

2.4 TEM images of epoxy layered silicate nanocomposites: diglycidyl ether of bisphenol A/diethyltoluene diamine/octadeclammonium (left) and tetraglycidyldiamino diphenylmethane/diethyltoluene diamine/ octadeclammonium (right).

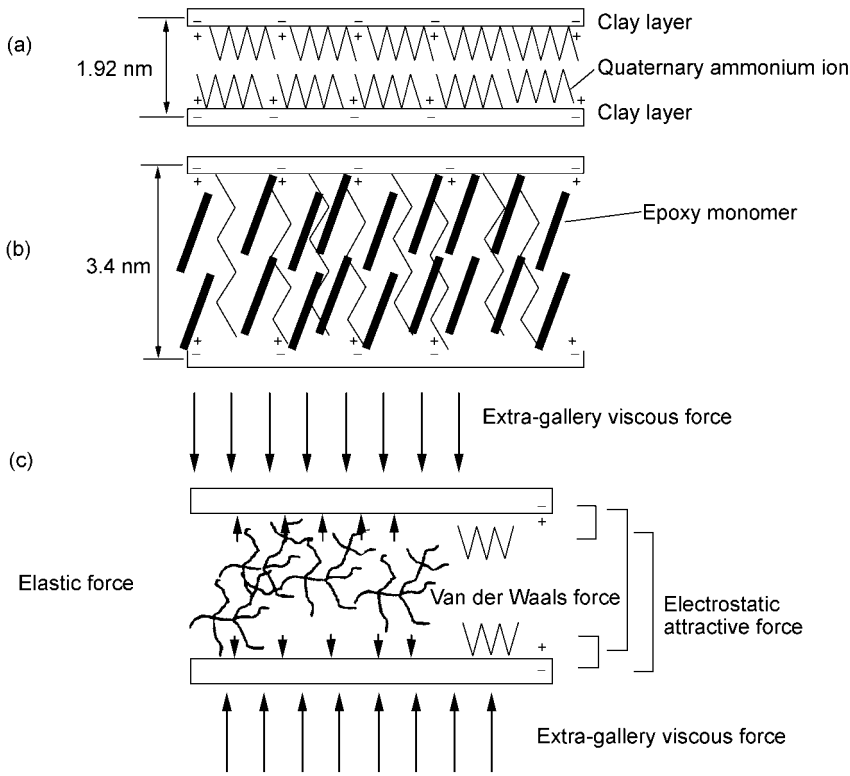

2.5 Schematic of various states of intercalation and exfoliation (a) organo-treated clay alone, (b) intercalated epoxy (c) force balance on tactoid consisting of two layered silicate sheets[25] (Figure 1, page 2760, Park, J.H., Jana, C.J. (2003) *Macromolecules* 36: 2758).

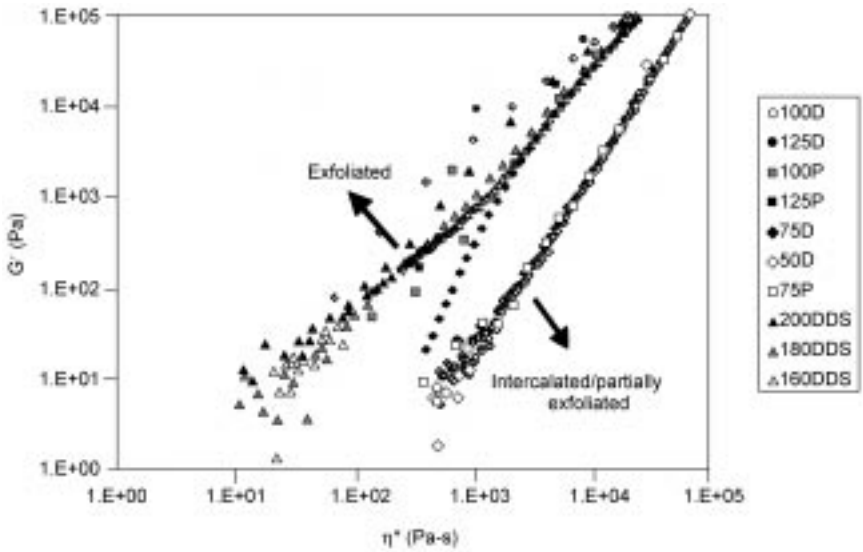

2.6 Relationship between storage modulus and viscosity as a function of cure with the standard epoxy resin (glycidyl ether of bisphenol A) with Jeffamine D230 (denoted P in the legend) or with DDS (denoted D in the legend). The numbers in the legend reflect the cure temperatures in °C.[25] (Figure 14, page 2765, Park, J.H., Jana, C.J., (2003) *Macromolecules* 36: 2758).

curing progresses. An important part of the understanding put forward is that the surface layers become removed first in a sequential manner, and that, in fact, they peel off from the edges because of the flexibility of the clay. Importantly, Park and Jana showed that manipulating and indeed matching, the intra- and extra-gallery reactions by addition of the chloride of the organic modifier changes the degree of exfoliation very little – demonstrating a reduced importance of surface treatment to what was previously thought.[25] With regards to the mechanism of formation of the nanocomposite, it was found (see data in Fig. 2.6) that if the ratio of shear modulus to complex viscosity (representing the recoil forces against viscous resistance) were greater than or equal to 2–4 s^{-1}, the clay layers could be pushed apart and exfoliation occurred.

Kong and Park[26] added further to the understanding with some elegant, real-time X-ray diffraction studies, which allowed the monitoring of changes in d-spacing with reaction. They found that slower curing rates (due to less reactive amines as indicated by their electronegativities, pK_a) or increased cure temperatures led to better exfoliation. It was found for the system investigated that the d-spacing occurs at a certain point (after approximately 9 minutes, see Fig. 2.7) when a sudden peak at 3.4 nm occurs. This indicates that the change in d-spacing can occur quite quickly and that simple diffusion alone of monomer into the galleries is not sufficient to push the clay apart, but rather that the elastic build-up described above by Park and Jana[25] is required. Indeed, three step-

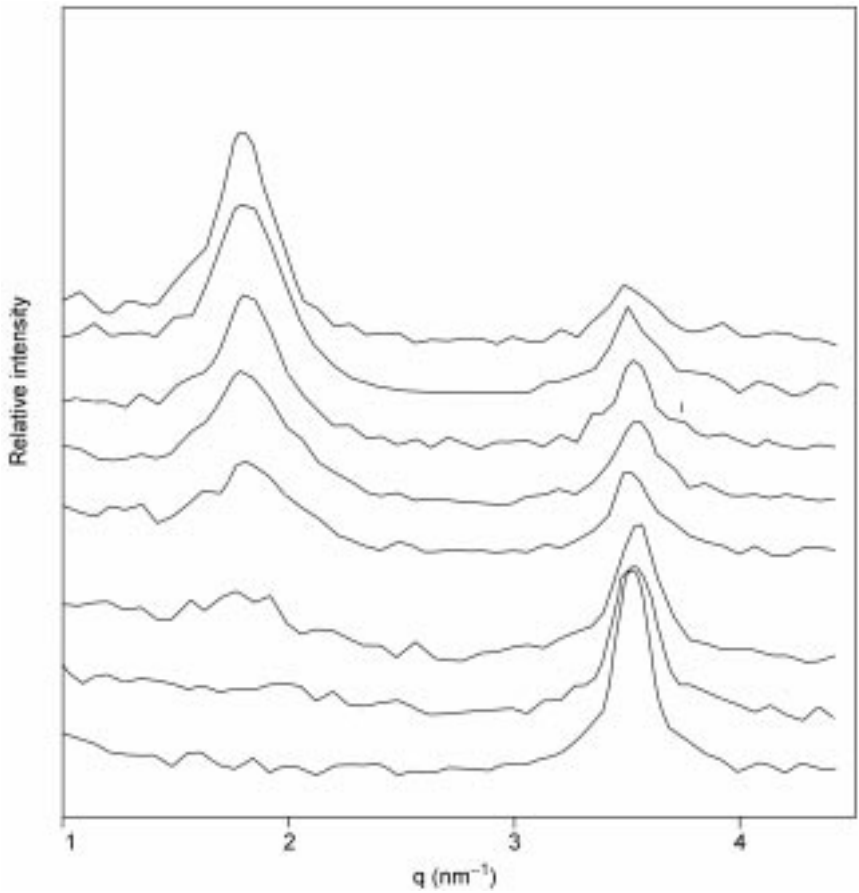

2.7 Time-resolved, isothermal SAX measurements for samples of DGEBA and an alkyl ammonium (18 units)-treated layered silicate with the scan times (from bottom) of 0, 3, 6, 9, 12, 15, 22.5, 30 and 60 minutes).[26] (Figure 4(b), page 422, Kong, D., Park, C.E. (2003) *Chemistry of Materials* 15: 419).

changes occur throughout cure (Fig. 2.8). The first is due to intercalation by the layered silicate of the epoxy monomer, the second is due to expansion of layers due to some early (organo-ion catalysed) epoxy reaction and the third is due to reaction and crosslinking within these clay layers.

It has been mentioned already and generally found that there are many factors influencing the degree of dispersion of the nanocomposites formed and these have recently been summarized by Becker and Simon.[27] Factors found to improve exfoliation include: lower charge density on the clays, a sufficiently long alkyl ammonium chain length, the use of primary or secondary onium ions and higher cure temperatures. These factors all relate to increased ability of the monomer to enter the clay and for the reaction between the clay layers to be promoted over that outside the galleries.

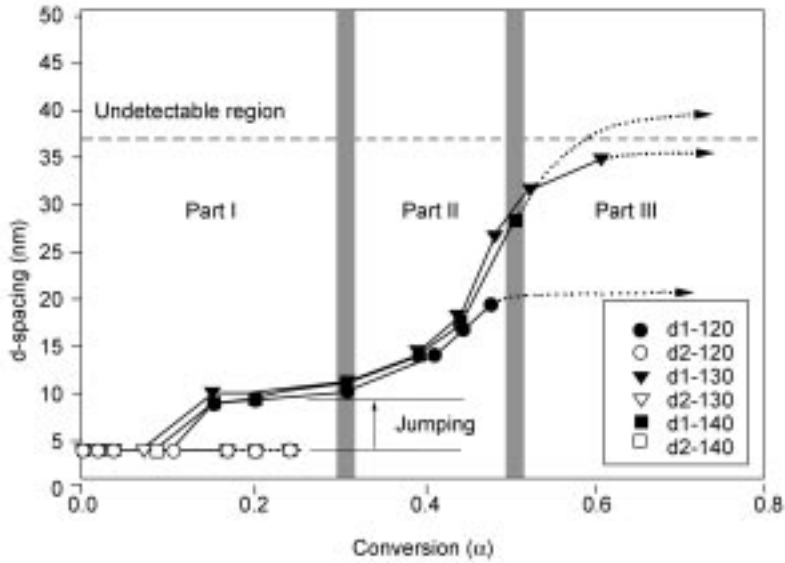

2.8 Changes in interlayer clay spacing (d), as a function of cure at various temperatures (120, 130 and 140°C).[26] (Figure 9, page 423, Kong, D., Park, C.E. (2003) *Chemistry of Materials* 15: 419).

2.2.4 Other strategies of layered silicate nanocomposite synthesis

A few other strategies for the synthesis of epoxy nanocomposites can be found in the literature. Brown *et al*.[23] and Salahuddin *et al*.[24] used acetone as a low-boiling solvent to enhance the processability of the network precursors. In both studies, the solvent is used as a processing aid only, i.e the acetone is removed under vacuum before thermal cure is initiated. Whilst the work by Brown *et al*. did not show any impact on the properties of the material after cure,[23] the processing aid allowed the production of highly filled epoxy nanocomposite systems, as reported by Salahuddin *et al*.[24]

Triantafillidis *et al*.[28,29] reduced the amount of organic modifier in the layered silicate by treating the clay mineral with diprotonated forms of polyoxypropylene diamines of the type α,ω-$[NH_3CHCH_3CH_2(OCH_2CHCH_3)_xNH_3]^{2+}$, with x = 2.6, 5.6, and 33.1. The amine modifier played a triple role of polymerization catalyst, curing agent and surface modifier. This strategy greatly reduced the plasticizing effect of the modifier, which can often be found with mono-amine modified layered silicates. Further, improved mechanical properties are reported for the resulting nanocomposites.

Recent work by Ma *et al*.[30] has shown some very promising results to achieve a disorderly exfoliated nanocomposite structure for the first time, by modifying the

layered silicate with a diamine hardener and precuring the organically modified layered silicate with the epoxy resin in suspension. In this reported work, the clay mineral was treated with an M-xylylenediamine hardener, where one amine group was previously converted into a cation in an acetic environment. The $–NH_3^+$ group could then be grafted to the negatively charged silicate surfaces in a water/layered silicate suspension. In a further step, dimerization between DGEBA and the free amine group of the surface modifier was initiated. After evaporation of any water present in the system, the blend was cured with stoichiometric amount of 4-aminophenyl sulfone (DDS). The reaction mechanism is illustrated in Fig. 2.9. TEM images of the resulting composite appeared to show a very disordered, exfoliated arrangement of the silicate platelets in the polymer matrix. The physical properties of this new material are yet to be reported.

Chen *et al.*[31] and Wang *et al.*[32,33] reported another approach of highly exfoliated epoxy nanocomposite synthesis using an organoclay slurry to improve the silicate layer dispersion. In the work by Wang *et al.*, the pristine clay was first swollen in water and than transferred into a clay-acetone slurry, including several steps to separate the water from the slurry. The slurry was further treated with low quantities of a coupling agent, (3-aminopropyl)trimethoxysilane, blended with some epoxy resin and separated from the acetone at 50ºC under vacuum and cured with the respective resin/hardener. TEM images of these materials revealed a well (disorderly) dispersed nanocomposite structure. Similar structural results were achieved in the work of Chen *et al.*[31] using 2,4,6-tris-(dimethylaminomethyl) phenol (DMP-30) as a clay surface modifier and cure accelerator and an acetone-layered silicate slurry.

2.2.5 Mechanical properties

In the early work on epoxy nanocomposites it was reported[34] that flexible resin systems with a low glass transition temperature showed greater improvement in mechanical properties upon forming nanocomposites, than those systems exhibiting higher glass transitions. A summary of improvement in mechanical properties of epoxy nanocomposites in both the rubbery and the glassy state is reported in this section.

Fracture properties

It is often stated in the literature[35] that toughening of a polymer matrix through incorporation of an additional phase occurs within a specific size range of the reinforcing filler. Hence, the silicate platelets in a fully dispersed (disordered exfoliated) arrangement would nominally be too thin to provide toughening of the polymer matrix. In contrast, the lateral, micron-sized structure of intercalated layered silicate tactoids can provide this toughening, mainly through a crack bridging mechanism and increased fracture surface area. Zerda and Lesser[35]

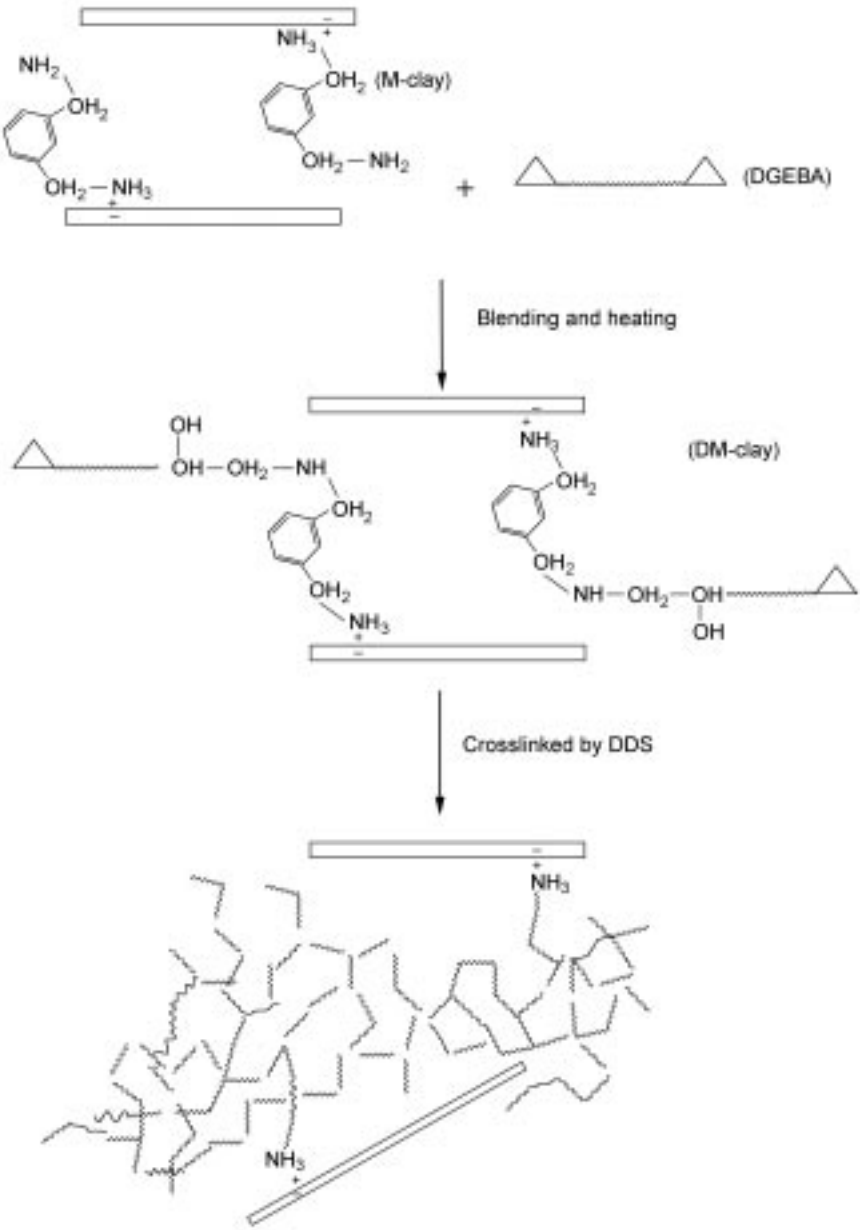

2.9 Reaction mechanism between M-xylylenediamine, sodium montmorillonite, followed by ingress of DDS hardener and epoxy resin[30] (Figure 1, page 758, Ma, J., Yu, Z.-Z., Zhang, Q.-X., Xie X.-L., Mai, Y.-W., Luck, I. (2004) *Chemistry of Materials* 16: 757).

investigated the fracture properties of intercalated diglycidylether of bisphenol A (DGEBA)/Jeffamine D230 layered silicate nanocomposites. The stress intensity factor, K_{IC}, a common indicator of the fracture properties, of these materials showed significant improvements at layered silicate contents of 3.5% in weight and above. The K_{IC} increased from initially 0.9 MPa/m^2 for the neat system to 1.5 MPa/m^2 (3.5 wt.% organically-modified layered silicate).

Generally, there has been good correlation in the literature between the degree of intercalation or exfoliation, respectively, and the correlating fracture toughness. The group of Mülhaupt[12,17,37] as well as Becker and Simon[38,39] provided much data underpinning the correlation between the nanoscale dispersion of layered silicate and the corresponding mechanical properties. Zilg *et al.*[12] showed for various anhydride cured DGEBA layered silicate nanocomposites using different layered silicate minerals and modifications, that a well dispersed intercalated epoxy nanocomposites primarily improves the toughness, whilst the exfoliated state more likely reinforces the stiffness of the materials. Recently, Fröhlich *et al.*[17] synthesized series of anhydride cured epoxy nanocomposites with glass transition temperatures above 100ºC. In their work, two types of phenolic imidazolineamides were used for the layered silicate modification. Although the interaction between the layered silicate modification and the polymer was low, some systems showed a decreased d-spacing in the composite compared to the modified mineral, and a steady increase in fracture toughness (K_{IC}) was observed for all systems investigated. The creation of additional surface areas on crack propagation is assumed to be the primary factor for the improvement in fracture toughness. SEM images of nanocomposites fracture surfaces[35] showed a tortuous path of crack propagation around areas of high silicate concentration in the nanocomposite compared to the neat system. Recently, Wang *et al.*[32] reported the formation of a large number of microcracks and the increase in fracture surface area as a result of crack deflection as the major toughening mechanism for their investigated nanocomposite systems. Similar images were presented for nanocomposites based upon an unsaturated polyester.[40]

Flexural and tensile properties

Since the pioneering work by Messersmith and Giannelis[41] and Lan and Pinnavaia[34] showed significant improvement in the flexural properties of epoxy nanocomposite systems, the modulus of these materials has probably been the most widely-reported mechanical property. Messersmith and Giannelis[41] reported an increase in flexural modulus by 58% in the glassy state for a nadic methyl anhydride-cured DGEBA system containing 4% by volume of layered silicate. The same system showed an improvement in modulus by some 450% in the rubbery state. Pinnavaia *et al.*[34] caused more than a 1000% increase in strength and modulus of an epoxy nanocomposites system containing an unusually high

concentration of 15% $CH_3(CH_2)_{17}NH_3^+$ modified montmorillonite. As discussed previously with regards to Zilg's work,[12] these results also identify that the degree of exfoliation significantly determines the surface area of the particles in the matrix, with higher layer separation thus yielding more rigidity. Wang *et al*.[3] showed, for a series of magadiite/epoxy/Jeffamine 2000 nanocomposites, the nature in which tensile strength improved in relation to the degree of exfoliation.

It is assumed[34] that the platelet particles align under strain in the rubbery polymer matrix, and form an arrangement with properties similar to a longer fibre in a fibre composite. This reinforcing mechanism would also explain the rather small improvement found for glassy epoxy nanocomposites with high glass transition temperatures. Kornmann *et al*.[37] reported an increase in Young's modulus by 38% for a 4,4′diaminodiphenyl sulfone (DDS) cured tetra-glycidyl 4,4′diaminodiphenyl-methane (TGDDM) containing 3.8% of well intercalated layered silicate. Similar results were found by Becker *et al*.[38,39] for a series of different diethyltoluene diamine (DETDA) cured glassy epoxy resin systems (DGEBA, TGAP, TGDDM).

2.2.6 Barrier properties and solvent uptake

It is reported in the literature that layered silicate-based polymer nanocomposites show improved barrier properties compared to the neat polymer matrix. Such an improvement in barrier properties of these materials is often explained by the presence of a more torturous path that the respective molecules have to traverse because of the dispersed silicate layers. However, only a few reports on barrier properties of thermosetting layered silicate nanocomposites can be found in the literature. Gensler *et al*.[42] investigated the water vapour permeability of a hexahydrophtalic anhydride-cured DGEBA nanocomposite, containing organically modified hydrotalcite as a platelet, nanostructured filler. Results for the water permeability of the intercalated nanocomposites showed a five to tenfold reduction at filler concentrations of between 3 and 5 wt.%.

A study by Shah *et al*.[43] on the moisture diffusion of a (non-epoxy) vinyl ester resin-based layered silicate nanocomposite also reported a decreased moisture diffusivity of the nanocomposite, ascribed to the restricted mobility of the polymer chains tethered to the clay particles. A reverse effect, however, could be observed for the equilibrium water uptake of one of the two fillers investigated. The equilibrium water uptake of a vinyl-monomer containing clay nanocomposites increased from 0.012% (neat resin) to 0.021 (5% clay). The water uptake of the other, an alkyl ammonium-treated montmorillonite clay, Cloisite 10A, remained relatively unaffected by the filler addition. The increase of the first nanocomposites system was related to the strong, hydrophilic behaviour of the clay, which remains to some degree in the surface treated state.

Becker *et al*.[44] investigated the water uptake of a series of highly crosslinked (high performance) epoxy nanocomposites containing 0–10% of a commercially

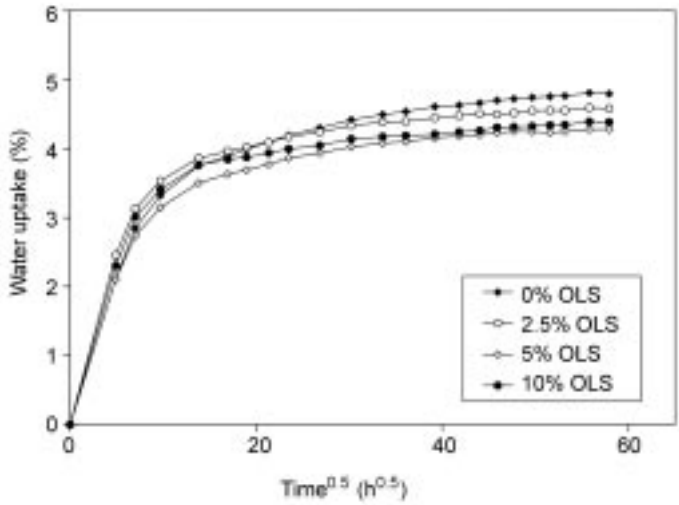

2.10 Water sorption curve of a series of triglycidyl p-amino phenol/diethyltoluene diamine nanocomposites containing different concentrations of octadeclammonium-layered silicate (OLS)[44] (Figure 2, page 190, Becker, O., Varley, R. J., Simon, G. P., (2004) *Eur. Polym. J.* 40: 187).

available modified layered silicate, Nanomer I30E. The equilibrium water uptake of all nanocomposites investigated in this study was reduced compared to the neat epoxy systems, whilst the rate of diffusion remained unaffected. Figure 2.10 illustrates an example of the % water uptake as a function of sorption time for a series of triglycidyl p-amino phenol/diethyltoluene diamine/Nanomer I30E nanocomposites. The variation in water uptake was related to the amount of bound water, rather than free water located in potential micro voids of the material. Massam *et al*.[45,46] have shown reduced absorption of methanol, ethanol and propanol for a glassy DGEBA-based epoxy layered silicate nanocomposite. The pristine polymer, for example, absorbed 2.5 times more propanol compared to the respective nanocomposites system. It was further shown in this study that the mechanical properties of the neat epoxy system were more affected (reduced) than those of the nanocomposites. It was found that the barrier to solvent uptake increased with increasing exfoliation.

2.2.7 Thermal and flame retardation properties

The effect of the addition of clay on the glass transition has shown a variety of behaviours, depending on the system used. An increase in T_g has been observed,[6] whilst others found a reduction.[47] Increases have been ascribed to retardation of molecular motion due to interaction with the high surface area platelets, whilst a decrease was explained by plasticization of the organo-ion, to

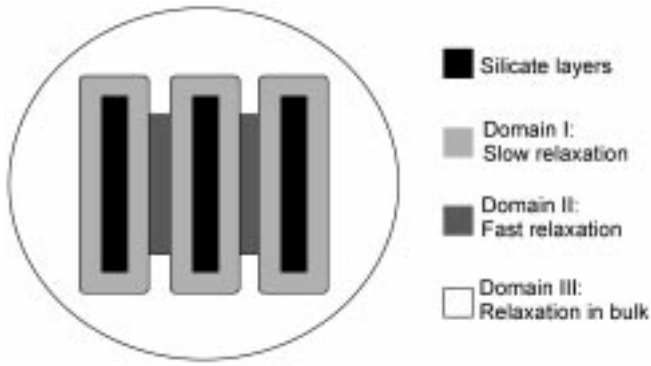

2.11 The domain-relaxation model of Lu and Nutt, which contains material which is attached to the platelets (I), confined between platelets (II) or in the bulk (III).[48] (Figure 6, page 4015, Lu, H., Nutt, S. (2003) *Macromolecules* 36: 4010).

disruption of the crosslinked structure, enhanced etherification or entrapment of unreacted monomer.[37] A more sophisticated view of this has been proposed recently by Lu and Nutt[48] and is illustrated in Fig. 2.11. This theory divides the molecular structure into three regions: Domain I: a slowly relaxing domain which is confined to the clay layers where the epoxy molecules are tethered to clay or organo-ions. Domain II: a region of faster motion where the material is isolated from the bulk and from the tethered state, and thus relaxes faster (due to a lack of such interactions) and has been observed particularly in thermoplastic nanocomposites, such as by NMR.[49] The final region (Domain III) is the bulk material, which has the same glass transition as if there were no added layered silicate. The ability to manipulate the size of these relative areas will vary the effect on T_g. Clearly greater exfoliation will result in a lack of fast relaxation Region II, and thus lead to the same or higher value. Since most epoxy nanocomposites do in fact show an intercalated structure, it is not surprising that most work has shown a decreased glass transition. Likewise, the mix of clay intercalation and exfoliation will lead to a broadness of relaxation.

At higher temperatures, thermal stability becomes an issue. This relates to degradation of both the organo-ion, as well as the epoxy resin. Most of the published work on the thermal stability of epoxy layered silicate nanocomposites to date is based on the widely used epoxy resin DGEBA.[13,50–52] The technique of thermogravimetric analysis (TGA) is often applied to investigate the degradation resistance to heat of such materials. Park *et al*.[50] found an increased activation energy of decomposition and an increased temperature value at which the maximum weight loss occurred. Lee and Jang[51] reported a shift in the onset of thermal decomposition towards higher temperatures for intercalated epoxy nanocomposite synthesized by emulsion polymerization of unmodified layered silicate, as indicated by TGA (in a nitrogen atmosphere). In

their study on the thermal degradation of DGEBA-based nanocomposites containing 2 and 10% octadecylammonium modified montmorillonite, Gu and Liang[52] found that the 10% nanocomposite had the lowest degradation temperature, whereas values for the nanocomposites containing 2% organo-modified clay were higher than the neat resin.

Wang and Pinnavaia[13] also found improved thermal stability with increasing layered silicate concentration. Comparison of TGA measurements of intercalated and exfoliated organically modified magadiite-based nanocomposites showed a low temperature weight loss at about 200ºC for the intercalated system, indicative of the thermal decomposition of the clay modifier, whilst the exfoliated nanocomposite did not show such a low onset temperature for weight loss. It was proposed that the interlayer exchanged ions were incorporated into the polymer network. However, the application of organically-modified layered silicates in high performance thermosetting systems with initially good thermal resistance and high T_gs may induce degradation of the compatibilizer at elevated temperatures and therefore decrease the thermal stability of the overall material. Becker *et al.*[44] recently reported slightly decreased onset temperatures for the thermal degradation of a series of high-performance epoxy nanocomposites.

Cone calorimetric measurements of these systems[53] showed an improvement in fire retardancy as indicated by a reduced peak release rate. Cone calorimetry determines fire relevant properties such as heat release rate (HRR) and carbon monoxide yield during combustion of the material using oxygen depletion-based calorimetry. Gilman *et al.*[54,55] have conducted a thorough study of the flammability of layered silicate-based thermosetting nanocomposites. The improved fire properties of epoxy layered silicate nanocomposites is often related to improved barrier properties and the torturous path for volatile decomposition products, which hinders diffusion out of the material[54,55] as well as diffusion of oxygen in.

A typical heat release rate curve for a neat epoxy system and the respective layered silicate nanocomposite, is shown in Fig. 2.12.[55] Both peak and average heat release rate, as well as mass loss rates, are all significantly improved through the incorporation of the nanoparticles. In addition, no increase in specific extinction area (soot), CO yields or heat of combustion is noticeable. However, the mechanism of improved flame retardation is still not clear and no general agreement exists as to whether the intercalated or exfoliated structure leads to a better outcome.[56] The reduced mass loss rate occurs only after the sample surface is partially covered with char. The major benefits of the use of layered silicates as a flame retardation additive is that the filler is more environmentally-friendly compared to the commonly used flame retardants and often improves other properties of the material at the same time. However, whilst the layered silicate strategy is not sufficient to meet the strict requirements for most of its application in the electrical and transportation industry, the use of layered silicates for improved flammability performance may allow the removal of a significant portion of conventional flame retardants.[55]

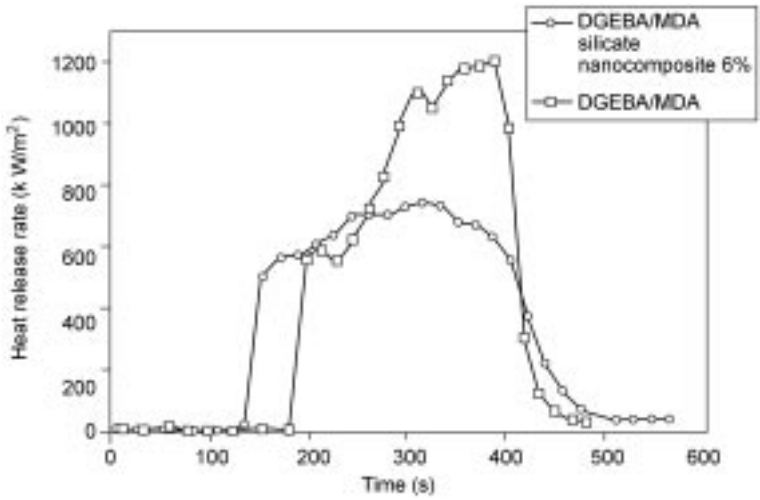

2.12 Heat release rate data for DGEBA epoxy resin cured by methylenedianiline (MDA) with and without 6 wt.% clay. The clay was a montmorillonite treated with dimethyl ditallow ammonium ions. The cone calorimeter was run at a heat flux of 35 kW/m^2.[54] (Figure 14.8, page 261 in Gilman, J.W., Kashiwagi, T., Nyden, M., Brown, J. E. T., Jackson, C. L., Lomakin, S., Giannelis, E. P., Manias, E. (1999), 'Flammability studies of polymer layered silicate nanocomposites: Polyolefin, epoxy, and vinyl ester resins', in *Chemistry and Technology of Polymer Additives*, Ak-Malaika, S., Golovoy, A., Wilkie, C. A. (eds) Malden, MA: Blackwell Science, pp. 249–65.

2.3 Epoxy-nanocomposites based on other nanofillers

A limited number of other instances of epoxy resins containing nanofillers have been discussed in the literature. Sue *et al*.[57,58] investigated the use of α-zirconium phosphate, $Zr(HPO_4)_2 \cdot H_2O$, a synthetic layer-type filler similar to the montmorillonite structure, as a nanostructured filler for epoxy systems. The layer structure of this material is formed by zirconium atoms, which are connected to the oxygen atoms of the phosphate group, with three oxygen groups contributing to the layer formation and the hydroxy-group facing the interlayer space. In their work, the α-zirconium phosphate was organically modified with a commercially available monoamine terminated polyether, Jeffamine M715. Composites containing 5.5 wt.% (1.9 vol.%) α-zirconium phosphate were synthesized using DGEBA/DDS as a polymer matrix. The resultant panels had a clear appearance, with no visible aggregations. TEM micrographs of the nanocomposites structure showed good dispersion of the platelets in an (ordered) exfoliated structure, the aspect ratio of the 0.75 nm thick platelets in the polymer estimated to be about 100–200. Dynamic mechanical measurements showed a significant decrease in T_g from 227ºC for the neat material, to 90ºC for the nanocomposites. Although a

decrease in T_g has been reported previously for glassy layered silicate-based nanocomposites systems, as mentioned above, the order of magnitude of this decrease is unusually high. The authors[57] proposed that the reduction in T_g is related to side reactions between the excess amount of monoamine modifier and the DGEBA. Investigations of the mechanical properties showed that the modulus of the nanocomposites is increased by 1 GPa (from an initial value of 2.9 GPa, to 3.9 GPa), albeit with a drastic reduction in ductility and a slightly reduced stress intensity factor (toughness).

Wetzel *et al*.[59] synthesized a series of Al_2O_3 nanocomposites based on a commonly-used cycloaliphatic polyamine-cured DGEBA resin system. The alumina filler is a dry powder, which consists of micron sized clusters of spherical particles with an average diameter of about 13 nm. The particles were dispersed in the resin using high shear forces under vacuum to additionally remove entrapped air. Investigation of the mechanical properties of the homogeneously dispersed composites showed a maximum in improvement for alumina concentrations of 2%. It was found that the filler simultaneously improved toughness (impact energy) and modulus of the epoxy. The improved properties were related to energy dissipating mechanisms (matrix shear yielding, crack pinning and particle pull out). Incorporation of a third, micron-sized phase ($CaSiO_3$) further improved the modulus and wear properties. Improvement was related to trans-particulate fracture.

Pan *et al*.[60] have synthesized a PbS epoxy resin nanocomposite through precipitation of the PbS/resin monomer in an aqueous environment. The precipitated emulsion was cured after isolating the PbS containing resin emulsion from solvents and solvated salts. TEM images of the final material revealed a flocculated composite, with individual particles of an estimated diameter of 7 nm according to XRD measurements.

2.4 Ternary epoxy nanocomposite systems

During the last fifteen years, the industrial and academic research in the field of polymer nanocomposites has grown dramatically and some promising results have been discovered. Lately, the increased knowledge in this area along with the promising results reported for this new class of materials has encouraged researchers to take the nanocomposite strategy a step further, incorporating it as a supplementary additive in combination with other phases such as fibres, rubbers or hyperbranched polymers.

2.4.1 Ternary composites containing layered nanoparticles and a rubbery phase

Lelarge *et al*.[61] investigated a ternary epoxy nanocomposite system involving DGEBA cured with poly(propylene glycol) bis (2-amino-propyl ether) as the

resin matrix, CTBN-rubbers (1300 × 8 and 1300 × 13) of differing polarity and a surface-treated octadecyl ammonium organo-ion montmorillonite as the nanostructured filler. Whilst the clay and epoxy formed a highly intercalated structure with d-spacings greater than 70 Å, this was reduced in the final ternary systems since not all rubber phase separated in the curing epoxy system and some remained soluble in the crosslinked matrix. Figure 2.12 shows that in the ternary blend, the clay remains in the epoxy-rich phase, while the rubber phase separated into fine particles away from the layered silicates. Flexural testing showed that the clay was able to retrieve some of the modulus lost by rubber addition. Whilst toughness of the resin increased with the addition of clay or rubber alone, the effect was not synergistic and the toughness of the ternary system was intermediate between that of the binary clay and the rubber epoxy system.

Another ternary system, consisting of DGEBA/triethylenetetramine/organo-treated-montmorillonite nanocomposites where the layered silicate was modified with the widely-used methyl, tallow, bis-2-hydroxyethyl quaternary ammonium ion and polyether polyol was investigated by Isik *et al*.[62] As with the work by Lelarge *et al*.,[61] both binary systems showed an improvement in toughness of the material, whilst the combination of the two did not show a further synergistic increase. The addition of layered silicate to the ternary system causes a decrease in impact strength, although still generally greater than the neat epoxy/amine system. The modulus was similar or slightly greater than the values of the neat resins, although the highest polyol concentrations (even at high clay concentrations) caused reduced values.

Fröhlich *et al*.[63,64] also investigated the combined use of compatibilized liquid rubber and organophilic rendered layered silicate to achieve simultaneous dispersion of rubber and layered silicate and improve toughness and stiffness of different epoxy resin systems. The investigation of a hexahydrophtalic acid anhydride-cured bisphenol A diglycidyl ether (BADGE) containing bis(2-hydroxyethyl) methyldodecylammonium and methyl stearate modified triol (PPO) rubber[64] showed that the PPO-stearate did not affect the intercalation of the layered silicate. Both the binary and the ternary nanocomposites showed an interlayer distance of 2.94 nm after cure, with the ternary system also containing phase-separated, spherical rubber particles of 50–200 nm when the liquid rubber concentration exceeded 9 wt.%. The best results with respect to the toughness/stiffness balance were achieved in the ternary systems with a separated polymer phase and higher amounts of layered silicate. These materials have shown improvement in fracture toughness by 300% compared to the neat resin, with slight reduction in toughness by about 10%. Fröhlich *et al*.[63] also investigated a high-performance resin system (DGEBA/TGDDM mixture, cured with DDS) containing organically modified fluorohectorite and compatibilized liquid six arm star rubber, poly(propylene oxide-block-ethylene oxide), PPO. Morphological studies of the resulting

material showed an intercalated clay particle structure along with separated PPO spheres distributed in the polymer matrix. Whilst stiffness of these materials was slightly increased, the strength was improved by 20%, which was mainly ascribed to the impact of the layered silicates on the resin. Interestingly, all the PPO-containing systems (both binary and ternary) showed reduced fracture toughness (K_{IC}) when compared to the neat DDS-cured epoxy system.

Sue *et al.*[58] incorporated the layered α-zirconium phosphate particles described above, into a ternary epoxy nanocomposites system, containing a preformed core-shell rubber (CSR) with a rubber core size of 90 nm and an epoxy-compatible, random copolymer shell of 10–20 nm. The use of core-shell rubber means that the rubber particle size can be controlled and is hence not affected by the addition of other particles. Further, this rubber-toughening strategy has the additional benefit that no soluble rubber will remain in the epoxy phase. Comparison between the epoxy/CSR system and the ternary system shows that the addition of the layered filler is able to compensate the loss in modulus, which can usually be observed in rubber-toughened epoxy systems. Table 2.1 illustrates the properties of the different epoxy systems (M indicating the Jeffamine modifier, α-ZrP the zirconium phosphate and CSR the core shell rubber). Surprisingly, the fracture toughness, as indicated by the measure of K_{IC}, showed no improvement in the binary epoxy/M-α-ZrP composite and only moderate improvement in the binary epoxy/CSR system. However, when both fillers are combined in the epoxy matrix, a significant increase in K_{IC} was observed. The weak delamination strength of intercalated α-ZrP leads to preferential delamination and crack propagation along the α-ZrP particles, whilst the main toughening mechanism in the ternary phase was the usual rubber particle cavitation, followed by matrix shear banding. However, the synergistic effect of the combined system on improving toughness is not fully understood.

Recently, Balakrishnan and Raghavan[65] investigated the tensile properties of an acrylic rubber containing DGEBA/pyridine/octadecylamine layered

Table 2.1 Properties of epoxy, epoxy CSR, epoxy nanocomposites and ternary epoxy/CSR nanocomposites[58]

	Neat epoxy	M-epoxy	Epoxy/ M-α-ZrP	M-Epoxy/ CSR	Epoxy/ M-α-ZrP/ CSR
T_g (°C)	227	129	124	129	124
Modulus (GPa)	2.85	3.10	3.97	2.56	3.77
Tensile strength (MPa)	69.4	89.7	103.4	78.8	93.3
Elongation at break (%)	3.5	7.1	6.3	6.5	6.6
K_{IC} (MPa $m^{0.5}$)	0.76	0.69	0.70	0.92	1.64

silicate nanocomposite containing 5.5% clay and 15% acrylic rubber dispersant. It was assumed that the improvement in strength, modulus and failure strain in the ternary phase were related to the stress-transfer capability of the layered silicate particles, as well as rubber particle cavitation and plastic flow and yielding of the matrix due to rubber particles. Ratna *et al.*[66] considered the use of a rubbery hyperbranched epoxy resin as a toughening agent. Both, toughened epoxy and ternary nanocomposites were synthesized using DGEBA/diethylene diamine as a resin matrix and epoxy functional dendritic hyperbranched polymer (Boltorn E1, Perstorp Speciality Chemicals, Sweden), which consists of a highly branched aliphatic polyester backbone with an average of 11 reactive epoxy groups per molecule. The ternary system further contained octadecyl ammonium modified montmorillonite as the nanostructured filler. The microstructure of the ternary composite consisted of regions of highly intercalated layered silicate (d-spacing 90–100 Å) and spherical hyperbranched epoxy particles of 0.8–1 μm. Both the clay and the hyperbranched polymer show improved toughness of the epoxy matrix. Once again, however, there is no synergistic effect and in the ternary blend the overall toughness is less than the toughness of the hyperbranched polymer/epoxy system alone.

2.4.2 Ternary systems with other nanoadditives

The impact of nano-scaled aluminium oxide, Al_2O_3, particles on the mechanical properties of a thermoplastic reinforced polyethylene terephthalate/O-benzene dicarboxyl anhydride-cured bisphenyl A type epoxy resin was investigated by Cao *et al.*[67] Samples were synthesized using 16 parts of polyester, 100 parts of epoxy and different concentrations of the Al_2O_3 filler with an average particle length of 40 nm and an average diameter of 10 nm. PET was used not only as a toughening phase, but also to increase the viscosity before cure, and therefore improve processability, by reducing particle sedimentation and agglomeration. TEM images of the cured composite showed that the nanoparticles were only located in the polyester phase. Addition of the PET improved the impact strength from initially 6.9 kJ/m^2 to 16.4 kJ/m^2, the tensile strength from 36.7 MPa to 67.9 MPa and the modulus from 2.5 to 2.8 GPa. Incorporation of the nano-aluminium oxide further improved the impact strength and tensile strengths. Optimal properties can be observed at about 8% concentration, where the impact strength is increased by 110% and the tensile strength by 45%. The elastic modulus increased steadily as a function of filler within the investigated range up to 25%. The improvement was related to the higher rigidity of the filler compared to the binary matrix. The ternary material further exhibited good dielectric properties and slightly increased glass transition temperatures.

2.4.3 Epoxy composites containing fibres and a nanostructured filler

Ternary epoxy, fibre, layered silicate nanocomposites

Rice *et al.*[68] presented the first results for a ternary carbon fibre epoxy nanocomposite based on a bisphenol F/epichlorhydrin epoxy resin/layered silica matrix. Investigation of the matrix-dominated properties of the composite through four-point flexure measurements showed no significant increase in z-directional properties. Only minor improvement was found for a fibre composite with low organoclay concentration. Composite systems containing higher organoclay concentrations even showed a decrease in flexural strength. The reduced performance was due to an increased void content in the matrix. The work showed that understanding the resin flow, kinetics and gel times are essential to improve the composite materials, as the effect of the carbon fibre upon the dispersion and exfoliation of the layered silicate is significant and apparently determined by the method of fabrication.

Becker *et al.*[69] investigated the mechanical properties of a series of DGEBA/diethyltoluene diamine/unidirectional carbon fibre composites that contain 0–7.5% octadecyl ammonium modified layered silicate. Mode I fracture toughness measurements showed improved in-plane resistance as indicated by the increased test load (+25% at 7.5% OLS compared to the neat system) and an increased G_{IC} initial (of 50% for the same comparison). Scanning electron microscopy images of the fracture surfaces revealed increased fracture surface area in the layered silicate containing composite. The increased surface area is indicative of a distorted path for the crack tip due to the platelets that make the crack propagation more difficult. Similar observations were reported previously for binary epoxy/layered silicate nanocomposites[35,40] and are found also to apply in composite systems. It is assumed, that it is the lateral micron dimension of stacks of layers that interact with the growing crack tip and hence improve the delamination properties.

Haque *et al.*[70] synthesized plain weave S2-glass fibre epoxy nanocomposites using a vacuum assisted resin infusion moulding process. The materials used for composite synthesis are a bisphenol-A/bisphenol-F blend and a cycloaliphatic amine hardener, with the required low viscosity for the process, an organically modified layered silicate I.28E by Nanocor and plies of the above mentioned glass fabric. Ternary composites of low layered silicate concentration (1% by weight) showed improved interlaminar shear strength by 44%, flexural strength by 24% and fracture toughness of 23% along with an increase in decomposition temperature by 26ºC, when compared to the neat glass fibre composite. Improvement was related to the increased interfacial surface areas and bond characteristics. Interestingly, the mechanical properties decreased at clay concentrations of 5% by weight and above, which was related to phase-separated structures and defects in the crosslinked structures.

Ternary nanocomposites containing epoxy, long fibres and nanoparticles

Chisholm *et al.*[71] investigated the use of micron (1 μm) and nanostructured spherical SiC particles with a diameter of 29 nm as a supplementary toughener of carbon/epoxy composites. The matrix resin used was SC-15, a mixture of DGEBA (60–70%), aliphatic diglycidylether (10–20%) and epoxy toughener (10–20%), by Applied Poleramic and a hardener consisting of cycloaliphatic amine (70–90%) and polyoxylalkylamine (10–30%). Ternary carbon fibre epoxy composites containing micron or nano-sized SiC particles of 0, 1.5 and 3%) were produced using satin weave carbon fibre preforms in a vacuum assisted resin transfer moulding process. The comparison showed that the nano-sized reinforcement of fibre composites gave better improvement in mechanical and thermal properties when compared with similar concentration of the micron sized filler. An optimum in improvement was found for concentrations around 1.5% by weight of the nanometer-sized SiC. At this load, the tension and flexural properties were improved by 20 to 30%. Improvement was related to enhanced cross-linking due to catalytic effects of the filler, as well as the ability of the filler to plug voids, thereby reducing void content in the matrix resin.

2.5 Future trends

Epoxy nanocomposites have stimulated much interest in this new area of nanotechnology, because of the ease of manufacture and the significant gain in properties. This review has shown potential for the different types of nanocomposites to have a range of benefits from increased modulus, strength, fracture toughness, impact resistance, gas and liquid barrier properties, flame retardance and wear properties, all at moderately low concentrations of about 0.5–5% by weight. Such low concentrations imply that there is little impact on processing of the materials in terms of their processing behaviour although additional mixing and specific processing steps may be required to achieve the required dispersion of the nanoscaled filler.

Work in this field continues to be active, with ternary systems becoming more widely reported, with other materials such as rubber, thermoplastics or fibres being present alongside the epoxy matrix and nanofiller. Other synergies likewise need to be explored between nanoparticles, with the addition of non-structural (but functional) additives such as flame retardants, since this is one of the most important, ongoing requirements in the transportation industries. In this vein, the effect of nanoparticulate addition on properties which take into account the increasingly high performance demanded of composites such as exposure to aggressive environments such as heat and moisture, needs to be investigated. Another crucial area in the development of these new materials is the effect of nanoparticle addition on their fatigue properties, particularly as a function of environmental conditions.

2.6 References

1. Njuguna, J., Pielichowski, K., (2003) *Advanced Engineering Materials* 5:769.
2. Chiao, L., (1990) *Macromolecules* 23:1286.
3. Wang, Z., Massam, J., Pinnavaia, T.J., (2000) *Epoxy-Clay Nanocomposites*, in *Polymer-Clay Nanocomposites*, T.J. Pinnavaia, Beall, G.W. (eds). Chichester: Wiley, p. 127.
4. Solomon, D.H., Hawthorne, D.G., (1983) *Chemistry of Pigments and Fillers*. New York: John Wiley & Sons.
5. Hoffmann, U., Endell, K., Wilm, D., (1933) *Z. Krist.* 86:340.
6. Lan, T., Kaviratna, P.D., Pinnavaia, T.J., (1995) *Chem. Mater*. 7:2144.
7. Kornmann, X., Lindberg, H., Berglund, L.A., (2001) *Polymer* 42:1303.
8. Theng, B.K.G., (1974) *The Chemistry of Clay-Organic Reactions*. London: A Hilger.
9. Theng, B.K.G., (1979) *Formation and Properties of Clay-Polymer Complexes*. Development in Soil Science 9. New York: Elsevier.
10. Giannelis, E.P., (1992) *Materials & Design* 13:100.
11. Akelah, A., Kelly, P., Qutubuddin, S., Moet, A., (1994) *Clay Minerals* 29:169.
12. Zilg, C., Mülhaupt, R., Finter, J., (1999) *Macromol. Chem. Phys*. 200:661.
13. Wang, Z., Pinnavaia, T.J., (1998) *Chem. Mater*. 10:1820.
14. Fletcher, R.A., Bibby, D.M., (1987) *Clays and Clay Minerals* 35:318.
15. Gu, B., Ouyang, X., Cai, C., Jia, D., (2003) *Journal of Polymer Science: Part B: Polymer Physics* 42:1192.
16. Le Pluart, L., Duchet, J., Sautereau, H., Gerard, J.-F., (2003) *Macromol. Symp.* 194:155.
17. Fröhlich, J., Golombowski, D., Thomann, R., Mülhaupt, R., (2004) *Macromol. Mater. Eng.* 289:13.
18. Mardis, W.S., (1984) *JAOCS* 61:382.
19. Pignon, F., Magnin, A., Piau, J.-M., (1998) *J. Rheol*. 42:1349.
20. Becker, O., Simon, G.,Varley, R., Halley, P., (2003) *Polym. Eng. Sci*. 43:850.
21. Becker, O., Sopade, P., Bourdonnay, R., Halley, P. J., Simon, G. P., (2003) *Polym. Eng. Sci*. 43:1683.
22. Le Pluart, L., Duchet, J., Sautereau, H., Halley, P., Gerard, J.-F., (2004) *Applied Clay Science* 25:207.
23. Brown, J.M., Curliss, D., Vaia, R.A., (2000) *Chem. Mater*. 12:3376.
24. Salahuddin, N., Moet, A., Hiltner, A., Baer, E., (2002) *Eur. Polym. J*. 38:1477.
25. Park, J.H., Jana, S.C., (2003) *Macromolecules* 36:2758.
26. Kong, D., Park, C.E., (2003) *Chem. Mater.* 15:419.
27. Becker, O., Simon, G.P., (2005) *Adv. Polym. Sci*. 179:29.
28. Triantafillidis, C.S., LeBaron, P., Pinnavaia, T.J., (2002) *Chem. Mater*. 14:4088.
29. Triantafillidis, C.S., LeBaron, P., Pinnavaia, T.J., (2002) *Journal of Solid State Chemistry* 167:354.
30. Ma, J., Yu, Z.-Z., Zhang, Q.-X., Xie, X.-L., Mai, Y.-W., Luck, I., (2004) *Chemistry of Materials* 16:757.
31. Chen, B., Liu, J., Chen, H., Wu, J., (2004) *Chem. Mater*. 16:4864.
32. Wang, K., Chen, L., Wu, J., Toh, M.L., He, C., Yee, A.F., (2005) *Macromolecules* 38:788.
33. Wang, K., Wang, L., Wu, J., Chen, L., He, C., (2005) *Langmuir* 21:3613.
34. Lan, T., Pinnavaia, T.J., (1994) *Chem. Mater*. 6:2216.
35. Zerda, A.S., Lesser, A.J., (2001) *J Polym Sci Part B: Polym Phys* 39:1137.

36. Nakatini, A.I., Hjelm, R.P., Gerspacher, M., Krishnamoorti, R., (2000) *MRS Proceedings* Vol. 661, KK7.2, MRS, Boston MA, Nov 27–Dec 1, 2000.
37. Kornmann, X., Thomann, R., Mülhaupt, R., Finter, J., Berglund, L.A., (2002) *Polym. Eng. Sci*. 42:1815.
38. Becker, O., Varley, R.J., Simon, G.P., (2002) *Polymer* 43:4365.
39. Becker, O., Cheng, Y.-B., Varley, R. J., Simon, G. P., (2003) *Macromolecules* 36:1616.
40. Kornmann, X., Berglund, L.A., Sterte, J., (1998) *Polym. Eng. Sci*. 38:1351.
41. Messersmith, P.D., Giannelis, E.P., (1994) *Chem. Mater*. 6:1719.
42. Gensler, R., Gröppel, P., Muhrer, V., Müller, N., (2002) *Part. Part. Syst. Charact*. 19:293.
43. Shah, A.P., Gupta, R.K., Gangarao, H.V.S., Powell, C.E., (2002) *Polym. Eng. Sci*. 42:1852.
44. Becker, O., Varley, R. J., Simon, G. P., (2004) *Eur. Polym*. J. 40:187.
45. Massam, J., Wang, Z., Oinnavaia, T. J., Lan, T., Beall, G., (1998) *Polym. Mater. Sci. Eng*. 78:274.
46. Massam, J., Pinnavaia, T.J., (1998) Clay Nanolayer Reinforcement of a Glassy Epoxy Polymer. *Mater. Res. Soc. Symp. Proc*.
47. Chen, J.-S., Poliks, M.D., Ober, C.K., Zhang, Y., Wiesner, U., Giannelis, E., (2002) *Polymer* 43:4895.
48. Lu, H., Nutt, S., (2003) *Macromolecules* 36:4010.
49. Zax, D.B., Yang, D. K., Santos, R. A., Hegemann, H., Giannellis, E. P., Manias, E., (2000) *J. Chem. Phys*. 112:2945.
50. Park, S.-J., Seo, D.-I., Lee, J.-R., (2002) *Journal of Colloid and Interface Science* 251:160.
51. Lee, D.C., Jang, L.W., (1997) *Journal of Applied Polymer Science* 68:1997.
52. Gu, A., Liang, G., (2003) *Polymer Degradation and Stability* 80:383.
53. Hussain, M., Varley, R. J., Mathys, Z., Cheng, Y.-B., Simon, G. P., (2003) *Journal of Applied Polymer Science* 91(2), 1233–1253.
54. Gilman, J.W., Kashiwagi, T., Nyden, M., Brown, J. E. T., Jackson, C. L., Lomakin, S., Giannelis, E. P., Manias, E., (1999) 'Chapter 14 – Flammability Studies of Polymer Layered Silicate Nanocomposites: Polyolefin, Epoxy, and Vinyl Ester Resins', in *Chemistry and Technology of Polymer Additives*, Ak-Malaika S., Golovoy, A., Wilkie, C. A. (eds). Oxford: Blackwell Science, p. 249.
55. Gilman, J.W., Kashiwagi, T., (2000) *Polymer-Layered Silicate Nanocomposites with Conventional Flame Retardants*. *Polymer-Clay Nanocomposites*, Pinnavaia, J.T. Beall, G. W. (eds), Chichester: Wiley, p. 193.
56. Anaheim, C., Kilger, H.S., Rasmussen, B., Pilato, L.A., Toile, T.B., (1998) Materials and Process Affordability Keys to the Future. SAMPE Symposium and Exhibition, 43rd International Proceedings. 43. Book 1 of 2 books. Society for the Advancement of Material and Process Engineering (SAMPE), 1053–1066.
57. Sue, H.J., Gam, K.T., (2004) *Chem. Mater.* 16:242.
58. Sue, H.J., Gam, K.T., Bestaoui, N., Clearfield, A., Miyamoto, M., Miyatake, N., (2004) *Acta Materialia* 52:2239.
59. Wetzel, B., Haupert, F., Zhang, M.Q., (2003) *Composites Science and Technology* 63:2055.
60. Pan, L., Chen, D., He, P., Zhu, X., Weng, L., (2004) *Materials Research Bulletin* 39:243.

61. Lelarge, R., Becker, O., Simon, G. P., Rieckmann, T., (unpublished data).
62. Isik, I., Yilmazer, U., Bayram, G., (2003) *Polymer* 44:6371.
63. Fröhlich, J., Thomann, R., Mülhaupt, R., Gryshchuk, O., Karger-Kocsis, J., (2004) *Journal of Applied Polymer Science* 92:3088.
64. Fröhlich, J., Thomann, R., Mülhaupt, R., (2003) *Macromolecules* 36:7205.
65. Balakrishnan, S., Raghavan, D., (2004) *Macromol. Rapid Communications* 25:481.
66. Ratna, D., Becker, O., Krishnamurthy, R., Simon, G. P., Varley, R., (2003) *Polymer* 44:7449.
67. Cao, Y., Sun, J., Yu, D.H., (2002) *Journal of Applied Polymer Science* 83:70.
68. Rice, B.P., Chen, C., Cloos, L., Curliss, D., (2001) *SAMPE* 37:7.
69. Becker, O., Varley, J. R., Simon, G. P., (2003) *Journal of Materials Science Letters* 22:1411.
70. Haque, A., Shamsuzzoha, M., Hussain, F., Dean, D., (2003) *Journal of Composite Materials* 37:1821.
71. Chisholm, N., Mahfuz, H., Rangari, V.K., Ashfaq, A., Jeelani, S., (2005) *Composite Structures* 67:115.

3

Biodegradable polymer/layered silicate nanocomposites

S SINHA RAY and M BOUSMINA, Laval University, Canada

3.1 Introduction

From the last decade of the twentieth century one of the rapidly growing areas for the use of plastics is packaging. Convenience and safety, low price and good aesthetic qualities are the most important factors determining rapid growth in the use of plastics for manufacturing of packing. Recently, out of total plastic production, 41% is used in packing industries, and of these 47% are used for the packing of foodstuffs.[1] These are generally made from polyolefins, polystyrene (PS), poly(vinyl chloride) (PVC), etc., are mostly produced from fossil fuels, consumed and discarded into the environment, ending up as spontaneously *undegradable* wastes. That means that a total of 40% of packaging refuse is practically eternal, and the question of what to do with plastics refuse is becoming a global environmental problem.

There are two approaches that can be used for protecting the environment from these plastic wastes: The first of these is the storage of wastes at landfill sites. But because of very fast development of society, satisfactory landfill sites are also limited. Moreover, burial of plastics wastes in landfill is a time bomb, with today's problems being shifted onto the shoulders of future generations.

The second approach can be divided into two steps: incineration and recycling. Incineration of plastic wastes always produces a large amount of carbon dioxide and creates global warming, and sometimes produces toxic gases, which again contribute to global pollution. On the other hand, recycling seems to solve the problem, even though it requires considerable expenditure of labour and energy: removal of plastics wastes, separation according to the types of plastics, washing, drying, grinding and, only then, reprocessing to final product. So this process makes packaging more expensive and the quality of the recycled plastic is also lower than that of the material produced directly by the primary manufacturer.

Given this background, there is an urgent need for the development of *green polymeric materials* that would not involve the use of toxic or noxious components in their manufacture and could degrade in the natural environment.

For these reasons, throughout the world today, the development of biodegradable materials with balanced properties has been a subject of much research within the community of materials scientists and engineers.

Preparation of blends or conventional composites using inorganic or natural fillers, respectively are among the routes to improve some of the properties of biodegradable polymers. Thermal stability, gas barrier properties, strength, low melt viscosity, and slow biodegradation rate are among the properties to be controlled. Nano reinforcements of biodegradable polymers have strong promise in designing eco-friendly green nanocomposites for several applications. A fairly new area of composites has emerged in which the reinforcing material has the dimensions in nanometric scale. Such composites are called nanocomposites. One of the reasons for this attention is that due to the 'nano-scale' dispersion, even with very low levels of nanofillers (= 5 wt.%), which results in high aspect ratio and high surface area, the reinforcement efficiency of nanocomposites can match that of conventional composites with 40 to 50% of loading of classical fillers. Currently various nano reinforcements are being developed, but the most heavily researched type of nanocomposites uses layered silicate clay mineral as the reinforcing phase.[2] Because of its easy availability, low cost and more importantly it is environmental friendly.[2]

This chapter highlights the major developments in this area during the last decade. The various techniques used to prepare biodegradable polymers/layered silicate nanocomposites, their physicochemical characterization, and the improved mechanical and materials properties, their biodegradability, processing, and future prospect of biodegradable nanocomposites will be discussed.

3.2 Definition and categories of biodegradable polymers

Biodegradable polymers are defined as those that undergo microbially induced chain scission leading to the mineralization. Specific conditions in terms of pH, humidity, oxygenation and the presence of some metals are required to ensure the biodegradation of such polymers. Biodegradable polymers may be made from bio-sources like corn, wood cellulose, etc. or can also be synthesized by bacteria from small molecules like butyric acid or valeric acid that give polyhydroxybutyrate (PHB) and polyhydroxyvalerate (PHV). Other biodegradable polymers can be derived from the petroleum sources or may be obtained from mixed sources of biomass and petroleum. The best known petroleum source-derived biodegradable polymers are aliphatic polyester or aliphatic-aromatic copolyesters, but biodegradable polymers made from renewable resources like polylactides (PLA) are attracting much more attention because of greater eco-friendliness in their origin in contrast to the fully petroleum-based biodegradable polymers and maintenance of carbon dioxide (CO_2) balance after their composting.

3.3 Properties and drawbacks of biodegradable polymers

Most biodegradable polymers have excellent properties comparable to many petroleum-based plastics, are readily biodegradable, and may soon be competing with commodity plastics. So, biodegradable polymers have great commercial potential for bio-plastic, but some of the properties such as brittleness, low heat distortion temperature, low gas permeability, low melt viscosity for further processing, etc., restrict their use in a wide range of applications. Therefore, modification of the biodegradable polymers through innovative technology is a formidable task for materials scientists. On the other hand, nano reinforcement of pristine polymers to prepare nanocomposites has already proven to be an effective way to improve these properties concurrently.[2] So, preparation to processing of biodegradable polymer-based nanocomposites, that is, green nanocomposites are the road to the future and considered as the next generation of materials.

3.4 Polymer/layered silicate nanocomposite technology

Recently, the utility of inorganic nanoparticles as additives to enhance the polymer performance has been established. Various nano reinforcements currently being developed are nano-clay (layered silicates),[2–6] cellulose nano-whiskers,[7] ultra fine layered titanate,[8] and carbon nanotubes.[9–11] Carbon nanotubes, however, are the most promising of the new nanomaterials. Carbon nanotube-based polymer composites are poised to exhibit exceptional mechanical, thermal and electrical properties.[11]

Of particular interest are polymer and organically modified layered silicate (OMLS) nanocomposites because of their demonstrated significant enhancement, relative to an unmodified polymer resin, of a large number of physical properties, including barrier, flammability resistance, thermal and environmental stability, solvent uptake, and rate of biodegradability.[2] These improvements are generally attained at lower silicate content (≤ 5 wt.%) compared to that of conventional filled systems. For these reasons polymer/OMLS nanocomposites are far lighter in weight than conventional composites, and this makes them competitive with other materials for specific applications. Furthermore, the nanoscale morphology affords opportunity to develop model systems consisting entirely of interfaces, and to study the structure and dynamics of confined and tethered chains using conventional bulk characterization techniques such as differential scanning calorimetry, thermally stimulated current, rheology, NMR and various kinds of spectroscopy.[12–15]

The main reason for these improved properties in nanocomposites is the nanometer scale of the dispersed fillers and the interfacial interaction between

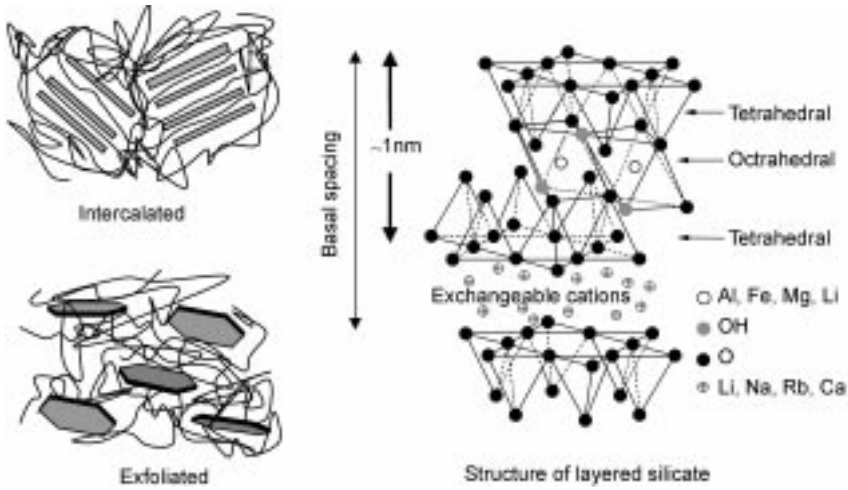

3.1 Structure of layered silicate and schematic illustration of two different types of thermodynamically achievable polymer/layered silicate nanocomposites.

matrix and OMLS as opposed to conventional composites.[16] Layered silicates have layer thickness in the order of 1 nm and very high aspect ratios (e.g. 10–1000). A few weight percent of OMLS that are properly dispersed throughout the matrix thus create a much higher surface area for polymer filler interactions than do conventional composites. On the basis of the strength of the polymer/OMLS interaction, structurally two different types of nancomposites are achievable (see Fig. 3.1): (i) intercalated nanocomposites, where insertion of polymer chains into the silicate structure occurs in a crystallographically regular fashion, regardless of polymer to OMLS ratio, and a repeat distance of few nanometers, and (ii) exfoliated nanocomposites, in which the individual silicate layers are separated in polymer matrix by average distances that depend totally on the OMLS loading.

One successful method to prepare polymer/layered silicate nanocomposites is to intercalate polymers into the silicate galleries. Generally, intercalation of polymer chains into the silicate galleries is done by using one of the following three approaches:

1. *Insertion of suitable monomers in the silicate galleries and subsequent polymerization*.[17–18] In this method, the layered silicate is swollen within the liquid monomer, or a monomer solution, so the polymer formation can occur between the intercalated sheets. Polymerization can be initiated either by heat or radiation, by the diffusion of a suitable initiator, or by an organic initiator or catalyst fixed through cation exchange inside the interlayer before the swelling step.
2. *Direct insertion of polymer chains into the silicate galleries from solution*.[19] This is based on a solvent system in which the polymer is soluble and the

silicate layers are swellable. The layered silicate is first swollen in a solvent, such as chloroform. When the polymer and layered silicate solutions are mixed, the polymer chains intercalate and displace the solvent within the interlayer of the silicate. Upon solvent removal, the intercalated structure remains, resulting in nanocomposite. The thermodynamics involved in this method are described in the following. For the overall process, in which polymer is exchanged with the previously intercalated solvent in the gallery, a negative variation in the Gibbs free energy is required. The driving force for the polymer intercalation into layered silicate from solution is the entropy gained by desorption of solvent molecules, which compensates for the decreased entropy of the confined, intercalated chains.[20] Using this method, intercalation only occurs for certain polymer/solvent pairs. This method is good for the intercalation of polymers with little or no polarity into layered structures, and facilitates production of thin films with polymer-oriented clay intercalated layers. However, from an industrial point of view, this method involves the use of copious amounts of organic solvents, which are usually environmentally unfriendly and economically prohibitive.

3. *Melt intercalation*.[21–25] Recently, the melt intercalation technique has become the standard for the preparation of polymer/layered silicate nanocomposites and is also quite compatible with the recent industrial techniques. During polymer intercalation from solution, a relatively large number of solvent molecules have to be desorbed from the host to accommodate the incoming polymer chains. The desorbed solvent molecules gain one translational degree of freedom, and the resulting entropic gain compensates for the decrease in conformational entropy of the confined polymer chains. Therefore, there are many advantages to direct melt intercalation over solution intercalation. For example, direct melt intercalation is highly specific for the polymer, leading to new hybrids that were previously inaccessible. In addition, the absence of a solvent makes direct melt intercalation an environmentally sound and an economically favourable method for industries from a waste perspective.

   This process involves annealing a mixture of the polymer and OMLS above the softening point of the polymer, statically or under shear.[26] While annealing, the polymer chains diffuse from the bulk polymer melt into the galleries between the silicate layers. A range of nanocomposites with structures from intercalated to exfoliate can be obtained, depending on the degree of penetration of the polymer chains into the silicate galleries. So far, experimental results indicate that the outcome of polymer intercalation depends critically on silicate functionalization and constituent interactions. The present authors observe that (a) an optimal interlayer structure on the OMLS, with respect to the number per unit area and size of surfactant chains, is most favorable for nanocomposite formation, and (b) polymer

intercalation depends on the existence of polar interactions between the OMLS and the polymer matrix.

In order to understand the thermodynamic issue associated with nanocomposite formation, Vaia *et al.*[20.26] applied a mean-field statistical lattice model, reporting that calculations based on the mean-field theory agree well with experimental results. Details regarding this model and explanation are presented in Vaia *et al.*[20] Although there is an entropy loss associated with the confinement of a polymer melt with nanocomposite formation, this process is allowed because there is an entropy gain associated with the layer separation, resulting in a net entropy change near to zero. Thus, from the theoretical model, the outcome of nanocomposite formation *via* polymer melt intercalation depends primarily on energetic factors, which may be determined from the surface energies of the polymer and OMLS.

3.5 Structure and properties of layered silicates

The commonly used layered silicates for the preparation of polymer/layered silicate (PLS) nanocomposites belong to the same general family of 2:1 layered- or phyllosilicates (see Fig. 3.1).[27] Their crystal structure consists of layers made up of two tetrahedrally coordinated silicon atoms fused to an edge-shared octahedral sheet of either aluminum or magnesium hydroxide. The layer thickness is around 1 nm, and the lateral dimensions of these layers may vary from 30 nm to several microns or larger, depending on the particular layered silicate. Stacking of the layers leads to a regular van der Waals gap between the layers called the *interlayer* or *gallery*. Isomorphic substitution within the layers (for example, Al^{+3} replaced by Mg^{+2} or Fe^{+2}, or Mg^{+2} replaced by Li^{+1}) generates negative charges that are counterbalanced by alkali and alkaline earth cations situated inside the galleries. This type of layered silicate is characterized by a moderate surface charge known as the cation exchange capacity (CEC), and is generally expressed as mequiv/100 gm. This charge is not locally constant, but varies from layer to layer, and must be considered as an average value over the whole crystal.

Montmorillonite, hectorite, and saponite are the most commonly used layered silicates for the preparation of nanocomposites. Layered silicates have two types of structure: tetrahedral-substituted and octahedral-substituted. In the case of tetrahedrally-substituted layered silicates the negative charge is located on the surface of silicate layers, and hence, the polymer matrices can interact more readily with these than with octahedrally-substituted material.

Two particular characteristics of layered silicates that are generally considered for PLS-nanocomposites are the ability of the silicate particles to disperse into individual layers, and the ability to fine-tune their surface chemistry through ion exchange reactions with organic and inorganic cations.

These two characteristics are, of course, interrelated since the degree of dispersion of layered silicate in a particular biopolymer depends on the interlayer cation. Pristine layered silicates usually contain hydrated Na^+ or K^+ ions.[28] Obviously, in this pristine state, layered silicates are only miscible with hydrophilic polymers, such as poly(ethylene oxide) (PEO),[19] or poly(vinyl alcohol) (PVA).[29] To render layered silicates miscible with biodegradable polymer matrices, one must convert the normally hydrophilic silicate surface to an organophilic one, making the intercalation of many polymers possible. Generally, this can be done by ion-exchange reactions with cationic surfactants including primary, secondary, tertiary, and quaternary alkylammonium or alkylphosphonium cations. Alkylammonium or alkylphosphonium cations in the organosilicates lower the surface energy of the inorganic host and improve the wetting characteristics of the polymer matrix, and result in a larger interlayer spacing. Additionally, the alkylammonium or alkylphosphonium cations can provide functional groups that can react with the polymer matrix, or in some cases initiate the polymerization of monomers to improve the adhesion between the inorganic and the polymer matrix.[30,31]

3.6 Techniques used for the characterization of nanocomposites

Generally, the state of dispersion and exfoliation of nanoparticles has typically been established using X-ray diffraction (XRD) analysis and transmission electron micrographic (TEM) observation. Due to its easiness and availability XRD is most commonly used to probe the nanocomposite structure[2–6] and occasionally to study the kinetics of the polymer melt intercalation.[32] By monitoring the position, shape, and intensity of the basal reflections from the distributed silicate layers, the nanocomposite structure (*intercalated* or *exfoliated)* may be identified. For example, in an *exfoliated* nanocomposite, the extensive layer separation associated with the delamination of the original silicate layers in the polymer matrix results in the eventual disappearance of any coherent X-ray diffraction from the distributed silicate layers. On the other hand, for *intercalated* nanocomposites, the finite layer expansion associated with the polymer intercalation results in the appearance of a new basal reflection corresponding to the larger gallery height.

Although XRD offers a convenient method to determine the interlayer spacing of the silicate layers in the original layered silicates and in the intercalated nanocomposites (within 1–4 nm), little can be said about the spatial distribution of the silicate layers or any structural nonhomogeneities in nanocomposites. Additionally, some layered silicates initially do not exhibit well-defined basal reflections. Thus, peak broadening and intensity decreases are very difficult to study systematically. Therefore, conclusions concerning the mechanism of nanocomposites formation and their structure based solely on

XRD patterns are only tentative. On the other hand, TEM allows a qualitative understanding of the internal structure, spatial distribution and dispersion of the nanopartilces within the polymer matrix, and views of the defect structure through direct visualization. However, special care must be exercised to guarantee a representative cross section of the sample.

Both TEM and XRD are essential tools[33] for evaluating nanocomposite structure. However, TEM is time-intensive, and only gives qualitative information on the sample as a whole, while wide-angle peaks in XRD allow quantification of changes in layer spacing. Typically, when layer spacing exceed 6-7 nm in intercalated nanocomposites or when the layers become relatively disordered in exfoliated nanocomposites, associated XRD features weaken to the point of not being useful. However, recent simultaneous small angle X-ray scattering (SAXS) and XRD studies yielded quantitative characterization of nanostructure and crystallite structure in some nanocomposites.[34–35]

3.7 Biodegradable polymers and their nanocomposites

3.7.1 Biodegradable polymers from renewable resources

Biodegradable polymers from renewable resources have attracted much attention in recent years.[36] Renewable sources of polymeric materials offer an alternative to maintaining sustainable development of economically and ecologically attractive technology. The innovations in the development of materials from biodegradable polymers, the preservation of fossil-based raw materials, complete biological degradability, the reduction in the volume of garbage and compostability in the natural cycle, protection of the climate through the reduction of carbon dioxide released, as well as the application possibilities of agriculture resources for the production of green materials are some of the reasons why such materials have attracted academic and industrial interest. So far the following renewable sources based biodegradable polymers have been used for the preparation of nanocomposites: polylactide (PLA),[37–64] poly(3-hydroxy butyrate) (P3HB)[65] and its copolymers,[66] thermoplastic starch,[67–73] plant oils,[74–76] cellulose,[77] gelatine,[78] Chitosan,[79–80] etc. In this section the synthesis and characterization of renewable sources-based biodegradable polymers/layered silicate nanocomposites are summarized.

PLA and its nanocomposites

Ogata *et al.*[37] first prepared PLA/OMLS blends by dissolving the polymer in hot chloroform in the presence of dimethyl distearyl ammonium modified MMT (2C18MMT). In the case of PLA/MMT composites, XRD and SAXS results showed that the silicate layers forming the clay could not be intercalated in the

PLA/MMT blends, prepared by the solvent-cast method. In other words, the clay existed in the form of tactoids, consisting of several stacked silicate monolayers. These tactoids are responsible for the formation of particular geometrical structures in the blends, which leads to the formation of superstructures in the thickness of the blended film, and that may lead to such a structural feature as an increase in theYoung's modulus of the hybrid. After that Bandyopadhyay *et al.*[38] reported the preparation of intercalated PLA/OMLS nanocomposites with much improved mechanical and thermal properties. In recent publications,[39–42] Sinha Ray *et al.* used the melt intercalation technique for the preparation of intercalated PLA/layered silicate nanocomposites. For nanocomposites (PLACNs) preparation, octadecyl ammonium modified MMT (C18MMT) and PLA were first dry-mixed by shaking them in a bag. The mixture was then melt-extruded using a twin-screw extruder operating at 190ºC to yield light gray strands of PLACNs. Nanocomposites loaded with a very small amount of *o*-PCL as a compatibilizer were also prepared in order to understand the effect of *o*-PCL on the morphology and properties of PLACNs.[41]

XRD patterns and TEM observations clearly established that the silicate layers of the clay were intercalated, and randomly distributed in the PLA matrix. Incorporation of a very small amount of *o*-PCL as a compatibilizer in the nanocomposites led to better parallel stacking of the silicate layers, and also to much stronger flocculation due to the hydroxylated edge-edge interaction of the silicate layers. Owing to the interaction between clay platelets and the PLA matrix in the presence of a very small amount of *o*-PCL, the strength of the disk-disk interaction plays an important role in determining the stability of the clay particles, and hence the enhancement of mechanical properties of such nanocomposites.

In subsequent research, Sinha Ray *et al.*[53] prepared PLACNs with organically modified synthetic fluorine mica (OMSFM). For the characterization of structure and morphology of prepared nanocomposites they first used XRD and conventional TEM (CTEM), and then CTEM and high resolution TEM (HRTEM), they examined the final structure of PLACNs. The compositions of nanocomposites of PLA with OMSFM are summarized in Table 3.1. The XRD

Table 3.1 Characteristic parameters of neat PLA and PLACNs

Characteristic parameters	Neat PLA	PLACN4	PLACN7	PLACN10
OMSFM	—	4	7	10
$M_w \times 10^{-3}$ (g.mol^{-1})	177	150	140	130
PDI	1.58	1.55	1.60	1.66
T_g (ºC)	60	56	55	55
T_m (ºC)	168.0	168.6	167.7	166.8
T_c (ºC)	127.2	99.4	97.6	96.5
X_c (%)	36	40	46	43

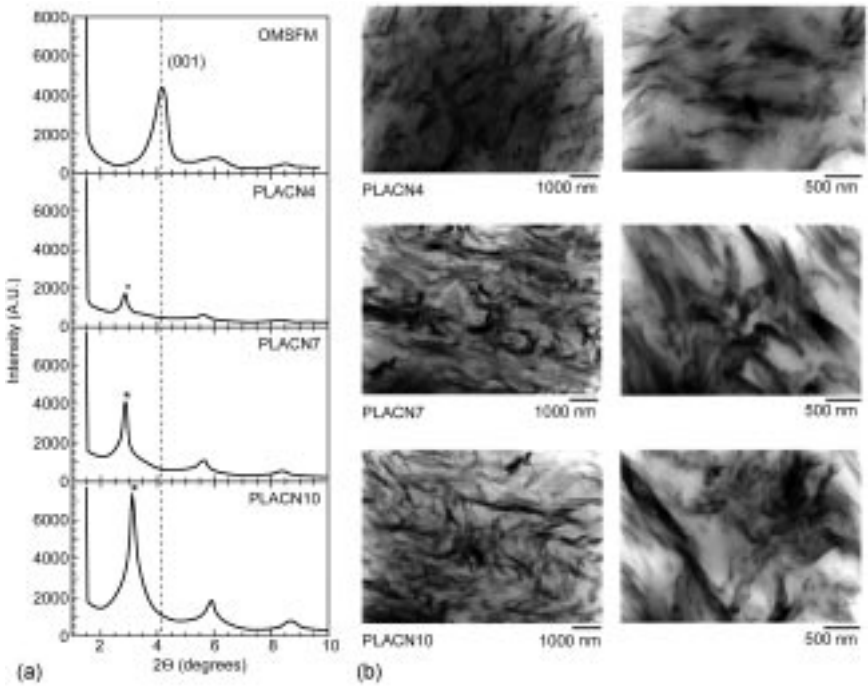

3.2 (a) XRD patterns of OMSFM powder and various PLACNs. The dashed line indicates the location of the silicate (001) reflection of OMSFM. The asterisks indicate the (001) peak for OMSFM dispersed in a PLA matrix.[53] Reproduced from Sinha Ray, Yamada, Okamoto, Ogami and Ueda by permission of American Chemical Society, USA. (b) Bright field CTEM images of various crystallized PLACNs pellets.[53] Reproduced from Sinha Ray, Yamada, Okamoto, Ogami and Ueda by permission of American Chemical Society, USA.

patterns of this series of nanocomposites are shown in Fig. 3.2(a). The mean interlayer spacing of the (001) plane (d_{001}) for the OMSFM powder obtained by XRD measurements is 2.08 nm. In the case of PLACN4, a sharp peak was observed at $2\theta = 2.86^{\circ}$, corresponding to the (001) plane of the stacked and intercalated silicate layers dispersed in the PLA matrix, accompanied by the appearance of a small peak at $2\theta = 5.65^{\circ}$. After calculation, it was confirmed that this peak was due to the (002) plane (d_{002}) of the dispersed OMSFM in the PLA matrix. With increasing OMSFM loading, these peaks become stronger and shifted toward the higher diffraction angle at $2\theta = 3.13^{\circ}$ and 5.9°, respectively, for PLACN10. These behaviours are due to a decrease in percentage of polymer chains to be intercalated and increase stacking of the intercalated silicate layers with increasing OMSFM loading. The width of the XRD peak, β (measured by the full-width at half-maxima), is inversely proportional to the coherence length of scattering intensities, D, and therefore reflects the coherent order of the silicate layers.[81] Since the width of the basal spacing of OMSFM decreased

sharply after nanocomposite preparation with PLA, therefore, the coherency of the intercalated silicate layers is much higher than that of un-intercalated silicate layers and increases with increasing OMSFM content. Thus, on the basis of XRD data the authors came to the conclusions that PLA chains were intercalated, have a strong effect on the layer structure of OMSFM, and sharply change the coherence length of the intercalated silicate crystallites with increasing OMSFM loading.[82]

Figure 3.2(b) shows the CTEM images of PLACNs pellets of two different magnifications in which dark entities are the cross section of the intercalated OMSFM layers and bright areas are the PLA matrix. TEM images clearly demonstrate the stacked and intercalated silicate layers, were nicely dispersed in the PLA matrix. In their further study, [44–46,49,57–59] Sinha Ray *et al.* prepared a series of PLACNs with various kinds of OMLS to investigate the effect of OMLS on the morphology, properties, and biodegradability of PLA.

Maiti *et al.*[47] prepared a series of PLACNs with three different types of pristine layered silicates, i.e. saponite (SAP), MMT, and mica, and each was modified with alkylphosphonium salts having different chain lengths. In their work, they first tried to determine the effect of varying the chain length of the alkylphosphonium modifier on the properties of organoclay, and how the various clays behave differently with the same organic modifier. They also studied the effects of dispersion, intercalation, and aspect ratio of the clay on the material properties. Recently, Paul *et al.*[48] reported the preparation of plasticized PLA/MMT nanocomposites by melt intercalation technique. The used OMLS was MMT modified with bis-(2-hydroxyethyl) methyl (hydrogenated tallow alkyl) ammonium cations. XRD analyses confirmed the formation of intercalated nanocomposites.

In further work, the same group reported the preparation of exfoliated PLA/clay nanocomposites by in-situ coordination-insertion polymerization method.[62] They used two different kinds of OMLS (C30B and C25A) for the preparation of nanocomposites. In a typical synthetic procedure, the clay was first dried overnight at 70ºC in a ventilated oven, and then, at the same temperature under reduced pressure, directly in the flame-dried polymerization vial for 3.5 h. A 0.025 molar solution of L,L-lactide in dried tetrahydrofuran (THF) was then transferred under nitrogen to the polymerization vial and the solvent was eliminated under reduced pressure. Polymerizations were conducted in bulk at 120ºC for 48 h, after 1 h of clay swelling in the monomer melt. When C30B was used, the polymerization was co-initiated by a molar equivalent of $AlEt_3$, with respect to the hydroxyl groups born by the ammonium cations of the filler, in order to form aluminium alkoxide active species, and was added before the L,L-lactide. $Sn(Oct)_2$ (monomer/$Sn(Oct)_2$ = 300) was used to catalyze the polymerization of L,L-lactide in the presence of C25A.

Figure 3.3 represents the XRD patterns of two different types of OMLS and their corresponding nanocomposites each containing 3 wt.% of OMLS. The

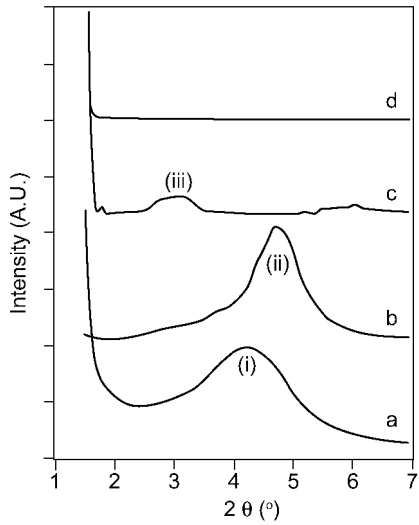

3.3 XRD patterns of (a) C25A, (b) C30B, (c) PLA/3 wt.% C25A, and (d) PLA/3 wt.% C30B; as noted for interlayer distances of (i) 2.04 nm, (ii) 1.84 nm, and (iii) 3.28 nm.[62] Reproduced from Paul, Alexandre, Degée, Calberg, Jérôme and Dubois by permission of Wiley-VCH Verlag GmbH, Germany.

XRD pattern of C30B-based nanocomposite shows completely featureless diffraction whereas C25A-based nanocomposite was a fully intercalated nanocomposite. Although the XRD pattern was featureless in the case of C30B-based nanocomposite, TEM images clearly indicates the stacking of the silicate layers. In general, many factors other than layer disorder such as intercalate composition and silicate concentration, may contribute to a featureless diffraction.[57] Thus, on the basis of XRD patterns it is very difficult to make conclusions about the structure of the nanocomposites exhibiting featureless diffraction patterns. Therefore, according to the present authors this is not an exfoliated nanocomposite, better to say intercalated or more precisely disordered intercalated nanocomposite.

To understand the effect of OMLS on the structure and properties of nanocomposites, Chang *et al.*[61] reported the preparation of PLA-based nanocomposites with three different kinds of OMLS via solution intercalation method. They used *N*, *N*′,-dimethylacetamide (DMA) for the preparation of nanocomposites. XRD patterns indicate the formation of intercalated nanocomposites whatever the OMLS. TEM images proved that most of the clay layers were dispersed homogeneously in the PLA matrix, although some clusters or agglomerated particles were also detected.

In a recent report, Krikorian and Pochan[63] explored the effect of compatibility of different organic modifiers on the overall extent of dispersion of layered silicate layers in a PLA matrix. Three different commercially available

OMLS were used as a reinforcement phase. Nanocomposites were prepared by using the solution-intercalation film-casting technique. For each composition, 100 mg of PLA was dissolved in 10 mL of dichloromethane. OMLS dispersions (<0.1 wt.%) were obtained by suspension of well-dried OMLS in a separate beaker of dichloromethane. Both the PLA solution and OMLS suspension were sonicated separately for 30 min at room temperature. The final mixture was further sonicated for 30 min. The mixture was then cast on a glass surface and kept in a desiccator for controlled evaporation of the solvent over 2 days.

According to the XRD and TEM studies an increase in miscibility of the surfactant with the matrix increases the tendency of the silicate layers to exfoliate. In the case of C30B clay, the favourable enthalpic interaction between diols present in the organic modifier with the C=O bonds present in the PLA backbone is a significant factor for driving the system toward exfoliation.

Very recently, Lee *et al.*[64] prepared PLA/MMT nanocomposite for the purpose of tailoring mechanical stiffness of PLA porous scaffold systems. They used a salt leaching/gas foaming method for the preparation of nanocomposites scaffold. A viscous solution with the concentration of 0.1 g/ml was prepared by dissolving PLA polymer in chloroform. NH_4HCO_3/NaCl salt particles sieved in the range of 150–300 μm and dimethyl dehydrogenated tallow ammonium modified MMT (2M2HT-MMT) clays were added to the PLA solution and mixed thoroughly. The amount of the 2M2HT-MMT clay was 2.24, 3.58, and 5.79 vol.% to PLA. The paste mixture of polymer/salts/solvent was then cast into a special device equipped with a glass slide as a sheet model. The cast film was obtained after being air-dried under atmospheric pressure for 2 h. When the film became semi solid, a two-step salt leaching was performed. The film was first immersed in 90ºC hot water to leach out the NH_4HCO_3 particles, concomitantly generating gaseous ammonium and carbon dioxide in the polymer matrix. When no gas bubbles were generated, the film was subsequently immersed into another beaker containing 60ºC water for 30 min to leach out the remaining NaCl particles, and then freeze dried for two days. The XRD patterns revealed that pure 2M2HT-MMT demonstrated a sharp peak at $2\theta = 3.76^{\circ}$ and this peak was not observed in the case of nanocomposite, indicating the formation of exfoliated PLA/2M2HT-MMT nanocomposite, but they did not report any TEM image.

PHB and its nanocomposites

PHB is a naturally occurring polyester produced by numerous bacteria in nature as intracellular reserve of carbon or energy. Maiti *et al.*[65] reported the first preparation of PHB/OMLS nanocomposites (PHBCNs) by melt intercalation method. They used three different kinds of OMLS for the preparation of nanocomposites. Nanocomposites were prepared by using a twin-screw extruder operated at 180ºC. The extruded strands were palletized and then dried under

vacuum at 80ºC to remove residual water. XRD patterns clearly show the formation of well-ordered intercalated nanocomposites. TEM image of PHBCN supports the formation of intercalated structure. The fate of the polymer after nanocomposites preparation was measured by GPC. The nanocomposites based on organically modified MMT shows severe degradation but surprisingly no degradation was found with nanocomposites based on organically modified fluoromica. There is no explanation for how organically modified fluoromica played to protect the system, but the present authors believe the presence of Al Lewis acid sites, which catalyze the hydrolysis of ester linkages at high temperature, may be one of the reasons.

Although thermoplastic PHB is a naturally occurring biodegradable material, it is very unstable and degrades at elevated temperature near its melting point. Because of this thermal instability, commercial applications of PHB have been extremely limited. For this reason, investigators have shown that copolymers of PHB, such as poly(3-hydroxybutyrate-co-3-hydroxyvalerate) (PHBV),[83] have much improved chemical and physical properties for a wide range of applications. The processing and the mechanical properties of PHBV have been improved over those of PHB; however, PHBV has some disadvantages such as slow rate of crystallization, relatively more complex processing condition, low elongation at break, etc., to be resolved for many applications. In order to overcome these drawbacks, Chen *et al.*[66] prepared nanocomposites of PHBV using the solution intercalation technique. Unfortunately they did not report the structure and morphology of the prepared nanocomposites.

Thermoplastic starch (TPS) and its nanocomposites

In the family of renewable sources-based biodegradable polymeric materials, starch has been considering as one of the most promising materials because it is readily available and may form cost effective end products.[84] Starch is known to be completely biodegradable in soil and water.[85] It also promotes the biodegradability of an undegradable plastic and can also be used together with fully biodegradable synthetic plastics;[86–87] producing biodegradable blends at low cost. The starch remains in granular form in the plastic matrix and thus may act as a filler.

One of the major problems with granular starch composites is their limited processability, due to the large particle sizes (5–100 μm). Therefore, it is very difficult to make blown thin films of starch for packing applications. For this reason, TPS has been developed by gelatinizing granular starch with 6–10 wt.% moisture in the presence of heat and pressure.[88–89] However, poor water resistance and low strength are limiting factors for the use of materials manufactured only from TPS, and hence it is often blended with other polymers. For example, it was found that the ductility of the gelatinized starch plasticized with approximately 15 wt.% of glycerol and 10 wt.% of water was improved by

adding EVOH.[90] Now if we are able to improve the mechanical properties of this polymer further by the addition of a small amount of environmentally benign filler, this polymer will find applications in more special or severe circumstances. On the other hand, OMLS is environmentally friendly, naturally abundant and economic. So, in order to realize the combination of the biodegradable TPS and the high strength and stability of the OMLS, TPS/OMLS nanocomposites were prepared using different techniques. The main objective of this section is to describe the preparation of biodegradable nanocomposites of TPS and OMLS, and to investigate the structure and morphology by using XRD and TEM.

De Carvalho *et al.*[67] reported the first preparation of TPS/kaolin hybrids by melt intercalation technique using a twin screw extruder. Subsequently Park *et al.*[68] reported the preparation of TPS/clay nanocomposites by melt intercalation in detail. Three organically modified MMT with different ammonium cations and one unmodified Na^+-MMT were used for the preparation of nanocomposites. In a typical preparative method TPS and clays were first dried under vacuum at 80ºC for at least 24 h. After that TPS was mixed with clays in a Haake-Rheocoder 600 roller mixer for 20 min. The contents of clays were fixed at 5 wt.%. The rotor speed was 50 rpm and the temperature was set at 110ºC. From the XRD patterns and TEM observation it is clearly established that the nanostructure of polymer/clay hybrids depends on the compatibility and interaction among the polymer, the silicate layers, and the nature of surfactant used for the modification of silicate layers. Due to the strong polar interactions between a small amount of polar hydroxyl group of water in the TPS chain and the silicate layer of the pristine MMT, the polymer chains were intercalated into the silicate layers of pristine MMT and formed an intercalated TPS/MMT nanocomposite. On the other hand, C6A and C10A were too hydrophobic and did not match the polarity of TPS, and discouraged TPS chain intercalation. The hydrophilicity of C30B is much higher than that of C6A or C10A, because of the presence of hydroxyethyl group, favouring the intercalation of TPS chains into the silicate layers. However, the introduction of these polar hydroxyethyl groups also enhances the interaction of the ammonium cation with the silicate surface. As a result, replacement of the surface contracts by TPS chains will be less favourable, impeding the extensive intercalation. For this reason TPS/C30B also did not show intercalation of TPS chains into the C30B silicate layers. In another publication[70] Park *et al.* reported the preparation of melt intercalated TPS/Na^+-MMT nanocomposites with high clay content.

Recently, Wilhelm *et al.*[71] modified glycerol-plasticized starch films by the addition of various layered compounds as filler, two being of natural origin (kaolinite, a natural mineral clay and hectorite, a cationic exchange mineral clay) and two synthetic (layered double hydroxide, LDH, an anionic exchanger, and brucite having a neutral structure). Glycerol-plasticized starch/layered compounds composite films were prepared from the respective aqueous

suspensions (30 ml) by casting. The starch/hectorite proportions were 100/0, 95/05, 90/10, 85/15, 80/20, and 70/30, relative to starch mass on a dry basis, with a total mass of 1.3 g. The composite films of starch with other layered compounds were prepared only in the 90/10 proportions. Initially, the layered material was dispersed in distilled water (10 ml) for 24 h and added to aqueous starch dispersion (20 ml). This suspension was degassed and heated to boiling point, in a sealed tube, for 30 min with continuous stirring in order to gelatinize the starch granules. Glycerol 920% w/w, relative to starch on a dry basis was added to the heated solution and the mixtures then poured into polypropylene dishes, allowing solvent evaporation at 40–50ºC. The films were maintained at 43% relative humidity atmosphere for 3 weeks. This level was obtained by exposing the films to the vapours of an aqueous potassium carbonate solution in a closed desiccator at 25ºC. In order to understand the hypothesis of glycerol and starch intercalation in the layered compounds, XRD analyses were carried out. XRD patterns demonstrated that the interplanar basal distance of kaolinite, LDH-CO_3 and brucite was not affected by the presence of a starch matrix while the hectorite showed an increase in interlayer spacing. In this composite, the hectorite dispersion was governed by the glycerol plasticizer. In unplasticized composite films, hectorite was exfoliated. Substitution of plasticized starch matrix by a plasticized oxidized starch or native/oxidized starch (the oxidation reaction was performed by de Nooy and Besemer procedure using 2,2,6,6-tetramethylpiperidine-oxyl (TEMPO))[91] blend gives rise to composite with higher interlayer basal distances, indicating that both short oxidized starch chains and glycerol molecules were intercalated between clay layers. In the absence of glycerol, oxidized starch was preferentially intercalated in relation to native starch chains due to its lower chain size and probable higher diffusion rate. In another recent report, McGlashan and Halley[72] reported the preparation of starch/polyester/clay nanocomposites. They also used melt-blending method for the preparation of nanocomposites. XRD data indicated that the best results were obtained for 30 wt.% starch blends, and the level of delamination depends on the ratio of starch to polyester and the amount of OMLS added.

Plant oils-based polymers and their nanocomposites

Recently, Uyama *et al.*[92–95] synthesized new reactive polymers from plant oils under mild reaction conditions. The single-step synthesis of plant oil-based crosslinkable polyesters has been achieved through lipase-catalyzed polymerization of divinyl sebacate and glycerol in the presence of unsaturated fatty acids under mild reaction conditions.[96–97] Furthermore, the unsaturated group in the side chain was converted to an epoxy group by the use of lipase as a catalyst.[98] These oil-based polymeric materials, however, do not show properties of rigidity and strength required for structural applications by themselves. On the basis of this background, Uyama *et al.*[74–76] synthesized new green nanocomposites

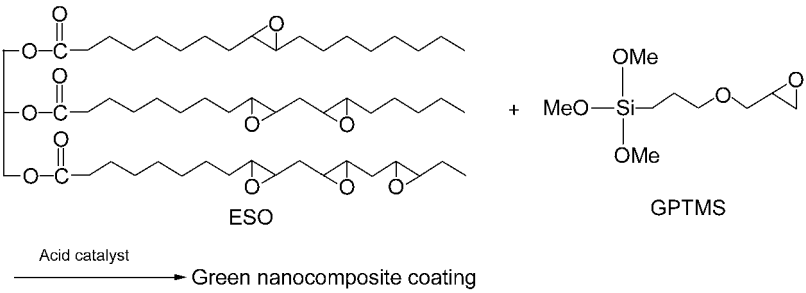

3.4 Synthetic procedure of green nanocomposite coating.[76] Reproduced from Tsujimoto, Uyama and Kobayashi by permission of Wiley-VCH Verlag GmbH, Germany.

consisting of plant oils and clay with much improved properties. They used epoxidized soybean oil (ESO) as an organic monomer. The nancomposite was synthesized by the curing of ESO using thermally latent cationic catalyst in the presence of octadecyl ammonium modified MMT (OMM) at 150ºC. During the thermal treatment, the cross-linking of the epoxy group took place, yielding an insoluble polymer network. The scheme of the nanocomposite synthesis is presented in Fig. 3.4.

Figure 3.5 shows XRD patterns of OMM and nanocomposites with four different OMM loadings. The mean interlayer spacing of the (001) plane (d_{001}) for OMM is 1.9 nm. In the case of the nanocomposite with 5 wt.% OMM content, the coherent order of silicate layers was completely destroyed, suggesting that silicate layers of OMM may be exfoliated. But when they used OMM content more than 10 wt.%, intercalated nanocomposites were formed. TEM

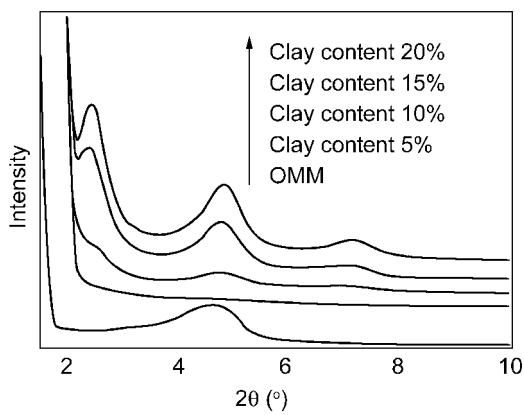

3.5 XRD patterns of octadecyl modified clay and ESO-clay nanocomposites with clay contents of 5, 10, 15, and 20 wt.%.[74] Reproduced from Uyama, Kuwabara, Tsujimoto, Nakano, Usuki and Kobayashi by permission of American Chemical Society, USA.

images clearly indicated the formation of mixed exfoliated and intercalated nanocomposites.

Cellulose and its nanocomposites

Cellulose from trees is attracting interest as a substitute for petroleum feedstock in making plastic in the commercial market.[99] Cellulose plastics like cellulose acetate (CA), cellulose acetate propionate (CAP), and cellulose acetate butyrate (CAB) are thermoplastic materials produced through esterification of cellulose. Recently, Misra *et al.*[77] successfully used melt intercalation technique for the fabrication of cellulose nanocomposites from CA, triethyl acetate (TEC) and organically modified clay. The effects of processing conditions, amount of plasticizer, various types (such as C30B, nanomer I.34TCN, I.34TCA, and I.44PA) and content of organo-clays on the performance of these nanocomposites has been evaluated. For the nanocomposites preparation, the CA and clay were first dried under vacuum at 80ºC for at least 24 h. The CA powder and TEC plasticizer (CA : TEC = 80 : 20 by wt.%) were then mixed mechanically with a high speed mixer for about 5 min. The CA plasticized mixture was then stored in a zip-lock bag for specific time periods. This pre-plasticized mixture was then mixed with desired quantities of organo-clays followed by mixing with the high-speed mixer. Then such mixtures (CA + TEC + organo-clay) were melt-compounded at 160–220ºC for 2–20 minute at 100 rpm with micro-compounding moulding equipment. XRD patterns and TEM observations revealed that only C30B exhibited the best exfoliation among all the organo-clay used in their work. In their subsequent research, they prepared CA/TEC-based nanocomposites of C30B with different clay content. For the CA/TEC/C30B nanocomposite system with 5 and 10 wt.% C30B content, no clear peaks were observed at around $2\theta = 2.75^{\circ}$ thus suggesting the exfoliated morphologies. The TEM images show that the CA/TEC/C30B nanocomposite system with 5 and 10 wt.% C30B shows better exfoliation and ordered intercalated structure than the counterpart nanocomposite having 15 wt.% clay content. The dispersion of clays becomes poorer with increasing clay content.

Gelatin and its nanocomposites

Gelatin (also called gelatine) is prepared by the thermal denaturation of collagen, isolated from animal skin and bones, with very dilute acid. It can also be extracted from fish skins. Gelatin contains a large number of glycine (almost 1 in 3 residues, arranged every third residue), proline and 4-hydroxyproline residues. This polymer can be used as a valuable biopolymer in tissue engineering;[100] its poor mechanical properties especially in wet state limit its application as a structural biomedical. Therefore, the reinforcement of gelatine materials becomes a challenge for worldwide researchers. Many attempts have

been made such as vapour crosslink,[101] orientation technique,[102] and gelatine-based composites filled with hydroxyapatite, tricalcium phosphate,[103] and carbon fibre[104] and great progress has been achieved. However, the strength is still not high enough, especially in the wet state. Given this background, Zheng *et al.*[78] prepared gelatine/MMT nanocomposites for the first time with the expectation that materials properties of gelatine will be improved after nanocomposite preparation. Nanocomposites were prepared directly with pristine MMT and gelatin in aqueous solution. In a typical preparative route 1 gm of gelatine powder was soaked in 50 ml of deionized water and heated at 70ºC to obtain a homogeneous solution. Then this solution was added drop wise into 2 wt.% ultrasonically prepared MMT suspension under vigorous stirring at 70ºC. The achieved homogeneous mixture was then poured into the specially self-made mould and dried at ambient temperature for several days. Unfortunately, these authors did not report the structure and morphology of prepared hybrids.

Chitosan and its nanocomposites

Chitosan, poly-β(1,4)-2-amino-2-deoxy-D-glucose, is the deacetylated product of chitin, poly(*N*-acetyl-D-glucosamine), a natural polymer found in the exoskeletons of crustaceans and insects and in the cell wall of fungi and microorganisms. Because of the polycationic nature of the chitosan in acidic media, this biopolymer also appears as an excellent candidate for intercalation in pristine MMT by means of cationic exchange process.[80] In a typical synthetic procedure, chitosan solutions were first prepared by the addition of the corresponding amounts of polysaccharide to 1% (v/v) acetic acid, and after the resulting solution was stirred for about 4 h, the pH of the polysaccharide solution was adjusted to 4.9 with NaOH before being mixed with the clay suspension. Chitosan solutions containing 20.1, 40.2, 80.5, and 161.0 mg of biopolymer in 25 ml of solution were slowly added to a 2% clay suspension, at 323 K, to obtain nanocomposites with initial chitosan/clay ratios of 0.25:1, 0.5:1, 1:1, and 2:1, respectively. For the preparation of nanocomposites with chitosan/clay ratios of 5:1 and 10:1, chitosan solutions with 402.5 mg of biopolymer in 125 ml and 805.0 mg in 250 ml, respectively, were mixed with the clay suspension. In all of the cases, the resulting mixture was stirred for 2 days and finally washed with purified water until free from acetate. The intercalation of the biopolymer in the silicate galleries was confirmed by the decrease of 2θ values in the XRD patterns while the chitosan/clay ratio increases. In acidic solutions, chitosan shows an extended structure that may facilitate the biopolymers intercalation in the clay interlayer space[105] in opposition to analogous polysaccharides with coiled or helicoidal structures that report only adsorbed in the external surface of silicate layers.[106] The XRD pattern of a chitosan film indicated a d_{001} spacing of 0.38 nm, indicating that chitosan film consists of arrays of parallel sheets of chains in a way similar to that of chitin.[107–108] Therefore, the interlayer space in

the nanocomposites prepared from chitosan/clay ratios of 0.25:1 and 0.5:1 can be related to the thickness of one chitosan sheet and, thus, to its intercalation as a monolayer covering the interlayer surface of the clay. Above such chitosan/clay ratios, the increase of the basal spacing can be explained as the uptake of two chitosan layers by the clay.

3.7.2 Biodegradable polymers from petroleum sources

Recently, a broad range of synthetic biodegradable resins based on aliphatic polyesters and their co-polymers have been commercialized by various companies. Demand for biodegradable materials with excellent materials properties is said to be growing at a rapid rate. Synthetic biodegradable polyesters are generally made by polycondensation method and raw materials are obtained from petrochemical feedstocks. Unlike other petrochemical-based resins that take centuries to degrade after disposal, these synthetic polyesters break down rapidly into carbon dioxide, water, and humus in appropriate conditions where they are exposed to the combined attacked of water and microorganisms. These products meet advanced composting standards (e.g. UK, USA and Japan), typically breaking down in twelve weeks under aerobic conditions. Poly(butylene succinate) (PBS),[109–118] poly(butylene succinate)-*co*-adipate (PBSA),[119] aliphatic polyesters,[120–122] poly(ϵ-caprolactone) (PCL),[123–144] poly(vinyl alcohol) (PVA)[29,140–144] are the most important polymers in this series. In this section the preparation and characterization of various petroleum sources based biodegradable polymers and their layered silicate nanocomposites are summarized.

PBS and its nanocomposites

One of the most promising polymers in the family of synthetic biodegradable polyesters is PBS under the trade name of 'Bionolle', and it is chemically synthesized by the polycondensation of 1,4-butanediol with succinic acid.[145,146] PBS is a commercially available, aliphatic polyester with many interesting properties, including biodegradability, melt processability, and thermal and chemical resistance.[147] PBS has excellent processability, so can be processed in the field of textile into melt blow, multifilament, monofilament, flat, and split yarn and also in the field of plastics into injection moulded products, thus being a promising polymer for various potential applications.[148–149] High molecular weight PBS is generally prepared by a coupling reaction of relatively low molecular weight PBS in the presence of hexamethylene diiocynate (OCN-C6H12-NCO) as a chain extender.[150]

So, increasing the realization of the various intrinsic properties of PBS, coupled with the knowledge of how such properties can be improved to achieve the compatibility with thermoplastics processing, manufacturing, and end-use

requirements, has fuelled technological and commercial interest in PBS. Of particular interest is recently developed nanocomposite technology consisting of a polymer and OMLS because they often exhibit remarkably improved mechanical and various other properties as compared to those of virgin polymer containing a small amount of layered silicate (≤ 5 wt.%).

Sinha Ray *et al.*[109,110] reported the first preparation of PBS/OMLS nanocomposites (PBSCNs) by simple melt extrusion of PBS and OMLS. Two different types of OMLS, MMT modified with octadecylammonium chloride (C18MMT) and saponite modified with quaternary hexadecyl tri-*n*-butylphosphonium bromide (qC16SAP), were used for the preparation of nanocomposites. For nanocomposites preparation, the PBS and OMLS were first dry-mixed by shaking them in a bag. The mixture was then melt-extruded using a twin screw extruder operated at 150ºC to yield nanocomposite strands. The colour of the strands depends on the colour of the OMLS used. The composition of PBSCNs is presented in Table 3.2. The strands were palletized and dried under vacuum at 75ºC. XRD pattern for the pure C18MMT powder and various representative PBSCNs are presented in Fig. 3.6(a). Figure 3.6(b) represents XRD patterns for pure qC16SAP powder, neat PBS and the corresponding PBSCNs respectively. Figure 3.7 show the results of TEM bright field images of various PBSCNs corresponding to the XRD patterns as shown respectively in Figs 3.6(a) and 3.6(b), in which dark entities are the cross section of intercalated organoclay layers. The figures show both larger view, showing the dispersion of the clay within the PBS matrix, and a higher magnification, permitting the observation of discrete clay layers. For PBSCN1, the silicate layers were intercalated but in the case of PBSCN3, the intercalated, stacked, and flocculated silicate layers were randomly oriented in the PBS matrix. Actually, there is a large anisotropy of the stacked silicate layers. The size of the some of the stacked-silicate layers appears to reach about 600–700 nm in length, however, the authors were not able to estimate precisely the thickness from the TEM images. On the other hand,

Table 3.2 Composition and characteristic parameters of PBSCNs.[110] Reproduced from Sinha Ray, Okamoto and Okamoto by permission of American Chemical Society, USA

Samples	Type of OMLS	Composition, wt.% PBS	OMLS	$M_w \times 10^{-3}$ (g/mol)	M_w/M_n
PBS	—	100	—	103	4.0
PBSCN1	C18MMT	98.5	1.5 [1.07]	100	3.8
PBSCN2	C18MMT	97.5	2.5 [1.73]	99	3.6
PBSCN3	C18MMT	96.0	4.0 [2.80]	97	4.3
PBSCN4	C18MMT	94.5	5.5 [3.60]	100	4.5
PBSCN5	qC16SAP	98.5	1.5 [1.04]	98	3.9
PBSCN6	qC16SAP	94.5	5.5 [3.84]	98	3.8

Value in the parenthesis indicates the wt.% of inorganic part.

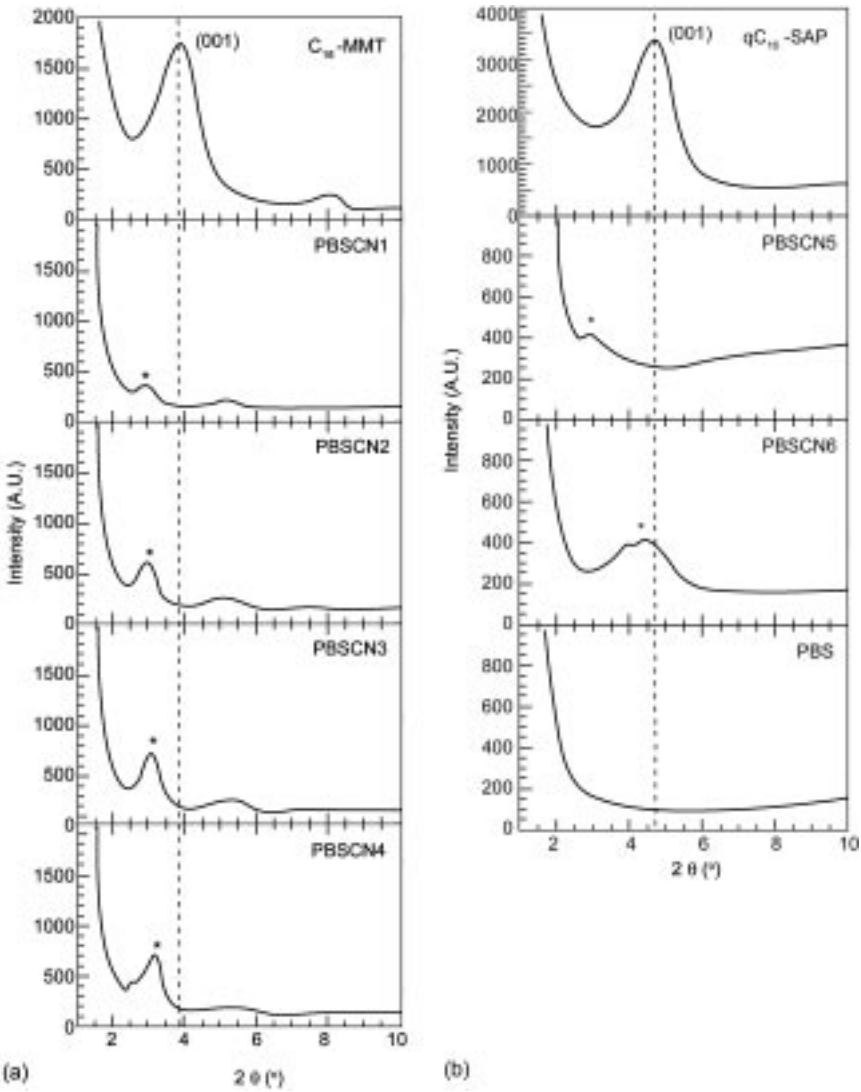

3.6 (a) XRD patterns for pure C18MMT powder and corresponding PBSCNs. The dashed line indicates the location of the silicate (001) reflection of C18MMT. The asterisks indicate (001) peak for C18MMT dispersed in PBS matrix. (b) WAXD patterns for pure qC16MMT powder and corresponding PBSCNs. The dashed line indicates the location of the silicate (001) reflection of qC16MMT. The asterisks indicate (001) peak for qC_{16}-mmt dispersed in PBS matrix.[110] Reproduced from Sinha Ray, Okamoto and Okamoto by permission of American Chemical Society, USA.

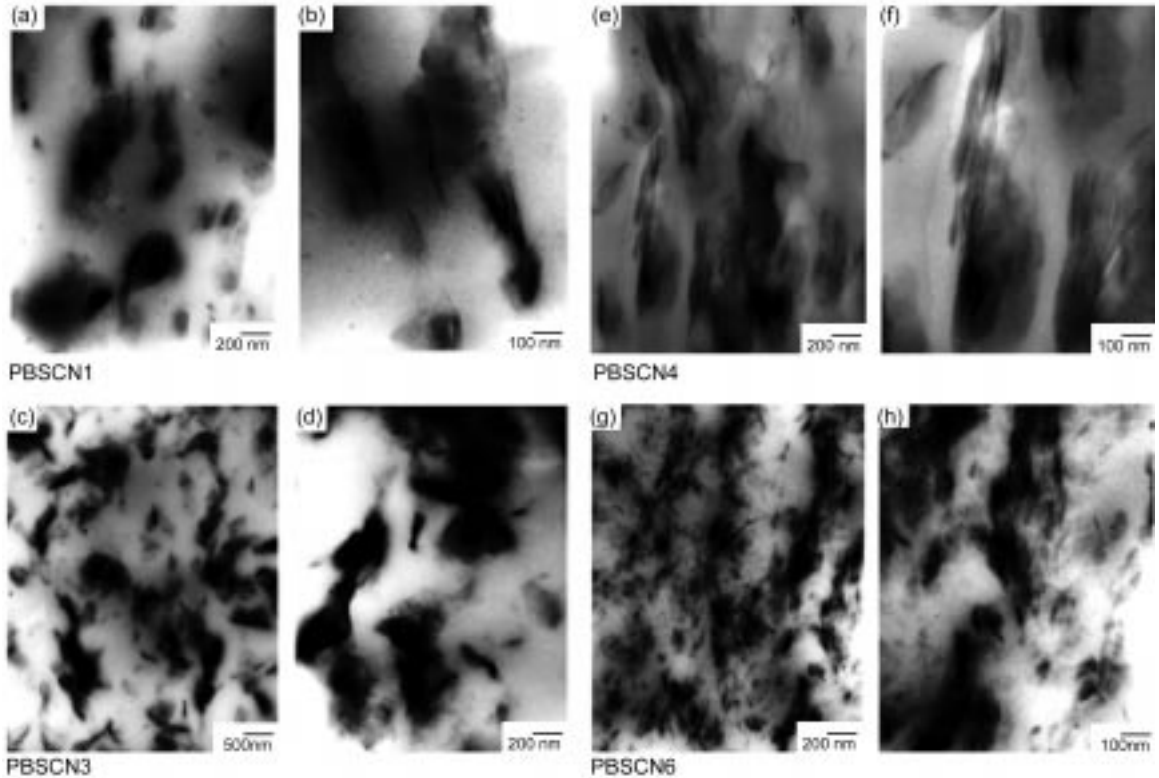

3.7 TEM bright field images of PBSCNs: (a) PBSCN1 (×100000), (b) PBSCN1 (×200000), (c) PBSCN3 (×40000), (d) PBSCN3 (×100000), (e) PBSCN4 (×100000), (f) PBSCN4 (×200000), (g) PBSCN6 (×100000), and (h) PBSCN6 (×200000) in which dark entities are the cross section of the intercalated or exfoliated silicate layers.[110] Reproduced from Sinha Ray, Okamoto and Okamoto by permission of American Chemical Society, USA.

silicate layers which were well intercalated with strong flocculated structure were formed with PBSCN4.

At the other extreme, the TEM images of PBSCN6 show fine and almost uniform distribution of clay particles in the PBS matrix where the clay particles exhibit both perpendicular and planar alignment to the sample surface. From the TEM images, it becomes clear that there were intercalated and disordered stacks of silicate layers coexisting in the PBSCN6 structure. The intercalated structures are characterized by a parallel stacking that gives rise to the XRD reflection of PBSCN6 in Fig. 3.6(b), whereas the disordered clay formations have no periodic stacking and thus remain XRD silent. Thus, on the basis of XRD patterns and TEM observations, the authors concluded that PBSCNs prepared using C18MMT lead to the formation of ordered intercalated nanocomposites with flocculated structure and coherence order of the silicate layers gradually increases with increasing OMLS content, while those prepared with qC16SAP leads to the formation of either near to exfoliate or disordered intercalated nanocomposites depending on the amount of clay loading. In their subsequent research,[112,115] they used dioctadecyl dimethyl ammonium modified MMT for the preparation of PBS nanocomposites. Recently, Mitsunaga *et al.*[113,114] prepared PBS/OMLS nanocomposites by melt extrusion technique. They used maleic anhydride grafted PBS for the preparation of nanocomposites. XRD patterns and TEM observations clearly indicates the formation of intercalated nanocomposites.

Biodegradable aliphatic polyesters

Biodegradable aliphatic polyesters (BAPs), which are usually synthesized from a diol and dicarboxylic acid through a condensation polymerization, are considered to be the most promising biodegradable plastics because of their low production costs and easy processability in large-scale production. Difficulties are encountered, however, in their practical application because of their low melting temperature and poor thermal stability. If the properties of BAPs can be further improved by preparation of nanocomposite with OMLS, this polymer will become more suitable for a wide range of applications. Lim *et al.*[120] prepared BAP/MMT nanocomposites by solvent cast method using chloroform as a co-solvent. XRD analyses and TEM observation established the intercalated structure of these nanocomposites. Recently, Lee *et al.*[121] reported the preparation of biodegradable polyester/OMLS nanocomposites using a melt intercalation method. Two kinds of OMLS, C30B and C10A, with different ammonium cations located in the silicate galleries were chosen for the nanocomposite preparation. The WAXD patterns and TEM observations showed a higher degree of intercalation for C30B-based nanocomposites as compared to that of C10A-based nanocomposites. It was hypothesized that this behaviour may be due to the stronger hydrogen-bonding interaction between the polymer

and the hydroxyl group in the galleries of C30B nanocomposites, compared with that of the polyester/C10A nanocomposites.

Recently, Bharadwaj *et al.*[122] describe the preparation of crosslinked polyester/clay nanocomposites by dispersing organically modified MMT in prepromoted polyester resin and subsequently crosslinked using methyl ethyl ketone peroxide catalyst at several clay concentrations. In a typical synthetic procedure, an appropriate amount of the OMLS was first added to the resin and mechanically stirred followed by sonication for 1 h, which resulted in well-dispersed, stable suspensions of the clay in the polyester resin. Crosslinking was initiated by adding ~1.5 vol.% of MEKP catalyst to the resin-clay mixture at room temperature. The crosslinking reaction was noticeably slower at the higher clay concentrations (> 2.5 wt.%). Samples were then allowed to cure for at least 24 h at room temperature. The formation of exfoliated nanocomposites was confirmed by XRD and TEM.

PCL and its nanocomposites

Polycaprolactone (PCL) is linear polyester, manufactured by ring-opening polymerization of ϵ-caprolactone. It is a semicrystalline polymer with a degree of crystallinity around 50%. It has rather low glass transition temperature and melting point. The PCL chain is flexible and exhibits high elongation at break and low modulus. Its physical properties and commercial availability make it very attractive not only as a substitute material for non-degradable polymers for commodity applications but also as a specific plastic in medicine and agricultural areas.[151] The main drawback of PCL is its low melting point (65ºC) which can be overcome by blending it with other polymers[152,153] or by radiation crosslinking processes resulting in enhanced properties for a wide rage of applications.[154] There have been many attempts to prepare PCL/OMLS nanocomposites with much improved mechanical and materials properties compared to those of neat PCL.

In 1993, Messersmith and Giannelis[123] reported the first preparation of PCL-based nanocomposites by in-situ intercalative polymerization method. They used Cr^{+3} exchanged fluorohectorite (FH) for the synthesis of nanocomposite. In a typical synthesis a mixture of 0.1 g of Cr^{+3}FH and 1 g of CL was stirred at 25ºC for 12 h, followed by heating at 100ºC for an additional 48 h. Upon cooling to room temperature, the reaction mixture solidified. The unintercalated PCL fraction of the composite was recovered by dissolving a portion of the product in acetone followed by centrifugation at 3000 rpm for 2 min. Intercalation of the CL monomer was revealed by powder XRD, which shows an increase in the silicate *d*-spacing from 1.28 to 1.46 nm. Energy minimization of the CL structure provided an approximate measure of monomer dimensions, which were then used along the known thickness of the silicate layers to predict layer spacing for various intercalation geometries. The d_{001} spacing observed prior to

polymerization was found to be consistent with the orientation of the CL ring perpendicular to the silicate layers. XRD analysis of the nanocomposite after polymerization indicates a reduction in the silicate *d* spacing from 1.46 to 1.37 nm as presented in XRD pattern. The decrease in the *d* spacing is consistent with the dimensional change accompanying polymerization of CL monomer. Opening of the lactone ring in the monomer to produce a monolayer of fully collapsed PCL chains is accompanied by a decrease in layer spacing as observed with XRD. The observed layer spacing of 1.37 nm correlates as well with the sum of the thickness of the silicate layer (0.96 nm)[155] and the known inter-chain distance (0.4 nm) in the crystal structure of PCL.[123] Repeated washing with a solvent for PCL did not alter the silicate layer spacing, indicating that the interaction between the intercalated polymer and the silicate surface is strong and that intercalation of the PCL is irreversible.

In another report[125] PCL nanocomposites were prepared by a synthetic procedure similar to that initially developed by Usuki *et al.*,[156,157] for nylon 6/OMLS nanocomposites. In its most basic form it involves dispersion of OMLS in an organic monomer, followed by polymerization of the monomer. The corresponding chemical shifts in ^{1}H NMR spectra clearly demonstrate conversion from CL to PCL. Complete conversion of CL to PCL was assumed because residual CL was not detected in the NMR spectra of any of the composites. The peak broadening effect seen in XRD pattern of PCLC2 is believed to be due to the strong attachment of PCL chains to the silicate layers, resulting in partial solid-like behaviour.

The ability to delaminate and disperse the silicate layers in a polymer matrix is directly related to a mumber of factors, including the exchange capacity of the layered silicate, the polarity of the medium, and the chemical nature of the interlayer cations.[2] Messersmith and Giannelis[31] did a series of experiments with different kinds of OMLS indicating that matching the polarities of the surfactant with those of the CL monomer was particularly critical to obtaining good dispersion. Evidence of the importance of the nature of the surfactant was demonstrated by the failure of the less polar dimethyl dioctadecyl ammonium exchanged OMLS to disperse in CL under similar experimental conditions. However, when the protonated form of 12-aminolauric acid was used, delamination of the OMLS into individual layers occurs. The dispersion is maintained after polymerization and the layers ultimately become dispersed within the polymer matrix.

The choice of 12-aminolauric acid, in addition to improving silicate layers delamination, was also useful by the potential of the carboxylic groups to initiate polymerization of CL. Polymerization of lactone monomers can be initiated using a number of different types of catalysts[158–165] including compounds containing labile protons, such as amines, alcohols, and carboxylic acids.[160–165] Initiation with these molecules has been shown to be the result of nucleophilic attack upon the lactone carbonyl group, resulting in ring opening and formation

of a new terminal hydroxyl group.[165] Subsequent propagation then occurs by similar nucleophilic attack by the terminal hydroxyl groups remaining on lactone monomers. By analogy, acid groups ionically bound to the silicate layers at the protonated amine terminus can act as nucleophiles, reacting with CL, which results in addition of one CL unit and production of a terminal hydroxyl group. The reactions occurring between the organic acid group of the OMLS and CL monomer are facilitated and maximized by molecular dispersion of the individual silicate layers in the liquid monomers.

PCL/layered silicate nanohybrids have also been synthesized by ring opening polymerization of CL according to a well-controlled coordination-insertion mechanism.[127] MMT were surface-modified by non-functional (trimethyl hexadecyl ammonium) and hydroxyl functional alkylammonium cations, i.e., (2-hydroxyethyl) dimethyl hexadecyl ammonium. The hydroxyl functions available at the clay surface were activated into tin (II or IV) or Al (III) alkoxide initiators for lactone polymerization, thus yielding surface grafted PCL chain.

Recently, Pantoustier *et al.*[128] used the in-situ intercalative polymerization method for the preparation of PCL-based nanocomposites. They compared the properties of nanocomposites prepared used both pristine MMT, and ω-amino dodecanoic acid modified MMT. For nanocomposite synthesis, the desired amount of pristine MMT was first dried under vacuum at 70ºC for 3 h. A given amount of CL was then added to a polymerization tube under nitrogen and the reaction medium was stirred at room temperature for 1h. A solution of initiator ($Sn(Oct)_2$) or $Bu_2Sn(Ome)_2$) in dry toluene was added to the mixture in order to reach a [monomer]/[Sn] molar ratio equal to 300. The polymerization was then allowed to proceed for 24 h at room temperature. The inorganic content of the composite was measured by TGA. After polymerization, a reverse ion-exchange reaction was used to isolate the PCL chains from the inorganic fraction of the nanocomposite. A colloidal suspension was obtained by stirring 2 g of the nanocomposite in 30 mL of THF for 2 h at room temperature. A solution of 1 wt.% of LiCl in THF was prepared separately. The nanocomposite suspension was added to 50mL of the LiCl solution and left to stir at room temperature for 48h. The resulting solution was centrifuged at 3000 rpm for 30 min. The supernatant was then decanted and the remaining solid washed in 30 mL of THF followed by centrifugation. The combined supernatant was concentrated and precipitated from petroleum ether. The white powder was dried in vacuum at 50ºC.

The polymerization of CL with pristine MMT gives PCL with a molar mass of 4800 g/mol and a narrow distribution. For comparison, the authors also conducted the same experiment without MMT, but found that there is no CL polymerization. These results demonstrate the ability of MMT to catalyze and to control CL polymerization, at least in terms of a molecular weight distribution that remains remarkably narrow. For the polymerization mechanism, the authors assume that the CL is activated through interaction with the acidic site on the

clay surface. The polymerization is likely to proceed via an activated monomer mechanism using the cooperative functions of the Lewis acidic aluminum and Brønsted acidic silanol functionalities on the initiator walls. On the other hand, the polymerization of CL with the protonated ω-amino dodecanoic acid modified MMT yields a molar mass of 7800 g/mol with a monomer conversion of 92% and again a narrow molecular weight distribution. The XRD patterns of both nanocomposites indicate the formation of intercalated structure. In another very recent publication,[129] the same group prepared PCL/MMT nanocomposites using dibutyl tin dimethoxide as an initiator/catalyst in an in-situ ring-opening polymerization of CL.

PCL-based nanocomposites have also been produced by dissolving the polymer in hot chloroform in the presence of OMLS.[140] SAXS and XRD results revealed that the silicate layers forming the clay could not be dispersed individually in the PCL matrix. In other words, the silicate layers existed in the form of tactoids, consisting of several stacked silicate layers. These are responsible for the formation of special geometrical structures in the blends, which leads to the formation of superstructures in the thickness of the blended film.

Recently, Di *et al.*[138] reported the preparation of PCL/OMLS nanocomposites in the molten state, using a twin-screw extruder. They used two different types of OMLS for the preparation of nanocomposites and attempted to determine the dependence of OMLS intercalation and/or exfoliation on the processing conditions and types of OMLS and also the thermal and rheological behaviour of the prepared nanocomposites. Nanocomposites were prepared using a Haake, co-rotating, twin-screw extruder, which was operated at 100 and 180ºC with a screw speed of 100 rpm and the residence time was 12 min.

XRD patterns clearly revealed that the delamination of silicate layers in the PCL matrix was directly dependent on the type of OMLS, the OMLS content, and the processing temperature. The strong interaction between the organic surfactants covering the clay layers and the PCL matrix molecules was favoured in the exfoliation process. Processing at low temperatures resulted in high stress in comparison with that at high temperatures, and this helped with the fracturing of the OMLS particles and caused a good dispersion of them in the PCL matrix. A higher OMLS content hybrid required more processing time for achieving an exfoliation structure than a lower OMLS content hybrid. Lepoittevin *et al.*[130] also used the same method for the production of PCL/OMLS nanocomposites. They also used master batch method for the preparation of PCL-based nanocomposites.[134]

PVA and its nanocomposites

In 1963, D.J. Greenland[139] reported the first fabrication of PVA/MMT composites by a solvent casting method using water as a co-solvent. After that, Ogata *et al.*[140] used the same technique for the production of PVA/MMT

composites. Recently, Strawhecker and Manias[141] have also used the solvent casting method in attempts to produce PVA/MMT nanocomposites films. PVA/MMT nanocomposite films were cast from a MMT/water suspension containing dissolved PVA. Room temperature distilled water was used to form a suspension of Na^+-MMT. The suspension was first stirred for 1h and then sonicated for 30 min. Low viscosity, fully hydrolyzed atactic PVA was then added to the stirring suspension such that the total solid (silicate plus polymer) was 5 wt.%. The mixtures were then heated to 90ºC to dissolve the PVA, again sonicated for 30 min, and finally films were cast in a closed oven at 40ºC for 2 days. The recovered cast films were then characterized by both WAXD and TEM. Both the *d*-spacing and their distribution decrease systematically with increasing MMT wt.% in the nanocomposites. The TEM photograph of 20 wt.% clay containing nanocomposite reveals the co-existence of silicate layers in the intercalated and exfoliated states.

At first glance, this dependence of the intercalated structure and *d*-spacing on the polymer/silicate mass ratio seems to be at odds with the theoretical expectations.[20,166–169] The equilibrium nanocomposite structure predicted from the thermodynamics corresponds to an intercalated periodic nanocomposite with *d*-spacing around 1.8 nm, which is expected to be independent of the polymer-to-silicate composition.[166] However, thermodynamics can only predict the equilibrium structure. In this case, the nanocomposite structure that they found is actually kinetically dictated; in the water solution of PVA and MMT the layers remain in colloidal suspension. Where this suspension is slowly dried, the silicate layers remain distributed and embedded in the polymer gel. Further drying removes all of the water, and although the thermodynamics would predict the MMT layers to re-aggregate in an intercalated fashion, the slow polymer dynamics trap some of the layers apart and therefore remain dispersed in the polymer matrix. Obviously, the kinetic constraints imposed by the polymer become less important as the polymer-to-silicate fraction decreases, and consequently, for higher amounts of MMT, intercalated structures are formed. For these periodic structures, the variation of the *d*-spacing with wt.% of MMT reflects the different polymer-silicate weight ratios, and upon increasing the amount of MMT the intercalated *d*-spacing converges to the equilibrium separation of 1.8 nm.

Recently, Chang *et al.*[143] reported the preparation of PVA-based nanocomposites with three different types of clays, pristine MMT and organically modified MMT. Dodecylammonium modified MMT (C12MMT) and 12-aminolauric modified MMT (C12OOHMMT) was used as OMLS. They used the same solvent casting method for the preparation of nanocomposites but the solvent used was N,N-dimethylacetamide (DMAc) in addition to water. In a typical preparative method, a 50.0 g mixture of DMAc dispersion containing 0.08 g of C12MMT, 4.0 g of PVA, and excess DMAc was stirred vigorously at room temperature for 1 h. The solution was cast onto glass plates, and the

solvent was evaporated in a vacuum oven at 50ºC for 2 days. The films were then cleaned in an ultrasonic cleaner three times for 5 min each time. These films with the solvent removed were dried again in a vacuum oven at 50ºC for 1 day. Na–MMT and Na–SPT (pristine saponite) hybrid films were cast from a water suspension where PVA was dissolved. The suspensions were heated to 70ºC to dissolve the PVA and sonicated for 5 min, and, finally, films were cast in a closed oven at 40ºC for 2 days. The film thickness was 10–15 μm.

XRD patterns and TEM observations respectively indicated the formation of exfoliated nanocomposites when pristine clays were used for the fabrication of nanocomposites. On the other hand, intercalated nanocomposites were produced with OMLS. This implies that the hydrophilic character of clay promotes dispersion of inorganic crystalline layers in water-soluble polymers.

Very recently, Yu *et al.*[144] reported the synthesis of a series of PVA/MMT nanocomposites via in-situ intercalative polymerization with AIBN as initiator. Organic vinyl acetate monomers were first intercalated into the organically modified MMT galleries and followed by a one-step free radical polymerization. The prepared poly(vinyl acetate)/OMLS solution were then saponified via direct hydrolysis with NaOH solution to form PVA/MMT nanocomposites. The synthesized nanocomposites were characterized by FTIR, XRD, SEM, OPM, and TEM. XRD patterns and TEM images established the formation of mixed intercalated/exfoliated structure of the PVA/MMT nanocomposites.

3.8 Properties

Biodegradable nanocomposites consisting of a biodegradable polymer and layered silicate (organically modified or not) frequently exhibit remarkably improved mechanical and various other properties when compared to those of virgin polymers. Improvements generally include a higher modulus both in solid and melt state, increased strength and thermal stability, decreased gas permeability, and increased biodegradability. The main reason for these improved properties in nanocomposites is the stronger interfacial interaction between the matrix and layered silicate, compared with conventional filler-reinforced systems.

3.8.1 Mechanical properties

Dynamic mechanical analysis

Dynamic mechanical analysis (DMA) measures the response of a given material to an oscillatory deformation as a function of temperature. DMA results are composed of three parameters:

(a) the storage modulus (or),
(b) the loss modulus (or), and

(c) tan δ, the ratio (G''/G'), useful for determining the occurrence of molecular mobility transition, such as the glass transition temperature (T_g).

DMA has been used to study temperature dependence of G' of PLA upon nanocomposite formation under different experimental conditions. Figure 3.8

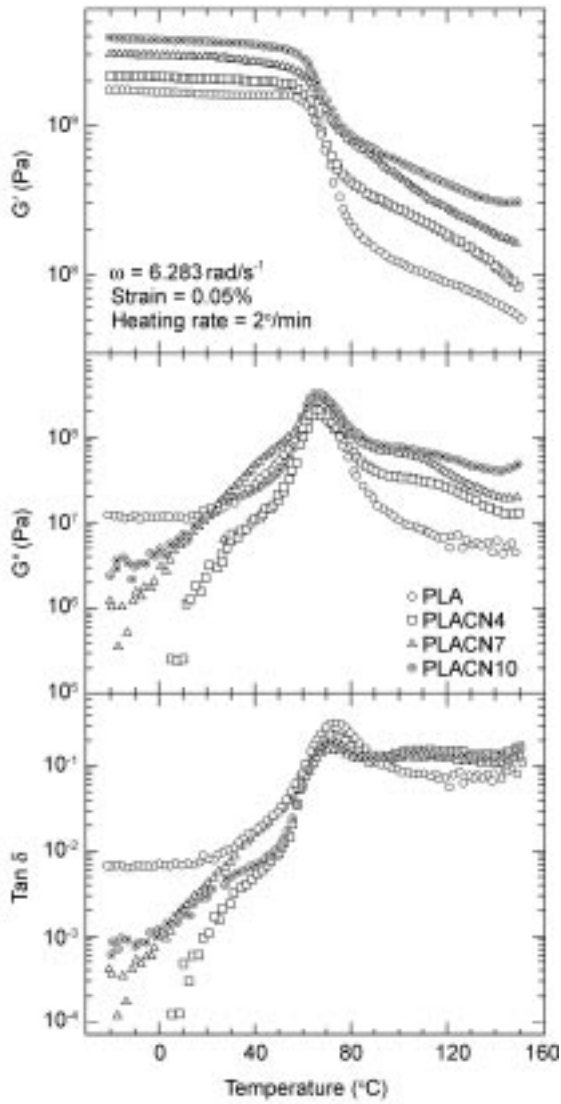

3.8 Temperature dependence of G', G'' and tan δ of neat PLA and PLA/OMSFM nanocomposites.[53] Reproduced from Sinha Ray, Yamada, Okamoto, Ogami and Ueda by permission of American Chemical Society, USA.

shows the temperature dependence of G', G'' and tan δ for various PLA/OMSFM nanocomposites and pristine PLA.[53] For all PLACNs, the enhancement of G' can be seen in the investigated temperature range when compared to the neat PLA, indicating that OMSFM has a strong effect on the elastic properties of virgin PLA. Below T_g, the enhancement of G' is clear for all nanocomposites. On the other hand, all PLACNs show a greater increase in G' at high temperature compared to that of the PLA matrix. This is due to both mechanical reinforcement by the silicate layers and extended intercalation at high temperature.[170] Above T_g, when materials become soft, the reinforcement effect of the silicate layers becomes prominent due to the restricted movement of the polymer chains. This is accompanied by the observed enhancement of G'.

The G' values over different temperature ranges of various PLACNs prepared with C18MMT with or without *o*-PCL and corresponding matrices are summarized in Table 3.3. PLACNs with a very small amount of *o*-PCL (PLACN4 and PLACN5) exhibited a very large enhancement of the mechanical properties compared with that of PLACN2 with comparable clay loading. One of the essential factors governing the enhancement of mechanical properties in the nanocomposites is the aspect ratio of the dispersed clay particles.[171] In TEM figures,[41] it was observed that, in the presence of a very small amount of *o*-PCL, flocculation of the dispersed silicate layers took place, due to the strong edge-edge interaction of the clay platelets. The two-dimensional aspect ratios of the dispersed clay particles L_{LS}/d_{LS} estimated from TEM observation are 22 for PLACN4 and 12 for PLACN2.[41] This large aspect ratio leads to the observed enhancement of mechanical properties. Another factor may be stacked and intercalated silicate layers.

Table 3.3 G' value of various PLACNs and corresponding matrices without clay at different temperature ranges.[41] Reproduced from Sinha Ray, Maiti, Okamoto, Yamada and Ueda by permission of American Chemical Society, USA

Samples	Storage modulus, G' (GPa)			
	-20°C	40°C	100°C	145°C
PLACN1	2.32	2.07	0.16	0.09
PLACN2	2.90	2.65	0.25	0.10
PLACN3	4.14	3.82	0.27	0.19
PLACN4	3.71	3.21	0.43	0.16
PLACN5	3.04	2.60	0.32	0.16
PLACN6	2.08	1.97	0.23	0.08
PLACN7	1.86	1.76	0.16	0.07
PLA	1.74	1.60	0.13	0.06
PLA1	1.73	1.60	0.13	0.06
PLA2	1.68	1.55	0.12	0.06
PLA3	1.67	1.62	0.12	0.06

The hypothesis that an increase in G' depends directly on the aspect ratio of dispersed clay particles is clearly observed in PBSCNs. The temperature dependence of G' for PBS and various PBSCNs are presented in Fig. 3.9. The nature of the enhancement of G' in PBSCNs with temperature is somewhat different from the well-established theories, which explains the similar behaviour observed in systems that are either intercalated (PP-MA/MMT)[171] or exfoliated (N6/MMT).[18] In the later system, G' typically increases by as much as 40–50%, when compared to that of the matrix well below T_g, while above T_g there is a strong enhancement (> 200%) in G'. This behaviour is common for the above reported nanocomposites, and the reason has been shown to be the strong reinforcement effect of the clay particles above T_g (when materials become soft). However, in the case of PBSCNs, the order of enhancement in G' is almost the same below and above T_g, and this behaviour may be due to the extremely low T_g (−29ºC) of the PBS matrix.

In the case of ESO polymer and ESO-$C_{11}CO_2H$-MMT hybrids with different OMLS contents above T_g, E' value of the hybrid became larger than that of the ESO polymer and increased as a function of the OMLS content, which is probably due to the mechanical reinforcement by the silicate layers.[74] The

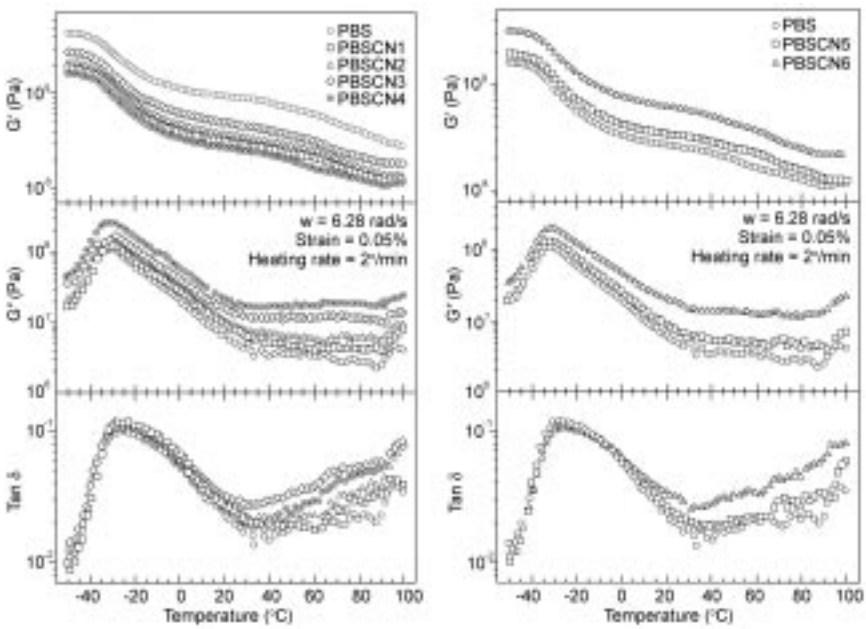

3.9 (a) Temperature dependence of G', G'' and their ratio tan δ for neat PBS and various nanocomposites prepared with C18MMT clay.[110] (b) Temperature dependence of G', G'' and their ratio tan δ for neat PBS and various nanocomposites prepared with qC16SAP clay.[110] Reproduced from Sinha Ray, Okamoto and Okamoto by permission of American Chemical Society, USA.

evolution of the dynamic modulus for the TPS matrix with four different types of layered silicates shows a significant increase in the modulus for the Na^+-Cloisite-based hybrids over a wide range of temperatures from -70 to 70ºC; while the modulus of the organically modified Cloisite-based hybrids is lower than those of the neat TPS.[68] According to the present authors, this behaviour is due to the difference in interaction between pristine Cloisite and organically modified Cloisite with the TPS matrix. Another reason may be the plasticized effect of the hybrids in the presence of excess glycerol used during preparation of TPS hybrids with OMLS. The shifts of the relaxations to lower temperatures supported this assumption. The relaxation processes associated with the glass transition of the amorphous phase of TPS were determined. The relaxation temperatures were taken at the maximum of the respective tan δ peaks**.** The TPS showed two transition peaks at around 7ºC and -64ºC due to the α-relaxation of starch (T_α) and the β-relaxation (T_β) of glycerol, respectively.[172]

When 5 wt.% of pristine clay was added to the TPS matrix, the temperatures of the two peaks were shifted toward higher temperatures indicating that the silicate layers in the hybrids have strong influenced on the TPS chain mobility. On the other hand, the hybrids of C10A and C6A, the two relaxation temperatures were decreased by about 10ºC compared to the pure matrix. The authors believe this behaviour is again due to the poor interaction between the hydrophilic TPS and the hydrophobic OMLS. For this reason, the TPS/C6A hybrid showed the largest shift toward the lower temperature for both of the two transition temperatures.

In the case of PCL/OMLS blends prepared by the solvent casting method,[124] whatever the clay content, was decreased with increasing temperature and a transition was observed at about -60ºC. From the figures it is clearly observed that PCL/OMLS hybrids showed a strong increase in compared to neat PCL. On the other hand, the tan δ curves showed a large maximum at $T = -54$ºC, which corresponds to the T_g of neat PCL; this value was similar to that reported for a crystalline annealed PCL.[173] DMA has also been used to study the temperature dependence G' of neat PVA upon nanocomposite formation. Results showed the storage modulus of PVA was remarkably improved after nanocomposite preparation with OMLS.

Tensile properties

The tensile modulus of a polymeric material has been shown to be remarkably improved when nanocomposites are formed with layered silicates. In the case of biodegradable polymer nanocomposites, most studies report the tensile properties as a function of clay content. In most conventionally filled polymer systems, the modulus increases linearly with the filler volume fraction, whereas for these nanoparticles much lower filler concentrations increase the modulus sharply and to a much larger extent.[2] The dramatic enhancement of the modulus

for such extremely low clay concentrations cannot be attributed simply to the introduction of the higher modulus inorganic filler layers. A theoretical approach is assuming a layer of affected polymer on the filler surface, with a much higher modulus than the bulk equivalent polymer.[174] This affected polymer can be thought of as the region of the polymer matrix that is physisorbed on the silicate surface, and is thus stiffened through its affinity for and adhesion to the filler surfaces.[174] Obviously, for such high aspect ratio fillers as our layered silicate, the surface area exposed to the polymer is huge and the significant increases in the modulus with very low filler content are not surprising. Furthermore, beyond the percolation limit the additional silicate layers are incorporated in polymer regions that are already affected by other silicate layers, and thus it is expected that the enhancement of modulus will be much less dramatic.

Figure 3.10(a) represents the tensile modulus of neat PLA and various nanocomposites prepared with three different kinds of OMLS. The modulus increased linearly with increasing OMLS content up to 4 wt.% for C16MMT and 6 wt.% for C25A. As the amount of C25A increased to 6 wt.%, the modulus of the hybrid increased to 296 MPa, a 1.4-fold increase over pure PLA (208 MPa). This behaviour is ascribed to the resistance exerted by the clay itself and to the orientation and aspect ratio of the intercalated silicate layers. Additionally, the stretching resistance of the oriented backbone of the polymer chain in the gallery also contributed to enhancing the modulus. In the case of C16MMT or C25A-based nanocomposites, when the OMLS content was greater than a critical weight percentage, the modulus of the nanocomposites started to decrease. But, the initial modulus of the PLA/DTAMMT hybrids increased linearly with increasing OMLS content from 2 to 8 wt.%.

The tensile strengths of the hybrid films with different OMLS contents are presented in Fig. 3.10(b).The figure shows that the ultimate strength of the hybrids increased remarkably with the OMLS content and possessed a maximum value for a critical OMLS loading. Above this critical loading, the strength values of all the hybrids started to decrease. This behaviour is mainly due to the high OMLS content which leads to a brittleness of materials.

The elongations at break of the nanocomposite films with various OMLS are shown in Fig. 3.10(c)**.** The elongation at break of neat PLA clearly increased with the incorporation of all OMLS and also with an increase in the OMLS loading. Like other tensile properties, the elongation at break also decreased after a critical OMLS loading. Form the above results; it appears that there is an optimal amount of OMLS needed in a nanocomposite to achieve the greatest improvement in its properties.

In a recent study, Lee *et al.*[64] reported the MMT content dependence tensile modulus of PLLA nanocomposites scaffolds. The modulus of the nanocomposites systematically increased with increasing MMT loading. According to them, the crystallinity and the glass transition temperature of PLLA nano-

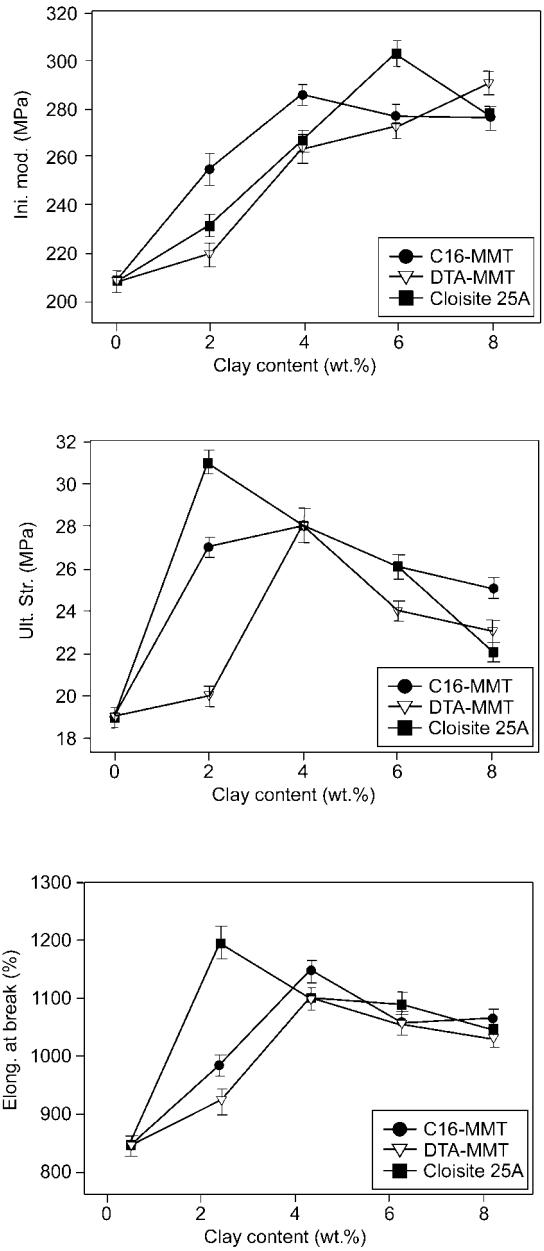

3.10 (a) Effects of the clay loading on the initial tensile modulus of the PLA hybrid films. (b) Effects of the clay loading on the ultimate tensile strength of the PLA hybrid films. (c) Effects of the clay loading on the elongation at break of the PLA hybrid films.[61] Reproduced from Chang, An and Sur by the permission of Wiley Periodicals, Inc, USA.

composites were lower than neat PLLA, but the modulus of neat PLLA was significantly increased in the presence of a small amount of MMT loading. This observation suggests that the layered silicates of MMT act as mechanical reinforcement of polymer chains.

The tensile data of kaolin-TPS-based composites represented an important increase of 135% in the modulus and an increase in tensile strength of 50% for the 50 phr composition.[67] On the other hand, a decrease in elongation was observed. Both modulus and strength have their maximum for the composition with 50 phr, while the elongation decreases almost monotonically. The maximum for the modulus and for the tensile strength correspond to the maximum quantity of mineral filler that may be incorporated, or wetted by the matrix. Above this point, increase in the amount of filler increases the fragility of the composite.

In comparison to the APS, the tensile strength and modulus have been improved with a slight decrease in elongation at break. APS/C30B nanocomposites exhibit a much higher tensile strength and modulus compared to the APS/C10A nanocomposites. This is attributed to the strong interaction between the matrix and clay, which ultimately leads to a better overall dispersion, as already observed by TEM analysis. Lim *et al.*[120] also observed the same behaviour of tensile properties in the case of BPA/C25A nanocomposites.

In the case of crosslinked polyester/OMLS nanocomposites,[122] the modulus was first seen to decrease with increasing clay content, and second, the drop in the value for the 2.5 wt.% nanocomposite was greater than expected. A combination of the morphology and the extent of crosslinking in the nanocomposites can be used to understand this phenomenon. It was proposed that the intercalation and exfoliation of the clay in the polyester resin serves effectively to decrease the number of crosslinks from a topological perspective. The overall decreases in the tensile modulus of the nanocomposites with increasing clay content lend credence to the hypothesis that the degree of crosslinking was indeed reduced. The origin of the greater drop in properties of the 2.5 wt.% nanocomposites may be traced to the morphology, where it was observed that the sample showed exfoliation on a global scale compared to the nanocomposite containing 10 wt.% clay. That means the crosslinking density is inversely proportional to the degree of exfoliation.

The modulus of neat PCL was increased significantly in the case of nanocomposites prepared with OMLS, but the modulus of the microcomposites formed by the pristine clay was basically independent of the clay content at least within the investigated range. Table 3.4 shows the Izod impact strength values of PCL-based composites prepared with three different types of clay as a function of clay content. The Izod impact strength decreases systematically with increasing clay content.

Tensile tests were also performed on PVA nanocomposites films with silicate loadings of 0, 2, 4, 6, and 10 wt.%. Yielding was found for any of the samples

Table 3.4 Izod impact properties of composites containing MMT-Na, MMT-Alk and MMT-$(OH)_2$.[130] Reproduced from Lepoittevin, Devalckenaere, Pantoustier, Alexandre, Kubies, Calberg, Jerome and Dubois by permission of Elsevier Ltd, UK

Filler content (wt.%)	Izod impact strength (J/m)		
	MMT-Na	MMT-Alk	MMT-$(OH)_2$
1	33 ± 5	28 ± 6	33 ± 3
3	22 ± 2	22 ± 2	18 ± 3
5	19 ± 1	15 ± 1	13 ± 1
10	15 ± 1	16 ± 3	13 ± 2

and all samples had an initial period of elastic deformation followed by a nearly monotonically increasing stress during plastic deformation, until failure.

Flexural properties

Nanocomposite researchers are generally interested in the tensile properties of final materials, but there are very few reports concerning the flexural properties of neat biodegradable polymer and its nanocomposites with OMLS. Very recently, Sinha Ray *et al.*[42,49] reported the detailed measurement of flexural properties of neat PLA and various PLACNs. They conducted flexural property measurements with injection-moulded samples according to the ASTM D-790 method. Table 3.5 summarizes the flexural modulus and flexural strength of neat PLA and various PLACNs (prepared with OMSFM) measured at 25ºC. There was a significant increase in flexural modulus for PLACN4 when compared to that of neat PLA, followed by a much slower increase with increasing OMLS content, and a maximum at 50% for PLACN10. On the other hand, the flexural strength shows a remarkable increase with PLACN7, and then gradually decreases with OMLS loading. According to the author, this behaviour may be due to the high OMLS content, which leads to brittleness in the material. They also measured the flexural properties of PLA nanocomposites prepared with various kinds of organically modified MMT but the results showed a similar trend. That means there is an optimal amount of OMLS needed in a nanocomposite to achieve the greatest improvement in its properties.

Table 3.5 Flexural properties of neat PLA and various PLACNs (prepared with OMSFM) measured at 25ºC.[53] Reproduced from Sinha Ray, Yamada, Okamoto, Ogami and Ueda by permission of American Chemical Society, USA

Samples	Neat PLA	PLACN4	PLACN7	PLACN10
Modulus (GPa)	4.84	6.11	5.55	7.25
Strength (MPa)	86	94	101	78

Heat distortion temperature

The nanodispersion of OMLS in biodegradable polymers also promotes a higher HDT. Sinha Ray *et al.*[53] examined the HDT of neat PLA and various PLA/OMSFM nanocomposites with different load conditions. As seen in Fig. 3.11(a), there was a marked increase of HDT with an intermediate load of 0.98 MPa, from 76ºC for the neat PLA to 93.2ºC for PLACN4. This value gradually increased with increasing clay content and in the case of PLACN10 with 10 wt.% of OMSFM, the value increased to 115ºC.

On the other hand, an imposed load dependence on HDT was clearly observed in the case of PLA-based nanocomposites. Figure 3.11(b) shows the typical load dependence in PLACN7. In the case of high load (1.81 MPa), it is very difficult to achieve high HDT enhancement without a strong interaction between the polymer matrix and OMLS, as observed in N6 based nano-

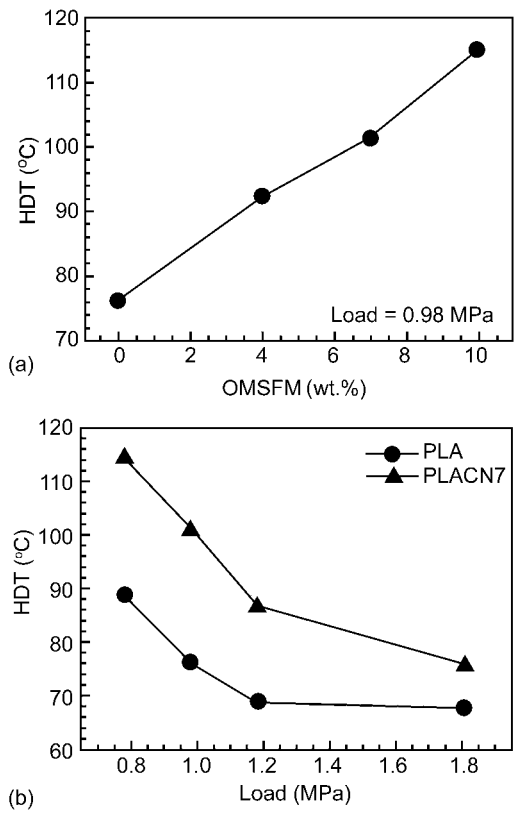

3.11 (a) OMSFM (wt.%) dependence of HDT of neat PLA and nanocomposites. (b) Load dependence of HDT of neat PLA and PLACN7.[53] Reproduced from Sinha Ray, Yamada, Okamoto, Ogami and Ueda by permission of American Chemical Society, USA.

composites.[18] For PLACNs, the values of T_m do not change significantly as compared to that of neat PLA. Furthermore, in XRD analyses up to $2\theta = 70^{\circ}$, no large shifting or formation of new peaks in the crystallized PLACNs was observed. This suggests that the significant improvement of HDT with intermediate load originates from the better mechanical stability, reinforcement by the dispersed clay particles, and higher degree of crystallinity and intercalation.

The increase of HDT due to clay dispersion is a very important property improvement for any polymeric material, not only from an application or industrial point of view, but also because it is very difficult to achieve similar HDT enhancements by chemical modification or reinforcement by conventional filler.

3.8.3 Thermal stability

The thermal stability of polymeric materials is usually studied by thermogravimetric (TG) analysis. The weight loss due to the formation of volatile products after degradation at high temperature is monitored as a function of temperature. When the heating occurs under an inert gas flow, a non-oxidative degradation occurs, while the use of air or oxygen allows oxidative degradation of the samples. Generally, the incorporation of clay into the polymer matrix was found to enhance thermal stability by acting as a superior insulator and mass transport barrier to the volatile products generated during decomposition.

Bandyopadhyay *et al.*[38] reported the first improved thermal stability of biodegradable nanocomposites that combined PLA and organically modified fluorohectorite (FH) or MMT clay. These nanocomposites were prepared by melt intercalation. They showed that the PLA that was intercalated between the galleries of FH or MMT clay resisted the thermal degradation under conditions that would otherwise completely degrade pure PLA. The authors argue that the silicate layers act as a barrier for both the incoming gas and also the gaseous by-products, which both increases the degradation onset temperature and also widens the degradation process. The addition of clay enhances the performance of the char formed, by acting as a superior insulator and mass transports barrier to the volatile products generated during decomposition.

Recently, there have been many reports concerned with the improved thermal stability of PLA-based nanocomposites prepared with various kinds of OMLS.[48,56] Very recently, Chang *et al.*[61] conducted detailed TG analyses of PLA-based nanocomposites of three different kinds of OMLS. In the case of C16MMT or C25A-based hybrids, the initial degradation temperatures of the nanocomposites were decreased linearly with an increasing amount of OMLS. On the other hand, nanocomposite prepared with DTAMMT clay, the initial degradation temperature was nearly constant over the clay loadings from 2 to 8 wt.%. This observation indicates that the thermal stability of the nanocomposites directly related to the stability of OMLS used for the preparation of nanocomposites.

Pluta *et al.*[43] also observed an increase in thermal stability of PLA nanocomposites with the clay content by TGA, with a maximum clay loading of 5 wt.%. When further increasing the filler content, a decrease in thermal stability was observed. Such behaviour was explained by the relative extent of exfoliation/delamination as a function of the amount of OMLS. Indeed at low filler content, exfoliation dominates but the amount of exfoliated silicate layers is not sufficient to promote any significant improvement of the thermal stability. Increasing the filler content leads to relatively more exfoliated particles, and increases the thermal stability of the nanocomposites. However, when the silicate content is more than some critical value, complete exfoliation of such high aspect ratio silicate layers becomes increasingly hindered because of the geometrical constraints within the limited space available in the polymer matrix and no more increase in thermal stability or even some decrease is detected.

The same types of behaviour were also observed in the case of TPS/clay nanocomposites.[68] The increase of the thermal stability with the addition of clays up to 5 wt.% was significant, after that the increase was levelled off with further increasing clay content. Like mechanical properties, TPS/CNa^+ hybrids showed better thermal stability than that of hybrids prepared with OMLS.

Thermal stability of chitosan/MMT nanocomposites was investigated from DTA and TG curves in the 300–1200 K range, under air flow conditions. The weight loss between room temperature and about 500 K was related to the absorbed water molecules. Such a weight loss was about 7.9% in the starting silicate, while the biopolymer/clay nanocomposites showed losses slightly higher, ranging from 8.4 to 10.5%. This result indicates the higher water-retention capacity of chitosan. The high thermal stability of these materials was evidenced by the elevated temperature required to eliminate the organic matter associated with the clay. This fact occurs between 500 and 800 K, corresponding to the combustion of the intercalated chitosan.

In the case of PVA-based nanocomposites, major weight losses were observed in the range of 200 to 500ºC for PVA and corresponding MMT-based nanocomposite fine powders, which may be correspondent to the structural decomposition of the polymer. Evidently, the thermal decomposition of nanocomposite materials shifted slightly toward the higher temperature range than that of PVA, which confirmed the enhanced thermal stability of confined polymers. After 600ºC, all the curves became flat and mainly inorganic residue remained. Recently, Strawhecker and Manias[141] also observed the same kind of thermal stability of PVA and its nanocomposites and they explained this behaviour as being possibly due to the fact that PVA can supply oxygen from within to initiate its decomposition.

The thermal stability of the PCL-based composites has also been studied by TGA. Generally, the degradation of PCL fits a two-step mechanism;[4,130] first random chain scission through pyrolysis of the ester groups, with the release of CO_2, H_2O and hexanoic acid, then in the second step, ϵ-caprolactone (cyclic

monomer) is formed as a result of an unzipping depolymerization process.[130] Both intercalated and exfoliated nanocomposites showed higher thermal stability when compared to the pure PCL or to the corresponding microcomposites. The nanocomposites exhibited a 25ºC high in decomposition temperature at 50% weight loss. The shift of the degradation temperature may be ascribed to a decrease in oxygen and volatile degradation products' permeability/diffusivity due to the homogeneous incorporation of clay sheets, to a barrier of these high-aspect ratio fillers, and char formation. The thermal stability of the nanocomposites increases systematically with increasing clay, up to a loading of 5 wt.%.

Different behaviour was observed in synthetic biodegradable aliphatic polyester BAP/OMLS nanocomposite systems, in which the thermal degradation temperature and thermal degradation rate systematically increases with increasing amounts of OMLS up to 15 wt.%.[120] A small amount of clay also increased the residual weight of BAP/OMMT because of the restricted thermal motion of the polymer chains in the silicate layers. The residual weight of various materials at 450ºC increased in the order BAP < BAP03 < BAP06 < BAP09 < BAP15 (here number indicates wt.% of clay). The role of clay in the nanocomposite structure may be the main reason for the difference in TGA results of these systems compared to the previously reported systems. The clay acts as a heat barrier, which enhances the overall thermal stability of the system, as well as assisting in the formation of char after thermal decomposition. In the early stages of thermal decomposition, the clay would shift the decomposition to higher temperature. After that, this heat barrier effect would result in a reverse thermal stability. In other words, the stacked silicate layers could hold accumulated heat that could be used as a heat source to accelerate the decomposition process, in conjunction with the heat flow supplied by the outside heat source.

3.8.4 Gas barrier properties

Clays are believed to increase the barrier properties by creating a maze or 'tortuous path' that retards the progress of the gas molecules through the matrix resin. The direct benefit of the formation of such a path is clearly observed in near to exfoliated PLA/OMSFM nanocomposites.[53] The relative permeability coefficient value, i.e. P_{PCN}/P_P, where P_{PCN} and P_P are the nanocomposite and pure polymer permeability coefficient, respectively, was plotted as a function of the wt.% of OMSFM in Fig. 3.12. The data were analyzed with the Nielsen theoretical expression (see below),[175] allowing prediction of gas permeability as a function of the length (L_{LS}) and thickness of filler particles (D_{LS}), as well as their volume fraction (ϕ_{LS}) in the PLA-matrix.

$$\frac{P_{PCN}}{P_P} = \frac{1}{1 + (L_{LS}/2D_{LS})\phi_{LS}} \tag{3.1}$$

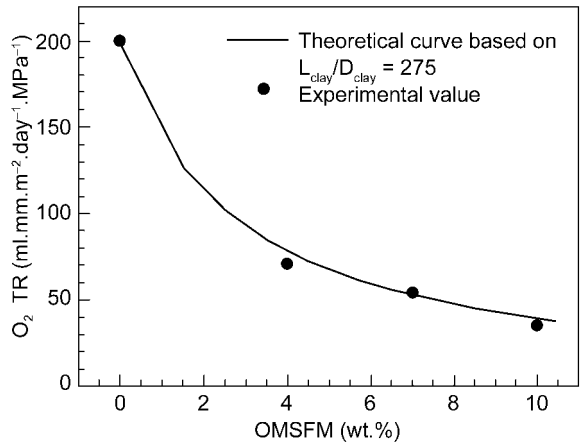

3.12 O_2 gas permeability of neat PLA and various PLACNs as function of OMSFM content (wt.%) at 20°C and 90% relative humidity. The filled circles represent the experimental data and the line based on Nielsen tortuosity model (Equation (3.1)) by considering L/D equal to 275.[53] Reproduced from Sinha Ray, Yamada, Okamoto, Ogami and Ueda by permission of American Chemical Society, USA.

Equation 3.1 clearly describes that the gas barrier property of nanocomposites depends primarily on two factors: one is the dispersed layered silicate particles dimension and other is the dispersion of layered silicate in polymer matrix. When the degree of dispersion of layered silicate in the matrix is the same, barrier property directly depends on the dispersed layered silicate particles dimension, i.e. the aspect ratio.

According to the above theoretical expression as described in Equation 3.1, Sinha Ray *et al.*[57] estimated the O_2 gas transmission coefficient of various PLA nanocomposites using experimentally obtained L_{LS}/D_{LS} value as summarized in Table 3.6. Among the five nanocomposites, the calculated values were almost well matched with the experimental values, with the exception of PLA/qC16SAP4 system (see Table 3.6), which shows higher value of permeability coefficient despite the much lower aspect ratio compared to that of other systems.

Güsev and Lusti[176] considered another factor, which is also responsible for the barrier property: changes in the local permeability due to the molecular level of transformation in the polymer matrix in the presence of silicate layers. This factor is directly related to the molecular level interaction of polymer matrix with the silicate layers. The PLA/qC16SAP4 is a disordered intercalated system, the favourable interactions between PLA and silicate layers probably due to the formation of phosphonium oxide caused by the reaction between the hydroxy edge group of PLA and alkylphosphonium cation. As a result, the barrier property of PLA/qC16SAP4 is much higher compared to that of other systems.[57]

Table 3.6 Comparison of O_2 gas permeability of neat PLA and various nanocomposite films.[57] Reproduced from Sinha Ray, Yamada, Okamoto, Fujimoto, Ogami and Ueda by permission of Elsevier Ltd, UK

Samples	O_2 gas permeability (ml. mm/m^2/ day.MPa)	O_2 gas permeability (ml. mm/m^2/ day.MPa)[a]	L_{Ls} (nm)	D_{Ls} (nm)
PLA	200	200	—	—
PLA/C18MMT4	172	180	450 ± 200	38 ± 17
PLA/qC^{2}18MMT4	171	181	655 ± 212	60 ± 15
PLA/qC18MMT	177	188	200 ± 25	36 ± 19
PLA/qC16SAP4	120	169	50 ± 5	2–3
PLA/qC$_{13}$(OH)-Mica4	71	68	275 ± 25	1–2

[a] Calculated on the basis of Nielsen theoretical equation (3.1).

Chang *et al.*[61] reported the oxygen gas permeability of PLA nanocomposites prepared with three different kinds of OMLS using a melt intercalation technique. The results show that O_2 gas permeability of nanocomposites were systematically decreased with increasing clay content and when the clay loading was as much as 10 wt.%, the permeability value of nanocomposites decreased to half of the PLA permeability value, regardless of the nature of OMLS for the nanocomposite preparation. This is attributed to the increase in the lengths of the tortuous paths in nanocomposites in the presence of high clay content.

Recently, Gorrasi *et al.*[133] reported the morphology dependent vapour barrier properties of PCL/MMT nanocomposites. They prepared different compositions of PCL/OMLS nanocomposites by melt blending or catalyzed ring opening polymerization of CL. Microcomposites were obtained by direct melt blending of PCL and pristine MMT. But exfoliated nanocomposites were obtained by in-situ ring opening polymerization of CL with an OMLS by using dibutyltin dimethoxide as an initiator/catalyst. Intercalated nanocomposites were formed either by melt blending with OMLS or in-situ polymerization within pristine MMT. The barrier properties were studied for water vapour and dichloromethane as an organic solvent. The sorption (S) and the zero concentration diffusion coefficients (D_0) were evaluated for both vapours. The water sorption increases with increasing the MMT content, particularly for the microcomposites containing the unmodified MMT. The thermodynamic diffusion parameters, D_0, were compared to the value of the parent PCL: both microcomposites and intercalated nanocomposites show diffusion parameters very near to PCL. At variance exfoliated nanocomposites show much lower values, even for small MMT content. In the case of organic vapour, the value of sorption at low relative pressure is mainly dominated by the amorphous fraction present in the samples, not showing any preferential adsorption on the inorganic component. At high relative pressure the isotherms showed an exponential increase of sorption, due to

plasticization of the polyester matrix. The D_0 parameters were also compared to those of the unfilled PCL; in this case, both exfoliated and the intercalated samples showed lower values, due to a more tortuous path for the penetrating molecules.

3.8.5 Optical transparency

Although layered silicates are microns in lateral size, they are just 1 nm thick. Thus, when single layers are dispersed in a polymer matrix, the resulting nanocomposite is optically clear in visible light. The UV/visible transmission spectra of pure PVA and PVA/Na^+-MMT nanocomposites with 4 and 10 wt.% MMT[141] show that the visible region is not affected by the presence of the silicate layers, and retains the high transparency of PVA. For UV wavelengths, there is strong scattering and/or absorption, resulting in very low transmission of UV light. This behaviour is not surprising, as the typical MMT lateral sizes are 50–1000 nm.

3.9 Biodegradability

The main objective of this section is to describe that the PLS nanocomposite technology is not only suitable for the concurrent improvement of mechanical and materials properties of virgin biodegradable polymers, it is also useful for the nanoscale control of the biodegradability of biodegradable polymers like PLA, PHB, PBS, SAP, etc.

3.9.1 PLA and its nanocomposites

A major problem with the PLA matrix is the slow rate of degradation as compared to the rate of waste accumulation. Despite the considerable amount of reports concerning the enzymatic degradation of PLA[177,178] and various PLA blend,[179] there remains very little regarding the compost degradability of PLA[180,181] except recent publications by one of the present authors.[52,53] Figure 3.13(a) shows the real picture of the recovered samples of neat PLA and three different kinds of PLA/OMLS nanocomposites from the compost with time. The decreased M_w and residual weight percentage (R_w) of the initial tests samples with time are reported in Figs 3.13(b) and 3.13(c), respectively. Based on Fig. 3.13(a), there was no significant discrepancy between PLA/C18MMT4 and PLA/qC18MMT4, though only the latter was indicated as an enhancer of biodegradability. Within one month, both extent of M_w and the extent of weight loss were almost the same for both pure PLA and PLA/qC18MMT4. However, after one month, a sharp change occurs in the weight loss of PLA/qC18MMT4, and within two months, it was completely degraded in compost.

Sinha Ray *et al*. also conducted a respirometric test to study the degradation of the PLA matrix in a compost environment.[57,58] Unlike weight loss or

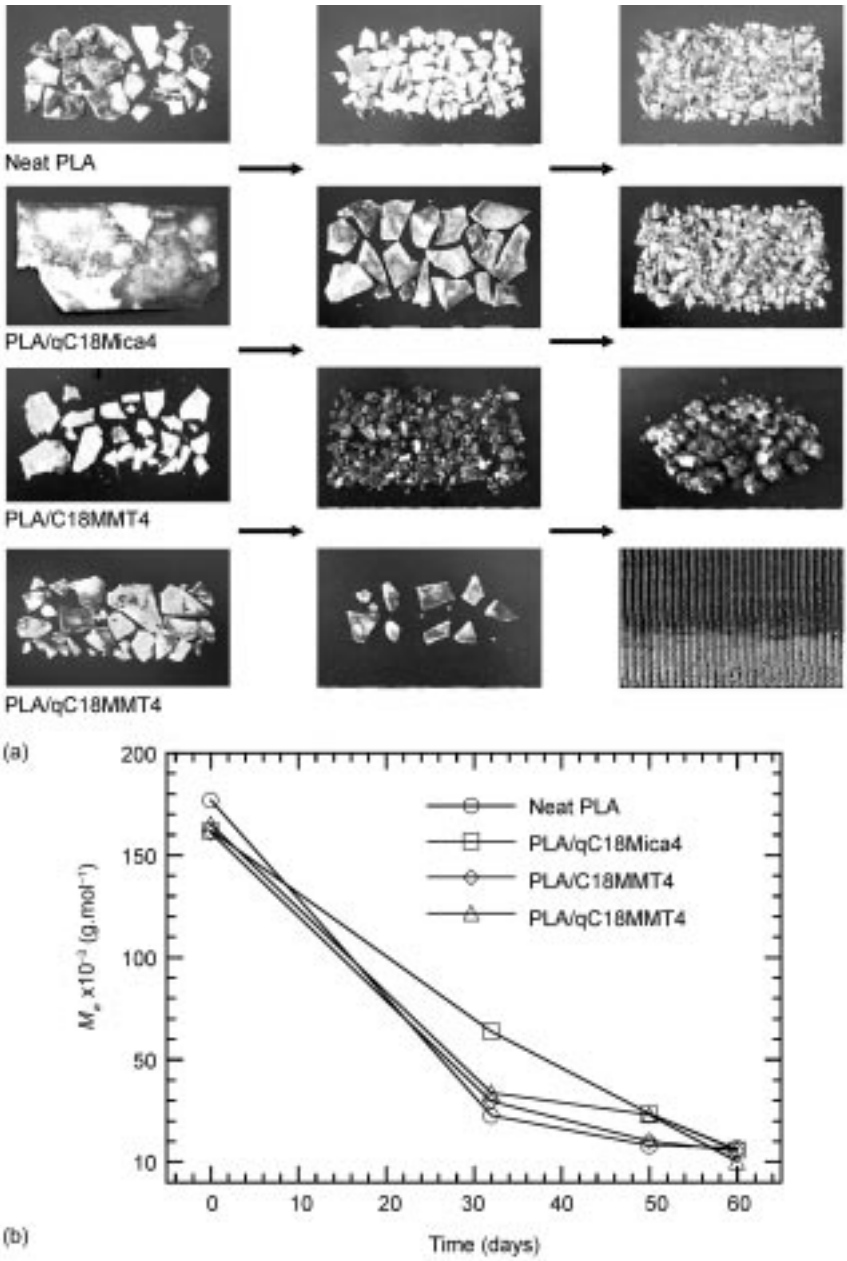

3.13 (a) Real picture of biodegradability of pure PLA and various nanocomposites recovered from compost with time. The initial shape of the crystallized samples was $3 \times 10 \times 0.1\ cm^3$. (b) Time-dependent change of matrix M_w of pure PLA and corresponding nanocomposites under compost. (c) Time-dependent weight percentage (R_w) of pure PLA and two different nanocomposites.

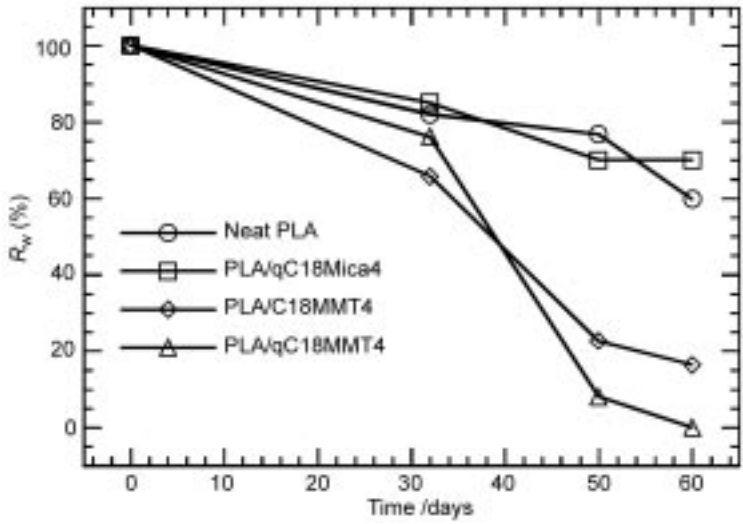

3.13 Continued

fragmentation, which reflects the structural changes in the test sample, CO_2 evolution provides an indicator of the ultimate biodegradability, that is, mineralization, of the test samples. The data clearly indicate that the biodegradability of PLA component in PLA/qC13(OH)-Mica4 or PLA/qC16SAP4 was enhanced significantly. On the other hand, PLA component in PLA/C18MMT4 showed a slightly higher biodegradation rate, while the rate of degradation of pure PLA and PLA/qC18MMT4 was almost the same.

The compost degradation of PLA occurs by a two-step process. During the initial phases of degradation, the high molecular weight PLA chains hydrolyze to lower molecular weight oligomers. This reaction can be accelerated by acids or bases and is also affected by both temperature and moisture. Fragmentation of the plastic occurs during this step at a point where the M_n decreases to less than about 40,000. At about this same M_n, microorganisms in the compost environment continue the degradation process by converting these lower molecular weight components to CO_2, water, and humus.[180,57] Therefore, any factor which increases the hydrolysis tendency of PLA matrix ultimately controls the degradation of PLA.

The incorporation of OMLS fillers into the PLA matrix resulted in a small reduction in the molecular weight of the matrix.[57] It is well known that PLA of relatively lower molecular weight may show higher rates of enzymatic degradation because of, for example, the high concentration of accessible chain end groups.[182] However, in these cases the rate of molecular weight change of pure PLA and PLA in various nanocomposites was almost the same (see Fig. 3.13(b)). So the initial molecular weight is not a main factor for controlling the

biodegradability of nanocomposites. Another factor that controls the biodegradability of PLA is the degree of crystallinity (χ_c) value because the amorphous phase is easy to degrade compared to that of the crystal phase. However, the χ_c value of the pure PLA sample was lower than that of nanocomposite samples except for PLA/qC16SAP4 and PLA/qC13(OH)-Mica4.[57,58] These two nanocomposite samples did not enhance the degree of crystallinity.

These data indicate that the incorporation of different types of OMLS in the PLA matrix resulted in a different mode of attack on the PLA component of the test samples that might be due to the presence of different kinds of surfactants and pristine layered silicates. Since PLA is an aliphatic polyester, it is conceivable that incorporation of different types of OMLS resulted in a different mode of disruption of some of the ester linkages due to the presence of different kinds of surfactants and layered silicates. The disruption of ester bonds is more facile in the presence of qC13(OH)-Mica or qC16SAP and less facile with qC18MMT. Therefore, this observation explores the role of OMLS as nanofiller to enhance the rate of biodegradation of pure PLA and the biodegradability of PLA can be controlled by judicious choice of OMLS.

3.9.2 PHB and its nanocomposites

Recently, Maiti *et al.*[65] reported the biodegradability of the PHB and its OMLS nanocomposites under compost. Apparently, the degradation started after just one week and at the initial stage the weight loss was almost the same for both PHB and its nanocomposites. Deviation occurred after three weeks of exposure, but degradation tendency of nanocomposites was suppressed. The authors assumed that the retardation of biodegradation of PHB was because of the improvement of the barrier properties of the matrices after nanocomposites preparation with OMLS. However, they did not report about the permeability. However, according to Sinha Ray *et al.*[57] in the case of PLA/OMLS nanocomposites, there is no relation between the biodegradability and the gas barrier properties. Some nanocomposites were degraded very fast having significantly improved barrier properties as compared with those of neat PLA.

3.9.3 PBS and its nanocomposites

Recently, Sinha Ray *et al.*[110,112] reported the biodegradability of neat PBS and its nanocomposites in two different modes: under compost and under soil field. Figure 3.13(a) shows the real pictures of recovered samples of neat PBS and various nanocomposites from the compost after 35 days. The compost used was prepared from a mixture of soybean dust (byproduct of tofu) and effective microorganism. Before use, this mixture was sealed and fermented for 20 days at outdoor temperature. For this test the compression moulded sample sheets with a thickness of 0.3 ± 0.03 mm were first clipped with a 35 mm slide holder

and then put into the compost. After 35 days, samples were recovered, washed with distilled water, and finally washed with methanol with an ultrasonic bath for 5 min.

Figure 3.14(a) indicates that many cracks appeared in nanocomposite samples as compared to those of pristine PBS. This observation indicates the improved biodegradability of nanocomposites in compost. This kind of fracture has an advantage for biodegradation because it is easy to mix with compost and create much more surface area for further attack by microorganisms, and the extent of fragmentation was directly related to the nature of OMLS used for the nanocomposites preparation. They also conducted the GPC measurement of recovered samples from compost. The GPC results show that the extent of molecular weight loss was almost the same for all samples.

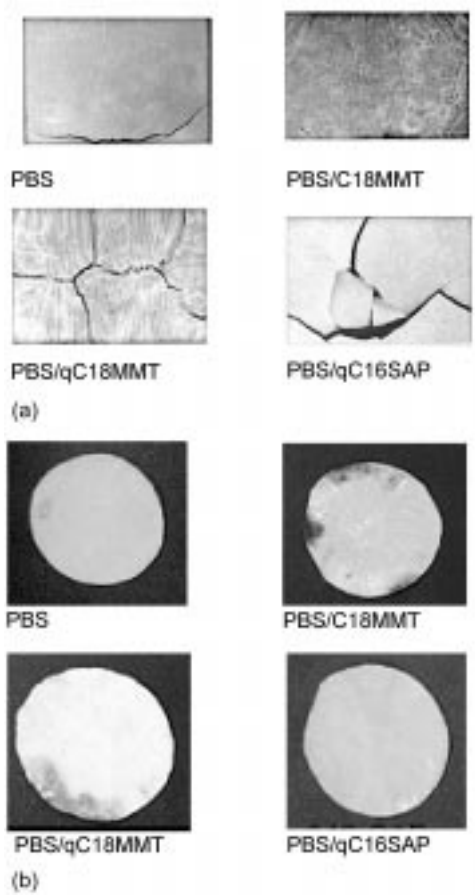

3.14 (a) Biodegradability of neat PBS and various nanocomposite sheets under compost and (b) under soil field.[112] Reproduced from Okamoto, Sinha Ray and Okamoto by permission of Wiley Periodicals Inc, USA.

Except for the nanocomposite prepared with qC16SAP, the degree of degradation was not different for other samples. This observation indicates that MMT or alkylammonium cations, as well as other properties, has no effect on the biodegradability of PBS. The accelerated degradation of PBS matrix in the presence of qC16SAP may be due to the presence of alkylphosphonium surfactant. This kind of behaviour was also observed in the case of PLA-based nanocomposites as described in the previous section.

They also observed the nature of degradation of PBS and various nanocomposites under soil field. For this test they used compression-moulded sample sheets with an average thickness of 1 mm and each sheet weighting 3 ± 0.03 g. The sample sheets were first put into mesh nets and then buried in the ground with leaf soil (the depth was *ca*. 15 cm). The experiment was conducted for 1, 2 and 6 months. After 1 and 2 months, there was no change in the nature of the sample surfaces, but after 6 months black or red spots appeared on the surface of the nanocomposites samples. Figure 3.14(b) represents the results of degradation of neat PBS and various nanocomposites sheets recovered from a soil field after 6 months. According to them these spots on the sample surface were due to the fungus attacked because when they put these parts into the slurry, they observed clear growth of fungus. These results also established that nanocomposites exhibit the same or a higher level of biodegradability as compared with the PBS matrix.

3.9.4 Other polyesters and their nanocomposites

Tetto *et al.*[183] first reported results on the biodegradability of nanocomposites based on PCL, reporting that the PCL/OMLS nanocomposites showed improved biodegradability compared to pure PCL. The improved biodegradability of PCL after nanocomposites formation may be due to a catalytic role of the OMLS in the biodegradation mechanism, but this is still not clear.

Recently, Lee *et al.*[121] reported the biodegradation of aliphatic polyester-based nanocomposites under compost. Results clearly showed that the biodegradability of polymer was depressed after nanocomposites preparation. They assumed that the retardation of biodegradation was due to the improvement of the barrier properties of the matrix after nanocomposites preparation with OMLS. However, like Maiti *et al.*,[65] they did not report any permeability data.

3.10 Melt rheology and structure-property relationship

The measurement of rheological properties of any polymeric material under molten state is crucial to gain fundamental understanding of the processability of that material. In the case of polymer/layered silicate nanocomposites, the measurements of melt rheological properties are not only important to understand the knowledge of the processability of these materials, but are also helpful

in finding out the strength of polymer-layered silicate interaction and the structure-property relationship in nanocomposites. This is because rheological behaviours are strongly influenced by their nanoscale structure and interfacial characteristics.

3.10.1 Dynamic oscillatory shear measurements

Dynamic oscillatory shear measurements of polymeric materials are generally performed by applying a time dependent strain of $\gamma(t) = \gamma_o \sin(\omega t)$ and measuring the resultant shear stress $\sigma(t) = \gamma_o[G' \sin(\omega t) + G'' \cos(\omega t)]$, where G' and G'' are the storage and loss moduli, respectively. Generally, the rheology of polymer melts depends strongly on the temperature at which the measurement is carried out. In the case of polymer samples, it is expected that at the temperatures and frequencies at which the rheological measurements were carried out, they should exhibit characteristic homopolymer-like terminal flow behaviour, expressed by the power laws $G' \propto \omega^2$ and $G'' \propto \omega$.

The master curves for G' and G'' of pure PLA and various nanocomposites with different weight percentages of C18MMT loading are presented in Fig. 3.15(a). At high frequencies ($a_T \cdot \omega > 10$), the viscoelastic behaviours of all nanocomposites were the same. On the other hand, at low frequencies ($a_T \cdot \omega < 10$) both moduli exhibited weak frequency dependence with increasing C18MMT content, and there were gradual changes of behaviour from liquid-like [$G' \propto \omega^2$ and $G'' \propto \omega$] to solid-like with increasing C18MMT content.

The terminal regions slope of the master curves for G' and G'' are presented in Table 3.7. The slope of and in the terminal region of the master curves of PLA matrix was 1.85 and 1, respectively, and these values are in the range expected for polydisperse polymers.[184] On the other hand, the slopes of G' and G'' were considerably lower for all PLACNs compared to those of pure PLA. In fact, for PLACNs with high C18MMT content, G'becomes nearly independent at low $a_t\omega$ and exceeds G'', characteristic of materials exhibiting a pseudo-solid-like behaviour.

The dynamic complex viscosity $|\eta^*|$ master curves for the pure PLA and nanocomposites, based on linear dynamic oscillatory shear measurements, are

Table 3.7 Terminal regions slopes of G' and G''.[60] Reproduced from Sinha Ray and Okamoto by permission of Wiley-VCH Verlag GmbH, Germany

Samples	G'	G''
PLA	1.85	1
PLACN3	0.25	0.5
PLACN5	0.18	0.4
PLACN7	0.1	0.3

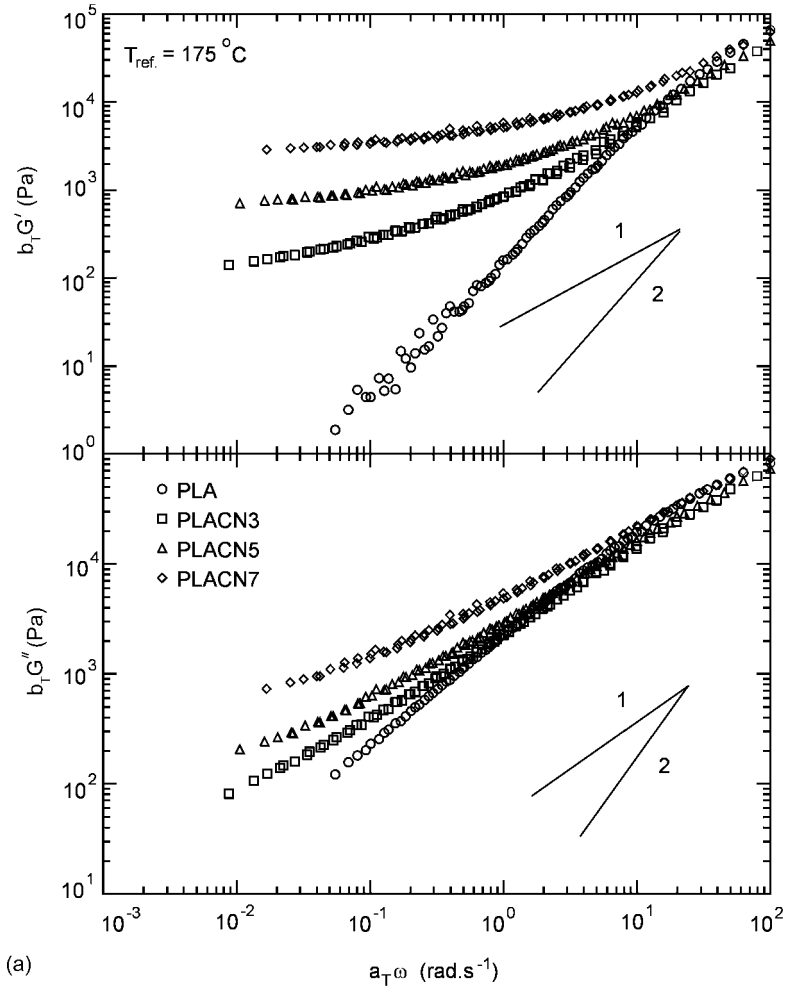

3.15 (a) Reduced frequency dependence storage modulus (G') and loss modulus (G'') of neat PLA and various nanocomposites.[60] (b) Reduced frequency dependence of complex viscosity of neat PLA and nanocomposites.[60] Reproduced from Sinha Ray and Okamoto by permission of Wiley-VCH Verlag GmbH, Germany.

presented in Fig. 3.15(b). At low $a_t\omega$ region (<10 rad.s^{-1}), pure PLA exhibited almost Newtonian behaviour while all nanocomposites showed very strong shear-thinning tendency. On the other hand, M_w and PDI of pure PLA and various nanocomposites were almost the same, thus the high viscosity of PLACNs were explained by the flow restrictions of polymer chains in the molten state due to the presence of MMT particles.

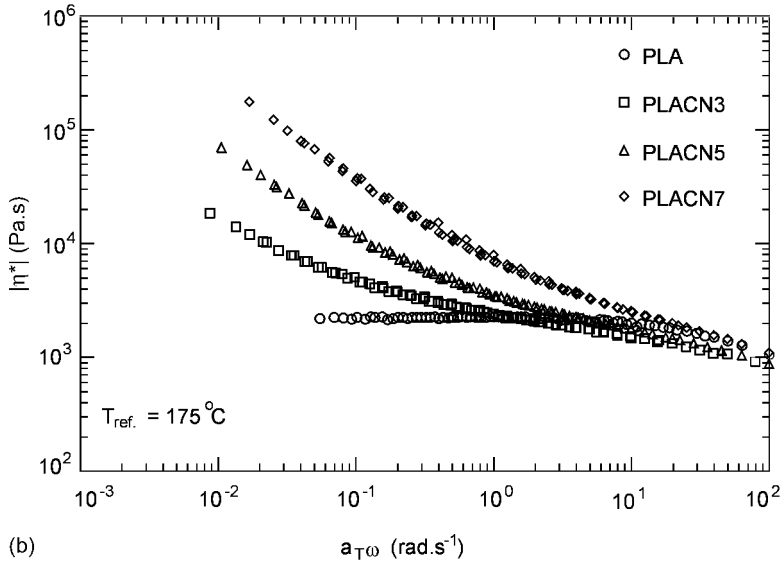

3.15 Continued

Figure 3.16 represents the master curves for G' and G'' of neat PBS and various PBSCNs prepared with two different types of OMLS. At all frequencies, both G' and G'' of nanocomposites increased monotonically with increasing OMLS loading with the exception of PBS/C18MMT1 and PBS/qC16SAP1 in which viscoelastic behaviours were almost identical to those obtained for neat PBS. At high frequencies ($a_T\omega < 5$), both moduli exhibited week frequency dependence with increasing clay content, which means that there are gradual changes of behaviour from liquid-like to solid-like with increasing clay content.

Melt rheological properties of PCL-based nanocomposites were first reported by Krishnamoorti and Giannelis[125] in the case of delaminated structures prepared by in-situ intercalative polymerization. Recently, Lepoittevin *et al.*[130] reported the detail melt rheology properties of PCL-based nanocomposites prepared by melt intercalation method. The rheological behaviour of the PCL filled with 3 wt.% of MMT-Alk and MMT-$(OH)_2$ was significantly different compared to the unfilled PCL and PCL/MMT-Na nanocomposites, for which the power law observed at low frequencies agrees with expectation for thermoplastics. The frequency dependence of G' and G'' was, however, perturbed by organically modified MMT. The effect was dramatic in the case of G' which drops from 2 to 0.14 and 0.24 for MMT-$(OH)_2$ and MMT-Alk, respectively.

When the clay content exceeded 1 wt.%, not only the classical power laws for the frequency dependence of G' and G'' were deeply modified, particularly in the case of G', but the moduli increased dramatically at low frequency. This behaviour is characteristic of a pseudo-solid-like response of the material. The

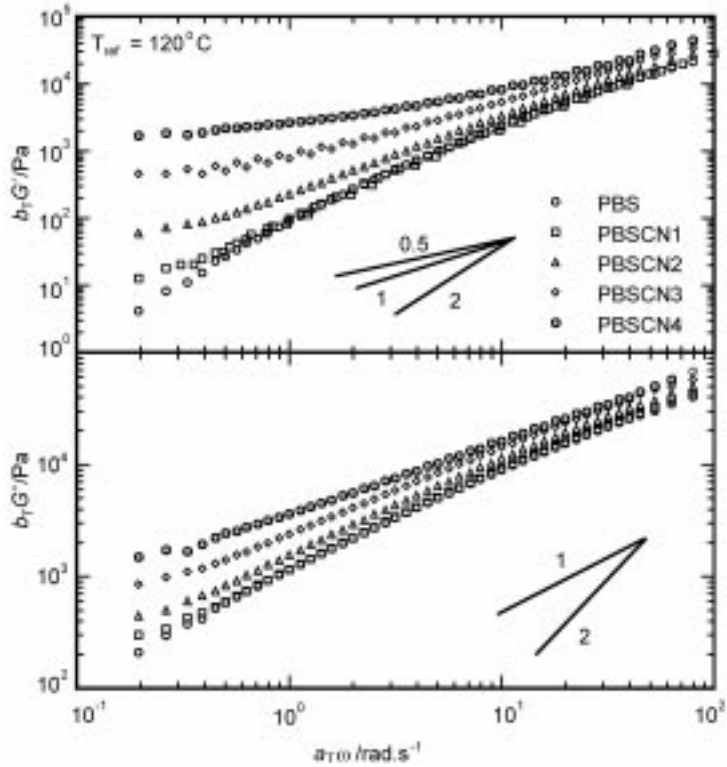

3.16 Master curves of storage modulus (G') and loss modulus (G'') of PBS and various nanocomposites.[110] Reproduced from Sinha Ray, Okamoto and Okamoto by permission of American Chemical Society, USA.

same behaviour was also observed in the case of PLA or PBS-based nanocomposites.

3.10.2 Steady shear measurements

The time dependent steady shear viscosity of neat PLA and a series of intercalated nanocomposites are shown in Fig. 3.17.[60] Steady-shear viscosity measurements were conducted at 175ºC using 25 mm diameter cone and plate geometry with a cone angle of 0.1 rad. The shear-viscosity of PLACNs is enhanced considerably at all shear rates with time, and at a fixed shear rate increases monotonically with increasing MMT content. On the other hand, all intercalated nanocomposites exhibited strong rheopexy behaviour, and this behaviour becomes prominent at low shear rate ($= 0.001\,s^{-1}$), while pure PLA exhibited a time independent viscosity at all shear rates. With increasing shear rates, the shear viscosity attains a plateau after a certain time (indicated by the arrows in Fig. 3.17), and the time required to attain this plateau decreases with

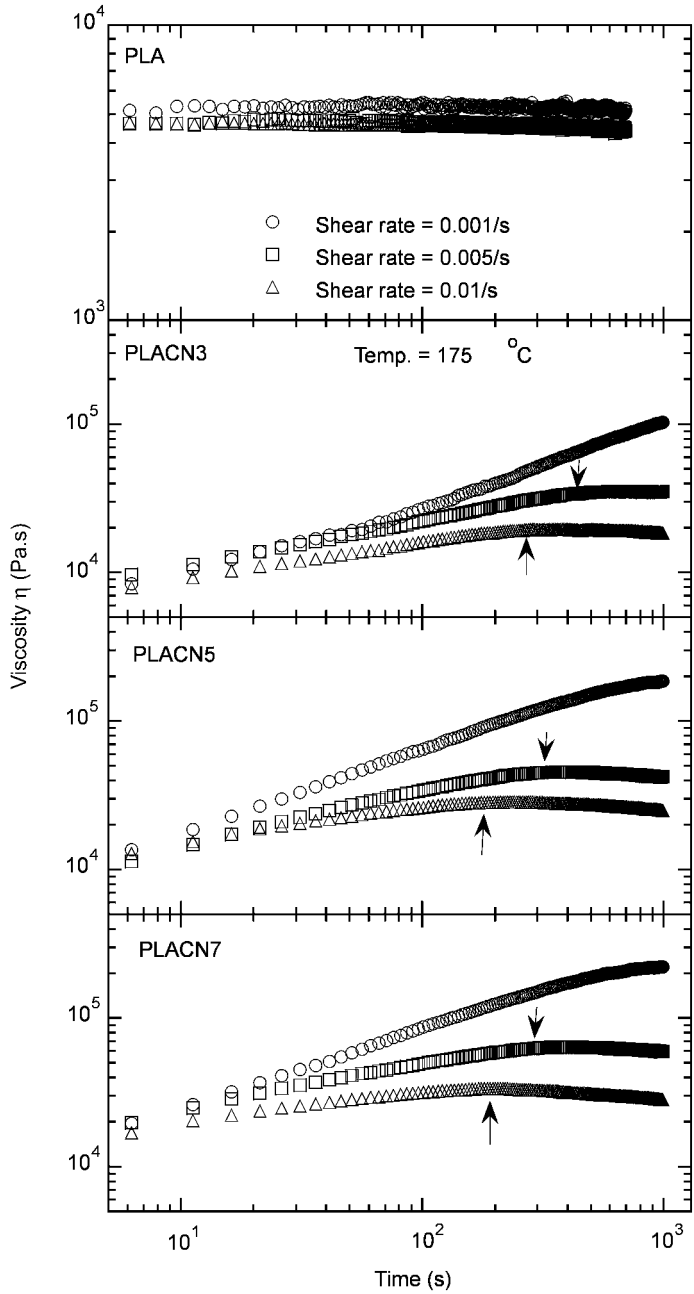

3.17 Steady shear viscosity of PLA and various nanocomposites as a function of time.[60] Reproduced from Sinha Ray and Okamoto by permission of Wiley-VCH Verlag GmbH, Germany.

increasing shear rate. The possible reason for this type of behaviour may be due to the planar alignment of the silicate particles towards the flow direction under shear. When the shear rate is very slow ($0.001\,s^{-1}$), silicate particles take a longer time to attain complete planar alignment along the flow direction, and this measurement (1000 s) was too short to attain such alignment. For this reason, nanocomposites showed strong rheopexy behaviour. On the other hand, under little high shear rates ($0.005\,s^{-1}$ or $0.01\,s^{-1}$) this time was sufficient to attain such alignment, and hence, nanocomposites showed time-independent shear viscosity after a certain time.

Figure 3.18 represents the shear rates dependent viscosity of pure PLA and various PLACNs measured at 175ºC. While the pure PLA exhibits almost Newtonian behaviour at all shear rates, the PLACNs exhibited non-Newtonian behaviour. All PLACNs showed a very strong shear-thinning behaviour at all measured shear rates and this behaviour is analogous to the results obtained in the case of oscillatory shear measurements (see Fig. 3.15(b)). Additionally, at very high shear rates, the steady shear viscosities of PLACNs were comparable to those of pure PLA. These observations suggest that the silicate layers are strongly oriented towards the flow direction (maybe perpendicular alignment of the silicate layers toward the stretching direction) at high shear rates and that of pure polymer dominates shear thinning behaviour at high shear rates. The same

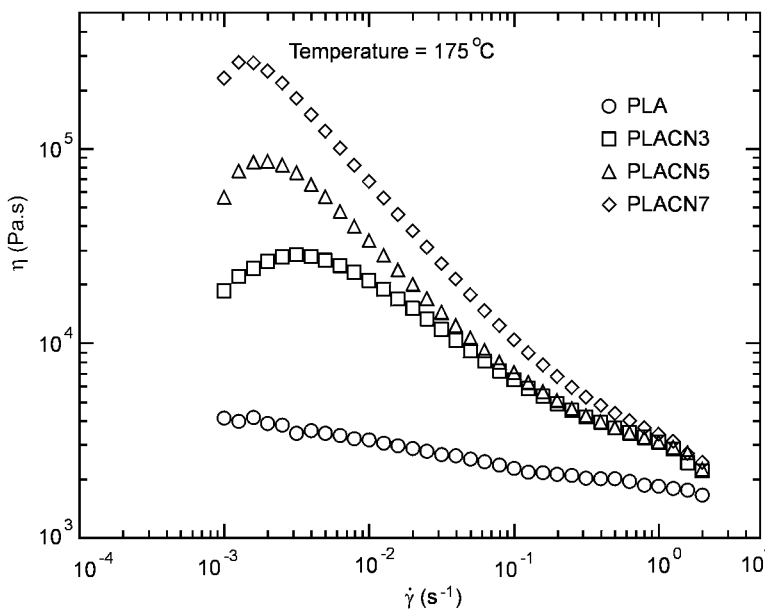

3.18 Steady shear viscosity of PLA and various nanocomposites as a function of shear rate.[60] Reproduced from Sinha Ray and Okamoto by permission of Wiley-VCH Verlag GmbH, Germany.

kind of steady shear rheological behaviours were also observed in the case of neat PBS and PBSCNs.

Like previous systems, the viscosity of the BAP/OMMT nanocomposites were also decreased with increasing shear rate. However, at very low shear rates, the shear viscosity data exhibited a Newtonian plateau even for high OMMT content. With increasing shear rate, the nanocomposites were exhibited higher degrees of shear-thinning behaviour compared to the pure polymer. A similar behaviour was also observed by Krishnamoorti and Giannelis[125] in the case of exfoliated PCL-based nanocomposites with several silicate loadings.

The increase in shear viscosity of the PLS nanocomposites was recently analyzed using a mean-field theory.[185] Furthermore, in the case of intercalated poly(styrene-isoprene) block copolymer/MMT nanocomposites, Krishnamoorti *et al.*[186] observed that the steady shear viscosities for the nanocomposites exhibited enhanced shear-thinning behaviour at low shear rates. In other words, the viscosity at high shear rates showed more decreased values from the zero-shear viscosities with increasing clay loading, and the values were identical to those of virgin polymer. Although the exact mechanism which causes the shear thinning behaviour is still not clear, it can be deduced that the orientation of the silicate layers under shear is the main cause. With increasing shear rate, the intercalated polymer chain conformations change as the coils align parallel to the flow.[186] Nevertheless, because of this shear thinning property, the nanocomposites can be processed in the melt state using the conventional equipment available in a manufacturing line.

PLS nanocomposites[2] always exhibit significant deviations from the empirical Cox-Merz relation,[187] while all neat polymers obey the empirical relation, which requires that, for $\gamma = \omega$, the viscoelastic data obeys the relationship $\eta(\gamma) = |\eta^*|(\omega)$. Two possible reasons may be offered for the deviation from the Cox-Merz relation in the case of nanocomposites. First, this rule is only applicable for homogeneous systems like homo-polymer melts, but nanocomposites are heterogeneous systems. Second, the structure formation is different when nanocomposites are subjected to dynamic oscillatory shear versus steady shear measurements.

3.10.3 Elongation flow rheology

Sinha Ray and Okamoto[60] first conducted elongation tests of PLACN5 (prepared with 5 wt.% of C18MMT) in the molten state at constant Hencky strain rate, $\dot{\epsilon}_0$ using elongation flow opto-rheometry.[188] On each run of the elongation test, samples of $60 \times 7 \times 1\,\text{mm}^3$ size were annealed at a predetermined temperature for 3 min before starting the run in the rheometer, and uniaxial elongation experiments were conducted at various $\dot{\epsilon}_0$ ranging from 0.01 to $1\,\text{s}^{-1}$. Figure 3.19(a) shows double-logarithmic plots of the transient elongation viscosity $\eta_E(\dot{\epsilon}_0; t)$ versus time t, observed for PLACN5 at 170ºC with

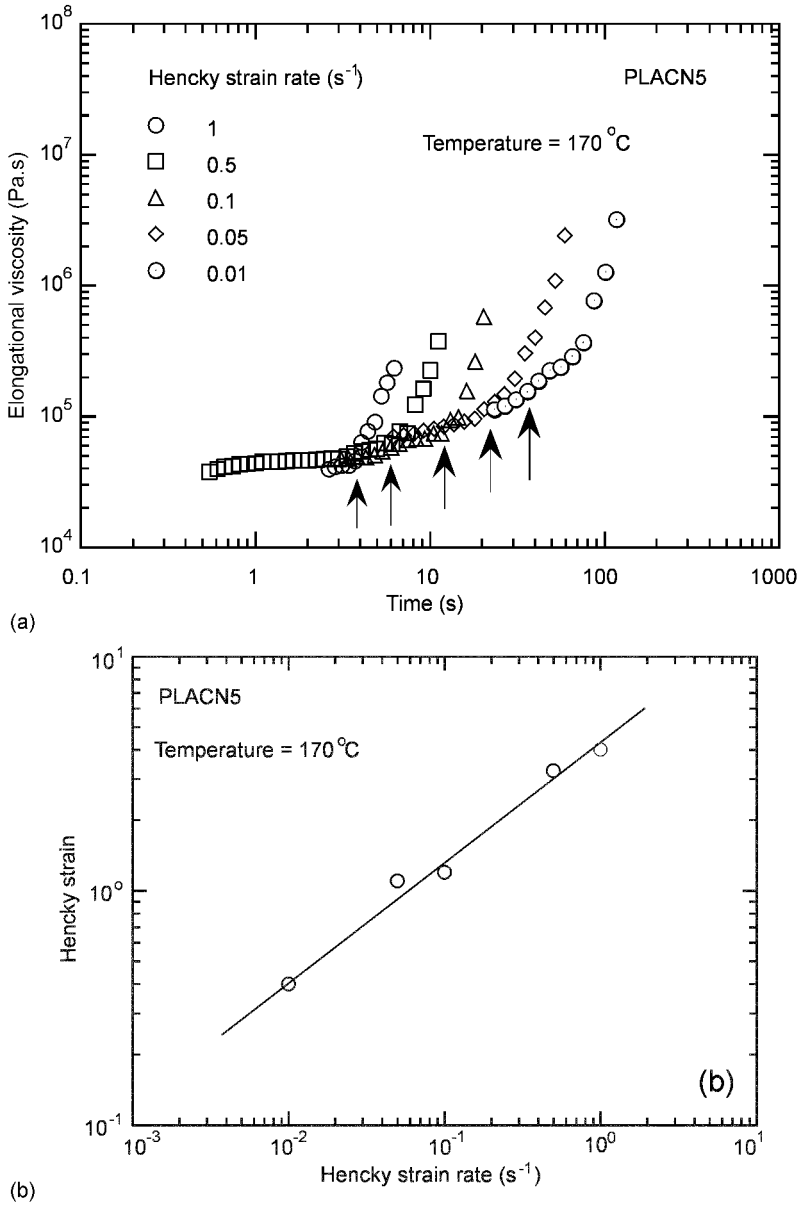

3.19 (a) Time variation of elongational viscosity for PLACN5 (PLA with 5 wt.% C18MMT) melt at 170°C. (b) Strain rate dependence of up-rising Hencky strain.[60] Reproduced from Sinha Ray and Okamoto by permission of Wiley-VCH Verlag GmbH, Germany

different $\dot{\epsilon}_0$ values ranging from 0.01 to $1.0\,s^{-1}$. This figure shows a strong *strain-induced hardening* behaviour for PLACN5. In the early stage, η_E gradually increases with t but almost independent of $\dot{\epsilon}_0$. This is generally called the *linear region* of the viscosity curve. After a certain time, t_{η_E} which is the *up-rising* time (marked with the upward arrows in the figure), was strongly dependent on $\dot{\epsilon}_0$, and a rapid upward deviation of η_E from the curves of the linear region was observed. On the other hand, the authors tried to measure the elongational viscosity of pure PLA but they failed to do that accurately. Low viscosity of pure PLA may be the main reason. However, they confirmed that neither strain-induced hardening in elongation nor rheopexy in shear flow took place in the case of pure PLA having the same molecular weights and polydispersity as that of PLACN3.

Like polypropylene/OMLS systems, the extended Trouton rule, $3\eta_0(\dot{\gamma};t) \cong \eta_E(\dot{\epsilon}_0;t)$, does not hold for PLACN5 melt, as opposed to the melt of pure polymers.[189] These results indicate that in the case of PLACN5, the flow induced internal structural changes also occurred in elongation flow, but the changes were quite different from shear flow.[190] The strong rheopexy observed in shear measurements for PLACN5 at very slow shear rate reflected the fact that the shear-induced structural change involved a process with an extremely long relaxation time.

As to the elongation-induced structure development, Fig. 3.19(b) represents the Hencky strain rate dependence of the up-rising Hencky strain $(\epsilon_{\eta_E}) = \dot{\epsilon}_0 \times t_{\eta_E}$ taken for PLACN5 at 170ºC. The ϵ_{η_E} values increased systematically with the $\dot{\epsilon}_0$. The lower the value of $\dot{\epsilon}_0$, the smaller is the value of ϵ_{η_E}. This tendency probably corresponds to the rheopexy of PLACN5 under slow shear flow.

3.11 Foam processing of biodegradable nanocomposites

Recently, polymeric foams are widely used as packing materials because they are lightweight, have a high strength/weight ratio, have superior insulating properties, and high energy absorbing performance. One of the most widely used polymers for the preparation of foam is PS. It is produced from fossil fuels, consumed and discarded into the environment, ending up as spontaneously *undegradable* waste. Now if foams were made from biodegradable polymeric materials, this problem would be solved. But biodegradable polymers such as PLA have some limitations in foam processing because such polymers do not demonstrate a high strain-induced hardening, which is the primary requirement to withstand the stretching force experienced during the latter stages of bubble growth. The branching of polymer chains, grafting with another copolymer, or blending of branched and linear polymers are the common methods used to improve the extensional viscosity of a polymer in order to make it suitable for foam formation. PLACNs have already been shown to exhibit a high modulus

and, under uniaxial elongation, a tendency toward strong strain-induced hardening. On the basis of these results, Sinha Ray *et al.*[54,60] first conducted foam processing of PLACNs with the expectation that they would provide advanced polymeric foams with many desirable properties. They used a physical foaming method, i.e. batch process, in order to conduct foam processing. This process consists of four stages:[191] (a) saturation of CO_2 in the sample at the

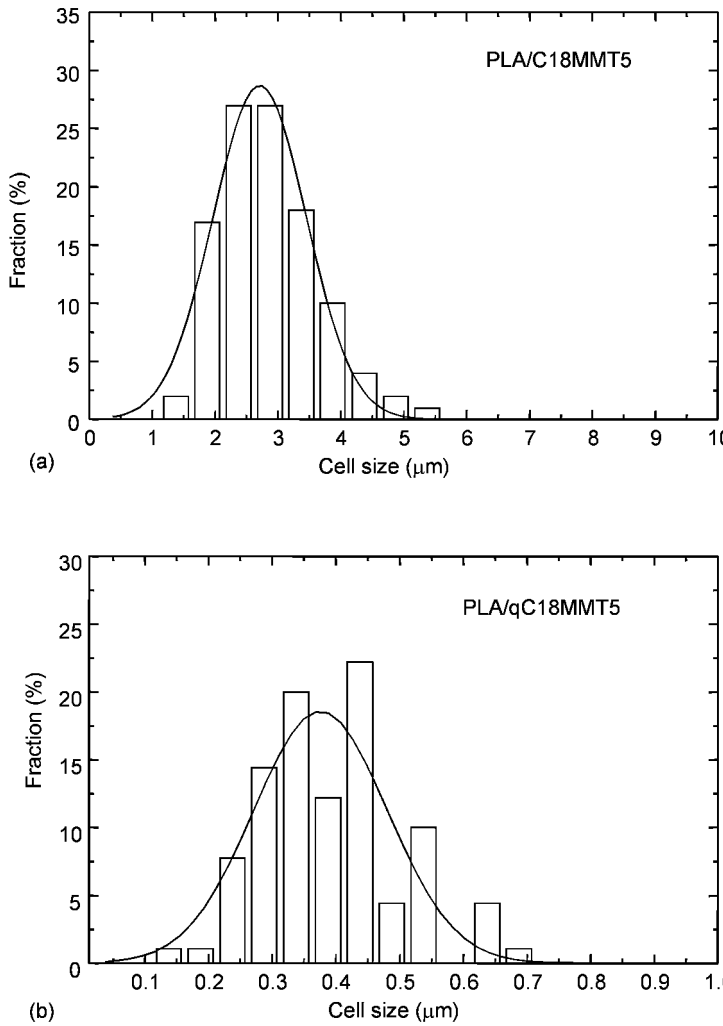

3.20 Cell-size distribution of two different nanocomposite foams. Average values of d in μm and variances σ_d^2 μm^2 in the Gaussian through the data are (a) 2.59 and 0.551 for PLA/C18MMT5 and (b) 0.36 and 0.11 for PLA/qC18MMT5 foams.[54] Reproduced from Fujimoto, Sinha Ray, Okamoto, Ogami and Ueda by permission of Wiley-VCH Verlag GmbH, Germany.

Table 3.8 Morphological parameters of the two different nanocomposite foams.[54] Reproduced from Fujimoto, Sinha Ray, Okamoto, Ogami and Ueda by permission of Wiley-VCH Verlag GmbH, Germany

Nanocomposite	ρ_f (g.cm^{-3})	d (μm)	$N_c \times 10^{-11}$ (cell. cm^{-3})	δ (μm)	d/ξ_{LS}	d/L_{LS}	δ/L_{LS}
PLA/C18MMT5	0.46	2.59	3.56	0.66	10.1	5.8	1.47
PLA/qC18MMT5	0.57	0.36	1172	0.26	4.5	1.8	1.3

desired temperature, (b) cell nucleation when the release of CO_2 pressure starts (forming supersaturated CO_2), (c) cell growth to an equilibrium size during the release of CO_2, and (4) stabilization of the cell via a cooling process of the foamed sample.

Nanocomposite foams exhibited a nice closed-cell structure with homogeneous cells, while the neat PLA foam showed non-uniform cell structure having large cell size (*ca*. 230 μm). Also, the nanocomposite foams showed a smaller cell size (d) and larger cell density (Nc) compared to neat PLA foam, suggesting that the dispersed silicate particles act as nucleating sites for cell formation.[191,192] In the case of nanocomposite foams, they calculated the distribution function of cell size from SEM images. Results are presented in Fig. 3.20. The nanocomposite foams conveniently obeyed a Gaussian distribution. In the case of PLA/qC18MMT5 (see Fig. 3.20), the width of the distribution peaks, which indicates the dispersity of cell size, became narrow accompanied by a finer dispersion of silicate particles. From SEM images, they quantitatively calculated various morphological parameters of the two different nanocomposite foams; these are summarized in Table 3.8. The PLA/qC18MMT5 (nanocellular) foam has a smaller d value (*ca*. 360 nm) and a huge Nc (1.2×10^{14} cell. cm^{-3}) compared to that of PLA/C18MMT5 (microcellular) foam ($d = 2.59$ μm and Nc = 3.56×10^{11} cell. cm^{-3}). These results indicate that the nature of the dispersion plays a vital role in controlling the size of the cell during foaming. On the other hand, the very high value of Nc in the case of the PLA/qC18MMT5 foam indicates that the final ρ_f is controlled by the competitive process in the cell nucleation, its growth, and coalescence. The cell nucleation, in the case of nanocomposite systems, took place in the boundary between the matrix polymer and the dispersed silicate particles. For this reason, the cell growth and coalescence were strongly affected by the characteristic parameter (see Table 3.8), and the storage and loss modulus ($\approx$ viscosity component) of the materials during processing. This may create nanocellular foams without the loss of mechanical properties in the case of polymeric nanocomposites.

3.12 Conclusions

Because of new environmental polices, societal concerns and growing environmental awareness have triggered the search for new products and processing that

are benign to the environment. Biodegradable polymers are considered as alternatives to the existing petroleum-based plastics. Several examples of biodegradable polymers, their synthetic procedures and properties have been discussed here. Incorporation of layered silicates, organically modified or not, into the biodegradable polymer matrix, i.e., the preparation of nanocomposites, has also been discussed. The resulting biodegradable nanocomposites possess several advantages:

- They generally exhibit improved mechanical properties both in solid and molten states compared to conventional filler composites, because reinforcement in nanocomposites occurs in 2D rather than 1D, and no special processing is required to laminate the composites.
- They show much improved barrier properties towards the small gases, e.g. oxygen, water, carbon dioxide, etc., because of the formation of a 'tortuous path' in the presence of layered silicate in the nanocomposites.
- Thermal stability of biodegradable polymers also increases after nanocomposites preparation, because clay acts as a heat barrier, which enhances the overall thermal stability of the system, as well as assisting in the formation of char after thermal decomposition.
- The compost degradation rate of some biodegradable polymers is significantly enhanced after nanocomposite preparation with organically modified layered silicate and we can control the biodegradability by judicious choice of clay.
- Melt viscosity of pure polymer increases after nanocomposites formation. This will help us for further processing.

The above improved properties are generally attained at low silicate content (≤ 5 wt.%) compared to that of conventional filler field composites.[193] For these reasons, these are far lighter in weight than conventional biodegradable composites and make them competitive with other materials for specific applications such as packaging. Biodegradable nanocomposite foams appear to have a very bright future for a wide range of applications. These are entirely new types of composite materials with various interesting properties and may soon be competitive with the existing fossil plastic materials. PLA-based nanocomposites have already started commercial application as a short-term packing material. Although, biodegradable nanocomposites have very strong future protects, the present low level of production and high costs restrict them for a wider range of applications. Therefore, the most important factors in the formation of a biodegradable polymer-based industry include cost reduction of biodegradable polymers as well as public and political acceptance.

Finally, for biodegradable nanocomposites to meet a wide range of applications, nanocomposites formulation must be further researched and modified so that mechanical and other properties can be easily manipulated depending on the end-user's requirements.

3.13 Acknowledgements

The Canada Research Chair on Polymer Physics and Nanomaterials supported this work financially.

3.14 References

1. Fomin V A, Guzeev V V (2001), 'Biodegradable polymers, their present state and future prospects', *Prog Rubb Plastics Tech*, 17, 186–204.
2. Sinha Ray S, Okamoto M (2003), 'Polymer/layered silicate nanocomposites: a review from preparation to processing', *Prog Polym Sci*, 28, 1539–641.
3. Biswas M, Sinha Ray S (2001), 'Recent progress in synthesis and evaluation of polymer montmorillonite nanocomposites', *Adv Polym Sci*, 155, 167–221.
4. Alexander M, Dubois P (2000), 'Polymer-layered silicate nanocomposites: preparation, properties and uses of a new class of materials', *Mater Sci Eng R*, 28,1–63.
5. Giannelis E P, Krishnamoorti R, Manias E (1999), 'Polymer-silicate nanocomposites: model systems for confined polymers and polymer brushes', *Adv Polym Sci*, 138, 107–47.
6. LeBaron P C, Wang Z, Pinnavaia T J (1999), 'Polymer-layered silicate nanocomposites: an overview', *J Appl Clay Sci*, 15, 11–29.
7. Mohanty A K, Drzal LT, Misra M (2003), 'Nano reinforcement of bio-based polymers-the hope and reality', *Polym Mat Sci Eng*, 88, 60–61.
8. Hiroi R, Sinha Ray S, 'Okamoto M (2004), 'Organically modified layered titanate: a new nanofiller to improve the performance of biodegradable polylactide', *Macromolecular Rapid Commun*, 25, 1359.
9. Mitchell C A, Bahr J L, Arepalli S, Tour J M, Krishnamoorti R (2002), 'Dispersion of functionalized carbon nanotubes in polystyrene', *Macromolecules,* 35, 8825–30.
10. Pötschke P, Bhattacharyya A, Janke A, Goering H (2003), 'Melt-mixing of polycarbonate/multi-wall carbon nanotube composites', *Comp Interfaces*, 10, 389–404.
11. Andrews R, Wisenberger M C (2004), 'Carbon nanotube polymer composites', *Curr Opinion Solid State Mat Sci*, 8, 31–37.
12. Hackett E, Manias E, Giannelis E P (1998), 'Molecular dynamics simulations of organically modified layered silicates', *J Chem Phys*, 108, 7410–15.
13. Hackett E, Manias E, Giannelis E P (2000), 'Computer simulation studies of PEO/layered silicate nanocomposites', *Chem Mater*, 12, 2161–7.
14. VanderHart D L, Asano A, Gilman J W (2001), 'NMR measurements related to clay dispersion quality and organic-modifier stability in nylon 6/clay nanocomposites', *Macromolecule*, 38, 3819–22.
15. Loo L S, Gleason K K (2003), 'Fourier transforms infrared investigation of the deformation behavior of montmorillonite in nylon 6/nanoclay nanocomposites', *Macromolecules*, 36, 2587–90.
16. Chen J S, Poliks M D, Ober C K, Zhang Y, Wiesner U, Giannelis E P (2002), 'Study of the interlayer expansion mechanism and thermal-mechanical properties of surface-initiated epoxy nanocomposites', *Polymer*, 43, 4895–904.
17. Usuki A, Kawasumi M, Kojima Y, Okada A, Kurauchi T, Kamigaito O (1993), 'Swelling behaviour of montmorillonite cation exchanged for ϵ-amine acid by ϵ-caprolactam', *J Mater Res*, 8, 1174–84.

18. Kojima Y, Usuki A, Kawasumi M, Okada A, Fukushima Y, Kurauchi T, Kamigaito O (1993), 'Mechanical properties of nylon 6-clay hybrid', *J Mater Res*, 8, 1185–89.
19. Aranda P, Ruiz-Hitzky E (1992), 'Poly(ethylene oxide)-silicate intercalation materials' *Chem Mater*, 4, 1395–403.
20. Vaia R A, Ishii H, Giannelis E P (1993), 'Synthesis and properties of two-dimensional nanostructures by direct intercalation of polymer melts in layered silicates', *Chem Mater*, 5, 1694–96.
21. Fisher H (2003), 'Polymer nanocomposites: from fundamental research to specific applications', *Mater Sci Eng C,*23, 763–72.
22. Mishra J K, Ha C.-S (2004), 'Heat shrinkable behavior and mechanical response of a low-density polyethylene/millable polyurethane/organoclay ternary nanocomposite', *Macromol Rapid Commun,* 25, 1851–55.
23. Schmidt D, Shah D, Giannelis E P (2002), 'New advances in polymerlayered silicate nanocomposites', *Curr Opin Solid State Mat*, 6, 205–12.
24. Sinha Ray S, Pouliot S, Bousmina M, Utracki L A (2004), 'Role of organically modified layered silicate as an active interfacial modifier in immiscible polystyrene/polypropylene blends', *Polymer,* 25, 8403–13.
25. Hsieh A J, Moy P, Beyer F L, Madison P, Napadensky E, Ren J, Krishnamoorti R (2004), 'Mechanical response and rheological properties of polycarbonate layered-silicate nanocomposites', *Polym Eng Sci,* 44, 825–37.
26. Vaia R A, Giannelis E P (1997), 'Polymer melts intercalation in organically-modified layered silicates: model predictions and experiment', *Macromolecules*, 30, 8000–09.
27. Brindly S W, Brown G, eds, *Crystal structure of clay minerals and their x-ray diffraction*, Mineralogical Society, London, 1980.
28. Krishnamoorti R, Vaia R A, Giannelis E P (1996), 'Structure and dynamics of polymer-layered silicate nanocomposites', *Chem Mater*, 8, 1728–34.
29. Fran Francis C W (1973), 'Adsorption of polyvinylpyrrolidone on reference clay minerals', *Soil Sci*, 115, 40–54.
30. Blumstein A (1965), 'Polymerization of adsorbed monolayers: II. thermal degradation of the inserted polymers', *J Polym Sci A3* 3, 2665–73.
31. Messersmith P B, Giannelis E P (1995), 'Synthesis and barrier properties of poly(ϵ-caprolactone)-layered silicate nanocomposites', *J Polym Sci Part A: Polym Chem*, 33, 1047–57.
32. Vaia R A, Jant K D, Kramer E J, Giannelis E P (1996), 'Microstructural evaluation of melt-intercalated polymer-organically modified layered silicate nanocomposites', *Chem Mater*, 8, 2628–35.
33. Morgan A B, Gilman J W (2003), 'Characterization of poly-layered silicate (clay) nanocomposites by transmission electron microscopy and X-ray diffraction: a comparative study', *J Appl Polym Sci*, 87, 1329–38.
34. Bafna A, Beaucage G, Mirabella F, Mehta S (2003), '3D Hierarchical orientation in polymer-clay nanocomposite films', *Polymer*, 44, 1103–15.
35. Bafna A, Beaucage G, Mirabella F, Mehata S (2002), Shear induced orientation and associated property enhancement in polymer/clay nanocomposites. Proc. Nanocomposites 2002 ECM Publication, Sept. 23–25, San Diego, California, USA.
36. Sinha Ray S, Bousmina M (2005), 'Biodegradable polymers and their layered silicate nanocomposites: in greening the 21st century materials world', *Prog Mater Sci*, 50, 962.

37. Ogata N, Jimenez G, Kawai H, Ogihara T (1997), 'Structure and thermal/mechanical properties of poly(L-lactide)-clay blend', *J Polym Sci Part B: Polym Phys*, 35, 389–96.
38. Bandyopadhyay S, Chen R, Giannelis E P (1999), 'Biodegradable organic-inorganic hybrids based on poly(l-lactide)', *Polym Mater Sci Eng*, 81, 159–60.
39. Sinha Ray S, Okamoto K, Yamada K, Okamoto M (2002), 'Novel porous ceramic material via burning of polylactide/layered silicate nanocomposite', *Nano Letts*, 2, 423–26.
40. Sinha Ray S, Yamada K, Okamoto M, Ueda K (2002), 'New polylactide/layered silicate nanocomposite: a novel biodegradable material', *Nano Letts*, 2, 1093–96.
41. Sinha Ray S, Maiti P, Okamoto M, Yamada K, Ueda K (2002), 'New polylactide/layered silicate nanocomposites. 1. Preparation, characterization and properties', *Macromolecule*, 35, 3104–10.
42. Sinha Ray S, Yamada K, Ogami A, Okamoto M, Ueda K (2002), 'New polylactide layered silicate nanocomposite: nanoscale control of multiple properties', *Macromol Rapid Commun,* 23, 493–97.
43. Pluta M, Caleski A, Alexandre M, Paul M-A, Dubois P (2002), 'Polylactide/montmorillonite nanocomposites and microcomposites prepared by melt blending: structure and some physical properties', *J Appl Polym Sci*, 92, 1497–506.
44. Sinha Ray S, Okamoto M, Yamada K, Ueda K (2002), 'New polylactide/layered silicate nanocomposites: concurrent improvement of materials properties and biodegradability', Nanocomposites 2002 Proc., ECM Publication, San Diego, USA.
45. Sinha Ray S, Okamoto M, Yamada K, Ueda K (2002), 'New biodegradable polylactide/layered silicate nanocomposites: preparation, characterization and materials properties', ICCE-9 Proc., 659–60, San Diego, USA.
46. Yamada K, Ueda K, Sinha Ray S, Okamoto M (2002), 'Preparation and properties of polylactide/layered silicate nanocomposites', *Kobunshi Robunshu*, 59, 760–65.
47. Maiti P, Yamada K, Okamoto M, Ueda K, Okamoto K (2002), 'New polylactide/layered silicate Nanocomposites: role of organoclay', *Chem Mater*, 14, 4654–61.
48. Paul M-A, Alexandre M, Degee P, Henrist C, Rulmont A, Dubois P (2003), 'New nanocomposite materials based on plasticized poly(L-lactide) and organo-modified montmorillonites: thermal and morphological study', *Polymer*, 44, 443–50.
49. Sinha Ray S, Yamada K, Okamoto M, Ueda K (2003), 'New polylactide/layered silicate nanocomposites. 2. Concurrent improvements of material properties, biodegradability and melt rheology', *Polymer*, 44, 857–66.
50. Isobe Y, Ino T, Kageyama Y, Nakanoa M, Usuki A (2003), 'Improvement of heat resistance for bioplastics', 2003 SAE World Congress, Detroit, Michigan, March 3–6, 2003.
51. Nam J Y, Sinha Ray S, Okamoto M (2003), 'Crystallization behaviour and morphology of biodegradable polylactide/layered silicate nanocomposite', *Macromolecules*, 36, 7126–31.
52. Sinha Ray S, Yamada K, Okamoto M, Ueda K (2003), 'Control of biodegradability of polylactide via nanocomposite technology', *Macromol Mater Eng*, 288, 203–8.
53. Sinha Ray S, Yamada K, Okamoto M, Ogami A, Ueda K (2003), 'New polylactide/layered silicate nanocomposites. 3. high performance biodegradable materials. *Chem Mater*, 15, 1456–65.
54. Fujimoto Y, Sinha Ray S, Okamoto M, Ogami A, Ueda K (2003), 'Well-controlled biodegradable foams: from microcellular to nanocellular', *Macromol Rapid*

Commun, 24, 457–61.
55. Sinha Ray S, Yamada K, Okamoto M, Ogami A, Ueda K (2003), 'New polylactide/layered silicate nanocomposites:4. structure, properties and biodegradability', *Comp Interfaces*, 10, 435–50.
56. Chang J H, An Y U, Cho D, Giannelis E P (2003), 'Polylactide nanocomposites: comparison of their properties with montmorillonite and synthetic mica (II)', *Polymer*, 44, 3715–20.
57. Sinha Ray S, Yamada K, Okamoto M, Fujimoto Y, Ogami A, Ueda K (2003), 'New polylactide/layered silicate nanocomposites:5. designing of materials with desired properties', *Polymer*, 44, 6633–46.
58. Sinha Ray S, Okamoto M (2003), 'Biodegradable polylactide/layered silicate nanocomposites: open a new dimension for plastics and composites', *Macromol Rapid Commun*, 24, 815–40.
59. Sinha Ray S, Yamada K, Okamoto M, Ueda K (2003), 'Biodegradable polylactide/montmorillonite nanocomposites', *J Nanosci Nanotech*, 3, 503–50.
60. Sinha Ray S, Okamoto M (2003), 'New polylactide/layered silicate nanocomposites: 6. melt rheology and foam processing', *Macromol Mater Eng*. 288, 936–44.
61. Chang J-H, Uk-An Y, Sur G S (2003), 'Poly(lactic acid) nanocomposites with various organoclays. I. Thermomechanical properties, morphology, and gas permeability', *J Polym Sci Part B: Polym Phys*, 41, 94–103.
62. Paul M A, Alexandre M, Degee P, Calberg C, Jerome R, Dubois P (2003), 'Exfoliated polylactide/clay nanocomposites by in-situ coordination-insertion polymerization', *Macromol Rapid Commun*, 24, 561–66.
63. Krikorian V, Pochan D (2003), 'Poly(L-lactide acid)/layered silicate nanocomposite: fabrication, characterization, and properties', *Chem Mater*, 15, 4317–24.
64. Lee J H, Park T G, Park H S, Lee D S, Lee Y K, Yoon S C, Nam J D (2003), 'Thermal and mechanical characteristics of poly(L-lactic acid) nanocomposite scaffold', *Biomaterials*, 24, 2773–78.
65. Maiti P, Batt C A, Giannelis E P (2003), 'Renewable plastics: synthesis and properties of PHB nanocomposites', *Polym Mater Sci Eng*, 88, 58–59.
66. Chen G X, Hao G J, Guo T Y, Song M D, Zhang B H (2004), 'Crystallization kinetics of poly(3-hydroxybutyrate-co-3-hydroxyvalerate)/clay nanocomposites', *J Appl Polym Sci*, 93, 655–61.
67. de Carvalho A J F, Curvelo A A S, Agnelli J A M (2001), 'A first insight on composites of thermoplastic starch and kaolin', *Carbohydrate Polym*, 45, 189–94.
68. Park H M, Li X, Jin C Z, Park C Y, Cho W J, Ha C K (2002), 'Preparation and properties of biodegradable thermoplastic starch/clay hybrids', *Macromol Mater Eng*, 287, 553–58.
69. Marques A P, Reis, R L, Hunt J A (2002), 'The biocompatibility of novel starch-based polymers and composites: in vitro studies', *Biomaterials*, 23, 1471–78.
70. Park H M, Lee W K, Park C Y, Cho W J, Ha C S (2003), 'Environmental friendly polymer hybrids: part 1. mechanical, thermal, and barrier properties of thermoplastic starch/clay Nanocomposites', *J Mater Sci*, 38, 909–15.
71. Wilhelm H M, Sierakowski M R, Souza G P, Wypych F (2003), 'The influences of layered compounds on the properties of starch/layered compound composites', *Polym Int*, 52, 1035–44.
72. McGlashan S A, Halley P J (2003), 'Preparation and characterization of

biodegradable starch-based nanocomposite materials', *Polym Int*, 52, 1767–73.
73. Wilhelm H M, Sierakowski M R, Souza G P, Wypych F (2003), 'Starch films reinforced with mineral clay', *Carbohydrate Polym*, 52, 101–10.
74. Uyama H, Kuwabara Mai, Tsujimoto T, Nakano M, Usuki A, Kobayashi S (2003), 'Green nanocomposites from renewable resources: plant oil-clay hybrid materials', *Chem Mater*, 15, 2492–94.
75. Tsujimoto T, Uyama H, Kobayashi S (2003), 'Green nanocomposites from renewable resources: biodegradable plant oil-silica hybrid coatings', *Macromol Rapid Commun*, 24, 711–14.
76. Uyama H, Kuwabara Mai, Tsujimoto T, Nakano M, Usuki A, Kobayashi S (2004), 'Organic-inorganic hybrids from renewable plant oils and clay', *Macromol Biosci*, 4, 354–60.
77. Misra M, Park H, Mohanty A K, Drzal L T (2004), 'Injection molded green nanocomposite materials from renewable resources. Paper presented at GPEC-2004, Feb. 18–19.
78. Zheng J P, Li Ping, Ma Y L, Yao K D (2002), 'Gelatine/montmorillonite hybrid nanocomposite.I. preparation and properties', *J Appl Polym Sci*, 86, 1189–94.
79. Watzke H J, Dieschbourg C (1994), 'Novel-silica-biopolymer nanocomposites: the silica sol-gel process in biopolymer organogel', *Adv Colloid Interface Sci*, 50, 1–14.
80. Darder M, Colilla M, Ruiz-Hitzky E (2003), 'Biopolymer-clay nanocomposites based on chitosan intercalated in montmorillonite', *Chem Mater*, 15, 3774–80.
81. Dritis V A, Tchoubar C (1990), X-ray diffraction by disordered lamellar structures. Springer- Verlag: New York, 21–22.
82. Cullity B D (1978), *Principles of X-ray diffraction*. Addison-Wesley: Reading, MA.
83. Konioka M, Tamaki A, Doi Y (1989), 'Crystalline and thermal properties of bacterial copolyesters: poly(3-hydroxybutyrate-co-3-hydroxyvalerate) and poly(3-hydroxybutyrate-co-4-hydroxybutyrate)', *Macromolecules*, 22, 694–97.
84. Liu W, Yang H, Wang Z, Dong L, Liu J (2004), 'Thermal properties of poly(3-hydroxybutrate-co-3-hydroxyvalerate) copolymer', *J Appl Polym Sci*, 93, 655–61.
85. Gibbons B J, Roach P J, Hurley T D (2002), 'Crystal structure of the autocatalytic initiator of glycogen synthesis, glycogenin', *J Mol Biol*, 319, 463–77.
86. Doi Y and Fukuda K (eds) (1994), *Biodegradable Plastics and Polymers*, Studies in Polymer Science, vol. 12, Elsevier, Amsterdam.
87. Zhou G W, Willett J L, Carriere C J (2001), 'Effect of starch content on viscosity of starch filled poly(hydroxyl ester ether) composites', *J Polym Sci Part B: Polym Phys,* 41, 1365–72.
88. Ke T Y, Sun X Z (2001), 'Effects of moisture content and heat treatment on the physical properties of starch and poly(lactic acid) blends', *J Appl Polym Sci*, 81, 3069–82.
89. George E R, Sullivan T M, Park E H (1994), 'Preparation of high moisture content thermoplastic polyester starch', *Polym Eng Sci*, 34, 17–24.
90. Reis R L, Cunha A M, Allan P S, Bevis M J (1997), 'Structure development and control of injection-molded hidroxyapatite-reinforced starch/EVOH composites', *Adv Polym Tech* 16, 263–77.
91. de Nooy A E J, Besemer A C, van Bekkum H (1995), 'Highly selective nitroxyl radical-mediated oxidation of primary alcohol groups in water-soluble glucans', *Carbohydr Res*, 269, 89–98.
92. Kobayashi S, Uyama H, Ohmae S (2001), 'Enzymatic polymerization for precision

polymer synthesis', *Bull Chem Soc Jpn*, 74, 613–35.
93. Kobayashi S, Uyama H, Kimura S (2001), 'Enzymatic polymerization', *Chem Rev*, 101, 3793–18.
94. Matsumura S (2002), 'Enzyme-catalyzed synthesis and chemical recycling of polyesters', *Macromol Biosci*, 2, 105–26.
95. Kobayashi S, Uyama H (2002), 'In vitro polyester synthesis via enzymatic polymerization', *Curr Org Chem*, 6, 209–22.
96. Tsujimoto T, Uyama H, Kobayashi S (2001), 'Enzymatic synthesis of cross-linkable polyesters from renewable resources', *Biomacromolecules*, 2, 29–31.
97. Tsujimoto T, Uyama H, Kobayashi S (2002), 'Enzymatic synthesis and curing of biodegradable crosslinkable polyesters', *Macromol Biosci*, 2, 329–35.
98. Uyama H, Kuwabara M, Tsujimoto T, Kobayashi S (2003), 'Enzymatic synthesis and curing of biodegradable epoxide-containing polyesters from renewable resources, *Biomacromolecules* 4, 211–15.
99. Mohanty A K, Wibowo A, Misra M, Drzal L T (2003), 'Development of renewable resource-based cellulose acetate bioplastic: Effect of process engineering on the performance of cellulosic plastics', *Polym Eng Sci*, 43, 1151–61.
100. Draye J P, Delaey B, Voorde A V D, Bulcke A V D, Rue B D, Schacht E (1998), 'In vitro and in vivo biocompatibility of dextran dialdehyde cross-linked gelatin hydrogel films', *Biomaterials*, 19, 1677–87.
101. Fakirov S, Sarac Z, Anbar T, Boz B, Bahar I, Evstatiev M, Apostolov A A, Mark J E, Kloczkowski A (1997), 'Mechanical properties and transition temperature of crosslinked oriented gelatine II. Effect of orientation and water content on transition temperatures', *Colloid Polym Sci*, 275, 307–14.
102. Bigi A, Panzavolta S, Roveri N (1998), 'Hydroxyapatite-gelatin films: a structural and mechanical characterization', *Biomaterials*, 19, 739–44.
103. Lin F H, Yao C H, Sun J S (1998), 'Biological effects and cytotoxicity of the composite composed by tricalcium phosphate and glutaraldehyde cross-linked gelatine', *Biomaterials*, 19, 905–17.
104. Wan Y Z, Wang Y L, Luo H L, Cheng G X, Yao K D (2000), 'Carbon fiber-reinforced gelatin composites. I. preparation and mechanical properties', *J* Appl Polym Sci, 75, 987–93.
105. Pan J R, Huang C, Chen S, Chung Y C (1999), 'Evaluation of a modified chitosan biopolymer for coagulation of colloidal particles', *Colloids Surf A*,147, 359–64.
106. Chenu C, Pons C H, Robert M (1987), 'Chitosan/clay composites', *Proceedings of the international clay conference*, Denver, CO.
107. Clarck G L, Smith A F (1936), 'X-ray diffraction studies of chitin, chitosan, and derivatives', *J Phys Chem*, 40, 863–79.
108. Blackwell J, Minke R, Gardner K H (1978), 'Determination of the structures of α- and β-chitins by x-ray diffraction'. Proceedings of the first international conference on chitin/chitosan; Muzzarelli R A A, Pariser E R (eds), MIT: Boston.
109. Sinha Ray S, Okamoto K, Maiti P, Okamoto M (2002), 'New poly(butylene succinate)/layered silicate nanocomposites.1. preparation, characterization, and mechanical properties', *J Nanosci Nanotech*, 2, 171–76.
110. Sinha Ray S, Okamoto K, Okamoto M (2003), 'Structure-property relationship in biodegradable poly(butylene succinate)/layered silicate nanocomposites', *Macromolecules*, 36, 2355–67.
111. Sinha Ray S, Okamoto K, Okamoto M (2002), 'New poly(butylene succinate)/

layered silicate nanocomposites. 1. Preparation, characterization, and properties', *JPPS Proceedings*, 233–35.
112. Okamoto K, Sinha Ray S, Okamoto M (2003), 'New poly(butylene succinate)/layered silicate nanocomposites. 2. Effect of organically modified layered silicates on morphology, materials properties, melt rheology, and biodegradability', *J Polym Sci Part B: Polym Phys*, 41, 3160–70.
113. Mitsunaga T, Okada K, Nagase Y (2002), Properties of biodegradable resin/clay nanocomposites. PPS Asia/Australia Meeting, Taipei, Taiwan, Paper No. 139.
114. Mitsunaga T, Okada K, Nagase Y (2002), Properties of biodegradable resin/natural fiber composites containing nano-scale particles. PPS Asia/Australia Meeting, Taipei, Taiwan, Paper No. 140.
115. Sinha Ray S, Okamoto K, Okamoto M (2006), 'New poly(butylene succinate)/layered silicate nanocomposites. 3. Materials properties and melt rheology', *J Appl Polym Sci*, in press.
116. Okamoto K, Sinha Ray S, Okamoto M (2006), 'Preparation, characterization and properties of poly(butylene succinate)/synthetic mica nanocomposites', *Polymer*, submitted.
117. Sinha Ray S, Okamoto K, Okamoto M (2006), 'Melt rheology and strain induced hardening behaviour of biodegradable poly(butylene succinate)/synthetic fluorine mica nanocomposites', *Langmuir*, submitted.
118. Sinha Ray S, Bousmina M (2005), 'Poly(butylene succinate-*co*-adipate)/montmorillonite nanocomposites: Effect of organic modifier miscibility on structure, properties, and viscoelasticity', *Polymer*, 46, 12430–12439.
119. Sinha Ray S, Bousmina M, Okamoto K (2005), 'Structure and properties of nanocomposites based on poly(butylene succinate-*co*-adipate) and organically modified montmorillonite', *Macromol Mater Eng*, 290, 759–68.
120. Lim S T, Hyun Y H, Choi H J, Jhon M S (2002), 'Synthetic biodegradable aliphatic polyester/montmorillonite nanocomposites', *Chem Mater*, 14, 1839–44.
121. Lee S R, Park H M, Lim H L, Kang T, Li X, Cho W J, Ha C S (2002), 'Microstructure, tensile properties, and biodegradability of aliphatic polyester/clay nanocomposites', *Polymer*, 43, 2495–500.
122. Bharadwaj R K, Mehrabi A R, Hamilton C, Trujillo C, Murga M Fan, Chavira A, Thompson A K (2002), 'Structure-property relationships in cross-linked polyester-clay nanocomposites', *Polymer*, 43, 3699–705.
123. Messersmith P B, Giannelis E P (1993), 'Polymer-layered silicate nanocomposites: in-situ intercalative polymerization of ε-caprolactone in layered silicates', *Chem Mater*, 5, 1064–66.
124. Jimenez G, Ogata N, Kawai H, Ogihara T (1997), 'Structure and thermal/mechanical properties of poly(ε-caprolactone)-clay blend', *J Appl Polym Sci*, 64, 2211–20.
125. Krishnamoorti R, Giannelis E P (1997), 'Rheology of end-tethered polymer layered silicate nanocomposites', *Macromolecules*, 30, 4097–102.
126. Pantoustier N, Alexandre M, Degee P, Calberg C, Jerome R, Henrist C, Cloots R, Rulmont A, Dubois P (2001), 'Poly(ϵ-caprolactone) layered silicate nanocomposites: effect of clay surface modifiers on the melt intercalation process', *e-Polymer*, 9, 1–9.
127. Lepoittevin B, Pantoustier N, Alexander M, Calberg C, Jerome R, Dubois P (2002), 'Polyester layered silicate nanohybrids by controlled grafting polymerization', *J*

Mater Chem, 12, 3528–32.
128. Pantoustier N, Lepoittevin B, Alexandre M, Kubies D, Calberg C, Jerome R, Dubois P (2002), 'Biodegradable polyester layered silicate nanocomposites based on poly(ϵ-caprolactone)', *Poly Eng Sci*, 42, 1928–37.
129. Lepoittevin B, Pantoustier N, Devalckenaere M, Alexandre M, Kubies D, Calderg C, Jerome R, Dubois P (2002), 'Poly(ϵ-caprolactone)/clay nanocomposites by in-situ intercalative polymerization catalyzed by dibutyltindimethoxide', *Macromolecules*, 35, 8385–90.
130. Lepoittevin B, Devalckenaere M, Pantoustier N, Alexandre M, Kubies D, Calberg C, Jerome R, Dubois P (2002), 'Poly(ϵ-caprolactone)/clay nanocomposites prepared by melt intercalation: mechanical, thermal and rheological properties', *Polymer*, 43, 4017–23.
131. Utracki L A (2002), Flow behavior of nanocomposites with polycaprolacton matrix. PPS2002 Meeting Proc. Taipei, Taiwan, Nov. 4–8.
132. Tortora M, Vittoria V, Galli G, Ritrovati S, Chiellini E (2002), 'Transport properties of modified montmorillonite-poly(ϵ-caprolactone) nanocomposites', *Macromol Mater Eng*, 287, 243–49.
133. Gorrasi G, Tortora M, Vittoria V, Pollet E, Lepoittenvin B, Alexandre M, Dubois P (2003), 'Vapor barrier properties of polycaprolactone montmorillonite nanocomposites: effect of clay dispersion', *Polymer*, 44, 2271–79.
134. Lepoittevin B, Pantoustier N, Devalckenaere M, Alexandre M, Calberg C, Jerome R, Henrist C, Rulmont A, Dubois P (2003), 'Polymer/layered silicate nanocomposites by combined intercalative polymerization and melt intercalation: a master batch processes, *Polymer*, 44, 2033–40.
135. Utracki L A, Simha R, Garcia-Rejon A (2003), 'Pressure-volume-temperature dependence of poly-ϵ-caprolactam/clay nanocomposites', *Macromolecules*, 36, 2114–21.
136. Shima R, Utracki L A, Garcia-Rejon A (2001), 'Pressure-volume-temperature relations of a poly-ϵ-caprolactam and its nanocomposite', *Composite Interfaces*, 8, 345–53.
137. Wu TM, Cheng J-C, Yan M-C (2003), 'Crystallization and thermoelectric behaviour of conductive-filler-filled poly(ϵ-caprolactone)/poly(vinyl butyral)/montmorillonite nanocomposites', *Polymer*, 44, 2553–62.
138. Di Y, Iannace S, Maio E D, Nicolais L (2003), 'Nanocomposites by melt intercalation based on polycaprolactone and organoclay', *J Polym Sci Part B: Polym Phys*, 41, 670–78.
139. Greenland D J (1963), 'Adsorption of poly(vinyl alcohols) by montmorillonite', *J Colloid Sci*, 18, 647–64.
140. Ogata N, Kawakage S, Ogihara T (1997), 'Poly(vinyl alcohol)-clay and poly(ethylene oxide)-clay blend prepared using water as solvent', *J Appl Polym Sci*, 66, 573–81.
141. Strawhecker K E, Manias E (2000), 'Structure and properties of poly(vinyl alcohol)/Na^+-montmorillonite nanocomposites', *Chem Mater*, 12, 2943–49.
142. Wang Y, Wang Y, Yan D (2003), 'Properties of poly(vinyl alcohol)/montmorillonite nanocomposite fiber', *Polym Prepr (USA),* 44, 1102–03.
143. Chang J H, Jang T G, Ihn K J, Sur G S (2003), 'Poly(vinyl alcohol) nanocomposites with different clays: pristine clays and organoclays', *J Appl Polym Sci*, 90, 3204–14.
144. Yu Y H, Lin C Y, Yeh J M, Lin W H (2003), 'Preparation and properties of poly(vinyl alcohol)-clay nanocomposite materials', *Polymer*, 44, 3553–60.

145. Bhari K, Mitomo H, Enjoji T, Yoshii F, Makuuchi K (1998), 'Radiation crosslinked poly(butylene succinate) foam and its biodegradation', *Polym Degrd Stab*, 62, 551–57.
146. Doi Y, Kasuya K, Abe H, Koyama N, Ishiwatari S, Takagi K, Yoshida Y (1996), 'Evaluation of biodegradabilities of biosynthetic and chemosynthetic polyesters in river water', *Polym Degrd Stab*, 51, 281–86.
147. Uesaka T, Nakane K, Maeda S, Ogihara T, Ogata N (2000), ' Structure and physical properties of poly(butylene succinate)/cellulose acetate blends', *Polymer*, 41, 8449–54.
148. Fujimaki T (1998), 'Processability and properties of aliphatic polyester, 'bionolle', synthesized by polycondensation reaction', *Polym Degrad Stab*, 59, 209–14.
149. Mani R, Bhattacharya M (2001), 'Properties of injection moulded blends of starch and modified biodegradable polyesters', *Euro Polym J*, 37, 515–26.
150. Yasuda T, Takiyama E (1995), Biodegradable poly(butylene succinate). US Pat. 5 391 644.
151. Nakayama A, Kawasaki N, Maeda Y, Arvanitoyannis I, Ariba S, Yamamoto N (1997), 'Study of biodegradability of poly(δ-valerolactone-*co*-L-lactide)s', *J Appl Polym Sci*, 66, 741–48.
152. Kesel C D, Wauven C V, David C (1997), 'Biodegradation of polycaprolactone and its blends with poly(vinylalcohol) by micro-organisms from a compost of household refuse', *Polym Degrad Stab*, 55, 107–13.
153. Ishiaku U S, Pang K W, Lee W S, Ishak Z A M (2002), 'Mechanical properties and enzymic degradation of thermoplastic and granular sago starch filled poly(ϵ-caprolactone)', *Eur Polym J*, 38, 393–401.
154. Rees R W (1985), In *Encyclopedia Polym Sci. Eng*, Mark J E (ed.), John Wiley and Sons: New York, p. 395.
155. Grim R E (1968), *Clay Mineralogy*. McGraw-Hill: New York.
156. Usuki A, Kojima A, Kawasumi M, Okada A, Fukushima Y, Kurauchi T, Kamigaito O (1993), 'Synthesis of nylon-6-clay hybrid', *J Mater Res*, 8, 1179–83.
157. Kojima Y, Usuki A, Kawasumi M, Okada A, Karauchi T, Kamigaito O (1993), 'One-pot synthesis of nylon-6-clay hybrid', *J Polym Sci, Part A: Polym Chem*, 31, 1755–58.
158. Johns D B, Lenz R W, Luecke A (1984), in *Ring-Opening Polymerization*, vol. 1, Ivin K J, Saegusa T (eds), Wiley: New York, p. 461.
159. Lundberg R D, Cox E F (1969), in *Ring-Opening Polymerization*, Frisch K C, Reegen S L (eds), Marcel Dekker: New York, p. 247.
160. Knani D, Gutman A L, Kohn D H (1993), 'Enzymatic polyesterification in organic media. Enzyme-catalyzed synthesis of linear polyesters. I. condensation polymerization of linear hydroxyesters. II. ring-opening polymerization of ϵ-caprolactone', *J Polym Sci, Part: A Polym Chem* 31, 1221–32.
161. Sawhney A S, Chandrashekhar P P, Hubbell J A (1993), 'Bioerodible hydrogels based on photopolymerized poly(ethylene glycol)-co-poly(α-hydroxy acid) diacrylate macromers', *Macromolecules*, 26, 581–87.
162. Cerrai P, Tricoli M, Paci F A M (1989), 'Polyether-polyester block copolymers by non-catalysed polymerization of ϵ-caprolactone with poly(ethylene glycol)', *Polymer*, 30, 338–43.
163. Hall H K, Schneider H K (1958), 'Polymerization of cyclic esters, urethans, ureas and imides', *J Amer Chem Soc*, 80, 6409–12.
164. Brown H C, Gerstein M (1950), 'Acid-base studies in gaseous systems. VII.

dissociation of the addition compounds of trimethylboron and cyclic imines; I-strain', *J Amer Chem Soc*, 72, 2926–33.
165. Wilson D R, Beaman R G (1970), 'Cyclic amine initiation of polypivalolactone', *J Polym Sci, Part: A-1*, 8, 2161–70.
166. Lee J Y, Baljon A R C, Loring R F, Panagiopoulos A Z (1998), 'Simulation of polymer melt intercalation in layered nanocomposites', *J Chem Phys*, 109, 10321–30.
167. Balazs A C, Singh C, Zhulina E (1998), 'Modeling the interactions between the polymers and clay surfaces through self-consistent field theory', *Macromolecules*, 31, 8370–81.
168. Balazs A C, Singh C, Zhulina E, Lyatskaya Y (1999), 'Modeling the phase behavior of polymer-clay composites', *Acc Chem Res*, 32, 651–57.
169. Ginzburg V V, Balazs A C (1999), 'Calculating phase diagram of polymer-platelet mixtures using density functional theory: implication for polymer/clay composites', *Macromolecules*, 32, 5681–88.
170. Maiti P, Nam PH, Okamoto M, Hasegawa N, Usuki A (2002), 'Influence of crystallization on intercalation, morphology, and mechanical properties of propylene/clay nanocomposites', *Macromolecules*, 35, 2042–49.
171. Nam P H, Maiti P, Okamoto M, Kotaka T, Hasegawa N, Usuki A (2001), 'A hierarchical structure and properties of intercalated polypropylene/clay nanocomposites', *Polymer*, 42, 9633–40.
172. Averous L, Fauconnier N, Moro L, Fringant (2000), 'Blends of thermoplastic starch and polyesteramide: processing and properties', *J Appl Polym Science*, 76, 1117–28.
173. Koleske J V, Lundberg R D (1969), 'Lactone polymers. I. Glass transition temperature of poly-ϵ-caprolactone by means on compatible polymer mixtures', *J Polym Sci, Part A-2*, 7, 795–807.
174. Shia D, Hui CY, Burnside S D, Giannelis E P (1998), 'An interface model for the prediction of Young's modulus of layered silicate-elastomer nanocomposites', *Polym Compos*, 9, 608–15.
175. Nielsen L (1967), 'Platelet particles enhance barrier of polymers by forming tortuous path', *J Macromol Sci Chem*, A1(5), 929–42.
176. Güsev A A, Lusti H R (20010, 'Rational design of nanocomposites for barrier applications', *Adv Mater,* 13, 1641–43.
177. Reeve M S, MaCarthy S P, Downey M J, Gross R A (1994), 'Polylactide stereochemistry: effect on enzymic', *Macromolecules,* 27, 825–31.
178. Iwata T, Doi Y (1998), 'Morphology and Enzymatic Degradation of Poly(L-lactic acid) Single crystals', *Macromolecules*, 31, 2461–67.
179. Hakkarainene M, Karlsson S, Albertsson A-C (2000), 'Rapid (bio)degradation of polylactide by mixed culture of compost microorganisms – low molecular weight products and matrix changes', *Polymer*, 41, 2331–38.
180. Drumright R E, Gruber P R (2000), 'Polylactic acid technology', *Adv Mater*, 23, 1841–46.
181. Lunt J (1998), 'Large-scale production, properties and commercial applications of polylactic acid polymers', *Polym Degrad Stab*, 59, 149–52.
182. Taino T, Fukui T, Shirakura Y, Saito T, Tomita K, Kaiho T, Masamune S (1982), 'An extracellular poly(3-hydroxybutyrate) depolymerase from Alcaligenes faecalis', *Eur J Biochem*, 124, 71–77.

183. Tetto J A, Steeves D M, Welsh E A, Powell B E (1999), 'Biodegradable poly(ϵ-caprolactone)/clay nanocomposites', *ANTEC'99*, 1628–1632.
184. Hoffmann B, Kressler J, Stoppelmann G, Friedrich Chr, Kim GM (2000), 'Rheology of nanocomposites based on layered silicate and polyamide-12', *Colloid Polym Sci*, 278, 629–36.
185. Hyun Y H, Lim S T, Choi H J, Jhon M S (2001), 'Rheology of poly(ethylene oxide)/organoclay nanocomposites', *Macromolecules*, 34, 8084–93.
186. Krishnamoorti R, Ren J, Silva A S (2001), 'Shear response of layered silicate nanocomposites', *J Chem Phys*, 15, 4968–73.
187. Cox W P, Merz E H (1958), 'Correlation of dynamic and steady flow viscosities', *J Polym Sci*, 28, 619–22.
188. Kotaka T, Kojima A, Okamoto M (1997), 'Elongational flow opto-rheometry for polymer melts-1. Construction of an elongational flow opto-rheometer and some preliminary results', *Rheol Acta*, 36, 646–57.
189. Okamoto M, Nam P H, Maiti P, Kotaka T, Hasegawa N, Usuki A (2001), 'A house-of-cards structure in polypropylene/clay nanocomposites under elongational flow', *Nano Lett*, 1, 295–98.
190. Krishnamoorti R, Koray Y (2001), 'Rheology of polymer/layered silicate nanocomposites', *Current opinion in Colloid Interface Sci*, 6, 464–70.
191. Nam P H, Maiti P, Okamoto M, Kotaka T, Nakayama T, Takada M, Ohshima M, Usuki A, Hasegawa N, Okamoto H (2002), 'Foam processing and cellular structure of polypropylene/clay nanocomposites', *Polym Eng Sci*, 42, 1907–18.
192. Okamoto M, Nam P H, Maiti M, Kotaka T, Nakayama T, Takada M, Ohshima M, Usuki A, Hasegawa N, Okamoto H (2001), 'Biaxial flow-induced alignment of silicate layers in polypropylene/clay nanocomposite foam', *Nano Lett*, 1, 503–5.
193. Mohanty A K, Misra M, Hinrichsen G (2000), 'Biofibres, biodegradable polymers and biocomposites: an overview', *Macrmol Mater Eng*, 276/277, 1–24.

4

Polypropylene layered silicate nanocomposites

K JAYARAMAN and S KUMAR, Michigan State University, USA

4.1 Introduction

Polypropylene is a commodity polymer used in a wide range of products ranging from automotive applications such as automotive bumpers and interior parts of automobiles to packaging applications such as pouches for ready-to-eat meals and other food containers. Conventional fillers such as talc and mica are used at a rather high loading of 20 to 40 wt.% to improve mechanical properties and dimensional stability while also increasing part weight. Silicate nanolayers have much larger aspect ratios and can enhance stiffness and scratch resistance significantly at a much lower loading.[1] They are also impervious to gases and when they are well dispersed and oriented, can yield greatly improved barrier properties as well as flame retardance in the composite. Hence the prospect of developing layered silicates such as montmorillonite as a multifunctional additive for polypropylene at 5 to 10 wt.% with minimal increase in weight is very attractive.

Montmorillonite is a 2:1 smectite; i.e., it has three atomic lattice layers in each of the nanolayers with an aluminum-oxygen-hydroxyl octahedral sheet sandwiched between two silicon-oxygen tetrahedral sheets.[2] Individual nanolayers are 1 nm thick and their lateral dimensions are about 100 nm. There are hydroxyl groups at the nanolayer edges, which are part of the aluminum lattice layer. The interlayer galleries contain exchangeable cations (usually sodium) because of the charge imbalance created by isomorphic substitution of the aluminum. The hydrophilic face of the clay platelets is modified by pre-intercalating long chain alkyl ammonium ions as surfactants, in order to enhance the interaction between the mineral and the organic polymer. The onium ion interacts with the surface of the clay while the hydrocarbon tails swell the clay and improve its dispersibility in organic materials. Other layered silicates with larger lateral dimensions have been investigated but they are harder to disperse, requiring much higher shear stresses for delamination and running the risk of damaging the particles.

Even after organic modification of the clays, polypropylene does not wet the surface of clays because it is nonpolar. It is necessary to blend in a functionalized polymer such as maleated polypropylene (PP-g-MA) that wets the modified clay surface more readily and is also miscible with the bulk polymer. Okada and coworkers[3–5] were the first to produce polypropylene layered silicate nanocomposites by melt compounding the modified clay with PP-g-MA and PP. The progress made since then in preparing and characterizing polypropylene layered silicate nanocomposites is reviewed in this chapter. We discuss advances in formulations, preparation methods and characterization; then proceed to effects of the dispersion state (intercalated vs. exfoliated) and of silicate loading on crystallinity, mechanical performance and other properties, and end with a summary of progress to date with these composites. All the results presented in this chapter refer to isotactic polypropylene nanocomposites with layered or smectite clays.

4.2 Chemical compatibilization and compounding

4.2.1 Formulations

Choices of surfactant, polymeric compatibilizer and other coupling agents are critical for optimizing the dispersion and properties of polypropylene clay nanocomposites. The interaction between the oxygen atoms on the clay surface and the polymeric compatibilizer must be stronger than the interaction between the clay surface and the surfactant in order to obtain delamination of the silicates.[6] The polymeric compatibilizer must also be miscible with the bulk PP; this puts a limit on the extent of functionalization of the polypropylene.[3] Hence the structure of surfactant and of the polymeric compatibilizer must be carefully engineered. The length of the surfactant chain is an important variable that influences the level of exfoliation. Reichert *et al.*[7] investigated the effectiveness of the chain length by exchanging synthetic sodium fluoromica with various protonated alkyl amines ranging from butyl (C4), to octadecyl (C18) amine. They concluded that the alkyl chain length must exceed 8 carbon atoms for the clay to be exfoliated in polypropylene and that the C18 onium ion yields high levels of exfoliation. Other variations include semi-fluorinated surfactants[6] that are more easily displaced by the maleated PP and surfactants with two alkyl tails[6,8] which appear to be more suited to polyolefins and also more thermally stable.

The coupling between the clay and the matrix can be further enhanced by silane treatment of the clays.[9] Some silanes move into the interlayer galleries and react with the gallery faces, leading to stronger intercalated structures.[10] Other silanes react with the edges alone and as seen from recent results obtained in our laboratory[11] and discussed in a later section, can lead to a greater degree of exfoliation as well. X-Ray diffraction patterns show no change in interlayer

spacing when an aromatic alkoxysilane is used, suggesting that this silane attaches to the edges of the clay platelets but does not enter the galleries. This selectivity arises from the chemical incompatibility of aryl silane which is unable to displace alkyl ammonium ions from the galleries.

The polymeric compatibilizer may be polypropylene grafted or terminated with maleic anhydride,[12] hydroxyl[4] or ammonium[13] groups; the hydroxyl group detracts from the flame retardance effect of the filler, as discussed in a later section. The maleic anhydride grafted polypropylene is commercially available and also most suited for flame retardance. It is important to note that the maleic anhydride in PP-g-MA may exist in three distinct forms:[14] unreacted maleic anhydride, oligomeric maleic anhydride and bound maleic anhydride attached to polymer chains. The fraction of bound maleic anhydride is usually considerably less than the overall maleic anhydride present and recent work in our laboratory has confirmed that it is important to determine the amount of bound maleic anhydride because it controls the effectiveness[15] of the compatibilizer for dispersion. The maleic anhydride moieties are grafted largely at the ends of the polymer chains[12] with a free radical reaction. When more than one maleic anhydride group is attached to a chain end, the potential for multiple interactions with the clay surface will enhance the ability of the compatibilizer to enter the clay gallery and lead to more effective stress transfer from the polymer to the clay in shear, allowing mechanical separation of the clay nanolayers. Hence a greater fraction of bound maleic anhydride should yield a greater degree of exfoliation. In early work,[3] a 3:1 ratio of compatibilizer to clay was used to obtain delamination of the clay. Recent work in our laboratory[16] with varying ratios of compatibilizer to clay for different compatibilizers has shown that a 2:1 ratio is adequate when the bound maleic anhydride content in the maleated polypropylene is greater than 1 wt.%. This proportion has been used effectively by other investigators[8] as well.

The primary limitation of using maleated PP as polymeric compatibilizer arises from chain degradation during the free radical reaction for grafting maleic anhydride. Higher maleic anhydride content is desirable for favorable interaction with the clay surface; but as more maleic anhydride is added, chain scission occurs leading to lower molecular weights. Among commercially available grades, for example, Polybond 3150 (Uniroyal) has a molecular weight of 330,000 and a bound maleic anhydride level of less than 0.5 wt.%; G3015 (Eastman) has a molecular weight of 47,000 and a bound maleic anhydride level of 0.9 wt.% and AC1325 (Honeywell) has a molecular weight of 28,200 with a bound maleic anhydride level of 1.3 wt.%. More than 5 wt.% maleic anhydride is usually obtained in very low molecular weight waxes and these compounds will not entangle adequately with the bulk polypropylene during compounding.[16] Large amounts of moderate molecular weight compatibilizer will lead to unacceptable mechanical properties.[17] The synthesis of grafted or functionalized polypropylenes with much higher molecular weight was reported recently by

Fibiger and coworkers[18] from Dow with a proprietary process; these high molecular weight compatibilizers lead to composites with much improved mechanical properties.

4.2.2 Compounding

Melt compounding of the three components is typically carried out in a twin screw extruder using lower temperatures of around 170ºC in the feed zone; this is because the alkyl ammonium surfactant in the interlayer galleries degrades at higher temperatures causing the galleries to collapse. The behavior of the surfactant is seen in the TGA scan shown in Fig. 4.1 for C-18 clay (I.30 P). The residence time of the clay must be manipulated to provide enough shear strain while avoiding degradation of surfactant or agglomeration of the clay;[19] this can be achieved by feeding the clay in a separate hopper downstream of the polymer feed, in addition to adjusting the screw rpm and the throughput rate.[19–20]

Batch mixers have been used effectively[15–16, 21–22] for small batches. The shear rates in the batch mixers ranged from 50 to 200 s^{-1} and the residence times used varied from 2 to 15 minutes. Dolgovskij *et al.*[21] reported that PP clay nanocomposites with 5 wt.% organically modified montmorillonite were most exfoliated when prepared by batch compounding for 15 minutes in a vertical, co-rotating twin screw extruder with a screw speed of 100 rpm. They noted that the dispersion level was much lower when a mixing time of 2 minutes was used.

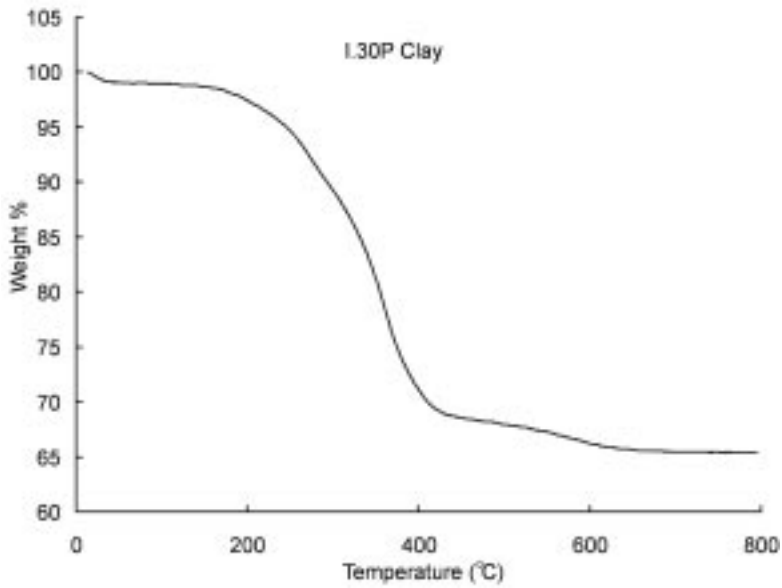

4.1 TGA scan of C-18 clay (Nanocor I.30 P), showing loss of organic surfactant from interlayer galleries above 200ºC.

Ultrasonication has been used after melt compounding to yield enhanced dispersion in some cases.[23]

The three components may be compounded all together or in stages. While direct compounding is appropriate for small scale (50 g) preparations, stagewise compounding with an intermediate concentrate, termed masterbatch is recommended for larger quantities. A variety of masterbatch concentrates have been used. For example, some investigators[9–10] prepared masterbatch concentrates consisting of all three components with up to 50 wt.% of montmorillonite and then let it down with the bulk PP and concluded that the dispersion was better than that obtained by direct compounding. Wang *et al.*[24] compounded maleated PP and montmorillonite in a 3:1 proportion into a masterbatch and then let it down with the bulk polypropylene to get a PP/PP-g-MA/silicate compound with 80/15/5 proportion by wt. X-ray diffraction patterns and viscosity measurements revealed that the dispersion in this compound was better than that obtained with direct compounding. Masterbatch concentrates without any compatibilizer were prepared by others[7-8] and let down with a mixture of compatibilizer and bulk PP to obtain better properties than with direct compounding. An in-situ compatibilization approach has been reported by Tjong *et al.*;[25] in this approach, maleic anhydride was used to swell and exfoliate vermiculite first and then the exfoliated vermiculite was compounded with polypropylene and dicumyl peroxide to prepare functionalized polypropylene in-situ. Kato *et al.*[26] injected an aqueous slurry of clay into a molten mixture of polypropylene, PP-g-MA and surfactant in a twin screw extruder and obtained exfoliated nanocomposite, using a 6:1 ratio of PP-g-MA to clay by wt.

4.3 Nanostructure

4.3.1 Morphology

Some assessment of the degree of dispersion is obtained from X-ray diffraction patterns. Figure 4.2 presents XRD patterns for three different polypropylene nanocomposites prepared in our laboratory with 5 wt.% of a C-18 organoclay (I-30 P from Nanocor), 85 wt.% of a 11 MFR PP and 10 wt.% of three different maleated polypropylenes. The bound maleic anhydride content in the graft PP varies from 0.37 wt.% to 1.3 wt.%. There is a hint of a peak for the nanocomposite (NC1) with the lowest bound MA content but not for the other two. This would indicate that the degree of exfoliation is least for NC1. Better discrimination of the structure of the three nanocomposites can be obtained from analysis of transmission electron micrographs. Two representative images are presented for the nanocomposite with the G-3015 compatibilizer in Fig. 4.3. In both images, exfoliated single platelets are seen along with intercalated stacks. Staggered arrangements of platelets sliding out of a stack when subjected to shear are seen in both these figures, like the formation termed ‘skewed stack’ by

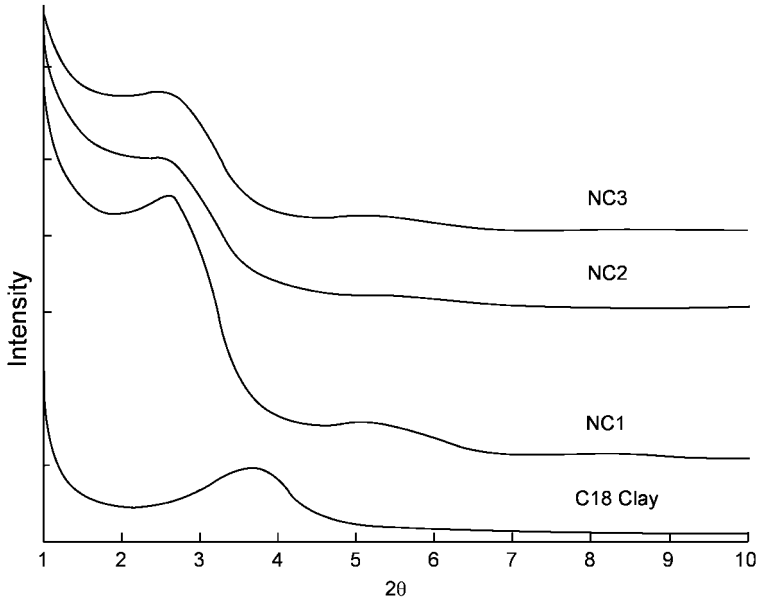

4.2 X-ray diffraction patterns for the organoclay and three polypropylene nanocomposites with 5 wt.% C18 clay and 10 wt.% PP-g-MA; the PP-g-MA grades were Eastman G-3003 (with 0.37 wt.% bound MA) in NC1, Eastman G-3015 (with 0.94 wt.% bound MA) in NC2 and Honeywell AC1325 (with 1.3 wt.% bound MA) in NC3.

Fornes *et al.*[27] in their analysis of nylon-6/layered silicate nanocomposites. A quantitative comparison of the degree of delamination in these composites can be obtained from an analysis of the fraction of single particles and the distribution of lengths of such particles in these samples. Several such images

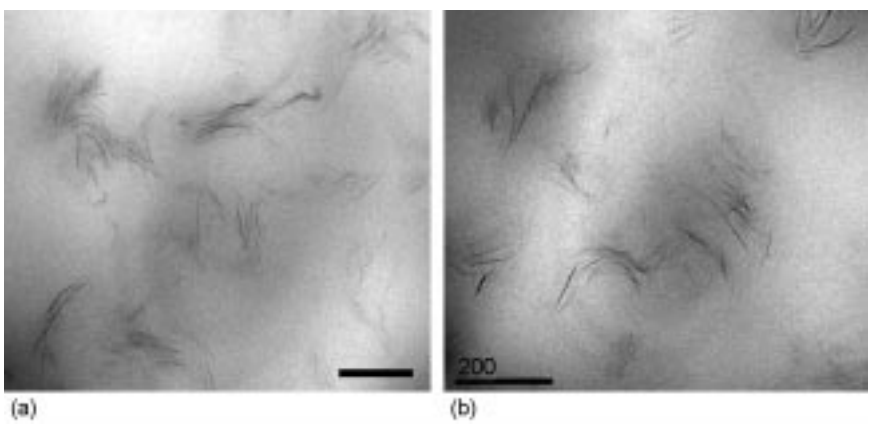

4.3 Two different TEM images for polypropylene nanocomposite NC2. The scale bar in each picture is 200 nm.

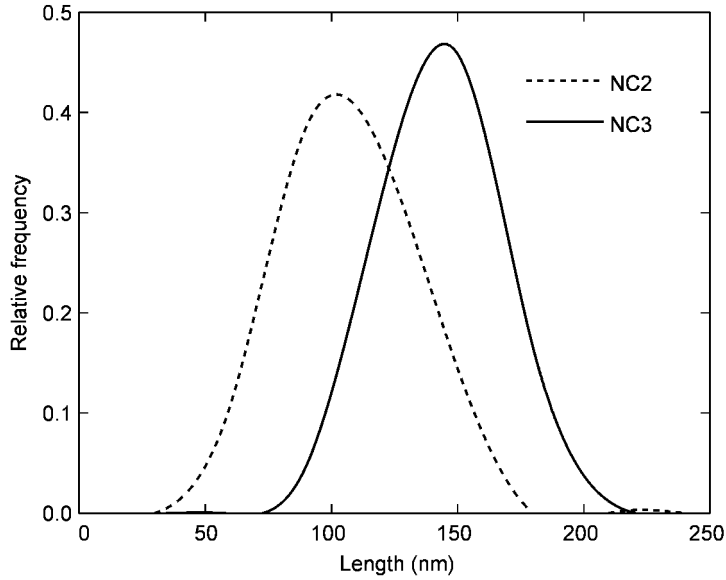

4.4 Length distributions for 'single particles' in polypropylene nanocomposites NC2 and NC3.

were analyzed to get a length distribution for each composite. The results of this analysis are presented for two of the composites in Fig. 4.4, which identifies NC3 – prepared with the PP-g-MA having the greatest bound MA fraction – clearly as the most exfoliated sample with the highest average platelet length.[15]

4.3.2 Rheology

The state of dispersion in the melt state as well as the orientation of nanolayers may be inferred from melt rheology. Both dynamic moduli – the storage modulus and the loss modulus – from small amplitude oscillatory shear of the nanocomposite melts increase with the loading of layered silicates.[28–29] The zero shear viscosity has been inferred from creep curves by Lele;[30] it is important to ensure that the material structure is stable over the long times required for linear viscoelastic creep data. The dynamic viscosity curves are more conveniently related to the mean aspect ratio and thus the degree of exfoliation[16] because the intrinsic viscosity of such suspensions increases with the average aspect ratio of the particles.[31] Marchant and Jayaraman[16] obtained a limiting value for the dynamic viscosity of some nanocomposite melts at low frequencies. However, other melts do not show such a limit. Figure 4.5 presents plots of the dynamic shear viscosity against the magnitude of complex shear modulus for two composites prepared in our laboratory[15] and the corresponding silicate free melts with PP and PP-g-MA in the same proportion as the composites. The dynamic

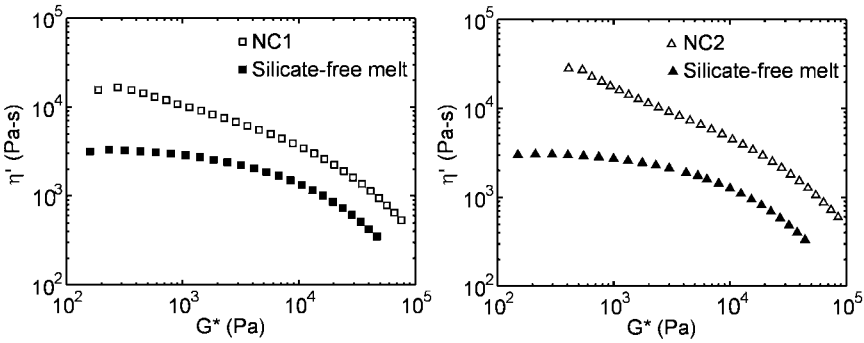

4.5 Dynamic viscosity vs. complex modulus G^* of the nanocomposite melts and the silicate-free melts for polypropylene nanocomposites NC1 and NC2.

viscosity curve for the composite NC2 increases sharply with decreasing stress at low shear stresses, indicating the presence of a yield stress. These plots allow us to evaluate the relative viscosity at a fixed value of shear stress as shown in Fig. 4.6. The relative viscosity is consistently higher for NC2 with the higher fraction of bound maleic anhydride. The dynamic storage modulus curves plotted for the two composites in Fig. 4.7 show a plateau at low frequencies for NC2, which is consistent with the presence of a yield stress. Lertwimolnun and Vergnes[20] have fitted a modified Carreau-Yasuda model that includes a yield stress to the complex viscosity curves of PP nanocomposites and found that the estimated yield stress value increases with increasing compatibilizer to clay ratio

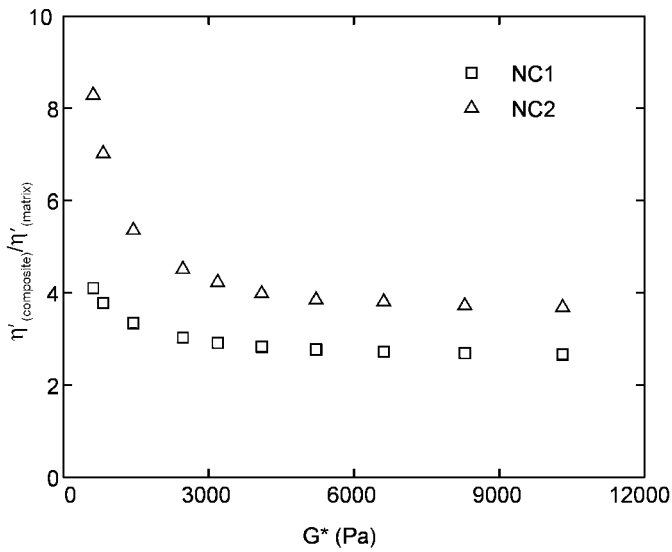

4.6 Relative viscosity vs. complex modulus G^* for polypropylene nanocomposites NC1 and NC2.

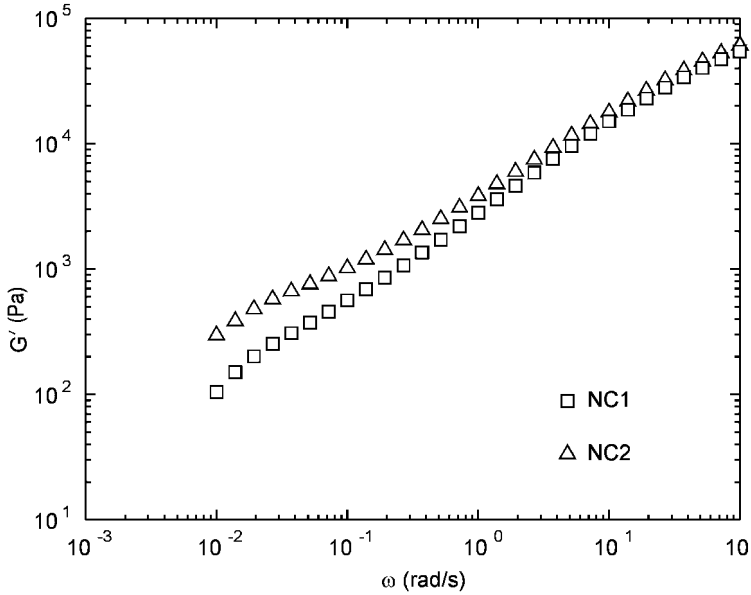

4.7 Dynamic storage modulus curves for polypropylene nanocomposites NC1 and NC2.

to a maximum of 800 Pa at a ratio of 5. These composites were prepared with 5 wt.% of Cloisite 20A clay and a PP-g-MA containing 1 wt.% maleic anhydride (including bound and free). Better characterization of the yield stress is required to relate the structure to rheology quantitatively.

Okamoto *et al.*[32,33] have observed that the evolution of nanostructure during uniaxial extension in an RME[32] and during biaxial extension in a foaming operation[33] led to significant strain hardening of a polypropylene nanocomposite melt whereas the polypropylene matrix alone did not show any strain hardening. The matrix was all maleic anhydride functionalized polypropylene. The nature and extent of aggregation as well as the predominant orientation were different in the two flow types. The aggregates in uniaxial extension were reported to be a 'house-of-cards' type while the aggregates in biaxial extension were mostly layered. The platelets were oriented with the normals along the flow direction in uniaxial extension while the platelets were oriented with the edges along the flow direction in biaxial extension. Kumar and Jayaraman[34] have noted that when other polypropylene nanocomposite melts were extruded through a converging die section with a strong uniaxial extensional flow in the center of the die, the platelets in the core of the extrudate had their edges oriented parallel to the flow direction. These nanocomposites were made with a silane coupling agent added to the organoclay in a mixture of neat polypropylene and maleic anhydride functionalized polypropylene as the matrix.

4.3.3 Stability of morphology

The stability of morphology to further melt processing is a measure of the degree of coupling or strength of interactions between the silicate nanolayers and the matrix polymer.[6,35] Reichert *et al.*[35] annealed injection molded PP nanocomposite specimens in an oven at 220ºC and observed a coarsening of morphology as displayed by two transmission electron micrographs in Fig. 4.8 taken before and after annealing. Manias *et al.*[6] processed different nanocomposite specimens by compression molding at 180ºC and observed the evolution of structure after different times of annealing by X-ray diffraction. The nanocomposites were prepared with the same organically modified clay where the surfactant had two alkyl tails (2C18), and two different matrices – neat PP alone in one case and PP-g-MA alone in the second case. In both cases the composite was precipitated from a co-suspension of the clay with the matrix in a common organic solvent and then compression molded at 180ºC. In the first case with the neat PP matrix, the structure which was mostly exfoliated at the start became strongly intercalated in 15 min. However, the second case with the PP-g-MA as matrix did not show much change over 30 min. The latter case evidently had stronger coupling between polymer and filler.

4.3.4 Crystallization

Addition of compatibilizer and the clay to polypropylene have competing effects on the rate of crystallization. The clay alone leads to a greater rate of nucleation

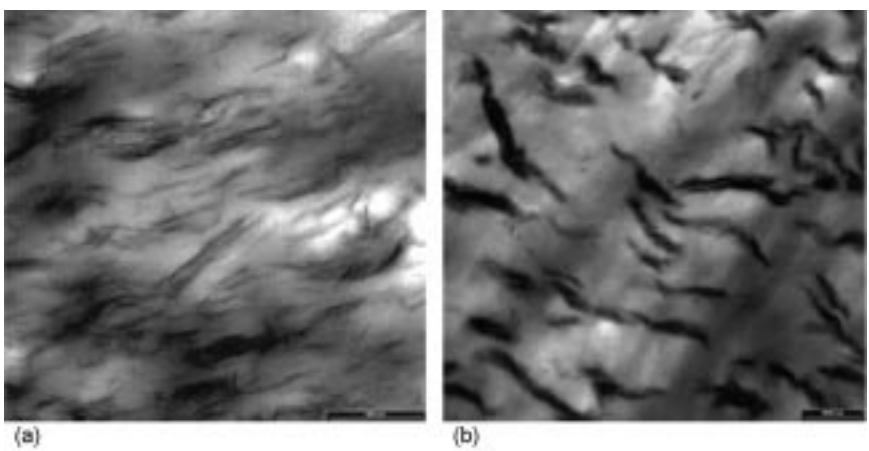

4.8 TEM images of injection molded PP nanocomposite samples: (a) not annealed (scale bar = 500 nm) and (b) annealed for 200 min at 220ºC (scale bar = 1000 nm). Reprinted with permission of John Wiley & Sons, Inc. from Reichert, P., Hoffman, B., Bock, T., Thomann, R., Mulhaupt, R. and Friedrich, C., 'Morphological stability of polypropylene nanocomposites', *Macromol. Rapid. Comm.*, **22**, 519–523 (2001) Copyright © 2001, Wiley.

and smaller spherulites, as reported by Ma *et al.*[36] for intercalated nanocomposites prepared with an intercalation polymerization process. As shown in Fig. 4.9 which presents optical micrographs taken from the work of Ma *et al.*,[36] spherulite sizes are of the order of 100 microns in pure PP and decrease progressively with clay loading. The addition of PP-g-MA alone to polypropylene reduces the rate of crystallization significantly;[37] a similar reduction in crystallization rate was observed in intercalated nanocomposites[37] confirming that the matrix in such composites is a mixture of PP and PP-g-MA. However, relative to PP-g-MA alone as the matrix, the presence of intercalated clay had the expected effect, producing smaller spherulites[38] particularly at crystallization temperatures below 100ºC. The rate of crystallization affects the nanolayer structure as well: during crystallization of intercalated nanocomposites, the

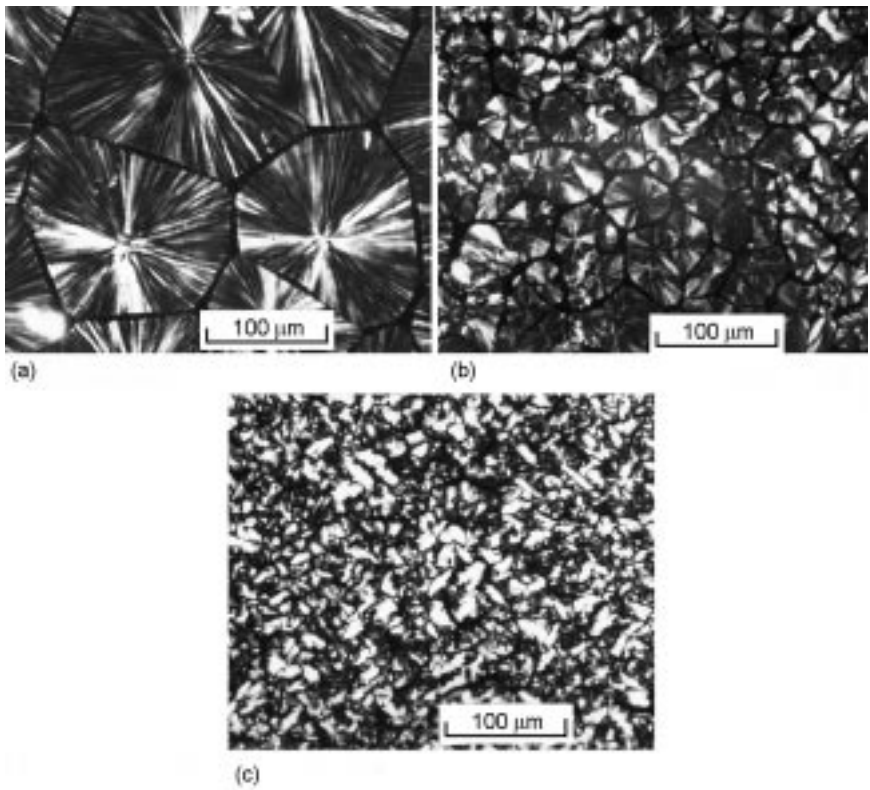

4.9 Micrographs of (a) pure PP, (b) PP/4.6 wt.% organoclay, and (c) PP/8.4 wt.% organoclay taken under a polarizing microscope. The nanocomposites were prepared via an intercalation polymerization process. Reprinted with permission of John Wiley & Sons, Inc. from Ma, J., Zhang, S., Qi, Z., Li, G. and Hu, Y., 'Crystallization behaviors of polypropylene/montmorillonite nanocomposites', *J. Appl. Polym. Sci.*, **83**, 1978–1985 (2002) Copyright © 2002, Wiley.

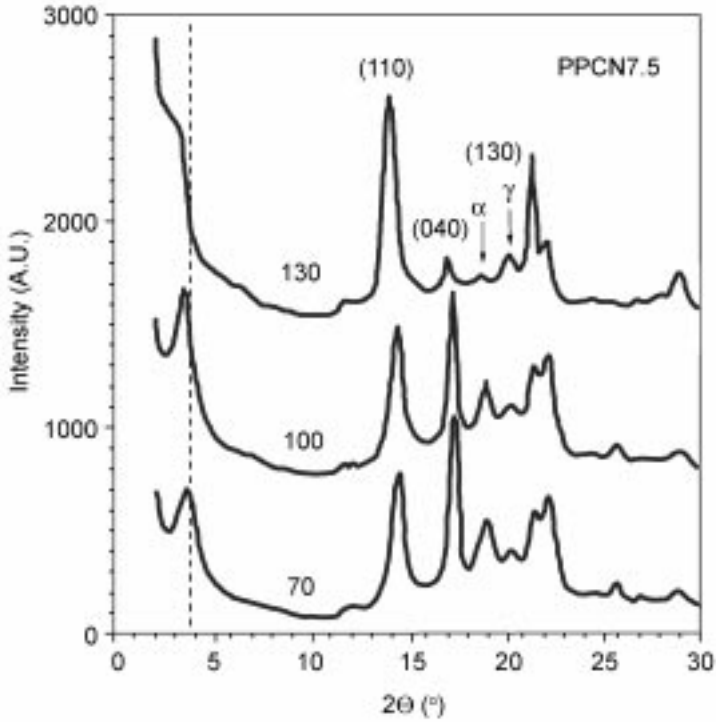

4.10 WAXD patterns for intercalated PP-g-MA/organoclay composites prepared by twin screw compounding (PP-g-MA: $M_w = 1.95$ kg/mol, $M_w/M_n = 2.98$ and MA content = 0.2 wt.%) with 7.5 wt.% clay with different crystallization temperatures – 70°C, 100°C and 130°C. Reprinted with permission of John Wiley & Sons, Inc. from Maiti, P., Nam, P.H., Okamoto, M., Kotaka, T., Hasegawa, N., and Usuki, A., 'The effect of crystallization on the structure and morphology of polypropylene/clay nanocomposites', *Polym. Eng. Sci.*, **42** (9), 1864–1871 (2002) Copyright © 2002, Wiley.

gallery spacing can be increased by raising the crystallization temperature.[39] Higher crystallization temperatures also lead to greater fractions of the γ-form and lower fractions of the α-form as shown by the WAXD patterns[39,40] of an intercalated PP nanocomposite in Fig. 4.10. The fraction of γ-form was also found to go up with increasing clay content. At crystallization temperatures of 110°C or higher, the clay was found to be predominantly located in the interspherulitic regions giving rise to higher modulus. The silicate nanolayers can in addition disrupt the crystal structure and increase the interchain distance in crystallites as pointed out by Nam *et al.*[41] This is important because defect-free crystal structure leads to better barrier properties.[42]

4.4 Performance

4.4.1 Mechanical properties

Much of the mechanical property data reported in the literature has been obtained with PP nanocomposites that have a largely intercalated structure. Figure 4.11 presents a plot of tensile modulus against clay loading in intercalated PP nanocomposites as reported by Svoboda *et al.*[17] A 1:1 wt. ratio of PP-g-MA compatibilizer to clay was used in preparing these composites. The rate of improvement is greater up to 2 wt.% than above it. This is in contrast to the trend found for fiber reinforced polymers where the modulus increases more steeply at higher loading. The observed trend for nanocomposites probably reflects poorer dispersion or lower d-spacing at higher loading in predominantly intercalated composites. This plot shows a 30% increase at a clay loading of 5 wt.%. Only a slight effect is seen of maleated PP molecular weight on the modulus. The tensile strength of intercalated PP nanocomposites increases sharply by about 12% at a clay loading of 1 wt.% clay and then levels off as shown in Fig. 4.12. The tensile strength of intercalated PP nanocomposites is brought down significantly by the addition of low molecular weight maleated PP, as shown in Fig. 4.12. Other authors[6–7,43] have reported similar improve-

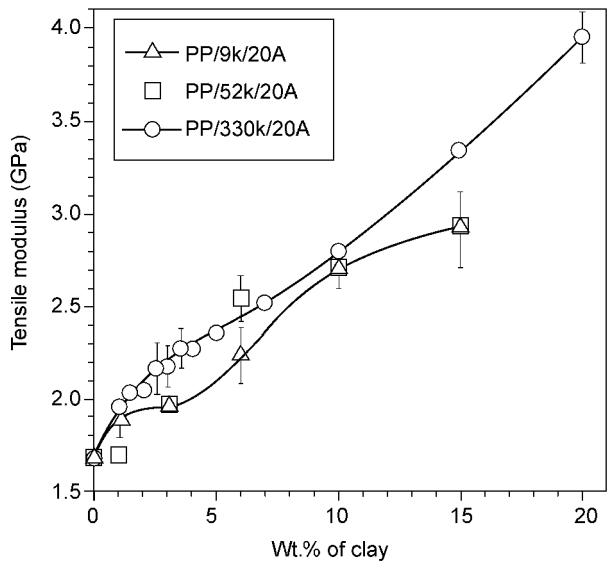

4.11 Tensile modulus as a function of clay content for intercalated PP/PP-g-MA/Cloisite 20A organoclay composites prepared by twin screw compounding with a 1:1 wt. ratio of PP-g-MA to clay. Reprinted with permission of John Wiley & Sons, Inc. from Svoboda, P., Zeng, C., Wang, H., Lee, L., and Tomasko, D., 'Morphology and mechanical properties of polypropylene/organoclay nanocomposites', *J. Appl. Polym. Sci.,* **85**(7): 1562–1570 (2002) Copyright © 2002, Wiley.

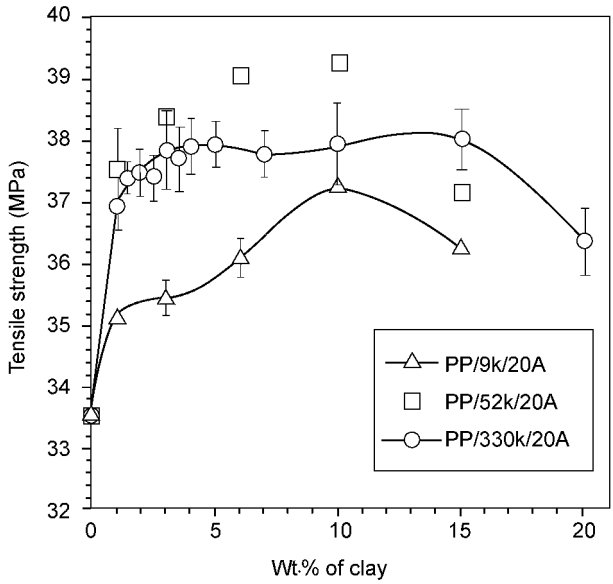

4.12 Tensile strength as a function of clay content for intercalated PP/PP-g-MA/Cloisite 20A organoclay composites prepared by twin screw compounding with a 1:1 wt. ratio of PP-g-MA to clay. Reprinted with permission of John Wiley & Sons, Inc. from Svoboda, P., Zeng, C., Wang, H., Lee, L., and Tomasko, D., 'Morphology and mechanical properties of polypropylene/organoclay nanocomposites', *J. Appl. Polym. Sci.,* **85**(7): 1562–1570 (2002) Copyright © 2002, Wiley.

ments with 5 wt.% clay. Reichert *et al.*[7] have reported that the tensile modulus is sensitive to the alkyl tail length in the surfactant as well as the compatibilizer molecular weight. A relevant question here is how much talc would be needed to provide similar improvements in properties. This is presented in Table 4.1 which is adapted from a table provided by Ellis and D'Angelo[10] It is readily seen from Table 4.1 that for a 30% increase in tensile modulus, we would need to add about 23% talc. The tensile strength is lowered by the addition of talc. Ellis and D'Angelo[10] obtained intercalated structures with I.31 PS, an organoclay with additional silane treatment. Composites were also prepared with the help of a masterbatch concentrate termed C.31 PS that contained 50 to 60 wt.% of the I.31 PS with the other two components. By both compounding methods, a 5 wt.% intercalated nanocomposite exhibited a 25% improvement in tensile modulus, which is equivalent to adding over 20 wt.% talc.

Higher property improvements have been reported in highly exfoliated nanocomposites for which the intercalation peak is missing from X-ray diffraction patterns. Ton-That *et al.*[8] obtained a 30% increase in tensile modulus by dispersing only 2 wt.% of Cloisite 15A with the help of a 330,000 molecular weight PP-g-MA compatibilizer. The effect of surfactant structure and of the

Table 4.1 Mechanical properties of intercalated PP nanocomposites and talc filled polypropylene at 25°C

Sample	Tensile strength (MPa)	Tensile modulus (GPa)	Flexural strength (MPa)	Flexural modulus (GPa)
Base PP	38.1	1.97	67.9	1.89
5 wt.% I.31PS in PP	38.7	2.38	66.3	2.13
5 wt.% I.31 PS in PP after extended mixing	40.2	2.40	—	—
20 wt.% talc filled PP	35.2	2.34	64.3	2.75
30 wt.% talc filled PP	35.3	3.13	—	—
40 wt.% talc filled PP	33.9	3.65	61.0	3.29
10 wt.% C.31PS in PP	40.7	2.43	—	—
20 wt.% C.31PS in PP	41.0	2.71	—	—
30 wt.% C.31PS in PP	40.2	2.92	—	—

compatibilizer molecular weight is shown in Fig. 4.13 which is reproduced from this work. The tensile strength was improved by 13%. Higher improvements were obtained in flexural modulus and in flexural strength. Ton-That *et al.*[8] also compared the performance of polypropylene nanocomposites prepared with 2 wt.% of two different surfactant treated clays – Cloisite 30B with one tallow tail and Cloisite 15A with two hydrogenated tallow tails. They found that the nanocomposite with Cloisite 15A had a noticeably higher tensile modulus and tensile strength.

Tjong *et al.*[25] produced polypropylene nanocomposites with 2 wt.% exfoliated vermiculite after pre-treating the vermiculite with maleic anhydride for in-situ compatibilizer generation; the vermiculite aspect ratio was at least twice that of the montmorillonite. The tensile modulus improved from 0.84 GPa for their neat PP to 1.3 GPa for the 2 wt.% nanocomposite. The tensile strength improvement was also more striking going up from 28 MPa to 37 MPa.

In addition to the state of dispersion, the strength of coupling between the matrix and the clay particles also affects the tensile modulus. Additional coupling can be obtained with silanes but in some instances they have been found to detract from the dispersibility of the clays.[10] A more careful selection of the silane coupling agent can produce further increases in tensile modulus as seen in our laboratory and presented in Fig. 4.14. This figure presents a comparison of tensile modulus values for polypropylene nanocomposites with 5 wt.% clay and 10 wt.% maleated polypropylene and prepared by direct batch compounding in a Banbury mixer for 10 minutes at 180ºC. The silane chosen in this work reacted primarily with the groups on the edges of the silicate layers and led to better coupling with the matrix and thus to higher modulus.

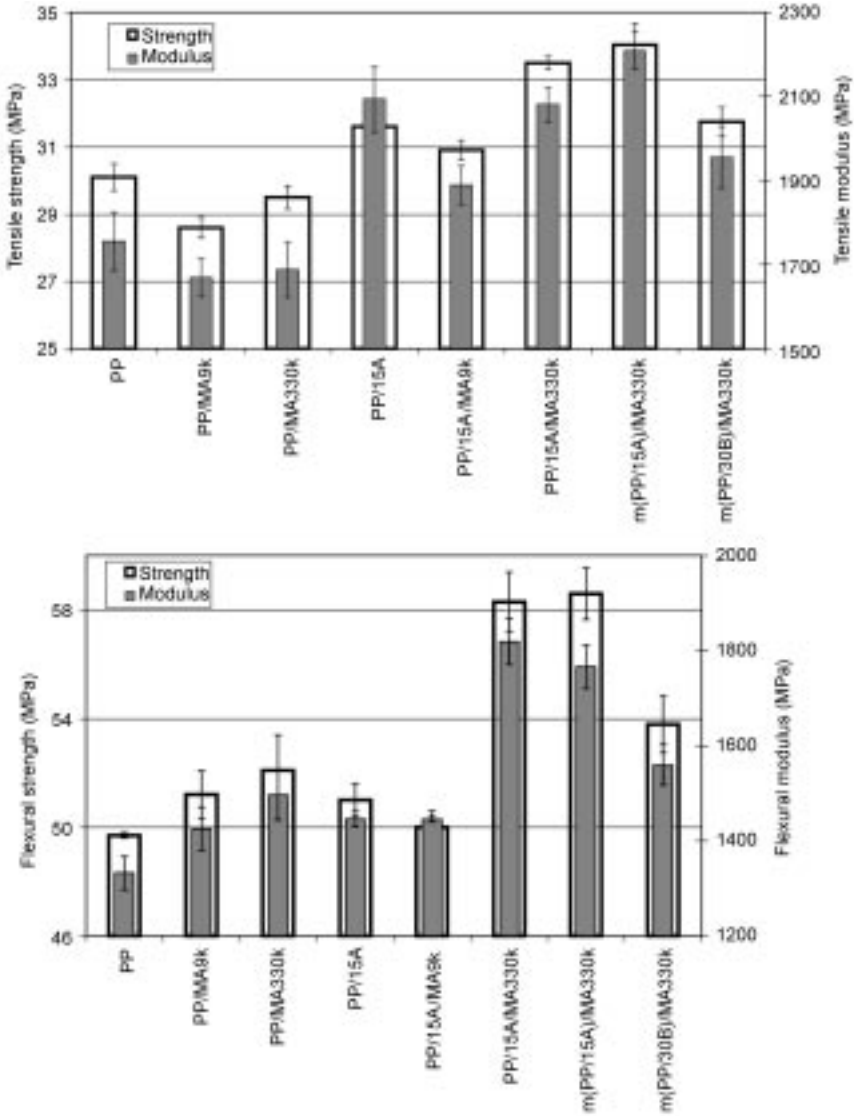

4.13 Tensile and flexural properties of PP, PP blends with PP-g-MA and PP nanocomposites with a 2:1 ratio of PP-g-MA to clay. Reprinted with permission of John Wiley & Sons, Inc. from Ton-That, M.T., Perrin-Sarazin, F., Cole, K.C., Bureau, M.N. and Denault, J. 'Polyolefin nanocomposites: formulation and development', *Polym. Eng. Sci.*, **44** (7), 1212–1219 (2004) Copyright © 2004, Wiley.

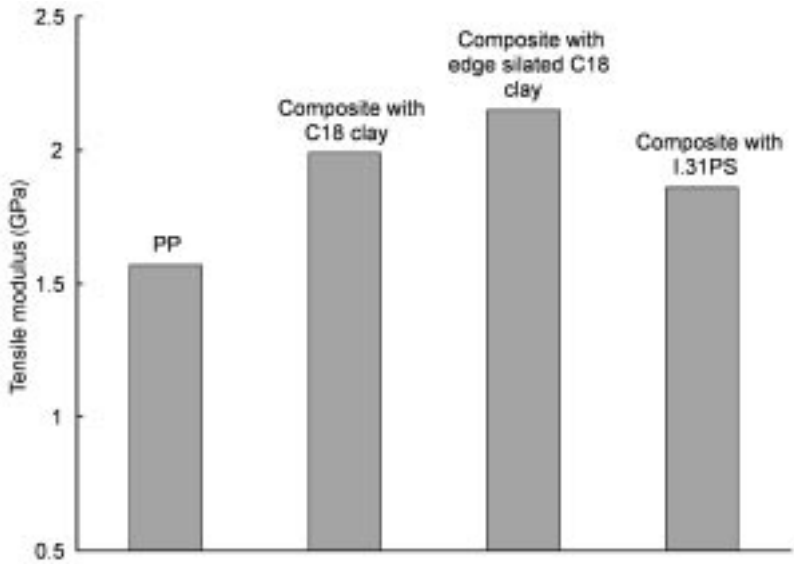

4.14 Tensile moduli of polypropylene and PP nanocomposites prepared by melt compounding with 10 wt.% of a fixed PP-g-MA and 5 wt.% of montmorillonite with different surface treatments including additional silane treatment.

4.4.2 Other properties

Incorporation of silicate nanolayers in semi-crystalline polymers like polypropylene can have a two-fold effect on the barrier properties, (1) well oriented large aspect ratio platelets will increase the tortuosity of the diffusion path and (2) the nanolayers will affect the crystalline order (size and interlamellar spacing) and possibly affect the barrier properties. The extent of orientation is greater in blown film than in extrusion cast film and this leads to similar trends in barrier properties of polypropylene nanocomposites with 7 wt.% I.31PS (silated) clay as reported by Qian *et al.*[44] With cast films, the nanocomposite had a lower permeability to oxygen by a factor of 1.5 compared to neat polypropylene. With blown films, the nanocomposite permeability to oxygen was lower by a factor of 2.5 compared to neat polypropylene. However, Ellis and D'Angelo[10] were able to prepare only intercalated polypropylene nanocomposites with the same I.31 PS and obtained no improvement in permeability to a solvent over that for neat polypropylene. This underlines the greater sensitivity of barrier performance to the level of dispersion and orientation.

The mechanism for flame retardance in polymer clay nanocomposites is the formation of an insulating char layer on the surface that is enriched in nanolayers[45] and also acts as a barrier. This is effective only when the clay is delaminated to a large extent.[46] Flame retardance is also quite sensitive to the

selection of polar group in the functionalized polypropylene used as compatibilizer: hydroxyl groups are detrimental while maleic anhydride is the most effective. Flame retardance is measured in terms of the peak heat release rate with a cone calorimeter. Gilman *et al.*[46] have tested PP nanocomposites including PP-g-MA with 2 wt.% and 4 wt.% layered silicates and found progressively lower values of the peak heat release rate with a maximum reduction of 75%. They also reported that better mixing had a noticeable effect on the reduction in peak heat release rate. This is accompanied by a reduction in mass loss rate during combustion. While the peak heat release rate is reduced significantly, the total heat released is not; this too can be reduced by combining the nanoclay with other intumescent flame retardants such as ammonium polyphosphate mixed with polyol and a blowing agent.[47–48]

4.5 Conclusions

Improvements in mechanical properties with polypropylene layered silicate nanocomposites are more modest than the improvements reported with nylon. This is a reflection not just of incomplete exfoliation in polypropylene but also of more complex and inadequate coupling between the bulk polypropylene matrix and the silicate layers usually in the presence of a compatibilizer. The fraction of bound maleic anhydride in the compatibilizer is important for both exfoliation and good coupling. The degree of coupling between polymer and nanolayers also affects the stability of morphology. The compatibilizer and the layered silicates have competing effects on the crystallization rate. Carefully chosen silanes can be used to provide additional coupling at the nanolayer edges. Detailed analysis of several TEM images has been used by investigators to assess the effectiveness of their formulations and methods; more work is required on developing less laborious characterization methods such as relating the structure to rheology quantitatively. Improvements in barrier properties depend on the level of orientation as well and more work is required to realize the potential of such nanocomposites in this area. Recently proposed approaches to exfoliate larger aspect ratio layered silicates such as vermiculite show promise.

4.6 Acknowledgements

This work was supported in part by a National Science Foundation NUE grant no. EEC-0407344.

4.7 References

1. Garces, J.M., Moll, D.J., Bicerano, J., Fibiger, R. and McLeod, D.G., 'Polymeric nanocomposites for automotive applications,' *Adv. Mater.*, **12** (3), (2000).
2. Van Olphen, H., *An Introduction to Clay Colloid Chemistry*; Interscience Publishers:

New York, 1962.
3. Kawasumi, M., Hasegawa, N., Kato, M., Usuki, A.and Okada, A. 'Preparation and Mechanical Properties of Polypropylene-Clay Hybrids,' *Macromolecules*, **30**, 6333–6338 (1997).
4. Kato, M., Usuki, A. and Okada, A., 'Synthesis of Polypropylene Oligomer-Clay Intercalation Compounds,' *J. Appl. Poly. Sci.*, **66**, 1781–1785 (1997).
5. Hasegawa, N., Kawasumi, M., Kato, M., Usuki, A., and Okada, A., 'Preparation and mechanical properties of polypropylene-clay hybrids using a maleic anhydride-modified polypropylene oligomer,' *J. Appl. Poly. Sci.*, **67** (1), 87–92 (1998).
6. Manias, E., Touny, A., Wu, L., Strawhecker, K., Lu, B. and Chung, T.C. 'Polypropylene/Montmorillonite Nanocomposites. Review of the Synthetic Routes and Materials Properties,' *Chem. Mater.*, **13**, 3516–3523 (2001).
7. Reichert, P., Nitz, H., Klinke, S., Brandsch, R., Thomann, R., Mulhaupt, R. 'Poly(propylene)/Organoclay Nanocomposite Formulation: Influence of Compatibilizer Functionality and Organoclay Modification,' *Macromol. Mater. Eng.*, **275**, 8–17 (2000).
8. Ton-That, M.T., Perrin-Sarazin, F., Cole, K.C., Bureau, M.N. and Denault, J. 'Polyolefin Nanocomposites: Formulation and Development,' *Polym. Eng. Sci.*, **44** (7), 1212–1219 (2004).
9. Lan, T. and Qian, G. 'Preparation of High Performance Polypropylene Nanocomposites,' *Additives 2000*, Clearwater Beach, FL (2000).
10. Ellis, T.S. and D'Angelo, J.S. 'Thermal and Mechanical Properties of a Polypropylene Nanocomposite,' *J. Appl. Polym. Sci.*, **90**, 1639–1647 (2003).
11. Kumar, S. and Jayaraman, K., 'Structure of PP Nanocomposites with Edge-Silated Layered Silicates,' Proc. SPE Automotive TPO Global Conference Material Development (2004).
12. De Roover, B., Sclavons, M., Carlier, V., Devaux, J., Legras,R. and Momtaz, A., 'Molecular Characterization of Maleic Anhydride-Functionalized Polypropylene,' *J Polym. Sci. Part A Polym. Chem.*, **33**, 829 (1995).
13. Wang, Z.M., Nakajima, H., Manias, E. and Chung, T.C., 'Exfoliated PP/Clay Nanocompsoites Using Ammonium-Terminated PP as the Organic Modification for Montmorillonite,' *Macromolecules*, **36**, 8919–8922 (2003).
14. Sclavons, M., Carlier, V., De Roover, B., Franquinet, P., Devaux, J. and Legras, R., 'The Anhydride Content of Some Commercial PP-g-MA: FTIR and Titration,' *J Appl. Polym. Sci.*, **62**, 1205 (1996).
15. Marchant, D. and Jayaraman, K. 'Effectiveness of PP-g-MA Compatibilizers for Nanolayer Dispersion in PP: Bound vs. Free Maleic Anhydride,' *Society of Plastics Engrs. Annual Tech. Conf.*, **61**, 2200–2204 (2003).
16. Marchant, D. and Jayaraman, K. 'Strategies for Optimizing Polypropylene-Clay Nanocomposite Structure,' *Ind. Eng. Chem. Res.*, **41**, (25), 6402 (2002).
17. Svoboda, P., Zeng, C., Wang, H., Lee, L., and Tomasko, D., 'Morphology and mechanical properties of polypropylene/organoclay nanocomposites,' *J. Appl. Polym. Sci.,* **85**(7): 1562–1570 (2002).
18. Fibiger, R., Garces, J.M., Palmieri, J., Traugott, T., 'Nanocomposite reinforced polypropylene,' Proc. SPE Automotive TPO Global Conference, pp 25–33 (2003).
19. Fasulo, P.D., Rodgers, W.R., and Ottaviani, R.A., 'Extrusion Processing of TPO Nanocomposites,' *Polym. Eng. Sci.*, **44** (6), 1036–1045 (2004).
20. Lertwilmolnun, W. and Vergnes, B., 'Influence of Compatibilizer and Processing

Conditions on the Dispersion of Nanoclay in a Polypropylene Matrix,' *Polymer*, **46** (10), 3462–3471 (2005).
21. Dolgovskij, M.K., Fasulo, P.D., Lortie, F., Macosko, C.W., Ottaviani, R.A., and Rodgers, W.R., 'Effect of Mixer Type on Exfoliation of Polypropylene Nanocomposites,' *Society of Plastics Engrs. Annual Tech. Conf.*, **61,** 2255–2259 (2003)
22. Gopakumar, T. and Page, D., 'Compounding of Nanocomposites by Thermokinetic Mixing,' *J. Appl. Poly. Sci.*, **96** (5), 1557–1563 (2005).
23. Lee, E., Mielewski, D., and Baird, R., 'Exfoliation and Dispersion Enhancement in Polypropylene Nanocomposites by In-Situ Melt Phase Ultrasonication,'*Polym. Eng. Sci.*, **44** (9), 1773–1782 (2004).
24. Wang, Y., Chen, F., and Wu, K., 'Twin-screw Extrusion Compounding of Polypropylene/Organoclay Nanocomposites Modified by Maleated Polypropylenes,' *J. Appl. Polym. Sci.*, **93** (1), 100–112 (2004).
25. Tjong, S.C., Meng, Y.Z. and Hay, A.S., 'Novel Preparation and Properties of Polypropylene-Vermiculite Nanocomposites,' *Chem. Mater.*, **14** (1), 44–51 (2002).
26. Kato, M., Matsushita, M., and Fukumori, K., 'Development of a new production method for a polypropylene-clay nanocomposite,' *Polym. Eng. Sci.*, **44** (7), 1205–1211 (2004).
27. Fornes, T. D., Yoon, P. J., Keskkula, H. and Paul, D. R., 'Nylon 6 nanocomposites: the effect of matrix molecular weight,' *Polymer*, **42**, 9929 (2001).
28. Krishnamoorti, R., and Giannelis, E.P., 'Rheology of End-Tethered Polymer Layered Silicate Nanocomposites,' *Macromolecules*, **30**, 4097 (1997).
29. Solomon, M.J., Almusallam, A.S., Seefeldt, K.F., Somwangthanaroj, A. and Varadan, P., 'Rheology of Polypropylene/Clay Hybrid Materials,' *Macromolecules*, **34**, 1864–1872 (2001).
30. Galgali, G., Ramesh, C. and Lele, A., 'A Rheological Study on the Kinetics of Hybrid Formation in Polypropylene Nanocomposites,' *Macromolecules*, **34**, 852–858 (2001).
31. Luciani, A., Leterrier, Y., and Manson, J., 'Rheological behavior of dilute suspensions of platelet particles,' *Rheol. Acta*, **38** (5), 437–442 (1999).
32. Okamoto, M., Nam, P.H., Maiti, P., Kotaka, T., Hasegawa, N. and Usuki, A., 'A House of Cards Structure in Polypropylene/Clay Nanocomposites under Elongational Flow,' *Nano Letters*, **1,** (6), 295 (2001).
33. Okamoto, M., Nam, P., Maiti, P., Kotaka, T., Nakayama, T., Takada, M., Ohshima, M., Usuki, A., Hasegawa, N., and Okamoto, H., 'Biaxial flow-induced alignment of silicate layers in polypropylene/clay nanocomposite foam,' *Nano Letters*, **1** (9), 503–505 (2001).
34. Kumar, S. and Jayaraman, K., 'Process induced orientation of nanolayers in polyolefin nanocomposites,' *Society of Plastics Engrs. Annual Tech. Conf.*, **62**, 1498–1502 (2004).
35. Reichert, P., Hoffman, B., Bock, T., Thomann, R., Mulhaupt, R. and Friedrich, C., 'Morphological Stability of Poly (propylene) Nanocomposites,' *Macromol. Rapid. Comm.*, **22**, 519–523 (2001).
36. Ma, J., Zhang, S., Qi, Z., Li, G. and Hu, Y., 'Crystallization Behaviors of Polypropylene/Montmorillonite Nanocomposites,' *J. Appl. Polym. Sci.*, **83**, 1978–1985 (2002).
37. Somwangthanaroj, A., Lee, E., and Solomon, M., 'Early stage quiescent and flow-

induced crystallization of intercalated polypropylene nanocomposites by time-resolved light scattering,' *Macromolecules*, **36** (7), 2333–2342 (2003).
38. Maiti, P., Nam, P.H., Okamoto, M., Hasegawa, N., and Usuki, A., 'Influence of crystallization on intercalation, morphology, and mechanical properties of polypropylene/clay nanocomposites,' *Macromolecules*, **35** (6), 2042–2049 (2002).
39. Maiti, P., Nam, P.H., Okamoto, M., Kotaka, T., Hasegawa, N., and Usuki, A., 'The effect of crystallization on the structure and morphology of polypropylene/clay nanocomposites,' *Polym. Eng. Sci.*, **42** (9), 1864–1871 (2002).
40. Ray, S.S. and Okamoto, M., 'Polymer layered silicate nanocomposites: a review from preparation to processing,' *Prog. Polym. Sci.*, **28**, 1539–1641 (2003).
41. Nam, P.H., Maiti, P., Okamoto, M., Kotaka,, T., Hasegawa, N., A. Usuki, 'A Hierarchical Structure and Properties of Intercalated Polypropylene/Clay Nanocomposites,' *Polymer*, **42**, 9633–9640 (2001).
42. Weinkauf, D.H., and Paul, D.R., 'Effects of Structural Order on Barrier Properties,' Chapter 3 in *Barrier Polymers and Structures*, W.J. Koros Ed., American Chemical Society (1990).
43. Liu, X. and Wu, Q., 'PP/clay nanocomposites prepared by grafting-melt intercalation,' *Polymer,* **42** (25), 10013–10019 (2001).
44. Qian, G., Cho, J.W. and Lan, T., 'Preparation and Properties of Polyolefin Nanocomposites,' *Polyolefins 2001*, Houston, TX (2001).
45. Manias, E., 'The Role of Nanometer-Thin Layered Inorganic Fillers as Flame Retardants in Polymers,' in *Flame Retardants in Our New World*, DEStech Publications, Inc., 2002.
46. Gilman, J., Jackson, C., Morgan, A., Harris, R., Manias, E., Giannelis, E., Wuthenow, M., Hilton, D., and Phillips, S., 'Flammability Properties of Polymer – Layered-Silicate Nanocomposites. Polypropylene and Polystyrene Nanocomposites,' *Chem. Mater.*, **12** (7), 1866–1873 (2000).
47. Bartholmai, M. and Schartel, B., 'Layered silicate polymer nanocomposites: new approach or illusion for fire retardancy? Investigations of the potentials and the tasks using a model system' *Polym. Adv. Tech.*, **15** (7), 355–364 (2004).
48. Tang, Y., Hu, Y., Li, B., Liu, L., Wang, Z., Chen, Z., and Fan, W., 'Polypropylene/montmorillonite nanocomposites and intumescent, flame-retardant montmorillonite synergism in polypropylene nanocomposites,' *J Polym. Sci. Polym. Chem.*, **42** (23), 6163–6173 (2004).

5

Polystyrene/clay nanocomposites

D-R YEI, H-K FU and F-C CHANG,
National Chiao-Tung University, Taiwan

5.1 Introduction

Polymerization of vinyl monomers intercalating into the montmorillonite (MMT) clay[1] was first reported in the literature as early as 1961. The most recent methods to prepare polymer-layered-silicate nanocomposites have primarily been developed by several other groups. In general these methods (shown in Fig. 5.1) are able to achieve molecular-level incorporation of the layered silicate (e.g. montmorillonite clay or synthetic layered silicate) in the polymer matrix by addition of a modified silicate either to a polymerization reaction (in situ method),[2–4] to a solvent-swollen polymer (solution blending),[5] or to a polymer melt (melt blending).[6,7] Recently, a method has been developed to prepare the layered silicate by polymerizing silicate precursors in the presence of a polymer.[8]

Several attempts to prepare polystyrene-clay composites have been reported. A common technique involves impregnating clay in styrene monomer followed by polymerization. The hydrophilic nature of untreated clay impedes its homogeneous dispersion in polymer matrix. Friedlander and Grink[9] reported a slight expansion of the 001 spacing of clay galleries and concluded that polystyrene was intercalated in clay galleries; but Blumstein[10] questioned intercalation by polystyrene because no increase in the basal spacing could be detected. Later Kato *et al.*[11] reported the intercalation of styrene into stearyltrimethyl-ammonium cation exchanged MMT. Kelly *et al.*[12,13] reported the modification of MMT by a variety of functional groups in their study of epoxy composites. Akelah and Moet[14,15] prepared polystyrene nanocomposites using a solvent (acetonitrile). Na-MMT was made organophilic by cation exchange with vinyl-benzyltrimethylammonium chloride. Polystyrene-clay intercalated nanocomposites with a maximum basal spacing of 2.45 nm were reported. Giannelis[16] and Vaia *et al.*[17] developed a new approach to fabricate polymer-clay nanocomposites via polymer melt intercalation. Polystyrene-clay intercalated nanocomposites were prepared using this method.[17] Recently, Doh and Cho[18] prepared polystyrene-clay intercalated nanocomposites by

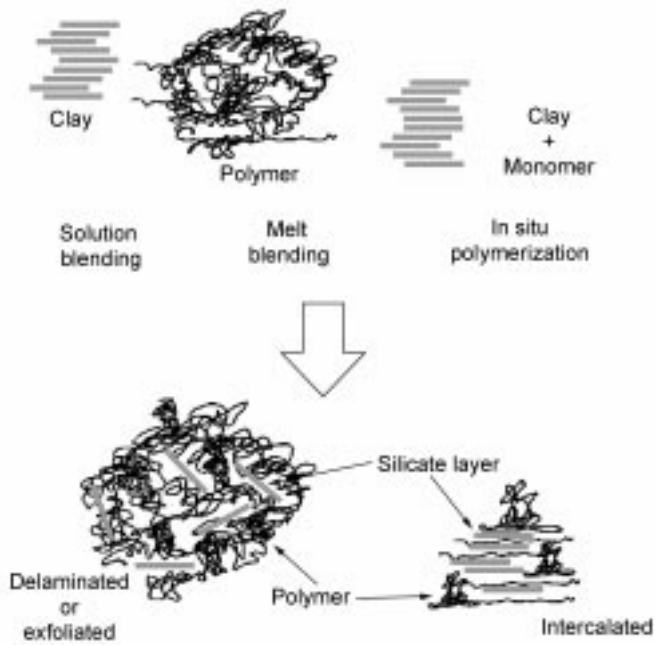

5.1 Schematic representation of various methods used to prepare polymer-layered-silicate nanocomposites.[38]

polymerization of styrene in the presence of organophilic clay. The intercalated polystyrene-clay nanocomposites exhibited thermal stability better than pure polystyrene.

5.2 Organically modified clay

Zhu and co-workers[19] reported the preparation of three new organically modified clays and their corresponding preparation of PS/clay nanocomposites from these clays by bulk polymerization. Two are functionalized ammonium salts while the third is a phosphonium salt and structures of these salts are shown in Fig. 5.2. TGA/FTIR showed that the phosphonium treatment results in the most thermally stable treatment when compared to the two ammonium salts.

Wang[20] used two different organic modifications of the montmorillonite, one contains a styryl monomer on the ammonium ion while the other contains no double bond. A double bond that may be involved in the polymerization reaction is present in the cation of the clay. Polystyrene-clay nanocomposite has been prepared by bulk, solution, suspension, and emulsion polymerization as well as by melt blending. The organic modification as well as the mode of preparation may determine whether the composite is either exfoliated or intercalated. Exfoliation is more likely to occur if the ammonium ion contains a double bond

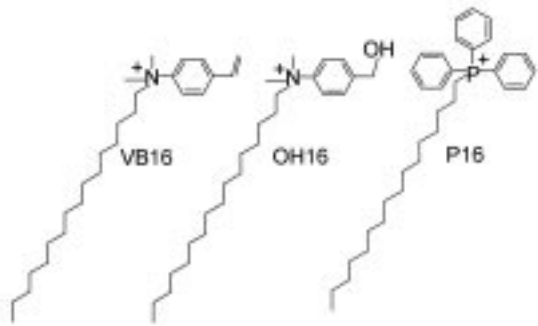

5.2 Structures of the salts used to prepare the organically modified clays.[19]

which can participate in the polymerization reaction. However, the mere presence of this double bond is not sufficient to always produce an exfoliated system.

In addition, Wang and Charles[21] also reported the preparation and characterization of an antimony-containing clay and the preparation of polystyrene nanocomposites from this clay. The structure of antimony is shown in Fig. 5.3. The objective of this study is to determine if this clay is more thermally stable than the common ammonium clays and thus could be used at higher temperatures for the processing of polymers, such as polycarbonate, that require processing at higher temperature.

Fu and Qutubuddin[22] reported the synthesis of exfoliated polystyrene-clay nanocomposite. A reactive cation surfactant vinylbenzyldimethyldodecylammonium chloride (VDAC) was synthesized and used for ion exchange with sodium ions in MMT. The structure of VDAC is shown in Fig. 5.4. The exfoliated polystyrene-clay nanocomposite was prepared by direct dispersion of organophilic MMT in styrene monomer followed by free radical polymerization.

Chang and co-workers[23] reported the preparation of two types of nanocomposites formed from cetylpyridinium chloride (CPC)- and aminopropylisobutyl polyhedral oligomeric silsesquioxane (POSS)-treated clays (Fig. 5.5). The PS/clay nanocomposite formed using the CPC-treated clay exhibited no

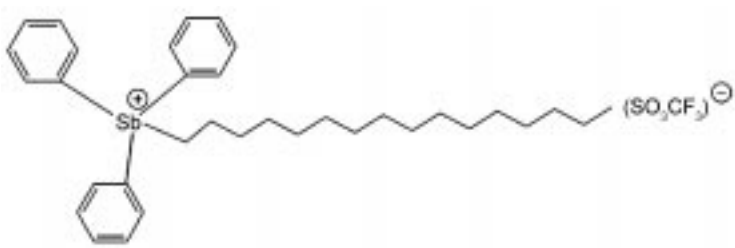

5.3 Structure of triphenylhexadecylstibonium trifluoromethylsulfonate.[21]

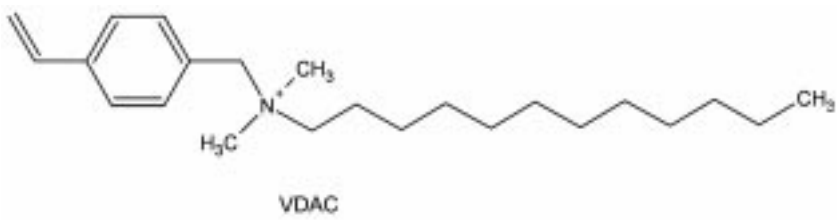

5.4 Structure of VDAC used to prepare the organically modified clay.

significant improvement in thermal properties.[24–28] The major advantage of choosing POSS molecules is its thermal stability up to 300ºC, higher than the thermal degradation temperatures of most organic molecules. POSS consists of a rigid cubic silica core with 0.53 nm side length, to which organic functional groups can be attached at the vertices for further reactions. POSS derivatives containing amine functional groups can play the role of surfactants for the treatment of clay and the thermal stability of the resulting nanocomposite is enhanced.

In addition, Yei and co-workers also reported the preparation of two types of PS/clay nanocomposites formed from clays treated with either cetylpyridinium chloride (CPC) or the CPC/α-CD inclusion complex.[29] Structures of these two intercalation agents were shown in Fig. 5.6. We found that CPC, a linear aliphatic surfactant, is able to form a crystalline complex with cyclodextrin. Including CPC within CD channels improves the thermal stability of the virgin

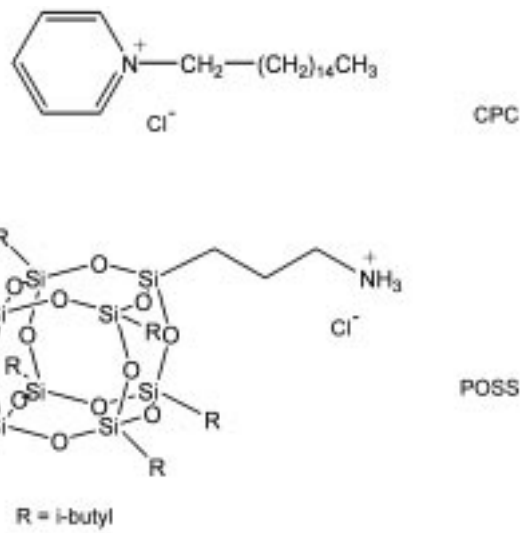

5.5 Chemical structures of the surfactants used to prepare the modified clays.[23]

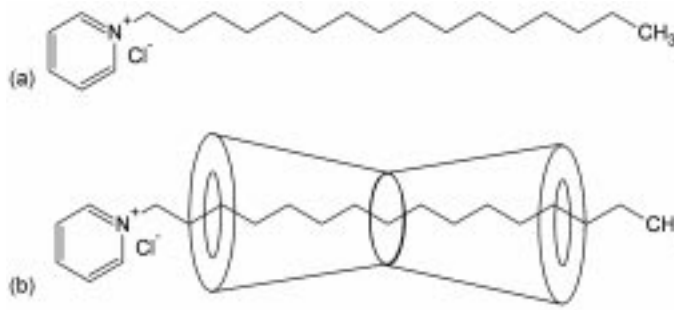

5.6 The structures of intercalation agent (a) CPC and (b) CPC/α-CD inclusion complex.

CPC. The linear aliphatic chain within the CPC/α-CD cannot bend within the galleries of the clay and the *d* spacing of clay intercalated by the CPC/α-CD inclusion complex is significantly higher than that formed using pure CPC. The CPC/α-CD inclusion complex can promote exfoliated structure of clay.

5.3 Surface-initiated polymerization (SIP)

Rather than modifying the clay with organic quaternized ammonium salts, cationically modified polymerization initiators can also be used to prepare organophilic clays. In this method, the in-situ polymerization is initiated by the activation of these initiators which are *ionically bound* to the clay particle surfaces, that is, through a surface-initiated polymerization (SIP) process. The advantage of SIP is based on the assumption that as the polymer chain grows through surface initiation, the ordered silicate layers can be gradually pushed apart, ultimately exfoliating to discrete laths, resulting in a well-dispersed structure of the final product. Also, theoretically, if all initiators are tethered to clay surfaces, a higher efficiency of intergallery polymerization is expected compared to that of free, or unattached initiators. Exfoliated polystyrene-clay nanocomposites with controllable MW have been prepared by intercalating a charged living free radical polymerization (LFRP) initiator into montmorillonite.[30] A (1,1-diphenylethylene) DPE derivative initiator was used to synthesize polystyrene-clay nanocomposite materials through living anionic surface-initiated polymerization (LASIP).[31–32] However, only intercalated structures were obtained.

In efforts to conduct SIP from clay surfaces, Xiaowu and co-workers[33] recently synthesized two initiators for free radical SIP, both contain quaternized amine endgroups for cation exchange with montmorillonite particles. The initiator molecule design is as follow:

- *symmetric*, with two cationic groups at both chain ends (named bicationic free radical initiator hereafter) and

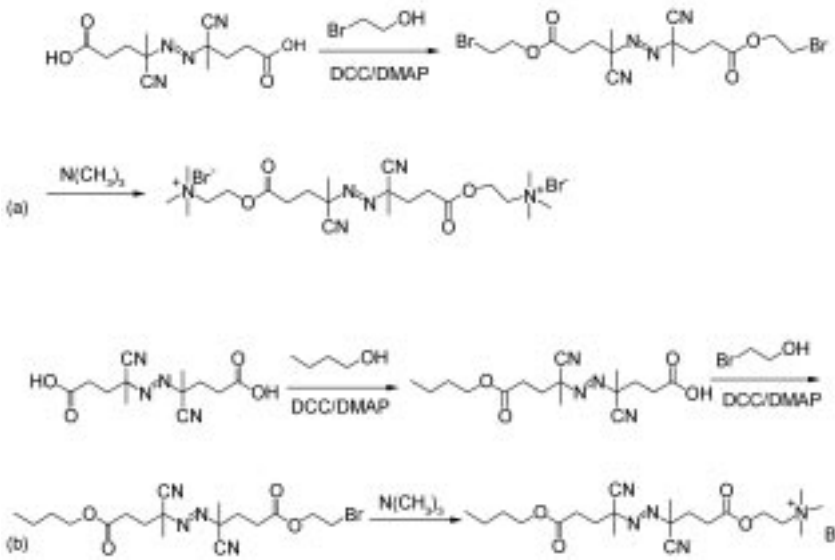

5.7 (a) Synthetic scheme and structure of the bicationic free radical initiator. (b) Synthetic scheme and structure of the monocationic free radical initiator.[33]

- *asymmetric*, with one cationic group at one end (named monocationic free radical initiator hereafter).

The synthetic schemes and structures of these initiators are shown in Figs 5.7(a) and 5.7(b). They are both AIBN-analogue initiators for free radical polymerization. The use of another symmetric bicationic azo compound, 2,2′-azobis(isobutyramidine hydrochloride) (AIBN), has also been proven to be feasible for styrene SIP on high surface area mica powder.[34] However, no structural information for these SIP products has been reported. Asymmetric azo initiators in the form of silanes have also been successfully employed to free radically polymerize styrene from spherical silica gel surfaces.[35–36] To the best of our knowledge, there have been no reports on a direct free radical SIP approach from surface-bound monocationic azo initiators on individual clay nanoparticles.

X-ray powder diffraction patterns of the pristine clay and two initiator-intercalated clay samples are shown in Fig. 5.8. Lamellar periodicity was maintained on the organophilic clay despite the rigorous sonication-centrifugation procedure to intercalate the initiators. By using the Bragg equation, $n\lambda = 2s \sin\theta$, the d spacing values of these samples were calculated and shown beside each peak.

The basal spacing of the pure montmorillonite Na^+ is 1.16 nm, which is in accordance with data from other sources.[37] The XRD patterns of the intercalated clays indicate the successful insertion of the initiator molecules into the galleries

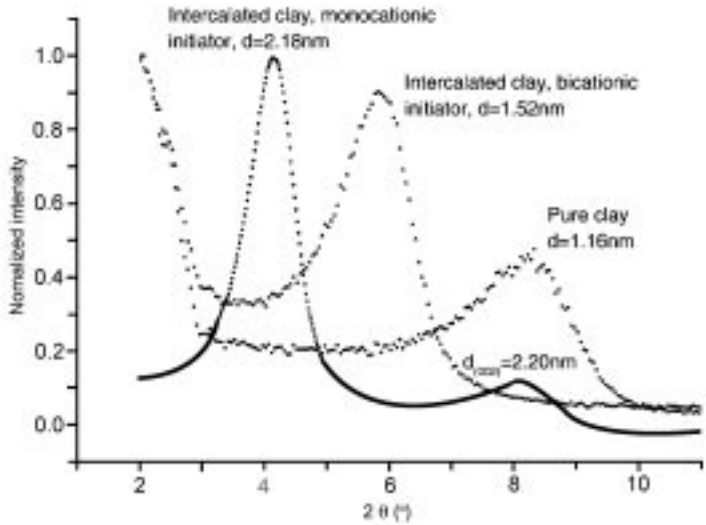

5.8 X-ray powder diffraction patterns of pure clay and two intercalated clay samples.[33]

of the silicate platelets since both intercalated clay samples gave increased *d* spacing values. In addition, the sharper shape and the higher diffraction intensities of these peaks after intercalation provide the evidence of a better-ordered swollen structure than that of the original clay. This result demonstrates that the layered framework of inorganic clay can accommodate the AIBN derivative molecules of various functionalities with better long-range periodicity.

On further analysis, the *d* spacing values seemed to be inconsistent with the steric sizes of the two initiators. The *d* spacing of bicationic intercalated clay (1.52 nm) is substantially smaller than that of the monocationic intercalated clay although their molecular dimensions are comparable (both chain length values are 2.20 nm, as estimated by Chem 3D software). The bicationic initiator molecule possesses charged groups on both ends that can have two intercalation possibilities:

1. these two cationic endgroups interact electrostatically with two different but neighboring platelets' surfaces, or
2. they interact on the same side surface of a single clay particle.

The combination of these two possibilities makes the intercalated structure less spatially ordered which accounts for the broadened reflection for this sample as compared with the peak of the clay intercalated by the monocationic initiator. Furthermore, since XRD collects the average information from a large area of a powder sample, a synergic effect of these two possibilities accounts for an intermediate *d* spacing value. This interpretation is schematically shown in Fig.

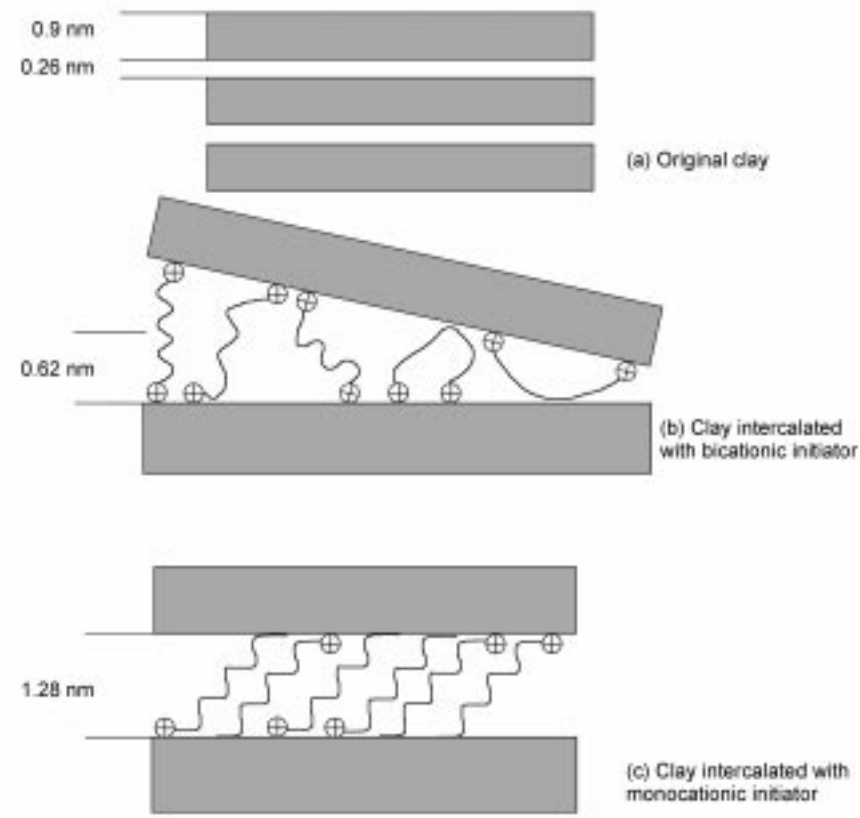

5.9 (a–c) Schematic diagrams of the intercalation: (a) original clay, (b) clay intercalated with bicationic initiator, and (c) clay intercalated with monocationic initiator.[33]

5.9. The interlamellar height shown in the figure is calculated by $\Delta d = d$ spacing – thickness of one platelet (~1.0 nm).

The X-ray diffractograms of the two final SIP products are shown in Fig. 5.10. The broad peaks of both samples at the higher angle regime are believed to be related to the long-range order of the polystyrene matrix. Similar broad peaks were also observed in the diffractogram of the PS-0 reference sample (not shown). Sample bi-PS-M-2 shows a small peak at $2\theta = 5.9^{\circ}$, which is about the same as the peak position of the corresponding intercalated clay (Fig. 5.8), implying that this product still contains fractions of the intercalated clay structure. On the contrary, there is no peak on the XRD trace of the mono-PS-M-2 sample, indicating that a completely exfoliated structure was achieved in this sample.

This observed result is quite unexpected. We would anticipate that these adjacent clay layers in the clay/bicationic initiator system will be gradually

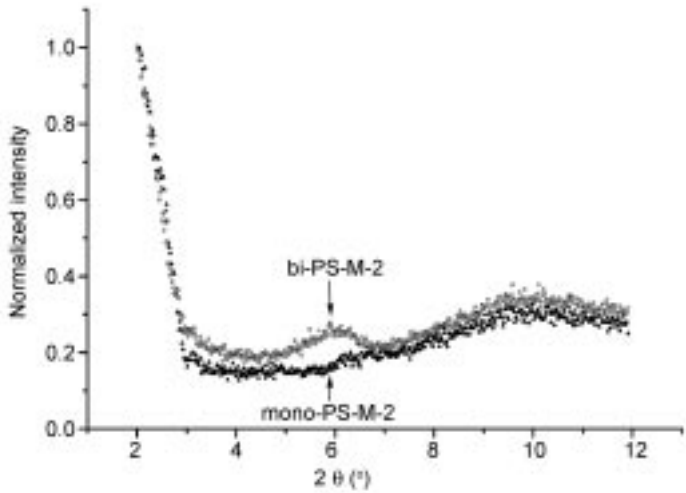

5.10 XRD spectra of the two SIP nanocomposites showing degree of exfoliation.[33]

pushed apart during SIP, if these two immobilized free radicals are simultaneously generated. As a result, the intercalated clay stacks would be totally delaminated, forming a fully exfoliated nanocomposite product. However, the polymer can only grow within the clay gallery when monomer molecules are able to diffuse and make contact effectively with the tethered radicals within the interlayer spacing. The time scale of diffusion is such that access to the monomer from within the layers is limited. Considering the rapid kinetics for free radical polymerization in solution, this intercalative monomer diffusion is significantly slower toward monomer addition. Thus, free initiators exhaust the monomers while SIP inside clay lamellar is delayed by diffusion. Furthermore, there is also competition from the surface-perimeter-attached initiators of the clay particles. Even if some of the bication initiators were activated and grew to become oligomers, the growing chains will likely be terminated by recombination or disproportionation by nearby immobilized growing chains/initiators in the same gallery. Hence the low molecular weight and high polydispersity obtained by bi-PS-M-2 can be explained.

By comparison, an intercalated monocationic initiator is more easily delaminated than a bicationic initiator. The monocationic initiator molecule is also more organophilic. The weaker van der Waals interaction between the alkyl headgroups of the monocationic initiator and clay surfaces makes the intercalated clay more easily swelled by the solvent and monomer. Once the clay intercalated with monocationic initiator is exfoliated by sonicating and stirring, the attached initiators have more accessibility to monomer and thus results in better monomer intercalative diffusion.

5.4 Syndiotactic polystyrene (s-PS)/clay nanocomposite

5.4.1 Clay effects on chain conformation and crystallization behavior of the s-PS

The highly stereoregular syndiotactic polystyrene (s-PS) has received considerable interest recently. Depending on the thermal history, s-PS possesses several polymorphic crystalline structures. Helical (TTGG) conformation is formed in solution recovered s-PS, whereas the thermodynamically favored all-trans (TTTT) conformations are formed from either melt or annealing at an elevated temperature.[39–44] The extent to which thermal history affects the crystalline structure and crystallization kinetics for s-PS has been extensively studied.[45–48]

Having been extensively applied to characterize polymers,[49] FTIR spectroscopy complements other techniques in providing detailed information on the chain conformation transition and crystallinity of a polymer with nondestructive characteristics.[50–52] The changes of chain conformation and crystallinity can be characterized by identifying FTIR spectral features of intensity, bandwidth, and position.

Wu *et al.*[53] reported effects of clay on chain conformation and crystallization behavior. Analyses of the effects of montmorillonite on the chain conformation and crystallization of syndiotactic polystyrene (s-PS) thin films are investigated using FTIR spectroscopy, X-ray diffraction, and TEM. The clay is dispersed into the s-PS matrix using a solution blending with scale in 1–2 nm or in a few tenths to 100 nm, depending on whether a surfactant is added or not. Upon adding clay, the chain conformation of s-PS tends to convert to TTTT from FFGG after drying because the highly dispersed clay overcomes the energy barrier of chain conformation transformation. This phenomenon leads to a change in the conventional mechanism of molecular packing for s-PS in the drying stage. During melt-crystallization, clay plays a vital role in facilitating the formation of the thermodynamically favored all-trans β form crystal, particularly on the s-PS thin film samples. When the s-PS is melt-crystallized at a cooling rate of 1ºC/min from 320ºC, the highest absolute crystallinity of β form up to 0.56 occurs in the clay dispersibility of few tenths to 100 nm in the s-PS matrix; then dispersibility is of 1–2 nm (0.49), and the final one is of pure s-PS (0.42). Evidently, clay significantly affects the chain conformation and crystallization of s-PS.

5.4.2 Crystallization kinetics of the s-PS/clay nanocomposite

Tseng *et al.*[54] investigated the effects of montmorillonite on the crystallization kinetics of syndiotactic polystyrene (s-PS) with isothermal differential scanning calorimetry analyses. The clay was dispersed into the s-PS matrix via melt

blending on a scale of 1–2 nm or up to about 100 nm, depending on the surfactant treatment. For a crystallization temperature of 240ºC, the isothermal crystallization data were fitted well with the Avrami crystallization equation. Crystallization data on the kinetic parameters (i.e., the crystallization rate constant, Avrami exponent, clay content, and clay/surfactant cation-exchange ratio) were also investigated. Experimental results indicated that the crystallization rate constant of the s-PS nanocomposite increased with increasing clay content. The clay played a vital role in facilitating the formation on the thermodynamically more favorable all-β-form crystal when the s-PS was meltcrystallized.

In isothermal DSC operations, the crystallization kinetics of the s-PS/clay hybrid is based on Avrami analysis. The following expression is used to measure the extent of crystallization:

$$X(t) = \frac{\int_0^t \frac{dH}{dt} dt}{\int_0^\infty \frac{dH}{dt} dt} \tag{5.1}$$

where the first integral is the heat generated at time t and the second is the total heat generated up to the end of the crystallization process. By equating the integrals to areas of the isothermal DSC curves, we can shape Equation (5.1) into

$$X(t) = \frac{A_t}{A_\infty} \tag{5.2}$$

where A_t is the area under the DSC curves from $t = 0$ to $t = t$ and A_∞ is the total area under the crystallization curve. On the basis of this equation, the weight fraction of the crystalline material $[X(t)]$ at a specific time can be calculated. Because the crystalline polymer can transform from an amorphous phase to a crystalline phase, $X(t)$ is called the reduced crystallinity. Figures 5.11–5.13 plot $X(t)$ versus time for each hybrid at the crystallization temperature (240ºC). The aforementioned results suggest that the clay content, ratio of clay and CPC, and methods for preparing the composite heavily influence the crystallization rate of s-PS. By following the Avrami treatment, Fig. 5.11 plots the relative crystallinity as a function of the crystallization times for neat s-PS and s-PS nanocomposites by different preparation methods. These curves reveal that the crystallization rate of s-PS nanocomposites prepared by melt blending (Figs. 5.11(d,e)) is faster than that of those prepared by solution blending (Figs 5.11(b,c)).

Figure 5.12 plots the relative crystallinity versus crystallization time for s-PS/clay-CPC hybrids with different ratios of clay to CPC. A higher clay/CPC ratio (Fig. 5.12(f)) results in a slower crystallization rate, implying that the presence of CPC, free or intercalated, tends to retard the s-PS crystallization. Better compatibility between CPC and s-PS makes better clay/CPC dispersion in the

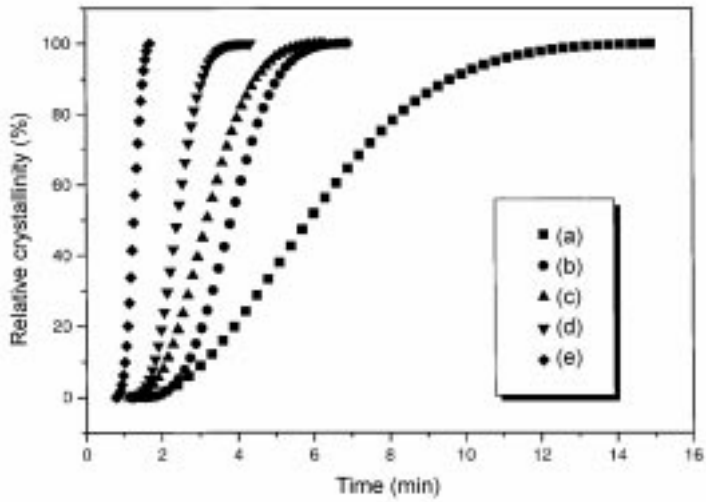

5.11 Plots of the relative crystallinity versus time at 240°C for (a) pure s-PS, (b) 95/5 s-PS/clayCPC (clay/CPC = 1/1) from solution blending, (c) 95/5 s-PS/clay from solution blending, (d) 95/5 s-PS/clay–CPC (clay/CPC = 1/1) from melt blending, and (e) 95/5 s-PS/clay from melt blending.[54]

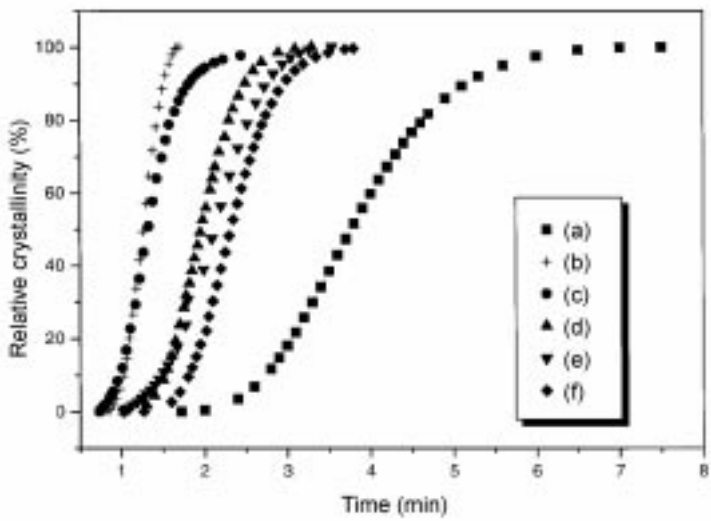

5.12 Plots of the relative crystallinity versus time for pure s-PS and 95/5 s-PS/clay–CPC hybrids at 240°C for various clay/CPC ratios from melt blending: (a) pure s-PS, (b) 1/0 clay/CPC, (c) 1/0.25 clay/CPC, (d) 1/0.5 clay/CPC, (e) 1/1 clay/CPC, and (f) 1/2 clay/CPC.[54]

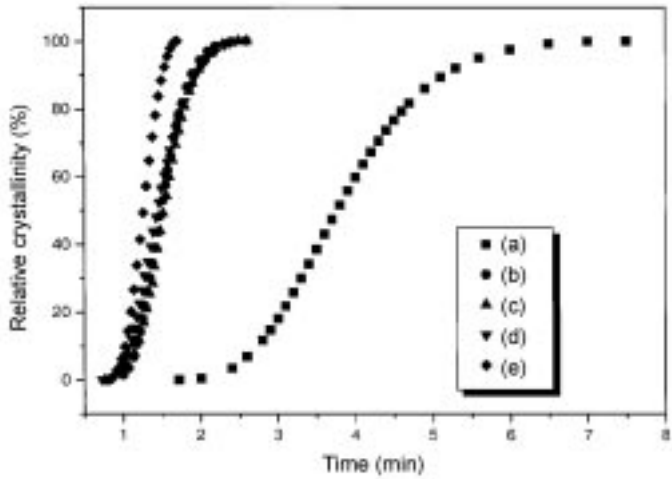

5.13 Plots of the relative crystallinity versus time for s-PS/clay hybrids at 240°C for various pure clay contents (wt.%) from melt blending: (a) pure s-PS, (b) 99.5/0.5 s-PS/clay, (c) 99/1 s-PS/clay, (d) 97.5/2.5 s-PS/clay, and (e) 95/5 s-PS/clay.[54]

s-PS matrix but tends to retard the s-PS crystallization rate by physical hindrance of s-PS chains.

Figure 5.13 plots the relative crystallinity versus crystallization time for s-PS/clay hybrids at different clay contents, indicating that the s-PS crystallization rate significantly increases, even with small clay content. The pure clay can act as an efficient nucleating agent to facilitate s-PS crystallization.

5.5 Properties of nanocomposites

5.5.1 Dimensional stability

Dimensional stability is critical in many applications. For example, if the layers of a microelectronic chip have different thermal or environmental dimensional stabilities, then residual stresses can develop and cause premature failure. Poor dimensional stability can also cause warping or other changes in shape that affect the function of a material. Nanocomposites provide methods for improving both thermal and environmental dimensional stability. The possible mechanism by which nanofillers can affect the coefficient of thermal expansion (CTE) of a polymer has also been observed in traditional fillers.

The dimension stability of nanocomposites was studied by Zeng and Lee.[55] Figure 5.14 shows the shape changes of injection molded PS and PS/clay nanocomposites under the aforementioned thermal cycle (50°C, 1 h; 75°C, 1 h; 105°C, 1 h; and 135°C, 1 h). The original sample shape is shown in the first row. Pure PS and the extruded PS/20A (dimethyl dehydrogenated tallow ammonium

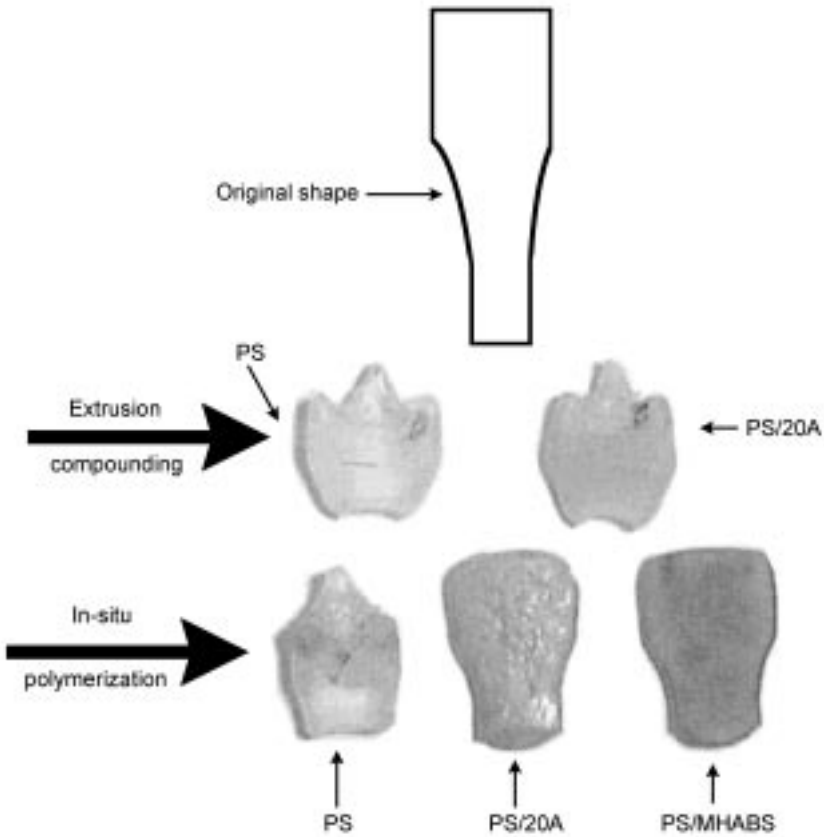

5.14 PS and PS/clay nanocomposites after dimension stability test. Clay loading is 5 wt.% for all nanocomposites.[55]

montmorillonite, 20A) nanocomposite are shown in the second row for comparison. The third row shows the in-situ polymerized pure PS, PS/20A, and PS/MHABS (2-methacryloyloxyethylhexadecyldimethylammonium bromide, MHABS) nanocomposites. All the nanocomposites contain 5 wt.% clay. In the absence of clay, the sample shrank greatly, and the shape became highly irregular. Dimension stability at elevated temperature was improved significantly when 5 wt.% of clay was present in the in-situ polymerized nanocomposites, as shown in the third row. The exfoliate PS/MHABS exhibited the best dimensional stability. After the heating cycle, although the sample shrank to a certain extent, the original shape and surface smoothness remained. It is noteworthy that the PS/20A nanocomposite prepared by extrusion compounding did not show much improvement in dimension stability at elevated temperature, as compared to the in-situ polymerized PS/20A nanocomposite with the same clay content.

5.5.2 Thermal stability and flammability

Delaminated composites have significantly higher degradation temperatures than intercalated nanocomposites or traditional clay composites.[56] Some speculate that this increase in stability is due to the improved barrier properties of the composites. If oxygen cannot penetrate, then it cannot cause oxidation of the resin.[57] In addition, the inorganic phase can act as a radical sink to prevent polymer chains from decomposing. The improved thermal stability of some composites may be limited by the lower thermal stability of alkylammonium ions. For example, in intercalated clay/polystyrene composites, the intercalating agent decomposes at about 250ºC. Bonding the intercalating ion to the polystyrene matrix noticeably improved the thermal stability.

Jin and co-workers investigated thermal property of polymer-clay nanocomposites by TGA and cone calorimetry.[19] The thermal stability of the nanocomposite is enhanced relative to that of virgin polystyrene and this is shown in Fig. 5.15. Typically, the onset temperature of the degradation is about 50ºC higher for the nanocomposites than for virgin polystyrene.

One invariably finds that nanocomposites have a much lower peak heat release rate (PHRR) than the virgin polymer. The peak heat release rate for polystyrene and the three nanocomposites are also shown graphically in Fig. 5.16. P16-3 means that the nanocompoite was formed using 3% of P16 clay with polystyrene. The peak heat release rate falls as the amount of clay was increased. The suggested mechanism by which clay nanocomposites function involves the formation of a char that serves as a barrier to both mass and energy transport.[58] It is reasonable that as the fraction of clay increases, the amount of char that can be formed increases and the rate at which heat is released is decreased. There has

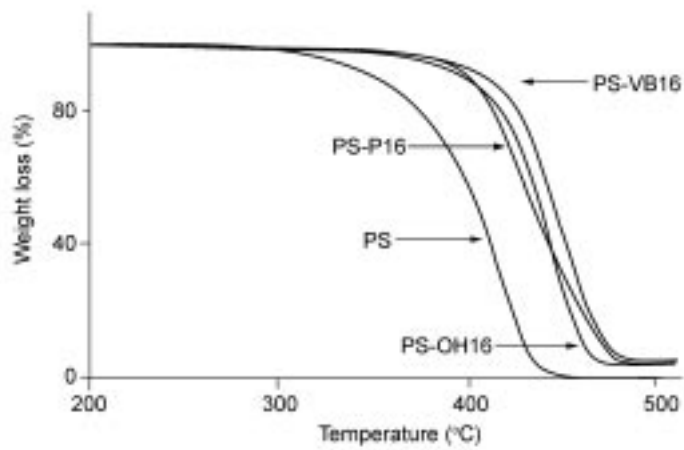

5.15 TGA cures for polystyrene, PS, and the nanocomposites.[19]

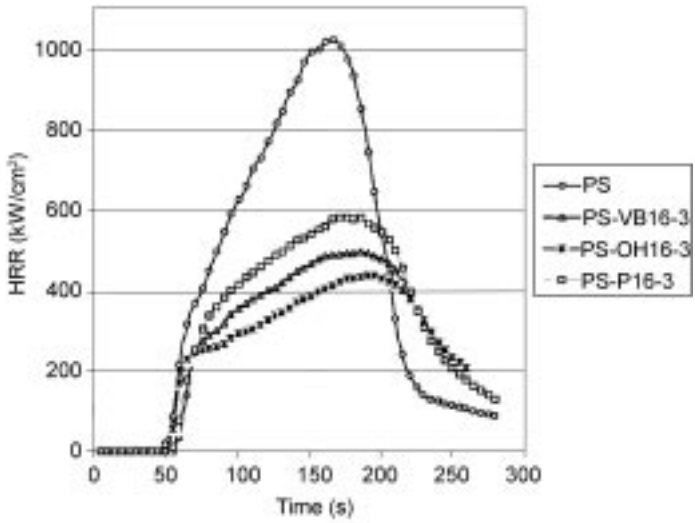

5.16 Peak heat release rates for polystyrene and the three nanocomposites.[19]

been a suggestion that an intercalated material is more effective than is an exfoliated material in fire retardancy.[19]

The production of a char barrier must serve to retain some of the polymer and thus both the energy released and the mass loss rate decrease. The amount of smoke evolved, and specific extinction area, also decreases with the formation of the nanocomposite. There is some variability in the smoke production but apparently the formation of the nanocomposite gives a reduction in smoke; however, the presence of additional clay does not decrease smoke.

5.5.3 Mechanical properties

The cyclic deformation of PS/MMT nanocomposites as a function of temperature was measured by DMA. The temperature dependence of storage modulus and tan δ are shown in Figs 5.17 and 5.18, respectively. The storage modulus of PS/MMT nanocomposites was greater than that of pure PS and monotonically increased with the clay content in both the glassy and rubbery regions. However, the improvements in the rubbery region were much greater than those in the glassy region. This behavior indicates that the restricted segmental motions at the organic-inorganic interface are due to large aspect ratios of the clay platelets, and the polymer chains were also well confined inside the clay galleries at the nanoscale level.[59–60] The storage modulus of PS/MMT-3 was 1.2 times higher than that of pure PS, which is comparable to the earlier reported data (1.4 times improvement).[59] The T_gs of the nanocomposites were estimated from the peak values of tan δ in Fig. 5.18, which were shifted towards higher temperature with

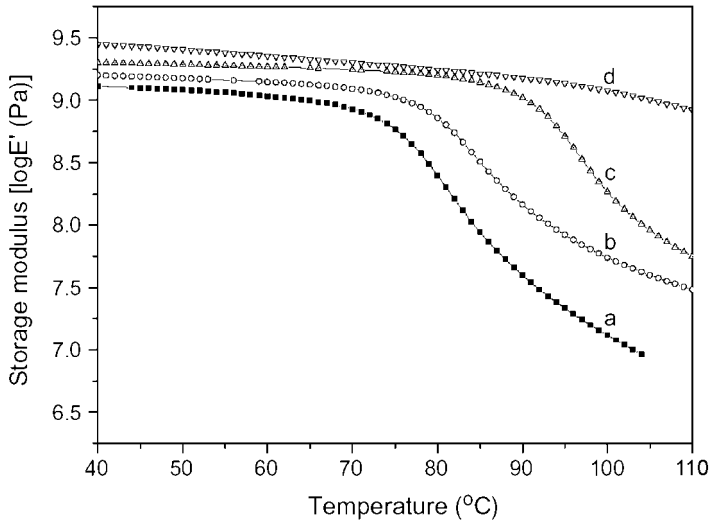

5.17 Storage modulus of (a) pure PS, (b) PS/MMT-1, (c) PS/MMT-2 and (d) PS/MMT-3.

increasing clay content. These results indicate that nanoscale clay platelets strongly restrict the polymer segmental motions, resulting in the significant increase in T_g. This improvement in T_g is higher than those of other researchers even though the smaller clay content was used in this experiment.[61,62]

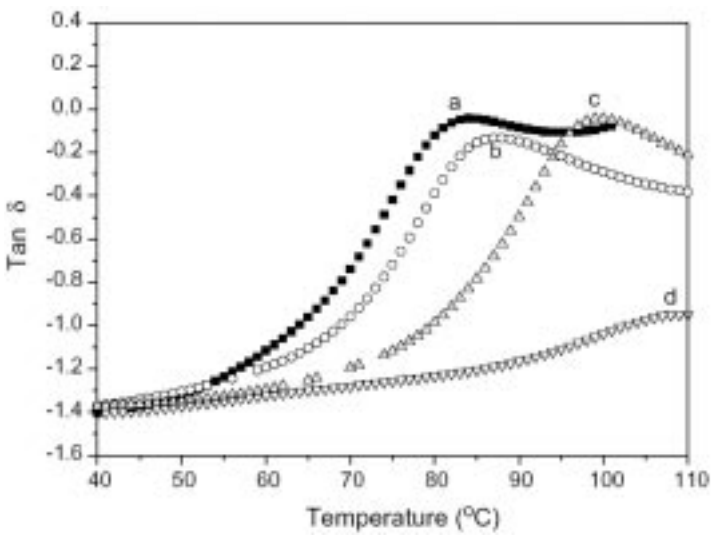

5.18 Tan δ values of (a) pure PS, (b) PS/MMT-1, (c) PS/MMT-2 and (d) PS/MMT-3.

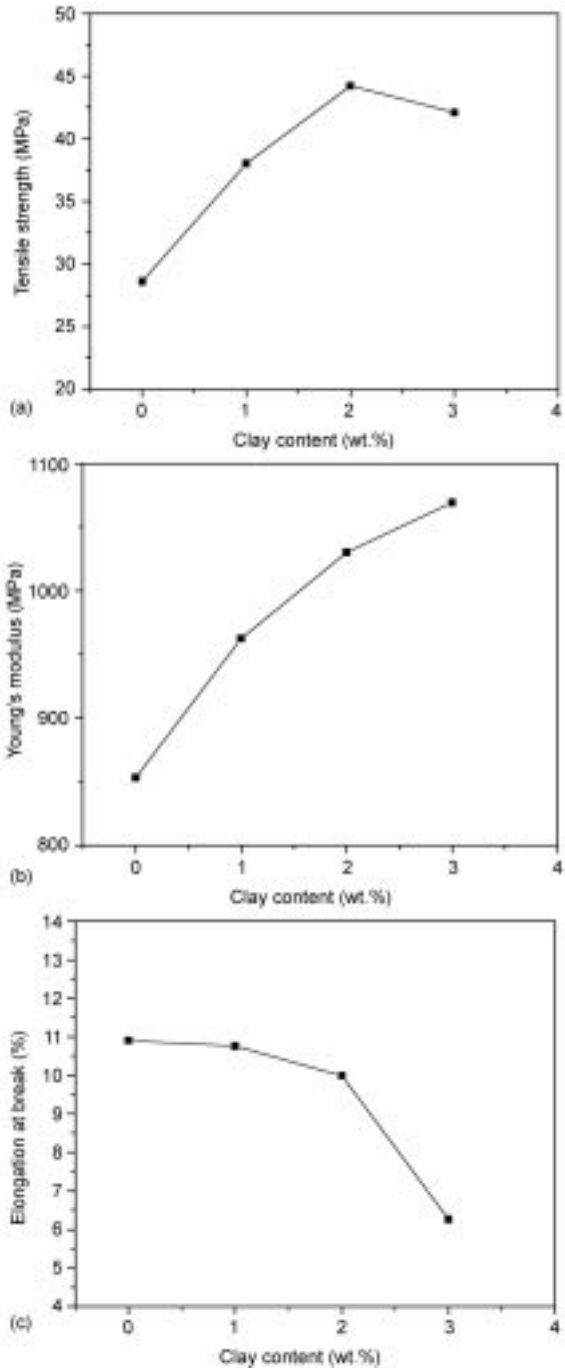

5.19 (a) Tensile strengths, (b) Young's modulus and (c) elongations at break of PS/MMT nanocomposites.[64]

The effects of clay loadings on tensile properties of the PS/MMT nanocomposites are shown in Fig. 5.19. The tensile strength and Young's modulus were significantly enhanced in the presence of the small content of clay, while the elongation at break was reduced with increasing the clay content. The increase in tensile strength was attributed to the stronger interfacial adhesion between PS and the clay platelets. However, the enhancement of modulus was reasonably ascribed to the high resistance exerted by the clay platelets against the plastic deformation and the stretching resistance of the oriented polymer backbones in the galleries. The improvement of tensile strength in PS/MMT-3 compared to pure PS was ~47%, which is greater than the earlier reported value in the literature (~21%) for PS/MMT nanocomposite with 3 wt.% MMT prepared by melt blending.[60] Similarly, the enhancement of Young's modulus in PS/MMT-3 compared to pure PS was ~25%, which is much greater than the reported value (7.4% improvement for PS/MMT nanocomposite with 5 wt.% clay prepared by emulsion polymerization).[63] However, the elongations at break were reduced with increasing the clay content. Similar results were earlier reported. For example, the reduction of elongation at break in PS/MMT nanocomposite with 4.4 wt.% MMT prepared by melt blending was reported to ~26%.[63]

5.6 Conclusions

The nanocomposite presented here is a composite material reinforced with silicate sheets. Silicate sheet is an ultrafine filler of nanometer size, which is almost equal to the size of the matrix polymer. Although the content of the filler is as little as several wt.%, individual filler particles exist at a distance as close as tens of nanometers from each other because of their ultrafine size. One end of the polymer is strongly restrained to the silicate sheet by polar interaction. Thus, the nanocomposite has a microstructure that has never been seen in conventional composites. The characteristic properties of the nanocomposite are derived from this very structure. Considering the properties, the nanocomposite may be, in a sense, an embodiment of the ideal polymer composite, or a completely novel composite. Silicate sheet can be regarded as a rigid inorganic polymer. In this sense, the nanocomposite realized is a molecular composite in which a silicate sheet is used instead of an organic rod-like polymer.

5.7 References

1. Blumstein, A. *Bull. Chim. Soc.* **1961**, 899.
2. Usuki, A.; Kojima, Y.; Kawasumi, M.; Okada, A.; Fukushima, Y.; Kurauchi, T.; Kamigaito, O. *J. Mater. Res.* **1993**, 8, 1179.
3. Lan, T.; Pinnavaia, T. J. *Chem. Mater.* **1994**, 6, 2216.
4. Usuki, A.; Kato, M.; Okada, A.; Kurauchi, T. *J. App. Polym. Sci.* **1997**, 63, 137.

5. Jeon, H.G.; Jung, H.T.; Lee, S.D.; Hudson, S. *Polymer Bulletin* **1998**, 41, 107.
6. Giannelis, E. *Adv. Mater.* **1996**, 8, 29.
7. Fisher, H.; Gielgens. L.; Koster, T. *Nanocomposites from Polymers and Layered Minerals*; TNO-TPD Report, 1998.
8. Carrado, K. A.; Langui, X. *Microporous Mesoporous Mater.* **1999**, 27, 87.
9. Friedlander, H. Z.; Grink, C. R. *J. Polym. Sci., Polym. Lett.* **1964**, 2, 475.
10. Blumstein, A. *J. Polym. Sci., Part A.* **1965**, 3, 2653.
11. Kato, C.; Kuroda, K.; Takahara, H. *Clay and Clay Minerals* **1981**, 29, 294.
12. Kelly, P.; Moet, A.; Qutubuddin, S. *J. Mater. Sci.* **1994**, 29, 2274.
13. Akelah, A.; Kelly, P.; Qutubuddin, S.; Moet, A. *Clay Minerals* **1994**, 29, 169.
14. Akelah, A.; Moet, A. *J. Mater. Sci.* **1996**, 31, 3189.
15. Akelah, A.; Moet, A. *Mater. Lett.* **1993**, 18, 97.
16. Giannelis, E.P.; *Adv. Mater.* **1996**, 8, 29.
17. Vaia, R.; Ishii, H.; Giannelis, E. *Chem. Mater.* **1993**, 5, 1694.
18. Doh, J.G.; Cho, I. *Polymer Bulletin* **1998**, 41, 511.
19. Zhu, J.; Alexander, B. M.; Frank, J. L.; Charles, A. W. *Chem. Mater.* **2001**, 13, 3774
20. Wang, D.; Jin, Z.; Qiang, Y.; Charles, A. W. *Chem. Mater.* **2002**, 14, 3837.
21. Wang, D.; Charles, A.W. *Polym. Deg. Stab.* **2003**, 82, 309.
22. Fu, X.; Qutubuddin, S. *Polymer* **2001**, 42, 807.
23. Yei, D.R.; Kuo, S.W.; Su, Y.C.; Chang, F.C. *Polymer* **2004**, 45, 2633.
24. Tseng, C.R.; Wu, J.Y.; Lee, H.Y.; Chang, F.C. *Polymer* **2001**, 42, 10063.
25. Tseng, C.R.; Lee, H.Y.; Chang, F.C. *J. Polym Sci Part B: Polym Phys* **2001**, 39, 2097.
26. Chen, H.W.; Chiu, C.Y.; Chang, F.C. *J. Polym Sci Part B: Polym Phys* **2002**, 40, 1342.
27. Tseng, C.R.; Wu, J.Y.; Lee, H.Y.; Chang, F.C. *J Appl Polym Sci* **2002**, 85, 1370.
28. Tseng, C.R.; Wu, H.D.; Wu, J.Y.; Chang, F.C. *J Appl Polym Sci* **2002**, 86, 2492.
29. Yei, D.R.; Kuo, S.W.; Fu, H.K.; Chang, F.C. *Polymer* **2005**, 46, 741.
30. Weimer, M.W.; Chen, H.; Giannelis, E.P.; Sogah, D.Y. *J. Am. Chem. Soc.* **1999**, 121, 1615.
31. Zhou, Q.; Fan, X.; Xia, C.; Mays, J.; Advincula, R. *Chem. Mater.* **2001**, 13, 2465.
32. Fan, X.; Zhou, Q.; Xia, C.; Crsitopholi, W.; Mays, J.; Advincula, R.C. *Langmuir* **2002**, 18, 4511.
33. Fan, X.; Xia, C.; Advincula, R.C. *Langmuir* **2003**, 19, 4381.
34. Meier, L.; Shelden, R.; Caseri, W.; Suter, U. *Macromolecules* **1994**, 27, 1637.
35. Pruker, O.; Ruhe, J. *Macromolecules* **1998**, 31, 592.
36. Pruker, O.; Ruhe, J. *Macromolecules* **1998**, 31, 602.
37. Kotov, N.A.; Haraszti, T.; Turi, L.; Zavala, G.; Geer, R.E.; Dekany, I.; Fendler, J. H. *J. Am. Chem. Soc.* **1997**, 119, 6821.
38. Jeffrey, W.G.; Catheryn, L.J.; Alexander, B.M.; Richard, H.J. *Chem. Mater.* **2000**, 12, 1866.
39. Ishihara, N.; Seimiya, T.; Kuramoto, N.; Uoi, M. *Macromolecules* **1986**, 19, 2464.
40. Kellar, E.J.C.; Galiotis, C.; Andrews, E.H. *Macromolecules* **1996**, 29, 3515.
41. Pellecchia, C.; Longo, P.; Grassi, A.; Ammendola, P.; Zambelli, A. *Markromol. Chem., Rapid Commun.* **1987**, 8, 277.
42. Musto, P.; Tavone, S.; Guerra, G.; De Rosa, C. *J. Polym. Sci., Part B: Polym. Phys.* **1997**, 35, 1055.
43. Woo, E.M.; Wu, F.S. *Macromol. Chem. Phys.* **1998**, 199, 2041.

44. Woo, E.M.; Wu, F.S. *J. Polym. Sci., Part B: Polym. Phys.* **1998**, 36, 2725.
45. Nakaoki, T.; Kobayashi, M. *J. Mol. Struct.* **1991**, 242, 315.
46. Reynolds, N.M.; Stidham, H.D.; Hsu, S. L. *Macromolecules* **1991**, 24, 3662.
47. Guerra, G.; Vitagliano, V.M.; De Rosa, C.; Petraccone, V.; Corradini, P. *Macromolecules* **1990**, 23, 1539.
48. Kobayashi, M.; Nakaoki, T.; Ishihara, N. *Macromolecules* **1989**, 22, 4377.
49. Strobl, G.R.; Hagedorn, W. *J. Polym. Sci., Polym. Phys. Ed.* **1978**, 16, 1181.
50. Vittoria, V.; Ruvolo Filho, A.; De Candia, F. *J. Macromol. Sci. Phys.* **1990**, B29, 411.
51. Kellar, E.J.C.; Evan, A.M.; Knowles, J.; Galiotis, C.; Andrews, E.H. *Macromolecules* **1997**, 30, 2400.
52. Vittoria, V. *Polym. Commun.* **1990**, 31, 263.
53. Wu, H.D.; Tseng, C. R.; Chang, F.C. *Macromolecules* **2001**, 34, 2992.
54. Tseng, C.R.; Lee, H.Y.; Chang, F.C. *J. Appl. Polym. Sci. Part B Polym. Phys.* **2001**, 39, 2097.
55. Zeng, C.; Lee, L.J. *Macromolecules* **2001**, 34, 4098.
56. Lee, J.; Giannelis, E. *Polym. Prepr.* **1997**, 38, 688.
57. Burnside, S.D.; Giannelis, E.P. *Chem. Mater.* **1995**, 7, 1597.
58. Gilman, J.W.; Jackson, C.L.; Morgan, A.B.; Harris, R.; Giannelis, E.P.; Phillips, S.H. *Chem. Mater*. **2000**, 12, 1866.
59. Hasegawa, N.; Okamoto, H.; Kawasumi, M.; Usuki, A. *J. Appl. Polym. Sci.* **1999**, 74, 3359.
60. Park, C.I.; Choi, W.M.; Kim, M.K.; Park, O.O. *J. Polym. Sci. Part B: Polym. Phys.* **2004**, 42, 1685.
61. Fu, X.; Qutubuddin, S. *Mater. Lett.* **2000**, 42, 12.
62. Kim, Y.K.; Choi, Y.S.; Wang, K.H.; Chung, I.J. *Chem. Mater.* **2002**, 14, 4990.
63. Noh, M.W.; Lee, D.C. *Polym. Bull.* **1999**, 42, 619.
64. Uthirakumar, P.; Song, M.K.; Nah, C.; Lee, Y.S. *Euro. Polym. J.* **2005**, 41, 211.

6

Poly(ethyl acrylate)/bentonite nanocomposites

T TANG, X TONG, Z FENG and B HUANG,
Chinese Academy of Sciences, People's Republic of China

6.1 Introduction

Polymer nanocomposite is a class of hybrid materials composed of an organic polymer matrix with dispersed inorganic nanofillers, which have at least one dimension in nanometer range.[1] At this scale, the large surface area of the nanofiller, even at very low concentration, can markedly change the macroscopic properties of the polymer and contribute many new characteristics to the polymer, such as increased moduli and strength, heat resistance, and decreased gas permeability and flammability. Polymer nanocomposites can commonly be obtained by either the sol-gel method or the intercalation method. Sol-gel nanocomposites (polymer/silica nanocomposite) are prepared by in situ hydrolysis and condensation of mononuclear precursors such as tetraethoxysilane (TEOS) and tetramethoxysilane (TMOS) in organic polymer matrices.[2,3] Recently, the intercalation method for synthesizing polymer/clay nanocomposites has received much attention, where polymer chains may penetrate into the host layers while ordered silicate registry remains (intercalated structure), or the exfoliated individual silicate layers (about 1nm thickness) are homogeneously dispersed in the organic polymer matrix (delaminated structure).[4] Since the successful synthesis of nylon 6/clay nanocomposite, many polymer/clay nanocomposites have been reported.[5] Research indicates that, compared to the intercalated nanocomposites, the exfoliated nanocomposites have higher Young's modulus,[6] a larger increase in elongation at break[7] and better thermal stability,[8] and the extent of exfoliation strongly influences the improvement of the properties.

Natural silicates have strong interaction between the layers due to negative charges and hydrogen bonding in their crystal structures. The basal space of pristine silicate is about 1 nm, which is smaller than the radius of gyration of general polymers. This might be an obstacle for polymers to penetrate into or delaminate between the silicate layers. So, most hydrophobic polymers are limited in penetrating into layer region of hydrophilic silicates. Up to now, the preparation of polymer/silicate nanocomposites has been based mainly on

organically modified layered silicates (OLS), where the sodium montmorillonite (Na^+-MMT) is modified with alkylammonium ions by means of replacing metal cation located interlayers of MMT through ion-exchange, showing hydrophobic characters. However, some disadvantages result from the presence of surfactant modifiers beyond any economic benefits. For example, there are two major concerns relating to the thermal stability of the surfactant during high-temperature melt processing and the long-term stability of the organic surfactant in the polymer/clay nanocomposite under various application conditions. In addition, the effectiveness of such surfactants is also limited by their chain length and the enthalpic interaction between the surfactant and the intercalating polymer.

The four main strategic processes for preparing polymer/layered silicate nanocomposites are exfoliation-adsorption, in situ intercalative polymerization, melt intercalation and template synthesis.[5b]

Exfoliation-adsorption in emulsion with Na^+-montmorillonite, known to readily delaminate clay in water has been studied to promote intercalation of water insoluble polymers. Studies by Lee et al showed that only intercalated nanocomposites were obtained in systems PMMA,[9] PS,[10] SAN[11–13] and epoxy.[14] Bandyopadhyay and Giannelis[15] have analyzed how the silicates affect the polymerization reaction in the cases of montmorillonite and fluorohectorite. Their results showed that well-exfoliated nanocomposites could be prepared and the dispersion was somewhat better in the montmorillonite-based nanocomposites.

Up to now, polymers used to prepare polymer/layered silicate nanocomposites by emulsion polymerization were almost glassy polymers with high T_g, such as PMMA, PS, SAN and epoxy. Meanwhile, all the above research showed that the information about structures and properties of this kind of polymer/clay nanocomposites came from the samples which were prepared through coagulation and separation of nanocomposite emulsions. As a new environmentally benign and simple synthesis method of nanocomposites, the significance of in situ emulsion polymerization is more attractive, if the resulting nanocomposite emulsion can be used directly to prepare the sample for avoiding coagulation and separation. Moreover, whether coagulation and separation can affect nanocomposite microstructure is still unclear. This makes the situation of fabricating nanocomposites through emulsion polymerization more complicated. A mixture of polymer and MMT is formed in emulsion polymerization, in which MMT dispersed differently depending on interaction of MMT with polymer chains. It was reported that the drying procedure of MMT had an important effect on the microstructure of MMT.[16] Pinnavaia found that the apparent pore openings of pillared MMT are determined principally by the method used to dry the flocculated reaction products. Generally, freeze-drying is a better route than air-drying to obtain a loose aggregated state of MMT. Exfoliated poly(methyl methacryalte) (PMMA)/Na^+-MMT nanocomposites were synthesized through a soap-free emulsion polymerization of MMA using 2-acrylamido-2-methyl-1-

propanesulfonic acid (AMPS) during polymerization from XRD results of the freeze dried samples because AMPS made the produced polymer end-tethered on pristine Na-MMT.[17]

Studies on rubbery polymers have rarely been reported. It was reported[18] that in the case of non-emulsion polymerization, clays exfoliated in a rubbery matrix performed better than in a glassy matrix. A new type of nanocomposite of clay with poly (butyl acrylate) (PBA) has been prepared successfully using intercalation-polymerization process.[19]

Here poly(ethyl acrylate) (PEA)/clay nanocompsite as the first example of rubbery polymer/clay nanocomposite synthesized by in situ emulsion polymerization is reported. The clay used is bentonite having extremely strong swelling characteristics in water. The resulting nanocomposite emulsion is directly cast to form film without coagulation process. This study focuses on microstructure, thermal and mechanical properties, and gas barrier permeability of the final PEA/clay nanocomposites.

6.2 Materials and characterization

6.2.1 Materials

Bentonite enriched in montmorillonite with 75 meq/100 g of cation exchange capacity, as determined in this laboratory, was provided by Linan Chemical Factory of Bentonite of Zhejiang Province. Ethyl acrylate monomer was purified by distillation under reduced pressure before use. All the water used was deionized. The initiator potassium persulfate (KPS) and the surfactant sodium dodecylsulphate (SDS) were used as supplied.

6.2.2 Characterization

Average molecular weights were determined by using gel permeation chromatography (GPC). GPC analyses were performed at a flow rate of THF 2.0 mL/min at room temperature using a Waters GPC system equipped with four styragel HR columns (two 500, two 10^3, 10^4, and 10^5).

X-ray diffraction was performed using a D/max IIB X-ray Diffractometer. Cu-Kα radiation (wavelength 0.15406 nm) was operated at 40 kV and 20 mA. Data were collected continually in diffraction angle 2θ ranging from 0.8 to 50º, with a step increment of 0.02º.

Observation of transmission electron microscopy (TEM) was performed on thin sections using a JEOL JEM 2010 transmission electron microscope. The samples were microtomed perpendicular to the coating direction with a LKB Ultratome III.

Differential scanning calorimeter DSC-7 instrument was used to measure the glass transition of the samples with a heating rate of 20ºC/min over the range

−60–150ºC under nitrogen atmosphere. Thermal degradation was followed by a Perkin-Elmer DSC-7 Thermogravimetric Analyzer. Scans were performed from room temperature to 700ºC at 20ºC/min.

Dynamic mechanical analysis (DMA) of the samples was performed on a Rheometric Scientific DMTA IV at a driving frequency of 10 Hz and a temperature scanning rate of 3ºC/min. Tensile tests were performed at room temperature using dumbbell-shaped specimens on an Instron 1121 electronic testing machine at a crosshead speed of 20 cm/min. An average value of five specimens was taken.

The permeability of water vapor was measured by the cup method.[20] The membrane to be measured was fixed on a standard cup half-filled with water. Cups were placed into a chamber with circulating air maintained at constant relative humidity of 37% and at constant temperature of 38ºC. The weight of cup with water was quickly measured on an electronic semimicro balance from time to time and the water vapor permeability (P_w) was determined by the following relationship:

$$P_w = q \cdot l/t \cdot A \cdot \Delta p \tag{6.1}$$

where q/t is the mean value of cup weight loss rate in g/sec; l is the membrane sample in cm^2, and Δp is the transmembrane water vapor pressure difference in cm Hg, which is equal to $S(R_1 - R_2)$, where S is the saturation pressure of water vapor at the test temperature in cm Hg and R_1, R_2 are the relative humidity of the upstream and downstream sides of the membrane, respectively. The permeability of oxygen was measured on a model K315-N-03 manometric permeation apparatus (Reikaseiki). The two-chamber, steady-state method was used. After evacuation to 10-2 torr for several hours, the permeating gas was introduced to the upstream side of the membrane and maintained constant at 1 atm. The flux of gas permeating through the membrane to the downstream side was monitored by the increase in pressure measured by an MKS Baratron.

6.3 Synthesis of PEA/bentonite nanocomposites through in situ emulsion polymerization

It is well known that, owing to the weak forces that stack the layers together, layered silicates can be easily dispersed in an adequate solvent. Bentonite with extreme water-swelling characteristics can delaminate into single layers in water. Bentonite was dispersed in water by agitation and, after standing overnight, sonicated for 1 h before adding the other components for emulsion polymerization in order to exfoliate all the layers of the bentonite. The monomer of ethyl acrylate, the initiator potassium persulfate, and the surfactant sodium dodecylsulphate were then added into the bentonite suspension. After agitating for 30 min at room temperature, the mixture was reacted for 5 h on heating to 70ºC. An evenly mixed emulsion of single silicate layers and polymer latex

particles was obtained. Finally, the resulting emulsion was cast into PTFE molds and dried at 20ºC. All samples were dried in vacuum before characterization.

The previous results showed that clays were known to be free-radical scavengers and traps.[21] The clay minerals inhibit the free-radical reactions by absorbing the propagating or initiating radicals to the Lewis acid surface. The radicals then either undergo bimolecular termination or form carbocations by electron transfer to the Lewis acid site. Minerals containing higher amounts of aluminosilicates are more effective inhibitors. In the case of PEA/bentonite nanocomposites, the molecular weights and molecular weight distribution (MWD) of the various PEA extracted from the nanocomposites were obtained by gel permeation chromatography (GPC) analyses with THF used as the eluant. The results showed that weight-average molecular weight (M_w) of PEA in the nanocomposites is in the range of 1.8–2.1 $\times$ 10^5. Compared with M_w (1.5 $\times$ 10^5) of control PEA sample synthesized under similar conditions in the absence of bentonite, M_w of PEA in the nanocomposites is slightly higher. The value of MWD in the PEA/bentonite nanocomposites is in the range of 2.5 to 3.1.

6.4 Preparation and microstructure of casting-film of PEA/bentonite nanocomposites from emulsion

Temperature is the critical factor in preparing cast-film from latex. The virgin latex, when applied onto a substrate and subsequently dried below a certain temperature, will result in a film consisting of non-transparent, powdery fragments. The opacity suggests that there are still many residual voids left within the film capable of scattering incident light. However, if it is dried above this temperature, the result will be a homogeneous, transparent film. This apparent critical temperature is called the minimum film-forming temperature (MFT) generally lying near T_g of the polymer. For PMMA ($T_g = 100$ºC) system,[22] nontransparent hybrid films were obtained at room temperature, although their TEM micrographs revealed that the phase size was smaller than 100 nm. For the PBMA ($T_g = 33$ºC) system,[23] transparent hybrid films were obtained at 35ºC. Instead, the films were opaque at room temperature. All the results showed that one can prepare transparent hybrids by choosing the polymer with lower T_g and a suitable casting temperature. In this work, the PEA/bentonite nanocomposites with different content of bentonite were cast at 20ºC which was below T_g of PEA. Transparent PEA/bentonite samples can be obtained, which were characterized by means of XRD and TEM.

During the past few years, use of latex blends has gained more and more attention. Several implicit or explicit aims in blending large and small latex particles underlie the development of latex blend films. Many studies[24–26] focus on blends of large and small particles, blends of film-forming and non-film-forming (i.e., hard and soft) particles, and blends with various sizes and hardness

to obtain films with desired properties. For latex blends, a critical volume fraction of small particles was required to obtain a continuous phase of small particles surrounding the large particles. Below this value, there are not enough small particles to create a continuous phase. A critical volume fraction might exist in our case. When the bentonite content is high enough, the close contact between PEA latexes becomes difficult as block of bentonite layers before the complete volatilization of water. The polymer latex particles are then fixed in the bentonite 'network'.

If the bentonite content is not high enough, the bentonite layers only exist as dispersed layers, in no way forming continuous bentonite layer 'networks'. After further coalescence of the PEA latex particles, bentonite as a dispersed phase is evenly dispersed in the PEA matrix. The smaller the size of latex particle, the higher the interfacial area between PEA and bentonite phases and the more intimate the mixing of the two phases. The above process can take place under conditions where the latex particles are stable enough in the whole drying process.

From the above, we can see that the mechanism of morphology formation is quite different from that of traditional polymer solution organic-inorganic nanocomposites. For traditional polymer solution systems, the phase separation mechanism is similar to that of polymer blends, i.e., nucleation and growth mechanism and spinodal decomposition mechanism.[27,28] Generally, the component with higher content is apt to form the continuous phase and the other the dispersed phase. However, for the PEA/bentonite emulsion system, whether PEA can be continuous or not depends mainly on whether the PEA latex particles are in close contact before the complete volatilization of water. Instead, it depends on whether the content of PEA is larger than that of bentonite.

XRD is a powerful technique to monitor the formation and microstructure of intercalated clays. Figure 6.1 shows a series of X-ray diffraction patterns for PEA/clay nanocomposites with different compositions. Compared with bentonite, the diffraction peaks corresponding to the pristine silicate disappear in PEA/clay hybrids, while a set of new peaks appears corresponding to the basal spacing of PEA/clay nanocomposites (from $d^{i}_{001} = 3.91$ nm to $d^{i}_{001} = 4.96$ nm). This means the existence of the intercalated clay by PEA in the hybrid.

However, it is difficult to draw definitive conclusions on the microstructure of the nanocomposites from XRD patterns exhibiting diffraction patterns, as the relatively featureless diffraction pattern of the exfoliated structure may have been covered up by the diffraction peak of the intercalated structure. In some cases, the featureless diffraction patterns do not mean exfoliated structure.[29] Therefore TEM is necessary to determine the nature of the nanocomposites and to provide additional information that will be helpful in the interpretation of the XRD results.

An interesting phenomenon was found in observing the microstructure of the nanocomposites with TEM. When a sample for TEM observation was prepared

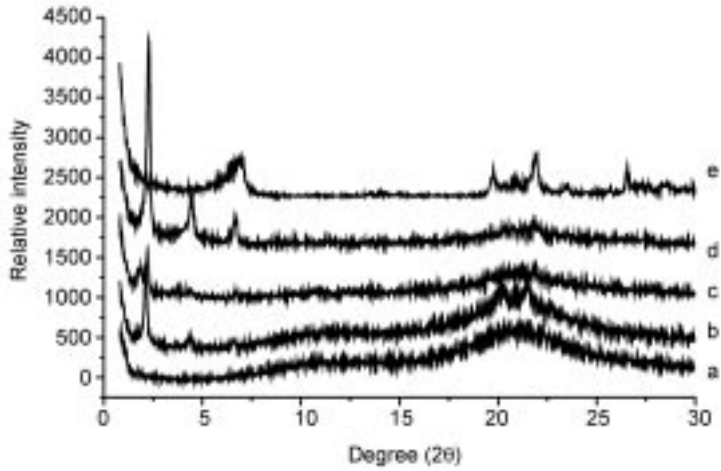

6.1 XRD patterns (Cu Kα) of PEA/bentonite nanocomposites with different composition PEA/bentonite (wt/wt): a. 100/0; b. 98/2; c. 95/5; d. 90/10; e. 0/100.

by dipping the emulsion containing clay directly onto the copper grid, only flakes of bentonite were observed in the dried PEA matrix (Fig. 6.2(a)). When the sample for TEM observation came from a vertical slice of the cast-drying nanocomposite film, the cross sections of the silicate layers were observed as dark lines (Fig. 6.2(b)). Some single silicate layers and ordered intercalated assemble layers of bentonite are well dispersed in PEA matrix. This means that most of bentonite layers are arranged in the direction parallel to the casting film,

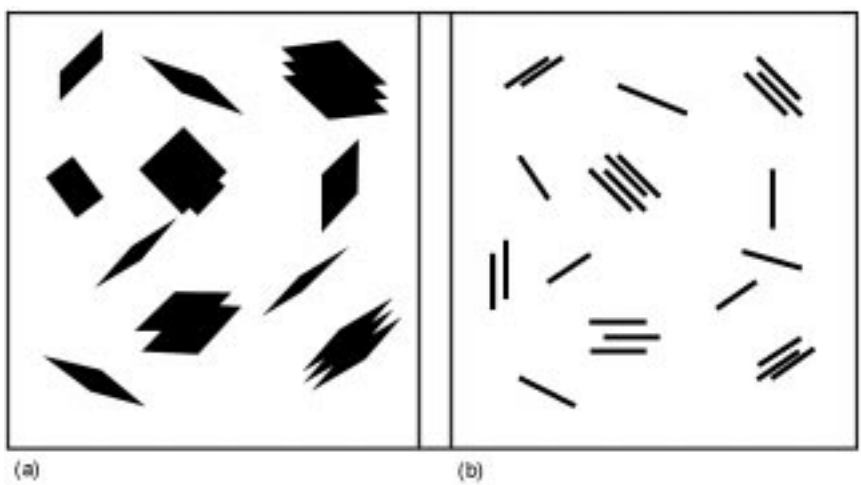

6.2 A schematic drawing of microstructure of PEA/bentonite = 95/5 (wt/wt) a dipping sample; b microtomed sample.

which is responsible for the improved barrier properties and thermal stability of the PEA. Based on the above TEM and XRD results, the direct-cast PEA/bentonite sample is apparently a nanocomposite with intercalated structure and disorderedly exfoliated structure of bentonite.

6.5 Performance of PEA/bentonite nanocomposites

6.5.1 DSC and TGA characterization of the nanocomposites

Thermal behavior of PEA/bentonite nanocomposites containing different amounts of bentonite as displayed in Fig. 6.3 shows that there is no great change in T_g of the resulting samples. Generally, movement of the polymer chains is strongly confined in the polymer/clay nanocomposites, especially when the polymer chain is intercalated into the interlayer of a silicate, leading to disappearance or increase in T_g.[10–12, 15] However, for the case of PEA/clay exfoliated-intercalated nanocomposites, the role of confinement between silicate layers to PEA is not obvious. The effect of M_w on the T_g can be excluded given the results from the previous section. The reason requires further investigation.

Thermal stability is an important property for which the nanocomposite morphology plays a vital role. The PEA/bentonite nanocomposites were analyzed by thermogravimetric analysis (TGA). The thermogravimetric (TG) curves under nitrogen are shown in Fig. 6.4. The temperature at which 5% of the degradation occurs, $T_{-5\%}$, a measure of the onset of degradation, the temperature at which 50% degradation occurs, the mid-point of the degradation process ($T_{-50\%}$), and the fraction of non-volatile material which remains at 700ºC, denoted as char, are listed in Table 6.1. These data reveal that PEA/bentonite nanocomposites show an obvious increase in $T_{-5\%}$ in the range of 0–5 wt.% bentonite. This phenomenon has been observed in other systems,[8] which is different from the results of polypropylene (PP) nanocomposites

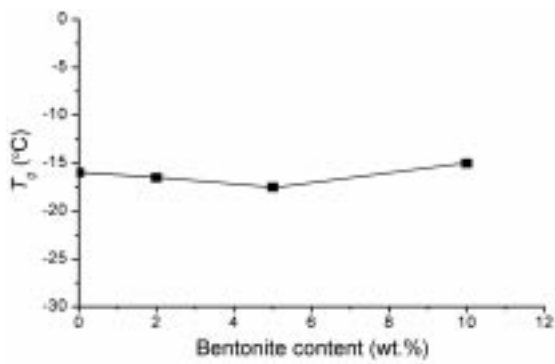

6.3 Dependence of T_g on clay loading for PEA/bentonite nanocomposites.

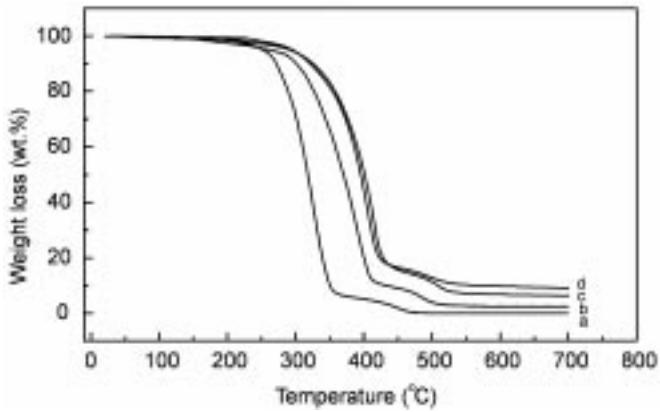

6.4 Thermogravimetric traces of PEA and PEA/bentonite nanocomposites. PEA/bentonite (w/w): (a) 100/0; (b) 98/2; (c) 95/5; (d) 90/10.

derived from organically modified montmorillonite.[30] Generally, there is a catalytic role played by the layered silicates deriving from the Hoffman reaction of hexadecyltrimethyl ammonium bromide, which may accelerate the charring process at the beginning of the degradation.[31] There is the intimate contact between the polymer molecules and the atoms of the inorganic crystalline layers in PP nanocomposite, which makes the catalytic role of layered silicates more obvious. In contrast, there is no modifier in PEA/bentonite nanocomposites, so the above-mentioned catalytic role will not occur. However, when the content of bentonite is 10 wt.%, $T_{-5\%}$ almost keeps constant compared with that of 5 wt.% bentonite containing system.

With increase in bentonite content, $T_{-50\%}$ also increases dramatically. Char residue of the nanocomposites tends to increase compared with those of polymer matrix. However, an obvious charring effect of bentonite for PEA was not found.

It is reasoned that the much better thermal stability is attributed to hindered out-diffusion of the volatile decomposition products, as a direct result of the usually observed decrease in permeability in polymer/clay nanocomposites. As improvements in the properties (such as thermal properties) of the nanocomposites can be realized at very low filler content, it often makes the material

Table 6.1 Properties of thermal degradation of PEA/bentonite nanocomposites

Bentonite (wt.%)	$T_{-5\%}$, °C	$T_{-50\%}$, °C	Char residue at 700°C (wt.%)
0	253	319	0
2	270	372	2.5
5	297	395	7.0
10	299	402	9.8

lighter and easier to process than more conventional microcomposites and is thus very promising for practical applications.

6.5.2 Mechanical properties of the nanocomposites

The tensile modulus, expressing the stiffness of a material at the start of a tensile test, is shown to be strongly improved in PEA/bentonite nanocomposites (Fig. 6.5). Lan *et al.*[32] reported that the tensile strength and the modulus of epoxide/*m*-phenylene- diamine/clay nanocomposites were only little improved relative to the pristine polymer. In contrast, for a low-T_g epoxide/amine system,[18] the reinforcement exhibited by the exfoliated clay is much more obvious. Owing to the increased elasticity of the matrix above T_g, the improvement in reinforcement may be in large part due to shear deformation and stress transfer to the platelet particles. In addition, platelet alignment under strain may also contribute to the improved performance of clays exfoliated in a rubbery matrix as compared to a glassy matrix.[18] In the present study, PEA is a rubbery polymer and the resulting PEA/bentonite nanocomposites are a combination of exfoliated structure and intercalated structure, so the mechanical properties are obviously improved, the tensile strength and modulus increasing from 0.65 and 0.24 to 11.16 and 88.41 MPa, respectively. In the case of simple intercalated structures without any exfoliation by emulsion polymerization, such as for PMMA or PS-based nanocomposites, the increase in tensile modulus is relatively weak, e.g. from 1.21 GPa for pristine PMMA to 1.3 GPa for PMMA nanocomposite containing 11.3 wt.% intercalated montmorillonite.[10] Therefore, our results further show the improved properties of clay exfoliation-intercalation in a rubber matrix over that in a glassy matrix.

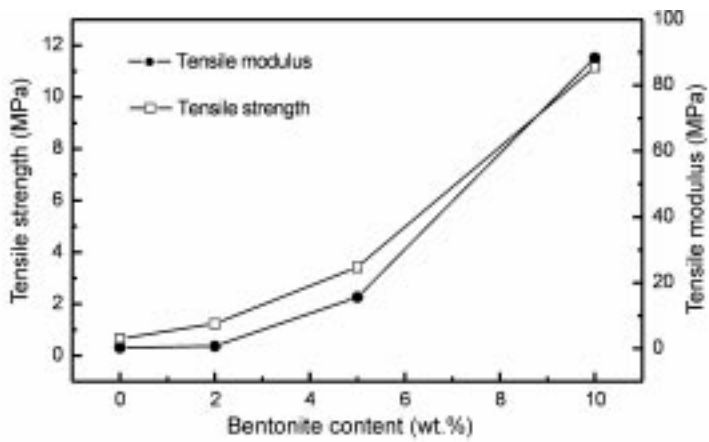

6.5 Dependence of tensile strength and modulus on bentonite loading for PEA/bentonite nanocomposites.

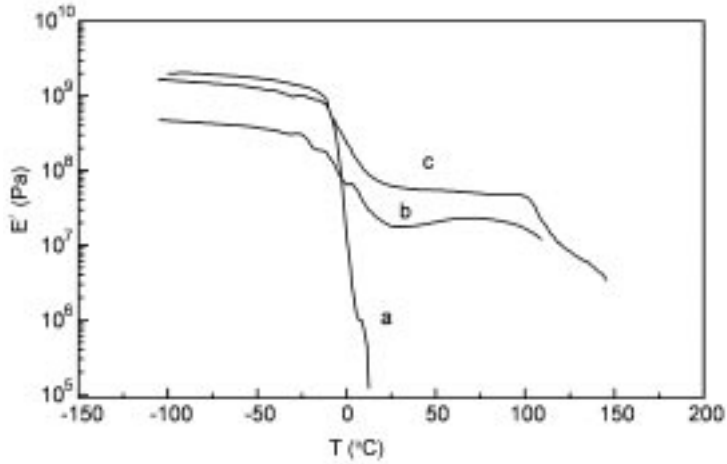

6.6 Dynamic mechanical analysis plot of PEA and PEA/bentonite nanocomposites. PEA/bentonite(w/w): (a) 100/0; (b) 95/5; (c) 90/10.

Generally, the strengthening of a polymer filled with an inorganic material is related to the thickness of the interlayer and the degree of the interfacial interaction. If the size of the filler is in nanoscale, the interfacial interaction is also very strong even without a compatibilizer, due to very large surface area of the nanofiller. Similarly, the volume fraction of the interlayer increases with the decrease in the size of the filler. If the volume fraction of the interlayer is high enough, it will play an important role in the properties of the composites. For the results in this paper, the M_w of PEA in the PEA/bentonite nanocomposites does not change dramatically compared with pure PEA control. Therefore uniform dispersion of layered silicate of only a few nanometers in polymer matrix and strong interaction at the interface between silicate layers and PEA through ionic-ionic interaction are the main reasons which lead to increase of the volume fraction of the interlayer obviously, so the mechanical properties are greatly improved.

In addition, dynamic mechanical analysis (Fig. 6.6) reveals a very marked improvement of the storage modulus above T_g. Similar behavior is observed for an elastomer such as nitrile rubber at room temperature.[33] A possible explanation for such an improvement could be the creation of a three-dimensional network of interconnected long silicate layers strengthening the material through mechanical percolation.

6.5.3 Barrier properties

The high aspect ratio of silicates nanolayers in exfoliated nanocomposites has been found to greatly reduce the gas permeability in films prepared from such nanomaterials. The dependence on factors such as the relative orientation and

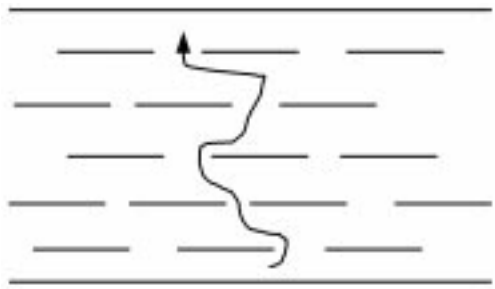

6.7 The tortuous path of gas through polymer/layered silicate nanocomposite.

dispersion (intercalated, exfoliated or some intermediate) is still not well understood. The gas will pass through the film of the nanocomposites by 'tortuous path' (Fig. 6.7).[34] From the above TEM results, there are a lot of clay layers well dispersed in the PEA matrix, which benefit the improvement of the barrier properties. However, beside the sheet length, and the concentration and state of the aggregation of clays, relative orientation of clay layers in the polymer matrix is also an important factor which affects barrier properties of the nanocomposites. Bharadwaj[35] addressed the modeling of barrier properties in PLS nanocomposites based completely upon the tortuosity arguments described by Nielsen.[36] Correlation between the sheet length, concentration, relative orientation, and state of aggregation is expected to provide guidance in the design of better barrier materials using the nanocomposite approach.

The permeabilities to water vapor and oxygen gas have been measured for the exfoliated-intercalated PEA-based nanocomposites (Figs 6.8 and 6.9). With increasing clay loading, the permeability coefficients of water vapor and oxygen gas for the PEA/bentonite nanocomposites decrease considerably. The main

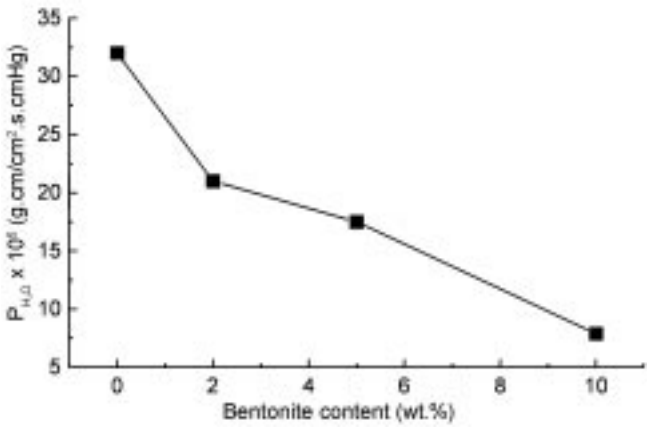

6.8 Dependence of PH_2O on bentonite loading for PEA/bentonite nanocomposites (PH_2O: permeability coefficient of H_2O).

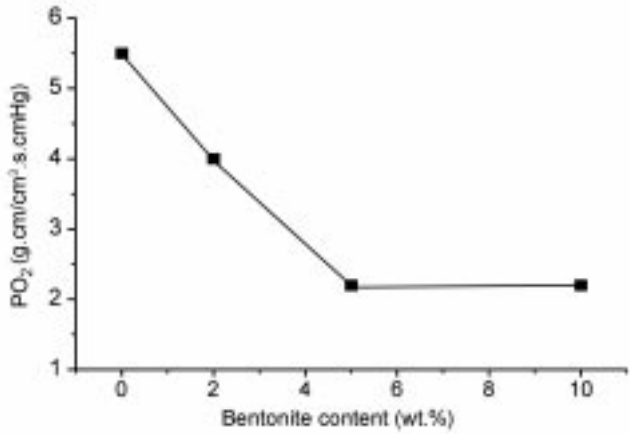

6.9 Dependence of PO_2 on bentonite loading for PEA/bentonite nanocomposites (PO_2: permeability coefficient of oxygen).

factor is that most of the clay layers are arranged in the direction parallel to the cast film, the partial exfoliated nanocomposites form the so-called 'tortuous path' by physically impeding the passage of gases through the matrix.[36] This is profitable to improve barrier properties and thermal stability of the PEA.

The enhanced barrier characteristics, which benefit from the hindered diffusion pathways through the nanocomposites, will lead to improvement of flame retardance and chemical resistance through reducing solvent uptake. On the other hand, the gas permeability of composites usually depends on the permeability of the continuous phase. It will assume an important position when the dispersion degree of the clay layers increases to some degree. Actually, the permeability of the nanocomposites is determined by that of the two components, generally between the two components. The barrier characteristic of the clay layers is better than that of the polymer with poor barrier property. Therefore, with the increase of the dispersion degree of the clay layers, the barrier characteristic of the nanocomposites filled with layered silicates increases dramatically.

6.6 Conclusions and future trends

Transparent exfoliated-intercalated PEA/bentonite nanocomposites are prepared by in situ emulsion polymerization in aqueous dispersions containing bentonite, following directly casting the resulting emulsion into film. XRD and TEM reveal that disorderedly exfoliated silicate layers and intercalated silicate layers coexist in the PEA matrix. Thermal stability, mechanical properties and barrier properties of the obtained materials were greatly improved. Because relatively small amounts (<10%) of nanometer-size clay particles can provide large

improvements in mechanical, thermal, as well as gas barrier properties without raising the density of the compound and reducing light transmission, the materials have many potential applications, such as packaging films. Since bentonite easily exfoliates into single layered silicate in water without modification by intercalative agent, we believe that the synthesis of polymer/layered silicate nanocomposite by in situ emulsion polymerization is a convenient avenue to prepare water-insoluble polymer-based exfoliated-intercalated nanocomposites, especially for the case which is difficult to be obtained by melt intercalation or in situ intercalative polymerization.

After surveying almost all of published reports in polymer/layered silicate nanocomposites so far, whatever the preparation methods for fabricating polymer nanocomposites, we did not find any in which all layered silicates were dispersed as a state of single layers in the polymer matrix. Therefore, all research in this field cannot but face this status quo, i.e., the exploration for effective dispersion of MMT in polymer matrixes is an important issue and even a challenge because there are, perhaps, a million or more platelets in each 8 μm particle awaiting effective dispersal in fabricating the nanocomposite.

Recently, emulsion polymerization and melt intercalation technique have become two common methods for preparing polymer nanocomposites from an environmentally sound and an economically favorable method for industries from a waste disposal perspective.[5b,5c] From the point of view of fabrication cost and properties of nanocomposites, it is best to use directly pristine layered silicates as raw material for synthesizing nanocomposites. Recently ammonium-terminated polypropylene (PP-t-$NH_3^+Cl^-$) was used in the modification of pristine Na^+-MMT clay via melt annealing for fabricating exfoliated PP/MMT nanocomposites.[37] It is clear that an organic surfactant is not needed to promote compatibility between PP-t-$NH_3^+Cl^-$ and pristine Na^+-MMT clay. However, improvement in thermal stability during high-temperature melt processing, similar to the case of surfactants, is still not clear, due to the presence of the ammonium group, besides the complicated synthesis procedure of PP-t-$NH_3^+Cl^-$.[38] Therefore further investigation into the search for a polymer as modifier of pristine MMT is urgently needed to stimulate further development in fabricating high-performance polymer nanocomposites.

6.7 Acknowledgements

We gratefully acknowledge the support by the National Natural Science Foundation of China (Project: 50473029) and the State Key Laboratory of Polymer Physics and Chemistry, Changchun Institute of Applied Chemistry, Chinese Academy of Sciences.

6.8 References

1. Giannelis, E. P. *Adv. Mater.* **1996**, *8*, 29.
2. Lan, T.; Kaviratna, P. D.; Pinnavaia, T. J. *Chem. Mater.* **1995**, *7*, 2144.
3. Tong, X.; Tang, T.; Feng, Z. L.; Huang, B. T. *J. Appl. Polym. Sci.* **2002**, *86*, 3532.
4. Krishnamoorti, R.; Vaia, R. A.; Giannelis, E. P. *Chem. Mater.* **1996**, *8*, 1728.
5. a. Kawasumi, M.; Hasegawa, N.; Usuki, A.; Okada, A. *Appl. Clay. Sci.* **1999**, *15*, 93; b. Alexandre, M.; Dubois, P. *Mater. Sci. Eng.* **2000**, *28*, 1; c. Ray, S. S.; Okamoto, M. *Prog. Polym. Sci.* **2003**, *28*, 1539.
6. Kojima, Y.; Usuki, A.; Kawasukmi, M.; Okada, A.; Kurauchi, T.; Kamigaito, O. *J. Polym. Sci Part A: Polym. Chem.* **1993**, *31*, 1755.
7. Wang, Z.; Pinnavaia, T. J. *Chem. Mater.* **1998**, *10*, 1820.
8. Burnside, S. D.; Giannelis, E. P. *Chem. Mater.* **1998**, *7*, 1597.
9. Lee, D. C.; Jang, L. W. *J. App. Polym. Sci.* **1996**, *61*, 1117.
10. Noh, M. W.; Lee, D. L.; *Polym. Bull.* **1999**, *42*, 619.
11. Noh, M. H.; Jang, L. W.; Lee, D. C. *J. Appl. Polym. Sci.* **1999**, *74*, 179.
12. Noh, M. H.; Lee, D. C. *J. Appl. Polym. Sci.* **1999**, *74*, 2811.
13. Kim, J. W.; Noh, M. H.; Choi, H. J.; Lee, D. C.; John, M. S. *Polym. Mater. Sci. Eng.* **1999**, *80*, 512.
14. Lee, D. C.; Jang, L. W. *J. Appl. Polym. Sci.* **1998**, *68*, 1997.
15. Bandyopadhyay, S.; Giannelis, E. P. *Polym. Mater. Sci. Eng.* **2000**, *82*, 208.
16. Pinnavaia, T. J.; Tzou, M. S.; Landau, S. D.; Raythatha, R. H. *J. Mol. Cat.*, **1984**, *27*, 195.
17. Choi, Y. S.; Choi, M. H.; Wang, K. H.; Kim, S. O.; Kim, Y. K.; Chung, I. J. *Macromolecules*, **2001**, *34,* 8978.
18. Lan, T.; Pinnavaia, T. J. *Chem. Mater.* **1994**, *6*, 2216.
19. Chen, Z. H.; Huang, C. Y.; Liu, S. Y.; Zhang, Y. H.; Gong, K. C. *J. Appl. Polym. Sci.* **2000**, *75*, 796.
20. Fu, H. Y.; Jia, L. D.; Xu, J. P. *J. Appl. Polym. Sci.* **1994**, *51*, 1405.
21. Solomon, D. H.; Swift, J. D. *J. Appl. Polym. Sci.* **1967**, *11*, 2567.
22. Tong, X.; Tang, T.; Zhu, N.; Feng, Z. L.; Huang, B. T. *Chem. J. Chin. Univ.-Chin.* **2002**, *23*, 306.
23. Tong, X.; Tang, T.; Zhang, Q. L.; Feng, Z. L.; Huang, B. T. *J. Appl. Polym. Sci.* **2002**, *83*, 446.
24. Winnik, M. A.; Feng, J. *J. Coat Technol.* **1996**, *68*, 39.
25. Chu, F. X.; Graillat, C.; Guyot, A. *J. Appl. Polym. Sci.* **1998**, *70*, 2667.
26. Eckersley, S. T.; Helmer, B. J. *J. Coat Technol.* **1997**, *69*, 97.
27. Silveira, K. F.; Yoshida, I. V. P.; Nunes, S. P. *Polymer* **1995**, *36*, 1425.
28. Rodrigues, D. E.; Risch, B. E.; Wilkes, G. L. *Chem. Mater.* **1997**, *9*, 2709.
29. Vaia, R. A.; Jandt, K. D.; Kramer, E. J.; Giannelis, E. P. *Chem. Mater.* **1996**, *8*, 2628.
30. Tang, Y.; Hu, Y.; Songa, L.; Zong, R.; Gui, Z.; Chen, Z.; Fan, W. C. *Polym. Degrad. Stab.* **2003**, *82*, 127.
31. Zanetti, M.; Kashiwagi, T.; Falqui, L.; Camino, U. *Chem. Mater.* **2002**, *14*, 881.
32. Lan, T.; Kaviratna, P. D.; Pinnavaia, T. J. *Polym. Mater. Sci. Eng.* **1994**, *71*, 528.
33. Okada, A.; Usuki, A. *Mater. Sci. Eng.* **1995**, *C3*, 109.
34. Yano, K.; Usuki, A.; Okada, A.; Kurauchi, T.; Kamigaito, O. *J. Polym. Sci., Part A: Polym. Chem.* **1993**, *31*, 2493.

35. Bharadwaj, R. K. *Macromolecules* **2001,** *34*, 1989.
36. Nielsen, L. *J. Macromol. Sci. Chem.* **1967**, *A1(5)*, 929.
37. Wang, Z. M.; Nakajima, H.; Manias, E.; Chung, T. C. *Macromolecules*, **2003**, *36*, 8919.
38. Xie, W.; Gao, Z. M.; Liu, K. L.; Pan, W.-P.; Vaia, R.; Hunter, D.; Singh, A. *Thermochimica Acta*, **2001**, *367–368*, 339.

7

Clay-acrylate nanocomposite photopolymers

C DECKER, Université de Haute-Alsace, France

7.1 Introduction

In recent years, there has been a growing interest in the scientific community for polymer/layered silicate (clay) nanocomposites, as shown by the annual number of publications devoted to this topic which has risen from 20 in 1997 to over 500 in 2004. Most of these nanocomposite materials are based on linear polymers[1–14] (polyamides, polyolefins, polystyrene, polyacrylate), which may show insufficient chemical and heat resistance for some applications. Moreover, when the organoclay filler is introduced into the melted polymer, thermodegradation of the organic surfactant may occur during the relatively long time required for swelling and exfoliation of the silicate platelets. This problem can be avoided through a solvent-based process, which releases large amounts of volatile organic compounds. In this respect, photoinitiated crosslinking polymerization of a solvent-free resin[15–17] appears the most effective way to produce nanocomposites showing enhanced chemical and thermal resistance by an environment-friendly process.

It was recently shown that clay/acrylate nanocomposite polymers can be easily synthesized by UV-radiation curing of multiacrylate monomers containing silicate nanoparticles.[18–20] As Chapter 6 deals with conventional clay/acrylate nanocomposites, we will restrict the scope of this chapter to the highly crosslinked nanocomposite materials obtained by photopolymerization of clay-based acrylate resins. The overall process is represented schematically in Fig. 7.1.

The solvent-free UV-curable resin, made of a photoinitiator, an acrylate functionalized oligomer and the mineral filler, is perfectly stable in the dark, thus allowing enough time for the resin to penetrate deeply into the organophilic clay lattice which will ultimately fall apart. A short UV exposure will generate free radicals capable of initiating polymerization of the acrylate double bond, with formation of a tridimensional polymer network. This UV-curing technology offers a number of advantages for the synthesis of nanocomposite materials:

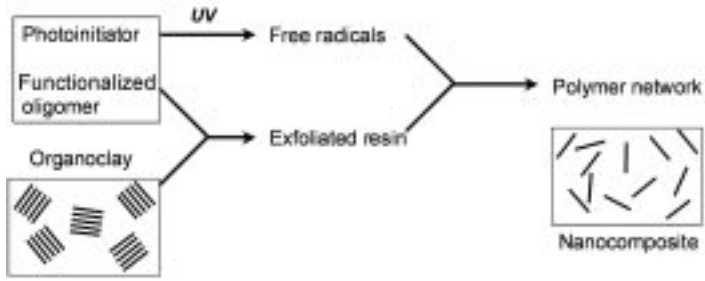

7.1 Reaction scheme of the synthesis of clay nanocomposite polymers by photopolymerisation.

- a solvent-free formulation, with essentially no emission of volatile organic compounds
- a fine control of the swelling time to ensure a perfect interpenetration of the resin into the lattice layers of the clay mineral
- operations in the presence of air at ambient temperature, thus preventing any thermodegradation of the clay surfactant
- an ultrafast curing by using the highly reactive acrylate-based resins and adequate photoinitiators
- a fine control of the polymerization rate in a large domain, simply by adjusting the light intensity
- a large range of mechanical properties, from soft and flexible composite materials to hard organic glasses, by a proper choice of the functionalized oligomer
- the production of photoset polymers very resistant to heat and chemicals because of their high crosslink density.

While research on clay-based nanocomposites has experienced an impressive growth over the past decade, only scant attention has been directed toward the synthesis of these materials by means of the UV-curing technology. Since our early work on photopolymer-clay nanocomposites,[21] a number of similar studies have been reported.[22–31] Wang *et al.*[22] produced intercalated nanocomposites by photopolymerization of a methacrylate or resin filled with montmorillonite, but the slow cure and the deep color of the final product make such a system ill-suited for industrial use. The performance of different types of photocured polymers (epoxides, vinyl ethers, acrylates) containing organically modified clays has been examined recently and shown to be superior for the nanocomposite than for the microcomposite (unmodified clay).[23] Uhl *et al.*[25–27] reported a moderate enhancement of some of the properties of UV-cured acrylate films containing layered silicates as nanomaterial. Paczkowska *et al.*[30] have synthesized polymer-clay nanocomposites by sunlight or laser-induced polymerization of methacrylate monomers in the presence of a xanthenic dye, but the composite materials thus obtained had poor mechanical properties. An

accelerating effect of synthetic clay on the photopolymerization of methacrylate monomers was reported by Shemper *et al.*[31] in their work on the synthesis of UV-cured nanocomposites which were characterized by Xray diffraction and transmission electron microscopy. These few studies have clearly demonstrated the great interest of such photochemical approach to produce polymer/layered silicate nanocomposites, especially with respect to the faster and cost-effective processing, as well as to the improvement of some of the properties of the final product. In the present survey, we have tried to summarize the most important findings of the recent work on the synthesis of clay/acrylate nanocomposite photopolymers.

7.2 Synthesis of clay-acrylate nanocomposites

7.2.1 Formulation of the nanocomposite resin

A typical formulation of a photocurable composite resin contains four basic components: a radical-type photoinitiator, an acrylate functionalized oligomer, a reactive diluent and the clay mineral filler. The photoinitiator is usually an aromatic ketone which cleaves into two radical fragments upon UV exposure. The telechelic oligomer consists of a short polymer chain (polyurethane, polyether, polyester) end-capped by the very reactive acrylate double bond. An acrylate monomer is generally used as reactive diluent to reduce the resin viscosity. Figure 7.2 shows some typical compounds used in UV-curable acrylic resins. Different types of phyllosilicates were selected as mineral filler: an organophilic clay (Nanomer I-30E from Nanocor), native hydrophilic clays (montmorillonite K10 and bentonite) and a synthetic clay (beidellite).

To obtain a true nanocomposite, the 1 nm thick silicate platelets need to be dispersed in the polymer matrix. The hydrophilic clays were therefore treated with a cationic surfactant, like an alkylammonium salt, which makes them organophilic and thus compatible with the acrylic resin. This cationic exchange treatment, described in detail in reference 18, leads to a widening of the clay galleries, as shown by the shift toward small angles of the X-ray diffraction (Fig. 7.3): the interlamellar spacing of native bentonite was found to increase from 1.24 nm to 1.76 nm after treatment with an alkylammonium chloride. The effectiveness of the exchange of the alcali cations of clay by the organocations has been confirmed by thermogravimetric analysis which revealed a 22% weight loss of the organoclay upon heating from 200ºC to 600ºC, compared to 3 wt.% only for the untreated clay (Fig. 7.4). The widening of the galleries, together with the organophilic character of the treated clay, allows an easy penetration of the UV-curable resin into the lamellar structure which will ultimately fall apart.

Exfoliation of the silicate platelets was demonstrated by the following observations:

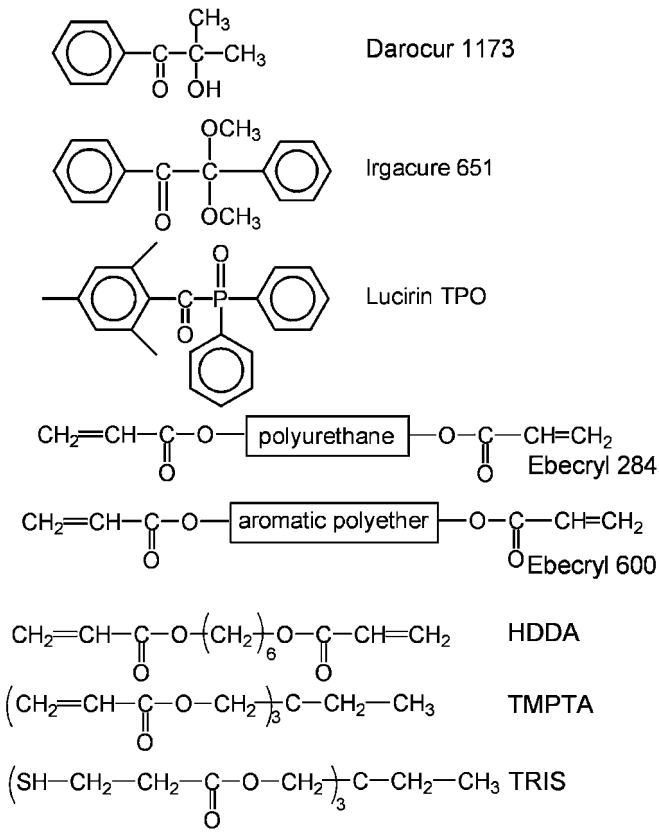

7.2 Typical compounds used in UV-curable acrylic resins.

- a total disappearance of the X-ray diffraction pattern in the organoclay and thus of the crystalline structure, which is not the case for the untreated clay (microcomposite)[1]
- a much slower sedimentation of the mineral particles in the nanocomposite resin than in the microcomposite resin[23]
- a greater transparency because light scattering by the nanoparticles is reduced, compared to the microparticles in the non-exfoliated sample[32]
- transmission electron microscopy pictures of the nanocomposite which show both isolated particles (exfoliation) and stacks of silicate platelets (intercalation).[32]

It should be noted that a total loss of the regular structure is still observed for an intercalated morphology where the nanoparticles are packed together in a disordered arrangement. Such microstructure was found to be favorable for improving the tensile properties of nanocomposites.[1,11]

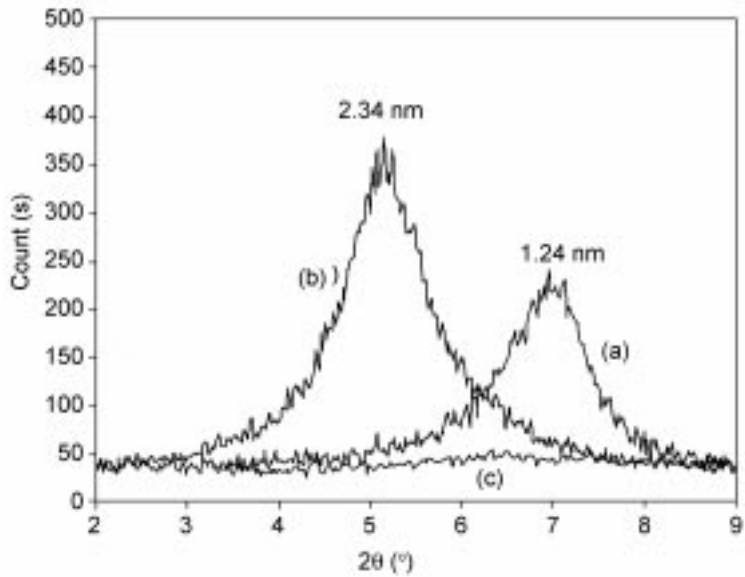

7.3 X-ray diffraction patterns of native bentonite (a), of the organoclay treated by an alkylammonium salt (b) and of the organoclay/acrylate nanocomposite (c). Numbers refer to the interlamellar spacing.[18]

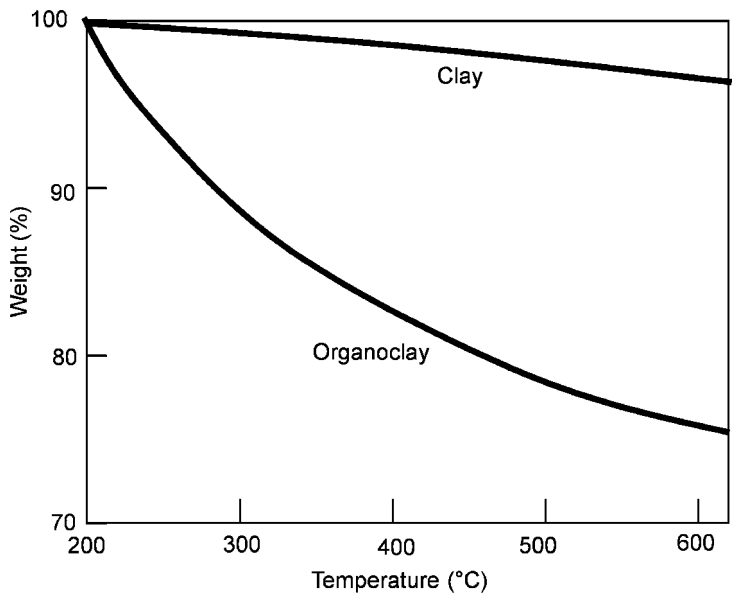

7.4 Thermogravimetric profiles showing the weight loss of natural clay and organoclay upon heating.

7.2.2 In-situ photopolymerization

The liquid resin containing the randomly distributed nanosize silicate platelets can be hardened by a short exposure to UV radiation, with formation of a nanocomposite polymer. Different techniques have been used to follow such ultrafast polymerization,[17] the most reliable one being infrared spectroscopy which monitors the light-induced chemical reaction (disappearance of the acrylate double bond), rather than one of its consequences (heat evolved, gelation, shrinkage). The degree of conversion after a given exposure can thus be evaluated accurately. The superior time resolution of FTIR spectroscopy (0.02 s, i.e. up to 50 spectra per second) allows one to directly record conversion *versus* time profiles for polymerizations occurring within less than 1 s upon UV or laser irradiation.[33,34] The influence of chemical and physical factors has thus been quantified for a variety of UV-curable resins.[35,36]

Real-time infrared spectroscopy proved particularly well suited to check whether the silicate platelets have any effect on the UV-curing process. The polymerization profiles recorded for a 25 μm thick polyurethane-acrylate film (Fig. 7.5) clearly show that the organoclay (5 wt.%) has no slowing down effect on the polymerization reaction which proceeds as extensively in the nanocomposite as in the unfilled resin. It means that the mineral filler is not acting as a radical scavenger and that the penetration of UV radiation into the sample is not reduced significantly by the nanoparticles. This is also true for up to 2 mm thick samples, where similar polymerization profiles were recorded

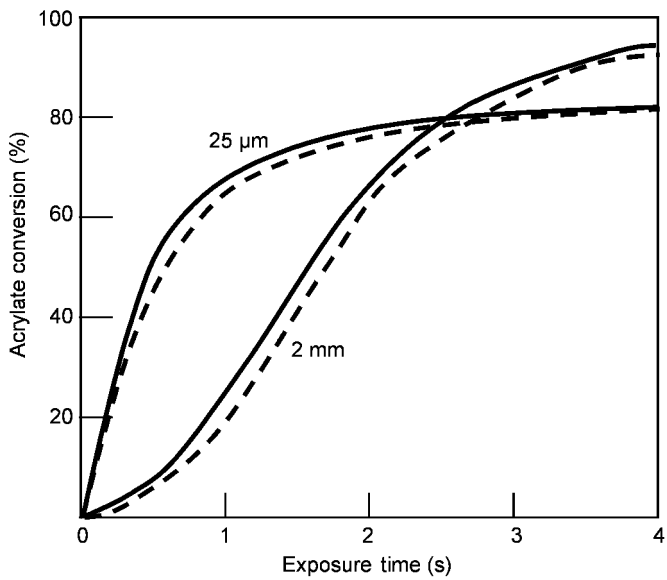

7.5 Influence of the organoclay filler on the polymerization of a polyurethane-acrylate resin. Organoclay (– – –) = 5 wt.%. Light intensity: 50 mW cm^{-2}.

with and without organoclay, by means of near-infrared spectroscopy (overtone at 6160 cm^{-1} of the acrylate double bond).

The photocuring of thick samples was achieved by using a photobleachable initiator which generates UV transparent photoproducts,[37] thus allowing the incident light to penetrate progressively deeper into the sample and promote a frontal polymerization.[38,39] Such a radiation filter effect is responsible for the slower cure observed in thick samples. This acylphosphine oxide photoinitiator absorbs in the near-UV and visible range, and is thus well suited for producing such nanocomposite materials by simple exposure to sunlight for 20 seconds.[20] The main advantage of solar curing is to allow an easy manufacturing of large dimension objects by a rapid and energy cost-free process.

The most complete polymerization observed in thick samples was attributed to a thermal effect, the rise in temperature caused by the exothermic polymerization being more pronounced in thick samples than in thin films,[40] as shown by the temperature profiles recorded by pyrometry (Fig. 7.6). This temperature rise will prevent the premature ending of the polymerization due to vitrification which is observed in thin films. For the latter, a more complete polymerization can still be achieved by rising the sample temperature up to 80ºC, either before or after the UV exposure, as shown in Fig. 7.7. This leads to a further hardening of the nanocomposite polymers, the Persoz pendulum hardness rising to 350 s on a scale which extends from 0 to 400 s for mineral glass.

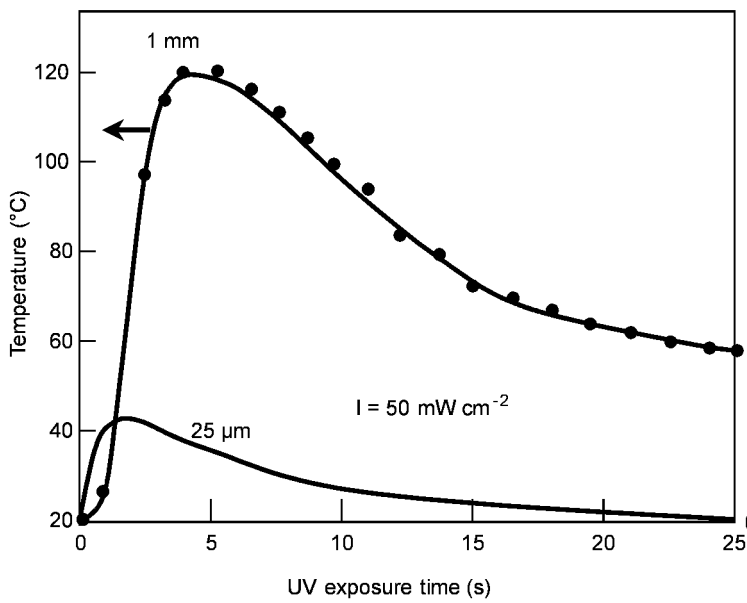

7.6 Temperature profiles recorded by pyrometry upon UV-curing of 25 μm and 1 mm thick polyurethane-acrylate nanocomposite samples. Light intensity: 50 mW cm^{-2}.[32]

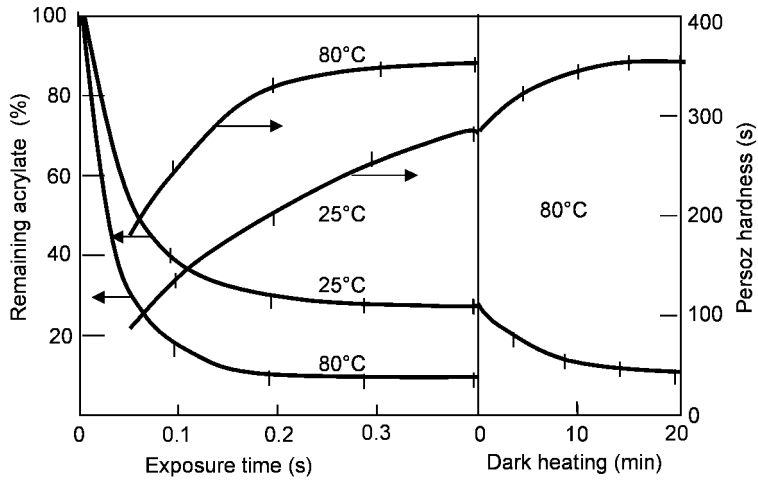

7.7 Influence of the temperature on the UV-curing of an aromatic polyether-acrylate nanocomposite.

In this respect, it should be mentioned that dual-cure systems, combining UV irradiation and a thermal treatment, have been developed to address the issue of the lack of cure in shadow areas of 3D objects, as well as in thick pigmented samples.[41,42] A few centimeter thick nanocomposite materials can be produced by this two-step process which associates the photopolymerization of the acrylate resin and the thermally-induced polyaddition of isocyanate and alcohol groups:

$$\mathrm{R{-}N{=}C{=}O + R'OH \longrightarrow R{-}NH{-}\underset{\underset{\mathrm{O}}{\|}}{C}{-}O{-}R'}$$

Figure 7.8 shows the doubly crosslinked polymer network formed by dual curing of an hydroxyl functionalized acrylate oligomer associated to a diisocyanate crosslinker. The UV exposure is usually perform on the hot sample (80ºC to 130ºC) emerging from the oven, so as to achieve a nearly complete curing of the acrylate double bonds. The relatively short heating time (15 min) at moderate temperature was found to have no significant detrimental effect on the organoclay.

7.3 Properties of clay-acrylic nanocomposites

The physico-chemical properties of photocrosslinked polymers depend primarily on the chemical structure of the functionalized oligomer, on the functionality of the monomer used as reactive diluent, as well as on the final cure extent. They can be varied in a large range, from soft aliphatic polyether elastomers to hard

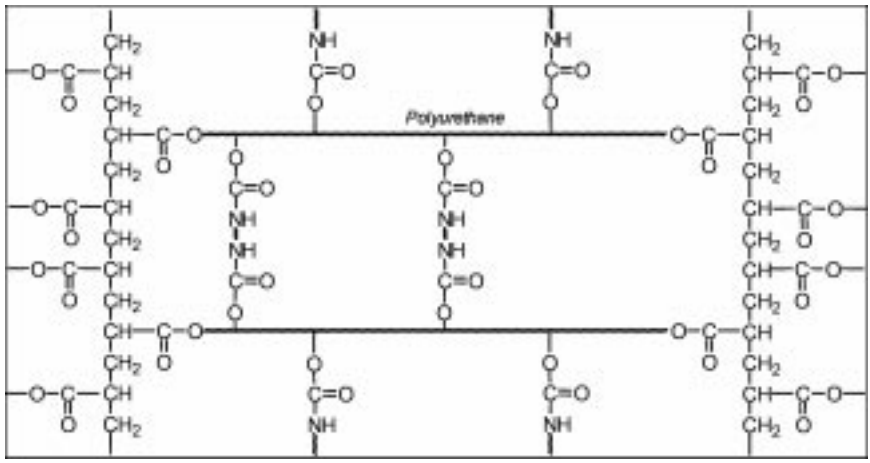

7.8 Dual polymer network formed by UV-curing and polyaddition of a hybrid acrylate/isocyanate resin.

and tough polyphenoxy glassy materials, depending on the considered application. The addition of clay nanoparticles was found to affect some of the polymer properties by imparting a greater tensile strength, a lower permeability to gas and a higher flame retardancy to the nanocomposite material.[1,11] Typical trends observed in UV-cured clay/acrylate nanocomposites have been recently reported for different kinds of materials.[20–31]

7.3.1 Chemical and heat resistance

Because of the high crosslink concentration, which ranges typically between 2 and 5 mol kg^{-1}, i.e. a number average molecular weight between crosslinks ranging from 500 to 200 g, respectively, UV-cured polymers exhibit an excellent resistance to organic solvents, as well as to heating. Total insolubilization is generally achieved within a few seconds upon UV-exposure, as shown in Fig. 7.9 for a polyurethane-acrylate by using chloroform as solvent. As expected, the swelling ratio decreases upon UV irradiation and increasing crosslink density, to reach very low values (less than 0.1) in the case of triacrylate monomers. UV-cured clay/acrylate nanocomposites proved to be quite resistant to thermal treatment,[26] as they start to decompose at temperatures above 350ºC. The loss of the alkylammonium surfactant which occurs above 250ºC is hardly detectable because of its very low content (1 wt.%).

The presence of nanoparticles in a polymer is generally considered to reduce its permeability to gases, because of a labyrinth effect. This feature could be of great interest for coating applications, in particular to improve the moisture resistance of such polymers when they are used in a humid environment. It can be seen in Fig. 7.10 that the water uptake (monitored by the increase of the OH infrared band) of a

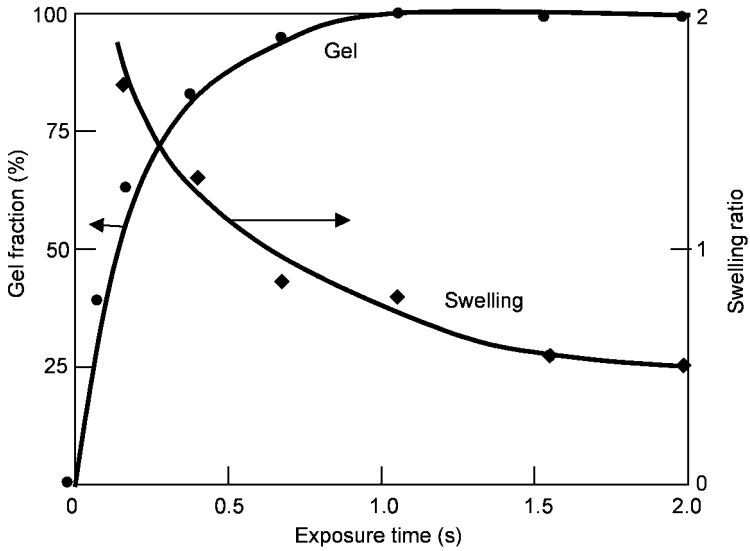

7.9 Insolubilization of a clay/acrylate resin upon UV exposure.

UV-cured polyurethane-acrylate film placed in a 100% humid atmosphere is cut by half when a small amount (3 wt.%) of organoclay is introduced in the resin. Consequently, the polymer softening caused by the plasticizing effect of the absorbed water was substantially reduced for the nanocomposite sample (Fig.

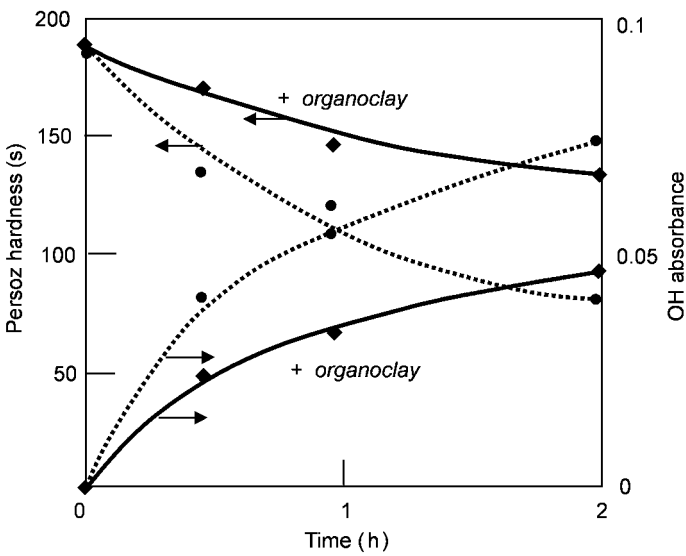

7.10 Influence of the organoclay (3 wt.%) on the water permeability of a UV-cured polyurethane-acrylate film.[32]

7.10). The moisture resistance can be further enhanced by the addition of a fluorinated acrylate monomer (0.5 wt.%) which concentrates at the film surface. The contact angle of a water droplet placed onto the coating was shown to increase from 60º to 110º for the fluorinated nanocomposite.[20]

7.3.2 Mechanical properties

The viscoelastic and tensile properties of UV-cured nanocomposites will depend primarily on the chemical structure of the acrylate functionalized oligomer selected. They can therefore be modulated in a large range, from flexible and impact resistant nanocomposites to hard and tough materials. Figure 7.11 shows some typical elastic modulus and tensile loss ($\tan\delta$) profiles recorded by dynamic mechanical analysis for two UV-cured clay/acrylate nanocomposites. The aliphatic polyurethane-acrylate associated to a monoacrylate diluent leads to a low modulus ($E = 500$ MPa) elastomer ($T_g = 15$ºC), while the aromatic polyether-acrylate generates a high modulus ($E = 2800$ MPa) glassy material ($T_g = 110$ºC). It should be noted that the addition of organoclay has hardly any effect on the elastic modulus and glass transition temperature of photoset acrylate polymers, while it was found to lower the T_g and increase the flexibility and impact resistance of epoxy-based UV-cured polymers.[23] These polymer materials proved to be as resistant to scratching as the thermoset polymers typically used as protective varnishes and topcoats.

Phyllosilicate nanoparticles have a beneficial effect on the tensile properties of UV-cured acrylate polymers. While the elongation at break and tensile

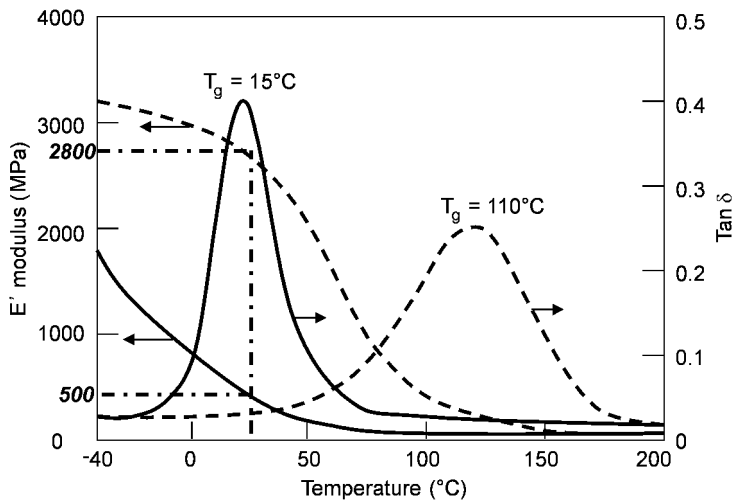

7.11 Viscoelastic properties of UV-cured clay/acrylate nanocomposite polymers. Low modulus polyurethane-acrylate (———); high modulus polyphenoxy-acrylate (– – –).

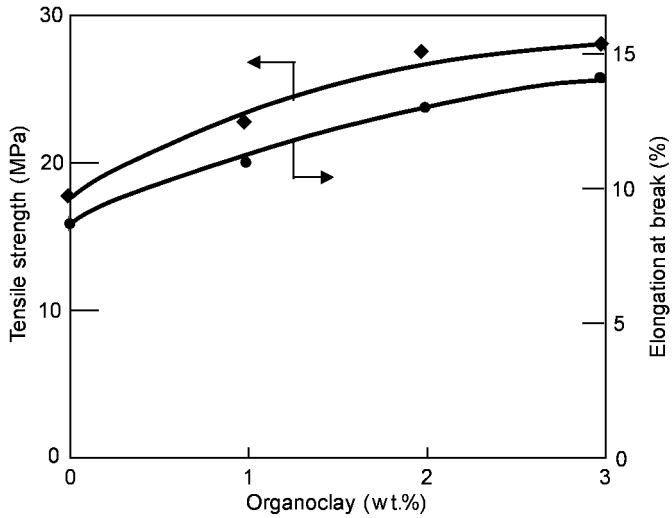

7.12 Influence of organoclay on the tensile properties of a UV-cured polyurethane-acrylate nanocomposite.

strength were both found to decrease with increasing amounts of natural clay (microcomposite), the opposite trend was observed with the organoclay (nanocomposite),[20] as shown in Fig. 7.12. The toughness of the polymer was thus improved significantly by the addition of just a few weight percent of organoclay. As expected, a greater effect was observed by working above the T_g of the polymer, as it allows an easier orientation of the nanoparticles upon stretching. Tensile strength values up to 60 MPa were reached with selected photocured phenoxy-acrylate polymers,[43] as required for some specific applications.

7.3.3 Optical properties

The presence of mineral particles in composite polymers is known to reduce the transparency of such material, as well as their gloss due to an increased surface roughness. This effect is yet less pronounced for nanocomposites than for microcomposites owing to the smaller size of the filler particles. The light transmitted at 500 nm by a 2 mm thick UV-cured polyurethane-acrylate sample was found to drop from 90% for the neat polymer to 75% for the nanocomposite containing 5 wt.% organoclay, and down to 50% for the nanocomposite containing 5 wt.% pristine clay. The best optical properties with respect to color and transparency were obtained with synthetic beidelitte.

Another effect of silicate nanoparticles is to reduce the gloss of UV-cured acrylic polymers, even at a relatively low filler load, as shown in Fig. 7.13. An organoclay content of 1 wt.% proved already sufficient to cut by half the gloss of

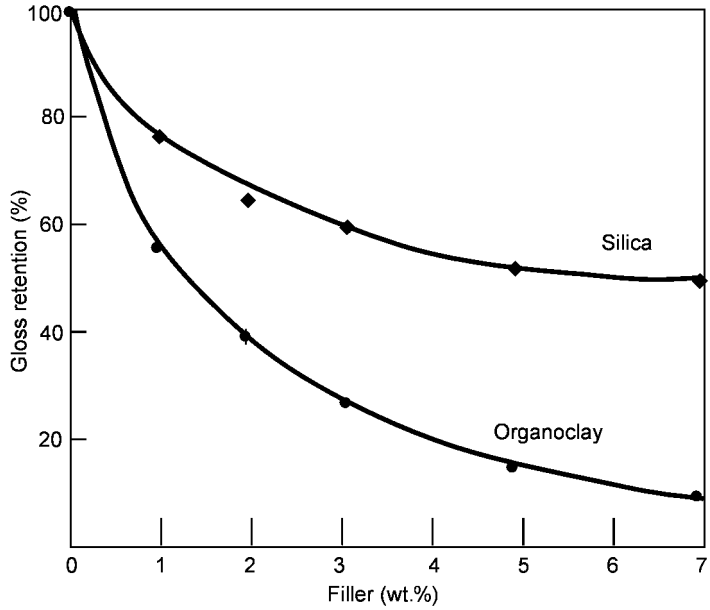

7.13 Influence of organoclay and of silica on the gloss of a UV-cured polyurethane-acrylate film.[32]

a UV-cured acrylate film, while it takes as much as a 5 wt.% content with a typical matting agent like finely powdered silica. This loss of gloss was attributed to an increase of the surface roughness, which is clearly apparent on surface mapping pictures.[32] The relief height was measured to be on the order of 0.5 μm for such nanoparticles arising from the intercalated morphology. While such matting effect will be a drawback for some applications (automotive topcoat, overprint varnishes), it can be advantageous in some others like for wood coatings or floor finishes. Non-glossy surfaces can be achieved with low amounts of organoclay, which appears an effective and cheap matting agent. Moreover, the addition of clay nanoparticles is making the surface of UV-cured coatings less slippery, as expected from the increased surface roughness.

7.3.4 Weathering resistance

Polymer materials used in outdoor applications need to have a longlasting resistance to natural weathering, i.e., the combined action of sunlight, heat, rain and pollutants. In this respect, UV-cured aliphatic polyurethane-acrylate polymers containing adequate light-stabilizers (UV-absorbers and hindered amine radical scavengers) were shown to be very resistant to photodegradation, partly because of their high crosslink density.[44,45] It was recently reported that the addition of organoclay decreases substantially the light stability of

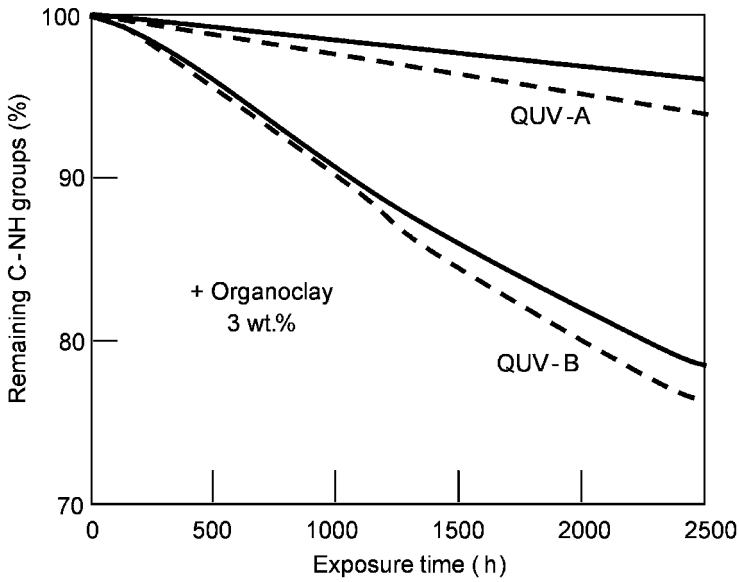

7.14 Photodegradation of stabilized UV-cured polyurethane-acrylate polymer (——) and nanocomposite (– – –) coatings upon exposure in a wet cycle QUV-A or QUV-B accelerated weatherometer.

polyolefins, presumably because of the detrimental effect of the montmorillonite and the alkyl-ammonium ion.[46–48] Consequently, the range of applications of such nanocomposites will be limited to indoor use.

Such detrimental effect of the organoclay filler was not observed with acrylate photopolymer nanocomposites exposed to accelerated weathering. The light-induced chemical modifications, monitored by infrared spectroscopy, were found to follow very similar trends with and without organoclay (5 wt.%), as shown in Fig. 7.14 for the loss of the urethane group (C-NH band at 1522 cm^{-1}) for UV-cured polyurethane-acrylate samples exposed to accelerated QUV weathering. It is quite remarkable that, in this well-stabilized UV-cured nanocomposite polyurethane-acrylate, only 20% of the CNH groups have been destroyed after a 2500 h exposure to the harsh QUV-B-313 weathering conditions, and as little as 6% under the milder QUV-A-340 conditions. By contrast to previous observations on linear polymer nanocomposites,[46] the organoclay is not interfering with the light stabilizers used which retain their full efficiency in the presence of the phillosilicate nanoparticles. UV-cured clay/acrylate nanocomposites can therefore be safely used in outdoor applications, like some previously developed photopolymers[49,50] in particular as protective coatings to improve the exterior durability of various materials (wood, plastics, metals).

7.4 Conclusions

Clay-acrylate nanocomposite polymers can be readily synthesized by photoinitiated polymerization of multifunctional acrylate monomers containing small amounts (3 wt.%) of an organophilic clay. This novel synthesis method offers the unique advantages of the UV-curing technology which are summarized in Fig. 7.15. The silicate filler does not affect at all the polymerization process, thus allowing a few millimeter thick samples to be extensively cured within seconds by a light-induced frontal polymerization, upon simple exposure to UV light at ambient temperature.

In the UV-cured nanocomposite polymer, the clay platelets are either packed together in a disordered arrangement (intercalated morphology) or dispersed as isolated nanoparticles (exfoliated morphology). They were found to have no major effect on the viscoelastic properties of acrylate based nanocomposites, probably because of the high crosslink density of the polymer network and the high T_g value of such photoset nanocomposites. The presence of silicate nanoparticles is reducing the permeability to gas, in particular to water vapor, thus improving the moisture resistance of UV-cured nanocomposite polymers. Another effect of this highly dispersed filler is to increase the surface roughness, which leads to a sharp drop of the gloss, and provides the matting effect desired for some coating applications. These highly crosslinked nanocomposite polymers are quite resistant to organic solvents, chemicals and weathering, as well as to mechanical aggression. They are therefore well suited for coating applications to protect and improve the surface properties of different types of materials, in particular those used in outdoor applications.

The UV-radiation curing technology is not restricted to the synthesis of clay-acrylate nanocomposites, but it can be extended to other types of polymer systems, such as crosslinked epoxides, vinyl ethers and interpenetrating polymer networks, as well as to other types of layered nanoparticles, such as superconductive nanofillers and magnetic particles. Future work should be

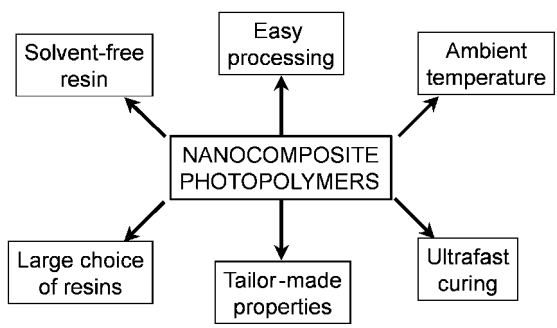

7.15 Performance of UV-radiation curing to produce nanocomposite polymers.

oriented in such directions to take full advantage of the remarkable performance of this new method of producing nanocomposite polymers.

7.5 References

1. M. Alexandre, P. Dubois, 'Polymer/layered silicate nanocomposites: preparation, properties and uses of a new class of materials', *Mater. Sci. Eng*. 2000, **R-28**, 1–63.
2. R.A. Vaia and E.P. Giannelis, 'Lattice Model of polymer melt intercalation in organically-modified layered silicate', *Macromolecules*, 1997, **30,** 7990–8009.
3. P. Reichert, J. Kressler, O. Thomann, R. Mülhaupt and G. Stöppelmann, 'Nanocomposites based on a synthetic layer silicate and polyamide 12', *Acta. Polym.*, 1998, **49,** 116–123.
4. P.C. Le Baron, Z. Wang, T.J. Pinnavaia, 'Polymer-layered silicate nanocomposites: an overview', *Appl. Clay. Sci*., 1999, **15**, 11–29.
5. C. Zilg, R. Mülhaupt and J. Finter, 'Morphology and toughness/stiffness balance of nanocomposites based on anhydride-cured epoxy resins and layered silicates', *Macromol. Chem. Phys*., 1999, **200,** 661–670.
6. P. Dubois, M. Alexandre, F. Hindrycks and R. Jerome, 'Polyolefin-based composites by polymerization-filling technique', *J. Macromol. Sci. Reviews*, 1998, **C38,** 511–565.
7. L. Wei, T. Tang, B. Huang, 'Synthesis and characterization of polyethylene/clay-silica nanocomposites. A montmorillonite/silica hybrid supported catalyst and in-situ polymerization', *J. Polym. Sci., Polym. Chem. Ed*., 2004, **42**, 941–949.
8. M. Zanetti, S. Lomakin, G. Camino, 'Polymer layered silicate nanocomposites', *Macromol. Mater. Eng*., 2000, **179**, 1–9.
9. A.R. Vaia, E.P. Gianellis, 'Polymer nanocomposites: Status and opportunities', *Mater. Res. Sci. Bulletin*, 2001, **26**, 394–401.
10. S.S. Ray, K. Okamoto, 'Structure-property relationship in biodegradable poly(butylene succinate)/layered silicate nanocomposites', *Macromolecules*, 2003, **36**, 2355–2367.
11. S.S. Ray, K. Okamoto, 'Polymer/layered silicate nanocomposites : a review from preparation to processing', *Progr. Polym. Sci.*, 2003, **28**, 1539–1641.
12. C. Chen, C. David, 'Processing and morphological developement of montmorillonite epoxy nanocomposites', *Nanotechnology*, 2003, **14**, 643–648.
13. S.J. Ahmadi, Y.D. Huang, W. Li, 'Synthetic routes, properties and future applications of polymer-layered silicate nanocomposites', *J. Mater. Sci*., 2004, **39**, 1919–1925.
14. M. Kurian, A. Dasgupta, F. Beyer, M.E. Galvin, 'Investigation of the effect of silicate modification on polymer-layered silicate nanocomposites morphology', *J. Polym. Sci., Polym. Physics Ed*., 2004, **42**, 4075–4083.
15. C. Decker, 'Photoinitiated crosslinking polymerization', *Progr. Polym. Sci*., 1996, **21**, 593–650.
16. S. Davidson, *Exploring the Science, Technology and Applications of UV and EB Curing*, SITA Technology, London, 1999.
17. C. Decker, 'Kinetic study and new applications of UV-radiation curing', *Macromol. Rapid. Comm*., 2002, **23**, 1067–1093.
18. C. Decker, K. Zahouily, L. Keller, S. Benfarhi, T. Bendaikha, J. Baron, 'Ultrafast synthesis of bentonite-acrylate nanocomposite materials by UV-radiation curing', *J. Mater. Sci*., 2002, **37,** 4831–4838.

19. K. Zahouily, C. Decker, S. Benfarhi, J. Baron, 'A novel class of hybrid organic clay UV-curable nanocomposite materials', *Proc. RadTech America 2002*, pp. 309–318.
20. L. Keller, C. Decker, K. Zahouily, S. Benfarhi, J.M. Le Meins, J. Miehe-Brendle, 'Synthesis of polymer nanocomposites by UV-curing of organoclay-acrylic resins', *Polymer*, 2004, **45**, 7437–7447.
21. K. Zahouily, S. Benfarhi, T. Bendaikha, J. Baron, C. Decker, 'Novel UV-curable nanocomposite materials', *Proc. RadTech Europe 2001*, pp. 583–591.
22. H. Wang, M. Mei, Y. Jiang, X. Zhang, S. Wu, 'A study on the preparation of polymer/montmorillonite nanocomposite materials by photopolymerization', *Polym. Inter*., 2001, **51**, 7–11.
23. S. Benfarhi, C. Decker, L. Keller, K. Zahouily, 'Synthesis of clay nanocomposite materials by light-induced crosslinking polymerization', *Europ. Polym. J*., 2004, **40**, 493–501.
24. Y.H. Yu, C.Y. Lin, J.M. Yeh, 'Poly(N-vinylcarbazole)-clay nanocomposite materials prepared by photoinitiated polymerization with triarylsulfonium salt initiator', *J. Appl. Polym. Sci*., 2004, **91**, 1904–1912.
25. F.M. Uhl, B.R. Hinderliter, S.P. Davuluri, S.G. Croll, S.C. Wong, D.C. Webster, 'UV-curable montmorillonite-acrylate nanocomposites', *Polymer Preprints*, 2003, **44(2)**, 247–248.
26. F.M. Uhl, S.P. Davuluri, S.C. Wong, D.C. Webster, 'Polymer films possessing nanoreinforcements via organically modified layered silicate', *Chem. Mater*., 2004, **16**, 1135–1142.
27. F.M. Uhl, S.P. Davuluri, S.C Wong, D.C Webster, 'Organically modified montmorillonite in UV-curable urethane-acrylate films', *Polymer*, 2004, **45**, 6175–6187.
28. J.Y. Kim, W.C Jung, K.Y. Park, K.D. Suh, 'Synthesis of Na^+ montmorillonite/amphilitic polyurethane nanocomposite via bulk and coalescence emulsion polymerization', *J. Appl. Polym. Sci*., 2003, **89,** 3130–3136.
29. J.M. Yeh, S.J. Liou, Y.W. Chang, 'Polyacrylamide clay nanocomposite materials prepared by photopolymerization with acrylamide as an intercalating agent', *J. Appl. Polym. Sci*., 2004, **91**, 3489–3496.
30. B. Paczkowska, S. Stzelec, B. Jederzejewska, L.A. Linden, J. Paczkowski, 'Photochemical preparation of polymer clay composites', *Appl. Clay Science*, 2004, **25**, 221–227.
31. B.S. Shemper, J.F. Morizur, M. Alirol, A. Domenech, V. Hulin, L.J. Mathias, 'Synthetic clay nanocomposite-based coatings prepared by UV-cure photopolymerization', *J. Appl. Polym. Sci.*, 2004, **93**, 1252–1263.
32. C. Decker, L. Keller, K. Zahouily, S. Benfarhi, 'Synthesis of nanocomposite polymers by UV-radiation curing', *Polymer*, 2005, **46**, 6640–6648.
33. C. Decker, K. Moussa, 'A new method for monitoring ultrafast photopolymerizations by real-time infrared spectroscopy', *Makromol. Chem*., 1988, **189**, 2381–2394.
34. C. Decker, K. Moussa, 'Real-time kinetic study of laser-induced polymerization', *Macromolecules*, 1989, **22,** 4455–4462.
35. C. Decker, B. Elzaouk, D. Decker, 'Kinetic study of ultrafast photopolymerization reactions', *J. Macromol. Sci*. *Pure Appl. Chem*., 1996, **A33**, 173–190.
36. C. Decker, F. Masson, C. Bianchi, 'Kinetic study of photoinitiated polymerization by RTIR spectroscopy', in *In situ Spectroscopy of Monomer and Polymer Synthesis*, J.E Puskas, T.E Long, R.F Storey (eds), Kluwer Academics, New York, 2002, pp. 109–124.

37. C. Decker, K. Zahouily, D. Decker, T. Nguyen Thi Viet, 'Performance analysis of acylphosphine oxide photoinitiated polymerization', *Polymer*, 2001, **42**, 7551–7560.
38. V. Ivanov, C. Decker, 'Kinetic study of photoinitiated frontal polymerization', *Polym. Intern*., 2001, **50**, 113–118.
39. C. Decker, 'Light-induced crosslinking polymerization', *Polym.Intern*., 2002, **51**, 1141–1150.
40. C. Decker, D. Decker, F. Morel, 'Real-time monitoring of high-speed polymerization', *Polym. Mater. Sci. Eng*., 1996, **74**, 350–351.
41. K. Maag, W. Lenhard, H. Löffles, 'New UV-curing systems for automotive applications', *Progr. Org. Coat*., 2000, **40**, 93–97.
42. C. Decker, F. Masson, R. Schwalm, 'UV-radiation curing of waterborne coatings', *Macromol. Mater. Eng*., 2003, **288**,17–28.
43. C. Decker, L. Keller, S. Benfarhi, K. Zahouily, C. Bianchi, 'Synthesis of composite materials by photopolymerization', *Polym. Prepr*., 2004, **45(2)**, 18–19.
44. C. Decker, S. Biry, 'Light-stabilization of polymers by radiation-cured acrylic coatings', *Progr. Org. Coat.*, 1996, **29**, 81–87.
45. C. Decker, K. Zahouily, 'Photodegradation and photooxidation of thermoset and UV-cured acrylate polymers', *Polym. Degr. Stab*., 1999, **64**, 293–304.
46. H. Qin, C. Hao, S. Zhang, G. Chen, M. Yang, 'Photooxidative degradation of polyethylene/montmorillonite nanocomposite', *Polym. Degr. Stab*. 2003, **81**, 497–500.
47. B. Mailhot, S. Morlat, J.L. Gardette, S. Boncard, J. Duchet, J.F. Gerard, 'Photodegradation of polypropylene nanocomposites', *Polym. Degr. Stab*., 2003, **82**, 163–167
48. S. Morlat, B. Mailhot, D. Gonzalez, J.L. Gardette, 'Photooxidation of polypropylene/montmorillonite nanocomposite. Influence of nanoclay and compatibilizing agent', *Chem. Mater*., 2004, **16**, 377–383.
49. C. Decker, K. Zahouily, 'Light-stabilization of polymeric materials by grafted UV-cured coatings', *J. Polym. Sci. A : Polym. Chem*., 1998, **36**, 2571–2580.
50. C. Decker, K. Zahouily, A. Valet, 'Weathering performance of thermoset and photoset acrylate coatings', *J. Coat. Technol.*, 2002, **74(924)**, 87–92.

8

Nanocomposites based on water soluble polymers and unmodified smectite clays

K E STRAWHECKER, Veeco Instruments Inc, USA and
E MANIAS, The Pennsylvania State University, USA

8.1 Introduction

Polymer/layered-silicate hybrids – nanocomposites – have attracted strong interest in today's materials research, as it is possible to achieve impressive enhancements of material properties compared to the pure polymers. Especially when these properties depend on the surface area of the filler particles, small amounts (typically less than 5%) of nm-thin layered inorganic fillers give rise to the same level of mechanical and thermal improvements as are typically achieved with loadings of 30–50% of micron-sized fillers. Examples of such materials enhancements are decreased permeability to gases and liquids, better resistance to solvents, increased thermal stability, and improved mechanical properties. Nanometer-thin layered materials used to form polymer nanocomposites include montmorillonite clays, synthetic 2:1 aluminosilicates, metal phosphates, transition metal chalcogenides, and complex oxides, to name a few.[1–6] In some cases, properties are observed in nanoscale materials that have not been realized in more conventional material structures, as for example flame retardant character.[7] Since this occurs without sacrificing properties such as optical clarity they are good choices as fillers in applications such as coatings and packaging.

Sodium montmorillonite (MMT) is a naturally occurring 2:1 phyllo-silicate, capable of forming stable suspensions in water. This hydrophilic character of MMT also promotes dispersion of these inorganic crystalline layers in water soluble polymers such as poly(vinyl alcohol)[8] and poly(ethylene oxide).[9,10] Inspired from those studies, this work is focused on investigating the properties of poly(vinyl alcohol)/MMT nanocomposite hybrids. Poly(vinyl alcohol) (PVA) is a water soluble polymer extensively used in paper coating, textile sizing, and flexible water soluble packaging films.[11] These same applications stimulate an interest in improving mechanical, thermal, and permeability properties of thin nanocomposite films, ultimately with the hope of retaining the optical clarity of PVA. PVA/layered silicate nanocomposite materials may offer a viable alternative for these applications to heat treatments (that may

cause polymer degradation) or conventionally filled PVA materials (that are optically opaque).

Polymer crystallization behavior near an inorganic surface has been the focus of extensive study.[12] In most cases the inorganic surface is shown to produce a nucleating or epitaxial effect,[2,13–15] which often stabilizes the bulk crystal phase or, in some cases, promotes growth of a different crystal phase. The polymer mechanical and thermal properties can be enhanced through this mechanism, where the surface-nucleated crystalline phase has better mechanical and thermal characteristics than the bulk crystal phases.[2,14–17] Fillers with large surface area maximize these filler-induced enhancements of the material properties; a dramatic manifestation of such a response is found in nylon-6/montmorillonite nanocomposites.[2,14,15] Less dramatic property enhancements are found in systems where the bulk crystalline phase is simply stabilized via the incorporation of heterogeneous nucleation sites, such as in polypropylene/organo-montmorillonite systems.[18]

The nylon-6/inorganic hybrids show dramatic enhancements in their mechanical and thermal properties upon addition of a minute amount (2–10 wt.%) of montmorillonite (MMT),[2] a nanometer thin mica-type layered silicate with a surface area of about 750 m^2/g. This was later attributed to a filler-stabilized γ crystalline phase of nylon-6 formed at the silicate surface.[14,15,19] PVA/layered-silicate nanocomposites also possess such filler-induced property enhancements,[19] which were also attributed to the existence of a non-bulk-like crystalline structure promoted when Na^+ montmorillonite (MMT) is added to PVA.[17]

8.2 Dispersion of Na^+ montmorillonite in water soluble polymers

Bright field TEM is used to view directly the hybrid structure for the nanocomposites formed, with the emphasis on the dispersion of the nanometer thin layered fillers in the polymer matrix. A typical TEM image is shown in Fig. 8.1 for the 20 wt.% MMT nanocomposite. Extensive TEM observations reveal a coexistence of silicate layers in the intercalated (label 'A') and the exfoliated ('B') states. We refer to intercalated layers/structures where the inorganic layers maintain the parallel registry of pristine silicates, and are separated by ultra-thin (1.3–5 nm) PVA films. Due to the periodic parallel assembly of the silicates, the intercalated structures give rise to X-ray diffraction peaks. We refer to exfoliated layers/structures where the layers are much further apart ($\gg$5 nm), and in general both the layer registry and the parallel stacking are lost.

The periodic intercalated structure can be quantified through powder XRD. Comparison of the intercalated gallery height with that of the pristine MMT (9.7 Å) measures the thickness of the PVA/Na^+ film. Fig. 8.2 shows XRD scans for concentrations of 20, 40, 60, 80 and 100 wt.% MMT; the inset shows the corresponding d-spacing distributions for the same concentrations. The

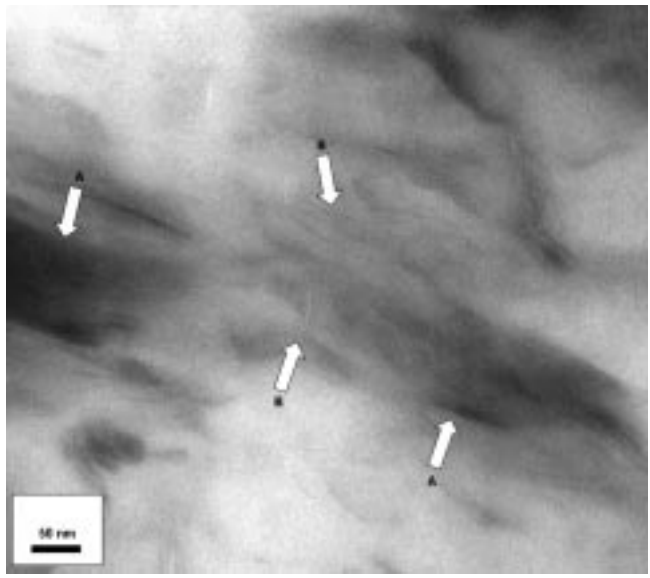

8.1 TEM image of 20 wt.% MMT/PVA nanocomposite revealing the coexistence of intercalated (A) and exfoliated (B) MMT layers. Copyright © *Chem. Mater.* 2000, vol. 12, pp. 2943–2949.

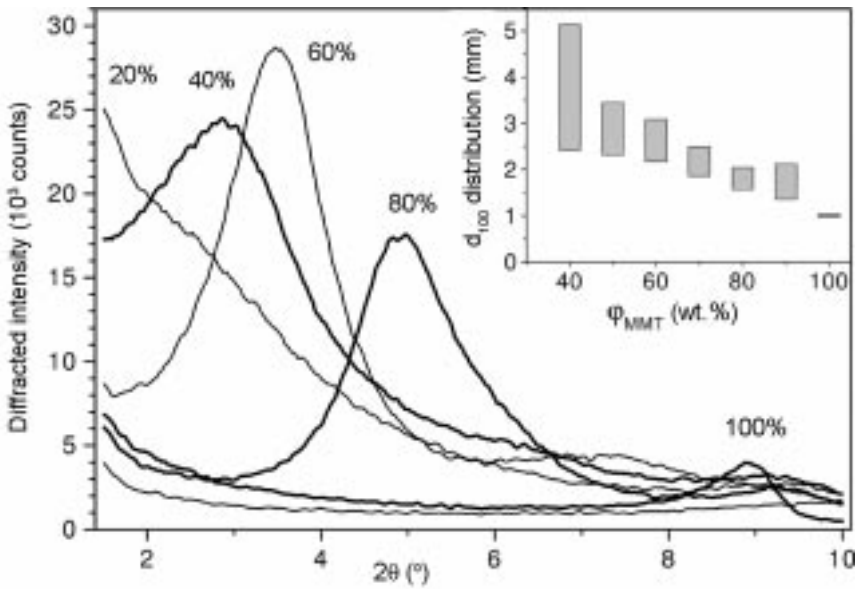

8.2 X-ray diffraction of the PVA/MMT hybrids as a function of ϕ_{MMT}. The inset shows the distribution of the MMT intercalated d-spacings for the respective hybrids. Copyright © *Chem. Mater.* 2000, vol. 12, pp. 2943–2949.

distribution of the intercalated d-spacings is calculated at half maximum of the d_{001} peak and the range of observed periodicities is given by bars (Fig. 8.2, inset) for each sample. Both the d-spacings, as well as their distributions, decrease systematically with higher silicate loadings, from 40 to 90 wt.% MMT. For lower inorganic filler concentrations, the XRD diffraction peak that corresponds to the silicate gallery d-spacing moves below $2\theta = 1.5^{\circ}$. This suggests that, if there still exist periodic assemblies of intercalated MMT layers, these are characterized by d-spacings larger than 5 nm. In addition, for all the nanocomposite XRDs, the background is higher than expected for simple mixtures of PVA and MMT, suggesting the existence of exfoliated inorganic layers throughout the polymer matrix. Thus, both XRD and TEM consistently show that these samples are in a hybrid structure where both intercalated and exfoliated silicate layers coexist in considerable ratios.

At first glance, this dependence of the intercalated structure and d-spacing on the polymer/silicate mass ratio seems to be at odds with the theoretical expectations.[20,21] The equilibrium hybrid structure predicted from the thermodynamics corresponds to an intercalated periodic nanocomposite (with a d-spacing around 1.8 nm) which is expected to be independent of the polymer/silicate composition.[20] However, thermodynamics can only predict the *equilibrium* structure. In our case, though, the hybrid structure that we find is actually kinetically dictated: In the water solution of poly(vinyl alcohol) and montmorillonite the layers remain in colloidal suspension. Where this suspension is slowly dried, the silicate layers remain distributed and embedded in the polymer gel. With further drying, to remove all water, although thermodynamics would predict the MMT layers to reaggregate in an intercalated fashion, the slow polymer dynamics trap some of the layers apart, and therefore remain dispersed in the polymer. Obviously, these kinetic constraints by the polymer become less important as the polymer-to-silicate fraction decreases, and consequently, for higher ϕ_{MMT}, intercalated structures are formed. For these periodic structures, the variation of the d-spacing with ϕ_{MMT} reflects the different polymer/silicate weight ratios, and with increasing ϕ_{MMT} the intercalated d-spacing converges to the theoretically predicted value of 1.8 nm.

Dispersion of silicates in water soluble polymers need not result in kinetically trapped systems, and such is the behavior of PEO/Na^{+}MMT hybrids. The structure of these polymer/inorganic hybrids is well known (Fig. 8.3), studied extensively both experimentally,[9,10,22] as well as by molecular simulations,[23,24] and is markedly independent of the filler loading. When enough PEO exists in the composite an intercalated structure is formed (with d-spacings distributed around 1.7 nm, which corresponds to a PEO bilayer of about 0.8 nm thickness). For composites with extremely small amounts of PEO ('polymer-starved' composites at montmorillonite loadings of $\phi_{MMT} > 90\%$), an intercalated monolayer of PEO can also be observed, with an intercalated d-spacing of about 1.37 nm. These latter structures are of no interest to this present work. For the

montmorillonite loadings of interest here (ϕ_{MMT} = 1–10 wt.%) the layered silicates retain their pristine parallel registry, but there is an increase in the d-spacing (Fig. 8.3(d)) due to the intercalation of PEO in the interlayer gallery (Fig. 8.3(c)). Successive single layers self-assemble in stacks (tactoids, Fig. 8.3(a)), in a highly parallel stacking that can give rise to 00*l* XRD diffraction peaks up to the 11th order.[9] These micron size tactoids are dispersed in the PEO matrix – either isolated or in groups of tactoids (agglomerates, Fig. 8.3(b)) – separated by regions of pure polymer (Fig. 8.3).

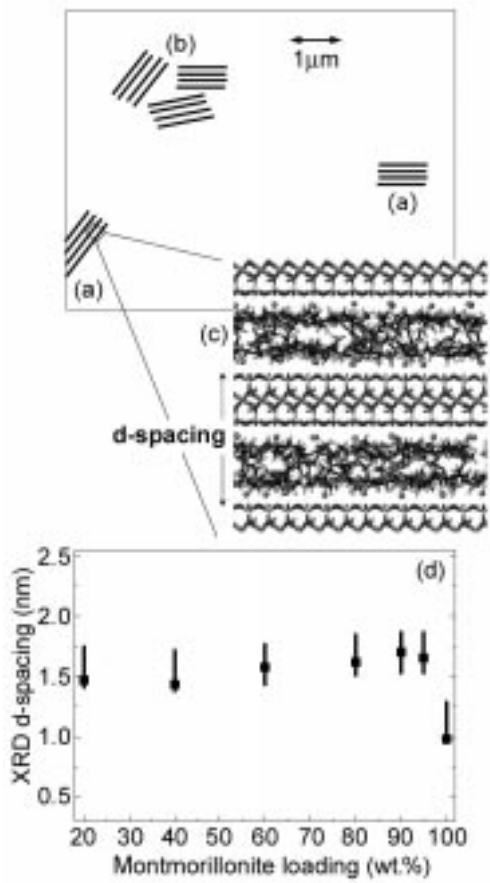

8.3 Schematic of the PEO/Na^+ MMT intercalated nanocomposites. The layered inorganic MMT layers assemble in a parallel fashion, creating stacks of layers referred to as tactoids (a), and most times tactoids are found in groups referred to as agglomerates (b), separated by bulk-like polymer regions. Within the tactoid, MMT layers are separated by a 0.8 nm film of PEO (c), which is stable through a wide range of MMT loadings as seen in the X-ray diffraction data (d). The MMT layers bear a large number of Na^+ (one cation per 70 $Å^2$), depicted by dots in (c). Copyright © *Chem. Mater.* 2003, vol. 15, pp. 844–849.

8.3 Crystallization behavior

Methods used to compare and contrast the crystallization behavior of water soluble crystalline polymers with dispersed silicates may include cross-polarization optical microscopy (CPOM) or atomic force microscopy (AFM), depending upon physical properties of the materials such as spherulite size and optical properties. Other methods used to study crystallization behavior of such materials include differential scanning calorimetry (DSC) and x-ray diffraction (XRD).

8.3.1 Cross-polarized optical microscopy and atomic force microscopy

PEO crystallization

Cross-polarized optical microscopy (CPOM) was used to compare the crystal morphology between filled and unfilled PEO, and subsequent DSC studies were used to further quantify the relevant crystallization kinetics. We focus on systems with low silicate loadings ranging from neat PEO (0 wt.% MMT) to PEO with 10 wt.% MMT. In Fig. 8.4 we compare the CPOM images of neat PEO and a PEO/5 wt.% MMT intercalate, both crystallized at 45ºC. The morphology of the crystals is shown at an early stage (neat: Fig. 8.4(a), intercalate: Fig. 8.4(c)) and at the final stage of crystallization (neat: Fig. 8.4(b), intercalate: Fig. 8.4(d)). For the neat PEO, it can be clearly seen that the spherulites are similar in size, and prior to impinging upon one another they appear circular, suggesting an isotropic (spherical) three dimensional shape. For the intercalated system (Figs 8.4(c)–(d)) the spherulite sizes vary a lot, and they are typically much smaller than the ones seen in neat PEO. Moreover, in these systems the spherulites are characterized by very anisotropic, non-spherulitic shapes (Fig. 8.4(d)) with jagged edges, even before impinging upon one another (Fig. 8.4(c)).

A CPOM time series, following a crystalline growth front in the same intercalated material, can provide some clues on the origin of these crystal morphologies. In Fig. 8.5 a progression of a growing crystallite is shown for the PEO/5 wt.% MMT system. The early and late stages are shown in Fig. 8.5(a) and Fig. 8.5(f), where silicate tactoids can be seen, manifested as either bright/white features (near the focused plane) or dark features (below and above the focused plane). Figs 8.5(b)–(e) are a higher magnification of the selected area (shown as the box in Figs 8.5(a)–(f)) as the spherulite growth-front encounters an MMT agglomerate (or a large tactoid). As the growth proceeds, the lamellar pathways are interrupted and they are forced to grow around the tactoid, breaking the spherical symmetry of the crystallite, and crystallization is delayed in the region downfield from the tactoid. The same behavior is also observed for the smaller tactoids in the image, albeit at smaller scale. At the end of crystallization (Fig.

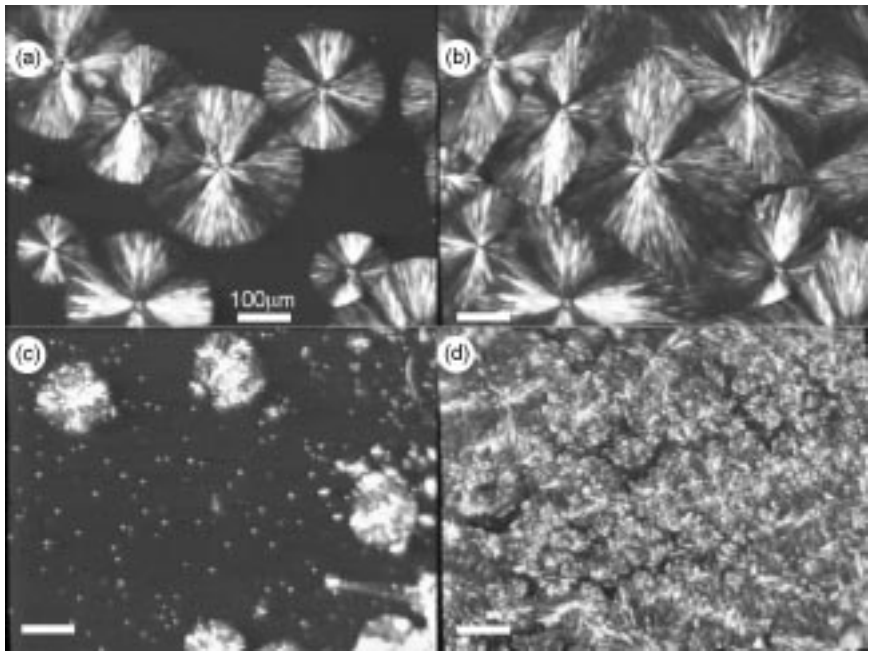

8.4 Cross-polarization optical microscope images of neat PEO (a,b) and PEO containing 5 wt.% MMT (c,d). Images on the left (a,c) are early in the crystallization process, while those on the right (b,d) are the final images. The scale bar is the same for all images (100 microns). White spots in (c) are tactoids found in the nanocomposite system. Image (d) illustrates the fact that later in the process many smaller spherulites grow to fill the space in the composite system. The growth front of the composite system (c) appears highly jagged in contrast with the very smooth front found in the neat PEO spherulites (a). Copyright © *Chem. Mater.* 2003, vol. 15, pp. 844–849.

8.5(f)) we see that the effect of the MMT on the crystallite growth resulted in 'spherulites' grown in a haphazard fashion with tortuous lamellar pathways and jagged edges. Also, the crystallite size is markedly smaller than the spherulites developed in neat PEO (Fig. 8.4(b) and (d)).

PVA crystallization

Before we consider the differences between neat and filled PVA systems, we shall briefly discuss how the crystallization of PVA develops in films cast from PVA/water solutions. As cast these films are mostly amorphous, and crystallites initiate predominately in the final drying stages; crystallization proceeds slowly thereafter, aided by the ambient humidity. If the ambient humidity is too low or absent, the drying polymer becomes glassy and crystal growth becomes arrested before extended crystallites can develop and impinge. Though PVA has a T_g

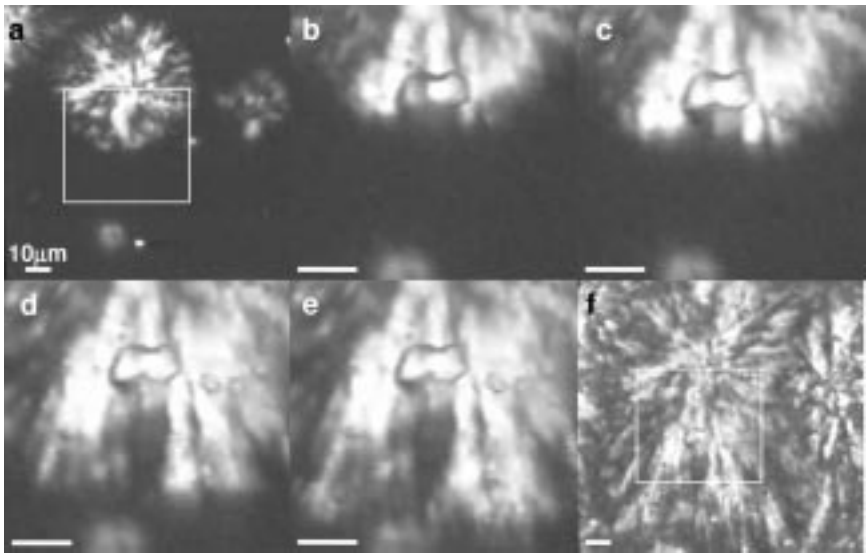

8.5 A time series of cross polarization optical microscopy images of a nanocomposite region from PEO containing 5 wt.% MMT. Images (a) and (f) have the same magnification and are at the beginning (a) and the end (f) of the crystallization. The box in (a and f) outlines the area shown in (b–e) at a higher magnification, which focus on the growth of a spherulite 'front' as it encounters an MMT agglomerate. The scale bar in all images is 10 microns. Copyright © *Chem. Mater.* 2003, vol. 15, pp. 844–849.

above room temperature, water cast films still form crystals at ambient temperatures due to the slow drying nature of the hydrophilic polymer. Subsequently, plasticization by ambient humidity allows for a slow, cold crystallization of PVA resulting in crystals, which are reminiscent of structures as those from row nucleated crystallization in the earlier stages, dendritic in the mid to latter stages (Fig. 8.6), and spherulitic in final stages after they impinge and fully develop. The final systems include mature crystallites of all these morphologies, and this mixture of morphologies can only be described loosely as PVA dendrites or hedrites[25] due to the branched nature of the crystalline lamellae. These mature crystal structures are still not sufficiently birefringent to be observed with cross polarization microscopy. Before impinging on each other, the prevailing shape of the PVA crystallites on the surface of the film is a multi-directional 'wheat sheaf' structure as shown in Fig. 8.6. These crystallites are not spherically symmetric, i.e. they do not have a spherulitic symmetry, however, they do conjure up images of young or immature spherulites grown from the melt. The fact that these crystals are grown from water cast films has no bearing on the fundamental foci of this research; this preparation was only chosen as it allows for crystallization studies at room temperature and over extended time scales.

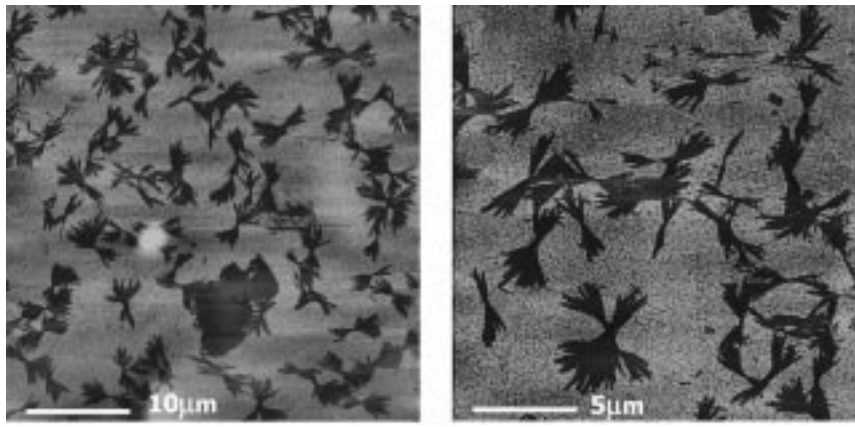

8.6 AFM images of bulk PVA (40 × 40 μm, and 20 × 20 μm) obtained in contact mode (lateral force images shown). A variety of branched crystal morphologies – nearly impinging – are found throughout the film, however the same film is non-birefringent when viewed under a crossed polarized optical microscope. Copyright © *Macromolecules*, 2001, vol. 34, pp. 8475–8482.

PVA crystal morphology

AFM was performed in all the above modes on bulk PVA films and on PVA filled with inorganic layers (4, 10, and 20 wt.% MMT) in order to measure differences in crystal morphology, with the emphasis on the initial stages of crystallization. As can be seen in Fig. 8.7(a), the bulk PVA has crystals which grow to sizes of about 5 microns and larger, before impinging upon neighboring crystallites and arresting further growth. In contrast, when inorganic filler layers are present (Fig. 8.7(b)) the crystallites are smaller and more linear in shape than the bulk crystallites. Crystallite sizes in the MMT-filled system are about 1–2 microns, when grown in the vicinity of the inorganic particles. The color scales used in both images, show the crystalline regions in lighter color, corresponding to higher apparent topography (i.e. smaller deformation under the constant applied force in addition to any true topography features). The behavior of PVA systems loaded with 10 and 20% MMT is similar to that of Fig. 8.7(b); i.e. crystals grow in a linear fashion, albeit in much higher density on the surface. Due to the higher crystallite densities the crystalline regions overlap, making it impossible to assign a diameter or length to these structures.

In order to elucidate the crystallization mechanisms responsible for this difference in morphology, we followed the evolution of the PVA crystals growing next to silicate layers or tactoids (the silicate particles imaged can be easily designated as layers or tactoids through their size: single layers are 1 nm thin, whereas tactoids – stacks of parallel packed single layers – are much larger, on the order of 100 nm). In Fig. 8.8, we follow the time evolution of PVA crystals in a 2.5 × 2.5 μm region of a PVA/4 wt.% MMT sample, at room

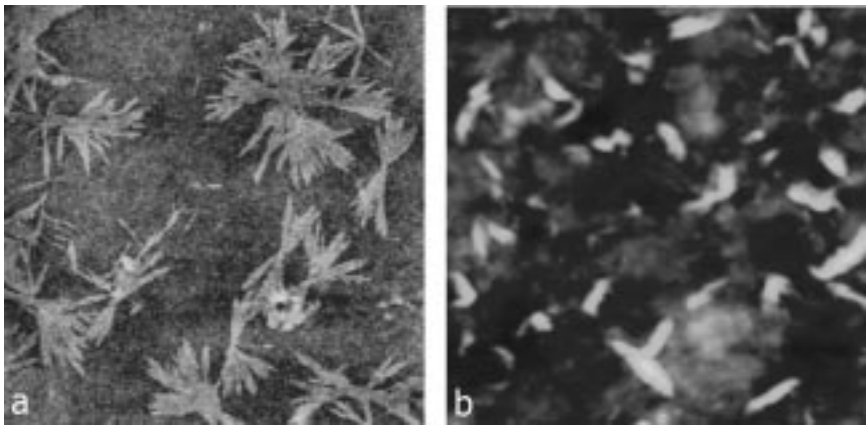

8.7 Comparison between bulk PVA (a) and PVA/4 wt.% MMT (b), both 15 × 15 μm. Contact mode (height) images are shown under the high normal forces; the 'apparent topography' under these scanning conditions shows crystalline material in lighter colors, since it undergoes smaller compressive deformations. The modulus of the amorphous polymer in the PVA/MMT system (b) is much higher than the amorphous bulk (a), resulting in much smaller deformation under the same normal force, and thus in less contrast of the 'apparent topography'. There is a marked decrease in crystallite size and a change in shape when submicron inorganic particles are introduced in the PVA. Copyright © *Macromolecules*, 2001, vol. 34, pp. 8475–8482.

temperature and 50% relative humidity (due to its strong hydrophilicity, PVA tends to absorb water from the ambient humidity, resulting in plasticization as well as crystallization of PVA well below its known crystallization temperature of 193ºC). This image depicts well the general behavior found in the silicate filled system, i.e. the crystalline material found in Fig. 8.8 is indicative of the crystallites found in most images of the PVA/silicate systems studied here, as is evident in Fig. 8.7. Figure 8.8 shows a time series of height images, obtained by tapping AFM in the vicinity of a protuberant inorganic filler particle (a tactoid in this case). The crystalline PVA regions correspond to the apparent 'higher' features in Fig. 8.8; concurrent phase and force imaging show that these 'higher' features are much stiffer than the surrounding material, which is also confirmed by subsequent lateral force contact imaging. Thus we may safely conclude that the light-colored material is crystalline, and the darker-colored regions are amorphous. The PVA crystal initiates next to the inorganic surface (Fig. 8.8(a)), grows in size (Figs 8.8 (b)–(d)), and eventually covers completely the surface of the silicate (Fig. 8.8(e)). Furthermore, once the silicate becomes covered with PVA, it appears to continue to recruit amorphous polymer for crystallization in the same region (Fig. 8.8(f)), albeit more slowly than before. The tendency of the PVA to completely cover the tactoid in Fig. 8.8, which is typical also in all other regions of this sample, is driven by the strong specific interactions between the PVA and the silicate,[16] which cause a strong wetting of the polymer on the

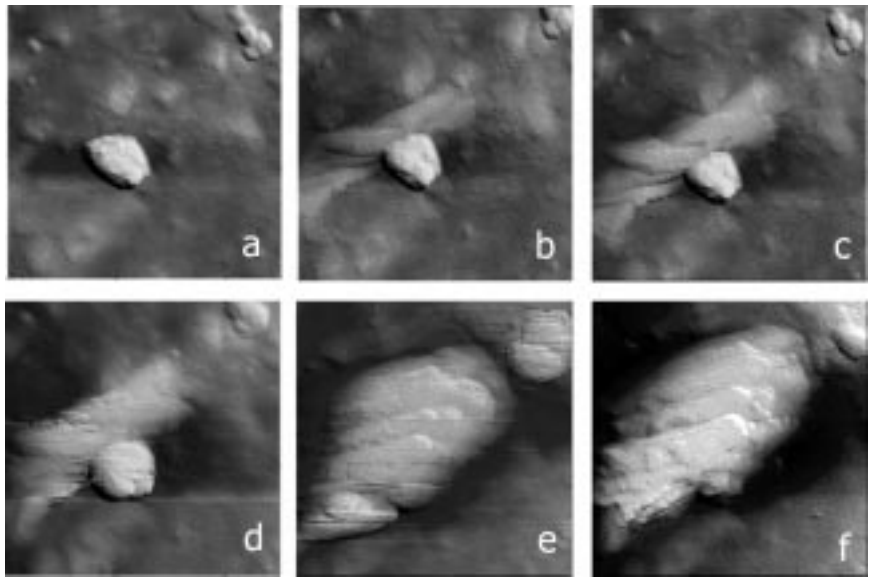

8.8 A time series of height images (2.5 × 2.5 μm), obtained by tapping mode AFM in the vicinity of a protuberant inorganic filler tactoid. Time after casting is as follows: (a) 36 hours, (b) 3 days, (c) 4 days, (d) 6 days, (e) 20 days and (f) 21 days. The height scale (light to dark) is 400 nm (a–d) and 500 nm (e–f). The PVA crystal initiates next to the inorganic surface (a), grows in size (b–d), and eventually covers completely the surface of the silicate (e). The same crystallization behavior observed near the central protuberant tactoid, can also be seen for a smaller inorganic particle in the top right corner. Copyright © *Macromolecules*, 2001, vol. 34, pp. 8475–8482.

inorganic surface. The fact that these crystals grow in a linear fashion suggests that nucleation prefers to begin near the inorganic surface, and that once nucleated, the crystals tend to grow upon one another.

The PVA vinyl alcohol group forms hydrogen bonds with the silicate oxygens, which dominate the cleavage plane of MMT. Moreover, due to the atomically smooth MMT surface, these specific interactions are expected to force chains to create long adsorbed trains,[26] which in turn will promote a strongly interacting second layer of PVA to crystallize on top of them. Thus this MMT surface epitaxial/nucleating effect can be 'felt' through many layers of polymer, causing a long range collection and crystallization of PVA from the surface of the silicate (Fig. 8.8). Therefore, these sites tend to act as nucleating sites for the PVA crystallites. Accordingly scans of the PVA/4 wt.% MMT show many more crystallites per area compared to the neat PVA, as all the inorganic silicate fillers nucleate polymer crystallites. The PVA/MMT specific interactions decrease the surface energy necessary to create/nucleate a polymer crystal, and thus, the crystalline regions tend to nucleate around the silicate surfaces. Furthermore, since the silicate surface can be felt through only a small

distance, the new crystallites formed only grow to a limited size of about 2 microns. Hence, it is not unexpected that the size falls from 5 microns, in the neat PVA, to 1–2 microns in the MMT filled PVA (Fig. 8.7).

8.3.2 Differential scanning calorimetry and X-ray diffraction

PEO crystallite size

The difference in crystallite size for PEO crystallized in the presence of silicates can be quantified by enumerating the number of crystallites/spherulites per area. In Fig. 8.9 we show the density of crystallites, as measured in the isothermal crystallization CPOM experiments at temperatures (T_{iso}) of 45 and 50ºC. It is seen that the density of crystallites increases by more than an order of magnitude when MMT layers are introduced in PEO, even at very small silicate loadings. Moreover, CPOM reveals that almost all of the crystal nuclei initiate in the bulk PEO, i.e. far away from the MMT fillers. Albeit this huge difference in the number of crystallites between neat and intercalated PEO, the polymer crystalline fraction – as measured through DSC experiments – does not show a marked change between these two systems. In Fig. 8.10 we plot the enthalpy of melting (ΔH_m) as measured by DSC, showing no strong effect of the silicate loading and/or the crystallization temperature on the final crystallinity of the systems. One of these DSC experiments is shown in Fig. 8.11(a) for neat PEO and PEO/5 wt.% MMT. The onset and peak crystallization temperatures (T_c) can also be measured from the cooling response (Fig. 8.11(b)). The addition of

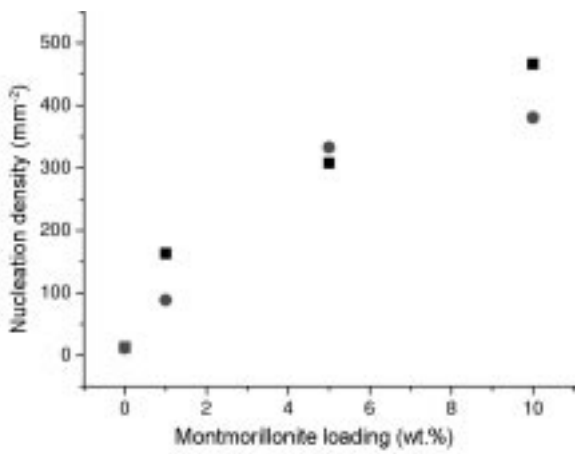

8.9 The nucleation density as a function of silicate loading, as measured from cross polarization optical microscopy. Crystallization is done at 45ºC (squares) and 50ºC (circles). The number of nucleated spherulites per unit area increases by more than tenfold, even at low silicate loadings. Copyright © *Chem. Mater.* 2003, vol. 15, pp. 844–849.

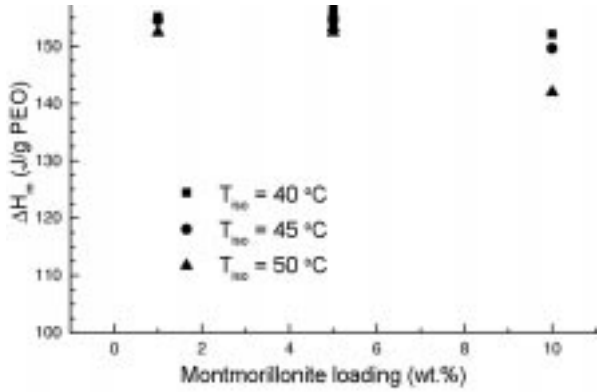

8.10 Enthalpy of melting for PEO versus filler loading. The PEO crystallinity does not change markedly with silicate loading, for various isothermal temperatures of crystallization (T_{iso} = 40, 45, and 50°C: squares, circles, and up triangles, respectively). All samples were melted and then rapidly cooled to the T_{iso}; after isothermal crystallization in the DSC, samples were heated at 10°C/min and ΔH was measured. Copyright © *Chem. Mater.* 2003, vol. 15, pp. 844–849.

MMT fillers in the PEO decreases the polymer T_c for all cooling rates used, suggesting that the MMT hinders the PEO crystallization, a conclusion which is in concert with the behavior seen in Fig. 8.5. As expected, the DSC-observed T_c decreases with increasing cooling rate, and the crystallization temperature of PEO/MMT composite deviates more from the neat polymer's T_c as more MMT filler is added. The fact that the dependence of T_c on the cooling rate is similar for the neat PEO and the filled PEO suggests that these differences are due to genuine changes in the polymer crystallization, rather than changes of the thermal conductivity caused by the incorporation of the inorganic fillers. In the latter case, if the DSC-observed decrease of T_c were actually due to changes in thermal conductivity, the *difference in* T_c between the neat and filled PEO would have been a strong function of the cooling rate.

PVA crystal nature

In contrast to the PEO crystal behavior, the strong interactions present between PVA and the silicate surfaces bring about changes in the inherent crystal nature, as evidenced by the following observations. Wide angle XRD provides evidence that not only the crystal morphology but also the crystalline structure changes when the inorganic filler is added to PVA. Namely, in the 2θ region between 14.0 and 25.5° (Fig. 8.12) PVA has its 100, $10\overline{1}$, 101 and 200 crystalline reflections (corresponding to $2\theta = 16.0$, 19.4, 20.1 and 22.7° respectively). The XRD scans in Fig. 8.12 (neat PVA and 4, 20, and 60 wt.% MMT) suggest that as silicate content increases from $\phi_{\mathrm{MMT}} = 0$ to 20 wt.%, the 101 and $10\overline{1}$ peaks

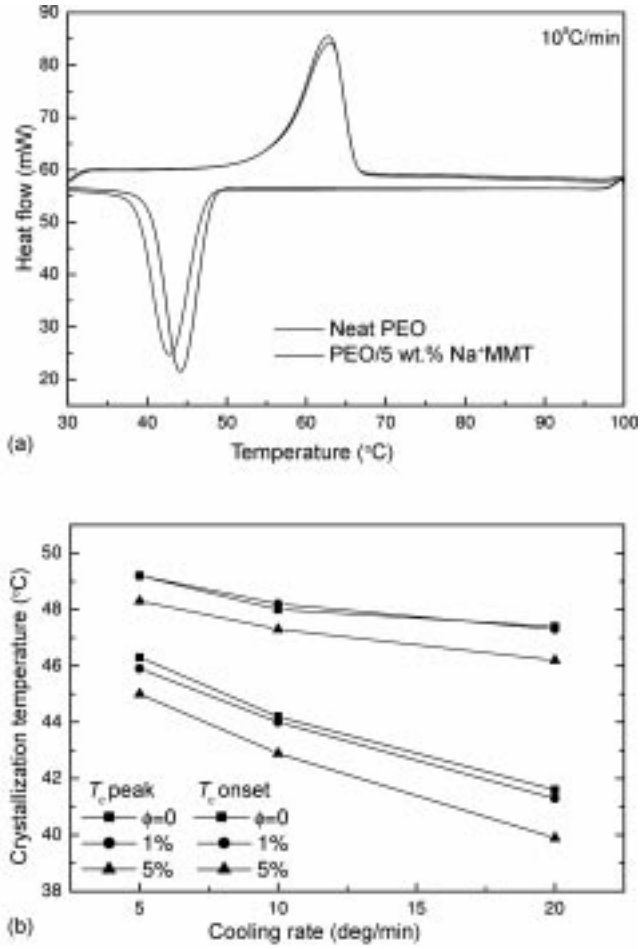

8.11 (a) A typical DSC scan for PEO and PEO/5 wt.% MMT, at a heating/cooling rate of 10°C/min. (b) Peak and onset of the crystallization temperature, as a function of DSC cooling rate, for PEO and PEO/MMT nanocomposites. The crystallization temperature is decreasing with silicate loading, showing that a higher degree of undercooling is needed for crystallization of composites. Copyright © *Chem. Mater.* 2003, vol. 15, pp. 844–849.

show a concerted decrease in intensity. This depression of the 101 and $10\overline{1}$ peaks is accompanied by the appearance of a single peak centered at $2\theta = 19.5^{\circ}$. This development of the diffraction peaks indicates that a new crystal structure forms with the addition of the silicate, at the expense of the bulk-like crystal structure. (For clarity, the XRD of the neat MMT is not given here. The appearance of the new peak, observed in the higher PVA loadings, is not connected in any way to crystalline reflections from the MMT structure.) Given the multiple overlapping peaks in the diffraction pattern, it is difficult to quantify with any accuracy either

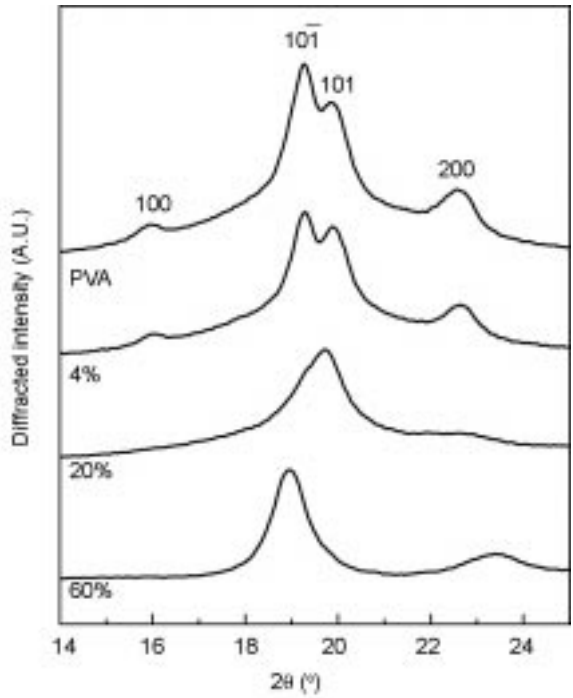

8.12 XRD curves of bulk PVA and silicate filled composites of various inorganic compositions. The bulk PVA reflections (100, 10$\bar{1}$, 101 and 200) are at 2θ: 16.0, 19.4, 20.1 and 22.7°, respectively. With increasing inorganic content, there appears a concerted decrease in intensity of the 101 and 10$\bar{1}$ peaks, accompanied by the appearance of a new peak centered at $2\theta = 19.5°$, suggesting a new crystalline form for the clay-induced PVA crystals. Copyright © *Macromolecules*, 2001, vol. 34, pp. 8475–8482.

the difference of the crystallite sizes,[27] or the simultaneous change in crystalline structure. However, the bulk-like and filler-induced crystals also have different melting temperatures (T_m) and DSC can be employed to quantify the change in crystalline structure with ϕ_{MMT}.

In Fig. 8.13(b), DSC traces are shown for the melting transitions of neat PVA films, as well as PVA films filled with MMT. Bulk PVA has a melting transition at $T_m = 225$ºC. As inorganic layers are added to PVA the polymer crystallinity does not change markedly, however a new, higher T_m crystalline form appears (Fig. 8.13(b)). Fig. 8.13(a) shows the inorganic content dependence of the fractions of the two melting transitions; these fractions are defined via the ratios of the corresponding enthalpies of melting over the total enthalpy of the sample, both for the bulk-like T_m, as well as for the new – higher T_m – melting transition observed in the presence of the inorganic fillers. Figure 8.13(a) clearly indicates that the presence of the inorganic surface induces a new higher T_m crystal at the

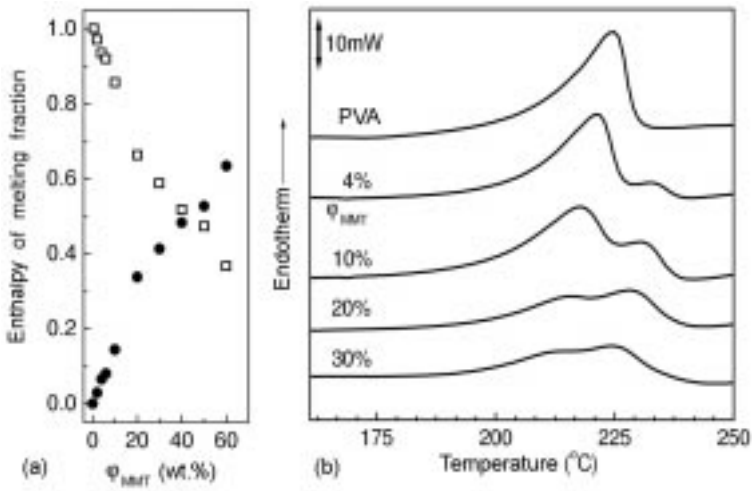

8.13 DSC traces showing the melting region of PVA/silicate composites of various chosen compositions. On the left, the fractions of the two melting enthalpies for the two crystalline forms for all the MMT concentrations studied [squares: bulk-like crystal ($T_m = 225°C$), circles: higher T_m crystal]. The dependence of the enthalpy fractions on the ϕ_{MMT} suggests that the inorganic surface promotes a new, higher T_m crystal form, at the expense of the bulk crystalline material. Copyright © *Macromolecules*, 2001, vol. 34, pp. 8475–8482.

expense of the bulk-like crystals. This behavior is consistent with the XRD observation (Fig. 8.12) of a new crystal phase that gradually appears with the addition of the fillers, with a parallel depression of the bulk-like crystal peaks. Our AFM scans (Fig. 8.8) show that the inorganic-induced crystals grow around the inorganic fillers, and this suggests that the higher T_m may originate from the specific interactions near the PVA/silicate interface, which result in a strong polymer/inorganic adhesion.

8.4 Overview of nanocomposite structure and crystallization behavior

Using non-isothermal and isothermal DSC, and cross-polarization optical microscopy, we have investigated the differences of crystallization behavior in neat PEO films and PEO films filled by MMT inorganic layers. The coordination of PEO to the montmorillonite Na^+ promotes the polymer-filler miscibility, but renders the PEO/MMT interface not conducive to crystallization, since it promotes amorphous polymer conformations in the vicinity of the inorganic fillers. Thus, MMT causes a retardation of the crystal growth front, and results in crystal morphologies which are characterized by non-spherical shapes with jagged edges. Moreover, this PEO crystal obstruction by the MMT allows for the

'homogeneous' nucleation of large numbers of crystallites, which grow to much smaller sizes than neat PEO spherulites. In the Na^+ MMT filled PEO, crystallization nucleation sites occur in the bulk of the PEO matrix, i.e. far from the silicate surfaces, in considerably larger numbers than in unfilled PEO at the same undercooling. This higher nucleation density is a manifestation of two effects: (a) the disruption of the spatial continuity by the inorganic layers, which allows for the independent nucleation of PEO crystallites in the spaces between the fillers, and (b) the characteristic PEO/Na^+ coordination, which markedly inhibits 'heterogeneous' nucleation by the MMT fillers. The absence of marked heterogeneous nucleation contrasts the PEO behavior against most of the other polymer/MMT systems studied, where heterogeneous nucleation and/or epitaxial crystallization are the dominant effects. Despite the different crystal morphologies between neat and filled PEO, there is no marked change in polymer crystal fraction for the small amounts of silicate ($\phi_{MMT} < 10\%$) studied here. For larger MMT loadings than studied here, the introduction of more PEO/MMT interfaces in the system decreases the PEO crystallinity proportionally to ϕ_{MMT}.[28,29]

Using AFM, we have investigated the differences in neat PVA films and PVA films filled by MMT inorganic layers. Mechanical variations across polymer surfaces – as those between amorphous and crystalline regions – are manifested in various AFM imaging modes, including contact, intermittent contact, and two force modes. Since in most cases the mechanical variations are superimposed on surface topographical features, sometimes comparative imaging with various modes is needed to unambiguously resolve polymer crystal, amorphous polymer, and filler particles.

When inorganic layers (MMT) are added to the PVA polymer, crystallites are initiated and grown in the immediate vicinity of the inorganic surface. We believe that this is due to the strong specific interactions between the inorganic surfaces and the polymer. The crystallites found near the inorganic fillers are about 2 microns in size, smaller than the crystallites found in the neat PVA film, which are 5 microns or larger. Moreover, the melting temperature of these crystals was found to be higher than the bulk T_m. At the same time, XRD also shows differences in the PVA crystalline structure when crystallized in the presence of MMT, suggesting that the inorganic fillers change also the crystal structure. This new, silicate-induced PVA crystal phase is promoted by the existence of the montmorillonite layers, and forms at the expense of the bulk PVA crystalline phase.

8.5 Materials properties of poly(vinyl alcohol)/ Na^+ montmorillonite nanocomposites

The purpose of this study is, first, to investigate the structure of the PVA/MMT nanocomposites, with the focus on the layered filler dispersion, as well as on the changes of the polymer crystallinity due to the inorganic layered fillers.

Subsequently, through the study of selected nanocomposite material properties, we attempt to correlate the hybrid structure with changes in the material response. The structure is explored over the full range of silicate compositions. On the other hand, properties are explored only for the low silicate loadings, which are relevant to potential applications.

8.5.1 Thermal properties

The model water soluble polymer/silicate nanocomposite systems presented here also possess unique thermal properties which can be studied using various techniques. These include DSC and thermal gravimetric analysis. Thermal properties for the PVA/silicate system are outlined in the following sections.

DSC and XRD analysis of PVA crystallites in the nanocomposite

Thermal characterization

Bulk PVA has a glass transition at $T_g = 70$ºC and a melting transition at $T_m = 225$ºC. For fully intercalated PVA hybrids (i.e. all the polymer is intercalated in MMT galleries) DSC does not detect any traces of thermal transitions between 35ºC and 250ºC (Fig. 8.14), hybrids with $\phi_{\mathrm{MMT}} > 60$ wt.%). For these 'neatly intercalated' nanocomposites, both the T_g and T_m are either too weak and/or too broad to measure, or they are suppressed due to the polymer confinement. Although the physical origins of this behavior are still under debate,[30,31] this absence of thermal events is in agreement with the general behavior of polymers intercalated in clays and synthetic silicates. In a plethora of systems studied: nylon-6,[2] PEO,[9,10] PMPS,[30] PS,[31] PCL,[32] PMMA[33] intercalated in naturally occurring silicates (MMT) and in synthetic layered alumino-silicates (fluorohectorite), there exist no detectable thermal transitions for the intercalated polymers, over a wide temperature range below the T_g and above the T_m. Despite the use of methods with an increasing resolution and sensitivity (such as DSC, thermally stimulated current, positron annihilation, NMR, and so on) no transitions can be detected in neatly intercalated systems. For example, TSC, DSC, and NMR studies[9,10] of an intercalated poly(ethylene oxide) (PEO, $M_w = 100{,}000$)/MMT hybrid (20 wt.% polymer), indicated the absence of any thermal transitions between -100ºC and 120ºC, that could correspond to the vitrification or the melting of PEO ($T_g = -55$ºC and $T_m = 65$ºC). On a local scale, intercalated polymers exhibit simultaneously fast and slow modes of segmental relaxations for a wide range of temperatures,[10,30,31] but again with a marked suppression (or even absence) of cooperative dynamics typically associated with the glass transition.

A systematic study of the DSC traces with ϕ_{MMT} (Fig. 8.14) shows that the T_g and T_m signals weaken gradually, and disappear for ϕ_{MMT} above 60 wt.%. This

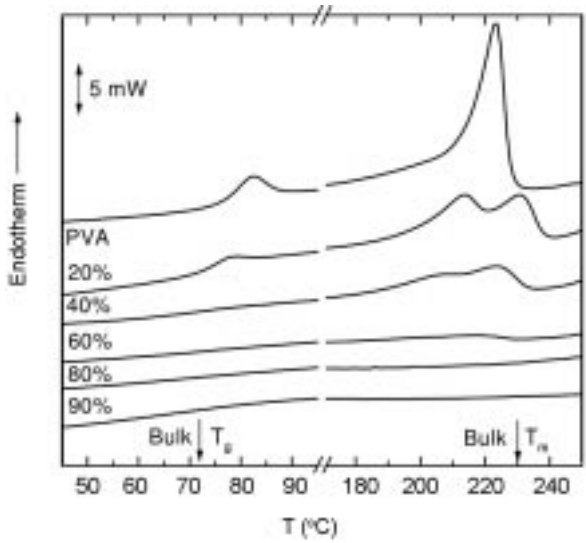

8.14 Differential scanning calorimetry of PVA/MMT nanocomposites with varying ϕ_{MMT} (20°C/min, second heating). For clarity a featureless region is omitted between 95 and 175°C. Copyright © *Chem. Mater.* 2000, vol. 12, pp. 2943–2949.

suggests that in these systems ($\phi_{MMT} > 60$ wt.%) all the polymer is affected by the inorganic layers, and there seems to be no bulk-like PVA present (at least not enough to manifest itself through thermal transitions). For higher polymer concentrations (e.g. 20 wt.% MMT) there appear two distinct and overlapping melting peaks, one around the bulk T_m and another one at higher melting temperature.

PVA crystallinity

The PVA melting was studied by performing DSC on several high PVA concentration nanocomposites ($2 < \phi_{MMT} < 30$ wt.%, Fig. 8.15(a).). Compared to the neat PVA, in the nanocomposites appears also a new higher-T_m crystal phase. This dual DSC melting trace is reminiscent of DSC endotherms belonging to a PVA system studied by Tanigami *et al.*[34] In their system, Tanigami *et al.* controlled the PVA stereoregularity by using blends of a syndiotactic-rich and an atactic poly(vinyl alcohol). What was observed was a crystalline-phase-separated system which exhibited a dual melting point. That dual melting point arose from two crystal phases: one formed primarily by syndiotactic sequences, the other primarily by atactic sequences. The two types of crystals have melting points which differ by about 15–22°C (T_m at 228 and 250°C). This T_m difference is comparable to the one measured for our PVA/MMT nanocomposites, as shown in Fig. 8.15. The width at half-maximum (FWHM), for the combined

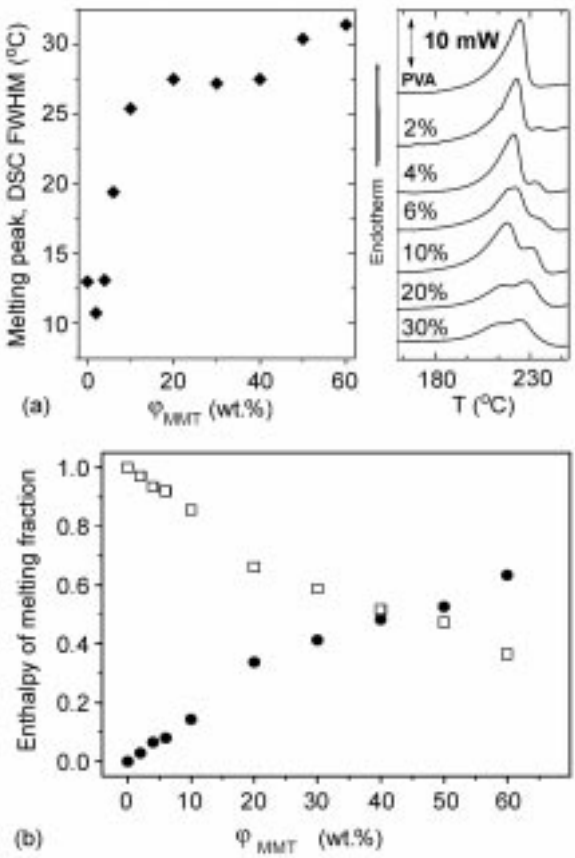

8.15 DSC of the melting region for the low MMT content nanocomposites (20°C/min); (a) FWHM of the combined melting endotherms and corresponding DSC traces around T_m; (b) the fractional heat of fusion owing to the MMT-induced crystal phase (circles, $T_m = 235$°C) and bulk-like crystal phase (squares, $T_m = 225$°C), as determined from the DSC peak fittings.

DSC melting peak, was used as an indicator of how the two crystal phases were present in the PVA blend. To calculate FWHM, the peak value of the DSC trace is located. The full width of the melting peak is then evaluated at a distance halfway between the peak value and the DSC trace baseline. In Tanigami's work, the melting peak FWHM increased to 25–35ºC when the atactic-rich and the syndiotactic-rich phases coexisted, whereas it remained approximately 10ºC when either of the two crystal phases was in excess. The FWHM for our nanocomposite combined/dual melting peaks is plotted in Fig. 8.15(a), as a function of the silicate loading (ϕ_{MMT}). The full width increases sharply from about 13ºC to above 25ºC as the silicate composition crosses the percolation

threshold (ϕ_{MMT} = 4 wt.%). This suggests that we have substantial volumes of bulk-like and of MMT-induced crystal phases coexisting for $\phi_{MMT} > 5$ wt.%.

In order to quantify the relative volumes of the two crystal phases present, we used the standard fitting method[35] and gaussian functions to estimate the melting enthalpies (heat of fusion, ΔH) for each of the two melting peaks in the DSC trace. The fraction of the two melting enthalpies (Fig. 8.15(b)) will reflect the relative amount of the respective crystalline phases in the polymer matrix. The new crystal form – which appears when MMT fillers are added to the PVA – seems to grow linearly with the MMT concentration, and at the expense of the bulk-like PVA crystal phase (Fig. 8.15(b)). This clearly suggests the high T_m phase is induced by the presence of the silicate layers. The shape of the melting peak and the relative peak areas remain the same in subsequent DSC scans, after cooling from the melt state (exotherms not shown). This indicates that this dual crystalline melting, is not an artifact of the solution casting or the thermal history, but is indeed induced by the presence of the silicate.

Wide angle XRD provides evidence that we actually have a new crystal phase in the nanocomposite. Namely, in the 2θ region between 14.0 and 25.5º (Fig. 8.12) PVA has its 100, $10\bar{1}$, 101 and 200 crystalline reflections (corresponding to $2\theta = 16.0$, 19.4, 20.1 and 22.7º, respectively). In the same region MMT also has its 101 reflection at 19.7º. We have annealed our samples at 245ºC for 35 minutes prior to scanning in order to allow for higher quality PVA crystals. Samples showed some degradation by becoming brown in color and overall crystallinity did decrease somewhat; however, the DSC of the annealed samples remains the same qualitatively (dual melting peak) and quantitatively (heat of fusion). The XRD scans in Fig. 8.12 suggest that as silicate content increases from ϕ_{MMT} = 0 to 20 wt.%, the 101 and $10\bar{1}$ peaks concurrently become lower in intensity and are replaced by what appears to be a single peak centered at $2\theta = 19.5$º. This is consistent with the DSC measured high-T_m crystal phase that appears at these compositions, and with its gradual enhancement at the expense of the bulk-like crystal. Unfortunately, a quantitative comparison between the DSC and the XRD is not possible, as the existence of 5 overlapping diffracted reflections does not allow for the unambiguous fitting of the XRD peaks.

In summary, the analysis of the PVA crystalline XRD and DSC data shows that at low silicate loadings (below 60 wt.%) there appears a new crystalline phase, which is induced by the presence of MMT. This phase grows linearly with ϕ_{MMT} at the expense of the bulk PVA crystal phase. For $\phi_{MMT} \geq 60$ wt.%, PVA is primarily intercalated and no melting endotherms are found for the confined polymer.

Thermal degradation

In addition to having a higher melting point, thermal degradation properties of PVA/MMT nanocomposites also show improvement. A comparative thermal

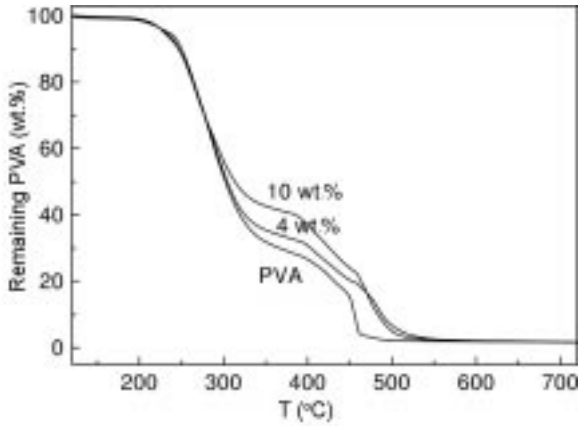

8.16 Polymer weight loss from TGA scans in air, for PVA and two nanocomposites containing 4 wt.% and 10 wt.% Na^+ MMT. Copyright © *Chem. Mater.* 2000, vol. 12, pp. 2943–2949.

gravimetric analysis (TGA) of pure PVA and two nanocomposites with 4 and 10 wt.% MMT (10ºC/min in air) is shown in Fig. 8.16. The weight loss due to the decomposition of PVA is nearly the same until the temperature of about 275ºC. After this point, the silicate inhibits the PVA weight loss, which reaches a maximum lag of about 75ºC. Unlike most other polymer/MMT nanocomposite systems,[33] this PVA/MMT suffers nearly the same weight loss as the bulk for its initial 50%, possibly due to the fact that PVA can supply oxygen from within to initiate its decomposition.

8.5.2 Mechanical properties

Exfoliated polymer/silicate systems have been found to exhibit mechanical, thermal and solubility properties, as well as water vapor transmission rates, which are superior to conventionally filled systems.[26] Furthermore due to their nanoscale dispersion of filler, they retain optical clarity.[36] In our PVA/MMT hybrids, and especially at the application relevant low ϕ_{MMT} (below 10 wt.%), TEM and XRD reveal a coexistence of intercalated and exfoliated silicate layers. For these systems we will briefly describe some of their materials properties.

Tensile tests were performed on PVA nanocomposite films with silicate loadings of 0, 2, 4, 6 and 10 wt.%. Because completely dry PVA films are quite brittle, tests were performed at a nominal relative humidity of 50%, according to the usual testing procedure for PVA.[37] Prior to testing, films were equilibrated in a humidity chamber at 90% r.h. Yielding was not found for any of the samples. All samples had an initial period of elastic deformation followed by a nearly monotonically increasing stress during plastic deformation, until failure. Figure 8.17 shows the Young's modulus, the stress-at-break and strain-at-break, and the

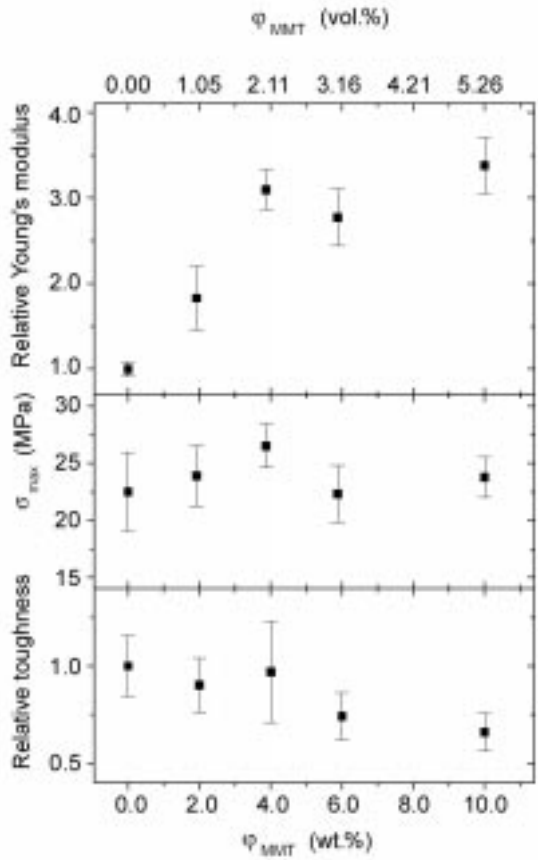

8.17 Tensile testing results as a function of MMT weight and volume content. Top: the Young's modulus normalized by the bulk value (68.5 MPa); middle: the maximum stress at break; bottom: the toughness of the hybrids normalized by the bulk values (45.8 kJ/m^2). Copyright © *Chem. Mater.* 2000, vol. 12, pp. 2943–2949.

measured fracture toughness, all as a function of silicate loading. For comparison, the Young's moduli are normalized by the measured bulk PVA value (68.5 MPa). At $\phi_{\mathrm{MMT}} = 4$ wt.%, the nanocomposite is characterized by a modulus about 300% larger than the one of the respective bulk PVA. In most conventionally filled polymer systems, the modulus increases linearly with the filler volume fraction; for these nano particles much lower filler concentrations increase the modulus sharply and to a much larger extent.[1] Accordingly, in the PVA/MMT systems the dependence of modulus on ϕ_{MMT} is very strong at very low content, and tends to level off after $\phi_{\mathrm{MMT}} = 4$wt.%, at about 3.5 to 4 times the value for bulk PVA. This behavior has been reported before for poly-(dimethyl siloxane)/MMT exfoliated hybrids.[38,39] The dramatic enhancement of

the Young's modulus for such extremely low MMT filler concentrations cannot be attributed simply to the introduction of the higher modulus inorganic filler layers. A recent theoretical approach is assuming a layer of affected polymer on the filler surface, with a much higher Young's modulus than the bulk equivalent polymer. This affected polymer can be thought of as the region of the polymer matrix which is physisorbed on the silicate surfaces, and is thus stiffened through its affinity for and adhesion to the filler surfaces.[38] Obviously, for such high aspect ratio fillers as our MMT layers, the surface area exposed to polymer is huge (for MMT is typically 700–800 m^2/g), and the dramatic increases in the modulus with very low ϕ_{MMT} are not surprising. Furthermore, beyond the percolation limit ($\phi_{MMT} > 4$ wt.%) the additional exfoliated layers are introduced in polymer regions that are already affected by other MMT layers, and thus it is expected that the enhancement of Young's modulus will be much less dramatic.

The stress at break (σ_{max}) is also plotted versus the silicate content in Fig. 8.17. The data shows that σ_{max} is relatively insensitive to the filler concentration. Finally, the toughness is also plotted in the same graph, again normalized by the bulk PVA value (45.8 kJ/m^2) for comparison; the toughness was calculated from the integrated area under the Instron stress/strain curve. There is a very moderate decrease of the toughness (3% at $\phi_{MMT} = 4$ wt.%, and 22% at $\phi_{MMT} = 6$ wt.%) for ϕ_{MMT}, which is caused by a comparable decrease of the strain-at-break.

8.5.3 Barrier properties

With the dispersion of these ultra-thin inorganic layers throughout the polymer matrix, the barrier properties of the nanocomposites are expected to be strongly enhanced compared to the respective polymer. The water vapor transmission rates were measured for the pure polymer and several of its low ϕ_{MMT} nanocomposites, and are plotted in Fig. 8.18. In the same figure, the resulting water permeabilities[40] are plotted as well. WVT and permeabilities were measured following ASTM E96, for PVA and PVA/MMT nanocomposite films of the same thickness ($8.98 \pm 0.33 \times 10^{-3}$ cm). The permeabilities decrease to about 40% of the pure WVT values for silicate loadings of only 4–6 wt.%. We believe that this enhancement in the water permeability originates both from the increased path tortuosity of the penetrant molecules – forced around the inorganic layers – as well as the enhanced modulus of the polymer matrix in the nanocomposites.

8.5.4 Optical properties

Because of the nanoscale dispersion of the silicates in the PVA matrix, optical clarity remains high at silicate contents which yield primarily exfoliated composites. This allows its potential use in paper coatings, one of the most

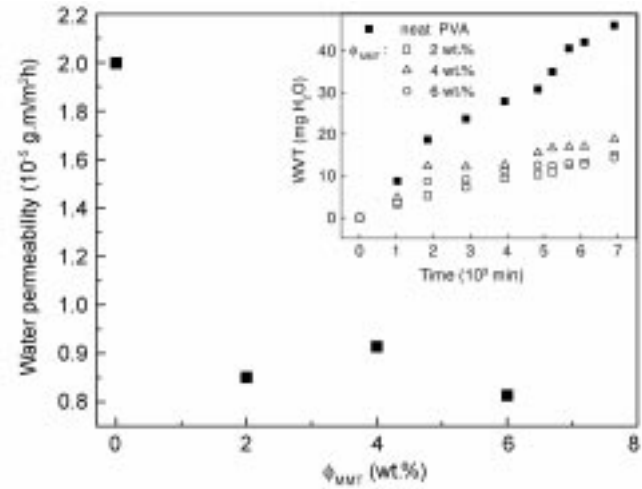

8.18 Water vapor permeability for the neat PVA and several PVA/MMT nanocomposites. The inset shows the water vapor transmission raw data collected for each composition, which were used to calculate the water permeabilities. Copyright © *Chem. Mater.* 2000, vol. 12, pp. 2943–2949.

common uses for pure PVA. Figure 8.19 shows the UV/VIS transmission spectra of pure PVA, and PVA/MMT hybrids with 4 and 10 wt.% MMT. These films have thicknesses of 0.17, 0.18 and 0.15 mm, respectively. The spectra show that the visible region (400–700 nm) is not affected at all by the presence of the silicate, and retains the high transparency of the PVA. For the ultraviolet wavelengths, there is strong scattering and/or absorption, resulting in very low

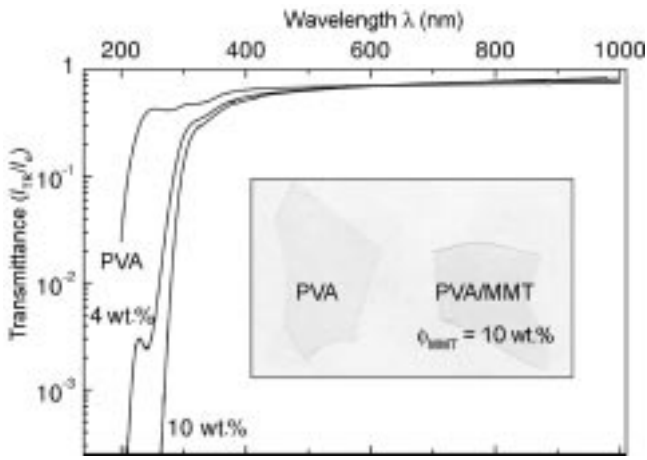

8.19 UV-VIS transmittance spectra of PVA and PVA/MMT nanocomposites containing 4 and 10 wt.% MMT. Copyright © *Macromolecules*, 2001, vol. 34, pp. 8475–8482.

transmission of the UV light. This is not surprising as the typical MMT lateral sizes are 50–1000 nm.

8.6 Conclusions

We have investigated the structure and properties of PVA/MMT nanocomposites formed by water casting, a solution intercalation method. From TEM and XRD studies, over the full range of silicate loadings, we find that there is a coexistence of exfoliated and intercalated silicate layers. The system becomes mostly intercalated as silicate loading increases beyond $\phi_{\mathrm{MMT}} \geq 60$ wt.%. The exfoliation of layers is attributed to the water casting method used, since the water suspended layers become kinetically trapped by the polymer and can not reaggregate. DSC studies find a suppression of the thermal transitions (T_g and T_m) for the purely intercalated systems. However, for the mostly exfoliated, low MMT loading nanocomposites, DSC unveils a new melting transition with higher T_m than the neat PVA. X-ray diffraction of the polymer crystals suggest that this is a new, silicate-induced PVA crystal phase, that is promoted by the existence of the montmorillonite layers at the expense of the bulk-like PVA crystalline phase.

Some basic materials characterization was also performed for the low ($\phi_{\mathrm{MMT}} \leq 10$ wt.%) MMT loadings. For these MMT concentrations the inorganic layers are well dispersed throughout the PVA matrix, i.e. the nanocomposites formed are mostly exfoliated hybrids. The mechanical/tensile properties of these nanocomposites were studied for low silicate loadings and Young's modulus was found to increase by 300% for 5 wt.% silicate, with only a 20% decrease in toughness, and no sacrifice of the stress at break compared to the neat PVA. In addition, for these low loadings, thermal stability from TGA measurements was shown to be slightly enhanced, and high optical clarity was retained. Additional properties at low silicate loadings, detailed studies of the PVA crystal morphology, and NMR investigations of the PVA segmental dynamics in intercalated structures, are currently under way.

8.7 References

1. Giannelis, E.P.; Krishnamoorti, R.K.; Manias, E. *Adv. Polym. Sci*. **1998**, *138*, 107.
2. Kojima, Y.; Usuki, A.; Kawasumi, M.; Okada, A.; Kurauchi, T.T.; Kamigaito, O. *J. Polym. Sci., Part A: Polym. Chem*. **1993**, *31*, 983. (b) Kojima, Y.; *et al. J. Polym. Sci., Part B: Polym. Phys*. **1995**, *33*, 1039.
3. Lan, T.; Kaviratna, P.D.; Pinnavaia, T.J. *Chem. Mater*. **1995**, *7*, 2144. (b) Wang, M.S.; Pinnavaia, T.J. *Chem. Mater*. **1994**, *6*, 468. (c) Pinnavaia, T.J. *Science* **1983**, *220*, 365.
4. Kanatzidis, M.G.; Wu, C.G.; Marcy, H.O.; DeGroot, D.C.; Kannewurf, C.R. *Chem. Mater*. **1990**, *2*, 222. (b) *Chem. Mater*. **1991**, *3*, 992. (c) *Chem. Mater*. **1996**, *8*, 525.
5. Vaia, R.A.; Ishii, H.; Giannelis, E.P. *Chem. Mater*. **1993**, *5*, 1694. (b) Vaia, R.A.;

Jandt, K.D.; Kramer, E.J.; Giannelis, E.P. *Macromolecules* **1995**, *28*, 8080. (c) Vaia, R.A.; Price, G.; Ruth, P.N.; Nguyen, H.T.; Lichtenhan, J. *Appl. Clay Sci*. **1999**, *15*, 67.
6. Krishnamoorti, R.K.; Vaia, R.A.; Giannelis, E.P. *Chem. Mater*. **1996**, *8*, 1728. (b) Giannelis, E.P. *Adv. Mater*. **1996**, *8*, 29.
7. Gilman, J.W.; Jackson, C.L.; Morgan, A.B.; Harris, R.; Manias, E.; Giannelis, E.P.; Wuthenow, M.; Hilton, D.; Philips, S.H. *Chem. Mater*. **2000**, *12*, 1866.
8. Carrado, K.A.; Thiyagarajan, P.; Elder, D.L. *Clays and Clay Minerals* **1996**, *44*, 506.
9. Vaia, R.A.; Vasudevan, S.; Krawiec, W.; Scanlon, L.G.; Giannelis, E.P. *Adv. Mater*. **1995**, *7*, 154. (b) Vaia, R.A.; Sauer, B.B.; Tse, O.K.; Giannelis, E.P. *J. Polym. Sci., Part B: Polym. Phys*. **1997**, *35*, 59.
10. Wong, S.; Vaia, R.A.; Giannelis, E.P.; Zax, D.B. *Solid State Ionics* **1996**, *86*, 547.
11. Bassner, S.L.; Klingenberg, E.H. *Am. Ceram. Soc. Bull*. **June 1998**, 71.
12. Bassett, D.C. *Principles of Polymer Morphology*; Cambridge University Press: Cambridge, 1981. (b) Lee, J.-C; Nakajima, K.; Ikehara, T.; Nishi, T. *J. Appl. Polym. Sc*i. **1997**, *64*, 797. (c) Mi, Y.; Chen, X.; Guo, Q. *J. Appl. Polym. Sci*. **1997**, *64*, 1267. (d) Wang, C.; Chen, C.-C. *Polym. Bull*. **1999**, *43*, 433. (e) Mucha, M.; Marszalek, J.; Fidrych, A. *Polymer* **2000**, *41*, 4137. (f) Stocker, W.; Schumacher, M.; Graff, S.; Thierry, A.; Wittmann, J.-C.; Lotz, B. *Macromolecules* **1998**, *31*, 807. (g) Doye, J.P.K.; Frenkel, D. *J. Chem. Phys*. **1998**, *109*, 10033.
13. Janigova, I.; Chodak, I. *Eur. Polym. J*. **1995**, *31*, 271. (b) Liang, J.Z.; Li, R.K.Y.; Tjong, S.C. *J. Appl. Polym. Sci*. **1999**, *71*, 687. (c) Tjong, S.C.; Xu, S.A. *Polym. Int*. **1997**, *44*, 95. (d) Alonso, M.; Velasco, J.I.; de Saja, J.A. *Eur. Polym. J*. **1997**, *33*, 255. (e) Radhakrishnan, S.; Saujanya, C. *J. Mater. Sci*. **1997**, *64*, 1267. (f) Stricker, F.; Bruch, M.; Mulhaupt, R. *Polymer* **1997**, *38*, 5347. (g) Trifonova, D.; Varga, J.; Vancso, G.J. *Polym. Mater. Sci. Eng*. **1998**, *41*, 341.
14. Davis, R.D.; Jarrett, W.L.; Mathias, L.J. *Polym. Mater. Sci. Eng*. **2000**, *82*, 272.
15. Liu, L.; Qi, Z.; Zhu, X. *J. Appl. Polym. Sci*. **1999**, *71*, 1133.
16. Strawhecker, K.; Manias, E. *Chem. Mater*. **2000**, *12*, 2943.
17. Strawhecker, K.; Manias, E. *Macromolecules* **2001**, *34*, 8475.
18. Manias, E.; Touny, A.; Wu, L.; Strawhecker, K.; Lu, B.; Chung, T.C. *Chem. Mater*. **2001**, *13*, 3516.
19. Lincoln, D.M.; Vaia, R.A.; Wang, Z.-G.; Hsiao, B.S.; Krishnamoorti, R. *Polymer* **2001**, *42*, 9975.
20. Vaia, R.A.; Giannelis, E.P. *Macromolecules* **1997**, *30*, 7990.
21. Balazs, A.C.; Singh, C.; Zhulina, E. *Macromolecules* **1998**, *31*, 8370.
22. Wu, J.; Lerner, M. *Chem. Mater*. **1993**, *5*, 835.
23. Hackett, E.; Manias, E.; Giannelis, E.P. *Chem. Mater*. **2000**, *12*, 2161.
24. Kuppa, V.; Manias, E. *Chem. Mater*. **2002**, *14*, 2171.
25. Bassett, D.C. *Principles of Polymer Morphology*; Cambridge University Press: Cambridge, 1981.
26. Israelachvili, J. *Intermolecular and Surface Forces*; Academic Press: London, 1991.
27. Guinier, A. *X-ray Diffraction in Crystals, Imperfect Crystals, and Amorphous Bodies*; W.H. Freeman: San Francisco, 1963.
28. Kuppa, V.; Menakanit, S.; Krishamonti, R.; Manias, E.J. *Polym. Sci. B: Polym. Phys.* **2003**, 41, 3285.
29. Strawhecker, K. PhD. Thesis, Penn State University, 2002.
30. Anastasiadis, S.H.; Karatasos, K.; Vlachos, G.; Giannelis, E.P.; Manias, E. *Phys. Rev. Lett*. **2000**, *84*, 915.

31. Zax, D.B.; Yang, D.K.; Santos, R.A.; Hegemann, H.; Giannelis, E.P.; Manias, E. *J. Chem. Phys*. **2000**, *112*, 2945.
32. Messersmith, P.B.; Giannelis, E.P. *Chem. Mater*. **1993**, *5*, 1064.
33. Bandiopadhyay, S.; Giannelis, E.P. *Polym. Mater. Sci. Eng*. **2000**, *82*, 2008.
34. Tanigami, T.; Hanatani, H.; Yamaura, K.; Matsuzawa, S. *Eur. Polym. J*. **1999**, *35*, 1165.
35. Perkin-Elmer DSC7 Manual, 1994.
36. Wang, Z.; Pinnavaia, T.J. *Polym. Mater. Sci. Eng*. **2000**, *82*, 278.
37. Sundararajan, P.R. In *Polymer Data Handbook*; Mark, J.E., Ed.; Oxford University Press: New York, 1999; p. 894.
38. Shia, D.; Hui, C.Y.; Burnside, S.D.; Giannelis, E.P. *Polym. Compos*. **1998**, *19*, 608.
39. Burnside, S.D.; Giannelis, E.P. *Chem. Mater*. **1995**, *7*, 1597.
40. ASTM Standard E 96-95, Standard Test Methods for Water Vapor Transmission of Materials, Annual Book of ASTM Standards, April 1999, p 829.

9

Poly(butylene terephthlate) (PBT) based nanocomposites

C-S HA, Pusan National University, Korea

9.1 Introduction

Polybutylene terephthalate (PBT) is a conventional semi-crystalline engineering polymer having a high degree and rate of crystallization, good chemical resistance, thermal stability, and excellent flow properties. PBT is used in various high volume automotive, electrical, and other engineering applications because it possesses good tensile strength, flexural modulus, and dimensional stability especially in water and high resistance to hydrocarbons.[1,2] PBT, however, has low impact strength. Thus, there have been attempts to improve impact strength by blending a rubber-like polymer into PBT.

Many attempts have been made to improve the impact properties of PBT by blending with a rubber-like polymer such as ethylene/vinyl acetate copolymer (EVA),[3,4] acrylonitrile-butadiene-styrene copolymer (ABS),[5,6] acrylate rubber,[7] and so on. Therefore, in the first part of this chapter, we will discuss the impact on PBT of rubber-like materials including especially EVA.

A relatively easy and cost-effective way to produce new combinations of properties is blending. However, most blends achieved by melt mixing are immiscible and thus show poor properties. Therefore, compatibilization is demanded to obtain a blend with desired properties. A common way to improve the compatibility and interfacial adhesion between two immiscible polymers is to add block or graft copolymers. Grafting reaction by reactive monomers, such as vinyl silane,[8] acrylic acid (AA),[9] or maleic anhydride (MAH),[10,11] on the main chain of a polymer in the presence of peroxide could be achieved. When a graft copolymer possessing functional groups reacts with a polymer, such as PBT, poly(ethylene terephthalate)(PET), or nylon containing —OH, —COOH or NH_2 groups on the chain end, a desired compatibilizer to improve the compatibility between two different polymers is produced through in situ reaction under the conditions of high temperature and shearing.[12] The compatibilizer produced by the reactive compatibilization exhibits more improved interfacial adhesion in blends than a common physical compatibilizer. Recently, the reactive compatibilizers have been extensively investigated to overcome the

poor properties of blends. Hence, reactive compatibilization of the PBT/EVA blend will be discussed in the second part of this chapter.

Unfortunately, however, the existence of a rubber-like polymer often decreased other properties of the PBT such as the tensile strength, modulus and heat distortion temperature. The disadvantages of the elastomer-toughened PBT can be overcome by introducing the polymer layered silicate (PLS) nanocomposite technique to the PBT/EVA blend system. Thus, PLS nanocomposites based on PBT and PBT/EVA blend are described in detail in the later section.

9.2 Impact modification of PBT by blending

9.2.1 Property changes of PBT by blending with functionalized polyolefins

Impact strength of PBT can be improved by blending with polyacrylate graft rubber,[12] nitrile rubber,[13] styrene-acrylonitrile (SAN) grafted ethylene propylene diene rubber (EPDM-g-SAN),[14] and ethylene propylene rubber (EPR). It was reported that the addition of about 10% polycarbonate (PC) and about 20% EPDM-g-SAN in the PBT gave a ten-fold improvement in the impact strength. Impact modification of PBT is usually possible by interaction between the chain ends of PBT such as hydroxyl group and carboxylic group and another functionalized rubber component. To be used for impact modification of PBT, EPR are usually functionalized by alcoholic or ester group.[15,16] EPDM is also functionalized by an epoxy monomer, or MAH. Glycidyl methacrylate (GMA) grafted on EPDM (EPDM-g-GMA) is as a good compatibilizer for PBT/EPDM blends to enhance impact strength, that is, dispersing a small amount of a low modulus polymer into PBT can lead to improvement in the impact strength.

In this way, the functionalization of one component in immiscible polymer blends has attracted great interest in terms of the compatibilization.[17–19] For example, Lambla and his coworkers reported a series of works on the in situ compatibilization of immiscible polymer blends by one-step reactive extrusion.[20–22] They described the chemical reactions related to compatibilizing polymer blends, especially for the PBT/polypropylene (PP) blend system. They stressed that the monomers used for functionalizing PP, such as acrylic acid (ACID), MAH, GMA, and oxazoline, are potentially reactive towards the carboxylic acid and/or hydroxyl groups at the chain ends of the PBT and are melt grafted onto the PP by free-radical reactions.

It was found that blends of PBT and EVA-g-MAH or ethylene metharylate-g-MAH (EMA-g-MAH) show better impact strength than those of other functionalized polyolefin containing blends at higher contents above 20 wt.%.[23] In this sense, the two blend systems are particularly interesting in the impact modification of PBT. As noted in the Introduction, the tensile modulus as well as the yield strength are, however, decreased monotonously with the added

functionalized polyolefin contents.[23] The reduction in the tensile modulus and the yield strength should be expected as the result of a flexible and amorphous nature of the functionalized polyolefins. This is the reason why further introduction of PLS nanocomposite technique into the PBT or PBT/EVA blend systems is needed, which will be discussed later.

The blending of functionalized polyolefins also affects the thermal properties of PBT. In general, PBT shows a single endotherm around 223ºC on the DSC thermogram at the first heating scan but exhibits a second endotherm at a temperature below that of the original endotherm as well as that of original higher-melting of crystals at the second heating scan. The second lower-melting endotherm peak of PBT is often displayed in a subsequent scanning thermal analysis at a temperature below that of the original endotherm, which can be observed at the first heating scan, when PBT is annealed. There are two kinds of crystallization of the originally amorphous material, coupled and not coupled to pre-existing crystals. The coupled amorphous material cannot crystallize without molecular rearrangements within the crystalline material to which it is coupled.[24] The amorphous material that can crystallize only at higher annealing temperature is likely to be coupled to pre-existing crystals.

Thus, the lower-melting peak on the DSC thermogram occur at the expense of a higher-melting peak because of annealing on the second heating scan when no chemical change is noted. Kim *et al.* proposed that the apparent transformation of high temperature to low temperature-melting material during annealing of PBT arises mainly from the coupled crystallization-recrystallization of amorphous and preexisting crystalline material.[24]

When EVA-g-MAH or EMA-g-MAH is added, the higher melting temperature of PBT slightly decreases with increasing the EVA-g-MAH and the EMA-g-MAH contents, but the lower melting temperature of PBT is not appreciably changed (see Table 9.1).[23] It suggests that the addition of EVA-g-MAH and EMA-g-MAH restricts the crystallization of higher-melting crystals in PBT but it does not affect the coupling of crystallization-recrystallization of amorphous and preexisting crystalline material in PBT. But when EVA or EMA is added, the higher and lower melting temperature of PBT are not changed, meaning that the addition of EVA and EMA do not affect the crystallization of higher and lower melting crystals in PBT.

EVA-g-MAH and EMA-g-MAH have better compatibility with PBT than EVA and EMA. Thus, the compatibility is closely related with the increase in the impact strength when either EVA-g-MAH or EMA-g-MAH was added to PBT.

The enhanced compatibility of the MAH modified EVA or EMA with PBT in comparison with non-MAH EVA or EMA may be expected because of the intermolecular dipole-dipole interaction between the carbonyl oxygen (δ^-) in MAH of the EVA-g-MAH or the EMA-g-MAH and the hydrogen in the hydroxyl group (δ^+) of PBT. The enhanced compatibility may be also ascribed

Table 9.1 The melting temperature of PBT/EVA and PBT/EVA-g-MAH blends (reprinted from ref. [23] with permission from Wiley)

Contents of EVA (wt.%)	T_m (H)[a] (°C)	T_m (L)[a] (°C)	Contents of EVA-g-MAH (wt.%)	T_m (H)[a] (°C)	T_m (L)[a] (°C)
0	223.4 ± 0.05	213.5 ± 0.04	0	223.4 ± 0.03	213.5 ± 0.04
20	222.4 ± 0.01	212.5 ± 0.02	20	222.9 ± 0.05	212.6 ± 0.04
40	222.2 ± 0.02	212.5 ± 0.02	40	222.0 ± 0.03	212.2 ± 0.04
50	222.4 ± 0.05	212.7 ± 0.05	50	221.5 ± 0.02	213.2 ± 0.05
60	222.3 ± 0.03	212.7 ± 0.05	60	221.2 ± 0.02	212.8 ± 0.04
80	221.0 ± 0.03	212.7 ± 0.03	80	220.7 ± 0.05	213.1 ± 0.03

[a] The H and L parentheses denote the higher-melting crystal and the lower-melting crystal, respectively. For example, T_m (H) indicates the melting point of higher-melting crystal of PBT.

to the potential reactivity of MAH with the hydroxyl ends of PBT to form the desired compatibilizer, a graft copolymer of the two component polymers, PBT-g-EMA or PBT-g-EVA.[23] The chemical aspects for the reactive compatibilization in the PBT/EVA blend will be described in more detail in next session.

9.2.2 Reactive compatibilization of the PBT/EVA blend

Blends of PBT and EVA can be prepared by reactive compatibilization of PBT and EVA by MAH. For a typical melt grafting,[25] EVA is dried prior to use in an oven for a given time (say, 5 h) at mild temperature (i.e. 70°C). The EVA can be functionalized in the presence of MAH and dicumyl peroxide (DCP) using an intensive mixer such as a plasticorder equipped with cam rotors. The melt grafting reaction is usually carried out at the set temperature (say, 175°C) for a given reaction time (i.e. *ca.* 10 min). EVA is mixed with MAH before adding DCP for inhibiting pre-crosslink of EVA. The concentration of MAH can be varied from 0.5 to 3.0 phr, and that of DCP from 0.1 to 0.4 phr. Torque–time behaviors are recorded as a measure of grafting reaction and crosslinking reaction. The formation of PBT-g-EVA copolymer as an in situ compatibilizer can be identified by the reaction of hydroxyl groups and/or carboxylic groups at the chain ends of PBT and MAH grafted onto EVA in the presence of DCP as an initiator. The amounts of the MAH grafted onto EVA in the presence of DCP are dependent on the concentrations of MAH and DCP, which affect final torque values in the torque–time behaviors because of the competitive reaction of the grafting and crosslinking of EVA (see Fig. 9.1).[25]

When EVA is blended with PBT, the in situ compatibilizer, i.e. PBT-g-EVA, is obtained from the reaction of MAH grafted onto EVA and the hydroxyl groups and/or carboxylic groups at the chain ends of PBT. The PBT-g-EVA in the blend can be confirmed from the PBT separated by extraction using Fourier-Transform infrared (FTIR) spectrometer.

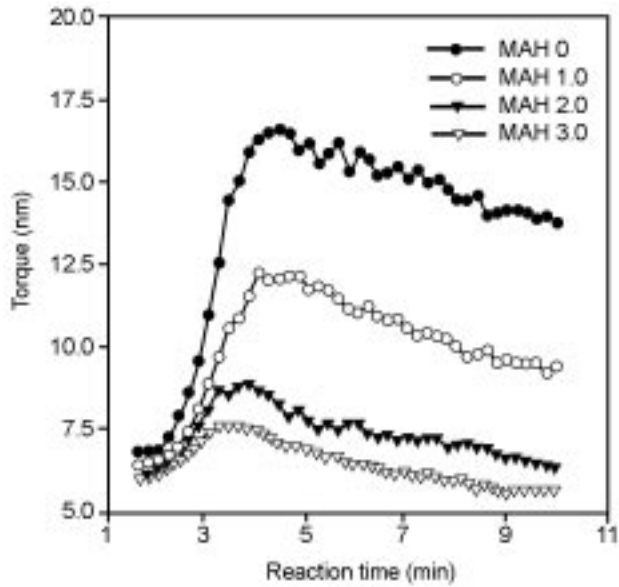

9.1 Rheographs of EVA as a function of MAH concentration (DCP, 0.1 phr) (reprinted from ref. [25] with permission from Elsevier).

Figure 9.2 shows the Izod impact strength of the blends of PBT with EVA-g-MAH as a function of MAH and DCP concentration. The Izod impact strength of the PBT/EVA-g-MAH blends is increased with increasing the concentration of MAH for a given concentration of DCP, but it is slightly decreased when 3.0 phr of MAH is added. In general, the Izod impact strength of the PBT/EVA (80/20) blend appears to a slight decrease in comparison with that of the pure PBT, whereas that of PBT/EVA-g-MAH (80/20) blends shows about three-fold increase. The result is surely attributed to the fact that the formation of the PBT-g-EVA copolymer has been achieved in the blend system. The scanning electron microscopy (SEM) micrographs also showed that the particle size of the dispersed phase (MAH grafted EVA) is reduced from about 5–10 to about 0.51 μm due to the reactive compatibilizing effects when EVA-g-MAH obtained at a higher concentration of DCP is blended with PBT.[25]

The grafting yield and the gel content during the reactive compatibilization processes are higher at higher DCP content. The mechanical properties of crosslinked polymeric materials are usually improved with the degree of crosslinking. As a result it was noticed that the flexural strength of the PBT-EVA-g-MAH blend is apparently affected by the crosslinked components of EVA-g-MAH, while the tensile strength is not. The tensile strength decreased but flexural strength increases with the increasing gel contents and grafting yield.[26]

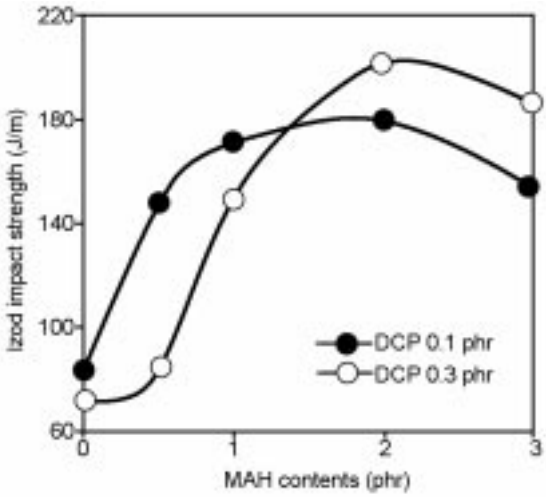

9.2 Impact strength of PBT/MAH-grafted EVA (80/20) as a function of MAH and DCP concentration (at 23°C) (reprinted from ref. [25] with permission from Elsevier).

Reactive compatibilization by the formation of in-situ grafting of PBT with EVA-g-MAH takes place competitively and simultaneously with the cross-linking of EVA and the grafting of MAH onto EVA. The maximum formation of the PBT-g-MAH-EVA takes place at a certain MAH content, producing the best reactive compatibilization in the PBT-EVA-g-MAH blend and thus the highest mechanical properties. The reactive compatibilzation of PBT and EVA-g-MAH can be also applied to other PBT-containing blend systems such as PBT/Nylon blend system.[27]

9.3 PBT/organoclay nanocomposite

As mentioned in the Introduction, the further property improvement of PBT can be done by the PLS technique, especially by the polymer melt intercalation method. In this session, we discuss on the preparation and characterization of PBT/organic montmorillonite (MMT) (PBT/organoclay) nanocomposites using three kinds of organoclays, each possessing different ammonium cations, in order to see their effects on the morphology of the PBT hybrids.[28] Table 9.2 shows the related structure information of three typical kinds of commercial organoclays produced by Southern Clay, Texas, USA (whose trade names are Cloisite 6A, Cloisite 10A and Cloisite 30B).

In addition, epoxy resin can be added as a third component in order to improve the dispersion state of the organoclay in the PBT matrix. Poly-(bisphenol A-*co*-epichlorohydrin), a glycidyl end-capped epoxy resin are usually used.

Table 9.2 Structural data for three kinds of organically modified MMT clays (organoclays) (reprinted from ref. [28] with permission from Wiley-VCH)

Organoclay	Ammonium cation[a]	XRD peak position (2θ) (°)	Basal spacing (001) (nm)
Cloisite 6A	$(CH_3)_2(HT)_2N^+$	2.49, 4.72	3.57
Cloisite 10A	$(CH_3)_2(HT)(CH_2C_6H_5)N^+$	4.52	2.00
Cloisite 30B	$(CH_3)(T)(CH_2CH_2OH)_2N^+$	4.73	1.88

[a]T = tallow (65% C18, 30% C16, 5% C14), HT = hydrogenated tallow.

9.3.1 Dispersion of organoclays in a PBT matrix

Figure 9.3 shows the X-ray diffraction (XRD) results of the PBT/organoclay hybrids containing 3 wt.% of organoclay. It can be seen that the results of the XRD analyses are dependent on the kind of organoclay used. The two original peaks of Cloisite 6A (at about 2.49° and 4.73°) remain in PBT/Cloisite 6A (2.44°, 4.93°), indicating that little or no intercalation has occurred. For PBT/Cloisite 30B, the original peak of the Cloisite 30B (at 4.73°) has shifted to 2.44°, meaning that the PBT has intercalated in the gallery of the silicate layers. The XRD pattern of PBT/Cloisite 10A shows a shoulder around 2.35°, indicating that the Cloisite 10A was partially exfoliated in the PBT matrix.[29,30]

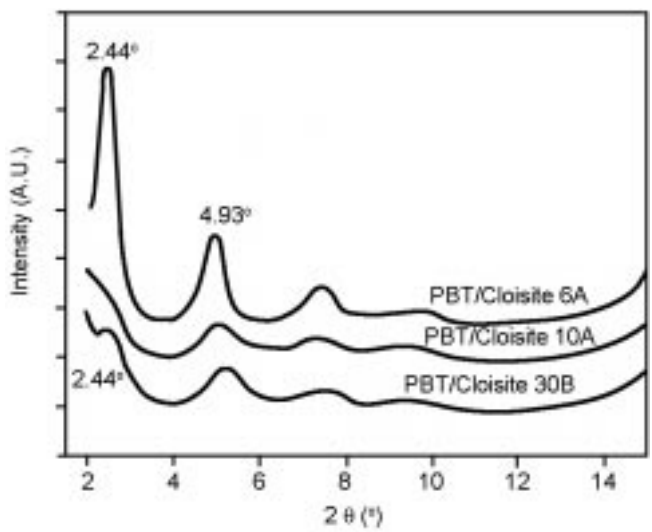

9.3 XRD patterns of PBT/organoclay nanocomposites containing different organoclays (reprinted from ref. [28] with permission from Wiley-VCH).

PBT/Cloisite 10A shows the finest dispersion of the silicate particles in the PBT matrix, based on the TEM images with lower magnification. The primary particles of Cloisite 10A have been partially exfoliated into single layers and thin multi-layer stacks which are disorderly and uniformly dispersed in the PBT matrix. The PBT/Cloisite 6A system shows the largest organoclay agglomerates and exhibits almost no further intercalation of PBT, consistent with the XRD analysis, while the PBT/Cloisite 30B system shows an intercalated structure with a basal spacing higher than 30nm, again in agreement with the XRD measurements. The difference between Cloisite 6A, 10A and 30B comes from the ammonium cations located in the gallery of the silicate layers. With two bulky tallow groups, the ammonium cations present in Cloisite 6A are the most hydrophobic, while those in Cloisite 30B are the most hydrophilic with their two hydroxyethyl groups.[28]

In order for the polymer to fully wet and intercalate the organic MMT tactoids, it is imperative that the surface polarities of the polymer and organic MMT be matched.[31] Polar-type interactions are also critical for the formation of intercalated and especially exfoliated nanocomposites via polymer melt intercalation.[32] Cloisite 6A shows the biggest initial gallery spacing (about 3.5 nm), allowing for easier intercalation of the PBT chains, but is too hydrophobic and does not match the polarity of PBT. Furthermore, lack of strong polar interactions between the ammonium cations present in Cloisite 6A and the PBT chains further discourages PBT intercalation. For these reasons, Cloisite 6A dispersed poorly, with large agglomerates present, and failed to form a nanocomposite when introduced into the PBT matrix.

Due to the existence of hydroxyl groups, the methyltallowbis-2-hydroxyethyl ammonium cation in the Cloisite 30B interlayer has strong polar interaction with the carboxyl groups present in PBT, favoring the intercalation of PBT chains and the formation of PBT/Cloisite 30B nanocomposites. However, the introduction of these polar hydroxyl groups also enhances the interaction of the ammonium cation with the silicate surface. As a result, replacement of the surface contacts by PBT chains will be less favorable, impeding the extensive intercalation and further exfoliation of Cloisite 30B in a PBT matrix.

It is expected that the moderate surface polarity of Cloisite 10A is responsible for the formation of a partially exfoliated PBT nanocomposite. In comparison to Cloisite 6A, the replacement of one hydrogenated tallow group by a benzyl group gives Cloisite 10A the proper hydrophobicity and compatibility with PBT, which in turn favors extensive intercalation. Furthermore, the lack of strong polar groups bound to the ammonium cation of Cloisite 10A ensures a relatively weak interaction between the ammonium cation and the silicate layers, make it possible to more readily delaminate the Cloisite 10A. It is again seen that compatibility and optimum interactions between polymer matrix, organic modifiers and the silicate layer surface itself are crucial to the formation of intercalated and especially exfoliated PLS nanocomposite.[33]

9.3.2 Effect of the addition of epoxy resin on the morphology of PBT/organoclay hybrids

As stated above, the formation of PLS nanocomposites in melt intercalation can be achieved by adequately matching the surface polarity and interactions of the organoclay and the polymer used. There are, however, too many cases where the organoclay and the polymer lack the compatibility for effective PLS nanocomposite formation. To realize nanoscale dispersion of such systems, a third component can be added in melt processing as a compatibilizer or a swelling agent,[31,34–36] in order to assist intercalation of the polymer chains. This seems to be a promising technique for nanocomposite formation.

Due to the existence of polar epoxy groups, epoxy resins can easily intercalate into the galleries of organoclay.[29,37] Epoxy resin is also miscible with PBT at temperatures above 210ºC with high agitation.[38] Based on these considerations, 2 wt.% of epoxy resin was added during melt blending of PBT with organoclay in order to investigate its effect on the dispersion state of the PBT/organoclay nanocomposites. Comparing PBT/Cloisite 6A with PBT/epoxy/Cloisite 6A, no obvious differences exist except that the average particle size of Cloisite 6A is marginally smaller in the presence of the epoxy resin. In both cases, the particles of Cloisite 6A are phase-separated from the PBT matrix, with almost the same basal spacing as the original silicate layers. Epoxy resin is ineffective in aiding the intercalation of PBT chains into the silicate galleries of Cloisite 6A.

The partially delaminated Cloisite 10A particles are larger in size, consisting of more silicate layers, and dispersed less uniformly than in the absence of epoxy resin. This indicates that the presence of epoxy resin in a PBT/Cloisite 10A nanocomposite disrupts the extensive intercalation of PBT into the silicate galleries, as well as subsequent exfoliation.

In contrast to the PBT/Cloisite 6A and PBT/Cloisite 10A systems, adding epoxy resin to the PBT/Cloisite 30B nanocomposites is an effective way to improve the nanostructure of the corresponding hybrids. The XRD pattern also indicates a high degree of intercalation with layer spacings higher than 4–5 nm, and/or exfoliation of the Cloisite 30B silicate layers.

9.4 EVA/organoclay nanocomposite

EVA/organic layered silicate nanocomposites can be also prepared by melt intercalation method.[39] Alexandre and Dubois[40] found that nanocomposites were only formed when EVA was melt-blended at 130ºC with nonfunctionalized organoclay, such as MMT exchanged with dimethyldioctadecyl ammonium. Zanetti *et al.*[41] prepared EVA nanocomposites with fluorohectorite-like synthetic silicate exchanged with octadecylammonium and studied their thermal behaviors.

9.4.1 Dispersion of organoclays in EVA matrix

Figure 9.4 shows the XRD patterns of the EVA/organoclay hybrids containing 3 wt.% of organoclays. In contrast to the Cloisite 6A, the EVA/Cloisite 6A hybrid shows no peak at 2.49º, and the peak at 4.72º has shifted to 4.31º, indicating the intercalated and even partially exfoliated hybrid structure. The XRD pattern of the EVA/Cloisite 30B hybrid shows almost no peak, meaning a high degree of intercalation with layer spacings higher than 4–5 nm and/or exfoliation of the silicate layers in the EVA matrix. For the EVA/Cloisite 10A hybrid, the original peak of the Cloisite 10A at about 4.6º still remains, but a new peak trace is observed at about 2º, indicating only partially intercalated structure of the EVA/Cloisite 6A hybrid.

In general, the outcome of polymer melt intercalation is determined by the interplay of entropic and enthalpic factors.[42] The confinement of the polymer chains inside the silicate galleries results in a decrease in the overall entropy of the polymer chains, and the increased conformational freedom of the tethered ammonium cations compensates the entropy loss as the silicate layers separate with each other. However, the small increase in the gallery spacing does not affect the total entropy change; rather, the total enthalpy will drive the intercalation. The enthalpy of mixing has been classified into two components: the interaction between polymer and ammonium cations and the interaction between the layered polar silicates and the polymer chains. In most conventional organomodified silicates, the tethered ammonium cations are apolar. The apolar interactions between the polymer and ammonium cations are unfavorable to the

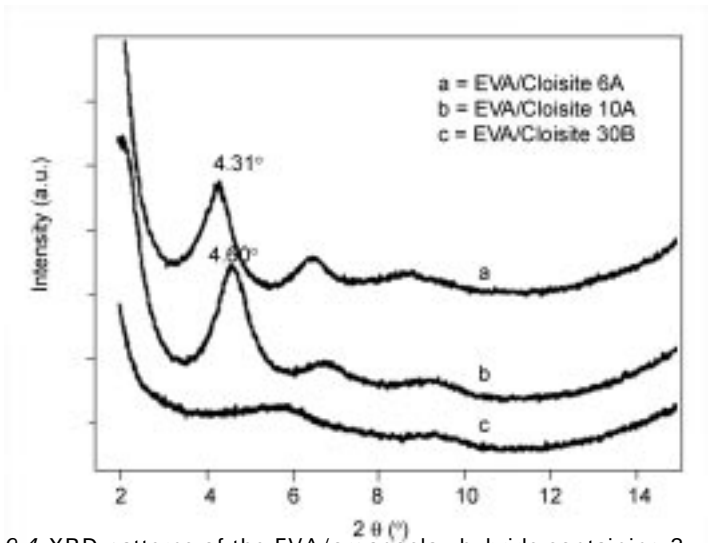

9.4 XRD patterns of the EVA/organoclay hybrids containing 3 wt.% of organoclay (reprinted from ref. [39] with permission from Wiley).

polymer melt intercalation. In such cases, the enthalpy of mixing can be rendered favorable by the establishment of polar polymer-silicate surface interactions.

The above theoretical concepts can be used to explain the results of the EVA/organoclay hybrids. With two bulky tallow groups, the ammonium cations present in the Cloisite 6A are the most hydrophobic. The biggest initial gallery spacing (*ca*. 3.57 nm) and the related weak interaction between the silicate layers of Cloisite 6A allow for easier intercalation of the EVA chains. The consequent expansion of the gallery and especially the partial exfoliation of the silicate layers compensate the entropy loss of the chain intercalation by the freedom of ammonium cations. On the other hand, the polar interactions between the carboxyl group of EVA and the silicate layers are necessary to drive the intercalation of EVA chains and partial exfoliation of the silicate layers. In this sense, the failure of PP and low density polyethylene (LDPE) to form nanocomposites with organoclays was reported to be in part due to the lack of polar interactions between the apolar polymer and the silicate layers.[43]

In contrast to the Cloisite 6A, the ammonium cations in Cloisite 30B contain two hydroxyethyl groups. The driving force of the intercalation and exfoliation for the EVA/Cloisite 30B hybrid should originate from the strong polar interaction between the carboxyl groups present in EVA and hydroxyl groups of the ammonium cations.

The hydrophobicity of the Cloisite 10A is in between those of the Cloisite 6A and the Cloisite 30B. In comparison to the Cloisite 30B, there are no strong polar interactions between EVA and ammonium cations of the Cloisite 10A, and the interlayer spacing of the Cloisite 10A is smaller than that of the Cloisite 30B. Thus, it is difficult for the EVA chains to intercalate into the galleries of Cloisite 10A, and EVA can form only partially intercalated hybrids with Cloisite 10A.

9.4.2 Nanostructure of EVA-g-MAH/organoclay hybrid

Figure 9.5 shows the XRD patterns of the EVA-g-MAH/Cloisite 6A and the EVA/Cloisite 6A hybrids, respectively. It is seen that the dispersion states of the Cloisite 6A in the EVA-g-MAH matrix become much better than those in the EVA matrix. The original peaks of the Cloisite 6A at around 2.49º and 4.72º have shifted to 2.23º and 4.45º, respectively, indicating an intercalated structure of the EVA/Cloisite 6A hybrid. However, the XRD pattern of the EVA-g-MAH/Cloisite 6A hybrid exhibits only one relatively weak peaks at lower 2θ of 2.17º. Therefore, the Cloisite 6A layers in the EVA-g-MAH matrix should be expected to intercalate with high degree and even partially exfoliated.

For the EVA/Cloisite 10A hybrid, the dispersion states of the Cloisite 10A in the EVA matrix have also been greatly improved by using the EVA-g-MAH instead of the EVA in the matrix. The existence of the original peak of the Cloisite 10A at around 4.6º suggests no intercalation, while the new peak at

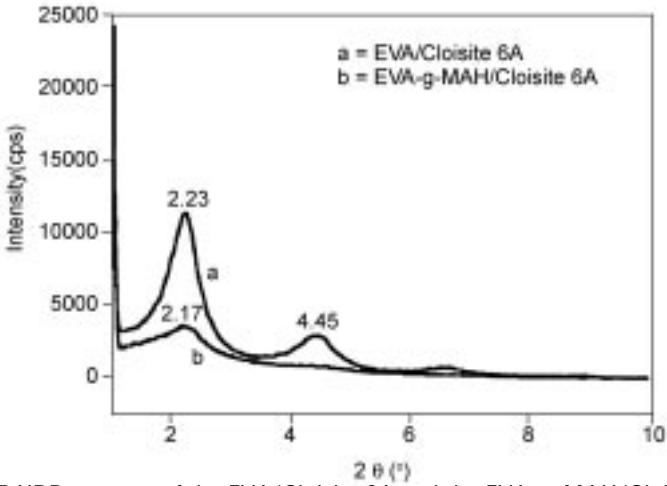

9.5 XRD patterns of the EVA/Cloisite 6A and the EVA-g-MAH/Cloisite 6A hybrids containing 3 wt.% of Cloisite 6A (reprinted from ref. [39] with permission from Wiley).

around 1.96º indicates the intercalation of EVA in the galleries of the Cloisite 10A. Thus, the EVA/Cloisite 10A hybrid exhibits only a partially intercalated nanostructure.

On the other hand, the EVA-g-MAH/Cloisite 10A hybrid exhibits a relatively small shoulder around 2.82º, with a gradual increase in the XRD strength toward low angle (Fig. 9.6). Completely exfoliated and dispersed PLS hybrids such as the nylon-clay hybrid exhibit no peak, but instead display a gradual increase in the diffraction intensity toward low diffraction angles.[44] Therefore, the silicate layers of the Cloisite 10A in the EVA-g-MAH matrix should be exfoliated and well dispersed. This was confirmed by the TEM images showing the homogeneous dispersion of completely delaminated single silicate layers in the EVA-g-MAH matrix. The effect of the grafting of MAH onto EVA on the nanostructure of the EVA/Cloisite 30B hybrid is quite different from that of the EVA/Cloisite 6A and the EVA/Cloisite 10A hybrids.

The variable effects of the grafting of MAH onto EVA on the dispersion states of organoclays in the polymer matrix can be interpreted based on the polymer melt intercalation thermodynamics. As mentioned above, the strong polar interactions between the polymer and organoclays are critical to the formation of intercalated and especially exfoliated nanocomposites. The driving force for the formation of mostly exfoliated EVA-g-MAH/Cloisite 6A nanocomposite and completely exfoliated EVA-g-MAH/Cloisite 10A nanocomposite originates from the strong hydrogen bonding between the MAH group (or —COOH group generated from the hydrolysis of the MAH group) and the oxygen groups or hydroxyl groups of the silicates.

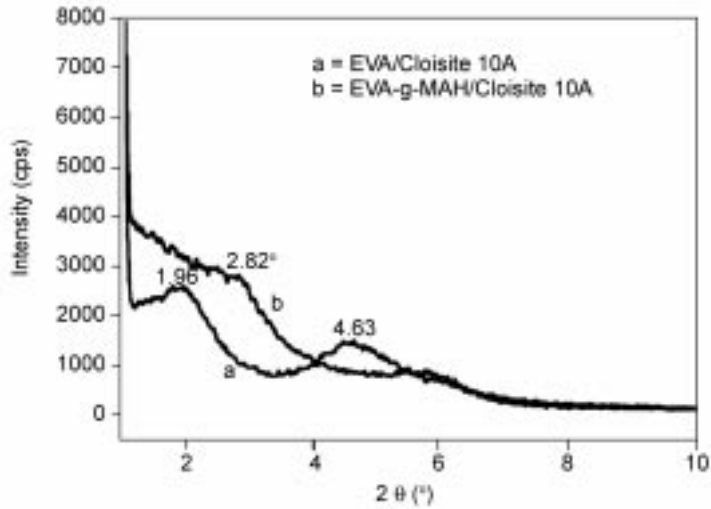

9.6 XRD patterns of the EVA/Cloisite 10A and the EVA-g-MAH/Cloisite 10A hybrids containing 3 wt.% of Cloisite 10A (reprinted from ref. [39] with permission from Wiley).

The existence of MAH groups along the EVA chains may disrupt the optimum combination of EVA with Cloisite 30B, or too strong polymer-organic silicate layer interactions may increase the frictional coefficient associated with polymer transport within the interlayer and result in slower melt intercalation kinetics.[45]

9.4.3 Effect of mixing temperature on nanostructure of EVA/organoclay hybrid

According to the kinetics of polymer melt intercalation,[46] the increasing temperature leads to higher polymer diffusion rates, thus favoring the hybrid formation. Vaia and Giannelis[42] found similar results in the preparation of polystyrene nanocomposites, in which higher anneal temperatures favor the hybrid formation. However, for EVA/organoclay hybrids, it is obvious that the high mixing temperature (175ºC) is unfavorable for well-dispersed PLS nanocomposites; even though the mixing time is 5 min longer at 175ºC than that at 140ºC, EVA/organoclay hybrids prepared at 175ºC still show worse dispersion state of the organoclays in the EVA matrix. The exfoliated silicate layers of Cloisite 30B are dispersed more uniformly when prepared at 130ºC. On the other hand, the hybrid prepared at high temperature, 175ºC, exhibits a weak peak around 6º in the XRD pattern, and less uniform dispersion of the silicate particles in the EVA matrix with a few large particles. Thus, we conclude that better dispersion states of Cloisite 30B in the EVA matrix were obtained at lower mixing temperature (130ºC).

The main reason for the above observations can be explained by the effect of an external shear on the formation of polymer/organoclay nanocomposites via melt intercalation process. The presence of an externally applied shear would promote the exfoliation of the silicate layers.[46] Huh and Balaz[47] also found that the polymer-clay mixture can readily form an exfoliated nanocomposites under shear, which can remove the bridging force between the two confining silicate layers. If the mixing temperature is lower, the torque or the shear will be higher in preparation of EVA/organoclay nanocomposites via melt intercalation at constant shear rate. This strong shear is necessary to promote the delamination of the silicate layers in the EVA matrix, due to the proper combination of the external shear and interaction between EVA and the organic silicate layers.

9.5 PBT/EVA-g-MAH/organoclay ternary nanocomposite

9.5.1 Microstructure and properties of ternary nanocomposites

Very few papers have been published on the preparation of polymer blend nanocomposite from organoclays and poly(ethylene oxide)/poly(methyl methacrylate) (PEO/PMMA) blend by the solution blending method.[48] In this section, we discuss how the blending sequence affects the microstructure of the ternary hybrid nanocomposites and especially the dispersion states of the organoclays in the polymer matrix.

In sections 9.3 and 9.4, microstructures of both the PBT/organoclay and the EVA/organoclay nanocomposites with different kinds of organoclays were discussed. It was found that the Cloisite 30B can form nanocomposites in both the PBT and the EVA-g-MAH matrix. Thus, the Cloisite 30B is selected to prepare PBT/EVA-g-MAH/organoclay temary nanocomposites.[49]

PBT/EVA-g-MAH/organoclay ternary nanocomposites are prepared through the melt intercalation method to obtain toughened PBT with higher tensile strength, modulus, and so on. It may be expected for the PLS hybrids based on the polymer blend system that the dispersion and migration of the silicate in the two phases will give important guides to the formation mechanism of the PLS nanocomposites.

The organoclays, PBT, and EVA pellets were dried under vacuum at 80ºC for at least 10 h before use. The ternary nanocomposite was prepared through two-step mixing in an internal mixer (Haake Rheocord Mixer) for 15 min.: first PBT, organoclay (3 wt.%) and epoxy resin (2 wt.%) to get PBT/organoclay nanocomposite, then the PBT/organoclay nanocomposite with MAH grafted EVA (EVA-g-MAH). The rotor speed was 50 rpm and the temperature was set at 230ºC. The ratio of PBT to EVA-g-MAH is 75/25 by weight. The mixed product was also injection molded to get bulk samples for characterization and property measurements.

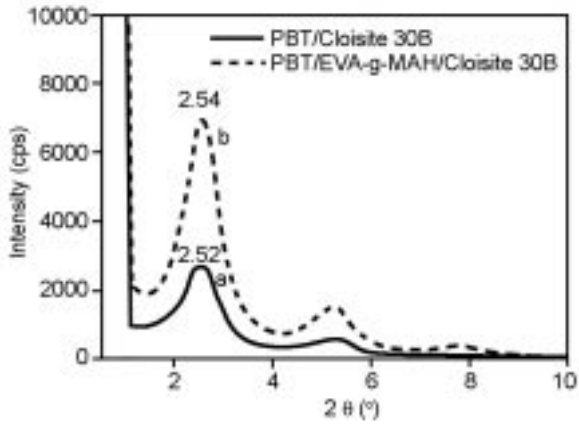

9.7 XRD patterns of the PBT/organoclay nanocomposite with epoxy (a) and PBT/EVA-g-MAH/organoclay nanocomposite (b). The amount of organoclays is 3 wt.% (reprinted from ref. [49] with permission from Wiley).

In the previous sections, we found that the organoclay can form nanocomposites in both the PBT and the EVA-g-MAH matrix. Figure 9.7 shows the XRD pattern of the PBT/EVA-g-MAH/organoclay ternary nanocomposite system with 3 wt.% Cloisite 30B. The ternary nanocomposites exhibit microstructure of intercalated PLS nanocomposites with 001 reflection moved from 4.72º (corresponding to the basal spacing of the organoclays) to around 2.54º. In all cases higher order peaks were also observed.

In order to confirm the dispersion state of organoclay and the morphology of the PBT/EVA-g-MAH blend in the presence of organoclay, TEM photomicrographs are presented in Fig. 9.8,[50] which show not only the dispersion state of the organoclay, but also the microstructure of the PBT/EVA-g-MAH blend. The TEM image in Fig. 9.8(a) shows clearly the two phase morphology (sea-island morphology) of the PBT/EVA-g-MAH blend with EVA-g-MAH domains (light portion) dispersed in the PBT matrix (dark portion). The identification of domains and the matrix was done by selective solvent etching technique. The existence of 3 wt.% organoclay influenced the dispersion of EVA-g-MAH within the PBT matrix. Comparing the TEM photomicrographs of lower magnification (2 μm scale bar) in Fig. 9.8(a) and (b), it can be seen that the ternary nanocomposite exhibits fine 'sea-island' morphology of EVA-g-MAH in the PBT matrix, as for the one without organoclay. Epoxy resin was used as a compatibilizer or a swelling agent to improve the dispersion of the organoclay in the PBT matrix as for the PBT/organoclay nanocomposite, as already mentioned in section 9.3.

In Fig. 9.7(b), the peak at 2.54º in the XRD pattern suggests the intercalated nanostructure of PBT/organoclay nanocomposite (3.5 nm basal spacing). The TEM image in Fig. 9.8(b) shows clearly that the primary particles of organoclay

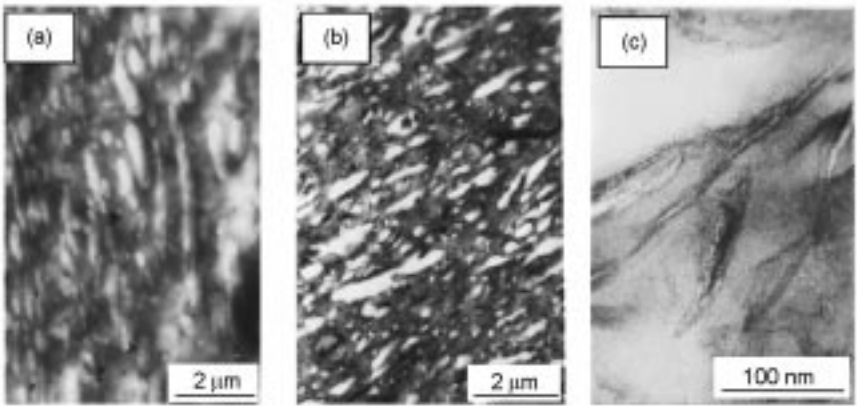

9.8 TEM images of the PBT/EVA-g-MAH blend (a) and PBT/EVA-g-MAH/organoclay nanocomposite with two different magnifications; (b) lower magnification and (c) higher magnification. The amount of organoclays is 3 wt.% (reprinted from ref. [50] with permission from VSP).

have been split to several layers of silicate crystallites dispersed uniformly in the PBT matrix with the interlayer spacing corresponding to the XRD result. Blending with EVA-g-MAH, the 001 reflection at 2.52–2.54º in the XRD pattern kept unchanged, indicating no further intercalation occurred during the second-step mixing. The TEM image in Fig. 9.8 gives further confirmation to the XRD results. More interestingly, no crystallites of organoclay migrated to the dispersed EVA-g-MAH phase during the second-step mixing as can be seen in Fig. 9.8(c) (high magnification). This is due to the strong interfacial interaction such as hydrogen-bonding among the hydroxyl group of organoclay, epoxy and PBT matrix,[28] which keeps the silicate crystallites in the PBT matrix from migrating to the dispersed EVA-g-MAH phase. The hydrogen bonding can be confirmed by FTIR spectra.

Table 9.3 gives the tensile and impact properties of the PBT/EVA-g-MAH/organoclay ternary nanocomposite as well as those of PBT and PBT/EVA-g-MAH blend.[50] It can be found that the impact strength of the ternary nanocomposite is in between that of the PBT and PBT/EVA-g-MAH blend. As shown in Fig. 9.8, the fine dispersion of elastic EVA-g-MAH in the continuous PBT phase is responsible for the remarkable impact strength improvement to the PBT.

Unfortunately, however, the impact strength of the ternary nanocomposite is lower than that of the PBT/EVA-g-MAH blend. It should be noted, however, the uniform dispersion of the intercalated organoclay in the continuous PBT phase leads to higher tensile strength and modulus of the ternary nanocomposite compared to the PBT/EVA-g-MAH blend. It was also reported that the thermal stability of the nanocomposite was improved in comparison to that of the PBT/EVA-g-MAH blends, due to the clay layer structure.

Table 9.3 Tensile and impact properties of PBT, PBT/EVA-g-MAH blend, and PBT/EVA-g-MAH/organoclay ternary nanocomposite (reprinted from ref. [50] with permission from VSP)

Sample	Tensile strength (MPa)	Elongation at break (%)	Tensile modulus (MPa)	Impact strength (J/m)
PBT	56.4	42.8	370	24.7
PBT/EVA-g-MAH	38.6	72.3	268	90.6
PBT/EVA-g-MAH/organoclay (3 wt.%)	42.4	45.6	325	65.4
PBT/EVA-g-MAH/organoclay (6 wt.%)	44.1	43.7	362	64.8

9.5.2 Effect of blending sequences

The effects of different mixing sequences were also investigated by Li *et al.*:[49]

- They attempted to mix PBT, EVA-g-MAH and organoclays in one step (Hybrid 'L-1')
- They tried mixing PBT with organoclays first, then the PBT/organoclay nanocomposite with EVA-g-MAH (Hybrid 'L-2'), (already discussed in section 9.5.1)
- They tried first preparing EVA-g-MAH/organoclay nanocomposites, then mixing with PBT to get the final nanocomposite (Hybrid 'L-3')
- They prepared the PBT/EVA-g-MAH blend first, then mixed the blend with organoclays (Hybrid 'L-4').

Table 9.4 gives the tensile and impact properties of various PBT/EVA-g-MAH/ Cloisite 30B hybrids prepared by different blending sequences. Comparing the impact strength of all the hybrids with that of PBT/EVA-g-MAH blend and pure PBT, the impact strengths of the ternary hybrids are between those of the PBT and PBT/EVA-g-MAH blend. The impact strength difference among the PBT/ EVA-g-MAH/ Cloisite 30B hybrids is related to the morphology of the blends in the presence of organoclays, and the dispersion of organoclays in the polymer matrix as well.

The fine dispersion of elastic EVAg- MAH in the continuous PBT phase is responsible for the remarkable impact strength improvement in the PBT. As for the PBT/EVA-g-MAH blend, the L-2 hybrid also shows fine two-phase 'sea-island' morphology with elastic EVA-g-MAH dispersed in the PBT/Cloisite 30B nanocomposite matrix, as already shown in Fig. 9.8. This is the reason why the L-2 hybrid exhibits higher impact strength than all the other PBT/EVA-g-MAH hybrids. Unfortunately, the impact strength of the L-2 hybrid is lower than that of the PBT/EVA-g-MAH blend. Usually, PLS nanocomposites show increased Young's modulus but simultaneously a loss in the impact strength, except in a few instances.[51] However, the uniform dispersion of the intercalated Cloisite

Table 9.4 Tensile and impact properties of PBT/EVA-g-MAH/Cloisite 30B ternary hybrids prepared through various blending sequences (reprinted from ref. [49] with permission from Wiley)

	PBT/EVA-g-MAH	L-1[a]	L-2[b]	L-3[c]	L-4[d]	PBT
Tensile strength (MPa)	38.6	38.1	42.4	39.6	38.7	58.4
Elongation at break (%)	72.3	28.2	45.6	28.0	33.0	42.8
Tensile modulus (MPa)	268	277	325	282	291	370
Impact strength (J/m)	90.6	36.4	65.4	36.9	48.7	24.7

[a] To mix PBT, EVA-*g*-MAH and organoclays in one step.
[b] To mix PBT with organoclays in the presence of epoxy first, then the PBT/organoclay nanocomposites with EVA-*g*-MAH.
[c] First to prepare EVA-g-MAH/organoclay nanocomposite, then mix it with PBT.
[d] To mix the organoclays with PBT/EVA-g-MAH blend.

30B in the continuous PBT phase leads to highest tensile strength and modulus of the L-2 hybrid compared to the PBT/EVA-g-MAH blend and three other hybrids.

The low impact strength of the hybrids L-1 and L-3 is mostly attributed to the layer-like two-phase nanostructure with large and irregular EVA-g-MAH domains and few large Cloisite 30B particles dispersed in PBT matrix. The EVA-g-MAH domains and large Cloisite 30B particles act as weak points or stress concentrators, resulting in low impact strength and tensile properties. Though the L-3 hybrid shows similar layer-like dispersion nanostructure with the L-1 hybrid, the existence of Cloisite 30B in the EVA-g-MAH phase makes the tensile strength a little higher than that of the L-1 hybrid.

Though the dispersion of EVA-g-MAH in the continuous PBT phase was a little disturbed after blending with the Cloisite 30B, the domain size of the dispersed phase was still smaller than that of the hybrids L-1 and L-3. Therefore, the L-4 hybrid exhibits slightly higher impact strength than that of the hybrids L-1 and L-3.

9.6 Conclusions

PBT is a good material for the automobile industry. For instance it can be used for wheel covers, components of door handles, and distributor caps because of its chemical resistance, thermal stability, and hydrolytic stability.[52] The hydrophobicity of the organically modified MMT and the polar interactions between the ammonium cations, silicate layers, and the PBT itself are critical to hybrid formation. As it possesses the proper hydrophobicity and compatibility with PBT, Cloisite 10A can be intercalated and partially exfoliated in a PBT matrix. Cloisite 30B, on the other hand, can only form intercalated nanocomposites with PBT, due to the strong interactions between the ammonium cation and silicate layers. Finally, PBT/Cloisite 6A systems exhibit the

morphology of traditional composites due to the high hydrophobicity and lack of compatibility between the PBT and the organoclay.

As a third component in the nanocomposite preparation, epoxy resin has varying effects on the dispersion and intercalation behavior of the three PBT/organoclay systems studied here, depending on the compatibility and polar interactions of the epoxy resin with the PBT and the organically modified silicate layers. Epoxy resin enhanced the intercalation and further exfoliation of Cloisite 30B in the PBT matrix, due to the strong hydrogen bonding interactions and even possible chemical reactions between the epoxy and the organoclay, and the compatibility between epoxy and PBT.

On the other hand, the dispersion of the organoclays in the EVA matrix depends on the hydrophobicity of the organoclays and especially the polar interactions between the silicate layers and EVA chains. For the strong hydrogen-bonding interactions between EVA and Cloisite 30B, the EVA/Cloisite 30B nanocomposite shows mostly exfoliated structure, while the EVA/Cloisite 10A hybrid can only possess a partially intercalated structure due to the lack of strong polar interactions and entropy compensation by the freedom of ammonium cations. By introducing the strong hydrogen bonding to the EVA/organoclay hybrids through grafting MAH onto EVA, the dispersion states of EVA/organoclay hybrids were greatly improved for both Cloisite 6A and Cloisite 10A hybrid systems. In the EVA-g-MAH/Cloisite 10A nanocomposite, a complete exfoliation is observed, whereas in the EVA-g-MAH/Cloisite 6A hybrid mostly exfoliated morphology is observed. Both hybrids show much better dispersion of organoclays in the EVA-g-MAH matrix than the corresponding EVA/organoclay hybrids. Though the different effects of the grafting MAH onto EVA on the dispersion of Cloisite 30B in the EVA matrix is not easily explained.

The dispersion state of organoclays in the matrix becomes worse with increasing the mixing temperature of EVA with organoclays, probably due to the decreased external shear at high temperatures, as the external shear is necessary for the nanocomposite formation.

The PBT/EVA-g-MAH/organoclay ternary nanocomposite shows much enhanced impact strength in comparison to PBT without severely sacrificing the tensile properties of PBT, due to fine ‘sea-island’ morphology of EVA-g-MAH in the continuous PBT/organoclay nanocomposite matrix, like the PBT/EVA-g-MAH blend. The strong polar interaction between PBT and organoclay in the presence of the compatibilizer, epoxy resin, keeps the organoclay from migrating to the dispersed EVA-g-MAH phase.

PBT/EVA-g-MAH/organoclay ternary nanocomposite also shows enhanced thermal stabilities compared to its pristine counterpart, due to the clay layer structure, which restricts the mobility of the small molecules produced during degradation.

For the PBT/EVA-g-MAH/organoclay intercalated ternary nanocomposites, the mixing sequence significantly affects the microstructure of the prepared

hybrids, the dispersion states of the organoclays in the polymer matrix, and thus the mechanical properties of the hybrids. To mix the PBT/Cloisite 30B nanocomposite with elastic EVA-g-W is the best way to prepare PBT/EVA-g-MAH/organoclay ternary nanocomposites with the best mechanical properties and desirable morphology. With the fine 'sea-island' morphology of the EVA-g-MAH in the continuous PBT/Cloisite 30B nanocomposite matrix, like the PBT/EVA-g-MAH blend, this PBT/EVA-g-MAH/organoclay hybrid exhibits higher tensile and impact strength than those of all the other hybrids that showed irregular morphology. The strong polar interaction between PBT and Cloisite 30B in the presence of the compatibilizer, epoxy resin, keeps the Cloisite 30B from migrating to the dispersed EVA-g-MAH phase.

Though the PBT nanocomposite was found to possess good mechanical and thermal properties, the application of PBT nanocomposite has not been revealed yet in detail. Recently, however, the potential application of PBT nanocomposites as high strength fibers was reported. Chang *et al.*[53,54] synthesized PBT nanocomposite from dimethyl terephthalate (DMT) and butane diol (BD) by using an in-situ interlayer polymerization approach. The PBT nanocomposites were melt spun at different organoclay contents to produce monofilaments. The hybrids were extruded with various draw ratios (DRs) to examine the tensile mechanical property of the fibers. At DR = 1, the ultimate tensile strength of the hybrid fibers increased with the addition of clay up to a critical content and then decreased.[54] However, the initial modulus monotonically increased with increasing amount of organoclay in the PBT matrix. When the DR was increased from 1 to 6, for example, the strength and the initial modulus values of the hybrids containing 3 wt.% organoclay decreased linearly. Table 9.5 shows the results.

The report may find some potential application of PBT nanocomposites as high strength fibers after property optimization. It is also expected that the PBT nanocomposite will replace PBT, though this requires improved thermal and mechanical properties in comparison to PBT for the applications where general purpose grade PBT cannot be used. In particular, the automobile industry may be expected to be one of the important future markets for PBT nanocomposites.

Table 9.5 Effect of the DR on the tensile properties of PBT nanocomposite fibers (reprinted from ref. [54] with permission from Elsevier)

	Ultimate Strength (MPa)			Initial Strength (GPa)		
Clay (wt.%)	DR = 1	DR = 3	DR = 6	DR = 1	DR = 3	DR = 6
0 (pure PBT)	41	50	52	1.37	1.49	1.52
3	60	35	29	1.76	1.46	1.39

9.7 Acknowledgements

The work was supported by the National Research Laboratory Program and the Center for Integrated Molecular Systems.

9.8 References

1. *Plast. World*, 1985, **8**, 122.
2. Mock J A, *Plast. Eng*., 1983, **2**, 13.
3. Kang T K, Kim Y, Cho W J, Ha C S, *Polym. Eng. & Sci.*, 1996, **36**(20), 2525.
4. Radusch H J, Androsch R, *Die Angew. Makro. Chem.*, 1994, **214**, 179.
5. Runt J P, Miley D M, Zhang X, Gallagher K P, *SPE ANTEC Tech. Papers*, 1992, **38**, 366.
6. Bohn L, *Angew. Makromol. Chem.*, 1971, **20**, 129.
7. Bohn, L, *Adv. Chem. Ser.*, 1975, **142**, 66.
8. Cartasegna S, *Rubber Chem Technol*., 1986, **49**, 722.
9. Steinkamp D G, Grail T J, US Patent 3,862,265 (Exxon Research and Engineering), 1975.
10. Gaylord N G, US Patent 4,506,056 (Gaylord Research Institute), 1985.
11. Gaylord N G, Mehta R, *J Polym Sci, Part A: Polym Chem.,* 1988, **26,** 1189.
12. Bier P, Rempel D, *SPE ANTEC Tech. Papers*, 1988, **34**, 1485.
13. Yates J B, U.S Patent 4,619,971.
14. Wefer J M, U.S Patent 4,485,212.
15. Immirzi B, Laurienzo P, Malinconico M, Martuscelli E, *J. Polym. Sci., Part A: Polym. Chem.*, 1989, **27**, 829.
16. Laurienzo P, Malinconico M, Martuscelli E,Volpe M G, *Polymer*, 1989, **30**, 835.
17. Ha C S, Choi H Y, Cho W J, *Polym. Bull.*, 1991, **25**, 185.
18. Simmons A, Baker W E, *Polym. Comm.*, 1990, **31**, 20.
19. Bonner J G, Hope P S, *Polymer Blends and Alloys*, Glasgow, M. J. Folkes and Blackie Acad. & Prof., 1993, pp. 46–74, and references therein.
20. Hu G H, Sun Y, Lambla M, *Polym. Eng. & Sci.*, 1996, **36**, 676.
21. Sun Y J, Hu G H, Lambla M, Kotlar H K, *Polymer*, 1996, **37**(18), 4119.
22. Vainio T, Hu G H, Lambla M, Seppala J V, *J. Appl. Polym. Sci.*, 1996, **61**, 843.
23. Kim S J, Kang C J, Chowdhury S R, Cho W J, Ha C S, *Polym. Eng. Sci*., 1997, **37**(3), 603.
24. Kim J K, Nichols M E, Robertson R E, *J. Polym. Sci., Part B: Polym. Phys*., 1994, **32**(5), 887.
25. Kim S J, Shin B S, Hong J L, Cho W J, Ha C S, *Polymer*, 2001, **42**, 4073.
26. Kim S J, Chowduhury S R, W J Cho, Ha C S, *J. Appl. Polym. Sci.*, 2003, **89**(5), 1305.
27. Kang T K, Kim Y, Cho W J, Ha C S, *Polym. Eng. Sci*., 1996, **36**(20), 2525.
28. Li X, Kang T, Cho W J, Lee J K, Ha C S, *Macromol. Rapid Commun*., 2001, **22**(16), 1306.
29. Kornmann X, Lindberg H I, Bergluad L A, *Polymer*, 2001, **42**, 1303.
30. Kawasumi M, Hasegawa N, Kato M, Usuki A, Okada A, *Macromolecules*, 1997, **30**, 6333.
31. Lebaron P C, Wang Z, Pinnavaia T J, *Appl. Clay Sci.*, 1999, **15**, 11.
32. Vaia R A, Jandt K D, Giannelis E P, *Chem. Mater*, 1996, **8**, 2628.

33. Lee S R, Park H M, Kang T, Li X, Cho W J, Ha C S, *Polymer*, 2002, **43**, 2495.
34. Reichert P, Nitz H, Klinke S, Brandsch R, Thomann R, Mulhaupt R, *Macromol. Mater. Eng.*, 2000, **275**(2), 8.
35. Galgali G, Ramesh C, Lele A, *Macromolecules*, 2001, **34**, 852.
36. Ishida H, Campbell S, Blackwell J, *Chem. Mater.*, 2000, **12**, 1260.
37. Kornmann X, Lindberg H, Bergluad I A, *Polyme*r, 2001, **42,** 4493.
38, Kim S, Jo W, Kim J, Lim S H, Choe C R, *J. Mater. Sci.*, 1999, **34**, 161.
39. Li X, Ha C S, *J. Appl. Polym. Sci*., 2003, **87**(12), 1901.
40. Alexandre M, Dubois P, *Mater Sci Eng*, 2000, **28**, 1.
41. Zanetti M, Camino G, Thomann R, Mülhaupt R, *Polymer*, 2001, **42**, 4501.
42. Vaia R A, Giannelis E P, *Macromolecules*, 1997, **30**, 7990.
43. Usuki A, Kato M, Okada A, Kurauchi T J, *J Appl Polym Sci*, 1997, **63**, 137.
44. Usuki A, Kawasumi Y, Kojima M, Fukushima Y, Okada A, Kurauchi T, Kamigaito O, *J Mater Res*, 1993, **8**, 1179.
45. Vaia R A, Jandt K D, Giannelis E P, *Chem Mater*, 1996, **8**, 2628.
46. Vaia R A, Jandt K O, Kramer E J, Giannelis E P, *Macromolecules*, 1995, **28**, 8080.
47. Huh J, Balazs A C, *Polym Mater Sci Eng*, 1999, **81**, 449, **22**
48. Kim S K, Chin I, Kim J W, Choi H J, *Polym. Mater. Sci. Eng.*, 2001, **84**, 555.
49. Li X, Park H M, Lee J O, Ha C S, *Polym. Eng. Sci.*, 2002, **42**(11), 2156.
50. Li X, Mishra J K, Seul S D, Kim I, Ha C S, *Comp. Interf*., 2004, **11**(4), 335.
51. Hoffmann B, Kressler J, Stöppelmann G, Friedrich C, Kim G M, *Colloid Polym. Sci.*, 2000, **278**, 629.
52. Parikh C J, Donatelli A A, Deanin R D, *Polym. Prepr.*, 1993, **34**, 2.
53. Chang J H, An Y U, Ryu S C, Giannelis E P, *Polym. Bull*., 2003, **51**(1), 69.
54. Chang J H, An Y U, Kim S J, Im S, *Polymer*, 2003, **44**(19), 5655.

10

Flammability and thermal stability of polymer/layered silicate nanocomposites

M ZANETTI, University of Turin, Italy

10.1 Introduction

Plastics and textiles find many uses and add greatly to the quality of modern day life. However, a major problem arises because most of the polymers on which these materials are based are organic and thus flammable. Most deaths due to fire are caused by inhalation of smoke and toxic combustion gases, carbon monoxide being the most common, and serious injuries can result from exposure to the heat involved. What is of major interest in the plastics and textiles industries is not the fact that their products burn but how to render them less likely to ignite and, if they are ignited, to burn much less efficiently. The phenomenon is termed 'flame retardance'.

Flame retardants (FR) act to break the combustion cycle, and thus extinguish the flame or reduce the burning rate, in a number of possible ways. Today, halogen-based fire retardants constitute the only effective systems able to reduce the flammability of a wide range of polymers, without forgoing the mechanical performance of the material. On the other hand, the ever increasing concern for the negative environmental effects of halogen-based fire retardant polymer materials has lead to intense activity in the search for halogen-free FR. Moreover, the 'sustainable growth' approach requires that plastic wastes are recycled as much as possible by environmentally sound recycling methods. In this respect halogen-based fire retardants increase the complexity of recycling processes since they can produce environmentally harmful toxic or supertoxic compounds in most recycling processes. This either increases the cost of recycling and/or may render negative the overall ecological balance of recycling the plastics waste.

At present, the flame retardant systems used to substitute halogens (intumescent formulation and inorganic hydroxides) are effective only at high loadings, strongly reducing the mechanical properties of the materials. Polymer layered silicate nanocomposites (PLSNs) constitute a new development in the area of flame retardants and offer significant advantages over conventional formulation where high loadings are often required.

Contrary to what many people think, PLSNs are not a recent discovery. One of the earliest systematic studies of the interaction between a clay mineral and a macromolecule dates backs to 1949, when Bower described the absorption of DNA by montmorillonite.[1] Even in the absence of X-ray diffraction (XRD) evidence, this finding implied insertion of the macromolecule in the lamellar structure of the silicate. In the case of synthetic polymers, Uskov[2] found in 1960 that the softening point of polymethylmethacrylate derived by polymerisation of methylmethacrylate was raised by montmorillonite modified with octadecylammonium, while in the following year Blumstein[3] obtained a polymer inserted in the structure of a montmorillonite by polymerising a previously inserted vinyl monomer. In 1965 Blumstein first reported the improved thermal stability of a PMMA/clay nanocomposite. He showed that PMMA inserted between the lamellae of montmorillonite clay resisted thermal degradation under conditions that would otherwise completely degrade pure PMMA.[4]

10.2 Nanocomposites and fire

In 1976 Unitika Ltd, Japan, first presented the potential flame retardant properties of polyamide 6 (PA6)/layered silicate nanocomposites. However, not until more recent studies did the serious evaluation of the flammability properties of these materials begin when Gilman *et al.* reported detailed investigations on flame retardant properties of PA6/layered silicate nanocomposite.[5] From this pioneering work many attempts have been made to study the flammability properties of polymer/layered silicate nanocomposites. A wide range of polymers has been employed to provide either intercalated or exfoliated nanocomposites, which exhibit enhanced fire retardant properties. These include various thermoplastic and thermosetting polymers, such as polystyrene (PS),[6–14] high impact polystyrene (HIPS),[13–15] poly(styrene-*co*-acrylonitrile) (SAN),[16] acrylonitrile-butadiene-styrene (ABS),[13–15,17] polymethyl methacrilate (PMMA),[14,18,19] polypropylene (PP),[6,9,12,14,15,19–22] polyethylene (PE),[14,15,19,23–27] poly(ethylene-*co*-vinylacetate) (EVA),[27–30] PA6,[9] PA66,[31] PA12,[9] epoxy resin (ER)[32] and polyurethane (PU).[33]

10.3 Flame retardant mechanism

The cone calorimeter is one of the most effective bench-scale methods for studying the fire retardants.[34] Fire-relevant properties such as the heat release rate (HRR), peak of HRR, smoke production, CO_2 and CO yield, are vital to the evaluation of the fire safety of materials. Heat release rate, in particular peak HRR, has been found to be the most important parameter to evaluate fire retardants. A typical cone calorimeter experimental result for a nanocomposite is reported in Fig. 10.1 where are reported the HRR plots for pure EVA; EVA with 5 wt.% of fluorohectorite exchanged with aminododecanoic acid, a micro-

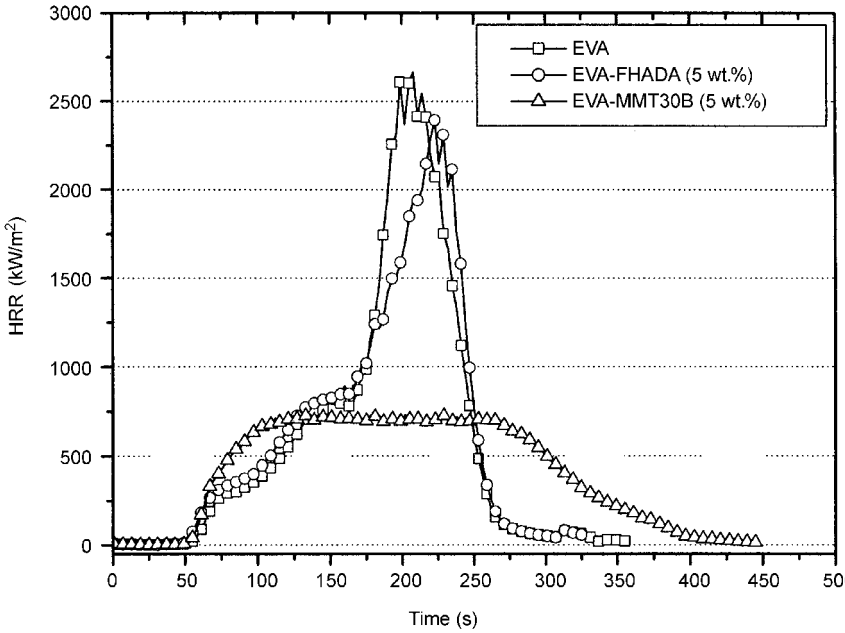

10.1 Heat release rate (HRR) plots for pure EVA; EVA with 5 wt.% of fluorohectorite exchanged with aminododecanoic acid, a microcomposite; and EVA with 5 wt.% of montmorillonite exchanged with methyl, tallow, bis-2-dihydroxyethylammonium, a nanocomposite, at a heat flux of 50 kW/m^2. Reprinted with permission from ref. [30]. Copyright © (2005) American Chemical Society.

composite; and EVA with 5 wt.% of montmorillonite exchanged with methyl, tallow, bis-2-dihydroxyethylammonium, a nanocomposite, at a heat flux of 50 kW/m^2. The nanocomposite shows a 78% lower peak HRR than the pure polymer and 75% lower than the microcomposite.

The cone calorimetry flammability data for a variety of PLSNs are shown in Table 10.1. The most relevant result is the delta that represents the lowering in the peak of HRR in %. The cone calorimetry data show that the peak HRR was reduced significantly for intercalated, exfoliated and intercalated/exfoliated nanocomposites with low silicate mass fraction. indicating that the lowering in peak HRR arising from PLSN is a general phenomenon, which reduced the flammability of both thermoplastic and thermoset resins.

The clearest proof of flame retardancy has been obtained with cone calorimetry. As a consequence, most studies done to understand the mechanism are dedicated to the reduction in peak of HRR. Most of the mechanisms proposed to explain the flame retardance attribute the reduction in heat release rate to the formation of a protective surface layer consisting of clay layers created during polymer ablation. Gilman first proposed the formation, during

Table 10.1 Cone calorimeter data

Polymer matrix	Filler (%)	Morphology	Cone heat flux (kW)	Peak HRR (kW/m^2)	Delta (%)	Ref.
ABS	MMT/3MC16 (2, 5, 10)	Exfoliated/intercalated	50	832, 772, 697	23, 28, 35	17
ABS	MMT/3MC16 (5)	Intercalated	50	772	28	56
EVA19	MMT/MOHT (2, 5, 10)	Exfoliated	50	1210, 584, 436	54, 78, 83	30
EVA	MMT/3MC16 (5)	Intercalated	50	640	40	29, 62
EVA19	MMT/MOHT (3, 5, 10)	Unknown	50	860, 780, 630	44, 50, 60	62
EVA18	MMT/M2HT (5)	Intercalated	35	574	63	27
EVA28	MMT/M2HT (5)	Intercalated	35	493	78	27
ER (anhydride)	MMT/MOHT (5)	Exfoliated/intercalated (tethered)	50	1063	13	32
ER (anhydride)	MMT/M2HT (5)	Exfoliated/intercalated	50	984	19	32
ER (aromatic amine)	MMT/M2HT (5)	Exfoliated/intercalated	50	1289	0	32
PA6	MMT/ ? (2, 5)	Exfoliated	35	686, 378	32, 63	9
PA6	MMT/3MC16 (2)	Exfoliated/intercalated	50	681	39	31, 57
PA66	MMT/? (2, 5, 10)	Exfoliated	35	496, 335, 209	38, 58, 74	31
PA12	MMT/ ? (2)	Exfoliated	35	1060	38	9
PE	MMT/M2HT(3)	Immiscible/intercalated	35	1340	35	24
PE	MMT/JSAc (2, 5, 10, 15)	Exfoliated	35	670, 620, 540, 390	54, 58, 63, 73	25
PE-g-MA	MMT/VB16 (3)	Immiscible/intercalated	35	1380	34	24
PE-g-MA	MMT/MOHT (3)	Immiscible/intercalated	35	1450	31	24
PE-g-MA	MMT/Si18 (3)	Immiscible/intercalated	35	1500	30	24
PE/PE-g-MA	MMT/M2HT	Intercalated	35	620	70	27
PMMA	MMT/Bz16 (3)	Intercalated	50	676	28	18
PMMA	MMT/Allyl16 (3)	Exfoliated/intercalated	50	744	20	18
PMMA	MMT/Bz16 (3)	Intercalated	50	676	28	18
PP	MMT/VB16 (3)	Immiscible/intercalated	35	1246	24	12
PP	MMT/2M2C18 (2, 5, 10)	Immiscible/intercalated	35	870, 459, 357	23, 60, 69	22
PP-g-MA	MMT/M2HT (2, 4)	Intercalated	35	450, 381	70, 75	6
PP-g-MA	MMT/MOHT (5)	Exfoliated/intercalated	35	382	48	21

Table 10.1 Continued

Polymer matrix	Filler (%)	Morphology	Cone heat flux (kW)	Peak HRR (kW/m^2)	Delta (%)	Ref.
PP-g-MA	MMT/3MC18 (5)	Exfoliated/intercalated	35	224	69	21
PS	MMT/VB16 (1, 3, 5)	Exfoliated/intercalated (tethered)	35	752, 584, 534	27, 43, 48	10
PS	MMT/OH16 (1, 3, 5)	Exfoliated/intercalated	35	766, 502, 429	25, 51, 58	10
PS	MMT/P16 (1, 3, 5)	Intercalated	35	749, 586, 496	27, 43, 51	10
PS	SMM/VB16 (0,1; 0,5, 1, 3, 5)	Exfoliated/intercalated (tethered)	35	758, 807, 785, 595, 444	26, 21, 23, 42, 57	11
PS	MMT/VB16 (0,1; 0,5, 1, 3, 5)	Exfoliated/intercalated (tethered)	35	890, 771, 752, 584, 534	13, 25, 27, 43, 48	11
PS	SMM/P18 (3)	Intercalated	35	556	46	11
PS	MMT/P18 (3)	Intercalated	35	566	45	11
PS	SMM/M2HTB (0,1; 0,5, 1, 3, 5)	Intercalated	35	793, 814, 806, 642, 517	22, 20, 21, 37, 49	11
PS	MMT/M2HTB (0,1; 0,5, 1, 3, 5)	Intercalated	35	593, 697, 663, 449, 412	42, 32, 35, 56, 60	11
PS	MMT/Sb18 (3)	Immiscible/intercalated	35	1111	20	12
PS	MMT/StyTro (3)	Exfoliated/intercalated	35	960	32	9, 53
PS	MMT/M2HT (3)	Intercalated	35	567	48	9
PS	MMT/M2HT (2, 5, 10)	Exfoliated/intercalated	50	847, 537, 379	55, 72, 80	7
PS	MMT/M2HT (1, 5, 10)	Intercalated	35	1079, 555, 446	17, 57, 65	8
PS	FH/M2HT (1, 5, 10)	Intercalated	35	910, 428, 513	29, 67, 60	8
SAN	MMT/MOHT (3, 6, 8, 11)	Exfoliated/intercalated	35	450, 420, 345, 320	10, 16, 30, 36	16
PU	MMT/M3C16 (5)	Intercalated	35	472	50	33

Note: MMT: Montmorillonite, FH, Fluorohectorite, SMM: Synthetic mica, Allyl16: hexadecylallyldimethyl ammonium, Bz16: hexadecylvinylbenzyldimethyl ammonium, MHTB: Hydrogenated tallow dimethylbenzylammonium, M2HT: Dimethyl dehydrogenated tallow ammonium, MOHT: Methyl tallow bis2hydroxyethyl ammonium, 3MC16: hexadecyltrimethyl ammonium, 3MC18: octadecyltrimethyl ammonium, 2M2C18, Dioctadecyldimethyl ammonium, JSAc: N-g-trimethoxylsilanepropyl) octadecyldimethylammonium, OH16: *N,N*-Dimethyl-*n*hexadecyl-(4-hydroxymethylbenzyl) ammonium, P16: n-Hexadecyl Triphenylphosphonium, P18: stearyltributylphosphonium, Si18: [3-(trimethoxysilyl) propyl] octadecyldimethy ammonium, StyTro: Styrene tropylium (styrylcycloheptatriene), Sb18: triphenylheadecylstibonium, VB-16: *N,N*-Dimethyl-*n*-hexadecyl-(4-vinylbenzyl) ammonium.

combustion, of a multilayered carbonaceous-silicate structure arising from recession of the polymer resin from the surface by pyrolysis with de-wetted clay particles left behind.[5] This multilayered carbonaceous-silicate structure appears to enhance the performance of the char through structural reinforcement acting as an excellent insulator and mass transport barrier, slowing the escape of the volatile products generated during decomposition. Thermal protection via ablation is achieved through a self-regulating heat and mass transfer process involving an insulator with low thermal conductivity and the sacrificial pyrolysis and concomitant formation of a tough refractory char on the insulator surface.

The formation of this high-performance carbonaceous-silicate char was first observed by studying the combustion residues using transmission electron microscopy (TEM) and X-ray diffraction (XRD).[9] The structure of the combustion residue of a PE/clay nanocomposite has been observed in scanning electron microscopy (SEM):[23] at nanoscale the residue resulted in a net-like structure of clay platelets and char, while at microscale showed a sponge-like structure, similar to those obtained from combustion of intumescent FR systems.[35]

In support of these results, studies of PA6/MMT nanocomposites by Vaia *et al.* found a similar fire retardancy enhancement through char formation.[36] Specifically, the nanocomposites showed the formation of a tough ceramic passivation layer on the polymer surface, when exposed to solid-rocket motor exhaust and plasma environments.

This effect is particularly surprising for non char forming polymers, such as EVA, PE, PP, etc. where, at the end of combustion, the residue is usually composed of 95% clay and 5% carbonaceous char as determined in TGA experiments performed under air flow.[23] The little amount of char present in the nanocomposite residue contributes to the flame retardant effect, acting as a binder of the clay layers to form a graphitic/clay protective layer. Char formation during polymer degradation is a complex process. It occurs in several steps, which include conjugated double bond formation, cyclisation, aromatisation, fusion of aromatic ring, turbostratic* char formation and graphitisation.[37] Benson and Nogia[38] proposed a mechanism to explain the complex oxidation chain reactions of organic molecules considering the existence of two competing mechanisms: in the first, at lower temperature, the oxidation involves free-radical chain and the main products are hydroperoxides and oxygenated species. In the second, at higher temperature, hydrogen abstraction becomes more likely resulting in oxidative dehydrogenation. In normal combustion conditions the first process prevails and the thermo-oxidation causes chain scission with

* A type of crystalline structure where the basal planes have slipped sideways relative to each other, causing the spacing between planes to be greater than ideal. In a char turbostratic structure the carbon atoms will be aligned in layers.

subsequent volatilisation of the polymer. On the other hand, the second mechanism seems to prevail in the nanocomposite where an enhanced aromatisation and a reduced rate of oxidation were observed,[39] indicating a catalyst effect of the clay in the char forming reaction. The role of catalysis in charring is indirectly supported by the fact that charring is only effective in the nanocomposite. In the microcomposite, volatilisation prevails over charring because this contact is weak and the clay layers collapse to form a powder.[23,28] A catalytic effect of the nanodispersed clay layers was found to be effective in promoting the char forming reaction in PP,[39] EVA,[40] PE[41] and PS[42] nanocomposites.

The alkyl ammonium used to render the clay organophilic is known to decompose with the Hofmann elimination or with an SN2 nucleophilic substitution reaction at a temperature as low as 155ºC.[43,44] As result a protonic site is created on the clay surface (Reaction 10.1).

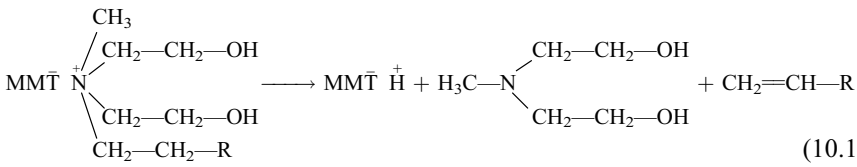

(10.1)

At the end of the thermal decomposition of the organic modifier the amount of this site will correspond to the cationic exchange capacity of the montmorillonite and the clay can be considered an acid-activated clay that possesses comparatively strong acid sites (Hammett acidity typically quoted in the range $-8.2 < H_0 < -5.6$[45]).

Clays are also characterised by Lewis acidity that can arise at the layer edge from partially coordinated metal atoms, such as Al^{3+}, or along the siloxane surface from isomorphic substitution of multivalent species, such as Fe^{2+} and Fe^{3+}, and crystallographic defect sites within the layer. These Lewis acid sites can accept single electrons from donor molecules with low ionisation potential, coordinate organic radicals, or abstract electrons from vinylic monomers. Zanetti *et al.*[39] suggested that the clay acts as a char promoter slowing down the degradation and providing a transient protective barrier to the nanocomposite in combination with the alumino-silica barrier which arises from the clay.

Another mechanism proposed by Zhu *et al.* is radical trapping by paramagnetic iron within the clay.[11] They observed that even when the clay was as low as 0.1% by mass fraction, the peak heat release rate of the clay/polystyrene nanocomposite was lowered by 40%, a value not much different from that observed with higher amounts of clay.

Char forming mechanisms are thus complementary of the clay layer accumulation mechanism proposed by Gilman. A schematic representation is reported in Fig. 10.2. Heat transfer from an external source or from the flame

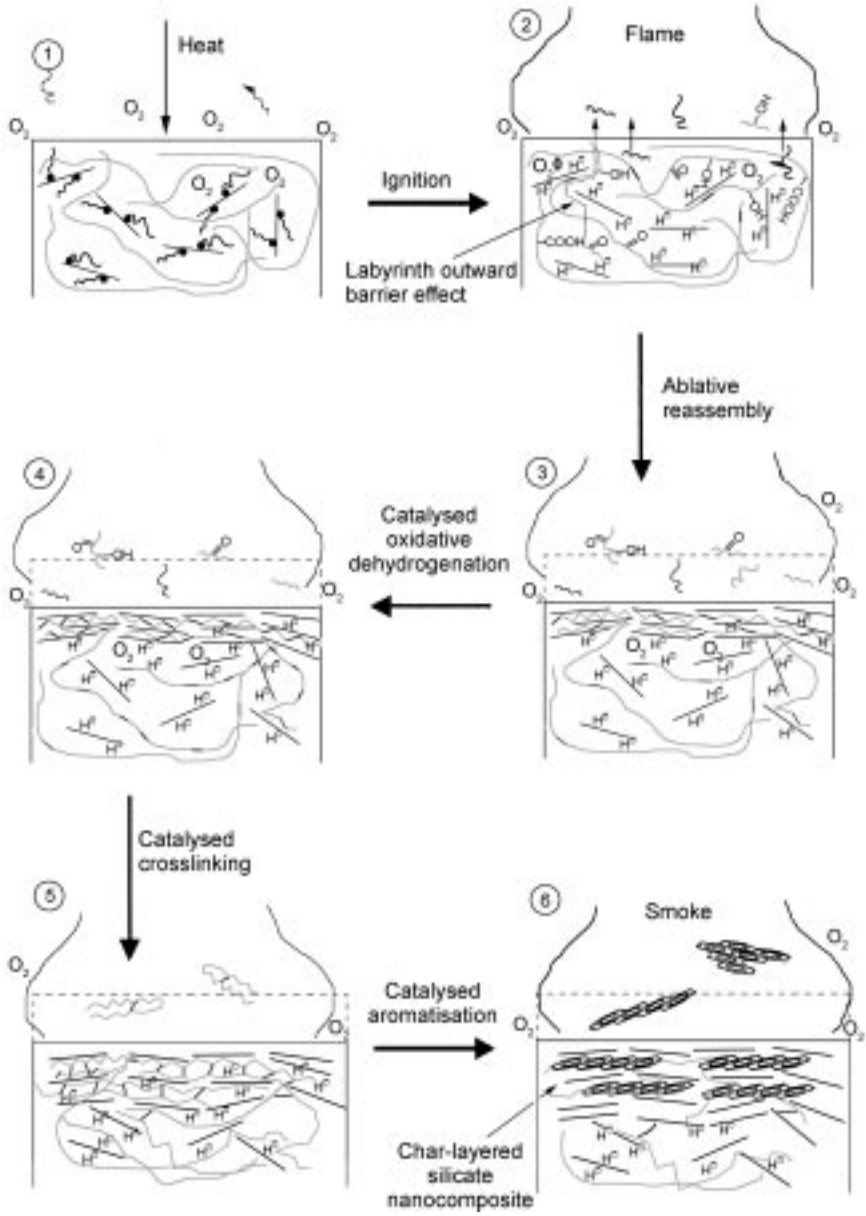

10.2 Schematic representation of combustion mechanism and ablative reassembly of a nanocomposite during cone calorimeter experiments. Reprinted with permission from ref. [30]. Copyright © (2005) American Chemical Society.

promotes thermal decomposition of the organoclay and thermal decomposition of the polymer (steps 1 and 2, Fig. 10.2). This results in the creation of protonic catalytic sites on the clay layers that reassemble on the surface of the burning material (step 3). The polymer undergoes competition between oxidation and chain scission to volatile partially oxidised fragments and catalysed dehydrogenation and oxidative dehydrogenation (step 4). The resulting conjugated polyene undergoes aromatisation, crosslinking and catalysed dehydrogenation to form a charred surface layer (step 5), which combines and intercalates with the reassembling silicate layers to provide the char-layered silicate residue (step 6).

A different approach based on the migration of clay platelets to the surface driven by the lower surface free energy of the clay has been proposed by Lewin.[46] This hypothesis is based on the fact that the organic treatment of the organoclay decomposes at temperatures lower than the pyrolysis and combustion of the polymer lowering the surface free energy of the clay platelet and driving to a decomposition of the nanocomposite structure. In these conditions the clay platelets migrate to the surface, aided by convection forces, arising from the temperature gradients, perhaps aided by the movement of gas bubbles. Accumulation of clay (as measured by XPS) has been observed by Wang *et al.*[47] on the surface of PS/clay nanocomposites at temperatures close to the decomposition temperature of the polymer. The bubbling of the nanocomposites during the combustion has been considered by Kashiwagi *et al.* as a disturbance element: the mechanism is described in terms of transportation of clay particles pushed by numerous rising bubbles of degradation products and the associated convection flow in the melt from the interior of the sample toward the sample surface.[48]

The ideal structure of the protective surface layer (consisting of clay particles and char) is net-like and has sufficient physical strength not to be broken or disturbed by bubbling. The protective layer should remain intact over the entire burning period. Bursting of the bubbles at the sample surface pushes the accumulated clay particles outward from the bursting area to form 'island-like' floccules instead of forming a continuous net-like structure of a clay filled protective layer decreasing the FR effect. The parameters influencing this phenomenon are: the initial content of clay in the polymer, the char forming characteristics of the polymer, the melt viscosity of the sample, and the aspect ratio of the clay platelets.

As can be seen in Fig. 10.1 the nanocomposite showed a lower time to ignition indicating an enhanced flammability in the very early stages of the combustion test. This can be considered a 'typical' behaviour since it has been observed in almost all combustion experiments made in the cone calorimeter. This phenomenon can be correlated with the thermal degradation of the organoclay. In cone calorimeter experiments the ignition takes place when a ignitable mixture of air and combustibles arising from thermal degradation of the polymer occurs. In other words the time to ignition depends on the thermal

stability of the polymer. As seen in Reaction (10.1) olefins are produced at a relatively low temperature anticipating the formation of a combustible mixture. The RHR of a whole organoclay was recorded by Zanetti *et al.*[20] showing that the peak of RHR occurred at the beginning of the experiment, at a time comparable with the ignition time of the nanocomposite. In addition, these olefins may be created during the melt compounding at temperatures near the decomposition temperature of the organoclay and 'stored' in the bulk of the material during the quenching. On the other hand, Reaction (10.1) can affect the thermal degradation of the polymer since olefin could combine with oxygen to give peroxidic radicals that would broaden the polydispersity through typical free radical processes.

This effect is very important during the preparation of the nanocomposite via melt blending, as observed by Gilman *et al.* for a PS nanocomposite, where gel permeation chromatography analysis of the samples, extruded without a nitrogen flow in the extruder, showed some evidence of degradation in the form of lower molecular weight.[32]

A catalyst effect of clay (not only the organoclay) on degradation of polymer matrix has also been observed by Qin *et al.* for a PP/MMT nanocomposite. They suggest that the addition of MMT can catalyse the initial decomposition of PP under oxygen because of the complex crystallographic structure and the habit of clay minerals that could result in some catalytically active sites, such as the weakly acidic SiOH and strongly acidic bridging hydroxyl groups present at the edges and acting as Bronsted acidic sites, un-exchangeable transition metal ions in the galleries, and crystallographic defect sites within the layers.[22]

In any case the thermal stability of the alkylammonium plays an important role in both thermal stability of the polymer and flame retardant effect. Many efforts have been made to generate new organically modified clays that have greater thermal stability than the common ammonium clay comprising: phosponium clays,[10] imidazolium clays,[49,50] crown ether clays[51] stibonium clays[52] and tropylium substituted clays.[53]

10.4 Nanocomposites and conventional flame retardants

For the past several years there was hope that the formation of a nanocomposite alone would permit one to impart fire retardancy to a polymer in all combustion conditions. Flame retardancy is achieved with nanocomposites alone, but not enough for an ignition resistance test such as the limiting oxygen index (LOI)[54] and the UL-94 vertical burning test (ANSI//ASTM D-635/77).

Cone calorimeter results show a reduction in the combustion rate of nanocomposites with respect to the polymer matrix, while in other tests, such as the UL-94, a self extinguishing behaviour is required to pass the test. The UL-94 test is, indeed, a qualitative pass/fail test performed on a plastic sample (125 ×

13 mm, with various thicknesses up to 13 mm) suspended vertically above a cotton patch. The plastic is subjected to two 10 s flame exposures with a calibrated flame in a unit which is free from the effects of external air currents. After the first 10 s exposure, the flame is removed, and the time for the sample to self-extinguish is recorded. Cotton ignition is noted if polymer dripping ensues; dripping is permissible if no cotton ignites. Then the second ignition is performed on the same sample, and the self-extinguishing time and dripping characteristics recorded. If the plastic self-extinguishes in less than 10 s after each ignition, with no dripping, it is classified as V-0. If it self-extinguishes in less than 30 s after each ignition, with no dripping, it is classified as a V-1, and if the cotton ignites then it is classified as V-2. If the sample does not self-extinguish before burning completely it is classified as failed.

With the exception of a PA6 nanocomposite that achieved a V-0 rating,[55] no other nanocomposites showed a self-extinguishing behaviour and at least slower burning times are observed for some of the samples. Nowadays it is unclear which measured parameter in the cone calorimeter experiments controls performance in the UL-94 test.

Recently, many researchers agreed that the approach to use with nanocomposites is to combine the nanocomposite with another flame retardant, such that the nanocomposite provides the base reduction flammability, and the secondary flame retardant provides the ignition resistance. This improves flammability performance and enhances the physical properties. It has been observed that the peak heat release rate of a PP nanocomposite (organoclay, 5 wt.%) was reduced still further when antimony oxide (AO, 6 wt.%) or decabromodiphenyloxide (DB, 22 wt.%) was present.[20] When both additives were present, a synergistic effect resulted, consisting in an increased time to ignition and in a further reduction in the peak HRR, which did not occur under identical testing conditions when antimony oxide and the brominated fire retardant were added to the virgin polymer.

Recently Wang *et al*. adopted the same approach to reduce the ignitability preparing flame retardant ABS nanocomposites (organoclay, 5 wt.%) by melt blending ABS, organophilic montmorillonite and conventional flame retardants (DB, 15 wt.% and AO, 3 wt.%).[56] Cone calorimeter experiments, UL-94 and LOI tests showed that the nanocomposites were superior to those of conventional flame retardant microcomposites. Improved effects were found between organoclay and DB and AO. When both ABS–DB–AO/organoclay and ABS–DB–AO achieved V-0 grade by UL-94 test, the peak HRR of ABS–DB–AO/OMT was 33% lower than that of ABS–DB–AO.

The advantage of this approach is the possibility to reach a desirable flame retardant effect with a lower amount of halogenated compound. Moreover, the addition of metal oxides, such as AO, to halogenated fire retardants increases their efficiency through the formation of antimony trihalide, a volatile product that slows reactions in the flame, even though the oxide itself has no effect. In

the case of nanocomposites a synergistic effect between the nanocomposites and the AO in absence of DB has been observed. This effect is presumably attributable to volatilisation of antimony trichloride formed by a reaction between AO and sodium chloride, present as an impurity in the commercial clay as a residue of clay exchange to intercalate the ammonium ion as in the following reactions:[20]

$$6MMT^{-+}H + 6NaCl + Sb_2O_3 \rightarrow 6MMT^{-+}Na + SbCl_3 + 3H_2O \qquad (10.2)$$

This reaction may be catalysed by the proton sites formed during Hoffman degradation on the reticular phyllosilicate layers dispersed in the matrix.

The reduced flammability of PLSNs allowed to obtain valuable UL-94 and LOI results even in absence of halogenated compounds. Song *et al*.[57] achieved a V-0 degree in the UL-94 test, preparing halogen-free flame-retarded polyamide 6 nanocomposite (organoclay, 2 wt.%) using magnesium hydroxide (MH, 6 wt.%) and red phosphorus (RP, 5 wt.%) as synergistic flame retardant. The LOI increased from 21 of PA6 to 31 of PA6 nanocomposite. The synergy in flame retardancy of PU nanocomposites was studied by Song *et al.*[33] They prepared via polymerisation route a polyurethane/organoclay nanocomposite based on polyether, organoclay, phenylmethane diisocyanate, diglycol, glycerine and melamine polyphosphate (MPP, 6 wt.%) as synergistic flame retardant. Cone calorimeter experiments and LOI tests showed that a synergistic effect occurs as MPP and OMT are added to PU. OMT and MPP co-enhanced the formation of carbonaceous char of PU at high temperature. The results confirmed that there are synergistic effects among clay, MPP and PU which retard the heat release rate, suppress the release of smoke and decrease the toxicity of gas released in the combustion process of PU.

10.5 Conclusion and future trends

Cone calorimetry experiments showed that the reduced flammability of PLSN is a general phenomenon of both thermoplastic and thermoset resins. There is no data indicating a preferencial morphology: the peak HRR is reduced significantly for intercalated, exfoliated and intercalated/exfoliated nanocomposites with low silicate mass fraction. Different views of the mechanism at the basis of the FR effect have been proposed. These proposals can be considered complementary since all agree on an ablative phenomenon. Exposed to heat the PLSN promotes the formation of a protective refractory shield composed of char and clay, that slows down the flame feeding thermal decomposition. Char formation is promoted catalytically by the clay and acts as a binder between the clay platelets to form a continuous net-like structure. In the absence of enhanced charring reaction (i.e the microcomposite), a continuous protective layer is not formed depending on the poor amount of char unable to link together the clay platelets that collapse to form an inconsistent powder.

However, many issues are still not resolved. There is, unfortunately, no theory as yet to explain the relationship between the reduction in peak HRR and dispersion of the clay in the polymer. This depends on uncertainties about the clay dispersion in the polymer matrix since the technique most used to characterise the PLSNs morphology is the TEM that examines only a very small portion of the polymer and one small sample will not necessarily be representative of the whole. On the other hand, cone calorimeter experiments are so sensitive that Wilkie proposed that the cone calorimetry must also be considered as another method to examine the bulk sample and infer if good dispersion has been achieved.[14]

PLSNs may be considered to be environmentally friendly alternatives to some traditional flame retardants. For instance, relatively low concentrations of clay are necessary compared with the amounts used for conventional FR in order to achieve a similar level of flame retardancy. Moreover, PLSNs can be processed with normal techniques used for polymers like extrusion, injection moulding and casting. In spite of the encouraging results obtained at the cone calorimeter and the environmentally friendly potential, PLSNs have been difficult to impose on the market. The main reason is because they leak in combustion tests such as LOI and UL-94. Nevertheless, this limitation can be avoided combining PLSNs with a conventional FR such that the nanocomposite provides the base reduction flammability, and the secondary flame retardant provides the ignition resistance. In this manner it is possible to reach the flame retardancy required by the market with a reduced amount of non-environmentally friendly FR and improved mechanical properties. Studies concerning the synergy between PLSNs and conventional FR are very few and many issues are to be understood. Once resolved, nanocomposites may fulfil the requirement for high-performance additive type flame retardant system.

The FR effect of nanocomposites is not limited to PLSNs. Carbon nanotubes are another candidate as FR additives because of their high aspect ratio. This was demonstrated by using carbon nanotubes in PP,[58,59] PMMA[60] and also EVA.[61]

10.6 References

1. Bower, C.A., 'Studies on the forms and availability of soil organic phosphorus'. *Iowa Agricoltural Experiment Station Research Bulletin*, 1949, **362**, 39–52.
2. Uskov, I.A., *Vysokomolekulyarnye Soedineniya (high molecular weight compounds)*, 1960, **2**, 926–930.
3. Blumstein, A., 'Etude des polymerisations en couche adsorbee I'. *Bull. Chim. Soc.*, 1961, 899–905.
4. Blumstein, A., 'Polymerization of adsorbed monolayers: II. Thermal degradation of the inserted polymer'. *Journal of Polymer Science A*, 1965, **3**, 2665.
5. Gilman, J.W., Kashiwagi, T., Lichtenhan, J.D. Nanocomposites: a revolutionary new flame retardant approach. In *42nd Internationl SAMPE Symposium*, 1997.

6. Gilman, J.W., Jackson, C.L., Morgan, A.B., Harris, R., Manias, E., Giannelis, E.P., Wuthenow, M., Hilton, D., Phillips, S.H., 'Flammability properties of polymer-layered-silicate nanocomposites. Polypropylene and polystyrene nanocomposites'. *Chemistry of Materials*, 2000, **12**, 1866–1873.
7. Morgan, A.B., Harris, R.H., Kashiwagi, T., Chyall, L.J., Gilman, J.W., 'Flammability of polystyrene layered silicate (clay) nanocomposites: carbonaceous char formation'. *Fire Materials*, 2002, **26**, 247–253.
8. Morgan, A.B., Chu, L.L., Harris, J.D., 'A flammability performance comparison between synthetic and natural clays in polystyrene nanocomposites'. *Fire Materials*, in press.
9. Gilman, J.W., 'Flammability and thermal stability studies of polymer layered-silicate clay nanocomposites'. *Applied Clay Science*, 1999, **15**, 31–49.
10. Zhu, J., Morgan, A.B., Lamelas, F.J., Wilkie, C.A., 'Fire properties of polystyrene-clay nanocomposites'. *Chemistry of Materials*, 2001, **13**, 3774–3780.
11. Zhu, J., Uhl, F., Morgan, A.B., Wilkie, C.A., 'Studies on the mechanism by which the formation of nanocomposites enhances thermal stability'. *Chemistry of Materials*, 2001, **13**, 4649–4654.
12. Wang, D. and Wilkie, C.A., 'In-situ reactive blending to prepare polystyrene–clay and polypropylene–clay nanocomposites'. *Polymer Degradation and Stability*, 2003, **80**, 171–182.
13. Su, S., Jiang, D.D., Wilkie, C.A., 'Novel polymerically-modified clays permit the preparation of intercalated and exfoliated nanocomposites of styrene and its copolymers by melt blending'. *Polymer Degradation and Stability*, 2004, **83**, 333–346.
14. Su, S., Jiang, D.D., Wilkie, C.A., 'Polybutadiene-modified clay and its nanocomposites'. *Polymer Degradation and Stability*, 2004, **84**, 279–288.
15. Zheng, X. and Wilkie, C.A., 'Nanocomposites based on poly (ϵ-caprolactone) (PCL)/clay hybrid: polystyrene, high impact polystyrene, ABS, polypropylene and polyethylene'. *Polymer Degradation and Stability*, 2003, **82**, 441–450.
16. Bourbigot, S., Vanderhart, D.L., Gilman, J.W., Bellayera, S.v., Stretz, H., Paul, D.R., 'Solid state NMR characterization and flammability of styrene–acrylonitrile copolymer montmorillonite nanocomposite'. *Polymer*, 2004, **45**, 7627–7638.
17. Wang, S., Hu, Y., Lin, Z., Gui, Z., Wang, Z., Chen, Z., Fan, W., 'Flammability and thermal stability studies of ABS/Montmorillonite nanocomposite'. *Polymer International*, 2003, **52**, 1045–1049.
18. Zhu, J., Start, P., Mauritz, K.A., Wilkie, C.A., 'Thermal stability and flame retardancy of poly(methyl methacrylate)-clay nanocomposites'. *Polymer Degradation and Stability*, 2002, **77**, 253–258.
19. Su, S., Jiang, D.D., Wilkie, C.A., 'Poly(methyl methacrylate), polypropylene and polyethylene nanocomposite formation by melt blending using novel polymerically-modified clays'. *Polymer Degradation and Stability*, 2004, **83**, 321–331.
20. Zanetti, M., Camino, G., Canavese, D., Morgan, A.B., Lamelas, F.J., Wilkie, C., 'Fire retardant halogen-antimony-clay synergism in polypropylene layered silicate nanocomposites'. *Chemistry of Materials*, 2002, **14**, 189–193.
21. Tidjani, A., 'Polypropylene-graft-maleic anhydride nanocomposites: fire behaviour of nanocomposites produced under nitrogen and in air'. *Polymer Degradation and Stability*, 2005, **87**, 43–49.
22. Qin, H., Zhang, S., Zhao, C., Feng, M., Yang, M., Shu, Z., Yang, S., 'Thermal stability and flammability of polypropylene/montmorillonite composites'. *Polymer*

Degradation and Stability, 2004, **85**, 807–813.
23. Zanetti, M. and Costa, L., 'Preparation and combustion behaviour of polymer/layered silicate nanocomposites based upon PE and EVA'. *Polymer*, 2004, **45**, 4367–4373.
24. Zhang, J. and Wilkie, C.A., 'Preparation and flammability properties of polyethylene–clay nanocomposites'. *Polymer Degradation and Stability*, 2003, **80**, 163–169.
25. Zhao, C., Qin, H., Gong, F., Feng, M., Zhang, S., Yang, M., 'Mechanical, thermal and flammability properties of polyethylene/clay nanocomposites'. *Polymer Degradation and Stability*, 2005, **87**, 183–189.
26. Lu, H., Hu, Y., Xiao, J., Kong, Q., Chen, Z., Fan, W., 'The influence of irradiation on morphology evolution and flammability properties of maleated polyethylene/clay nanocomposite'. *Materials Letters*, 2005. **59**, 648 651.
27. Preston, C.M.L., Amarasinghe, G., Hopewell, J.L., Shanks, R.A., Mathys, Z., 'Evaluation of polar ethylene copolymers as fire retardant nanocomposite matrices'. *Polymer Degradation and Stability*, 2004, **84**, 533–544.
28. Zanetti, M., Camino, G., Mulhaupt, R., 'Combustion behaviour of EVA/fluorohectorite nanocomposites'. *Polymer Degradation and Stability*, 2001, **74**, 413–417.
29. Tang, Y., Hua, Y., Wanga, S.F., Guia, Z., Chen, Z., Fan, W.C., 'Preparation and fammability of ethylene-vinyl acetate copolymer/montmorillonite nanocomposites'. *Polymer Degradation and Stability*, 2002, **78**, 555–559.
30. Zanetti, M., Kashiwagi, T., Falqui, L., Camino, G., 'Cone calorimeter combustion and gasification studies of polymer layered silicate nanocomposites'. *Chemistry of Materials*, 2002, **14**, 881–887.
31. Qin, H., Su, Q., Zhang, S., Zhao, B., Yang, M., 'Thermal stability and flammability of polyamide 66/montmorillonite nanocomposites'. *Polymer*, 2003, **44**, 7533–7538.
32. Gilman, J.W., Kashiwagi, T., Morgan, A.B., Harris, R.H., Brassell, L., Van Landingham, M., Jackson, C.L., 'Flammability of polymer clay nanocomposites consortium: year one annual report'. 2000, NISTIR 6531, NIST (National Institute of Standards and Technology): Gaithersburg, MD, pp. 1–55.
33. Song, L., Hu, Y., Tang, Y., Zhang, R., Chen, Z., Fan, W., 'Study on the properties of flame retardant polyurethane/organoclay nanocomposite'. *Polymer Degradation and Stability*, 2005, **87**, 111–116.
34. Babrauskas, V., 'Specimen heat fluxes for bench-scale heat release rate testing'. *Fire Materials*, 1995, **19**, 243–252.
35. Bertelli, G., Camino, G., Goberti, P., Marchetti, E., Luda, M.P., Costa, L., *Structure-Char Forming Relationship in Intumescent Fire Retardant Systems*, in *Fire Safety Science – Proceedings of the third international symposium*, G. Cox and B. Langford (eds), 1991, Elsevier Applied Science: London, pp. 537–546.
36. Vaia, R.A., Price, G., Ruth, P.N., Nguyen, H.T., Lichtenhan, J., 'Polymer-layered silicate nanocomposites as high performance ablative materials'. *Applied Clay Science*, 1999, **15**, 67–92.
37. Levchik, S. and Wilkie, C., *Char formation*, in *Fire retardancy*, A. Grand and C. Wilkie, (eds), 2000, Marcel Dekker Inc.: New York.
38. Benson, S.W. and Nangia, P.S., 'Some unresolved problems in oxidation and combustion'. *Acc Chem Res*, 1979, **12**, 223–228.
39. Zanetti, M., Camino, G., Reichert, P., Mulhaupt, R., 'Thermal behaviour of

poly(propylene) layered silicate nanocomposites'. *Macromolecular Rapid Communications*, 2001, **22**, 176–180.
40. Zanetti, M., Camino, G., Thomann, R., Mulhaupt, R., 'Synthesis and thermal behaviour of layered silicate/EVA nanocomposites'. *Polymer*, 2001, **42**, 4501–4507.
41. Zanetti, M., Bracco, P., Costa, L., 'Thermal degradation behaviour of PE/clay nanocomposites'. *Polymer Degradation and Stability*, 2004, **85**, 657–665.
42. Bourbigot, S., Gilman, J.W., Wilkie, C.A., 'Kinetic analysis of the thermal degradation of polystyrene montmorillonite nanocomposite'. *Polymer Degradation and Stability*, 2004, **84**, 483–492.
43. Xie, W., Gao, Z., Pan, W.-P., Hunter, D., Singh, A., Vaia, R., 'Thermal degradation chemistry of alkyl quaternary ammonium montmorillonite'. *Chemistry of Materials*, 2001, **13**, 2979–2990.
44. Xie, W., Gao, Z., Liu, K., Pan, W.-P., Vaia, R., Hunter, D., Singh, A., 'Thermal characterization of organically modifed montmorillonite'. *Thermochimica Acta*, 2001, 367–368.
45. Vaccari, A., 'Clays and catalysis: a promising future'. *Applied Clay Science*, 1999, **14**, 161–198.
46. Lewin, M., 'Some comments on the modes of action of nanocomposites in the flame retardancy of polymers'. *Fire Materials*, 2003, **27**, 1–7.
47. Wang, J., Dua, J., Zhu, J., Wilkie, C.A., 'An XPS study of the thermal degradation and flame retardant mechanism of polystyrene-clay nanocomposites'. *Polymer Degradation and Stability*, 2002, **77,** 249–252.
48. Kashiwagi, T., Jr, R.H.H., Zhang, X., Briber, R.M., Cipriano, B.H., Raghavan, S.R., Awad, W.H., Shields, J.R., 'Flame retardant mechanism of polyamide 6-clay nanocomposites'. *Polymer*, 2004, **45**, 881–891.
49. Davis, C.H., Mathias, L.J., Gilman, J.W., Scirald, D.A., Shields, R., Trulove, P., Sutto, T.E., Delong, H.C., 'Effects of melt-processing conditions on the quality of poly(ethylene terephthalate) montmorillonite clay nanocomposites'. *J Polym Sci Part B: Polym Phys*, 2002, **40**, 2661–2666.
50. Gilman, J.W., Awad, W.H., Davis, R.D., Shields, J., Harris, R.H., Davis, C., Morgan, A.B., Sutto, T.E., Callahan, J., Trulove, P.C., DeLong, H.C., 'Polymer/layered silicate nanocomposites from thermally stable trialkylimidazolium-treated montmorillonite'. *Chemistry of Materials*, 2002, **14**, 3776–3785.
51. Yao, H., Zhu, J., Morgan, A., Wilkie, C.A., 'Crown ether-mofified clays and their polystyrene nanocomposites'. *Polymer Engineering and Science*, 2002, **42**, 1808–1814.
52. Wang, D. and Wilkie, C.A., 'A stibonium-modified clay and its polystyrene nanocomposite'. *Polymer Degradation and Stability*, 2003, **82**, 309–315.
53. Zhang, J. and Wilkie, C.A., 'A carbocation substituted clay and its styrene nanocomposite'. *Polymer Degradation and Stability*, 2004, **83**, 301–307.
54. ASTM D2863.
55. Inoue, H. and Hosokawa, T., in *Japan Patent Application*. 1998, Showa Denko K.K., Japan: Japan, pp. 81–510.
56. Wang, S., Hu, Y., Zong, R., Tang, Y., Chen, Z., Fan, W., 'Preparation and characterization of flame retardant ABS/montmorillonite nanocomposite'. *Applied Clay Science*, 2004, **25**, 49–55.
57. Song, L., Hu, Y., Lin, Z., Xuan, S., Wang, S., Chen, Z., Fan, W., 'Preparation and properties of halogen-free flame-retarded polyamide 6/organoclay nanocomposite'.

Polymer Degradation and Stability, 2004, **86**, 535–540.
58. Kashiwagi, T., Grulke, E., Hilding, J., Harris, R., Awad, W., Douglas, J., 'Thermal degradation and flammability properties of poly(propylene)/carbon nanotube composites'. *Macromolar Rapid Communications*, 2002, **23**, 761–765.
59. Kashiwagi, T., Grulke, E., Hilding, J., Groth, K., Harris, R., Butler, K., Shields, J., Kharchenko, S., Douglas, J., 'Thermal and flammability properties of poly-propylene/carbon nanotube nanocomposites'. *Polymer*, 2004, **45**, 12 4227–4239.
60. Kashiwagi, T., Du, F., Winey, K.I., Groth, K.M., Shields, J.R., Bellayer, S.P., Kim, H., Douglas, J.F., 'Flammability properties of polymer nanocomposites with single-walled carbon nanotubes: effects of nanotube dispersion and concentration'. *Polymer*, 2005, **46**, 471–481.
61. Beyer, G., 'Short communication: Carbon nanotubes as flame retardants for polymers'. *Fire and Matrerials*, 2002, **26**, 291–293.
62. Duquesne, S., Jama, C., Bras, M.L., Delobel, R., Recourt, P., Gloaguend, J.M., 'Elaboration of EVA–nanoclay systems–characterization, thermal behaviour and fire performance'. *Composites Science and Technology*, 2003, **63**, 1141–1148.

11

Barrier properties of polymer/clay nanocomposites

A SORRENTINO, G GORRASI, M TORTORA and V VITTORIA, University of Salerno, Italy

11.1 Introduction

In this chapter we review the current literature associated with the barrier properties of polymer/layer silicate nanocomposites, with a special focus on the use of clay nanoparticles to affect permeability to gases and vapours.

The majority of papers on nanocomposites have been focused on the use of smectite type clays as nanoparticles. They are a group of *swelling* clay minerals including montmorillonite, nontronite, saponite, sauconite, and hectorite. Mostly smectite clays have been studied because they are naturally occurring minerals that are commercially available and exhibit platy morphology with high aspect ratio and substantial cation exchange capacities. The platelet structure of these aluminosilicate materials has proven its ability to improve the barrier properties of polymeric materials, according to a tortuous path model in which a small amount of platelet particles significantly reduces the diffusivity of gases through the nanocomposite. The key for nanocomposite technology is exfoliation of the clay into its individual platelets, thereby achieving the greatest barrier improvement as well as the lowest haze. The advantage of this approach is based on the use of conventional cheap polymers with barrier improvement arising from dispersion of low levels of inexpensive clay minerals.

Several models for barrier properties have been proposed for predicting the behaviour of polymer nanocomposites. This chapter examines in some detail the existing literature on barrier properties of polymer nanocomposites, comparing the results and trying to correlate the different experimental results, where possible.

11.2 Background on polymer barrier properties

Polymer materials come into contact with solvents or low molecular weight species in several applications such as packaging, polymer processing, drying of polymer coatings, drug release, sensors, etc.[1–5] Therefore there is a need to understand gas and liquid transport through polymers. Although numerous

studies are available in the literature about gas transport in polymers[6–14] the development of a suitable polymeric system for a given application is still, to a large extent, empirical. The reason is related to the complex relations between the structure of both the polymer and the permeant molecules. This issue includes both local chemical structure and longer range order described as morphology. In addition, temperature, solubility, pressure, polymorphism, reactivity, orientation, filler content, and composition modify the transport process.

Polymers usually have a wide spectrum of relaxation times associated with the motion of the polymer segments. An increase of either temperature or concentration of the permeant in the polymer leads to a decrease of the relaxation times, and thus to an enhanced motion of the polymer segments. The diffusion of liquid and gases in polymers is associated with the finite rates at which the polymer structure changes in response to the motion of the permeant molecules.

At temperatures below their glass transition temperature the polymers are in a glassy state. In this state, a polymer is hard and may be brittle due to its restricted chain mobility. Glassy polymers are very dense structures, with very little internal void space. Hence, it is not surprising that penetrant diffusivities and, as a consequence, permeability through such a structure are low.

In contrast, polymers in the rubbery state typically are tough and flexible, with a larger amount of free volume in which diffusion may take place.[9] In this case, larger segments are thought to participate in the diffusion process due to internal micro-motions of chain rotation and translation, as well as vibration.

The diffusion behaviour in a rubbery state is generally well described by Fick's laws with constant or concentration-dependent diffusivity. The rate of diffusion is much lower than the rate of relaxation and the polymer chains adjust so quickly to the presence of the liquid that they do not cause diffusion anomalies. The amount of liquid transferred at time t, C_t, as a fraction of the total amount of liquid transferred at infinite time, C_{eq}, is very often expressed as a function of time by the relationship (Equation 11.1):

$$\frac{C_t}{C_{eq}} = kt^n \tag{11.1}$$

with $n = \frac{1}{2}$ when the diffusion is Fickian.

In glassy polymers, diffusion is very rapid compared with the rate of the relaxation process. The liquid advances with a constant velocity; this advancing front marks the innermost limit of penetration of the liquid and it is the boundary between a swollen gel and the glassy part free of liquid. This process is characterized by $n = 1$ in Equation (11.1). Non-Fickian diffusion occurs when the relaxation and diffusion rates are comparable. In this anomalous diffusion the n exponent takes an intermediate value between $\frac{1}{2}$ and 1.

Formally, when a gas or vapour permeates through a polymer film, the global process involves three-steps:

1. The gas is sorbed at the entering face and dissolves there, with equilibrium rapidly being established between the two phases.
2. The dissolved penetrant molecules then diffuse through the polymer, via a random walk hopping mechanism, equilibrating their concentration inside the film.
3. On the low-concentration (low partial pressure) side of the film, the molecules can desorb into the gas phase.[12]

After a certain period of time, which depends on the diffusion coefficient and on the film thickness, a steady state of flux through the film is obtained and the concentration profile remains constant in time. The mechanism of permeation, then, involves both solution and diffusion.

A polymeric system is, thus, characterized by three transport coefficients, which are the permeability, the solubility, and the diffusion coefficients. The permeability coefficient, P, indicates the rate at which a permeant traverses polymer film. The solubility coefficient, S, is a measure of the amount of permeant sorbed by the polymer when equilibrated with a given pressure of gas or vapour at a particular temperature. Finally, the diffusion coefficient, D, indicates how fast a penetrant is transported through the polymer system. For steady state permeation of simple gases into a homogeneous film, the permeability coefficient, P, can be written as the product of diffusion coefficient D and solubility S (Equation 11.2):

$$P = DS \tag{11.2}$$

When specific interactions between penetrant and polymer become important, such as when hydrogen bonding is involved, the relationship among diffusivity, solubility and measured permeability is more complicated. In the presence of swelling liquids or vapours, such as water in ethyl cellulose and many hydrocarbons in olefinic polymers, diffusivity and solubility show concentration dependence.[11] The system can progressively lose its compactness and, as a consequence, at higher concentrations the polymeric film can dissolve completely in the vapour.

The solubility of a penetrant in a polymer matrix is described by the sorption isotherm. It correlates, at a constant temperature, the amount of sorbed penetrant to the pressure or to the activity of the phase outside the polymer (Fig. 11.1). Depending on the nature of the polymer-penetrant system, sorption isotherms may show considerable differences in shape.[11] The micro-voids in a glassy polymer can immobilize a portion of the penetrant molecules by entrapment or by binding at high energy sites at their molecular peripheries (Langmuir type isotherm). As a result, this system typically shows concave shaped sorption isotherms (I in Fig. 11.1). On the contrary, for high penetrant concentration of vapours in rubbery polymers, the sorption isotherm turns upwards into a convex shaped curve (II in Fig. 11.1). This kind of isotherm can be explained by a

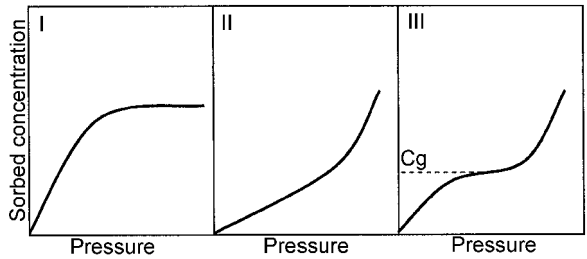

11.1 Theoretical sorption isotherm model. I) Langmuir type isotherm; II) Flory-Huggins type isotherm; III) Dual sorption (BET-mode) type isotherm.

preference for the formation of penetrant-penetrant pairs of entering molecules, so the solubility coefficient continuously increases with the activity (Flory-Huggins type isotherm).[11]

More generally, dual sorption mode (BET-mode), that is a combination of two isotherm types, is observed in complex polymeric systems (III in Fig. 11.1). At low activity, there is a preferential sorption of the solvent on specific sites, while, at high activity, strong interactions with the penetrating molecules lead to a high mobility of polymer chains, that can induce structural transformations, as clustering of solvent molecules, crazing or partial dissolution.[10,12]

The concentration at the transition point, *Cg*, represents the concentration of penetrant molecules at which the glass transition temperature of the polymer-penetrant system is equal to the experimental temperature.

In both glassy and rubbery states, solubility and diffusivity can be further modified by the presence of the crystalline phase, by molecular orientation and by the presence of inorganic fillers. In semi-crystalline polymers, the chains are aligned in crystalline regions, whereas they are randomly coiled in the amorphous regions connecting the crystalline phase. Generally, sorption only takes place in the amorphous phase, not in the crystalline regions. Hence crystallites act as local constraints fixing the chains in a three-dimensional network. Therefore, by increasing the crystallinity, there is a decrease in sorption due to a reduced amorphous volume and a decrease in diffusion due to a more tortuous path for the diffusing molecules.[12]

Inorganic fillers are believed to increase the barrier properties by creating a maze or 'tortuous path' that retards the progress of the gas molecules through the polymeric matrix. The direct benefit of the formation of such a path is clearly observed in all the prepared nanocomposites by dramatically improved barrier properties.[15]

There is also evidence that the nano-sized clay restricts the molecular dynamics of the polymer chains surrounding the clay, thus retarding the relaxation of polymer chains. The retarded relaxation, in turn, reduces the diffusion of small molecules through the nanocomposites.[16] Osman and Atallah[17] suggest that plate-like particles strongly reduce the permeability coefficient of the

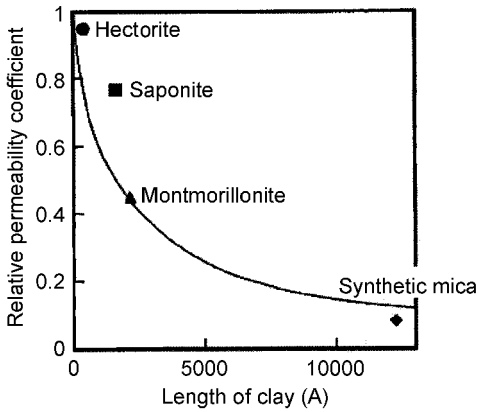

11.2 Clay length dependence on relative permeability coefficient (reprinted from ref. [18], Copyright © 1997, with permission of John Wiley & Sons, Inc.).

polymer and their effect depends on the aspect ratio, which in turn depends on the degree of exfoliation. In contrast, spherical particles do not influence the gas permeability of the polymer, irrespective of their diameter.

Yano *et al.*[18] prepared polyimide-clay hybrid films with four different sizes of clay minerals in order to investigate the effect of the aspect ratio on the properties of the hybrids. Hectorite, saponite, montmorillonite and synthetic mica were used as clay minerals. They found[18] that, at constant clay content (2 wt.%), the relative permeability coefficient decreases on increasing the length of the clay (Fig. 11.2).

11.3 Experimental methods

The transport characteristics are related to each other obeying Equation (11.2). Often, two of these parameters are experimentally determined and the third one can be evaluated from Equation (11.2). However, in most cases, concentration and time dependence of the transport parameters cannot be neglected, requiring independent experimental measurements of the three parameters.

Experimental methods employed in the determination of the transport parameters can be divided into two basic types:

1. sorption experiments
2. permeation experiments.

In the sorption experiments, a polymeric sample is suspended to a quartz spring balance, having a measured extension, in a vacuum chamber. A vapour or a gas is then introduced and maintained at a constant pressure. The gas or vapour dissolves and diffuses into the polymer and the weight gain is gravimetrically measured. The analysis is focused on the initial part of the mass-gain curves,

which provides a value of the diffusivity parameter, and on the equilibrium vapour uptake. From measurements realized at different activities, the concentration of sorbed solvent as a function of the applied pressures can be obtained.

In the permeation experiments, the two sides of the membrane, which are initially under vacuum, are sealed off from one another. Then the gas is introduced on the upstream side and kept at constant pressure p_{in}. On the downstream side the p_{out} slowly rises as the total amount permeated through the polymer into the calibrated volume changes in time.

An initially non-linear pressure increase in the transient state is followed by a linear increase in the steady state when an equilibrium concentration profile in the film is reached. From the slope of the steady state pressure increase it is possible to calculate the permeability of a penetrant through a polymeric sample.[12] The time to reach the stationary flux conditions is called lag-time and it allows us to determine the diffusivity of the system. Alternatively, in the pressure decay methods, a polymer sample and a gas are closed in a constant volume. The pressure decreases in time due to the sorption of the gas into the polymer are monitored.[13]

Permeability is so low that, in sorption experiments, large pressure differences and membranes of small thickness have to be employed. These restraints do not apply to condensable vapours or highly permeant gas. In the last case, relaxation processes in the polymer matrix cause changes in the transport behaviour and make the permeability time-dependent. In contrast, only vapours of sufficiently high solubility are suitable for the gravimetric measurements used in the sorption experiments. Consequently, there are only few systems for which both sorption and permeation results have been reported. Low *et al.*[16] conducted the two types of moisture transport experiments on a polyamide 6/clay nanocomposite. The authors found that the activation energy of moisture permeation obtained from the sorption experiment is lower than that derived from the permeation measurement. They concluded that the interaction and contribution of the diffusion and solubility parameters show complex transport behaviour in these nanocomposite films.

An elegant alternative method to measure sorption into polymers is the Attenuated Total Reflectance Fourier Transform Infrared (ATR-FTIR) method.[19,20] It allows in situ acquisition of the kinetic data and at the same time records the changes that occur in the polymer matrix due to the influence of the diffusant. Effects such as swelling, changes in morphology and polymer solvent interactions can all be simultaneously monitored. To calculate the diffusion coefficients from ATR-FTIR data, the mass uptake equation used in gravimetric diffusion experiments has to be modified to take into account the convolution of the evanescent field with the diffusion profile.

11.4 Permeation and diffusion models relevant to polymer nanocomposites

As reported by several authors and as proved by our studies on the transport behaviour, nanocomposites exhibit substantial improvements in gas and vapour permeability. This phenomenon has traditionally been explained by a tortuous path model where the high aspect ratio platelets acts as physical barrier for diffusion of molecules.[21]

In his model Nielsen[21] assumed that the filler particles are impermeable to the permeant molecules, and are uniformly and completely dispersed in the polymer. Moreover the plates are oriented parallel to the polymer film surface and the filler has no effect on the mobility of the polymer chains. Figure 11.3 illustrates the general type of path that molecules must take to get through the polymer. Based on simple geometrical considerations the following Equation (11.3) can be derived:

$$\frac{P_{\text{eff}}}{P_0} = \frac{1-\phi}{\tau} = \frac{1-\phi}{1+\left(\frac{L}{2t}\right)\phi} \tag{11.3}$$

where P_{eff} and P_0 are the permeabilities of the filled and unfilled polymer, ϕ is the volume fraction of the filler, τ the tortuosity factor, L and t are the length and the thickness of the filler particles.

These assumptions maximize the distance that the diffusing molecules must travel and thus define the maximum decrease in permeability that geometrically can be expected for the addition of filler to a polymer. In the same article, Nielsen[21] developed a second model for predicting a change in permeability that can be expected when the permeant is partially soluble in the polymer and when the concentration of sorbed molecules at the filler-polymer interface is different from the concentration in the polymer. He proposed that around each filler particle there is an interfacial layer which shows properties different from the bulk polymer saturated with sorbed molecules. In this case the total permeability is divided into two parts (Equation 11.4):

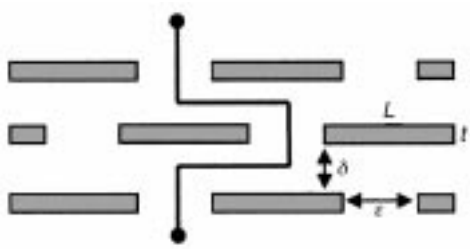

11.3 Model for the path of a diffusing molecule through a polymer filled with square plates.

$$\frac{P_{\text{eff}}}{P_0} = \frac{P_{\text{i}}}{P_0\phi^n + P_{\text{i}}(1-\phi^n)}\left(\frac{\phi_{\text{i}}}{\tau^0}\right) + \left(\frac{\phi_{\text{P}} + \phi_{\text{L}}}{\tau}\right) \tag{11.4}$$

P_{eff}, P_0 and P_{i} are the permeabilities of liquid through the filled polymer, the unfilled polymer and the interfacial region, ϕ, ϕ_{i}, ϕ_{P} and ϕ_{L} are the volume fraction of the filler, the liquid collected in the interfacial region, the dry polymer and the liquid dissolved in the bulk polymer, respectively. τ and τ_0 are the tortuosity factor for the polymer bulk and the interfacial part, respectively; they may or may not be equal. The constant n ranges between zero and one and denotes the fractional length of the average diffusional path that crosses the polymer. It depends upon particle shape and orientation as well as upon such factors as aggregation of filler particles.

Despite the large success of the tortuosity model in the polymer nanocomposites literature, no one has adopted this second model. It is probably due to the numerous numerical parameters that are not obtainable experimentally. The original idea, however, is so interesting that very recently Beall[22–24] proposed a new model essentially based on the same considerations. This model employs the concept of a constrained polymer region around the nano-particles. The constrained polymer region characteristics are dependent upon a number of factors involving both the type of nano-particle and the characteristics of the polymer. Beall defines three regions around the clay plates.[23] The first is near the surface of the clay and it is occupied by the surface modifier utilized to compatibilize the clay with the polymer. This region can be easily measured with x-ray diffraction of the organo-clays. The second region is a constrained polymer region. This region is less defined and it is determined by a number of variables including the type of bonding between the surface modifier and the polymer, the strength of interaction between polymer molecules, and the extent of nucleation imparted by the clay. The third region is the unconstrained polymer that is not directly affected by the clay. The model can explain some experimental results not predicted by the simple tortuous path model, such as the value of the relative permeabilities depending on the type of permeant and/or on the clay surface modification.

One of the principal assumptions of the Nielsen model is that the plates are oriented parallel to the polymer surface. In literature some results where the plates are randomly oriented along the film thickness are reported.[25] In order to overcome this problem, Bharadwaj[26] proposed an extension of the Nielsen model able to describe the effects of the sheet orientation on the relative permeability. The new study addressed both of these issues by modifying a simple model developed to describe permeability in filled polymers on the basis of tortuosity arguments. The tortuosity factor is modified to include the orientational order, and the relative permeability is given by Equation (11.5):

$$\frac{P_{\text{eff}}}{P_0} = \frac{1-\phi}{1 + \frac{2}{3}\left(\frac{L}{2t}\right)\phi\left(S + \frac{1}{2}\right)} \tag{11.5}$$

where the order parameter (S) represents a conventional Hermans orientation factor defined by relation (11.6):

$$S = \frac{1}{2}\langle 3\ \cos^2\theta - 1\rangle \tag{11.6}$$

where θ represents the angle between the direction of preferred orientation (n) and the sheet normal vectors, the angular bracket indicate the average value over all the system.

This geometrical approach may reduce the deviations between experimental data and model predictions but it cannot resolve the main limitation of the tortuous path theory. This model is based on the assumption that the presence of nano-particles does not affect the diffusivity of a polymer matrix.

Diffusion in heterogeneous media with dispersed impermeable domains had been described in several publications. Maxwell[27] solved the problem of a suspension of spheres in a continuum and obtained an expression for the effective diffusion coefficient of the composite medium. Cussler *et al.*[28] solved the problem of a suspension of impermeable flakes oriented perpendicular to the diffusion and obtained the following relation (11.7) for the effective diffusion coefficient:

$$\frac{D_{\text{eff}}}{D_0} = \left(1 + \frac{\alpha^2\phi^2}{1-\phi}\right)^{-1} \tag{11.7}$$

where ϕ is the loading, α is the particles aspect ratio, D_{eff} and D_0 are the diffusion coefficient with and without flakes, respectively.

In order to take into account the resistance to diffusion in the slits between adjacent flakes in the same horizontal plane, Aris[29] proposed the following model (Equation 11.8):

$$\frac{D_{\text{eff}}}{D_0} = \left(1 + \frac{\alpha^2\phi^2}{1-\phi} + \frac{\alpha\phi}{\sigma} + \frac{4\alpha\phi}{\pi(1-\phi)}\ln\left(\frac{\pi\alpha^2\phi}{\sigma(1-\phi)}\right)\right)^{-1} \tag{11.8}$$

where σ is the slit shape (the ratio between slit width (ϵ) and slit thickness (t), see Fig. 11.3).

The result for flakes given in Equations (11.7) and (11.8) has experimental support, especially for barrier membranes used in packaging.[28,30,31] It also has some analytical support as the result of Monte Carlo simulations.[32,33] In the latter case,[33] Monte Carlo simulations were run in two and in three dimensions to determine the effective diffusion coefficients for typical polymer-clay systems. A comparison of simulation results with the predictions using Equation (11.8) shows that the model of Aris over predicts the effective diffusion coefficient, especially if compared to the 3D simulations.[33]

Very recently, Sorrentino *et al.*[34] proposed a model that predicts effective diffusivity in heterogeneous systems with dispersed impermeable domains of variable orientation and distribution. In addition to the sinuous pathways

formation, the model takes into account the formation of an interface region between the polymer bulk and the clay sheets that can influence the barrier properties of the composite. The relative diffusivity can be expressed by the following relationship (11.9):

$$\frac{D_{\text{eff}}}{D_0} = \frac{(1-\beta\phi)}{\left[(1-\phi)+\phi\left(1+\dfrac{L+2t}{L\,\sin\,\theta+2t\,\cos\,\theta}\right)^2\right]} \tag{11.9}$$

where θ represents the orientation angle and β represents the ratio between the interface diffusivity and the bulk polymer diffusivity.[34] Due to the difficulty in the interface diffusivity measurements, β can be used as fitting parameter.

Drozdov *et al*.[35] developed a constitutive equation for moisture diffusion through an intercalated nanocomposite made with vinyl ester resin matrix and montmorillonite clay filler. Observations in diffusion tests showed that water transport in the neat resin is Fickian, whereas it becomes anomalous (non-Fickian) with increasing clay content. This transition is attributed to immobilization of penetrant molecules on the surfaces of the hydrophilic clay layers. Observations in uniaxial tensile tests demonstrate that the response of vinyl ester resin is strongly elasto-plastic, whereas an increase in the clay content results in a severe decrease of plastic strains observed as a noticeable reduction in the curvatures of the stress-strain diagrams.[35] This is explained by the slowing down of the molecular mobility in the host matrix driven by the confinement of chains in galleries between platelets. Adjustable parameters in these relations are found by fitting the experimental data. Fair agreement is demonstrated between the observations and the results of numerical simulation. The moisture uptake by the host matrix increases on increasing the clay content. With reference to the free-volume concept, this observation is explained by the clustering of water molecules in the close vicinity of stacks of platelets, where diffusivity dramatically falls down.[35]

11.5 Polymer nanocomposites diffusivity

Nanocomposites based on isotactic and syndiotactic polypropylene (iPP and sPP) and synthetic fluorohectorite modified octadecyl ammmonium ions (OLS) obtained by melt blending, were studied.[36,37] Maleic-anhydride-grafted isotactic polypropylene (iPP-g-MA) was used as compatibilizer in both cases. The composition of the inorganic material varied between 2.5 and 20 wt.%. The transport properties were measured for dichloromethane and *n*-pentane. The zero concentration diffusion parameter strongly decreased with increasing OLS content. However, for higher vapour activities, dichloromethane is able to completely plasticize the polymer, and this leads to a high mobility of the polymer chains that determines a transition in the diffusion-concentration curve, thus

leading to very similar diffusion coefficients for different samples. Practically, the system loses its compactness and diffusion becomes less dependent or even independent of concentration.[36,37]

A systematic study was realized on Poly(ϵ-caprolactone) (PCL) nanocomposites: the influence of different percentages of montmorillonite (MMT), of MMT intercalation degree and of different organic modifiers of MMT on the diffusion coefficient of water and dichloromethane were analyzed.[38,39]

In the case of water vapour transport, the micro-composites as well as the intercalated nanocomposites show diffusion parameters very near to PCL, while the exfoliated nanocomposites strongly deviate showing much lower values, even at low montmorillonite content (Fig. 11.4). This is an indication that in the former cases the water molecules on specific sites are not immobilized but can jump from one site to another. Only in the case of the exfoliated samples, the inorganic platelets, dispersed in a disordered distribution, can constitute a barrier to the path of the hydrophilic molecules.

For the organic solvent (dichloromethane) also the intercalated samples show lower values of the diffusion parameters confirming that it is not the content of clay alone but the type and size of dispersion of the inorganic component in the polymer phase that is important for improving the barrier properties of the samples (Fig. 11.5).

Particularly interesting are the results on the MMT dispersion degree in the polymeric matrix. In the case of dichloromethane, for samples with 3 wt.% of MMT it was shown that the diffusion parameter decreases going from micro-composites (values very similar to pure PCL) to exfoliated nanocomposites; intermediate values of diffusion were measured for the intercalated nanocomposites. In the case of water, both micro-composites and intercalated nano-

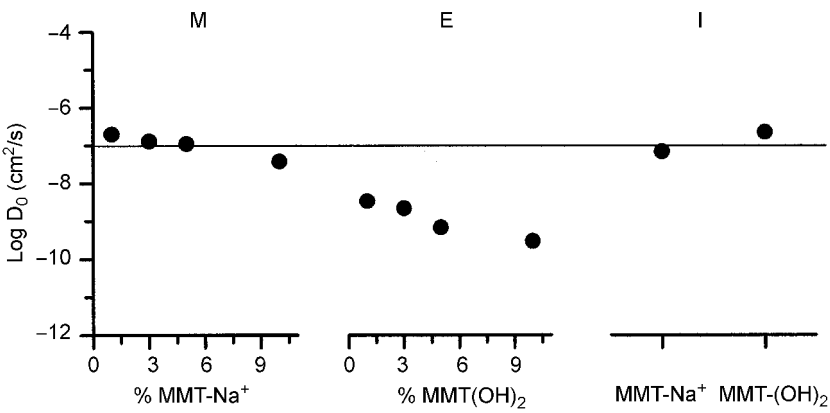

11.4 log D_0 (D_0 in cm^2/s) to water vapour, as function of clay content for the microcomposite (M), the exfoliated nanocomposites (E) and the 3 wt.% intercalated nanocomposites (I) (reprinted from ref. [38], Copyright © 2003, with permission of Elsevier Science Ltd).

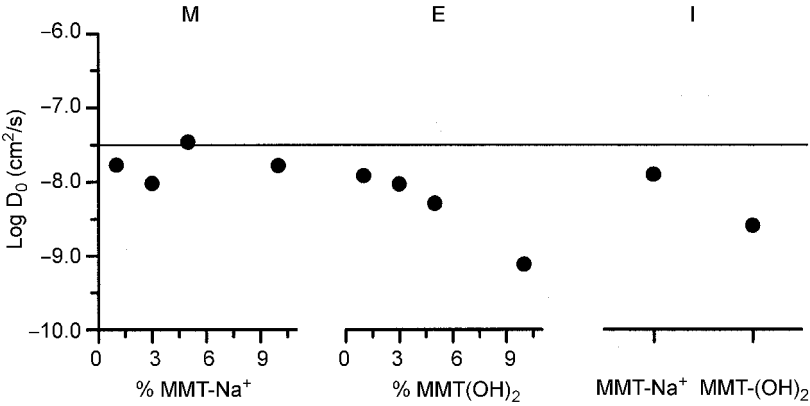

11.5 log D_0 (D_0 in cm^2/s) to dichloromethane vapour, as function of clay content for the microcomposite (M), the exfoliated nanocomposites (E) and the 3 wt.% intercalated nanocomposites (I) (reprinted from ref. [38], Copyright © 2003, with permission of Elsevier Science Ltd).

composites show diffusion parameters very near to PCL. At variance exfoliated nanocomposites show much lower values, even for small montmorillonite content.[38]

Poly(ϵ-caprolactone) chains grafted onto montmorillonite modified by a mixture of non functional ammonium salts and ammonium-bearing hydroxyl groups were studied in order to understand the influence of different polymer chain-grafting density on the diffusion coefficient. The clay content was fixed to 3 wt.%, whereas the hydroxyl functionality was 25, 50, 75, and 100%, obtaining intercalated or exfoliated systems.[39] In the case of water vapour, the diffusion parameters decreased when the hydroxyl content increased, up to the 100% sample, which showed zero diffusion. As the increase in polymer chain-grafting density induces a better exfoliation of the clays, a more tortuous pathway was created, limiting the diffusion of permeant water molecules. Moreover, a combination of exfoliation and PCL crystallization lead to the formation of an even more closed structure that further limited water diffusion by formation of a hybrid three-dimensional labyrinth. The diffusion parameters of dichloromethane also exhibited a decreasing value on increasing the hydroxyl content in the nanocomposites. In this case, however, the zero diffusion coefficients of the samples were very similar, with the only exception of the 100% sample which showed the lowest diffusion to dichloromethane vapours.[39]

The moisture diffusion in Polyamide 6/clay nanocomposites, containing 2 wt.% of clay, has been studied by Low *et al.*[16] The Authors found that the diffusion coefficient shows an U-shape dependence, while the solubility coefficient monotonically decreases as the relative humidity (RH) increases. The maximum value of the diffusion coefficient was attributed to the onset of water clustering in the polyamide, whereas the decrease of the diffusion coefficient was attributed to

the presence of water clusters. As the cluster molecules become larger in size, their diffusion through the polymer is slower, resulting in a lower diffusion coefficient. The dependence of the diffusion coefficient on the relative humidity for the polyamide 6/clay nanocomposite shows a sharp decrease between 30% and 50% RH if compared to that of polyamide 6. This may indicate that the presence of clay interfered with the water clustering in the polyamide matrix. Also Murase *et al.*[40] found from the evaluation of the Zimm-Lundberg cluster function that the clustering tendency of water sorbed into the nylon-6 matrix was reduced by polymer hybridization with the silicate compounds.

Shah *et al.*[41] studied the moisture diffusion behaviour through vinyl ester samples containing up to 5 wt.% of organically treated montmorillonite. Two different kinds of treated clay were used: a commercial montmorillonite treated with benzyl (hydrogenated tallow alkyl) dimethyl quaternary ammonium chloride, Cloisite 10A®, and a vinyl monomer clay (VMC) prepared by treating a montmorillonite with vinyl benzyl trimethyl ammonium. TEM pictures showed that the two different surface treatments resulted in different dispersion characteristics. The diffusivity of moisture was measured by soaking the samples in 25ºC water and measuring the increase of weight with increasing time of immersion. It was found that water diffusivity was reduced to half its value in the neat resin when the clay content was only 1 wt.% regardless of the nature of clay surface treatment. Although the diffusion coefficient rapidly and progressively reduces, there are diminishing returns, and a plateau appears to be reached at about 5 wt.% organoclay. Since Cloisite 10A® platelets are better separated and distributed than VMC platelets, it was expected that former nanocomposites would show a larger decrease in the moisture diffusion coefficient as compared to VMC nanocomposites. Shah *et al.*[41] theorize that the mobility of polymer chains for the two systems is quite different. In the case of the VMC nanocomposite samples, the clay platelets are not exfoliated but the movement of the polymer chains is more restricted than in the case of Cloisite 10A® samples because of the reactive nature of the clay surface. This leads to longer relaxation times and a slower rearrangement of polymer chains in the former case, resulting in comparable diffusion coefficients in the two cases.

The barrier properties of biodegradable melt-mixed polyesteramide/octadecylamine treated montmorillonite clay have been studied by Krook *et al.*[42] Density measurements indicated that shear-induced voids were formed in the nanocomposite, and these were, according to transmission electron microscopy, almost exclusively located between the clay sheets. The presence of voids limited the improvement in barrier properties with increasing filler content. The voids were the major reason for the low efficiency of the nano-fillers in blocking diffusion of the penetrant molecules.

Krook *et al.* associated the subsequent improvement of the barrier properties achieved by compression moulding the sample, to the combined effect of the increase in crystallinity as well as the small decrease in void content.

11.6 Polymer nanocomposites sorption

The transport properties of blends of a commercial high molecular weight poly(ϵ-caprolactone) with different amounts of a montmorillonite-poly(ϵ-caprolactone) nanocomposite containing 30 wt.% clay were studied by Gorrasi *et al.*[43] Water and dichloromethane were used for the sorption and diffusion analysis in the range of vapour activity between 0.2 and 0.8. Gorrasi *et al*.[43] observed that at each activity of water vapour, the sorption of the modified montmorillonite is much higher than that of PCL, indicating the higher hydrophilicity of clay with respect to the pure PCL polymer. The equilibrium concentration of water vapour increases on increasing the montmorillonite content in the composites. The type of sorption curve changes too, showing a dual sorption mode for all the blends. However, the sorption value at very low value of clay content (2%) is equal to that of pure PCL, indicating that at this concentration clay does not appreciably affect the sorption. For dichloromethane, the very strong interaction between solvent and PCL induces a plasticizing effect of the vapour, with a strong mobilization of the polymeric matrix. However, especially at high concentration of clay content, a significant reduction in sorption coefficient (evaluated as the slope of the curve at low concentration) was recorded.[43]

Low *et al.*[16] carried out a series of moisture sorption experiments on polyamide 6/clay nanocomposite film. The moisture absorption of the nanocomposites showed a maximum followed by a reduced sorption. The sorption maximum is believed to be caused by various factors, such as restricted chain relaxation in the presence of clay and moisture-induced crystallization.

Andrade *et al*.[44] investigated the transport properties and the solvent induced-crystallization phenomena in poly(ethylene terephthalate) (PET) and PET clay nanocomposites, prepared by melt intercalation. Results of non-isothermal crystallization showed that cold crystallization temperature, and percent of crystallinity of nanocomposites are higher than those of pure PET. The sorption of all the solvents is accompanied by a large-scale structural rearrangement, leading to the induced crystallization of the original amorphous state. The solvent induced crystallization caused an increasing of more than four times the percent of crystallinity.

Burnside and Giannelis[45] presented the relationship between nanostructure and properties in polysiloxane layered silicate nanocomposites. It was found that the nanocomposites show a significant decrease in swelling, even for very low filler loading (1 vol.%), compared to conventional composites, though intercalated nanocomposites and immiscible hybrids exhibited more conventional behaviour. Burnside and Giannelis suggest that strongly interacting fillers reduce swelling, while non-reinforcing fillers result in solvent uptake which may exceed that of the unfilled polymer. This behaviour has been attributed to the formation of ‘bonds’ in close proximity to the filler which is either physically or chemically sorbed and therefore restricts swelling.

Bohning *et al.*[46] prepared nanocomposites from solution using poly (bisphenol-A carbonate) as matrix polymer and the SiC nano-particles as filler. Gas sorption was measured gravimetrically using an electronic high pressure microbalance placed in a temperature controlled air-bath. Pressure dependent permeation experiments revealed a significant tendency to plasticization of the pure PC film in the region above 10 bar. Corresponding diffusion coefficients also strongly increase above 10 bar. At variance the nanocomposite film containing 5 wt.% SiC does not exhibit this plasticization behaviour. Similarly, Chen *et al.*[47] found that by blending a poly(methyl methacrylate), prepared via bulk polymerization of methyl methacrylate monomer in the presence of montmorillonite intercalated with an ammonium salt of octadecylamine, with plasticized poly(vinyl chloride), the resulting composite exhibited excellent barrier property in preventing the plasticizer migration from the inner matrix to the surface of the product.

The structural characteristics and moisture sorption properties of two kinds of nylon-6/clay hybrids were investigated by Murase *et al*.[40] The moisture sorption isotherms of the hybrid samples were a typical sigmoid shape similar to that of the pure nylon-6 sample, even if the extent of moisture regain of the hybrid films was comparatively low. All the isotherms obtained were explained through quantitative analysis in terms of the BET multilayer adsorption theory and complementally with the aid of the FloryHuggins solution theory.[40]

11.7 Polymer nanocomposites permeability

Several studies were realized on the gas barrier in different polyimide/clay nanocomposites.[18,48–53] Chang *et al.*[48–50] prepared poly(amic acid)/organoclay hybrids by the solution intercalation method with organophilic montmorillonites. A polyimide hybrid was obtained from poly(amic acid) hybrid by heat treatment at various temperatures. The permeability of the hybrid films decreased when the organoclay content increased, and it was not dependent on the gas. With the addition of only 2 wt.% clay loading, the permeability decreased of one order of magnitude and then reached a constant low value regardless of clay loading up to 6 wt.% in the case of the O_2. Dodecylamine (C_{12}) and hexadecylamine (C_{16}) were used as aliphatic alkylamines in organoclays.[50] As can be seen in Figs 11.6 and 11.7, C_{16}-organoclay is more effective than C_{12}-organoclay in increasing the gas barrier in a polyimide matrix. In the case of water vapour, the relative permeability rates of C_{12}- and C_{16}-organoclay are monotonically decreased with increasing clay loading from 2 to 8 wt.%. Similar to the O_2 permeability, the gas barrier effect of C_{16}-organoclay was also better than that of C_{12}-organoclay in permeability to water vapour.

The best fit of the Nielsen model (Equation 11.3) to the experimental data for O_2 and water gave apparent particle aspect ratios of 46 and 130, respectively. Chang *et al*. suggest that the clay retains a crystallographic regular layer

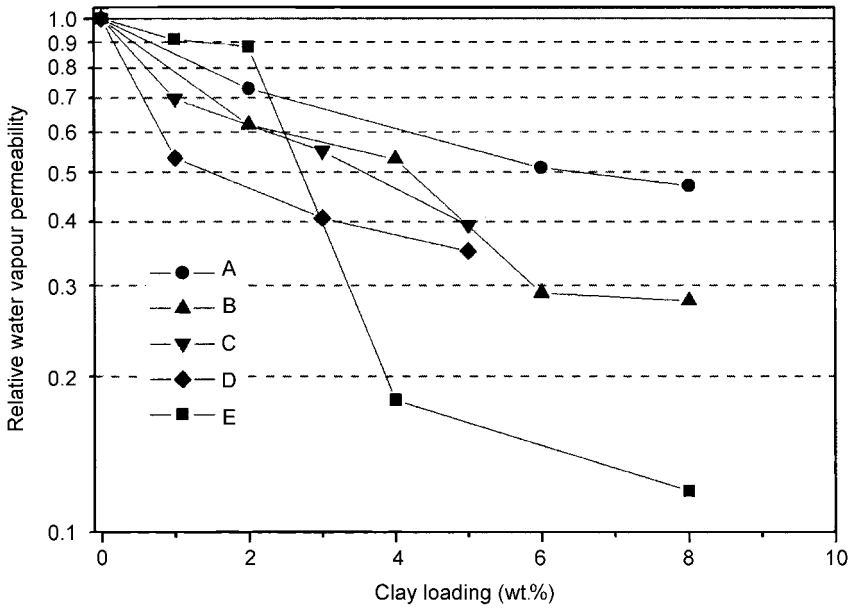

11.6 Water vapour permeability of polyimide nanocomposites as a function of clay content. (A) Polyimide/dodecylamine-clay nanocomposites (from Chang *et al.*[50]); (B) Polyimide/hexadecylamine-clay nanocomposites (from Chang *et al.*[50]); (C) Polyimide (BATB–ODPA)–clay nanocomposite (from Yeh *et al.*[52]); (D) Non-coplanar soluble polyimide (NSPI)–clay nanocomposite (from Yu *et al.*[53]); (E) Polyimide/hexadecylamine-clay nanocomposites (from Chang *et al.*[49]).

stacking order with a monolayer of polymer intercalated between the layers. The retention of the crystallographic order is in part a consequence of the unique intercalation mechanism, wherein the onium ions are displaced from the galleries and the polyamic acid becomes encapsulated upon removal of the solvent.

In Figs 11.6 and 11.7 the relative water vapour permeability and the relative oxygen permeability, respectively, of different polyimide/clay nanocomposites were reported as functions of organoclay content. It is evident from the experimental data distribution how different organoclay, as well as different preparation methods can produce dissimilar behaviour in the final properties. Regarding water vapour, more flexibility in the bone or the presence of –OH groups reduces the relative permeability, while an opposite trend is observed in the case of oxygen vapour. Permeability of heterogeneous media containing impermeable anisotropic domains is strongly influenced by domain orientation relative to the diffusion direction, as well as by their concentration and interactions with polymer bulk. The development of interface regions between polymer bulk and clay sheets can influence the barrier properties of the composite. The presence of these regions around the single slabs can be

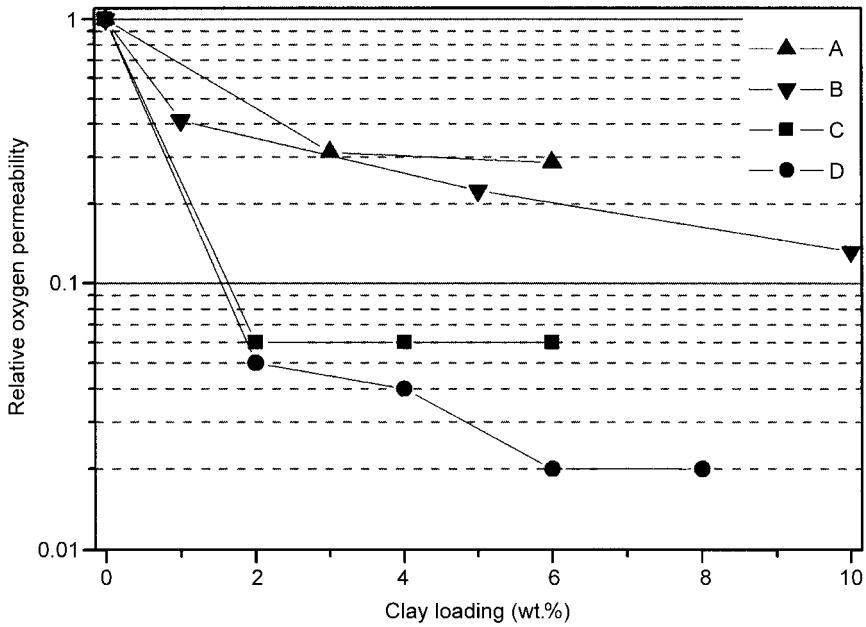

11.7 Permeability to oxygen as a function of the organoclay content in the polyimide nanocomposite. (A) Polyimide–dodecylamine–clay nanocomposites (from Khayankarn *et al.*[51]); (B) Polyimide (BATB–ODPA)–clay nanocomposite (from Yeh *et al.*[52]); (C) Polyimide/dodecylamine–clay nanocomposites (from Chang *et al.*[50]); (D) Polyimide/hexadecylamine–clay nanocomposites (from Chang *et al.*[50]).

occasionally responsible for a diffusional enhancement, as observed in some experiments.[22–24]

A variety of polyurethanes have been investigated as the continuous polymer phase in nanocomposites with dispersed clay.[54–57] Tortora *et al.*[54] prepared nanocomposites of polyurethane and organically modified montmorillonite covering a wide range of inorganic composition, up to 40 wt.%. Sorption and diffusion were measured for water vapour and dichloromethane. For both vapours the sorption did not drastically change on increasing the clay content. At variance the zero-concentration diffusion parameter strongly decreased on increasing the inorganic content. The permeability, calculated as the product of the sorption and the zero-concentration diffusion coefficient (D_0) showed a remarkable decrease up to 20% of clay and a levelling off at higher contents. Therefore permeability was largely dominated by the diffusion parameter.

Adhesive nanocomposites of polyurethane and montmorillonite modified with different organic residues have been synthesized and their permeability to oxygen and water vapour has been measured by Osman *et al.*[56] The oxygen transmission rate asymptotically decayed with increasing aluminosilicate volume fraction and a 30% reduction was achieved at 3 vol.%, when the clay

was coated with bis(2-hydroxyethyl) hydrogenated tallow ammonium or alkyl-benzyl-dimethyl-ammonium ions. In contrast, coating the clay surface with dimethyl di-hydrogenated tallow ammonium ions led to an increase in the gas transmission rate with increasing the inorganic fraction. This was attributed to a probable change in morphology resulting from phase separation at the interface between the apolar pure hydrocarbon clay coating and the relatively polar PU. This led to a decrease in density of the organic material (higher free volume) at the interface around the platelets and consequently to an increase in the permeation rate through the composite. The water vapour permeation through the PU nanocomposites was more strongly reduced than oxygen and a 50% reduction was observed at 3 vol.% silicate fraction. This might be due to the difference in size of the mobile units as well as to interactions of the water molecules with the matrix. Differences in the hydrophobicity of the clay coating influenced the water transmission rate.

The influence of the inclusion size, shape, and surface treatment on the gas permeability of polyethylene in its micro- and nanocomposites has been investigated in various papers.[17,58,59] Kato *et al.*[58] report the N_2 permeability of nanocomposites based on polyethylene (PE) melt compounded with maleic anhydride grafted polyethylene (MA-g-PE) and octadecylamine (C18-MMT) modified montmorillonite. The gas permeability coefficient for all the prepared samples are reported in Fig. 11.8. Interestingly, polyethylene, maleic anhydride grafted polyethylene, a 70/30 blend of PE/MA-g-PE and a blend of PE/MA-g-PE/MMT have almost the same permeability coefficient. Only the composites obtained by mixing the polymeric matrices with the modified montmorillonite show for PE/MA-g-PE/C18-MMT (PECH1) a decrement of 30% in permeability and for MA-g-PE/C18-MMT (PECH3) a decrement of 35%. The differences in the gas barrier property were attributed to the different dispersion of the clay silicate layers in the matrix.

In another paper, Mehrabzadeh *et al.*[59] measured the oxygen and toluene permeabilities of the exfoliated HDPE/modified clay with dimethyl-dihydrogenated tallow-quaternary ammonium nanocomposites. It was found that by addition of 5 wt.% clay the oxygen and toluene permeability was reduced by 61.5% and 48% respectively.

In several papers the PLA-organically modified layered silicate nanocomposites were studied.[60–62] All the nanocomposites exhibited dramatic improvement in many properties as compared to those of neat PLA. These improvements include the rate of crystallization, the mechanical and flexural properties, the heat distortion temperature, and the O_2 gas permeability, with a simultaneous improvement in biodegradability of neat PLA.[60,61]

Nitrile rubber (NBR)-clay nanocomposites were prepared by different methods.[63–65] The NBR-clay nanocomposites exhibited excellent gas barrier properties. Compared to gum NBR vulcanizate, the oxygen index of the NBR-clay nanocomposites slightly increased.[63,64]

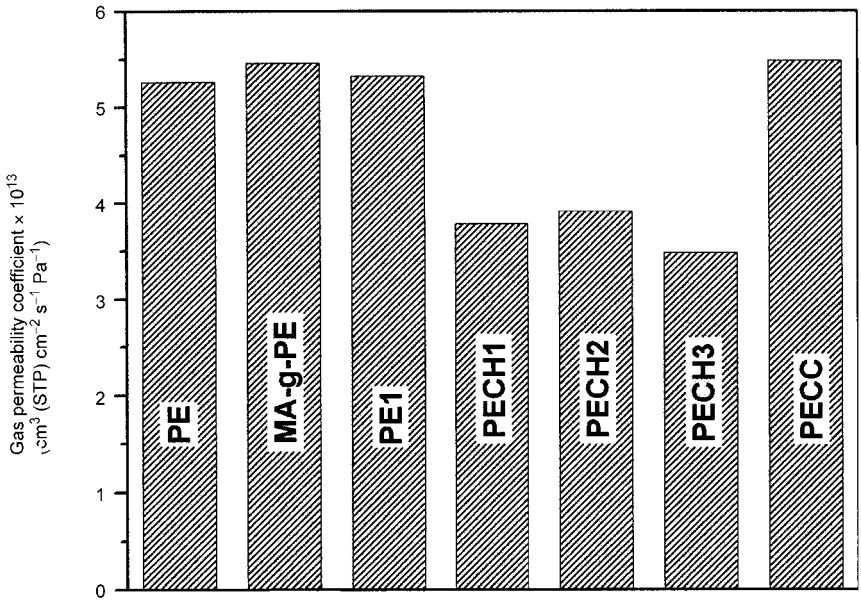

11.8 N_2 Permeability of the polyethylene-clay hybrids. PE: Polyethylene; MA-g-PE: Maleic anhydride grafted polyethylene; PE1: 70% Polyethylene/30% Maleic anhydride grafted polyethylene; PECH1: 67% Polyethylene/28% Maleic anhydride grafted polyethylene/5% C18-MMT; PECH2: 68% Polyethylene/29% Maleic anhydride grafted polyethylene/3% C18-MMT; PECH3: 95% Maleic anhydride grafted polyethylene/5% C18-MMT; PECC: 67% Polyethylene/28% Maleic anhydride grafted polyethylene/5% MMT (data from Kato *et al.*[58]).

The effect of clay concentration on the oxygen permeability of a modified poly(vinyl-alcohol) was studied by many authors,[66–68] it was found that sodium montmorillonite led to an improvement in the prevention of the water-soluble property.

Biodegradable thermoplastic starch (TPS)/clay nanocomposites were prepared through melt intercalation method.[69,70] Different kinds of clays, modified and one unmodified montmorillonite, were chosen in the nanocomposite preparation. Park *et al.*[69,70] found that the dispersion of the clays in the TPS matrix depends on both the hydrophilicity of the clays and the polar interaction between the silicate layers and TPS. The strong interaction between TPS unmodified clay leads to higher tensile properties and lower water vapour transmission rate than the pristine TPS.

11.8 Conclusions and future trends

In the previous pages, several examples of new barrier materials based on nanocomposites of polymers and layered silicates have been presented. The

investigations have shown that, generally, polymers filled with impermeable nanoparticles have a lower permeability than the corresponding virgin polymers. However, although the diffusion and the solubility are equally important for the overall mass transport, in the nanocomposites they can have very different influence – even opposite – on the permeability.

The improvement of the barrier properties for the hybrids is maximally due to the decreasing of the diffusion coefficient that, in the low vapour pressure range, is significantly reduced compared to that of the unfilled polymers.

With respect to the clay particles, dispersion, polymer nanocomposites show extremely complex morphologies. As a consequence, detailed morphological studies results are difficult to obtain by means of electron microscopy and X-ray diffraction alone. The transport properties characterization can be quite successful in elucidating structural aspects at a level which may be insensitive to the other techniques.

Micro-composites as well as intercalated nanocomposites generally have diffusion parameters very near to the pure polymers, while exfoliated nanocomposites show much lower values, even at low silicate content.

The uniform nano-filler distribution, combined with the presence of the continuous silicate phase, formed during the preparation of hybrids, represents the key to advance structural materials with simultaneous improvement of several important physical properties, such as mechanical, thermal and barrier properties.

Although a significant amount of work has already been conducted on several aspects of polymer nanocomposites, much research still remains in order to understand the complex processing-structure-properties relationships in polymer nanocomposites.

A better explanation of the mechanism that controls the transport properties of these materials and how it can be modified by suitable thermal, mechanical or chemical treatments may make possible the development of materials with permeation properties more advantageous for a given application.

Furthermore, biodegradable polymer-based nanocomposites appear to have a very bright future for a wide range of applications as high-performance biodegradable materials.

In conclusion, due to the unique combination of their key properties and potentially low production costs, polymer nanocomposites have opened new technological dimensions in the development of efficient and low cost barrier materials.

11.9 References

1. Paul D R and Yampol'skii Y P, *Polymeric gas separation membranes*, Boca Raton, CRC Press, 1994.
2. Piringer O G and Baner A L, *Plastic Packaging Materials for Food*, Weinheim, Germany, Wiley-VCH, 2000.

3. Friedman M and Walsh G, 'High performance films: review of new materials and trends', *Polym. Eng. Sci.*, 2002 **42**(8) 1756–88.
4. Lange J and Wyser Y, 'Recent innovations in barrier technologies for plastic packaging – a review', *Packag. Technol. Sci.*, 2003 **16** 149–58.
5. Vergnaud J M, *Drying of Polymeric and Solid Materials*, Berlin, Springer Verlang, 1992.
6. Fujita H, 'Diffusion in Polymer-Diluent Systems', *Advance in Polym. Sci.*, 1961 **3** 1–47.
7. Frisch H L and Rogers C E, 'Transport in Polymers', *J. Polym. Sci.: Part C*, 1966 **12** 297–315.
8. Crank J, *The Mathematics of Diffusion*, 2nd edn, Oxford Science Publications, 1975.
9. Frisch H L, 'Sorption and transport in glassy polymers – a review', *Polym. Eng. Sci.*, 1980 **20**(1) 2–13.
10. Comyn J, *Polymer Permeability*, London, Elsevier Applied Science, 1985.
11. Van Krevelen D W, *Properties of Polymers*, 3rd edn, New York, Elsevier, 1990.
12. Vieth W R, *Diffusion In and Through Polymers: Principles and Applications*, New York, Hanser, 1991.
13. Neogi P, *Diffusion in Polymers*, New York, Marcel Dekker Inc., 1996.
14. Cussler E L, *Diffusion: Mass Transfer in Fluid Systems*, New York, Cambridge University Press, 1997.
15. Ray S S and Okamoto M, 'Polymer/layered silicate nanocomposites: a review from preparation to processing', *Prog. Polym. Sci.,* 2003 **28** 1539–641.
16. Low H, Liu T, Loh W, 'Moisture sorption and permeation in polyamide 6/clay nanocomposite films', *Polym. Int.*, 2004 **53** 1973–8.
17. Osman M A and Atallah A, 'High-density polyethylene micro- and nanocomposites: effect of particle shape, size and surface treatment on polymer crystallinity and gas permeability', *Macromol. Rapid Commun.*, 2004 **25** 1540–4.
18. Yano K, Usuki A, Okada A, 'Synthesis and properties of polyimide-clay hybrid films', *J. Polym. Sci., Part A: Polymer Chemistry*, 1997 **35**(11) 2289–94.
19. Doppers L-M, Breen C, Sammon C, 'Diffusion of water and acetone into poly(vinyl alcohol)-clay nanocomposites using ATR-FTIR', *Vibrational Spectroscopy*, 2004 **35** 27–32.
20. Sloan J M and Hsieh A, 'Diffusion studies in polymerized poly (methyl methacrylate) nanocomposites by FT-IR', Annual Technical Conference, Society of Plastics Engineers, 2001 **59**(3), 3540–3.
21. Nielsen L E, 'Models for the permeability of filled polymers', *J. Macromol. Sci.* (*Chem*.), 1967 **A1**(5) 929–42.
22. Beall G W and Kamena K, 'A new family of intercalated clays for clay/polymer nanocomposites', Annual Technical Conference, Society of Plastics Engineers, 1999 **57**(3) 3973–4.
23. Beall G W, 'A new model for interpreting nanocomposite behavior', Annual Technical Conference, Society of Plastics Engineers, 2001 **59** 2195–202.
24. Beall G W, 'Molecular Modeling Of Nanocomposite Systems', Annual Technical Conference, Society of Plastics Engineers, 1999 **57**(2) 2398–401.
25. Osman M A, Mittal V, Lusti H R, 'The aspect ratio and gas permeation in polymer-layered silicate nanocomposites', *Macromol. Rapid Commun.*, 2004 **25** 1145–9.
26. Bharadwaj R K, 'Modeling the Barrier Properties of Polymer-Layered Silicate Nanocomposites', *Macromolecules*, 2001 **34** 9189–92.

27. Maxwell J C, *Electricity and Magnetism*, 3rd edn, vol. 1, New York, Dover, 1891.
28. Cussler E L, Hughes S E, Ward W J, Aris R, 'Barrier membranes', *J. Membrane Sci.*, 1988 **38** 161–74.
29. Aris R, 'On a problem in hindered diffusion', *Arch. Ration. Mech. Anal.*, 1986 **95**(2) 83–91.
30. Kamal M R and Jinnah I A, 'Permeability of oxygen and water vapor through polyethylene/polyamide films', *Polym. Eng. Sci.*, 1984 **24**(17) 1337–47.
31. Perry D, Ward W J, Cussler E L, 'Unsteady diffusion in barrier membranes', *J. Membrane Sci.*, 1989 **44** 305–11.
32. Falla W R, Mulski M, Cussler E L, 'Estimating diffusion through flake-filled membranes', *J. Membrane Sci.,* 1996 **119** 129–38.
33. Swannack C, Cox C, Hirt D, Liakos A, 'A 3D simulation study of barrier properties of nanocomposite films', Annual Technical Conference, Society of Plastics Engineers, 2003 **61**(l–2) 2100–4.
34. Sorrentino A, Tortora M, Vittoria V, 'Diffusion Behaviour in Polymer-Clay Nanocomposites', *J. Polym. Sci.: Part B: Polymer Physics*, 2006, **44**(2) 265–274.
35. Drozdov A D, Christiansen J C, Gupta R K, Shah A P, 'Model for anomalous moisture diffusion through a polymer–clay nanocomposite', *J. Polym. Sci.: Part B: Polymer Physics*, 2003 **41** 476–92.
36. Gorrasi G, Tammaro L, Tortora M, Vittoria V, Kaempfer D, Reichert P, Mulhaupt R., 'Transport properties of organic vapors in nanocomposites of isotactic polypropylene', *J. Polym. Sci.: Part B: Polymer Physics*, 2003 **41** 1798–805.
37. Gorrasi G, Tortora M, Vittoria V, Kaempfer D, Mulhaupt R, 'Transport properties of organic vapors in nanocomposites of organophilic layered silicate and syndiotactic polypropylene', *Polymer* 2003 **44** 3679–85.
38. Gorrasi G, Tortora M, Vittoria V, Pollet E, Lepoittevin B, Alexandre M, Dubois P, 'Vapor barrier properties of polycaprolactone montmorillonite nanocomposites: effect of clay dispersion', *Polymer* 2003 **44** 2271–79.
39. Gorrasi G, Tortora M, Vittoria V, Pollet E, Alexandre M, Dubois P, 'Physical properties of poly(ϵ-caprolactone) layered silicate nanocomposites prepared by controlled grafting polymerization', *J. Polym. Sci.: Part B: Polymer Physics*, 2004 **42** 1466–75.
40. Murase S, Inoue A, Miyashita Y, Kimura N, Nishio Y, 'Structural characteristics and moisture sorption behavior of nylon-6/clay hybrid films', *J. Polym. Sci.: Part B: Polymer Physics*, 2002 **40** 479–87.
41. Shah A P, Gupta R K, Gangarao H V S, Powell C E, 'Moisture diffusion through vinyl ester nanocomposites made with montmorillonite clay', *Polym. Eng. Sci.*, 2002 **42**(9) 1852–63.
42. Krook M, Albertsson A C, Gedde U W, Hedenqvist M S, 'Barrier and mechanical properties of montmorillonite/polyesteramide nanocomposites', *Polym. Eng. Sci.*, 2002 **42**(6) 1238–46.
43. Gorrasi G, Tortora,M, Vittoria V, Galli G, Chiellini E, 'Transport and mechanical properties of blends of poly(ϵ-caprolactone) and a modified montmorillonite-poly(ϵ-caprolactone) nanocomposite', *J. Polym. Sci.: Part B: Polymer Physics,* 2002 **40** 1118–24.
44. Andrade M L Q, Manrich S, Pessan L A, 'Transport properties and solvent induced-crystallization in PET and PET-clay nanocomposite films', *J. Metastable Nanocryst. Mater.*, 2004 **22** 51–6.

45. Burnside S D, Giannelis E P, 'Nanostructure and properties of polysiloxane-layered silicate nanocomposites', *J. Polym. Sci.: Part B: Polymer Physics*, 2000 **38** 1595–604.
46. Bohning M, Goering H, Hao N, Mach R, Oleszak F, Schonhals A, 'Molecular mobility and gas transport properties of polycarbonate-based nanocomposites', *Rev. Adv. Mater. Sci.*, 2003 **5** 155–9.
47. Chen G, Yao K, Zhao J, 'Montmorillonite clay/poly(methyl methacrylate) hybrid resin and its barrier property to the plasticizer within poly(vinyl chloride) composite', *J. Appl. Polym. Sci.*, 1999 **73** 425–30.
48. Chang J-H and Park K M, 'Polyimide nanocomposites: comparison of their properties with precursor polymer nanocomposites', *Polym. Eng. Sci.*, 2001 **41**(12) 2226–30.
49. Chang J-H, Park D-K, Ihn K J, 'Polyimide nanocomposite with a hexadecylamine clay: synthesis and characterization', *J. Appl. Polym. Sci.*, 2002 **84** 2294–301.
50. Chang J-H, Park K M, Cho D, Yang H S, Ihn K J, 'Preparation and characterization of polyimide nanocomposites with different organo-montmorillonites', *Polym. Eng. Sci.*, 2001 **41**(9) 1514–20.
51. Khayankarn O, Magaraphan R, Schwank J W, 'Adhesion and permeability of polyimide–clay nanocomposite films for protective coatings', *J. Appl. Polym. Sci.*, 2003 **89** 2875–2881.
52. Yeh J-M, Chen C-L, Kuo T-H, Su W-F, Huang H-Y, Liaw D-J, Lu H-Y, Liu C-F, Yu Y-H, 'Preparation and properties of (BATBODPA) polyimide–clay nanocomposite materials', *J. Appl. Polym. Sci.*, 2004 **92** 1072–9.
53. Yu Y-H, Yeh J-M, Liou S-J, Chen C-L, Liaw D-J, Lu H-Y, 'Preparation and properties of polyimide–clay nanocomposite materials for anticorrosion application', *J. Appl. Polym. Sci.*, 2004 **92** 3573–82.
54. Tortora M, Gorrasi G, Vittoria V, Galli G, Ritrovati S, Chiellini E, 'Structural characterization and transport properties of organically modified montmorillonite/ polyurethane nanocomposites', *Polymer* 2002 **43** 6147–57.
55. Chang J-H, An Y U, 'Nanocomposites of polyurethane with various organoclays: thermomechanical properties, morphology, and gas permeability', *J. Polym. Sci.: Part B: Polymer Physics*, 2002 **40** 670–7.
56. Osman M A, Mittal V, Morbidelli M, Suter U W, 'Polyurethane adhesive nanocomposites as gas permeation barrier', *Macromolecules*, 2003 **36** 9851–8.
57. Xu R, Manias E, Snyder A J, Runt J, 'New biomedical poly(urethane urea)-layered silicate nanocomposites', *Macromolecules*, 2001 **34** 337–9 .
58. Kato M, Okamoto H, Hasegawa N, Tsukigase A, Usuki A, 'Preparation and properties of polyethylene–clay hybrids', *Polym. Eng. Sci.*, 2003 **43**(6) 1312–6.
59. Mehrabzadeh M, Kamal M R, Mollet V, 'Synthesis and characterization of high density polyethylene clay nanocomposites', Annual Technical Conference, Society of Plastics Engineers, 2003 **61**(2) 2260–4.
60. Ray S S, Yamada K, Okamoto M, Ogami A, Ueda K, 'New polylactide/layered silicate nanocomposites. 3. High-performance biodegradable materials', *Chem. Mater.*, 2003 **15** 1456–65.
61. Ray S S, Yamada K, Okamoto M, Ueda K, 'Polylactide-layered silicate nanocomposite: a novel biodegradable material', *Nano Letters*, 2002 **2**(10) 1093–6.
62. Chang J-H, An Y U, Sur G S, 'Poly(lactic acid) nanocomposites with various organoclays. I. Thermomechanical properties, morphology, and gas permeability', *J. Polym. Sci.: Polymer Physics*, 2003 **41** 94–103.

63. Wu Y-P, Jia Q-X , Yu D-S, Zhang L-Q, 'Structure and properties of nitrile rubber (NBR)–clay nanocomposites by co-coagulating NBR latex and clay aqueous suspension', *J. Appl. Polym. Sci.*, 2003 **89** 3855–8.
64. Nah C, Ryu H J, Kim W D, Choi S-S, 'Barrier property of clay/acrylonitrile butadiene copolymer nanocomposite', *Polym. Adv. Tecknol.,* 2002 **13** 649–52.
65. Kim J, Oh T, Lee D, 'Curing and barrier properties of NBR/organo-clay nanocomposites', *Polym Int,* 2004 **53** 406–11.
66. Grunlan J C, Grigorian A, Hamilton C B, Mehrabi A R, 'Effect of clay concentration on the oxygen permeability and optical properties of a modified poly(vinyl alcohol)', *J. Appl. Polym. Sci.*, 2004 **93** 1102–9.
67. Strawhecker K E and Manias E, 'Structure and properties of poly(vinyl alcohol)/Na^+ montmorillonite nanocomposites', *Chem. Mater.*, 2000 **12** 2943–9.
68. Yeh J-M, Yu M-Y, Liou S-J, 'Dehydration of water-alcohol mixtures by vapor permeation through PVA/clay nanocomposite membrane', *J. Appl. Polym. Sci.*, 2003 **89** 3632–8.
69. Park H-M, Li X, Jin C-Z, Park C-Y, Cho W-J, Ha C-S, 'Preparation and properties of biodegradable thermoplastic starch/clay hybrids', *Macromol. Mater. Eng.,* 2002, **287** 553–8.
70. Park H-M, Lee W-K, Park C-Y, Cho W-J, Ha C-S, 'Environmentally friendly polymer hybrids. Part I Mechanical, thermal, and barrier properties of thermoplastic starch/clay nanocomposites', *J. Mater. Sci.,* 2003, **38** 909–15.

12

Rubber-clay nanocomposites

A MOHAMMAD and G P SIMON, Monash University, Australia

12.1 Introduction

Since the early days of the rubber industry, fillers in the form of fine particulates have been used in rubber compounding. Particulate fillers are usually divided into two groups, inert fillers and reinforcing fillers. Inert fillers are added to the rubber to increase the bulk and reduce costs. In contrast, reinforcing fillers such as carbon black and silica are incorporated in the rubber to enhance the mechanical properties, to change the electrical conductivity, to improve the barrier properties or to increase the resistance to fire and ignition.[1,2] However, a minimum of 20 wt.% of the filler content is usually needed for a significant property enhancement. This high loading of fillers may reduce the processability of the rubber compounds and cause the end products to weigh significantly more than the neat rubber, and thus limit their application in some industries. The expansion of the polymer industry and the continuous demand for new, low-cost composites with improved properties and lower particle content are some of the many new and exciting challenges for this industry.[3,4]

Nanocomposites based on layered silicates offer the possibility for new paradigms of material properties. Although clay nanocomposites have been prepared and tested for many thermoplastic and thermosetting polymers, much less attention has been given to the rubber-clay nanocomposites.[5–11] Rubbery polymers with their low modulus stand to gain much in terms of modulus and strength from the addition of nanoparticles. In addition, the effect of clay addition on rubber tear properties, fracture toughness and abrasion properties is only starting to become known.

12.2 Overview of rubbers (elastomers)

The term elastomer is used to describe vulcanized polymeric materials, whose glass transition is sub-ambient and, amongst other properties, has the ability to

be extensively deformed and on release of stress, return to its original length.[12] The common characteristics of elastomers are their elasticity, flexibility, and toughness. Beyond these common characteristics, each elastomer has its own unique properties, often requiring additives to achieve the appropriate behaviors. It is customary when discussing the formulation of rubber compounds to classify the additives by the function they serve. Rubber compounding ingredients can be categorized as: vulcanizing or crosslinking agents, processing aids, fillers, antidegradants, plasticizers and other specialty additives.[1,13]

The rubbers in the marketplace are of two main types: crosslinking systems and thermoplastic elastomers. Most of the commonly-used rubbers are polymeric materials with long chains, which are chemically crosslinked during the curing process. This type of elastomer cannot be reshaped, softened, melted nor reprocessed by subsequent reheating, once formed.[13,14] Thermoplastic elastomers, on the other hand, are rubbers which act at room temperature in a manner similar to crosslinked materials but are copolymers, with one phase being rubbery and the other crystallizable. However, it is crosslinked elastomers which will be the subject of this review. These elastomers are generally hydrocarbon-based polymers consisting of carbon and hydrogen atoms, although some are polar and may contain other moieties. They include styrene-butadiene rubber, butyl rubber, polybutadiene rubber, ethylene propylene rubber and polyisoprene-rubber, both natural and synthetic. Such rubbers are classified as general-purpose rubbers because of their use in high volume rubber products such as tyres, belting, seals and hoses.[13,15] Key aspects of the structure and properties of the range of common elastomers available are given below, prior to a discussion of work done to date in their nanocomposite manifestations.

12.2.1 Natural rubber (NR)

Natural rubber is a linear polymer with repeat units being isoprene (C_5H_8), its sub-ambient glass transition temperature is about −70ºC and its specific gravity is 0.93 at 20ºC. It crystallizes when stretched or stored at temperatures below 20ºC due to its regularity of structure. Temperature and type (grade) of natural rubber are factors which influence this rate of crystallization.[15] NR contains small amounts of fatty acids and proteinaceous residues, which act to promote sulfur curing, the main route used in industry to vulcanize (cure) natural rubber.[16] Peroxide-cured, natural rubber vulcanizates are found to have lower strength properties than those obtained by sulphur curing, but have other good properties such as lower compression set, lower creep, and excellent resistance to aging with suitable antioxidant incorporation.[17] Important commercial applications of NR are in the production of tyres, bumpers, and in thin-walled, high strength products such as balloons and surgical gloves.[16]

12.2.2 Synthetic polyisoprene (IR)

Synthetic polyisoprene is produced anionically and by Ziegler-Natta polymerization. Whilst natural rubber has up to a 95% cis-1,4 microstructure, synthetic polyisoprene may be as much as 98% stereoregular. Even though the difference in stereoregularity is small, IR is substantially more crystallizable. IR compounds have a lower modulus and higher elongation to failure than similarly-formulated NR compounds due to less strain-induced crystallization at high rates of deformation.[13,15] The most important commercial application of IR is in the preparation of chlorinated and isomerized rubbers for the surface coatings industry.[1] Synthetic polyisoprene rubber is often used in the same applications as natural rubber,[16] behaving during the mixing and processing stages like natural rubber due to their chemical similarity.[18]

12.2.3 Styrene-butadiene rubber (SBR)

Styrene-butadiene rubber is the most-widely used synthetic rubber in the elastomer industry, with the largest volume production. It is a copolymer of styrene ($C_6H_5CH{=}CH_2$) and butadiene ($CH_2{=}CH{-}CH{=}CH_2$), typically containing about 23% styrene and 77% butadiene. SBR can be produced by emulsion and solution polymerization, but almost 85–90% of the world production of SBR is prepared by emulsion polymerization.[15] Most SBR compound formulations use a reasonable amount of reinforcing filler, carbon black being the commonest improving both tensile and tear properties.[1,15] Conventional accelerated sulphur systems are the usual package used to crosslink SBR. Being an intrinsically slower curing material compared to natural rubber, SBR usually incorporates accelerators in its compounding formulations.[1]

The tyre industry consumes almost 70% of the total SBR production, since SBR has suitable properties of very good abrasion resistance, ageing resistance and low temperature properties.[1]

12.2.4 Butyl rubber (IIR)

Butyl rubber is a copolymer of isobutylene with a small amount of isoprene (2–3% by weight), which represent sites that allow crosslinking. IIR has unusually low resilience for an elastomer with such a low T_g of about -70ºC. Since butyl rubber is largely a saturated elastomer with no double bonds, it has excellent resistance to ozone, oxygen, chemicals and heat. Another outstanding feature of this rubber is its low gas permeability and is thus widely used in inner tubes and tyre liners.[13,15] Other butyl rubber industrial applications are in cable insulations and jacketing, roof membranes and pharmaceutical stoppers.[16]

12.2.5 Polybutadiene (BR)

Polybutadiene is the homopolymer of butadiene (C_4H_6) and is widely used in blends with other rubbers and is a difficult material to process on its own.[15] The largest portion of the global polybutadiene production is made by solution polymerization.[15,16] Some of the good properties of polybutadiene are: heat ageing resistance, abrasion resistance, ozone resistance, and their ability to accommodate large quantities of fillers and oil whilst retaining good rubbery properties.[1] Poor tack, poor road grip of tyre treads, and poor tear and tensile strength as compared those of natural and styrene-butadiene rubber are the limitations of polybutadiene.[1]

The tyre industry has been attracted by these outstanding properties and BR is often used in blends with SBR in the manufacture of car tyres, and with natural rubber in manufacturing truck tyres. It is the third most important and consumed (by volume) elastomer in the tyre industry after SBR and NR.[1]

12.2.6 Ethylene-propylene rubber (EPM, EPDM)

Ethylene propylene copolymers (EPM) are made by Ziegler-Natta and metallocene polymerization and are the commercial rubbers with the lowest density. EPM cannot be vulcanized and thus is not reactive to peroxide curing. To introduce an unsaturated site suitable for crosslinking, a non-conjugated diene termonomer such as ethylidene norbornene, 1,4 hexaadiene or dicyclopentadiene, is employed to produce the rubber known as EPDM. Ethylene propylene diene rubber has small number of double bonds, external to the backbone, introduced in this way. In EPDM, the 'E' stands for ethylene, the 'P' for propylene, the 'D' for diene and the 'M' indicates that the rubber has saturated chain of the polymethylene type.[13,15,16,19,20] The main desirable properties of EPM and EPDM are:[16]

- aging and ozone resistance of EPM and EPDM compounds is excellent
- EPM and EPDM compounds have a low temperature flexibility compared with that of natural rubber compounds
- high and excellent level or resistance to chemicals
- excellent electrical insulation properties
- the heat resistance of EPM and EPDM compounds is much better than that of SBR and NBR compounds.

The applications of EPDM and EPM include roofing, sealing, gaskets, hoses, cable insulations and jacketing, and in other goods that require heat and weather resistance.[13,15,16,19,20]

12.2.7 Silicone rubbers

Silicone rubbers are unlike the previously discussed elastomers which have carbon-carbon backbones, but rather contain the very flexible siloxane backbone. Silicone rubbers (polyorganosiloxanes) consist of repeat —Si—O— units, with the organic side groups attached to the silicon atoms. Despite the high price of silicone rubbers, they are very important elastomers, with many industrial applications as a result of their good thermal stability, excellent resistance to ozone, oxygen, and sunlight, good electrical insulation properties, and show reliable and consistent properties over a wide temperature range.[1] Despite silicone rubbers having excellent characteristics, they have some limitations such as the low tensile strength, high gas permeability, poor resistance to hydrocarbon oil and solvent, and a fairly high price.[1] It is important in nearly all silicone rubber applications to incorporate reinforcing fillers because of their very low tensile strength. On account of their excellent properties, silicone rubbers are used in many applications such as shaft sealing, spark plug caps, O-rings, embossing rollers and gaskets, cables, corona-resistant insulating tubing, keyboards and contact mats, window and door profile seals.[1]

12.2.8 Nitrile rubber (NBR)

The importance of NBR (a polar rubber) is due to its excellent resistance to non-polar or weakly polar materials (solvents) such as hydrocarbon oils, fuels, and greases. Nitrile rubber, which is a copolymer of butadiene and acrylonitrile, is prepared by an emulsion polymerization process.[1,15,16]

Acrylonitrile content varies in nitrile rubber grades from 20 to 50% by weight, most NBR properties are greatly affected by the acrylonitrile content. With increasing acrylonitrile content, the oil resistance increases, heat resistance improves, cure rate increases, and processability becomes easier.[15] It is very important to incorporate reinforcing fillers during the nitrile rubber compounding process to obtain compounds with a reasonable level of tensile strength, tear strength, and abrasion resistance, since NBR lacks self-reinforcing properties. Cure of nitrile rubber is usually achieved by an accelerated sulphur curing system, however peroxide curing may be used in particular instances. Sulphur has a lower solubility level in nitrile rubber than natural rubber, which inhibits a totally uniform distribution in NBR matrix, leading to over and under-cured regions.[15] Nitrile rubber has advantage over may type of elastomers as a result of its general vulcanizate properties:[1,16] excellent resistance to hydrocarbon materials (oil, fuels, and greases), very good heat resistance (with the air absence) very low level of gas permeability, high electrical conductivity, moderate tensile strength, tear strength, and ozone resistance, and low temperature flexibility.

12.3 Fillers predominantly used in the rubber industry

Fillers have been used in the formulation of rubber compounds since the early days of the rubber industry. Whilst their primary function is to reduce cost, it has been found that fillers have a reinforcing effect in the rubber mechanical properties such as tensile strength, modulus, tear resistance and abrasion resistance and thus very few rubber compounds are prepared without substantial quantities of filler.[1,21,22] The performance of filler in the rubber matrix is governed by its characteristics, such as the particle size and concentration, particle shape, surface activity, degree of interactions with rubber matrix and structure of the particle agglomerates.[1,23]

Increasing the area of contact between rubber matrix and filler particles seems to be the most important factor in providing a strong reinforcement effect. The interfacial contact area between rubber matrix and filler is controlled by the size of filler particles and filler volume fraction.[22] The degree of bonding between rubber matrix and filler particles is a key factor in determining the degree of an elastomer reinforcement.[22,24] Carbon black is the most widely used and most effective conventional reinforcing filler in the rubber industry because it gives excellent properties to general-purpose elastomers.[25] However, for colored rubber compounds, non-black fillers are needed, and silicon dioxide (silica) is the most effective reinforcing filler in this category due to its high specific surface area.[26] Since rubber compounds are largely reinforced by carbon back and silica, these two conventional fillers will first be overviewed before discussing layered silicate nanocomposites.

12.3.1 Carbon black

Carbon black (CB) is the most extensively used reinforcing filler in rubber compounds, since the discovery of colloidal carbon black reinforcing qualities in 1904.[27,28] Carbon black is composed of carbon particles solidly fused together by covalent bonds, thus forming aggregates which cannot be broken into smaller sizes during the normal material processing conditions. Another feature of the aggregates is that the bonding between them is weak and they do not retain their integrity during materials processing.[29] Carbon black particle diameters are less than 20 nm in some of furnace CB grads and up to few hundred nanometers in the thermal CB, whilst the carbon black aggregate dimensions fall in the range of 100 nm to a few micrometers.[30] Carbon black surfaces contain a number of functional groups such as carbon-oxygen, carbon-hydrogen surface groups, carbon-nitrogen moieties, and carbon-halogen surface compounds, and the most important groups between them are the carbon-oxygen surface groups.[29]

The incorporation of CB with high surface area in an elastomer results in a high level of reinforcement and higher tensile strength, tear strength, and abrasion resistance, but also results in a compound with high hysteresis, high cost, and one

which is more difficult to mix and process.[17,31] The dramatic improvement in properties such as tensile strength, modulus, tear strength, and abrasion resistance when carbon black is added to elastomers has motivated much research into the mechanisms of such a reinforcement.[21] There are likely both chemical and physical interactions between carbon back and the rubber matrix, resulting in property improvement, but the understanding of the nature of carbon black reinforcement is still growing.[21] Creating an interfacial contact area between a rigid solid phase (CB) and a soft rigid phase (rubber) is a result of carbon black incorporation in an elastomer matrix, and results in chemical or physical adsorption of rubber molecules onto carbon black surface.[29] The consequence of this adsorption is the formation of 'bound rubber' on the surface of carbon black.[29] Bound rubber is the portion of elastomer which can not be separated from the filler surface when the rubber mix is extracted by a good solvent for the rubber such as toluene, over a specific period of time at room temperature.[29,32] The formation of bound rubber structures, are believed to enhance the mechanical and physical properties of the carbon black-filled rubber compounds.[25]

12.3.2 Silica

Synthetic silicon dioxide (silica) can be produced either by precipitation or by a pyrogenic (thermal) process.[1,24] According to the method of production, synthetic silicon dioxide can be classified into two groups: precipitated and pyrogenic (fumed) silica.[1,24] Precipitated silicas have been used extensively in many rubber applications, much more than fumed silica.[24] In the rubber industry, the use of fumed silicas is limited due to expense, mainly being used as reinforcing fillers for silicon rubbers.[1,16,24] Non-black fillers such as silica are chosen over CB for one or more of the following reasons:[21,26–28,33,34]

- the end products have to be white, translucent or light colored
- lower cost clay, ground limestone, and silica are cheaper than carbon black
- certain unique properties arise when silica is used, such as reduced rolling resistance in rubber.

Silica is thus the most important filler that competes with carbon black in the area of rubber reinforcement technology.[21,33] However, in the early stages of silica usage, their uses as reinforcing filler instead of carbon black were limited due to a number of problems:[34]

- silica-filled compounds have higher viscosities
- they are more difficult to mix and process
- there is a concomitant increase in vulcanization time
- silica-filled compounds often show lower crosslinking density.

The silanol groups, which are on the surface of silica, show strong filler-filler interactions and cause the adsorption of the polar materials such as the curatives

on the surface. Such an adsorption of the curatives on the surface results in a reduction in the crosslinking density and delays in the scorch time of the silica filled rubber compounds.[35]

For these reasons, the use of silica as a reinforcing filler in the rubber compounds was hampered until the discovery of silane coupling agents.[27,34] Silane agents are able to react with the silanol groups on surface of silica and form stable bonds between the filler and silane. Silanes also often contain a second functional group, which permit the formation of covalent bonds with the polymer.[27,34,36] As well as filler/rubber coupling, silane coupling agents are used in the silica-filled rubber compounds to improve silica dispersion in the rubber matrix, reduce agglomerate size and prevent curative adsorption on their surface.[35]

12.4 Rubber crosslinking systems

The versatile properties of rubbers result from their low glass transition temperatures (T_g) and the ability to manipulate (increase) this by various types of crosslinking or vulcanization (also known as curing).[37] Sulphur and peroxide, respectively, are the most widely-used crosslinking agents.[12,38]

12.4.1 Sulphur vulcanization

Vulcanization is a very complex reaction and involves activators for the breakage of the sulphur ring (S_8) and accelerators for the formation of sulphur intermediates, which facilitate sulphur-to-double bond crosslinking. Elastomer vulcanization by sulphur without any accelerators takes several hours and is of no commercial importance. By using accelerators in the sulphur curing system, the optimum curing time can be decreased to as little as 2–5 min.

In general, the most widely used technique in curing various industrial applications is the accelerated sulphur curing method, since it provides better physical properties, provides a considerable fast crosslinking rate and it has the capability to provide the delayed actions needed for processing, shaping, and forming before the formation of the rubber vulcanized network.[39] According to the level of sulphur and the ratio of accelerator to sulphur, sulphur vulcanization systems are classified as conventional, semi-efficient (semi-EV), and efficient (EV).[37]

12.4.2 Peroxide curing

The production of free radicals is the driving force for peroxide crosslinking. Radicals are atoms or molecular fragments with unpaired electrons. These radicals cause an unstable situation and react to allow the electron to pair with another. Rubber peroxide crosslinking reaction consists of three basic steps as follows.[40]

A. Homolytic cleavage

When peroxide is heated to a sufficient temperature, the oxygen–oxygen bond ruptures. The resultant molecular fragments from these ruptures are called radicals, which are highly energetic, reactive species.[40]

$$ROOR' \longrightarrow RO^* + {}^*OR'$$

B. Hydrogen abstraction

Radicals that have been formed from the peroxide decomposing are reactive toward hydrogen atoms in chains. Hydrogen abstraction is a process where the radical removes a hydrogen atom from another nearby atom, and is a very important step in the peroxide curing reaction, as it is the mechanism by which radicals are transferred from peroxide molecular fragments to the rubber backbone.[40]

$$RO^* + P\text{-}H \longrightarrow ROH + P^*$$

C. Radical coupling (formation of crosslinking)

Elastomer radicals are highly reactive species and when two of these radicals come in contact, the unpaired electrons will couple and form a covalent bond or crosslink between the elastomer chains.[40]

$$P^* + P^* \longrightarrow P\text{-}P \text{ (crosslink)}$$

The complexity of the peroxide curing system arises from a range of possible side reactions such as β-cleavage of the oxy radical, addition reaction, polymer scission, radical transfer, dehydrohalogenation, oxygenation, and acid catalyzed decomposition of the peroxide.[40]

Rubber composites are usually a complex mixture of many additives (curatives, oils, fillers, antidegradants and coagents) and each of these additives is added to impart a specific benefit to the final rubber compound. The incorporated additives can also affect the peroxide crosslinking reaction because of the ability of the radicals to react with many of the functional groups of these additives.[40]

12.5 Types of rubber-clay nanocomposite

Rubber-clay nanocomposites have attracted, in recent years, the attention and interest of many industrial and academic researchers, since they often exhibit at low loading levels of clay outstanding properties compared with unfilled rubber compounds or conventional filled composites. Research on the rubber-clay nanocomposites has focused mainly on four well-known rubbery materials,

natural rubber (NR), ethylene propylene diene rubber (EPDM), styrene-butadiene rubber (SBR), and nitrile rubber (NBR). However, some other reports of work on other types of elastomers such as silicon rubber, polybutadiene rubber, and ethylene propylene rubber also exist.

12.5.1 Rubber-clay nanocomposite preparation methods

In general, rubber-clay nanocomposite preparation methods can be divided into four major groups according to the processing techniques:[2,41,42]

- in-situ polymerization
- intercalation of rubber via solution blending
- direct melt intercalation method
- intercalation of rubber via latex compounding.

In-situ polymerization

In this method, layered silicate is swollen within the monomer solution (or liquid monomer) so the formation of rubber can occur between and around the intercalated layers. The polymerization can be initiated either by the incorporating of curing agent or initiator or by increasing the temperature if it is sufficiently reactive.[2,41,42]

Intercalation via solution

This method uses a solvent system in which the rubber is soluble and the layered silicate is swellable. The organically modified layered silicate is first swollen and comes apart in the solvent. The rubber is then dissolved in solvent and added to the solution. Upon solvent removal, the clay layers reassemble around the polymer, resulting in rubber-clay nanocomposite.[2,41–43]

Direct melt intercalation method

This is the most promising method and it has great advantages over both previously mentioned methods being both compatible with current industrial processes and environmentally benign, due to the absence of solvents. In this method rubber and modified layered silicate mixture are blended in the molten state under shear. The rubber chains reptate from the molten mass into the silicate galleries to form either intercalated or delaminated nanocomposites.[2,41,42]

Intercalation of rubber via latex compounding

Latex compounding is also a promising method in preparing rubber-clay nanocomposites. The latex compounding technique starts with dispersing layered

silicates in water that acts as a swelling agent owing to hydration of the intergallery cations. Rubber latex is then added and mixed for a period of time, with the dispersion of layered silicate in water followed by coagulation.[42,44]

12.5.2 Types of rubber-clay nanocomposite structure

The incorporation of a few weight percent of modified layered silicates which are properly dispersed in the rubber matrix can result in very high surface areas for rubber-clay interactions, as compared to the conventional rubber-filler composites. According to the strength of the interfacial interactions between rubber matrix and layered silicate four type of rubber-clay composites can be produced:[2,41,42]

- *Conventional composites*: in the conventional rubber composite, layered silicate acts as conventional, micron-sized fillers such as carbon black clusters or other inorganic fillers.
- *Intercalated nanocomposite*: intercalated nanocomposites are formed by the insertion of a rubber chains between the unaltered silicate layers, maintaining their regular alternation of galleries and laminas.
- *Exfoliated nanocomposite*: in exfoliated nanocomposites the individual layers of the nanoclay are totally delaminated and dispersed in the rubber matrix. The ordered structure of layered silicate is lost and the average distances between the exfoliated layers depend on clay loading.
- *Intermediate nanocomposites*: rubber-clay nanocomposites which are partially intercalated and partially exfoliated, are an intermediate (and often observed) type of nanocomposite.

12.5.3 Natural rubber-clay nanocomposites

Rubber nanocomposites based on natural rubber (NR) with organic-modified layered silicate reinforcement have mainly been prepared on a two-roll mill, via a vulcanization curing process.[45–48] López-Manchado *et al.*[46] made NR nanocomposites with unmodified clay and with an organoclay (organic modified layered clay), the loading content of clays being 10 phr. Another natural rubber composite containing the octadecylamine in the absence of clay and organoclay was also prepared to determine the effect of the pristine octadecylamine on the crosslinking density of natural rubber.[46] The untreated clay (Na^+–bentonite) presented a diffraction peak at $2\theta = 7^\circ$ (d-spacing = 12.6 Å) and the organoclay had a peak at $2\theta = 5^\circ$ (d-spacing = 17.6 Å). Figure 12.1(a) shows the XRD spectra of NR-clay composite, NR-organoclay nanocomposite before curing, and NR-organoclay nanocomposite after curing.[46]

It can be seen from Fig. 12.1 (a and b) that the incorporation of clay in natural rubber compounding results in the formation of a conventional rubber

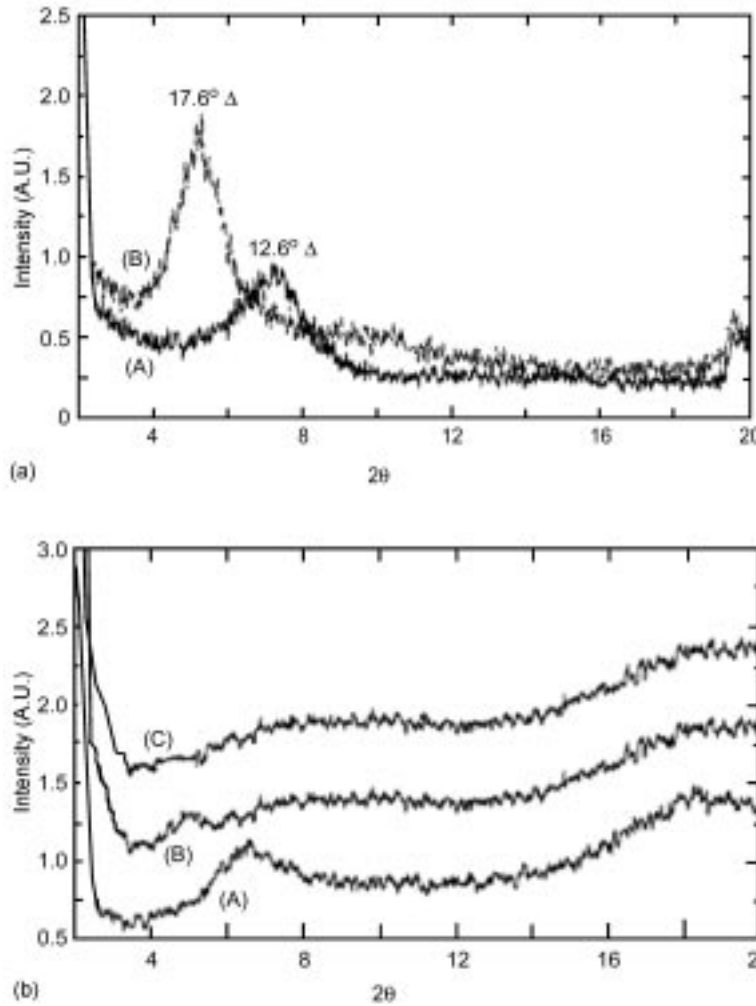

12.1 (a) XRD patterns of (A) unmodified clay and (B) unmodified organoclay.[46] (Figure 1, page 1072, López-Manchado, M.A., Herrero, B., Arroyo, M. (2003) *Polymer International* 52: 1070–1077.)
(b) XRD Patterns of (A) NR-clay composite, (B) NR-organoclay nanocomposite before curing, (C) NR-organoclay nanocomposite after curing.[46] (Figure 4, page 1073, López-Manchado, M.A., Herrero, B., Arroyo, M. (2003) *Polymer International* 52: 1070–1077.)

composite, with the interlayer gallery spacing remaining that of the untreated clay. The peak that corresponded to the organoclay interlayer spacing disappeared in the case of NR/organoclay nanocomposite, which indicates that the organoclay nanolayers have largely been exfoliated in the natural rubber

matrix.[46] There is no significant difference between NR/organoclay nanocomposite XRD patterns before and after vulcanization, implying that the formation of nanometer-scale dispersion structure in NR matrix is largely achieved during the mixing process.

The cure characteristics of pristine NR have been found to be affected by the presence of organoclay, where the optimum curing (vulcanization) time of natural rubber was sharply reduced with the incorporation of organoclay (Fig. 12.2).[46] This reduction in NR curing time is basically due to the amine groups present in the organoclay structure which arises from the treatment of the gallery surface.[46] It is also important to note from Fig. 12.2 that the intercalation of the octadecylamine into the organoclay galleries further facilitates the sulphur curing reaction of NR by sharply decreasing the curing time of NR-organoclay as compared to the blend with only octadecylamine.[46]

The incorporation of organoclay also resulted in a noticeable increase in the value of mixing torque of NR-organoclay nanocomposite, as compared to the pristine NR.[6,43,46] This is due to the octadecylamine intercalation between the layers of the clay increasing the interlayer distance, thus easing the intercalation and confinement of natural rubber chains in the galleries of the layered-silicate. Thus a better interaction between the silicate and natural rubber is obtained, which also increases the torque required for blending.[6,43,46]

The addition of organoclays also influences the thermal properties of natural rubber (Table 12.1).[46] The glass transition temperature (T_g) of NR shifts to slightly higher temperatures with the presence of the organoclay. This

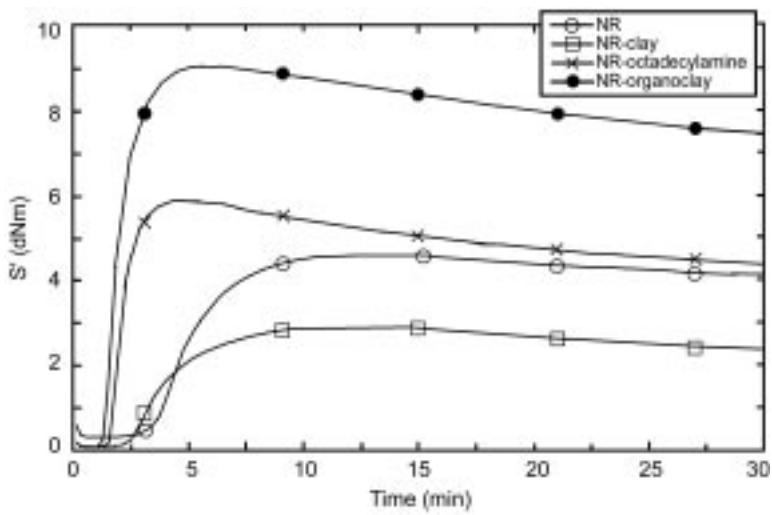

12.2 Vulcametric curves obtained at 160°C of all studied materials.[46] (Figure 5, page 1073, López-Manchado, M.A., Herrero, B., Arroyo, M. (2003) *Polymer International* 52: 1070–1077.)

Table 12.1 Thermal properties of the studied materials.[46] (Table 4, p. 1075, López-Manchado, M.A., Herrero, B., Arroyo, M. (2003) *Polymer International* 52: 1070--1077)

Material	TGA Degradation peak (°C)	DSC			
		t_{50} (min)	t_{97} (min)	ΔH_c (J g^{-1})	T_g (°C)
NR	382.9	10.81	23.00	9.20	−62.0
NR-clay	385.1	8.50	21.90	11.41	−60.4
NR-organoclay	393.1	1.71	6.46	19.61	−57.4
NR-octadecylamine	387.9	3.02	8.13	15.82	−59.7

is due to the intercalation of the rubber chains into the organoclay galleries, resulting in a restriction of motion of the natural rubber chains segments.[46] Organoclay addition also shifted the thermal decomposition temperature of NR-organoclay nanocomposite to a higher temperature, due to the confinement of NR chains into the galleries of the organoclay. The exfoliated nanolayers form a strong interaction with the rubber chains and prevent the volatile decomposition products from diffusing out during the thermal degradation process.[46,49]

López-Manchado *et al.,*[43] studied and investigated two different nanocomposite production methods (mechanical and solution mixing method), in order to find the optimal method of obtaining an exfoliated organoclay-natural rubber nanocomposite. It was been found that the solution blending method resulted in nanocomposites with higher amounts of bound rubber (R_B) values (15.2%) compared to those obtained by the mechanical blending (10.6%). This implies that the compatibility between the organo-layered silicate and NR matrix is much higher when a natural rubber nanocomposite is prepared by the solution mixing method.[43] Both mechanical and solution mixing methods resulted in a uniform dispersion (intercalation or exfoliation) of organoclay nanolayers in the natural rubber matrix, as can be seen from the disappearance of the organoclay peak in the XRD spectra.[43]

12.5.4 EPDM-clay nanocomposites

Ethylene propylene diene rubber is a well-known general-purpose rubber with a significant commercial importance. It has been one of the main rubbers to be investigated with organo-treated layered silicates to study the effects of nano-reinforcement on properties.[8,9,50–52] EPDM nanocomposites with clays have been prepared by simple static mixing in confined chamber such as Haake, solution blending, and on a laboratory two roll mill. However, most EPDM/clay nanocomposites have been produced by conventional, internal melt blending process.[8,9,50–53]

The nature of the curing systems (peroxide or sulphur) has an effect on the preparations and morphologies of EPDM/organic montmorillonite (OMMT) nanocomposites. Zheng *et al.*[51] found that the peroxide curing system of EPDM/OMMT composites resulted in a shift of the diffraction peak to lower angles than of the OMMT, due to the intercalation of EPDM chains into the OMMT galleries. However, the sulphur curing system caused the disappearance of the diffraction peak angle of EPDM/OMMT composites, which indicates that there is considerable delamination or exfoliation of OMMT layers throughout the rubber matrix.[51] The advantages of the internal melt blending process are its compatibility with present polymer processing methods, its versatility, and its friendly environmental characteristics due to the absence of organic solvents from this process.[51] The internal melt blending process was also found to result in better physical properties than other methods, as demonstrated in a comparative study between two mixing techniques; internal melt blending and the two roll mill, which showed that the internal melt blending technique at a temperature of 100ºC imparted higher tensile strength and elongation at break to EPDM-clay nanocomposites, than does preparation by a two roll mill.[52] This was due to the higher shear rates (shear stress) leading to nanocomposites with better clay dispersion, and consequently higher mechanical properties. Zheng *et al.*[50] reported that the tensile strength and the elongation at break of EPDM/MMT-C12 (Na-type montmorillonite treated with methylbiscocoalkylamine) nanocomposite increased respectively up to 25 MPa and 666% with increasing the rotor speed due to the high shear stresses produced for the addition of 15 wt.% clay.

Intercalation of EPDM molecules into the clay galleries, as well as the exfoliation of clay layers in EPDM rubbery matrix, leads to outstanding properties to EPDM/clay composites.[8,9,50–52] The tensile strength of EPDM/OMMT nanocomposites was enhanced 3-4 times more than the pristine EPDM composite for 15 wt.% clay, this improvement attributed to a strong interaction between EPDM matrix and organoclay and weaker interactions between filler particles.[50,51] The exfoliation of silicate layers in EPDM increased the elongation at break of EPDM/MMT-C12 (100/15) by 140%, compared to pristine EPDM compound.[50] The mechanism of elongation at break improvement is not clear at present, but could be due to better silicate layers dispersion and 'physical bonding' between silicate layers and the EPDM matrix.[8,50] The tear strength, a measure of rubber resistance to crack propagation, was effectively enhanced (1.5–2.0 times higher than gum EPDM vulcanized) by the incorporation of organic modified silicates in EPDM. This increase in tear resistance was attributed to the uniform dispersion of the silicate nanolayers in the EPDM rubbery matrix forming a physical barrier to the growing crack.[9,50,51] Another important characteristic of EPDM/clay nanocomposites is their excellent gas barrier properties, the permeability of oxygen and nitrogen decreased in EPDM/clay nanocomposites by the introduction of organically modified

silicates.[8,9] In EPDM/LEP-C18-MMT nanocomposites the oxygen permeability was reduced by 60%, compared to gum EPDM compounds with only 10phr filler content, due to the uniform dispersion of silicate nanolayers with planar orientation in the EPDM matrix increasing the tortuous path for oxygen molecules.[9]

12.5.5 SBR-clay nanocomposites

Styrene-butadiene rubber is one of the promising elastomers for the future rubber/clay nanocomposites industry. SBR-clay nanocomposites have been successfully prepared with properties such as tensile strength, hardness, and tear strength exceeding those of SBR composites reinforced with carbon black.[44] SBR-clay nanocomposites have been prepared by solution blending, with the solvent being toluene, but other successful SBR-clay nanocomposites have also been produced by other methods such as latexes.[5,44,54,55] SBR-clay nanocomposites prepared by this method involve dispersing the clay in water with vigorous stirring, causing the clay layers to separate. The SBR latex is then added to the clay-water solution and mixed for a period of time, resulting in a uniform dispersion of the clay particles inside the latex.[44] A comparative study between two reinforcing systems showed that the latex method resulted in SBR-clay nanocomposites with better tensile strength, tear strength, and hardness than those prepared by the solution method. This could be due to better dispersion of the silicate layers and better interaction between silicate layers and SBR matrix. The solution method, however, leads to SBR-clay nanocomposites with higher elongation at break and higher permanent set.[44]

Styrene content in SBR also has an influence on the mechanical properties of SBR-clay nanocomposites, this influence has been investigated by selecting three different grades of styrene-butadiene rubber with 15, 23, and 40% of styrene contents. Figure 12.3 shows that increasing the styrene contents up to 40% resulted in production SBR-clay nanocomposites with higher tensile strength and 50% modulus for clay contents of 4 phr, as well as increasing the glass-transition temperature of the nanocomposites.[55] Styrene moieties traditionally have been found to readily enter alkyl-ammonium treated clay galleries, and thus it is not surprising that the SBR grade with 40% styrene was the most effective grade in increasing the spacing between clay layers, which made the exfoliation of clay layers in the rubber matrix much easer during the preparation process. The bulky styrene group promotes ease of intercalation and pushes apart silicate layers.[55]

SBR-clay nanocomposites were cured by peroxide and sulphur curing system to study the effect of the curing agents on their mechanical properties. The amount of curing additives for both systems was optimized in such a way that the volume fraction values of rubber were comparable for both systems, and is directly proportional to the rubber crosslinking density. SBR-clay nano-

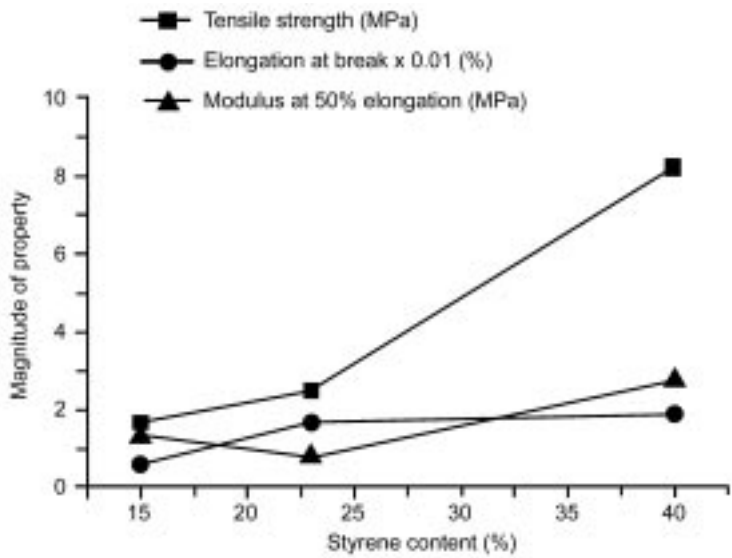

12.3 Variation of the mechanical properties with the styrene content of SBR nanocomposites filled with 4 phr of modified montmorillonite.[55] (Figure 10, page 706, Sadhu, S., Bhowmick, A.K. (2004) *Journal of Applied Polymer Science* 92: 698–709.)

composites with very similar crosslink density for either peroxide or sulphur systems resulted in compounds of very comparable modulus and tensile strength. However, the elongation at break of sulphur cured SBR-clay nanocomposites was much higher that the peroxide cured nanocomposites, the formation of polysulfidic bonds which are more flexible than the peroxide system carbon–carbon bonds were responsible for this increase in ductility.[55]

12.5.6 Nitrile rubber-clay nanocomposites

Nitrile rubber (NBR)-clay nanocomposites have been successfully prepared with mainly exfoliated and partially-intercalated structures in some cases, and intercalated structure in others.[54,56–58] The preparation of NBR-clay has been reported via different processing techniques such as melt intercalation (internal blending), solution blending, ball milling of surfactant treated layered clay in emulsified solution and followed by latex shear blending, and by co-coagulating the nitrile rubber latex and layered silicate aqueous suspension followed by two-roll mill compounding.[54,56–58] Kim *et al.*[56] studied the influence of clay-organic modification on the properties of the nitrile rubber-organomontmorillonite nanocomposites. They used three different modifiers, octylamine (CH_3 $(CH_2)_7$ NH_2), dodecylamine (CH_3 $(CH_2)_{11}$ NH_2), and octadecylamine (CH_3 $(CH_2)_{17}$ NH_2), to treat Na-montmorillonite (MMT), and the organically modified montmorillonites were termed as C8-MMT, C12-MMT, and C18-MMT

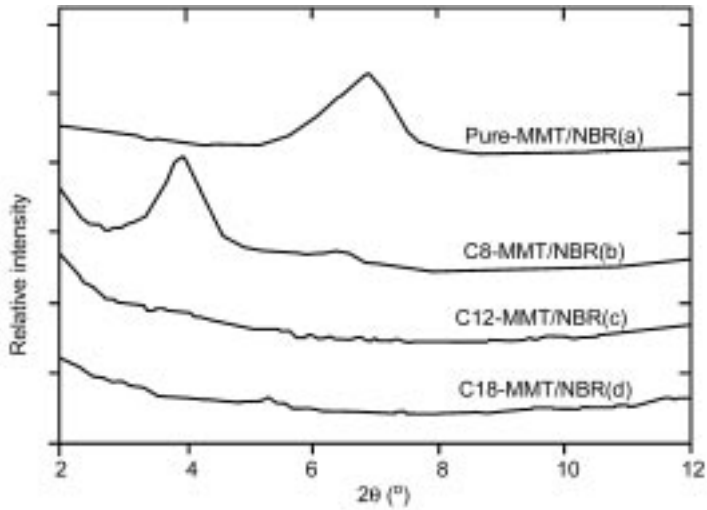

12.4 X-ray diffraction patterns of NBR hybrids with 4.52 wt.% of MMT: (a) pure-MMT/NBR, (b) C8-MMT/NBR, (c) C12-MMT/NBR, (d) C18-MMT/NBR.[56] (Figure 2, page 1060, Kim, J.-T., Oh, T.-S., Lee, D.-H. (2003) *Polymer International* 52: 1058–1063.)

respectively.[56] X-ray diffraction (XRD) and transmission electron microscopy (TEM) were used to characterize organomontmorillonite-NBR nanocomposites. Figure 12.4 shows the X-ray diffraction patterns of pure MMT/NBR, C8-MMT/NBR, C12-MMT/NBR, and C18-MMT/NBR hybrids.[56] It has been found that the diffraction peaks of C12-MMT/NBR and C18-MMT/NBR nanocomposites totally disappeared, which implied that the organo-MMT layers were exfoliated and randomly dispersed in the nitrile rubber matrix. Whilst in the case of C8-MMT/NBR nanocomposite, the diffraction peak was significantly shifted to 3.92º of 2θ (d_{001} = 2.25 nm) as compared with C8-MMT of 6.5º of 2θ (d_{001} = 1.36 nm), this shift indicating that NBR molecules intercalated between the galleries of C8-MMT.[56] To verify these XRD data regarding the dispersion of organo-MMT layers in NBR matrix, and to examine the nanostructure of the organo-MMT/NBR nanocomposites, transmission electron microscopy was used and TEM images of C18-MMT/NBR nanocomposite with 8.7 wt.% have been produced. The images reported show that C18-MMT layers have been successfully exfoliated into nanoscale layers (about 10–20 nm thickness) from their original particle size (40 μm) and the nanoscale layers were uniformly distributed in the nitrile rubber matrix.[56]

12.5.7 Silicon rubber-clay nanocomposites

Silicon rubber/organomontmorillonite hybrid nanocomposites were successfully prepared via a melt-intercalation process.[59] The organo-MMT XRD patterns

showed a peak at $2\theta = 4.38^{\circ}$, while the peak of the silicon rubber/organo-MMT nanocomposites can be found at $2\theta = 2.38^{\circ}$. According to Bragg equation calculations the galleries distance of organo-MMT and silicon rubber/organo-MMT nanocomposite are 20.2 Å and 37.1 Å, respectively, confirming that silicon rubber molecules can indeed be intercalated between the layers of the organo-MMT.[59] The presence of a strong diffraction peak at $2\theta = 2.38^{\circ}$ in the silicon nanocomposite indicates that some order of the organo-MMT layered structure still exists in the silicon rubber hybrid, despite the enlargement in the galleries distance due to the intercalation.[59] TEM showed that the organo-MMT particles were also exfoliated into nanoscale layers of about 50 nm dimensions from initial 40 μm dispersion, and the layers were homogeneously dispersed in the silicon rubber matrix.[59]

The mechanical properties (tensile strength and elongation at break) of silicon rubber nanocomposites were improved with the incorporation of the organo-clay and it has been found that these properties were close to the mechanical properties of aerosilica-filled silicon rubber composites.[59]

The thermal stability of silicon rubber compounds was evaluated with thermogravimetric analysis (TGA). The decomposition temperatures of unfilled silicon rubber, silicon rubber/organo-MMT nanocomposite, and silicon rubber/aerosilica filled compound were 381ºC, 433ºC, and 440ºC, respectively, as shown in Fig. 12.5. This advantageous elevation in the decomposition temperatures of silicon rubber with organo-MMT or aerosilica incorporation can be attributed to the favorable interaction between the silicon rubber matrix and filler particles, which increases the physical and chemical crosslinks which prevents the silicon chains from the degradation. It is also likely that these

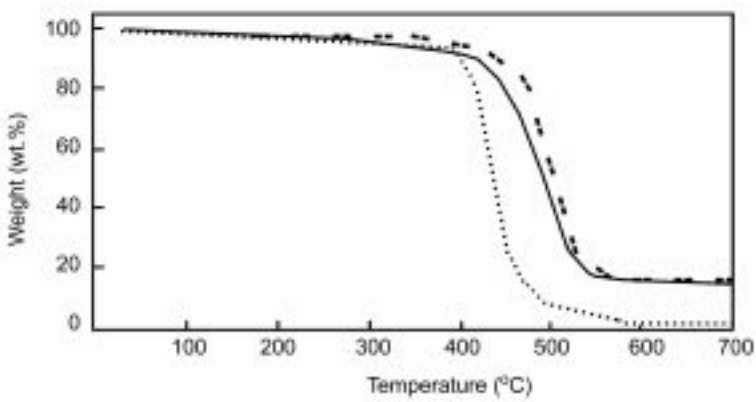

12.5 TGA traces for silicone rubber and its composites with 8.1 vol.% of filler: (– – –) silicone rubber without filler; (——) silicone rubber/organo-MMT hybrid; and (-- -- --) silicone rubber/aerosilica.[59] (Figure 5, page 1560, Wang, S., Long, C., Wang, X., Li, Q., Qi, Z. (1998) *Journal of Applied Polymer Science* 69: 1557–1561.)

incorporated fillers aided in deactivating the active centers of silicone chain decomposition.[59]

12.5.8 Polybutadiene rubber-clay nanocomposites

Polybutadiene rubber-clay nanocomposites reported to date were obtained by the solution method. The organically-modified layered clay was dissolved in solvent (toluene) with continuous stirring, and a polybutadiene-toluene solution was added to the organoclay-toluene solution and vigorously stirred for some 12 hours. Solvent was subsequently removed, resulting in polybutadiene rubber-clay nanocomposite preparation.[44] The data obtained by XRD showed that the basal spacings in the modified layered clay and polybutadiene rubber-clay nanocomposite were 1.90 and 4.41 nm, respectively. This expansion in the galleries of the layered silicate confirms the intercalation of some polybutadiene molecules between the galleries.[44] On the other hand, TEM micrographs showed that the layered silicates were dispersed uniformly in the polybutadiene matrix at a nanoscale size, which indicated the formation of polybutadiene nanocomposite.[44]

Table 12.2 summarizes the mechanical properties of polybutadiene rubber-clay nanocomposites. The hardness, tensile strength, elongation at break, and permanent set all improved with increasing the clay content (5–40 phr).[44] The mechanical properties of polybutadiene rubber-clay nanocomposite with 20 phr clay content have been compared to those of the polybutadiene composites filled with 20 phr carbon black (SFR and N330), as presented in Table 12.3. This data shows that the organically-modified layered silicate was as effective a reinforcing filler, as carbon black. Some of the mechanical properties of polybutadiene nanocomposite such as hardness, tear strength, and tensile strength even exceeded those of the carbon black filled compounds.[44] These excellent mechanical properties of the nanocomposites resulted from the uniformly dispersed layered silicate in the elastomer matrix, and the strong interaction between the nanoclay layers and rubber chains. Thus layered silicates could be used in the polybutadiene industry as a promising reinforcing filler, if the layers

Table 12.2 Properties of BR-clay nanocomposites.[44] (Table V, p. 1882, Wang, Y., Zhang, L., Tang, C., Yu, D. (2000) *Journal of Applied Polymer Science* 78: 1879–1883)

Clay (phr)	Hardness (Shore A)	Tensile strength (MPa)	Elongation (%)	Permanent set (%)
5	44	1.6	225	4
10	45	3.1	360	8
20	48	6.4	724	28
40	50	8.9	670	48

Table 12.3 Properties of BR by comparative reinforcing method (20 phr clay).[44] (Table VII, p. 1883, Wang, Y., Zhang, L., Tang, C., Yu, D. (2000) *Journal of Applied Polymer Science* 78: 1879–1883)

Method	Hardness (Shore A)	Tear strength (kN/m)	Tensile strength (MPa)	Elongation (%)	Permanent set (%)
Solution	48	15.7	6.4	724	28
SRF	48	19.6	3.5	476	4
N330	50	19.6	5.9	500	4

were able to be dispersed uniformly in the rubbery matrix on the nanometer size scale.[44]

12.5.9 Ethylene propylene rubber-clay nanocomposites

Ethylene propylene rubber-clay nanocomposites were successfully obtained by melt compounding maleic anhydride modified ethylene propylene rubber (EPR-MA) and organophilic montmorillonite in a twin-screw extruder at 200ºC for contents of 2.9 to 8.3 wt.% clay (CNs). A range of carbon black and talc filled compounds were also prepared in the same manner, for comparison purposes. The XRD patterns of the nanocomposites showed no peak for EPR-CNs, which indicated that these nanocomposites were well delaminated and TEM images confirmed that the layers were exfoliated on the nanometer size scale.[60]

Tensile test results indicated that increasing the organophilic montmorillonite content in the nanocomposites rubbery matrix caused the tensile modulus to increase and the elongation at break to decrease, since the tensile modulus of EPR-CN 8 was three times higher than the unfilled maleic anhydride modified ethylene propylene rubber composite (EPR-MA). These mechanical property improvements are thought to be due to the restriction of polymer chain rearrangement by the dispersion and interaction of the montmorillonite layers. Comparing the mechanical properties of nanocomposites with the conventional filled compounds at the same filler content (approximately 5 wt.%) showed that the nanocomposites had much higher modulus and much lower elongation at break. Indeed, the tensile modulus was similar to that of the conventional compounds filled with 30 wt.% carbon black.[60]

12.6 Comparison of properties achieved in rubber-clay nanocomposites

The previous section has looked largely at the nanocomposites from the point of view of the different materials, the methods of processing and degree of dispersion. In this section, the effect of nanoclay addition of the most widely measured rubbery properties are summarized and contrasted.

12.6.1 Cure characteristics

The vulcanization characteristics of filled rubber compounds are expressed in terms of scorch time, optimum cure time, and torque value.[6,9,43,46] For NR nanocomposites, the scorch time and optimum cure time were sharply reduced with the addition of organoclay. This behavior was a result of the existence of amine groups in the nanosilicate structure which come from the organophilization of the layered silicate, as well as the intercalation of octadecylamine between clay galleries which further facilitate the vulcanization reaction.[46] The torque value of NR nanocomposites increased remarkably with the presence of organoclay, as compared with the unfilled NR. As torque value is related to the crosslinking density, it can be assumed that the organoclay increased the crosslinking density of natural rubber.[46] On the other hand, the curing times of EPDM clay nanocomposites were prolonged with increasing organoclay content in the nanocomposites, which was most probably due to the adsorption of curing agents on the surface of organoclay.[9,50] In other work, Chang *et al.*[9] found no difference between the torque maximum values of pristine EPDM and MMT filled EPDM nanocomposite, which implied that organoclay did not affect the crosslinking density of EPDM nanocomposites. Sulphur and peroxide curing systems showed different impacts on the curing characteristics of EPDM/organo-clay nanocomposites.[51] The optimum curing time of sulphur cured EPDM nanocomposites was increased with increasing the clay content, possibly due to the adsorption of the curatives on the organoclay surface, whilst little change was noticed in the optimum curing time of the peroxide cured EPDM nanocomposites with increasing the organoclay content.[9,50,51]

12.6.2 Tensile properties

The tensile properties of the rubbers improved remarkably when nanocomposites are obtained with the addition of organically-modified layered silicates. It has been found that the tensile properties of these rubbers were influenced by one or more of the following factors: clay loading level, type of curing system, mixing conditions, rubber grade, nanocomposite preparation method, and type of alkyl-ammonium (clay modifier) used. NR-organoclay nanocomposite with 10 phr octadecylamine-modified montmorillonite showed higher tensile strength, 100% modulus, and elongation at break than those of the NR composite reinforced with 40 phr carbon black.[6] The tensile strength of NR-organoclay (10 phr) nanocomposite was more than three times greater than the tensile strength of the pristine NR.[6] When layered-silicate was incorporated at less that 20 phr in styrene butadiene rubber (SBR) nanocomposites, the tensile strength of nanocomposite exceeded those of the SBR composites reinforced with carbon black (SRF and HAF), silica, and commonly used clay (TC).

Increasing the filler content up to 40 phr in SBR matrix resulted in nanocomposites with tensile strengths greater than that of silica/SBR composites but lower than carbon black (HAF)/SBR composites at the same filler loading content.[5] It should be noted that clay loading content, nanocomposite preparation methods, and the level of styrene content in SBR all have an effect on the tensile properties of SBR nanocomposites.[5,44,55] For example, increasing the layered-silicate content or styrene level (in SBR) in the SBR nanocomposites resulted in an increase in the maximum tensile strength, elongation at break and modulus of the nanocomposites.[44,55] The investigation on the influence of curing systems on the tensile properties of SBR nanocomposites showed that elongation at break is the main property affected by the type of curing systems, and sulphur curing provides the nanocomposites with higher elongation at break due to the formation of the flexible polysulfidic bonds.[55]

The addition of 30 phr of organo-montmorillonite to nitrile rubber (NBR) led to preparation of NBR nanocomposite with tensile strength ten times higher than that of the gum NBR vulcanizate.[58] The tensile strength and modulus of NBR nanocomposites are proportionally related with the level of clay content in the studied range (0–16 phr clay).[56] Layered-silicate (20 phr) was found to provide polybutadiene rubber nanocomposites with good tensile properties even higher than those provided by carbon black.[44] Increasing the clay content from 5 to 20 phr in polybutadiene rubber nanocomposites led to a fourfold increase in tensile strength and 222% increase in the elongation at break.[44] In ethylene propylene rubber (EPR) the incorporation of organophilic montmorillonite resulted in raising the tensile modulus and lowering the elongation at break. The tensile modulus of EPR filled with 6 phr layered silicate was similar to that of 30 wt.% carbon black filled EPR.[44]

All improvements in the tensile properties of rubber nanocomposites were mainly due to the intercalation of rubber chains into layered-silicate galleries, which provided strong interaction between rubber matrix and organoclay and this strong interaction was often seen by the decreasing of $\tan\delta$ height of the glass transition relaxation and an increase of the T_g towards higher temperatures.[44,50,51,58]

12.6.3 Tear strength

Tear strength represents the level of resistance to crack propagation in rubbers. Organically-modified layered silicates effectively enhance the tear strength of NR, EPDM, SBR, and NBR nanocomposites.[5,9,44,48,50,51,57] The excellent tear strength property of these nanocomposites was attributed to the unique layer structure of the layered-silicate in the nanocomposites, the strong interfacial action between clay nano-particles and rubber matrix, and the ability of layer bundles to slide during the tearing process, which forms a physical barrier against growing cracks and reduces the energy of crack growth.[5,50,51] For

example, the tear strength of EPDM nanocomposite was found to be twice that of unfilled EPDM compound for 20 wt.% clay.[51] Sulphur curing systems, higher mixing temperature, and higher clay loading content resulted in EPDM nanocomposites with much improved tear strength.[50.51] SBR nanocomposites also showed outstanding tear strength, which exceeded those of SBR compounds reinforced by carbon blacks, silica and commonly used clay even at high filler loading level (60 phr).[5] 7.5 wt.% was the loading level and it provided NBR nanocomposite with the highest tear strength; further increasing the clay content in fact resulted in a lowering of the tear strength.[57]

12.6.4 Hardness

Rubber nanocomposite researchers are usually interested in investigating the tensile properties of the final nanocomposite products, but there are fewer studies into the hardness property of pristine rubber and its organoclay-filled nanocomposites.[5,6,43,44,50] Studies performed showed that the uniform dispersion of the layered structured clay increased the interfacial action between clay layers and rubber, resulting in nanocomposites with higher strength, and therefore, higher hardness. SBR nanocomposites, for example, exhibited two times higher hardness than the unfilled SBR and much higher than those of carbon blacks, silica, and commonly used clay composites for the same filler loading levels.[5] The addition of 10 phr of layered-silicate to natural rubber nanocomposites caused an improvement in hardness which was higher than NR composite's hardness filled with 40 phr carbon black.[6]

12.6.5 Gas permeability

The exceptional decrease in gas permeability is another advantage of rubber-clay nanocomposites. Layered silicate with planar orientations are believed to improve and elevate the barrier properties of rubber nanocomposite by forming a tortuous path which increases the gas diffusion distance, slowing down the gas molecules forward movement in the nanocomposite matrix.[9,58] For example, the oxygen permeability of 10 phr layered clay filled EPDM nanocomposite was reduced to 60% as compared with the pristine EPDM compound.[9] Increasing the amount of filler in the rubber matrix was also found to further decrease the nitrogen permeability of NBR compounds.[58] The barrier properties of NBR clay nanocomposites to nitrogen was also found to be much better than the barrier property of comprable silica-filled NBR compounds.[58]

12.6.6 Solvent resistance

As the gas permeability decreases with the enhancement of barrier properties of rubber-clay nanocomposites, the solvent uptake also decreases in the few studies

to date. A study conducted on NR-clay nanocomposites showed that the pristine natural rubber had much higher toluene uptake at 25ºC than NR-clay nanocomposites.[49] Similar behavior of swelling resistance had been noticed with silicon–clay nanocomposites: these nanocomposites showed significant reduction in organic solvent (toluene) uptake even at very low loading levels (1 vol.%).[61,62] This improvement of rubber nanocomposites solvent uptake resistance is due to the strong interaction between rubber matrixes and organoclay particles, as well as to the presence of large surface area of impermeable clay layers in the nanocomposites which increased the average diffusion path length for the solvents.[49,61,62]

12.6.7 Thermal stability

Thermo-gravimetric analysis (TGA) devices are often used to investigate rubber-clay nanocomposite thermal stability by monitoring the change in sample weight at high temperatures. It has been found that the addition of organoclay shifted the thermal decomposition temperature of natural rubber to higher values, which indicated the enhancement of the NR/organoclay nanocomposite thermal stability as compared with the unfilled NR.[46] NR nanocomposite filled with 10 wt.% fluorohectorite (synthetic layered clay) were more thermally stable than those filled with 10 wt.% bentonite (natural layered clay) at 450ºC, due to better clay dispersion and stronger interaction between NR matrix and clay layers.[49] Increasing the organoclay content in NBR nanocomposites also resulted in elevating their thermal degradation temperatures,[57] and Wang *et al.*[59] found that the decomposition temperatures of neat silicon rubber, silicon rubber/organo-MMT hybrid, and silicon rubber/aerosilica were increased in the order 381ºC, 433ºC and 440ºC, respectively. The improvement in the thermal stability is probably due to the high surface area of such nanocomposites, which prevents the volatile decomposition products from diffusing out during the high temperature degradation process.[46,49,57,59]

12.7 Conclusions

Compared to the vast literature on most of the thermoplastic or thermosetting polymer-clay nanocomposites, reports of rubber-clay nanocomposites are much more limited. Much more research is needed to understand the complex nature of these nanocomposites and to identify the factors that have the most significant influence on their physical, mechanical, thermal, barrier, and dynamic mechanical properties. The several examples of rubber-clay nanocomposite that have been covered in this chapter indicate that to date rubber nanocomposite research has largely concentrated on the natural rubber, ethylene propylene diene rubber, styrene-butadiene rubber, and nitrile rubbers. The main factors found to influence final properties were: type of clay and its treatment, clay

loading levels, curing system used, mixing conditions, rubber grade and preparation method. The remarkable enhancement in the physical, mechanical, thermal, and barrier properties of rubber-clay nanocomposites at low loading levels of organically-modified clay will likely boost the future use of such elastomers and create new industrial applications where lighter, higher performance rubber products are needed.

12.8 References

1. Brydson, J.A., *Rubbery Materials and their Compounds*. 1988, London and New York: Elsevier Applied Science.
2. Alexandre, M. and P. Dubois, Polymer-layered silicate nanocomposites: Preparation, properties and uses of a new class of materials. *Materials Science and Engineering: R: Reports*, 2000. **28**(1–2): 1–63.
3. Maniar, K.K., A Literature Survey on Nanocomposites, in *Plastics Engineering*. 2002, University of Massachusetts Lowell: Massachusetts.
4. Marco, Z., L. Sergi, and C. Giovanni, Polymer Layered Silicate Nanocomposites. *Macromolecular Rapid Communications*.
5. Zhang, L., *et al.*, Morphology and mechanical properties of clay/styrene-butadiene rubber nanocomposites. *Journal of Applied Polymer Science*, 2000. **78**(11):1873–1878.
6. Arroyo, M., M.A. López-Manchado, and B. Herrero, Organo-montmorillonite as substitute of carbon black in natural rubber compounds. *Polymer*, 2003. **44**(8): 2447–2453.
7. Nah, C., *et al.*, Fracture behaviour of acrylonitrile-butadiene rubber/clay nanocomposite. *Polymer International*, 2001. **50**(11): 1265–1268.
8. Usuki, A., A. Tukigase, and M. Kato, Preparation and properties of EPDM-clay hybrids. *Polymer*, 2002. **43**(8): 2185–2189.
9. Chang, Y.-W., *et al.*, Preparation and properties of EPDM/organomontmorillonite hybrid nanocomposites. *Polymer International*, 2002. **51**(4): 319–324.
10. Wu, Y.-P., *et al.*, Structure of carboxylated acrylonitrile-butadiene rubber (CNBR)-clay nanocomposites by co-coagulating rubber latex and clay aqueous suspension. *Journal of Applied Polymer Science*, 2001. **82**(11): 2842–2848.
11. Duquesne, S., *et al.*, Elaboration of EVA-nanoclay systems – Characterization, thermal behaviour and fire performance. *Composites Science and Technology*, 2003. **63**(8): 1141–1148.
12. Heinisch, K.F., *Dictionary of Rubbery*. 1966, London: Applied Science Publishers Ltd.
13. Hamed, G.R., Material and Compounds, in *Engineering with Rubbers: How to Design Rubber Components*, Gent, A.N. (ed.), 2001, Hanser Gardner, Germany, pp. 11–19.
14. Walker, B.M., *Handbook of Thermoplastic Elastomers*. 1979, New York: Van Nostrand Reinhold. xv, 345.
15. Barlow, F.W., *Rubber Compounding Principles, Materials, and Techniques*. 1988, New York: Marcel Dekker, Inc.
16. Hofmann, W., *Rubber Technology Handbook*. 1989, Munich; New York: Hanser Publishers; distributed in the USA by Oxford University Press. xxv, 611, 15, 18.

17. Whelan, A. and K.S. Lee, *Developments in Rubber Technology. 1. Improving product performance*. Developments series. 1979, London: Applied Science Publishers. x, 285p.
18. Morton, M. and American Chemical Society. Division of Rubber Chemistry, *Rubber Technology*. 2nd edn. 1973, New York: Van Nostrand Reinhold. viii, 603.
19. Markovic, M.G., *et al.*, Cure behavior of EPDM compounds influence of different accelerated sulfur systems. *KGK-Kautschuk und Gummi Kunststoffe*, 1999. **52**(3): 170–175.
20. Van Duin, M., Chemistry of EPDM cross-linking. *KGK-Kautschuk und Gummi Kunststoffe*, 2002. **55**(4):150–154.
21. Barlow, F.W., *Rubber Compounding: Principles, Materials, and Techniques*. 1988, New York: M. Dekker. ix, 325.
22. Moshev, V.V. and S.E. Evlampieva, Filler-reinforcement of elastomers viewed as a triboelastic phenomenon. *International Journal of Solids and Structures*, 2003. **40**(17): 4549–4562.
23. Siriwardena, S., H. Ismail, and U.S. Ishiaku, A comparison of white rice husk ash and silica as fillers in ethylene-propylene-diene terpolymer vulcanizates. *Polymer International*, 2001. **50**(6): 707–713.
24. Rothon, R.N. and Rapra Technology Limited., *Particulate-filled Polymer Composites*. 2nd edn. 2003, Shrewsbury: Rapra Technology. x, 544.
25. Ono, S., *et al.*, Structure development in silica-filled rubber composites. *Polymer International*, 1999. **48**(10): 1035–1041.
26. Sae-Oui, P., U. Thepsuwan, and K. Hatthapanit, Effect of curing system on reinforcing efficiency of silane coupling agent. *Polymer Testing*, 2004. **23**(4): 397–403.
27. Ansarifar, A., *et al.*, Reinforcing Effect of Silica and Silane Fillers on the Properties of Some Natural Rubber Vulcanizates. *Rubber Chemistry and Technology*, 2003. **76**(5): 1290.
28. Blow, C.M. and Institution of the Rubber Industry, *Rubber Technology and Manufacture*. 1971, London: Butterworths for the Institution of the Rubber Industry. 22; 527p.
29. Donnet, J.-B., R.C. Bansal, and M.-J. Wang, *Carbon Black: Science and Technology*. 2nd rev. and expand edn. 1993, New York: Marcel Dekker. xviii, 461.
30. Rodgers, B., *Rubber Compounding: Chemistry and Applications*. 2004, New York: Marcel Dekker. viii, 645.
31. Evans, C.W., *Practical Rubber Compounding and Processing*. 1981, London: Applied Science. xiii, 205.
32. Wu, J., *et al.*, Preparation of modified ultra-fine mineral powder and interaction between mineral filler and silicone rubber. *Journal of Materials Processing Technology*, 2003. **137**(1–3 spec): 40–44.
33. Kim, K.-J. and J.L. White, Silica surface modification using different aliphatic chain length silane coupling agents and their effects on silica agglomerate size and processability. *Composite Interfaces*, 2002. **9**(6): 541–556.
34. Schwaiger, B. and A. Blume, Silica/silane – a winning reinforcement formula. *Rubber World*, 2000. **222**(1): 32.
35. Choi, S.-S., C. Nah, and B.-W. Jo, Properties of natural rubber composites reinforced with silica or carbon black: Influence of cure accelerator content and filler dispersion. *Polymer International*, 2003. **52**(8): 1382–1389.

36. Bokobza, L. and O. Rapoport, Silica and carbon black reinforcement of natural rubber. *Macromolecular Symposia*, 2003. **194**: 125–133.
37. Akiba, M. and A.S. Hashim, Vulcanization and crosslinking in elastomers. *Progress in Polymer Science (Oxford)*, 1997. **22**(3): 475–521.
38. Smith, L.P., *The Language of Rubber*, 1st edn. 1993, Oxford: Butterworth-Heinemann Ltd.
39. Mark, J.E., B. Erman, and F.R. Eirich, *Science and Technology of Rubber*, 2nd edn. 1994, San Diego: Academic Press. xvi, 751, [2] of plates.
40. Dluzneski, P.R., Peroxide Vulcanization of Elastomers. *Rubber Chemistry and Technology*, 2001. **74**(3): 451.
41. Sinha Ray, S. and M. Okamoto, Polymer/layered silicate nanocomposites: A review from preparation to processing. *Progress in Polymer Science (Oxford)*, 2003. **28**(11): 1539–1641.
42. Karger-Kocsis, J. and C.-M. Wu, Thermoset Rubber/Layered Silicate Nanocomposites. Status and Future Trends. *Polymer Engineering and Science*, 2004. **44**(6): 1083–1093.
43. López-Manchado, M.A., B. Herrero, and M. Arroyo, Organoclay-natural rubber nanocomposites synthesized by mechanical and solution mixing methods. *Polymer International*, 2004. **53**(11): 1766–1772.
44. Wang, Y., *et al.*, Preparation and characterization of rubber-clay nanocomposites. *Journal of Applied Polymer Science*, 2000. **78**(11): 1879–1883.
45. Bala, P., *et al.*, Organomodified montmorillonite as filler in natural and synthetic rubber. *Journal of Applied Polymer Science*, 2004. **92**(6): 3583–3592.
46. López-Manchado, M.A., B. Herrero, and M. Arroyo, Preparation and characterization of organoclay nanocomposites based on natural rubber. *Polymer International*, 2003. **52**(7): 1070–1077.
47. López-Manchado, M.A., *et al.*, Vulcanization kinetics of natural rubber-organoclay nanocomposites. *Journal of Applied Polymer Science*, 2003. **89**(1): 1–15.
48. Varghese, S. and J. Karger-Kocsis, Melt-Compounded Natural Rubber Nanocomposites with Pristine and Organophilic Layered Silicates of Natural and Synthetic Origin. *Journal of Applied Polymer Science*, 2004. **91**(2): 813–819.
49. Varghese, S. and J. Karger-Kocsis, Natural rubber-based nanocomposites by latex compounding with layered silicates. *Polymer*, 2003. **44**(17): 4921–4927.
50. Zheng, H., *et al.*, Influence of clay modification on the structure and mechanical properties of EPDM/montmorillonite nanocomposites. *Polymer Testing*, 2004. **23**(2): 217–223.
51. Zheng, H., *et al.*, A comparison between cure systems for EPDM/montmorillonite nanocomposites. *Polymers and Polymer Composites*, 2004. **12**(3): 197–206.
52. Gatos, K.G., R. Thomann, and J. Karger-Kocsis, Characteristics of ethylene propylene diene monomer rubber/organoclay nanocomposites resulting from different processing conditions and formulations. *Polymer International*, 2004. **53**(8): 1191–1197.
53. Acharya, H., *et al.*, Synthesis and evaluation of high-performance ethylene-propylene-diene terpolymer/organoclay nanoscale composites. *Journal of Applied Polymer Science*, 2004. **93**(5): 2429–2436.
54. Sadhu, S. and A.K. Bhowmick, Preparation and properties of nanocomposites based on acrylonitrile-butadiene rubber, styrene-butadiene rubber, and polybutadiene rubber. *Journal of Polymer Science, Part B: Polymer Physics*, 2004. **42**(9): 1573–1585.

55. Sadhu, S. and A.K. Bhowmick, Preparation and Properties of Styrene-Butadiene Rubber Based Nanocomposites: The Influence of the Structural and Processing Parameters. *Journal of Applied Polymer Science*, 2004. **92**(2): 698–709.
56. Kim, J.-T., T.-S. Oh, and D.-H. Lee, Preparation and characteristics of nitrile rubber (NBR) nanocomposites based on organophilic layered clay. *Polymer International*, 2003. **52**(7): 1058–1063.
57. Hwang, W.-G., K.-H. Wei, and C.-M. Wu, Preparation and mechanical properties of nitrile butadiene rubber/silicate nanocomposites. *Polymer*, 2004. **45**(16): 5729–5734.
58. Wu, Y.-P., *et al.*, Structure and properties of nitrile rubber (NBR)-clay nanocomposites by Co-coagulating NBR latex and clay aqueous suspension. *Journal of Applied Polymer Science*, 2003. **89**(14): 3855–3858.
59. Wang, S., *et al.*, Synthesis and properties of silicone rubber/organomontmorillonite hybrid nanocomposites. *Journal of Applied Polymer Science*, 1998. **69**(8): 1557–1561.
60. Hasegawa, N., H. Okamoto, and A. Usuki, Preparation and properties of ethylene propylene rubber (EPR)-clay nanocomposites based on maleic anhydride-modified EPR and organophilic clay. *Journal of Applied Polymer Science*, 2004. **93**(2): 758–764.
61. Burnside, S.D. and E.P. Giannelis, Nanostructure and properties of polysiloxane-layered silicate nanocomposites. *Journal of Polymer Science, Part B: Polymer Physics*, 2000. **38**(12): 1595–1604.
62. Giannelis, E.P. and S.D. Burnside, Synthesis and properties of new poly(dimethyl-siloxane) nanocomposites. *Chemisty of Materials*, 1995. **7**(9): 1597.

Part II

Nanotubes, nanoparticles and inorganic–organic hybrid systems

13

Single-walled carbon nanotubes in epoxy composites

K LIAO and Y REN, Nanyang Technological University, Singapore
and T XIAO, Shantou University, People's Republic of China

13.1 Introduction

Carbon nanotubes (CNTs) are seamlessly rolled sheets of hexagonal array of carbon atoms with diameter ranging from a few Ångstroms to several tens of nanometers across. These nanometer-sized tubes exist in two forms, single-walled carbon nanotube (SWNT) in which the tube is formed from only a single layer of graphitic carbon atoms, and multi-walled carbon nanotubes (MWNT), in which the tube consists of several layers of coaxial carbon tubes. The arrangement of hexagonal carbon lattice in a CNT can further be categorized into 'zigzag', 'armchair', and 'chiral' tubes, as shown in Fig. 13.1. The chirality of a CNT is defined by its chiral vector $C_h = n\mathbf{a_1} + m\mathbf{a_2}$, where $\mathbf{a_1}$ and $\mathbf{a_2}$ are unit vectors, and n and m are integers. For convenience, the chirality can also be denoted by (n, m). A zigzag tube, for instance, is specified by $(n, 0)$. It has been shown that the physical properties of a carbon nanotube are strongly dependent on its chirality.[1–3] Since their discovery in 1991,[4] carbon nanotubes have attracted a great deal of attention and have been the focus of extensive research efforts as model systems in nanotechnology because of their potential applications including electronic devices, field emitters, and reinforcement for advanced materials. The extensive interest in CNTs arises from their unique structural and physical properties: their small size in the nanometer scale; their unique electronic behavior in that they can be either metallic or semi-conducting depending on their geometrical structure; their exceptional properties of ballistic transport; their extremely high thermal conductivity and high optical polarizability; as well as their unparalleled mechanical properties such as high elastics modulus and tensile strength.

CNTs can be produced using a wide variety of processes such as electric arc-discharge, pyrolysis of hydrocarbons, laser vaporization, solar carbon vaporization, and electrolysis of carbon electrodes. Electric arc-discharge involves applying a direct current through two high-purity graphite electrodes

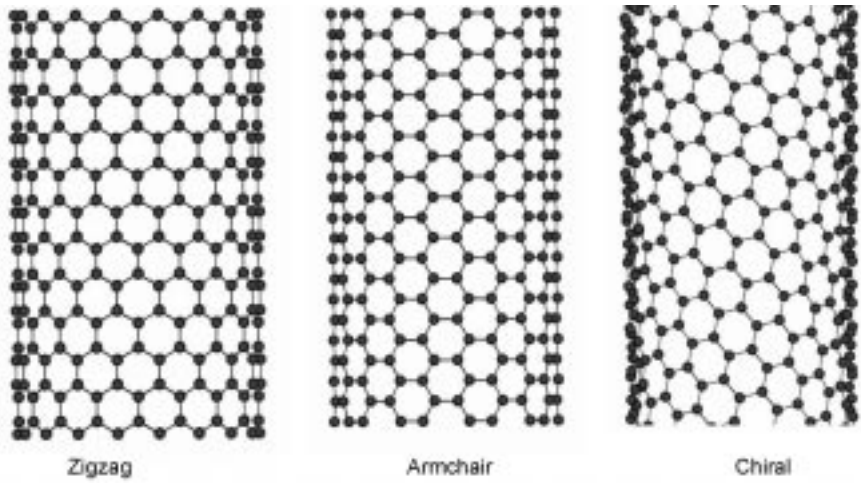

13.1 Schematics of hexagonal carbon lattice arrangements in carbon nanotubes.

in a He atmosphere.[5–9] Both SWNT and MWNT (with the use of metal catalyst) can be produced with high yields. Laser vaporization of graphite targets is usually carried out at about 1200ºC, using pure graphite target in Ar atmosphere with the use of metal catalyst.[10,11] Pyrolysis of hydrocarbons (such as methane, benzene, acetylene, etc.) involves decomposition of the hydrocarbon gases over metal catalyst. This process is able to produce fullerenes and CNTs in large quantities.[12–18] Electrolysis of carbon electrodes in molten ionic salts is a liquid phase process where graphite electrodes are immersed in molten LiCl under an Ar atmosphere, with application of DC voltage between the electrodes. The process is able to generate 20–40% of MWNTs.[19] In solar carbon vaporization, solar energy is focused on carbon-metal target in an inert atmosphere and vaporizes the graphite-metal target, to produce fullerenes and nanotubes.[20]

With breakthroughs in synthesizing long and aligned CNTs and CNT ropes,[21–26] ribbons,[27] and CNT composite fibers in recent years,[28] the potential applications of CNTs as an ideal class of super strong reinforcement for high-performance composite materials are better realized. However, many issues pertaining to the mechanical behavior and performance of CNTs and their composites remain unclear at present. In this chapter, we focus on issues relating to mechanical behavior of carbon nanotubes (SWNTs and MWNTs) and their polymer-based composites. In particular, we will discuss in some detail CNT tensile strength and tensile strength distribution, CNT-polymer interfacial characteristics, fatigue behavior and fatigue mechanisms of SWNT rope reinforced composites, and a molecular level life prediction scheme for SWNT.

13.2 Mechanical properties: elastic properties and strength

13.2.1 Tensile strength distribution of SWNT ropes

Remarkable progress has been made recently on experimental characterization of CNT tensile strength. By stretching suspended SWNT bundles using an atomic force microscope (AFM), Walters *et al.* estimated that the tensile strength of SWNT was 45 ± 7 GPa.[29] By pulling 2 mm long MWNT ropes, Pan *et al.* obtained Young's modulus of 0.45 ± 0.23 TPa and tensile strength of 1.72 ± 0.64 GPa.[30] Yu *et al.* performed tensile tests on individual MWNT and SWNT ropes using AFM,[31,32] and reported that the tensile strengths of SWNT rope and MWNTs ranged from 11 to 63 GPa and 13 to 52 GPa, respectively. Tensile strength of SWNT bundles ranging from 2.3 ± 0.2 GPa to 14.2 ± 1.4 GPa was obtained by Li *et al.*.[33] Zhu *et al.* characterized the Young's modulus and tensile strength of SWNT strands and showed that the tensile strength was in the range of 49 to 77 GPa.[23] In their study, the lowest value of elastic modulus of SWNT was only about 100 GPa, owning to inter-nanotube defects.

Because of the difficulties in producing defect-free CNTs,[34,35] CNT tensile strength is not a single-valued quantity, and has to be described on the basis of probability approach. However, report on the distribution of CNT tensile strength is still absent to date. Here we present the results of a study on direct tensile tests of SWNT bundle and use a two-parameter Weibull distribution to describe its tensile strength distribution.

All SWNT samples used in this study were synthesized by catalytic decomposition of hydrocarbon.[18] Long (several tens of centimeters), aligned SWNT ropes with diameter of about 100 μm were obtained. These SWNT ropes were carefully separated manually into several thinner, 3 mm long SWNT bundles for testing. The diameters of the SWNT bundles, determined by scanning electron microscopy, were in the range of 15 to 25 μm. A nano-mechanical testing device with a force and displacement resolution of 0.2 μN and 1 nm, respectively, was used for testing. Each SWNT bundle was mounted vertically between a rigid stage surface and a loading tip using epoxy (Fig. 13.2). The strain rate was controlled at $0.1\,s^{-1}$ during testing. A total of 12 SWNT bundles were tested.

All of the samples were broken in the region between the two mounting ends, typical images of a SWNT bundle before and after tensile testing are shown in Fig. 13.2. Taking into account the 65% volume fraction of SWNT in the bundle,[33] the tensile strengths of SWNT bundles were estimated in the range of 10 to 52 GPa (mean 23 GPa), comparable to published data (Table 13.1). The stress-strain curves of four SWNT bundles tested are shown in Fig. 13.3. Worth noticing are the kinks on these curves. These kinks, presented in all of the samples tested and appearing at more or less regular load intervals and span

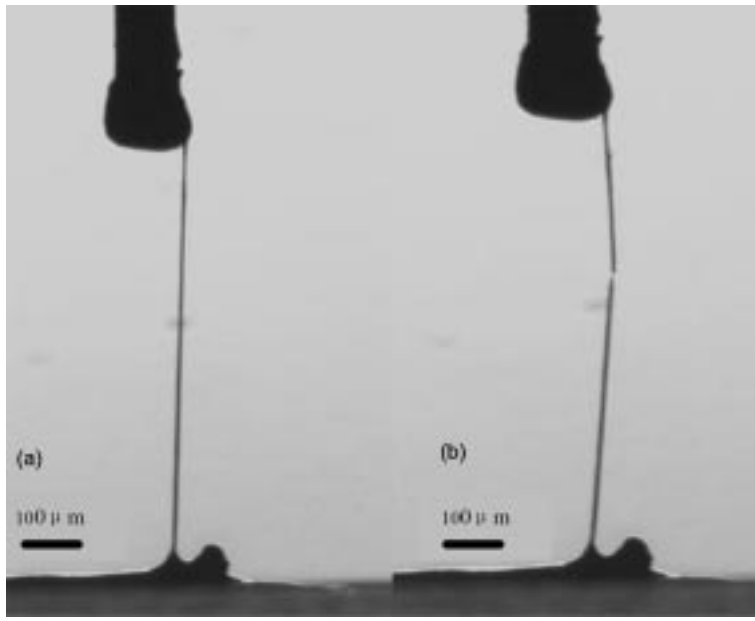

13.2 A mounted SWNT bundle subjected to tensile loading: (a) before breaking, (b) moments after being broken into two parts.

from low to high load (1.92–54.6 GPa), are indicative of sub-bundle failures. On average, there are nine kinks on each stress-strain curve.

The as-prepared SWNT ropes consist primarily of many rope-like sub-bundles of SWNT with diameter of 10 to 40 nm, and it is estimated that each of the SWNT bundles prepared for the tensile test contain from a few hundred to

Table 13.1 A comparison of tensile strength results of CNTs

Type of CNT	Young's modulus (GPa)	Tensile strength (GPa)	Strain	Reference
MWNT	0.27–0.95	11–63	$\sim$12%	Yu *et al.*[32]
	0.45$\pm$0.23	1.72$\pm$0.64	—	Pan *et al.*[30]
SWNT (ropes)	0.32–1.47 (Mean: 1.0)	13–52 (Mean: 30)	$<$5.3%	Yu *et al.*[31]
	—	3.6–22.2$\pm$2.2	—	Li *et al.*[33]
	—	45$\pm$7	$<$6.7%	Walters *et al.*[29]
	—	49–77	—	Zhu *et al.*[23]
	0.23–1 (Mean: 0.59)	6–55	3.3–10%	Present study

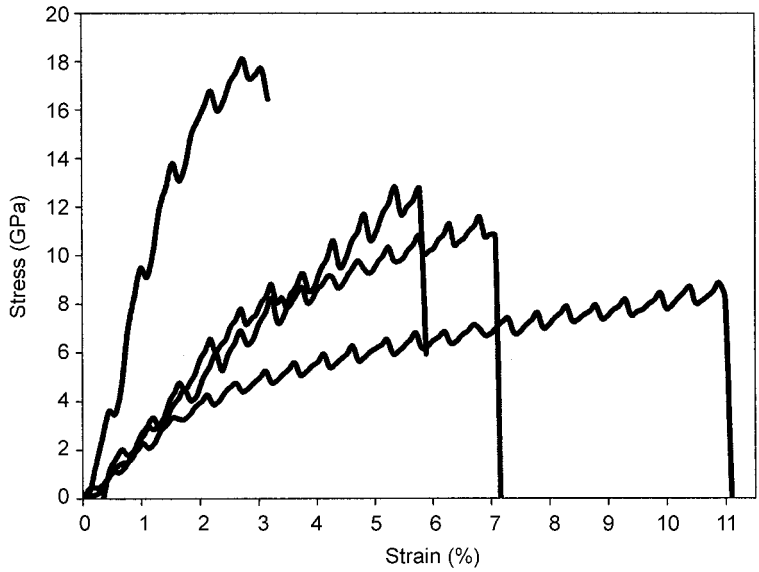

13.3 Stress-strain curves of four SWNT bundles. Each kink on these curves represents one or more sub-bundles in the bundle that have failed, while the surviving sub-bundles bear the remaining load until final rupture of the sample.

about a thousand sub-bundles. It is assumed that there is no interaction among SWNT sub-bundles, thus each SWNT sub-bundle is equally stressed during loading. The applied tensile load on a SWNT bundle is evenly redistributed among the remaining intact sub-bundles after failure of one or more sub-bundles at a specific load, until final failure of the entire SWNT bundle. Because only a limited number of kinks is observed on a stress-strain curve, and there are at least a few hundred sub-bundles within a SWNT bundle, many SWNT sub-bundles could have failed at a kink point. Within a SWNT sub-bundle, however, there could be local load-sharing as a result of weak van der Waals interactions.

It is assumed that the tensile strength of SWNT sub-bundles follows a two-parameter Weibull distribution, a statistical model based on weakest link concept that has been widely used for describing the strength of a broad spectrum of engineering materials.[36] The probability of failure of a sub-bundle, P_f, at an applied stress, σ, is

$$P_f = 1 - \exp\left[-\left(\frac{\sigma}{\sigma_0}\right)^m\right] \tag{13.1}$$

where m and σ_0 are the Weibull modulus and characteristic strength, respectively. Here the two parameters are evaluated by analyzing collectively all of the stress-at-the-kink on the 12 stress-strain curves. Since the effective cross-sectional area or the amount of ruptured SWNT sub-bundle is difficult to measure at any instant during tensile loading, it is assumed that the amount of

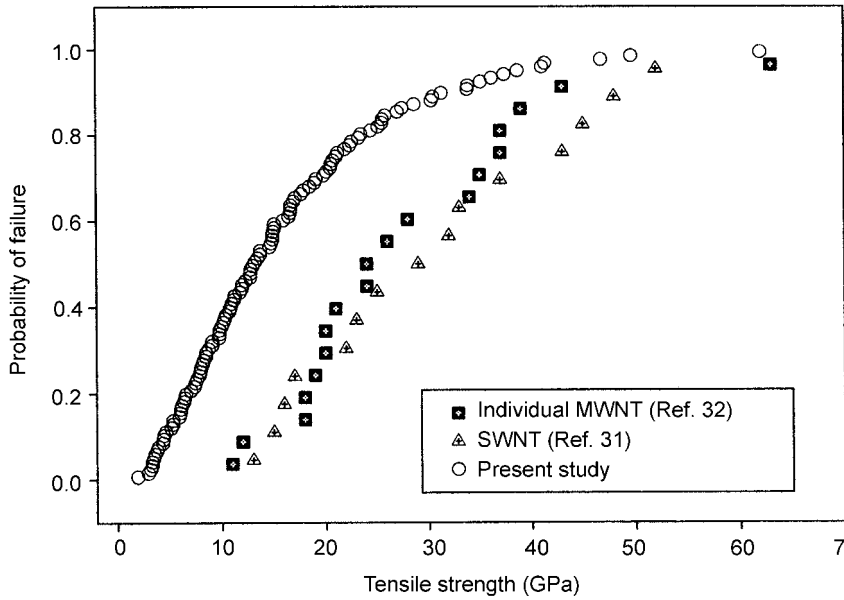

13.4 The cumulative failure probability versus strength of SWNT sub-bundles. A total of 114 kinks from 12 samples are included. Also included are data from refs 31 and 32.

load drop is proportional to reduction in cross-sectional area, and that SWNT sub-bundles are carrying equal load prior to failure.

The cumulative probability of failure, P_f, is estimated by the median rank method: $P_f = (i - 0.3)/(n + 0.4)$, where i is the rank of tensile strength in ascending order and n is the total number of samples. In our case, n is 114, the total number of kinks collected from stress-strain curves of all 12 SWNT bundles tested. The accumulative probability of failure of SWCNT sub-bundles is shown in Fig. 13.4. Values of m and σ_0 obtained from linear regression of the strength data are 1.71 and 17.8 GPa, respectively, with a coefficient of correlation of 0.964, indicating a reasonably good fit of data to the Weibull model. The probability density function of the Weibull model for tensile strength using $m = 1.71$ and $\sigma_0 = 17.8$ GPa is shown in Fig. 13.5.

Also included in Fig. 13.4 are tensile strength data of individual MWNTs and SWNT ropes from Yu *et al.*[31,32] The Weibull modulus, m, is 2.6, and the characteristic strength, σ_0, is 31.4 GPa, calculated from the 19 tensile strength data of individual MWNTs; m is 2.5 and σ_0 is 34 GPa for the 15 tensile strength data of SWNT ropes. The low Weibull modulus obtained from the present study and those from Refs. 31 and 32 all indicate a wide scattering of tensile strength of CNTs. As a comparison, the Weibull modulus for T300 carbon fiber is 8.26 (and $\sigma_0 = 3.58$ GPa),[37] indicating a much narrow distribution. Note that the characteristic strength is considerably higher for data from Refs. 31 and 32

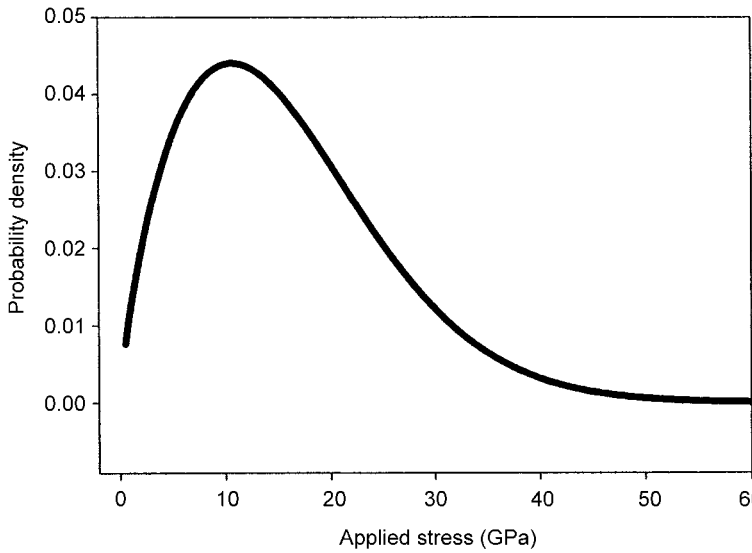

13.5 Probability density function (Weibull distribution) of SWNT sub-bundle strength using $m = 1.71$ and $\sigma_0 = 17.8$ GPa.

because the lengths of the samples used in those studies were substantially shorter (average length about 5 μm) than ours (3 mm).

The Weibull modulus calculated from the present study and those from Yu and co-workers all indicate substantial dispersion of CNT tensile strength, suggesting that CNTs may contain defects of different size and form, and they are distributed along a CNT. Moreover, these defects may interact when stressed, leading to lower tensile strength.

13.2.2 Mechanical properties of CNT-reinforced polymer composites

The unparalleled high elastic modulus and tensile strength of CNTs, when incorporated in polymer matrix, does not necessarily warrant a composite with enhanced mechanical properties. Recent research using CNTs in polymer composites showed both encouraging and discouraging results. In some studies, enhancement in mechanical properties were not seen when CNTs were added to a polymer matrix. Lau and Shi showed that flexural strength of a CNT/epoxy composite did not increase with the addition of 2 wt.% CNT.[38] Bhattacharyya *et al.* studied melt blended SWNT/Polypropylene (PP) composite, and saw a slight drop in tensile strength, elastic modulus, and breaking strain of the composite with addition of 0.8 wt.% CNT.[39] In a study by Jia *et al.* on CNT/poly(methyl methacrylate) (PMMA) composites, decrease in tensile strength, toughness, and hardness were seen with untreated CNT. When CNT was treated with 2,2′-

azobisisobutyronitrile (AIBN), a moderate increase in tensile strength was seen, but there was little increase in toughness and hardness.[40]

Some studies showed moderate increase in elastic modulus with slight or no increase in mechanical strength for CNT/polymer composites. Xu *et al.* studied MWNT/epoxy composite thin films from a spin-coating process. Compared to net resin thin films, a 24% increase in elastic modulus was seen when 0.1 wt.% MWNTs was added. However, the fracture load of the composite film is somewhat lower than that of the neat epoxy film.[41] In a study by Wong *et al.* on MWNT/polystyrene (PS) rod samples from an extrusion process, it was shown that there was a moderate increase in tensile stiffness (about 10%) and a slight increase in tensile strength.[42] Miyagawa and Drzal showed that the storage modulus of a diglycidyl ether of bisphenol F (DGEBF) epoxy at room temperature was increased up to 20% with the addition of only 0.30 wt.% of fluorinated SWNT. In the same study, the Izod impact strength showed slightly decreased when 0.3 wt.% of fluorinated SWNT was added to the epoxy.[43] Haggenmueller *et al.* showed, for an aligned SWNT/PMMA composite, moderate increase in elastic modulus and yield strength with an increase in nanotube loading and draw ratio.[44] Schadler *et al.* showed that tensile and compressive modulus of a CNT/epoxy composite showed 20% and 24% improvement, respectively, after adding 5 wt.% of CNT to the matrix.[45]

In some cases, significant improvement of the mechanical properties were seen with CNT as reinforcement. Ganguli *et al.* showed that 1 wt.% MWNT reinforcement increased the ultimate strength of a bifunctional epoxy and strain to failure by about 139 and 158%, respectively, and there is a 170% increase in the fracture toughness of the MWNT composites.[46] Gong *et al.* studied surfactant-assisted processing of CNT/epoxy composites with a nonionic surfactant, improved dispersion and interfacial bonding resulted in a 30% increase in elastic modulus with 1 wt.% CNT.[47] Liu *et al.* showed, compared with neat nylon-6 (PA6), that the elastic modulus and the yield strength of the MWNT/PA6 composite were greatly improved by about 214% and 162%, respectively, when incorporating only 2 wt.% MWNT.[48] Allaoui *et al.* showed that the Young's modulus and yield strength of a MWNT/epoxy composite were doubled and quadrupled for 1 and 4 wt.% nanotube added.[49] Gou *et al.* showed that for a SWNT/epoxy (EPON 862) composite, a 250–300% increase in storage modulus can be achieved with addition of 20–30 wt.% of SWNT.[50] Qian *et al.* showed that with the addition of only 1 wt.% CNT, a 36–42% increase in elastic modulus and a 25% increase in tensile strength were seen in MWNT/PS composite.[51]

These mixed experimental results on the mechanical properties of CNT/polymer imply that further research in terms of processing methods, CNT treatment, its dispersion and alignment in the matrix, as well as a better understanding and control of CNT-polymer interfacial adhesion are necessary in order to obtain CNT/polymer nanocomposites with desirable and predictable properties and performance. In the subsequent section, we will discuss in more

detail one of the critical issues concerning composite behavior: CNT-polymer interfacial characteristics.

13.3 Carbon nanotube – polymer interface

Previous studies on CNT-polymer composite systems suggested that chemical bonding between CNT and the polymer matrix may or may not exist, and adhesion between CNT and certain polymer systems are strong, although there are also contrasting views. Upon close examination of the fracture surface of a MWNT/poly(hydroxyaminoether) composite, Bower *et al.* observed contact and adherence of the polymer to most of the nanotubes, and in some cases the entire surface of the nanotube was covered with a layer of polymer.[52] Chang *et al.* also observed CNTs were well coated by polypyrroles in a CNT/polypyrroles composite produced by in-situ polymerization, and Raman scattering and X-ray diffraction data suggested there was no chemical reaction between CNT and the polymer.[53] In a study by Jia *et al.* on CNT/PMMA using an in-situ polymerization process, chemical bonding between CNT and PMMA was confirmed using infrared transmission spectra.[40]

From a mechanical point of view, the available literature to date also offered evidence of strong CNT-polymer interactions. Lourie and Wagner first showed CNT fragmentation in epoxy matrix, implying that force was transmitted to the CNT from the surrounding matrix.[54,55] From fragmentation experiments, these authors estimated that the CNT-matrix stress transfer ability is at least one order of magnitude larger than that measured in conventional micro fiber-based composites. Compared to CNT-polymer interface, they attribute the lower interfacial strength of conventional micro fiber-polymer interface to larger defects that facilitate interfacial crack propagation.[54] Furthermore, Qian *et al.* showed that tensile load can be transferred effectively from the polystyrene matrix to the CNT, because a high elastic modulus increase (42%) was seen using just 1 wt.% CNT.[51] Similar results were also shown by Xu *et al.*,[41] using CNT/epoxy thin film composite system. Using an expanded form of Kelly-Tyson approach, Wagner showed that high interfacial shear strength between CNT and polymers is possible.[56] Cooper *et al.* showed that interfacial shear strength between MWNT and epoxy ranged from 35 to 376 MPa, from pullout experiments using atomic force microscope (AFM).[57] More recently, Barber *et al.* showed that the average interfacial shear stress required to remove a single MWNT from a polyethylene-butene matrix is about 47 MPa, from direct pullout experiments using AFM.[58] Despite this positive evidence of strong CNT-polymer interactions, that CNT-polymer interface only offers poor stress transfer was also reported. Based on evidence of micro Raman spectroscopy, Schadler *et al.* showed that load transfer between CNT-epoxy was poor.[45,59] Although these studies have provided some insights into the nature of CNT-polymer interactions at the interface, the physics of CNT-polymer interactions still await further

elucidation, both qualitatively and quantitatively. To illustrate, in this section, we first show interfacial morphology of CNT/polystyrene and CNT/epoxy composites at micro- and nanometer scale. We then describe how molecular mechanics simulations can be used to estimate CNT-polymer interfacial shear stress, for a range of polymers. In addition, we also show that thermal residual stress and mechanical interlocking arise from waviness of CNTs also play a role in the interfacial characteristics of the nanocomposites.

13.3.1 Morphology of CNT-polymer interface

We illustrate CNT-polymer interface morphology using a CNT/PS and a CNT/epoxy system.[41,42] Rod specimen of CNT/PS composite with 1 mm diameter was fabricated using an extrusion process, with a CNT content of about 1 wt.%. Tensile failure surfaces of the CNT/PS composite rod were examined under a field emission scanning electronic microscope (FESEM) and transmission electron microscope (TEM). CNT/epoxy (EPON SU-8 photo resist) thin film with 0.1 wt.% CNT and 5.8 μm in thickness was fabricated by spin-coating mixture of CNT and epoxy on to a silicon wafer. The fracture surface of CNT/epoxy specimens was examined under FESEM and TEM after shaft-loaded test (inset of Fig. 13.7).

Results of tensile tests for CNT/PS rod samples showed that there was a moderate increase in tensile stiffness (about 10%) and only a slight increase in tensile strength (about 5%). Although the extrusion process is believed to align CNTs somewhat in the flow direction, from FESEM images shown in Fig. 13.6(a), it is seen that CNTs still exist in the form of agglomerates, ranging approximately from 5 to 20 μm in diameter. The reinforcing effect of the CNT agglomerate, if any, was offset by the fact that they were also acting as flaws or stress concentrators in the composite. At present, effective dispersion CNT in a polymer matrix still poses a challenge in processing of CNT composites.

Close examination of individual CNT in the agglomerate revealed that they are all coated by PS, suggesting good wetting of CNT by PS and that surface energies favors CNT-PS contact (Fig. 13.6(b)). Failure around the CNT agglomerate occurred within the PS matrix but not between CNT and its PS coating, suggesting strong CNT-PS adhesion. Extensive examinations of the CNT/PS interface by TEM indicate that these CNTs are in intimate contact with the PS matrix, suggesting excellent adherence between CNT and PS. In Fig. 13.6(c), a cross-sectional view of a CNT (located in the middle of the image) embedded in the PS matrix is shown. The circumference of the CNT is seen in close contact with the polymer matrix, with no obvious gaps observed at nanometer resolution. The darker regions in Fig. 13.6(c) are other CNTs embedded in the matrix. Again, they are seen tightly bound to the matrix. A longitudinal section of a CNT embedded in PS is shown in Fig. 13.6(d), where a change in tube diameter due to defect is obvious. This kind of mechanical

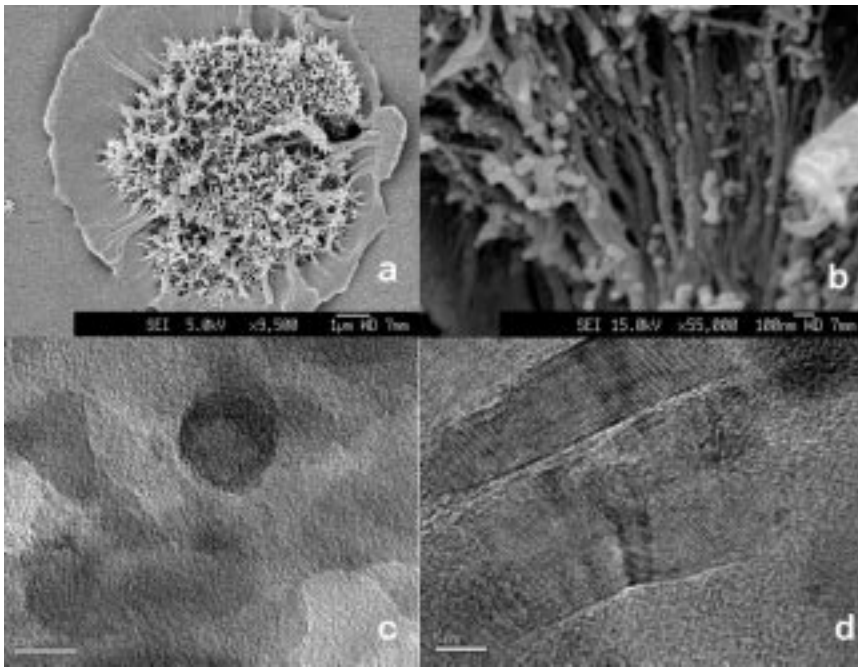

13.6 Images of fracture surface of CNT-PS composite: (a) FESEM image of a CNT agglomerate being pulled half way out from the PS matrix, (b) FESEM image of CNT bundles, note that most nanotubes are coated with PS (scale bar is 100 nm), (c) TEM image of CNTs embedded in PS. Dark circular region is the cross section of a CNT embedded in PS matrix. Other dark regions are other randomly oriented CNTs (scale bar is 20 nm), (d) TEM image of CNT-PS interface, note the kink and change in diameter of the CNT, which is believed to promote mechanical interlocking. In most TEM images that we have examined, no physical gaps between CNT and the polymer matrix are found.

interlocking is believed to contribute to the CNT-polymer adhesion. More will be said on this later.

Results of shaft-loaded test on epoxy and CNT/epoxy thin films showed that 0.1 wt.% of CNT can increase the elastics modulus of the epoxy thin film by 24%, suggesting that CNTs were aligned in the radial direction upon spin coating.[41] FESEM observations of the fracture mode showed that cracks originate at the central loading point and propagate in the radial direction to the edge of film-silicon boundary. MWNTs were found confined parallel to the plane of the thin film, and most MWNTs were seen running circumferentially, that is, they were oriented perpendicular to the crack direction, a consequence of CNT realignment under the action of centrifugal force during spin coating.

A fracture surface of the MWNT/epoxy film is shown in Fig. 13.7, where pullouts near the matrix crack are seen. Close examination indicate that these pullouts were MWNTs covered by epoxy. The pullout morphology indicates

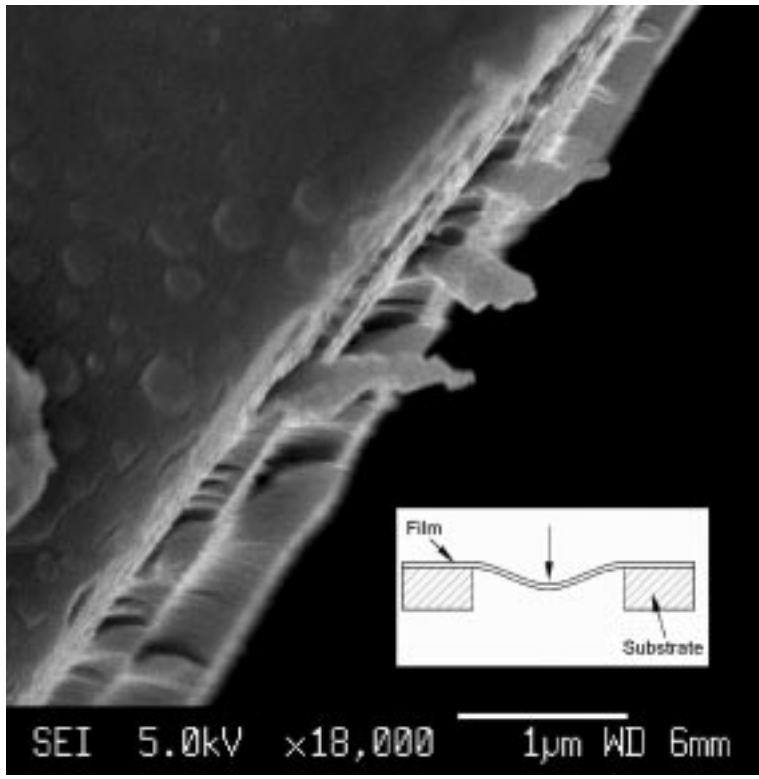

13.7 Fracture surface of CNT/epoxy thin film, oriented in radial direction. CNT bundles are seen coated with epoxy. Schematic of the shaft-loaded test setup is shown in the inset.

failure of the epoxy matrix but not the CNT-epoxy interface, suggesting a stronger interfacial adhesion between MWNT and the matrix. However, MWNT agglomerate also existed at places, where 'clean' MWNTs were found directly separated from the matrix, a result of poor local dispersion of MWNT, and was probably the cause of failure initiation.

A TEM image of CNT embedded in epoxy film is shown in Fig. 13.8(a). Covered by epoxy molecules, it is seen from these images that the lattice of the CNTs was blurred, and so were the boundaries between the nanotubes and the epoxy matrix. Similar to the case of CNT/PS, extensive examination did not reveal clear physical gaps between CNT and epoxy molecules. It was known that microtoming introduces shear force to the material and may result in CNT pullout from the matrix.[60] However, no obvious CNT pullout from the epoxy was observed in the CNT/epoxy slices after microtoming, and most of the CNTs remained in the epoxy, suggesting good adherence of polymer to CNT. Image in Fig. 13.8(b) for individual CNTs pulled out from the epoxy matrix clearly shows that a thin layer of epoxy (about 3 nm thick) was adhered on the CNT,

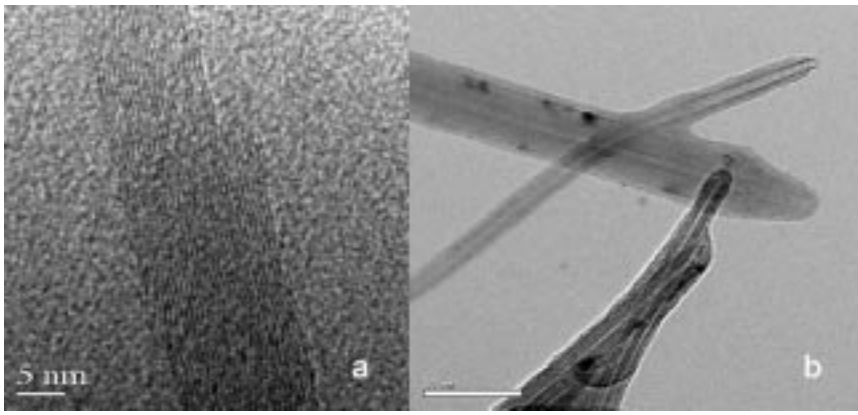

13.8 TEM of CNT in epoxy: (a) a longitudinal section of CNT, no physical boundary is seen between CNT and the matrix, (b) CNT pulled out from the matrix. Note that a thin layer (about 3 nm) of polymeric material adheres to the surface of CNT.

suggesting very strong CNT-epoxy interfacial adhesion. From these morphology studies, it can be concluded that PS and epoxy adhere strongly to CNTs, as also suggested by other workers.

13.3.2 Molecular mechanics study of CNT-polymer interface

Due to the difficulties in devising experiments to study the CNT-polymer interface, molecular modeling may serve to elucidate the importance of various factors constituting the interfacial characteristics of CNT reinforced polymer composites. To extend our understanding on CNT-polymer interactions, the interfacial adhesion characteristics between CNTs and a group of polymers (Table 13.2) are studied through molecular mechanics simulations. In this study, we are only concerned with non-bond interactions.

Table 13.2 Interfacial shear stress for CNT/polymer systems from molecular mechanics simulations

CNT/polymer systems	Interfacial shear stress (MPa)
CNT/poly (iso butyl-ethylene)	224
CNT/poly (ethyl-ethane)	211
CNT/polyvinyl chloride (PVC)	198
CNT/polystyrene (PS)	186
CNT/polyethylene (PE)	170
CNT/polypropylene (PP)	164
CNT/epoxy	138

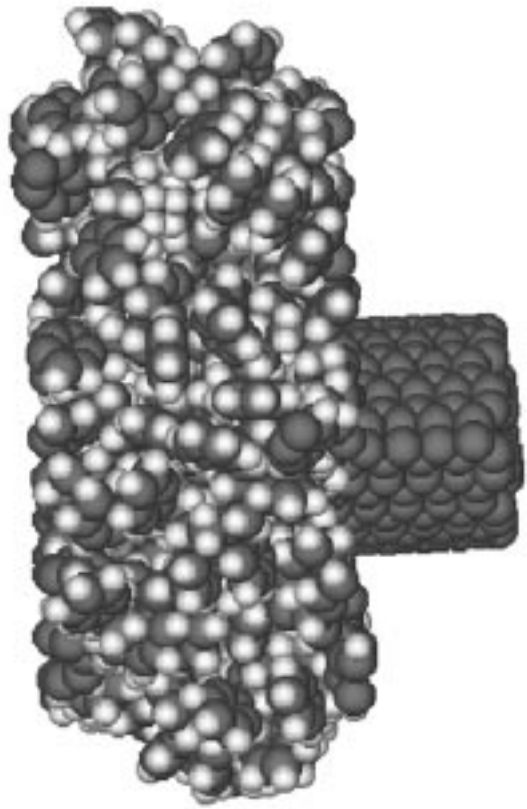

13.9 A molecular model of a CNT in PS matrix, the CNT is pulled out half way from the matrix.

Molecular models of SWNT embedded in a polymer block are constructed. The SWNT is of armchair configuration with outer diameter of 13.4 Å and length of 20 Å. The outer diameter of the polymer block consists of randomly oriented polymer chains, approximately 56 Å about 20 Å in thickness. No chemical bonding exists between the CNT and the polymer. To validate the polymer molecular model, the density for polyethylene (PE) and polypropylene are calculated to be 0.705 g/cm^3 and 0.73 g/cm^3, respectively, agreeing well with those by Frankland *et al.*[61]

Geometry optimization for each of the composite systems (i.e., both the CNT and the polymer matrix) was performed with a SWNT fully embedded in the matrix, and its potential energy was obtained. The SWNT was then 'pulled' out from the polymer matrix in a stepwise manner, as shown in Fig. 13.9. The pullout energy, W, work required for CNT pullout, is related to the interfacial shear stress, τ_i, between the CNT and the polymer matrix by[62]

$$W = \int_{x=0}^{x=L} 2\pi r(L-x)\tau_i \, dx \tag{13.2}$$

where r is the outer radius of the CNT. It follows from Eq. (13.2) that pullout energy is directly related to the interfacial shear stress between the CNT and the polymer

$$\tau_i = W/\pi r l^2 \tag{13.3}$$

Results of τ_i for seven different CNT-polymer systems are tabulated in Table 13.2.

For CNT/polymer composite systems with non-bond interactions, electrostatic and Van der Waals forces are primary contributors to the pullout energy and hence the adhesion strength between CNT and polymer. The nature and magnitude of non-bond interactions rely on the chemical structure, tacticity, and conformation of the polymer. Of the several different types of polymers constructed, PP, PS, PE and PVC are of atactic configurations, while poly(ethyl-ethane) and poly (isobutyl-ethylene) are of isotactic configurations. The isotactic configuration is known to have a tendency to form helix. The stronger adhesion between the CNTs and the polymers with helical conformation could be attributed to the fact that it allows the polymers to form entanglement around the CNTs more easily, which agrees with the results of Yao and Lordi.[63] Comparing CNT/PP with CNT/PE, it is expected that the pullout energy for CNT/PE is larger than CNT/PP because the later has a small side chain that causes spatial hindrance and the PP molecule is less conformable to the CNT surface. However, comparing CNT/PS and CNT/PE or CNT/PP, the situation is reversed. The spatial hindrance from rigid benzene rings of PS is thought to have a negative effect on polymer-CNT adhesion because the polymer chain is less conformable to CNT. Nonetheless, the interfacial shear stress or pullout energy of CNT/PS is larger than that of CNT/PE or CNT/PP, suggesting that the interactions between the surfaces of phenyl-groups and CNT are stronger than the spatial hindrance effects induced by rigid benzene rings. The larger pullout energy of CNT/PVC, as compared with CNT/PS, CNT/PE and CNT/PP, could be attributed to the strong interaction between the CNT and the polar group of PVC. It is found that the interfacial shear strength for SWNT/epoxy system is the lowest, among all of the SWNT/polymer systems. This could be attributed to the more rigid, cross-linked epoxy network.

13.3.3 Thermal mismatch

Mismatch in the coefficients of thermal expansion (CTE) between CNT and polymer results in thermal residual radial stress and deformation along the tube when the polymer is cooled from its melt. Compressive radial stress results in closer CNT-polymer contact which could enhance CNT-polymer non-bond interactions; and local CNT deformation which promotes mechanical

interlocking. To calculate radial stress using the concentric cylinder model based on elasticity theory,[64] the elastic modulus in the radial direction of CNT, E_r, need to be known. From Lu,[65] the stiffness coefficient perpendicular to the basal plane, C_{33}, of a SWNT is 0.397 TPa. E_r is related to C_{ij} by:

$$E_r = C_{33} - [2C_{13}{}^2/(C_{11} + C_{12})] \tag{13.4}$$

From data of graphite crystal,[66] the contribution from the second term of the previous equation is less than 1%, therefore E_r for SWNT is taken as 0.39 TPa in our calculations. The longitudinal and transverse Young's modulus of SWNT were taken as 1 TPa and 0.41 TPa, respectively, and the Poisson's ratio of a SWNT is taken as 0.16.[66]

Since CNT has a similar hexagonal arrangement of carbon atoms as the graphite crystal, the CTE of graphite crystal, such as α_c of 25×10^{-6}/K (15–800ºC) in *c*-axis and α_a of -1.5×10^{-6}/K (0–150ºC) in *a*-axis,[66] were used as CTE of CNT in the calculations. The CTEs of PS and SU-8 epoxy are 28×10^{-6}/K and 52×10^{-6}/K, respectively.[67] From concentric cylinder model of elasticity,[64] the radial stresses for SWNT/PS and SWNT/epoxy are estimated to be about -45 MPa/K and -26 MPa/K. Hence thermal residual stress from CTE mismatch could be a significant factor contributing to CNT-polymer adhesion, in terms of promoting closer contacts and thus mechanical interlocking mechanisms.

13.3.4 Mechanical interlocking

Local non-uniformity along a CNT, including varying diameter and bends and kinks at places as a result of non-hexagonal 'defects,' contribute to CNT-polymer adhesion by mechanical interlocking (Fig. 13.6(d)). In the case of CNT pullout, for instance, extra mechanical work has to be provided for CNT and the polymer to deform at 'rough contacts' in order for them to slip past each other, compared to CNT-polymer contact along a smooth CNT surfaces. To illustrate the idea, a molecule model of a CNT with diameter variation embedded in an array of linear polymer is constructed and the CNT was pulled through the polymer 'brush' from the end with smaller diameter (Fig. 13.10). The diameter of the larger and smaller ends of the CNT are 20.1 and 13.3 Å, respectively, and its length is about 31 Å.

As the CNT and the polymer are being displaced relative to each other against the 'interlock' (represented by the changing CNT diameter), extra energy is needed to deform the polymer. This is shown in Fig. 13.10, where a steep rise in potential energy of the system is seen when the portion of CNT with larger diameter is draw into the polymer and causes deformation of the polymer. Close contact between CNT and polymer as well as non-uniformity in CNTs suggest that mechanical interlocking could be an important contributor for CNT-polymer adhesion.

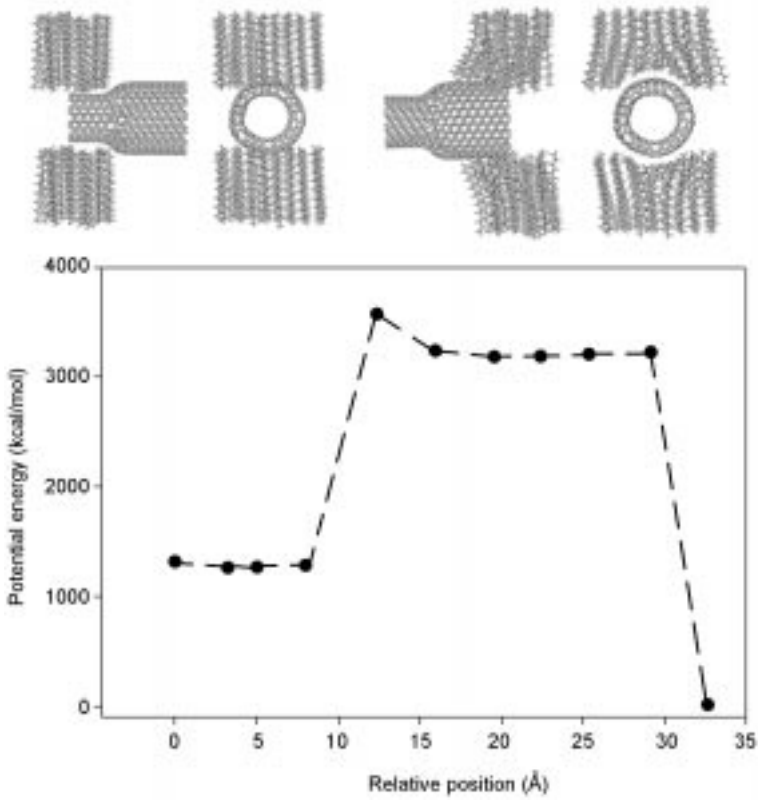

13.10 A molecular model of a CNT embedded in two layers of short linear polymer array. Extra energy is needed to pull the CNT through the 'interlock', modeled as a change in CNT diameter.

Taken together, CNT-polymer interactions have the following contributions at the nanometer scale:

1. Under no chemical bonding between CNT-polymer, the origins of CNT-polymer interactions are electrostatic and van der Waals forces.
2. Mismatch in CTEs is a significant factor contributing to both non-bond interactions and mechanical interlocking, because compressive thermal residual stress may increases the contact area between CNT and the surrounding polymers.
3. Local non-uniformity of a CNT embedded in polymer matrix may result in nano-mechanical interlocking, an effect similar to the clenching of gears.

It is believed that the high CNT-polymer interfacial shear stress obtained from molecular simulation is attributed, to a large extent, to the intimate contact between CNT and the polymer matrix at nanometer scale. CNTs offer a much

smoother contact surface deprived of local cavities for polymer adsorption, in contrast to polymer-micro fiber interface which might be full of local irregularities that are prone to micro crack development under applied load.

13.4 Long-term performance of unidirectional CNT/epoxy composites

Although many important mechanical properties of CNT, such as tensile strength and elastic modulus have been measured and/or simulated, as discussed earlier, studies on the long-term performance of CNT or CNT reinforced composites are still lacking. An understanding of their behavior under repeated mechanical loads will enable the potentials of CNT for structural applications to be better realized. In this section we present a study on the fatigue behavior of unidirectional, aligned SWNT rope reinforced epoxy composite, its fatigue failure mechanisms, and a molecular mechanics-based life prediction scheme for CNT time-dependent behavior.

13.4.1 Fatigue behavior

The SWNT ropes used were the same as those used for bundle strength measurements discussed earlier. The matrix material used was Epicote 1006 epoxy resin, a room temperature curing system. 32 dog-bone SWNT/epoxy specimens with dimensions of 40 mm × 3.5 mm × 0.4–0.6 mm were obtained. The gauge length of the specimens was about 15 mm, and the length of SWNT ropes embedded in the epoxy was about 20 mm. Details of the fabrication method can be found elsewhere.[68] The volume fraction of SWNT ropes in the composite was controlled within the range of 0.1–0.9%. Specimens were cyclically tested by an Instron 8800 Microforce Tester under tension-tension at 5 Hz, using a sinusoidal wave function at R ratio (ratio of minimum to maximum cyclic stress) of 0.1.

The S-N data of the SWNT/epoxy composite is shown in Fig. 13.11. Also included in the figure is the tensile strength data of SWNT, obtained previously.[33] Since the SWNT volume fraction varied from sample to sample, stress on SWNT cannot be inferred directly if the composite stress were used in the S-N plot. Therefore, the maximum cyclic stress of SWNT, calculated using rule-of-mixture, is plotted against the number of cycles to failure of the composite. The Young's modulus of SWNT was estimated as 800 GPa,[33] and the maximum cyclic stress of SWNT was calculated to be between 5.37 and 24 GPa.

The S-N data of unidirectional carbon fiber reinforced epoxy, shown in the gray rectangular region of Fig. 13.11, are adapted from Ref. 69, which encompasses unidirectional carbon/epoxy data from a variety of sources. In Fig. 13.11, the maximum cyclic stress of the carbon fiber instead of that of the composite is used in order to make a comparison with the data from the present study. A

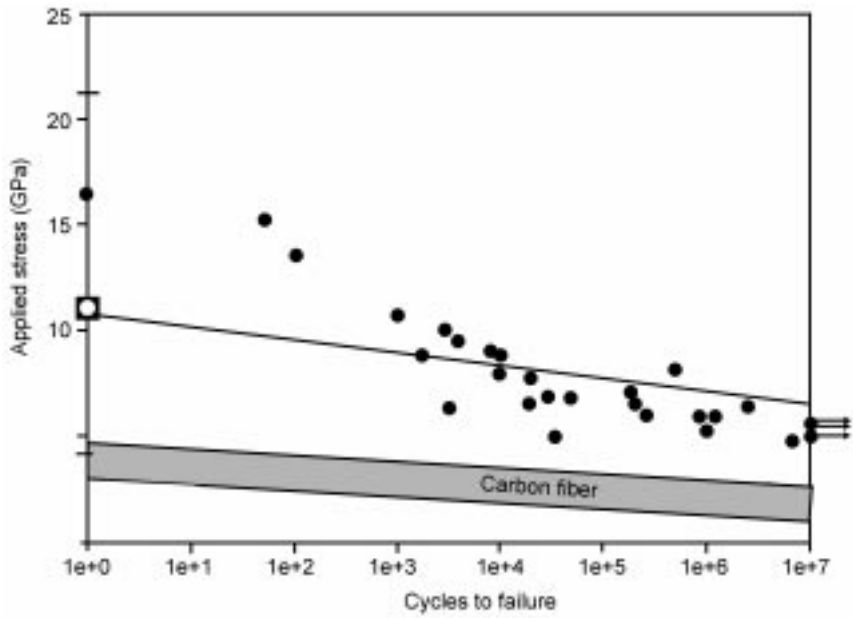

13.11 S-N diagrams. Filled circles are data obtained from this study. Quasi-static tensile data (square with white circle) are adapted from Ref. 33, error bar represents standard deviation. The gray rectangular region covers most S-N data for unidirectional carbon fiber reinforced epoxy composites, adapted from ref. 69.

simple linear relation often used for S-N curve is $\sigma_a/\sigma_{ult} = 1 - m \log N$, where σ_a and σ_{ult} are applied and ultimate stress, respectively, N the number of cycles to failure, and m the slope of the normalized S-N curve. Despite considerable scattering within 10^3 cycles, the S-N curve of the SWNT/epoxy composite is quite flat, similar to the characteristics of the unidirectional carbon/epoxy composites. According to Ref. 69, slope m for most unidirectional carbon/epoxy composites ranged from 0.035 to 0.057. For SWNT/epoxy composites, a m value of 0.042 was obtained from linear regression, which is within the range of the unidirectional carbon/epoxy composites. However, it is should be mentioned that the estimated maximum cyclic stress of SWNT is at least twice that of the carbon fiber in unidirectional composites. In other words, the fatigue strength of SWNT in epoxy is at least twice that of carbon fibers.

13.4.2 Fatigue mechanisms

All fatigue fracture of SWNT/epoxy samples occurred within the gauge region. Nanotube-matrix splitting is not seen, as compared to fatigue damage of carbon fiber composites where fiber-matrix splitting is a common damage mode. Macroscopically, the SWNT/epoxy composite exhibited a brittle type fatigue

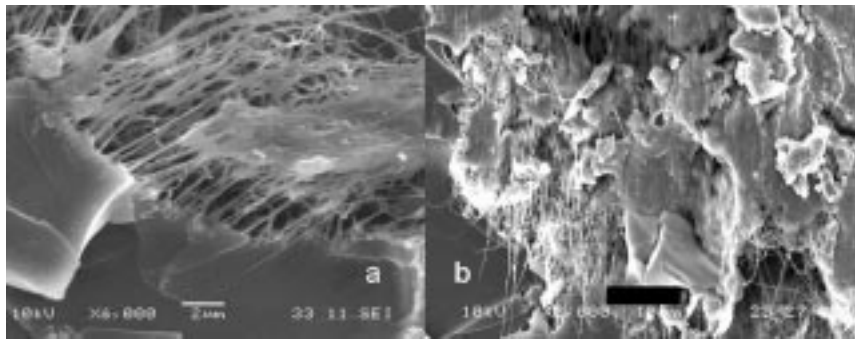

13.12 FESEM images of SWNT/epoxy fracture surface: (a) Pulled out CNT bundles as long as 30–40 μm can be seen. Plastic deformation of the matrix is obvious. Scale bar is 2 μm. (b) Fracture surface in lower magnification. The failure modes of the composite portion include SWNT pullout, matrix cracks bridged by SWNT. Scale bar is 10 μm.

failure with flat fracture surfaces, similar to the fracture surface of unidirectional carbon/epoxy composites. However, local failure modes around the SWNT ropes showed ductile-like failure with plastic deformation of the epoxy and pullout of SWNT ropes, as are seen from Fig. 13.12. Matrix cracks bridged by SWNT ropes are also obvious. Pullout of SWNT bundle can be seen on the fatigue fracture surface. Pullout length of SWNT ropes from the epoxy matrix, examined from SEM images, is about 30 μm, some can even reach 40 μm or longer. Long pullout length of SWNT ropes from the epoxy matrix and the strong interfacial shear stress suggests that CNT can be ideal reinforcement for composites with high fracture toughness.

TEM was used extensively to unravel SWNT fatigue failure mechanisms at the nanometer level, and several fatigue damage/failure modes were revealed:

- splitting of SWNT bundles,
- kink formation in the SWNT bundle and subsequent failure, and
- fracture of SWNT bundles.

Splitting

Two kinds of SWNT splitting are seen: (a) dendrite-like splitting at the very fracture tip, and (b) splitting within a rope away from the fractured tip (Fig. 13.13(a)). Both kinds of splitting are observed extensively. Splitting of SWNT rope is believed caused by differences in interactions between the SWNTs of the outer-layer of a bundle with the polymer matrix, and inter-tubular interactions within a bundle during cyclic loading. The dendrite-like morphology of pulled-out SWNT ropes at the fractured tips is found to be a ubiquitous damage mode, possibly as the result of debonding and splitting of individual SWCNT from a rope inside the matrix during fatigue.

Kink formation and failure of SWNT ropes

Kinks on the SWNTs are characterized by sharp angle on the convex side, with occasional failures, as shown in Fig. 13.13(b). It is likely that they are the result of repeated loading of misaligned SWNTs, or SWNTs debonded from the matrix. CNTs have been found to have excellent resilience, even larger bending deformations would not produce plastic deformation involving the observed kink formation. Thus the kink formation and subsequent failure suggest possible fatigue damage (i.e., accumulated carbon bond dissociation over time) has occurred within the vicinity of the kink. Kink formation is observed extensively. Repeated kinking could eventually lead to rupture of SWNT bundles. Since kinks are associated with splitting, and a split SWNT rope does not necessarily contain a kink, it can be deduced that kinks come after splitting.

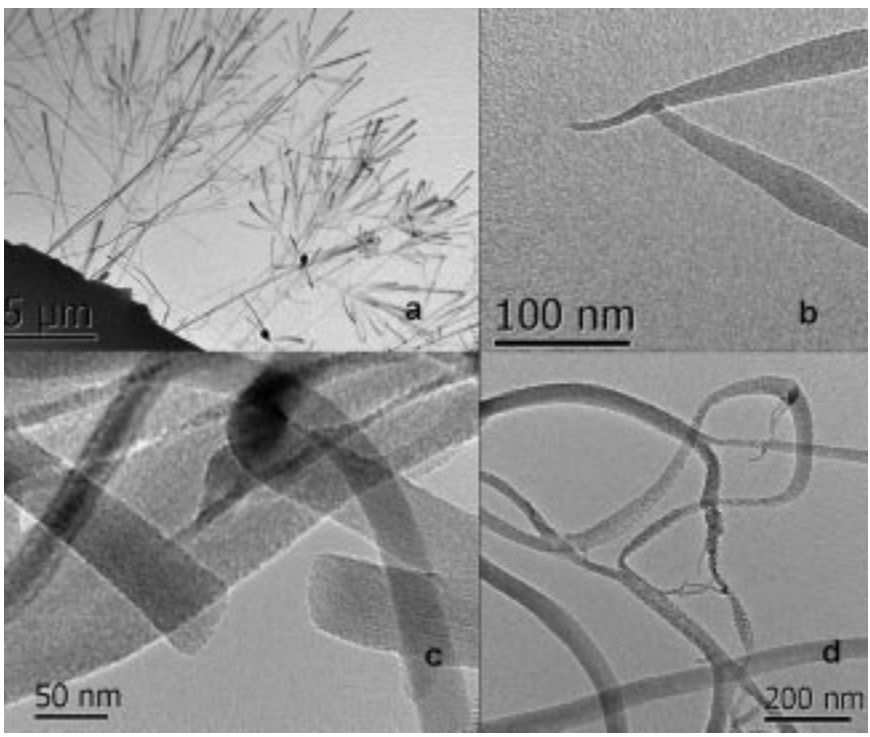

13.13 TEM images of fatigue failure surfaces: (a) very tips of pulled-out SWNTs on a fracture surface. The pulled out SWCNT bundles showed a dendrite-like morphology, believed resulted from splitting of SWCNT rope during fatigue, (b) kink-induced failure of a SWNT bundle, (c) brittle-like failure and (d) ductile-like failure of SWNT bundle.

SWNT fatigue fracture mode

SWNT fractures are observed at the very tips of pulled-out SWNTs (Fig. 13.13(a)), and within SWNT bundles away from the tips. Some of the SWNT failures are characterized with rather flat fracture surfaces, a characteristic of brittle-like failure (Fig. 13.13(c)). It should be mentioned that the fractured bundle shown in Fig. 13.13(c) may contain many SWNTs. In Fig. 13.13(d), tearing fractures are seen, where SWNT ropes are torn apart, leaving a ductile-like fracture surface. For some SWNT ropes, stepwise, abrupt changes in diameter are seen, indicating that SWNTs within a rope may not be broken at the same time or at the same location.

Recent studies on CNT defects and fractures suggested that topological defects of CNTs could be explained by the Stone–Wales mechanism,[35,70] and fracture of CNTs can be attributed to the plastic deformation of CNTs as a result of the gliding and separation of 5-7-7-5 defects. Molecular mechanics simulations of fracture patterns of six different SWNTs (defect-free armchair and zigzag SWNT, and these two types of SWNT with a single Stone-Wales defect) suggest that simulated results do bear a resemblance to the observed fracture surfaces shown in Fig. 13.13(c)–(d),[71] and they also agree with the simulation results of Belytschko *et al.*[70] The subsequent question is, can we predict time-dependent behavior of CNT based on molecular level simulations?

13.4.3 Prediction of SWNT time-dependent behavior

Based on the kinetic concept of fracture of Zhurkov,[72] it is assumed that a CNT will rupture along the direction where the bond has the comparative larger strain energy, due to the result of the atomic thermal motion and the preference of bond dissociation under a strain that is smaller than the critical value. The process of CNT fracture is described in a statistical scheme where the probability of bond breakage is only determined by two parameters, the energy gap of the bonds before and after the dissociation, and the temperature.

To illustrate the idea, we consider the time-dependent fracture of a zigzag type SWNT subject to axial tension, as shown in Fig. 13.14, where the process of onset and propagation of an atomic-sized crack (shaded region) in the nanotube is illustrated. The two C-C bonds at the crack front (represented in bold) oriented parallel to the axis are sustaining greatest strain. We identify each of the discrete crack geometries with i, the number of broken C-C bonds within the crack, and denote u_0 and u_i the strain energy associated with the C-C bond of an intact nanotube, and an i-th mode crack front C-C bond oriented parallel to the tube axis, respectively. In light of Zhurkov's model,[72] we postulate that the lifetime, t_i, of a strained i-th mode crack front C-C bond in a CNT is

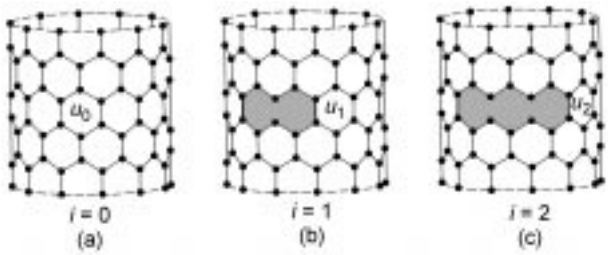

13.14 Schematic diagram of cracking modes of a zigzag type carbon nanotube. The number of broken bonds is denoted by parameter *i*. The crack front C-C bond with strain energy u_i is represented in bold.

$$t_i = \tau_0 \exp\left(\frac{U_0 - u_i}{kT}\right) \tag{13.5}$$

where k is the Boltzmann constant, U_0 is the bond dissociation energy, and u_i represents the strain energy of the bond near absolute zero before dissociation, such that $U_0 - u_i$ is the energy barrier.[73]

At present direct experimental determination of u_i is not possible due to CNTs' extremely small size. Alternatively, the strain energy can be estimated through molecular mechanics calculations. Owing to the discrete atomic structures of CNTs, we propose 'strain energy concentration' for CNT fracture analysis. The strain energies, E_i, for the nanotube and u_i for the crack front C-C bond can be approximately fitted into quadratic functions at small strains, ϵ, such that

$$E_i = a_i \epsilon^2 \tag{13.6a}$$

$$u_i = b_i \epsilon^2 \tag{13.6b}$$

The tensile force per unit length (of the nanotube circumference), T_i, applied at the ends of the CNT is the first-order derivative of the strain energy

$$T_i = \frac{\partial E_i}{\partial \epsilon} = 2a_i \epsilon \tag{13.7}$$

Taking into account CNT bundles as solid ensembles in a matrix material, we approximate the cross-sectional area, A, of a CNT by $\pi(r+h)^2$, in which r is the radius of the nanotube and $2h$ the gap between two adjacent nanotubes. Using Eq. (13.7), the stress at the end of the nanotube is

$$\sigma = \frac{2\pi r T_i}{A} = \frac{4a_i r}{(r+h)^2}\epsilon \tag{13.8}$$

Substituting Eq. (13.8) into Eq. (13.6b), the strain energy of the bond is

$$u_i = \gamma_i \sigma^2 \tag{13.9}$$

where γ_i is the coefficient of strain energy concentration and it reads

$$\gamma_i = \frac{b_i(r+h)^4}{16a_i^2 r^2} \tag{13.10}$$

γ_i is a function of the cracking mode, radial dimension, and chirality of the nanotube. It characterizes the non-uniform local strain energy distribution as a result of a flaw in the CNT. Knowing γ_i, the lifetime, t_i, of a bond and the time-to-failure of a nanotube can be determined.

Here we consider a zigzag type (18, 0) carbon nanotube. Molecular mechanics simulations reveal that a crack expands along the circumference of a zigzag SWNT perpendicular to the loading direction, thus the time-to-failure of an intact nanotube, t, is the summation of the lifetime, t_i, of each individual C-C bond around its circumference

$$t = \sum_{i=0}^{17} t_i = \sum_{i=0}^{17} \tau_0 \exp\left(\frac{U_0 - \gamma_i \sigma^2}{kT}\right) \tag{13.11}$$

In the present case there should be 18 C-C bonds to be broken for complete separation. According to Ref. 70, the strain at the inflection point on the curve of the potential energy of C-C bond, which is believed to be the critical point for bond dissociation, is 19%, and the corresponding bond dissociation energy, U_0, is 1.84×10^{-19} J. The reciprocal of the fluctuation frequency of atoms, τ_0, is usually taken as 10^{-13} s, the Boltzmann constant k is 1.38×10^{-23} J/K, and room temperature is assumed to be 300 K. Using r of 1.4 nm, $2h$ of 0.34 nm (the representative distance between two adjacent graphite layers[64]), and simulation results of a_i and b_i in Eq. (13.10), γ_i are obtained for a range of crack size and applied strains. The increase of γ_i as the crack grows leads to a rapid decline of C-C bond lifetime, t_i, in Eq. (13.11). The results of time-to-failure are shown in Fig.13.15: the dashed lines are lifetime curves of crack front C-C bonds with i broken bonds within a crack (i = 0 - 5), and solid lines are time-to-failure curves of a nanotube with a crack of the i-th mode (i = 0–5). Thus time-to-failure for a zigzag (18, 0) SWNT with a preexisted defect of i-th mode is the summation from t_i to t_{17}, according to Eq. (13.11), i.e., each solid line in Fig. 13.15 is the superposition of the dashed lines underneath. It is seen that the i-th solid curve (of the SWNT) is very close to the dashed curve of t_i when the stress is relatively large, implying that the time-to-fracture of a nanotube is dominated by the lifetimes of a few C-C bonds after initial bond dissociation. When the stress is low, more bonds contribute their lifetime to the total time-to-failure of the nanotube, resulting in a flattening of the solid curve, so that the stress versus logarithm of time-to-failure curve is approximately linear. A comparison of the model prediction and fatigue data presented earlier is also shown in Fig. 13.15. Note that each data point in Fig. 13.15 represents failure of a SWNT rope/epoxy composite sample. The 'composite effect' begins to emerge at low load, long life region, where fatigue data 'outperforms' predictions. Nonetheless, the data do fall within the range of predications of the current kinetic model. It is realized

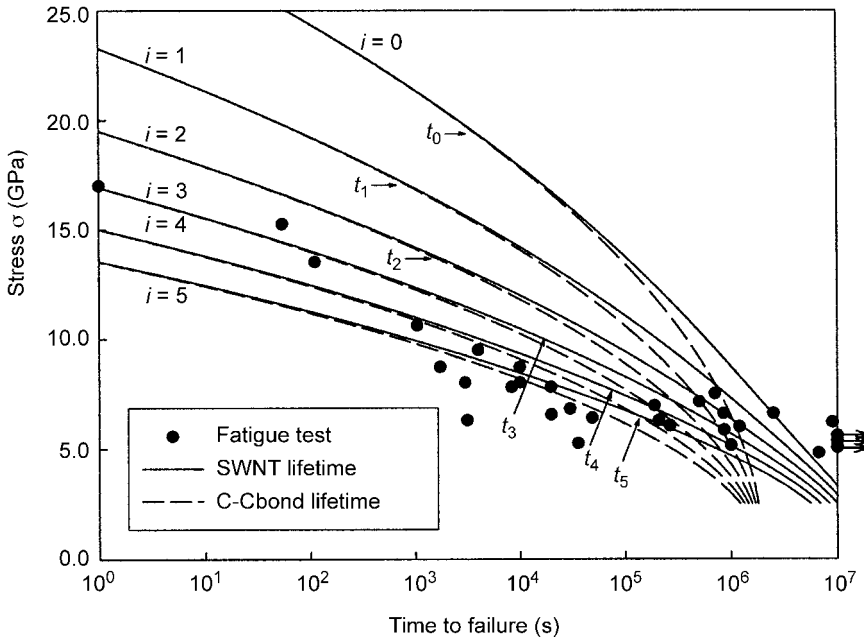

13.15 Time-to-failure of zigzag (18, 0) SWNTs versus applied stress. Dashed lines are lifetime curves of crack front C-C bond; solid lines are time-to-failure curves of intact nanotube ($i = 0$), and of nanotubes with preexisted flaw ($i > 0$). Only the results of the first six cracking modes are shown. Solid circles are results of fatigue experiments.

that frequency effect, SWNT size effect, and multiple SWNT fractures, may also exercise influence, to various extent, on the lifetime of a SWNT, which could be topics for further studies.

13.5 Conclusions

In this chapter we have addressed several issues concerning strength, interface, and long-term behavior of carbon nanotubes and carbon nanotube reinforced polymeric composites, from mechanics point of view. Although tensile strength of CNTs was experimentally determined and simulated at the molecular level in previous studies, a fundamental understanding of the atomic mechanisms leading to the observed wide statistical distribution is still lacking. In particular, what kind of defects exist in the CNTs from a specific synthetic process, how they are distributed along a CNT, how they interact under applied load, and more importantly, how they can be controlled in synthesis are problems to be addressed in the future.

Intricate experiments and modeling at both molecular and microscopic level have been performed to elucidate CNT-polymer interactions at the interface.

The majority of the results seem to suggest that CNT-polymer interfacial strength is much higher than that of conventional micro-fiber reinforced polymeric composites. Nonetheless, mysteries still remain. For instance, it has been observed in some cases that 'interfacial failure' during CNT pullout was not occuring at the CNT-polymer boundary but rather it was a polymer failure near the CNT-polymer boundary. Despite our very limited current understanding, there is still a lot of room for clarifying the physics at the CNT-polymer interface. A better understanding on the strength (and weakness) of CNTs and CNT-polymer interface issues enable us to design and create nanocomposites with predictable properties and performance.

We have just begun to study the long-term behavior of CNT/polymer composites, but are far from understanding it. Although only a few studies on CNT/polymer composite long-term behavior are available to date, the results are encouraging in comparison with unidirectional carbon fiber reinforced composites. Continuing and extended efforts in this direction are needed to better realize the potential of CNT/polymer composites for long-term structural applications. It should be mentioned that currently there is no creep or creep rupture data for CNTs and CNT/polymer composites, nor is there data for fatigue behavior of CNTs, to the best of our knowledge. Although a simple molecular framework has been proposed for predicting the time-dependent behavior of CNTs, many related issues, such as the effects of defects and defect interactions on the time-dependent behavior still await future efforts for a more accurate description of the physical processes.

13.6 References

1. Dresselhaus M S, Dresselhaus G, Avouris P H (eds), *Carbon Nanotubes Synthesis, Structure, Properties, and Applications*, Berlin, Springer, 2001.
2. Meyyappan M, *Carbon nanotube: science and applications*, Boca Raton, CRC Press, 2003.
3. Terrones M, 'Science and technology of the twenty-first century: Synthesis, properties and applications of carbon nanotubes', *Annual Review of Material Research*, 2003 **33** 419–501.
4. Ijima S, 'Helical microtubules of graphitic carbon', *Nature*, 1991 **354** 56.
5. Journet C and Bernier P, 'Production of carbon nanotubes', *Appl. Phys.* A, 1998 **67** (1) 1–9.
6. Ebbesen T W and Ajayan P M, 'Large-scale synthesis of carbon nanotubes', *Nature*, 1992 **358** (6383) 220–222.
7. Iijima S and Ichihashi T, 'Single-shell carbon nanotube of 1-nm diameter', *Nature*, 1993 **363** (6430) 603–605.
8. Bethune D S, Kiang, C H, de Vries M S, Gorman G, Savoy R, Vazquez J, and Beyers R, 'Cobalt-catalyzed growth of carbon nanotubes with single-atomic-layer walls', *Nature*, 1993 **363** (6430) 605–607.
9. Journet C, Maser W K, Bernier P, Loiseau A, Lamy de la Chapelle M, Lefrant S, Deniard P, Lee R and Fischer J E, 'Large-scale production of single-walled carbon

nanotubes by the electric-arc technique', *Nature*, 1997 **388** (6644) 756–758.
10. Guo T, Nikolaev P, Rinzler A G, Tomanek D, Colbert D T, Smalley R E, 'Self-assembly of tubular fullerenes', *J. Physical Chemistry*, 1995 **99** (27) 10694–10697.
11. Thess A, Lee R, Nikolaev P, Dai H, Petit P, Robert J, Xu C, Hee Lee Y, Gon Kim S, Rinzler A G, Colbert D T, Scuseria G E, Tománek D, Fischer J E and Smalley R E, 'Crystalline ropes of metallic carbon nanotubes', *Science*, 1996 **273** (5274) 483–487.
12. Hernadi K, Fonseca A, Nagy J B, Siska A and Kiricsi I, 'Production of nanotubes by the catalytic decomposition of different carbon-containing compounds', *Appl. Cat. A*, 2000 **199** (2) 245–255.
13. Colomer J F, Stephan S, Lefrant S, Van Tendeloo G, Willems I, Kónya Z, Fonseca A, Laurent Ch and Nagy J B, 'Large-scale synthesis of single-wall carbon nanotubes by catalytic chemical vapor deposition (CCVD) method', *Chem. Phys. Lett.*, 2000 **317** (1–2) 83–89.
14. Bacsa R R, Laurent C, Peigney A, Bacsa W S, Vaugien T and Rousset A, 'High specific surface area carbon nanotube from catalytic chemical vapor deposition process', *Chem. Phys. Lett.*, 2000 **323** (5–6) 566–571.
15. Li W Z, Xie S S, Qian L X, Chang B H, Zou B S, Zhou W Y, Zhao R A and Wang G, 'Large-scale synthesis of aligned carbon nanotubes', *Science*, 1996 **274** (5293) 1701–1703.
16. Dai H J, Rinzler A G, Nikolaev P, Thess A, Colbert D T, Smalley R E, 'Single-wall nanotubes produced by metal-catalyzed disproportionation of carbon monoxide', *Chem Physics Letters*, 1996 **260** (3–4) 471–475.
17. Lee C J, Lyu S C, Kim H W, Park C Y and Yang C W, 'Large-scale production of aligned carbon nanotube by the vapor phase growth method', *Chem. Phys. Lett.*, 2002 **359** (1–2) 109–114.
18. Cheng H M, Li F, Su G, Pan H Y, He L L, Sun X, Dresselhaus M S, 'Large-scale and low-cost synthesis of single-walled carbon nanotubes by the catalytic pyrolysis of hydrocarbons', *Applied Physics Letters*, 1998 **72** 3282–3294.
19. Hsu W K, Hare J P, Terrones M, Kroto H W, Walton D R M, Harris P J F, 'Condensed-phase nanotubes', *Nature*, 1995 **377** (6551) 687.
20. Laplaze D, Bernier P, Maser W K, Flamant G, Guillard T, Loiseau A, 'Carbon nanotubes: the solar approach', *Carbon*, 1998 **36** (5–6) 685–688.
21. Liu C, Cheng H M, Cong H T, Li F, Su G, Zhou B L, Dresselhaus M S, 'Synthesis of macroscopically long ropes of well-aligned single-walled carbon nanotubes', *Advanced Material*, 2000 **12** 1190.
22. Zheng L X, O'connell M J, Doorn S K, Liao X Z, Zhao Y H, Akhadov, E A, Hoffbauer M A, Roop B J, Jia Q X, Dye R C, Peterson D E, Huang S M, Liu J, Zhu YT, 'Ultralong single-wall carbon nanotubes', *Nature Materials*, 2004 **3** 675–676.
23. Zhu H W, Xu C L, Wu D H, Wei B Q, Vajtai R, Ajayan P M, 'Direct synthesis of long single-walled carbon nanotube strands', *Science*, 2002 **296** 884–886.
24. Jiang K, Li Q, Fan S, 'Spinning continuous carbon nanotube yarns', *Nature*, 2002 **419** 801.
25. Li Y L, Kinloch I A, Windle A H, 'Direct spinning of carbon nanotube fibers from chemical vapor deposition synthesis', *Science*, 2004 **304** (5668) 276–278.
26. Dalton A B, Collins S, Munoz E, Razal J M, Ebron V H, Ferraris J P, Coleman J N, Kim B G, Baughman R H, 'Super-tough carbon-nanotube fibres', *Nature*, 2003 **423** 703.
27. Terranova M L, Orlanducci S, Fazi E, Sessa V, Piccirillo S, Rossi M, Manno D, and

Serra A, 'Organization of single-walled nanotube into macro-sized rectangularly shaped ribbons', *Chem. Phys. Lett*., 2003 **381** (1–2) 86–93.
28. Ko F, Gogotsi Y, Ali A, Naguib N, Ye H, Yang G, Li C, and Willis P, 'Electrospinning of continues carbon nanotube-filled nanofiber yarns', *Advanced Materials*, 2003 **15** (14) 1161.
29. Walters D A, Ericson L M, Casavant M J, Liu J, Colbert D T, Smith K A, Smalley R E, 'Elastic strain of freely suspended single-wall carbon nanotube ropes', *Appl. Phys. Lett.*, 1999 **74** (25) 3803–3805.
30. Pan Z W, Xie S S, Lu L, Chang B H, Sun L F, Zhou W Y, Wang G, Zhang D L, 'Tensile tests of ropes of very long aligned multiwall carbon nanotubes', *Appl Phy Lett.*, 1999 **74** (21) 3152–3154.
31. Yu M F, Files B S, Arepalli S, Ruoff R S, 'Tensile loading of ropes of single wall carbon nanotubes and their mechanical properties', *Phys Rev Lett*, 2000 **84** 5552–5555.
32. Yu M F, Lourie O, Dyer M J, Moloni K, Kelly T F, Ruoff R S, 'Strength and breaking mechanism of multiwalled carbon nanotubes under tensile load', *Science*, 2000 **287** 637–640.
33. Li F, Cheng H M, Bai S, Su G, Dresselhaus M S, Tensile strength of single-walled carbon nanotubes directly measured from their macroscopic ropes', *Appl Phys Lett*, 2000 **77** 3161–3163.
34. Charlier J C, 'Defects in carbon nanotubes', *Acc. Chem. Res.*, 2002 **35** (12) 1063–1069.
35. Girifalco L A, Hodak M, Lee R S, 'Carbon nanotubes, buckyballs, ropes, and a universal graphitic potential', *Phys. Rev. B*, 2000 **62** (19) 13104–13110.
36. Bryan, D. *Weibull Analysis.* ASQC Quality Press, Wisconsin, 1994.
37. Zhou Y X and Xia Y M, 'In situ strength distribution of carbon fibers in unidirectional metal-matrix composite wires', *Composites Science and Technology*, 2001 **61** (14) 2017–2023.
38. Lau K T, Shi S Q, 'Failure mechanisms of carbon nanotube/epoxy composites pretreated in different temperature environments', *Carbon*, 2002 **40** 2961–2973.
39. Bhattacharyya A R, Sreekumar T V, Liu T, Kumar S, Ericson L M, Hauge R H, Smalley R E, 'Crystallization and orientation studies in polypropylene/single wall carbon nanotube composite', *Polymer*, 2003 **44** 2373–2377.
40. Jia Z, Wang Z, Xu C, Liang J, Wei B, Wu D, Zhu S, 'Study on poly(methyl methacrylate)/carbon nanotube composites', *Mater. Sci. & Eng. A*, 1999 **271** (1–2) 395–400.
41. Xu X J, Thwe M M, Shearwood, C, and Liao K, 'Mechanical properties and interfacial characteristics of carbon nanotube reinforced epoxy thin film', *Applied Physics Letters*, 2002, **81** (15) 2833–2835.
42. Wong M H, Paramsothy M, Ren Y, Xu X J, Li S, and Liao K, 'Physical interactions at carbon nanotube–polymer interface', *Polymer*, 2003 **44** 7757–7764.
43. Miyagawa H, Drzal L T, 'Thermo-physical and impact properties of epoxy nanocomposites reinforced by single-wall carbon nanotubes', *Polymer*, 2004 **45** (15) 5163–5170.
44. Haggenmueller R, Gommans, H H, Rinzler, A G, Fischer J E, Winey, K I, 'Aligned single-wall carbon nanotubes in composites by melt processing methods', *Chemical Physics Letters*, 2000 **330** 219–225.
45. Schadler L S, Giannaris S C, Ajayan P M, 'Load transfer in carbon nanotube epoxy

composites', *Appl. Phys. Lett*., 1998 **73** (26) 3842.
46. Ganguli S, Aglan H, Dean D, 'Microstructural origin of strength and toughness of epoxy nanocomposites', *J. Elastomers and Plastics*, 2005 **37** (1) 19–35.
47. Gong X, Liu J, Baskaran S, Voise R D, Young, J S, 'Surfactant-assisted processing of carbon nanotube/polymer composites', *Chemistry of Materials*, 2000 **12** (4) 1049–1052.
48. Liu T X, Phang I Y, Shen L, Chow S Y, Zhang W D, 'Morphology and mechanical properties of multiwalled carbon nanotubes reinforced nylon-6 composites', *Macromolecules*, 2004 **37** (19) 7214–7222.
49. Allaoui A, Bai B, Cheng, H M, Bai, J B, 'Mechanical and electrical properties of a MWNT/epoxy composite', *Composites Science and Technology*, 2002 **62** 1993–1998.
50. Gou, J H, Minaie, B, Wang, B, Liang, Z Y, Zhang C, 'Computational and experimental study of interfacial bonding of SWNT reinforced epoxy composites', *Computational Materials Science*, 2005 **31** (3–4) 225–236.
51. Qian D, Dickey E C, Andrew R, and Rantell T, 'Load transfer and deformation mechanisms in carbon nanotube-polystyrene composites', *Applied Physics Letters*, 2000 **76** (20) 2868–2870.
52. Bower C, Rosen R, Jin L, Han J, Zhou O, 'Deformation of carbon nanotubes in nanotube-polymer composites', *Applied Physics Letters*, 1999 **74** (22) 3317–3319.
53. Chang B H, Liu Z Q, Sun L F, Tang D S, Zhou W Y, Wang G, Qian L X, Xie S S, Fen J H, and Wan, M X, 'Conductivity and magnetic susceptibility of nanotube/polypyrrole nanocomposites', *Journal of Low Temperature Physics*, 2000 **119** (1/2) 41–48.
54. Wagner H D, Lourie O, Feldman Y, Tenne R, 'Stress-induced fragmentation of multiwall carbon nanotubes in a polymer matrix,' *Appl Phys Lett*, 1998 **72** (2) 188–190.
55. Lourie O and Wagner H D, 'Transmission electron microscopy observations of fracture of single-wall carbon nanotubes under axial tension', *Applied Physics Letters*, 1998 **73** (24) 3527–3529.
56. Wagner H D, 'Nanotube-polymer adhesion: a mechanics approach', *Chemical Physics Letters*, 2002 **361** 57–61.
57. Cooper C A, Cohen S R, Barber A H, Wagner H D, 'Detachment of nanotubes from a polymer matrix', *Appl Phys Letts*, 2002 **81** (20) 3873–3875.
58. Barber, A H, Cohen S R, Wagner H D, 'Measurement of carbon nanotube-polymer interfacial strength', *Appl Phys Letts*, 2003 **82** (23) 4140–4142.
59. Ajayan P M, Schadler L S, Giannaris S C, Rubio A, 'Single-walled carbon nanotube-polymer composites: strength and weakness', *Advanced Materials*, 2000 **12** (10) 750–753.
60. Jin L, Bower C, Zhou O, 'Alignment of carbon nanotubes in a polymer matrix by mechanical stretching', *Applied Physics Letters*, 1998 **73** (9) 1197–1199.
61. Frankland S J V, Caglar A, Brenner D W, Griebel M, 'Molecular simulation of the influence of chemical cross-links on the shear strength of carbon nanotube interfaces', *J. Phys. Chem. B*, 2002 **106** (12) 3046–3048.
62. Liao K and Li S, 'Interfacial characteristics of a carbon nanotube-polystyrene composite system', *Applied Physics Letters*, 2001 **79** (25) 4225–4227.
63. Yao N and Lordi V, 'Young's modulus of single-walled carbon nanotubes', *J Appl Phys*, 1998 **84** (4) 1939–1943.

64. Liao K and Tan Y M, 'Influence of moisture-induced stress on in-situ strength degradation of fiber in unidirectional composite', *Composites Part B: Engineering*, 2001 **32** 365–370.
65. Lu J P, 'Elastic properties of carbon nanotubes and nanoropes', *Physical Review Letters*, 1997 **79** (7) 1297–1300.
66. Kelly B T, *Physics of Graphite*, London, Applied Science Publishers, 1981.
67. Shackelford J F, and Alexander W, *Materials Science and Engineering Handbook*, Boca Raton, CRC Press, 1990.
68. Ren Y, Liao K, Li F, and Cheng H M, 'Tension-tension fatigue behavior of unidirectional single-walled carbon nanotube reinforced epoxy composite', *Carbon*, 2003 **41** 2177–2179.
69. Harris B, Reiter H, Adam T, Dickson R F, Fernando G, 'Fatigue behavior of carbon fiber reinforced plastics', *Composites*, 1990 **21** (1) 232–243.
70. Belytschko T, Xiao S P, Schatz G C, and Ruoff R S, 'Atomistic simulation of nanotube fracture', *Phys. Rev. B*, 2002 **65** (23) 235–430.
71. Ren Y, Fu Y Q, Liao K, Li F, and Cheng H M, 'Fatigue failure mechanisms of single-walled carbon nanotube ropes', *Applied Physics Letters*, 2004 **84** (15) 2811–2813.
72. Zhurkov S N, 'Kinetic concept of the strength of solids', *Int. J. Fracture Mechanics*, 1965 **1** (4) 311–323.
73. Xiao T, Ren Y, and Liao K, 'A kinetic model for time-dependent fracture of carbon nanotubes', *Nano Letters*, 2004 **4** (6) 1139–1142.

14

Fullerene/carbon nanotube (CNT) composites

T KUZUMAKI, The University of Tokyo, Japan

14.1 Introduction

This chapter focuses on the preparation of nanocomposite materials using carbon nanotubes (CNTs) as the fibre material and carbon 60 (C_{60}) crystals as the matrix. CNTs are a type of higher order fullerene and have a seamless cylindrical structure formed by the rolling of a graphene sheet.[1] The transmission electron microscope (TEM) image of a CNT and its atomic structure models are shown in Fig. 14.1. In several cases, the atomic configuration of the hexagonal carbon network of CNT takes a helical structure. Band structure calculations predict that chiral CNTs are either semi-conducting or metallic depending on their diameter and helical angle;[2,3] therefore, the CNT is a candidate for novel electronic devices. The remarkable features of CNTs are not limited to the electrical properties but extend to the mechanical properties. It has been reported that the Young's modulus of a CNT is extremely high and is of the order of TPa.[4–7] Moreover, CNTs are not brittle and can be bent plastically. In-situ TEM observations show that bending of a CNT above the elastic limit leads to structural defects, such as the folding of the cylindrical wall or an exfoliation of the layers, which result in a plastically deformed CNT.[8,9] On the other hand, bending of conventional carbon fibre above the elastic limit causes brittle fracture. Owing to the mechanical properties, CNTs are expected to be an ideal fibre material for composites.[10,11] For practical applications, the development of a CNT mass production process is indispensable. The technical problems are now being solved by the application of chemical vapour deposition (CVD) techniques. In the near future, CNTs will be widely used as fibre materials for composites.

On the other hand, C_{60} is a type of fullerene with a highly spherical molecular structure. The spherical molecules crystallise at room temperature in the form of a face-centred cubic (fcc) structure with C_{60} molecules at eight corners and six centres of a cube (Fig. 14.2). The C_{60} crystal has unique mechanical properties owing to its highly symmetrical fcc structure. Similar to common metals, the $\{111\} <1\bar{1}0>$ slip system allows the deformation of C_{60} crystals. The elongation of a nanocrystalline C_{60} specimen (approximately 50 nm in grain size) is larger

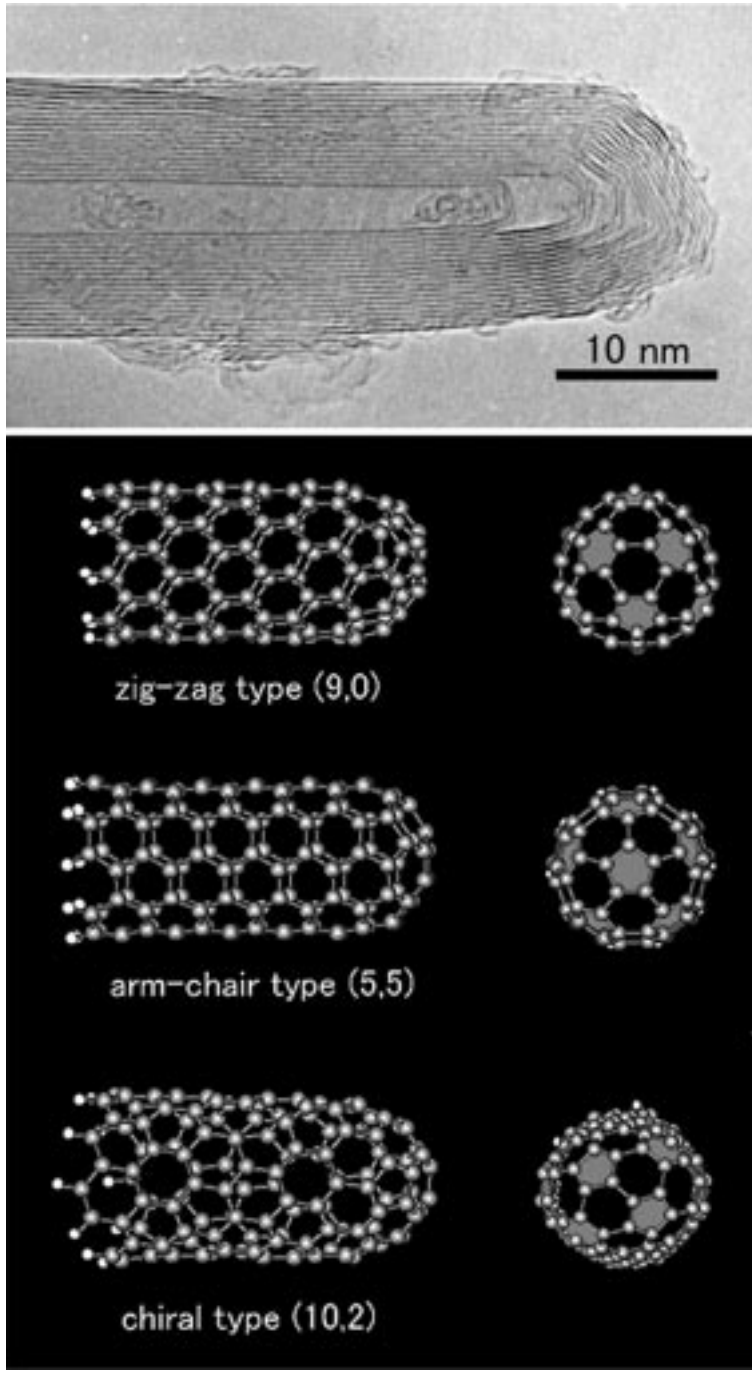

14.1 High-resolution TEM image and typical atomic structure models of a CNT.

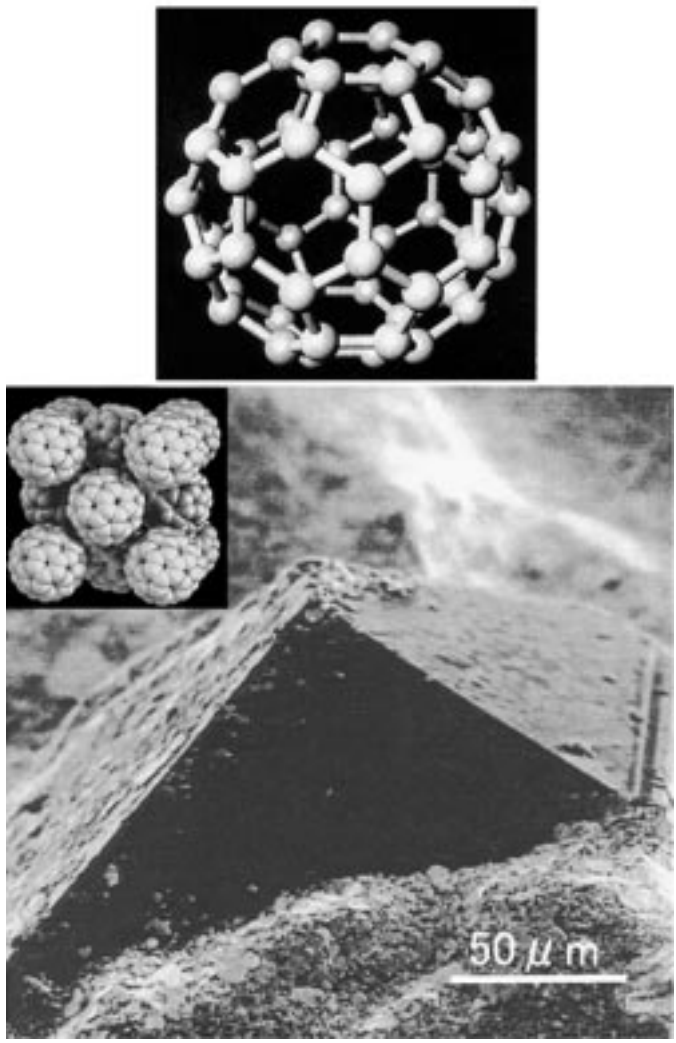

14.2 Molecular structure of C_{60} and a vapour-grown C_{60} crystal.

and the work hardening rate is either similar to or lesser than those of polycrystalline C_{60}.[12,13] Moreover, the C_{60} crystal is known to be polymerised by ultra high pressure sintering.[14–19] The polymerised C_{60} crystal is insoluble in organic solvents such as toluene, and it hardens in comparison with a pristine C_{60} crystal. These characteristic differences of C_{60} crystals are interesting in terms of material design.

The above-mentioned features of these novel carbons may contribute to the production of novel carbon/carbon (C/C) composites. This chapter consists of three main sections. The first section discusses the fabrication of the C_{60}/CNT

composite by the drawing process. A novel C/C composite was produced at room temperature by drawing a silver tube containing CNTs as the fibre material and nanocrystalline C_{60} as the matrix. An aim of this preparation method is to control the orientation of the CNTs in the matrix. The second section discusses the fabrication of the composite by ultra high pressure sintering. The obtained structure of the C_{60} matrix was characterised by X-ray diffraction (XRD), TEM and electron energy loss spectroscopy (EELS). In the third section, a possible application of the drawn composite is presented. The application potential of the composite as an electron source is investigated by evaluating the electron emission characteristics of the CNTs.

14.2 Fabrication of the composite by the drawing process

14.2.1 Introduction

The composite structure design involving orientation of the fibres in the matrix is an important factor in fibre-reinforced composite fabrication. Since CNTs can be deformed plastically by the application of external forces, plastic working such as drawing and extrusion can be applied for the production of composites. In this section, the preparation of the CNT reinforced nanocrystalline C_{60} matrix composite by the drawing process is presented, followed by a description of the composite structure and mechanical characteristics.[20,21]

14.2.2 Preparation of the composite

The CNTs and C_{60} were synthesised by the carbon DC arc discharge method (25 V, 300 A) in a helium (purity: 99.999%) atmosphere at 5.3 kPa.[8,9] The carbon powder obtained from the cathode debris on a graphite block was dispersed into ethanol by sonication to separate CNTs from other admixtures. The CNT content of the refined carbon powder used in this experiment was approximately 60 vol.%. The average length and diameter of the CNTs were approximately 2.1 μm and 15 nm, respectively.

The nanocrystalline C_{60} powder was prepared by the inert gas condensation method. C_{60} purified by high performance liquid chromatography was evaporated in a helium (purity: 99.9999%) atmosphere at 1.3 kPa. Ultra fine particles were collected on the surface of a stainless steel cylinder cooled by liquid nitrogen. The average grain size of nanocrystalline C_{60} was determined to be approximately 50 nm by TEM. A mixture of nanocrystalline C_{60} and carbon powder (C_{60}:C powder = 6:4) was packed in a silver sheath and drawn to produce a multicore wire, as shown in Fig. 14.3. In the first step, the mixture packed in the sheath was drawn to produce a hexagonal shaped wire with a diameter of 1 mm. Next, seven such wires were closely packed in another

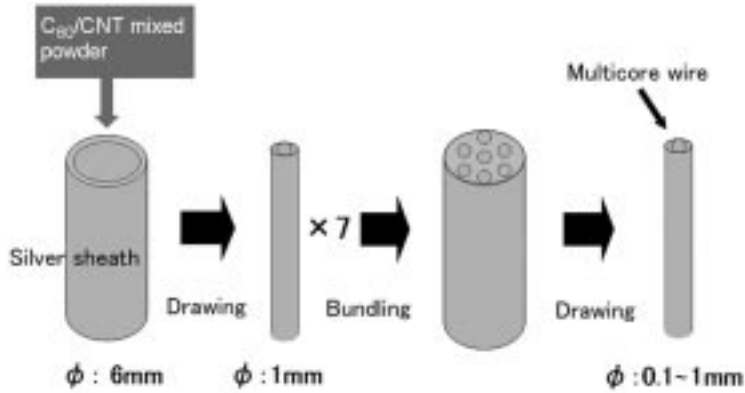

14.3 Processing scheme of the C_{60}/CNT composite.

sheath, and the diameter of the new sheath was reduced from 6.0 mm to 0.1 mm by the drawing process.

14.2.3 Nanostructural characterisation

Structure of the as-drawn composite specimen

The specimen with seven composite regions can be observed in a cross section of the drawn wire, as shown in Fig. 14.4. The CNTs are not damaged and are aligned along the longitudinal direction of the wire, as shown in Fig. 14.5. The

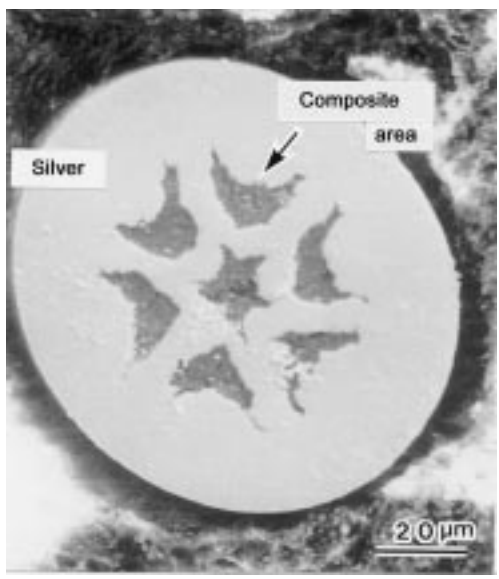

14.4 Cross-sectional view of the drawn composite.

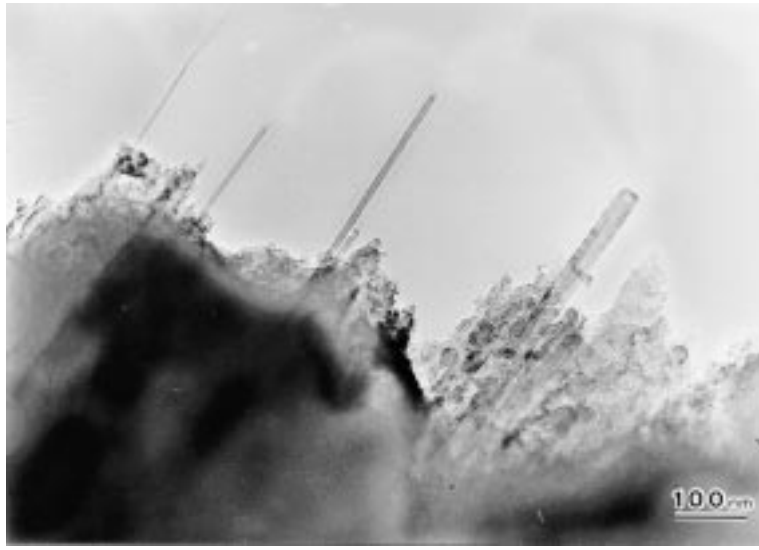

14.5 TEM image of the tip of the drawn composite. CNTs were aligned along the longitudinal direction of the composite wire.

microstructure of the composite is complex and comprises straight CNTs, deformed CNTs and carbon nanoparticles.

Structure of the heat-treated composite specimen

C_{60} crystal is thermally unstable and sublimes above approximately 853 K in an open atmosphere. In the present composite, however, the original morphology remained unchanged when subjected to a heat treatment at 1243 K for 54 ks. The Raman scattering spectrum shown in Fig. 14.6 exhibits no obvious peak of C_{60}, diamond or graphite; however, a broad spectrum is observed near the graphitic and disordered bands. High-resolution TEM observations of the heat treated C_{60} matrix revealed an amorphous phase along with the (111) plane of a C_{60} crystal. These results suggest that the C_{60} matrix loses much of its molecular crystallinity and becomes amorphous during the heat treatment. The CNTs in the matrix are not damaged by the heat treatment.

14.2.4 Bonding interaction at the interface

Tensile test of the heat treated composite

The mechanical properties of the composite that was desheathed by the evaporation of silver during the heat treatment at 1243 K and 54 ks were investigated by a conventional tensile test (Autograph, AGS-D Type 3, Shimadzu) at room temperature. The desheathed composite specimen yielded a tensile strength

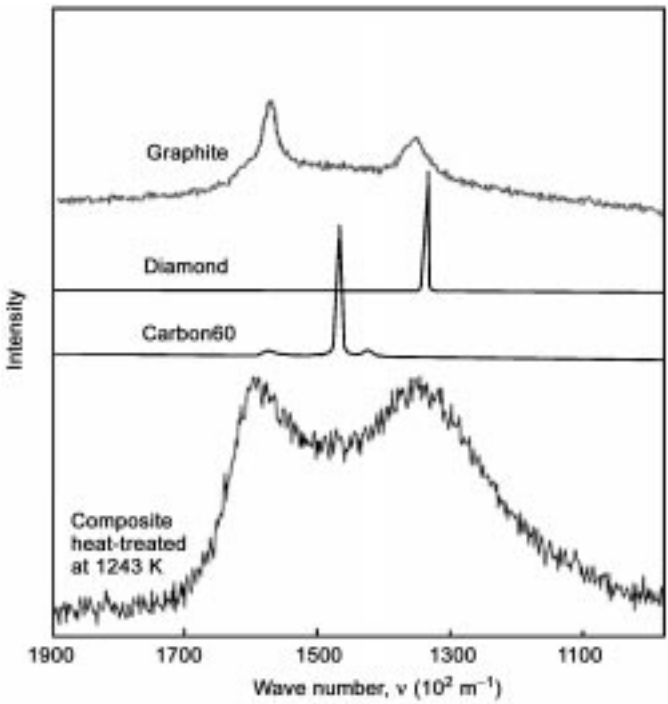

14.6 Raman spectrum of the composite that was heat-treated at 1243 K. Raman measurement was carried out at room temperature by an Ar+ laser (514.4 nm) with an incident power of 0.1 mW/1 $\mu m\phi$. The spectra of graphite, diamond and C_{60} crystal are shown for reference.

of 18 MPa and a fracture strain above 10% (Fig. 14.7). The fracture stress of the composite was found to be approximately 20 times that of polycrystalline C_{60} (1 MPa). Neither an elastic region nor a yield point of the specimen could be specified. Necking of the specimens was rarely observed during the tensile test. The fractured surface of the composite specimen indicates that the CNTs were pulled out without breaking the C_{60} matrix (cf. Fig. 14.5). The inhomogeneity of the composite, which is due to the fact that the carbon powder used in this experiment contained impurities such as carbon nanoparticles or flake like glassy carbon, resulted in the scattering of the data points in the tensile tests, yielding the average values of the tensile strength and fracture strain as 17 MPa and 11%, respectively.

Hardening mechanism of the matrix

The new C/C composite shows an excellent fracture strain greater than 10%. On the contrary, the fracture strain of conventional carbon materials is only 1–2%, although they have an extremely high strength and rigidity.

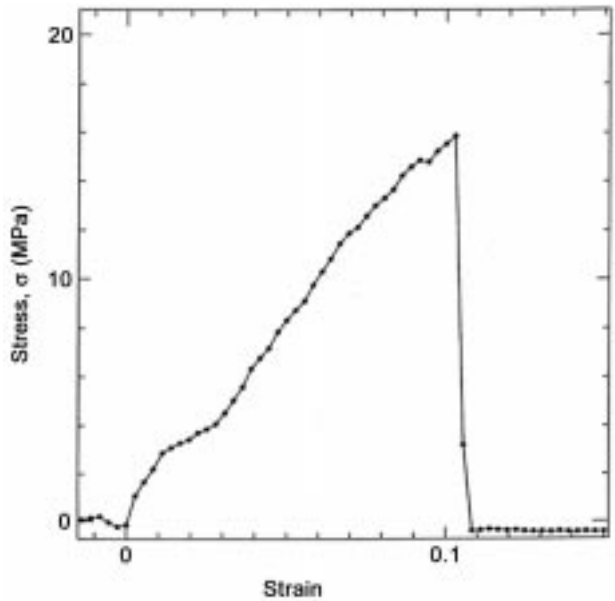

14.7 An example of the stress-strain curve of the heat-treated composite.

The nanocrystalline C_{60} specimen exhibits a behaviour similar to that of superplasticity and demonstrates a large strain at room temperature, which may be due to grain boundary sliding that originates from the weak bonding of molecular forces.[12] In the present experiments, however, the stress-strain curve and the fractured surface indicate an absence of the superplastic behaviour. This may be due to the decomposition of the C_{60} phase into the amorphous phase during the heat treatment.

This decomposition is supported by the Raman spectrum and TEM observations, which clarify that the structural features of the C_{60} crystal disappear due to the heat treatment along with the appearance of the amorphous phase. The Vickers hardness of polycrystalline C_{60} is known to increase with the heat-treatment temperature. Therefore, it can be speculated that the amorphous phase contributes to the hardening of the matrix and suppresses grain boundary sliding in the remaining nanocrystalline C_{60}. These considerations suggest that the possible role of the plasticity of matrix due to crystallographic slip or grain boundary slip may not affect the observed ductility of the composite.

Mechanical properties and nanostructure of the matrix/fibre interface

Microstructural observations of the composites suggest that their elongation originates due to sliding that occurs at the interface between the CNT and the C_{60} matrix. In this subsection, the interfacial structure is observed by using an electron microscope, and the mechanical properties of the interface are

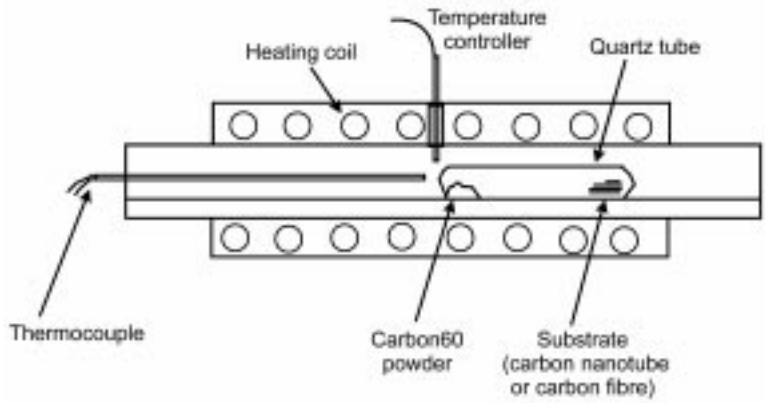

14.8 Schematic diagram of the equipment used for the preparation of the composite.

examined by a micro pull-out test performed using pitch-based high modulus carbon fibres deposited by the C_{60} single crystal instead of the C_{60}/CNT composite.[20–22]

A single crystal of C_{60} was grown on a CNT by vapour phase growth, as shown in Fig. 14.8. The CNTs and C_{60} powders were placed separately at the opposite ends of an evacuated and sealed quartz tube and heated in a temperature gradient (873–723 K).

For the pull-out test, a single crystal of C_{60} was vapour deposited on high modulus pitch-based carbon fibres (Young's modulus: 700 GPa, Tohnen Co. Ltd.) by the above-mentioned method. The fibres have a diameter of 10 μm and their surface structure is similar to that of the CNTs. The shear strength of the interface was estimated from the load-displacement (L-D) curve of the pull-out test, which was performed in an Instron-type tensile testing machine (Autograph AGS-D Type 3, Shimadzu) at room temperature with a cross head speed of 0.5 mm/min.

The fine C_{60} single crystal grown on a CNT is faceted by {111} planes of the fcc structure as in the case of a large bulk specimen. The epitaxial orientation relationship of the C_{60}/CNT interface is restricted to the parallel direction because of the cylindrical shape of the CNT. The fibre axis of the CNT is observed to be parallel to <110> of the C_{60} crystal, as shown in Fig. 14.9. In the case of a carbon fibre-C_{60} composite, C_{60} crystals of sizes ranging from micrometres to millimetres were formed on the carbon fibre (Fig. 14.10). As shown in Fig. 14.11, the interfacial structure of C_{60}/CNT is morphologically similar to that of the C_{60}/carbon fibre. The pull-out tests were performed on three specimens in which the carbon fibre axis was parallel to <110> of the C_{60} crystal. The L-D curve exhibits a nonlinear behaviour; the 'steps' are indicated by arrows from the beginning of the test (Fig. 14.12). The fibre was pulled out immediately once the maximum load was realised. Load fluctuation due to

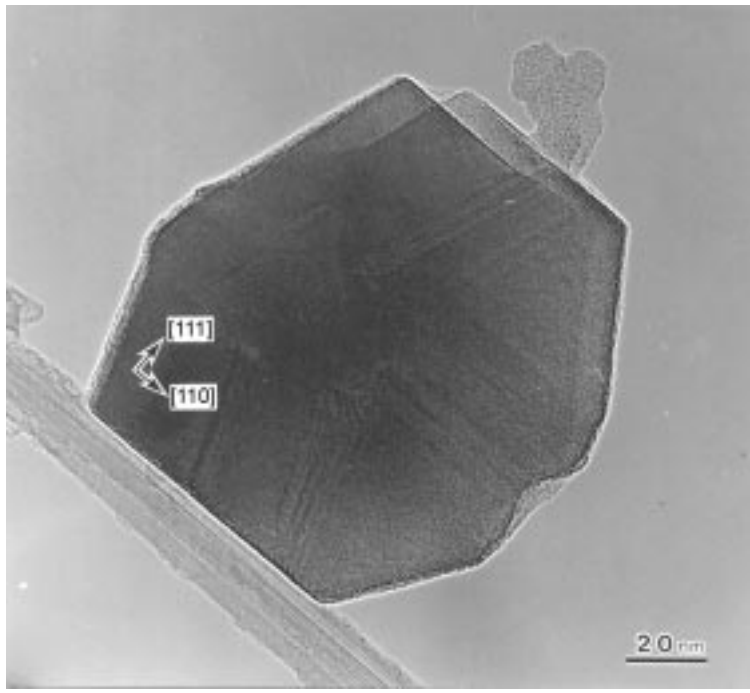

14.9 TEM image of a C_{60} crystal epitaxially grown on a CNT.

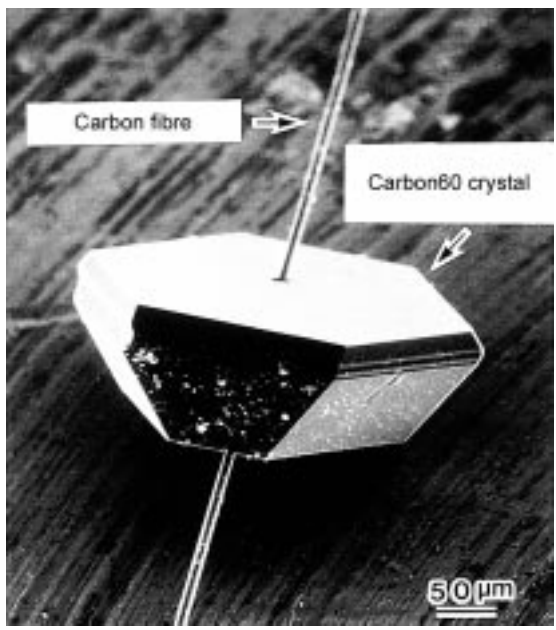

14.10 SEM image of a C_{60} crystal grown on a carbon fibre.

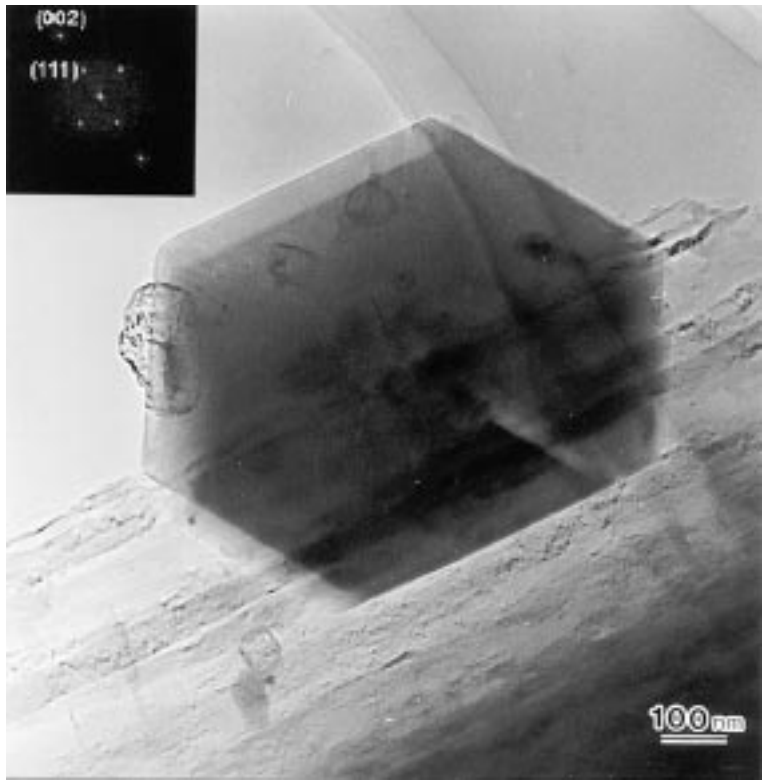

14.11 TEM image of a C_{60} crystal grown on a carbon fibre.

pulling out of the fibres, i.e. 'stick slip' could not be detected within the experimental resolution.

In the scanning electron microscope (SEM) image of the C_{60} crystal obtained from the pull-out test, no substantial evidence of the plastic deformation, such as the slip line, is observed near the hole edge. This result indicates that the nonlinear behaviour of the composite is caused by the microscopic debonding of the interface that begins at the surface and moves along the fibre and the sequential interfacial sliding, but not by the plastic deformation of the matrix. The shear strength of the interface was evaluated by the maximum load ($= 1.4$ mN) and embedded length of the carbon fibre ($= 1.0$ mm) to be approximately 4.4×10^{-2} MPa.

The fracture behaviour and mechanical properties of the composites are generally influenced by the interfacial structure or the fibre/matrix interactions. The nonlinear behaviour in the L-D curve and the pull-out of the fibre from the matrix without plastic deformation have demonstrated experimentally that the weak bonding between the fibres and C_{60} by the van der Waals force allows the shear sliding deformation at the interface. The weak interaction between the

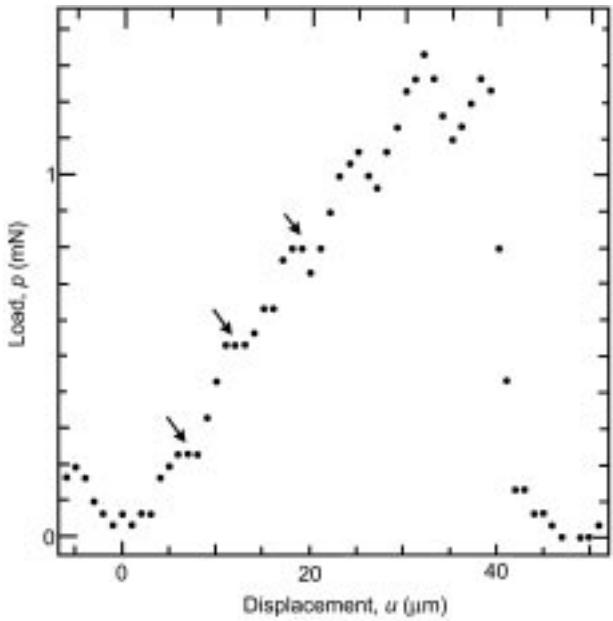

14.12 An example of the load-displacement (L-D) curve of a C_{60}/carbon fibre composite during the pull-out test.

fibres and C_{60} can be comprehended qualitatively from the following structural analyses of the interface.

The geometrical configuration of C_{60} molecules in the graphitic basal plane is shown in Fig. 14.13. The epitaxial orientation relationship between the CNT and C_{60} crystal is ineffective in reducing the interface energy even if the composite has a planar interface because the lattice constant of C_{60} crystals (1.147 nm, the nearest neighbour intermolecular distance is 1 nm) is significantly different from that of the graphitic basal planes (the *a*-axis lattice constant is 0.236 nm). Moreover, the bonding of the graphitic basal plane with C_{60} is weaker than that with the metallic substrate. Further, the graphitic basal plane has no specific trap sites for the C_{60} molecules because graphite, unlike the silicon substrate, lacks dangling bonds. This explains why the long-range epitaxial relationship is difficult to achieve in the C_{60}/graphite interface.

If the rotations of the C_{60} molecules occurring in the fcc lattice can be prevented by the π-electronic interaction at the interface with the graphite substrate, there exists a possibility that the epitaxial relationship may hold locally because of the correspondence of the hexagonal carbon ring in C_{60} with that in graphite. However, the epitaxial relationship between C_{60}/CNT is likely to be ineffective in reducing the interface energy because the curved plane (side wall) of the CNT with a small curvature radius restricts the area of the epitaxial relationship to the range of 2–3 unit cells in the C_{60} crystals.

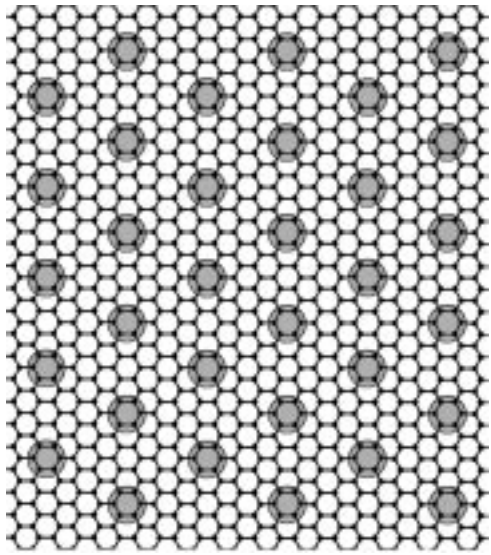

14.13 Comparison of the lattice spacing at the interface between C_{60} and CNT. The shaded circles represent the configuration of the C_{60} (111) plane in the CNT.

The scanning tunnelling microscope observation of the C_{60} molecules that are vapour deposited on highly oriented pyrolytic graphite (HOPG) revealed that the bonding at the C_{60}/graphite interface is not strong and the C_{60} molecules can easily migrate to the HOPG. Therefore, interfacial debonding and sliding deformation can easily occur in the C_{60}/graphite interface. The experiments have thus indicated that the ductility of the C_{60}/CNT composite does not originate from the matrix deformation but from the interfacial sliding between the C_{60} matrix and CNT. Further discussions with energy calculations are required in order to perform a quantitative analysis of the C_{60}/CNT interface.

Moreover, if C_{60} molecules rotate on the graphite surface, they will behave as molecular bearings at the interface, which is interesting from a tribological viewpoint.

14.2.5 Summary

A novel C/C composite with excellent ductility was prepared using CNTs as the fibre and nanocrystalline C_{60} as the matrix. The CNTs were not damaged during the drawing process and were aligned in the longitudinal direction of the wire. The composite wire that is desheathed by the evaporation of silver has a fracture stress approximately 20 times that of polycrystalline C_{60} and a high fracture strain greater than 10%.

The pull-out test of the C_{60}/carbon fibre specimen is performed to analyse the effect of the interaction at the interface on the mechanical properties of the C_{60}/

CNT composite. The sliding deformation readily occurs at the C_{60}/graphite crystal interface with slight deformation of the matrix. Structural analyses of the C_{60}/CNT composites based on high-resolution TEM observations indicate that the epitaxial relationship of the interface is ineffective in stabilising the interface. It is concluded that the ductility of the C_{60}/CNT composite is caused by the sliding at the interface between the CNT and C_{60}, which is due to the weak bonding between the graphitic basal plane and C_{60}. Interfacial sliding is observed between single crystals of C_{60} and carbon fibres without either deformation of the C_{60} matrix or the fracture of fibre. It is inferred that shear sliding, which is caused by the weak bonding between C_{60} and the graphitic basal plane, is responsible for the pull-out of the carbon fibre from the C_{60} matrix. The experiments also indicate that the ductility of the C_{60}/CNT composite probably originates from the sliding at the interface between the C_{60} matrix and CNT.

14.3 Fabrication of the composite by ultra high-pressure sintering

14.3.1 Introduction

The C_{60} crystal is known to be polymerised by heating under a high pressure. The structural change effects a change in the chemical or mechanical characteristics. To date, the structural characterisation of the high-pressure sintered C_{60} has been performed by XRD, Fourier transformed infrared spectroscopy and Raman scattering spectroscopy.[14–19] Four polymerised structures, namely, fcc, rhombohedral, tetragonal and orthorhombic structures have been proposed on the basis of the experimental results and theoretical calculations. However, very few studies have been conducted on the microstructural analyses using TEM.[23] Further, the behaviour of the CNT under high compression stress is noteworthy. In this section, the C_{60}/CNT composite is fabricated by heating in a high pressure, and the nanostructures of the C_{60} matrix and the CNT are subsequently characterised by high-resolution TEM observations and EELS measurements.[24]

14.3.2 Preparation of the composite

The CNTs and C_{60} were synthesised by the carbon DC arc discharge method.[8,9] The CNTs were purified from the fibrous masses by using a combination of an ultrasonic processor and centrifugation in a disperse medium. C_{60} powders of 99.95% purity were mixed with 20 mass% CNTs in an agate mortar. Approximately 130 mg of this mixed powder was encapsulated in a gold case. The specimen was precompacted into a cylindrical shape and was compressed in a belt-type compaction apparatus for 1 h at 1073 K and 5.5 GPa. Figure 14.14 shows a schematic diagram of the cross-sectional view of the high-pressure

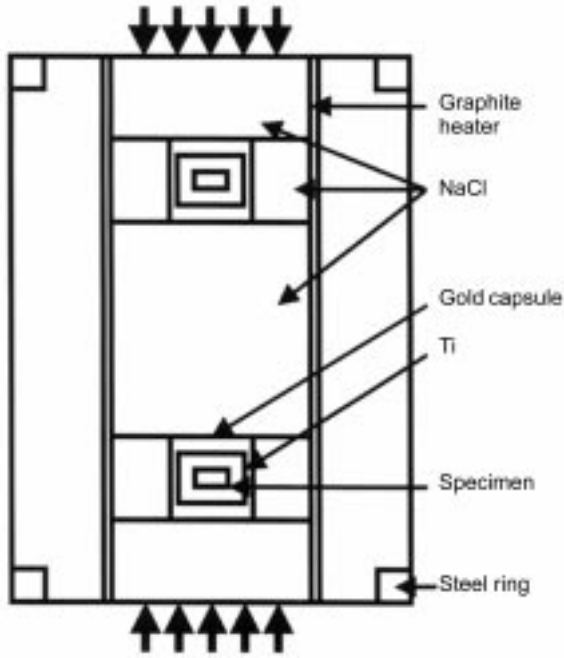

14.14 Schematic diagram of the cross-sectional view of a high-pressure anvil.

anvil. The rates of applying stress and heating were 0.18 GPa/min and 35.8 K/min, respectively. The specimens were furnace cooled to room temperature and then the pressure was released. The obtained specimen is pellet shaped with a thickness of 1 mm.

14.3.3 Nanostructural characterisation

XRD was performed on the compaction surface, cross section and crushed powder of the specimen. The XRD profiles shown in Fig. 14.15(b) reveal the (200) reflection that does not appear in the pristine C_{60} phase. The relatively strong intensity of the (220) reflection may be due to the <110> preferred orientation along the compact direction, probably caused by the (111) $<1\bar{1}0>$ slip system that allows considerable deformation of the C_{60} crystals.[13] The XRD chart in Fig. 14.15(b) indicates that the matrix phase can be indexed as the fcc structure with a lattice constant $a \fallingdotseq 1.31$ nm. The lattice constant decreases by approximately 8% relative to that of the pristine C_{60} ($a = 1.42$ nm) and is approximately equal to the minimum value ($a \fallingdotseq 1.32$ nm) reported by Takahashi *et al.*[23] In this specimen, an endothermic peak at approximately 563 K has been confirmed by differential thermal analysis. These results suggest that the h-C_{60} phase, a C_{60} phase that is subjected to high pressure, can be regarded as a polymerised C_{60} phase.[14,24]

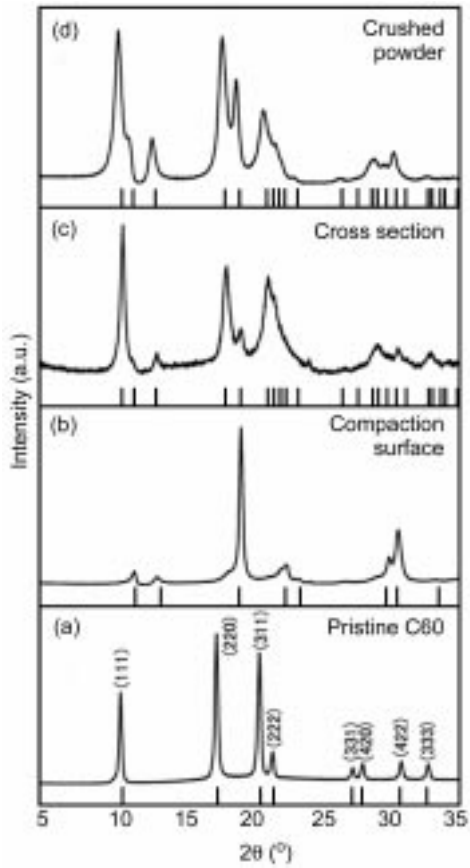

14.15 X-ray diffraction chart obtained using monochromated Cu kα for (a) pristine C_{60}, (b) compaction surface, (c) cross section and (d) crushed powder.

It is assumed that a more densely-packed structure may be stabilised under high pressure such that the three-dimensional polymerisation of C_{60} may proceed with the fcc symmetry. However, the XRD charts shown in Fig. 14.15(b)–(d) suggest that the polymerised structure does not consist of the simple fcc phase. Figure 14.16 shows a TEM image of the matrix and the electron diffraction pattern. The TEM observation was performed at an accelerating voltage of 120 keV. Although the observed structure closely resembles the fcc structure, the angle between the (111) planes (= 69º) slightly deviates from that of the cubic structure angle (angle between (111) and $(1\bar{1}1)$ = 70.5º). The observed angle is closer to the angle of either the tetragonal distortion ($a \fallingdotseq 1.25$ nm, $c \fallingdotseq 1.32$ nm, angle between (111) and $(11\bar{1})$ = 69.1º) or the rhombohedral distortion ($a \fallingdotseq 0.98$ nm, $\alpha = 56.3$, angle between (020) and $(00\bar{2})$ = 69.1º). Hence, the obtained polymerised structure cannot be confirmed from the TEM image alone. As a result of the chart fitting, the distorted structure can possibly be approximated by the rhombohedral

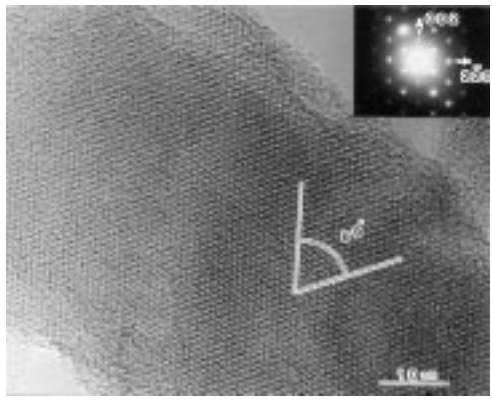

14.16 High-resolution TEM image of a polymerised C_{60} crystal and the electron diffraction pattern.

structure, as shown in Fig. 14.15(c) and (d). The inhomogeneity of the polymerised structure may be ascribed to the mechanical characteristics of the C_{60} crystal, the stress distributions or the anisotropy of the pressure during the high pressure treatment.

On the other hand, a typical example of the fcc structure is shown in Fig. 14.17. In several cases, the fcc phase is accompanied by stacking faults. The polymerisation of C_{60} with maintaining fcc symmetry is severely restricted by the symmetry of C_{60} molecule,[23] so that the minor deviations of the intermolecular bonding may not be allowed to form the long-range ordering of the fcc C_{60} polymerisation. It is expected that the minor deviations resulting from the loss of the fcc symmetry during the polymerisation of C_{60} molecules or

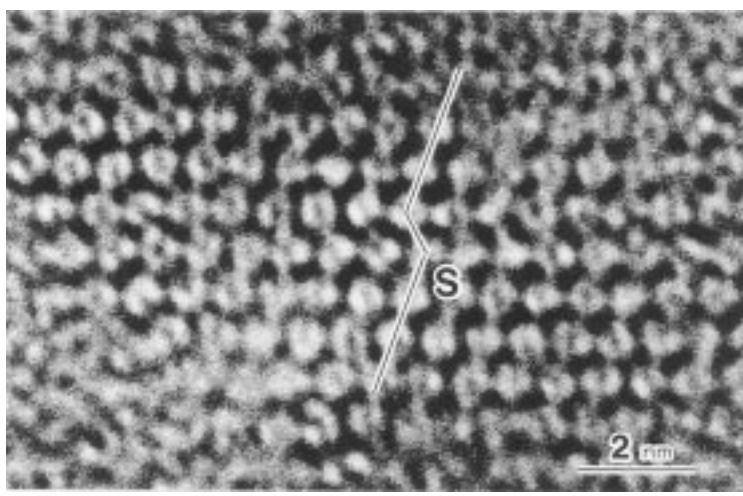

14.17 High-resolution TEM image of a polymerised C_{60} with stacking fault.

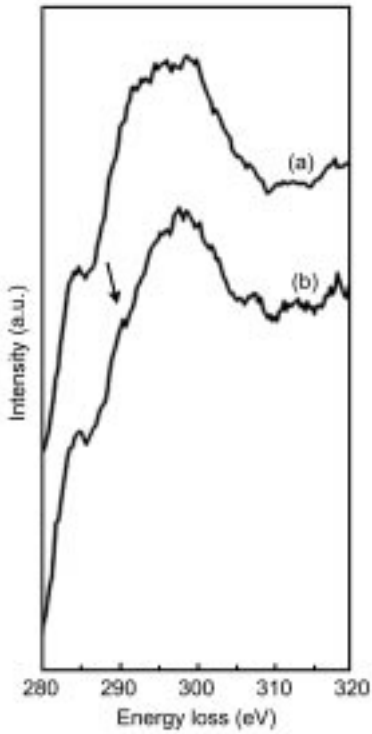

14.18 EELS spectrum of (a) high-pressure treated C_{60} and (b) pristine C_{60} specimens.

the lattice distortion caused by anisotropic high compression may be relaxed by introducing the stacking fault.

Figure 14.18 shows the result of the EELS measurements. The EELS spectrum was obtained by a TEM equipped with a Gatan PEELS spectrometer with an energy resolution of 1.5–1.8 eV. The h-C_{60} phase can be distinguished from the pristine C_{60} by EELS. The EELS spectrum of pristine C_{60} shows a peculiar peak near 290 eV (the arrowed peak in Fig. 14.18(b)). In contrast, such a peak is scarcely obtained in the h-C_{60} specimen within the experimental resolution, as shown in Fig. 14.18(a). An EELS spectrum simulation estimated by the multiscattering method (FEFF 7[25]) suggests that the difference in the spectra near 290 eV is possibly caused by the difference in the intermolecular distance in C_{60}.

The cylindrical structure of the CNT is also affected by the high-pressure compaction. Figure 14.19 is an example of a partially collapsed CNT. A contrast corresponding to the bend contour of the compressed part is observed. As shown in Fig. 14.20, the innermost layer shows the π-bonding interaction due to the interaction between p electrons. The interlayer spacing of the bonded layer is

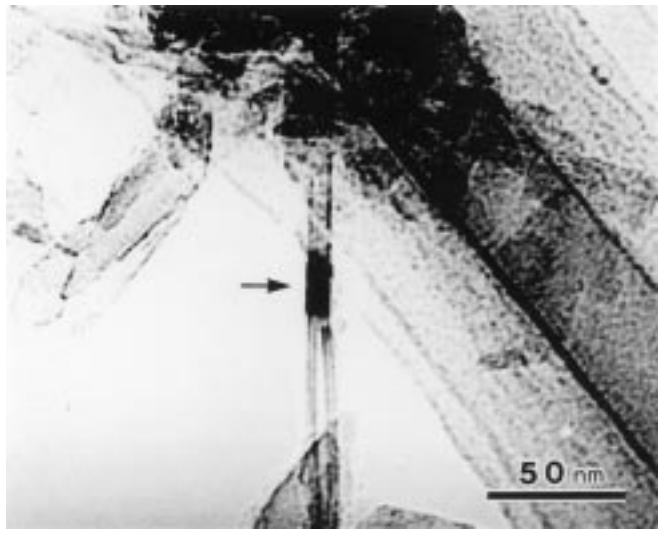

14.19 TEM image of a partially collapsed CNT.

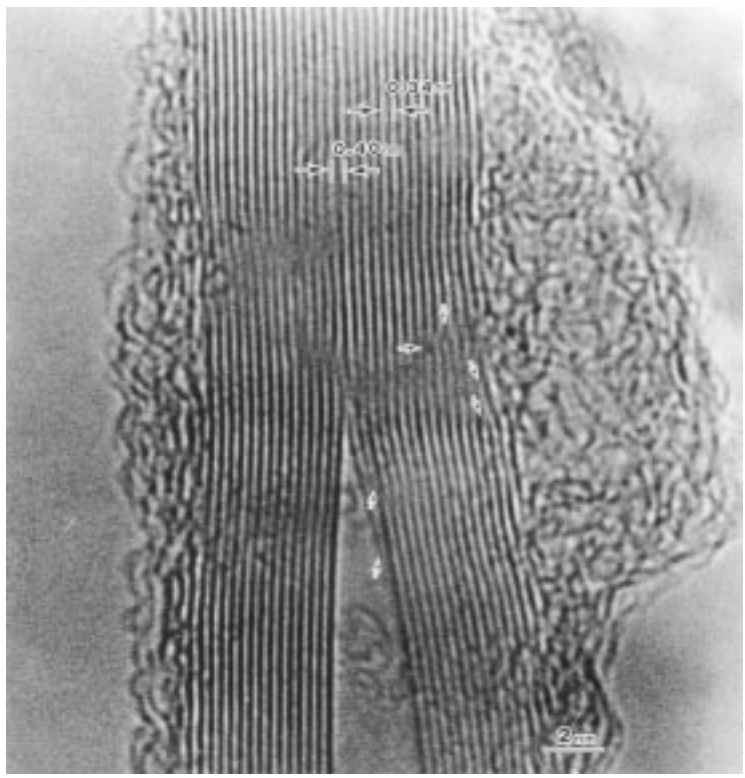

14.20 High-resolution TEM image of the collapsed CNT. The arrows indicate structural damage in the carbon layers.

larger (≒ 0.44 nm) than that of the other interlayers (≒ 0.34 nm). The high-pressure compaction causes certain structural defects in the CNT such as the fracture of the graphitic layer and mismatches of the tube walls (see arrowed sections in Fig. 14.20). The existence of these defects in the CNT suggests that the dissociation of the C–C covalent bonding and the reconstruction of the graphitic layer possibly occur under the high-pressure sintering.

The geometric configuration of the polymerised C_{60} on the CNT may be predicted from the interfacial structure of C_{60}/CNT.[20, 22] Further investigations are required on the details of the intermolecular bonding of the polymerised C_{60} and the interfacial polymerisation between C_{60} and CNT.

14.3.4 Summary

The high-pressure sintering transformed the C_{60} matrix into a polymerised phase with the fcc structure or a distorted phase. The polymerised C_{60} matrix phase can be distinguished from the pristine C_{60} by EELS. The cylindrical structure of the CNT was also affected by the high compression stress. A partially collapsed CNT with structural defects was observed in this experiment. The nanoscale porous structure of the polymerised C_{60} matrix may be advantageous for use as materials in negative electrodes of secondary lithium ion batteries or hydrogen occlusion. However, the charge–discharge characteristic of lithium ion or the hydrogen occlusion characteristic is insufficient for practical use. Further investigations are required for the elucidation of these mechanisms.

14.4 Application potential

14.4.1 Introduction

CNTs possess not only excellent mechanical characteristics but also electrical characteristics that are important in engineering applications. After the mechanism of field electron emission from CNTs was elucidated, one of the most expected applications of the CNT is as an electron source for novel thin flat-panel displays.[26–31] However, fundamental investigations related to the emission mechanism of the CNTs are insufficient to estimate their potential as an electron source, although the practical application of CNTs in field emission displays is expected. As regards the electronic states of the various tip structures that were applied to field emission microscopy and scanning tunnelling microscopy,[32–36] few investigations are available for reference. A direct observation using TEM will provide more reliable information on the electron emission mechanism of CNTs. The C_{60}/CNT composite that has the oriented structure of CNTs is not only an ideal material as an electron source but also an ideal specimen for the evaluation of the field emission characteristics of individual CNTs by TEM observations. In this section, the field emission characteristics of CNTs[37] and a

tip structure during field emission[38] were investigated in order to evaluate the potential of CNTs as an electron source.

14.4.2 Field emission characteristics of CNTs

In order to measure the field emission characteristics, the C_{60}/CNT composite, which was produced by the drawing process, was mounted on a copper grid using an adhesive and a silver paste and was used as an electron emission source (Fig. 14.21). Six readings of the emission current (I) in a sample for the applied voltage (V) were measured in a high vacuum chamber with a base pressure of approximately 6.5×10^{-6} Pa. The distance between the electrodes was fixed at 200 μm using a mica spacer.

The I–V characteristics of the CNTs are shown in Fig. 14.22(a). For the first run, the threshold voltage was high and the current increased quickly. However, after the second run, the emission began at a rather lower voltage and increased gradually. The Fowler-Nordhiem (F-N) plots (inset in Fig. 14.22(a)) show that the first run cannot be expressed as a straight line and is separated into different stages. This characteristic emission suggests that the electron emission is affected by surface conditions such as gas adsorption or structural changes in the CNT tips. On the other hand, another emission experiment conducted after exposing the sample to the atmosphere shows identical behaviour in terms of the electron emission. A decrease in the threshold voltage after the second run suggests the structural change of the CNT tip.

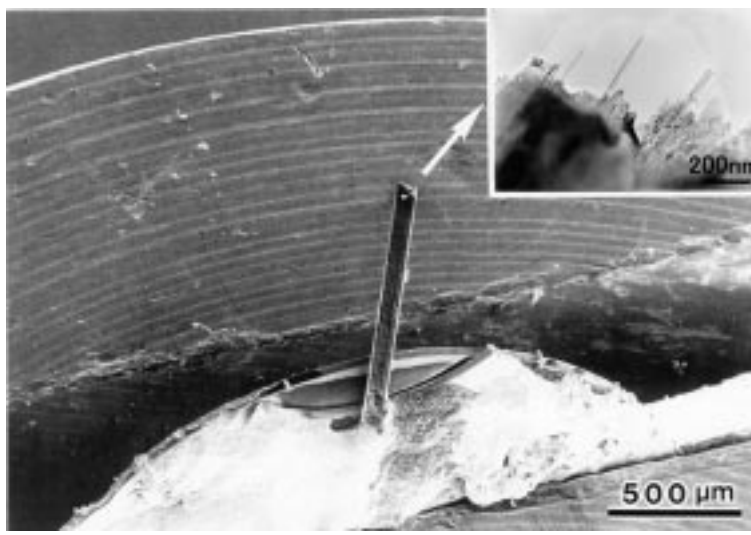

14.21 SEM image of the sample. The inset shows the surface morphology at the tip of the rod. The CNTs were aligned along the longitudinal direction of the rod within an angular deviation of 30°.

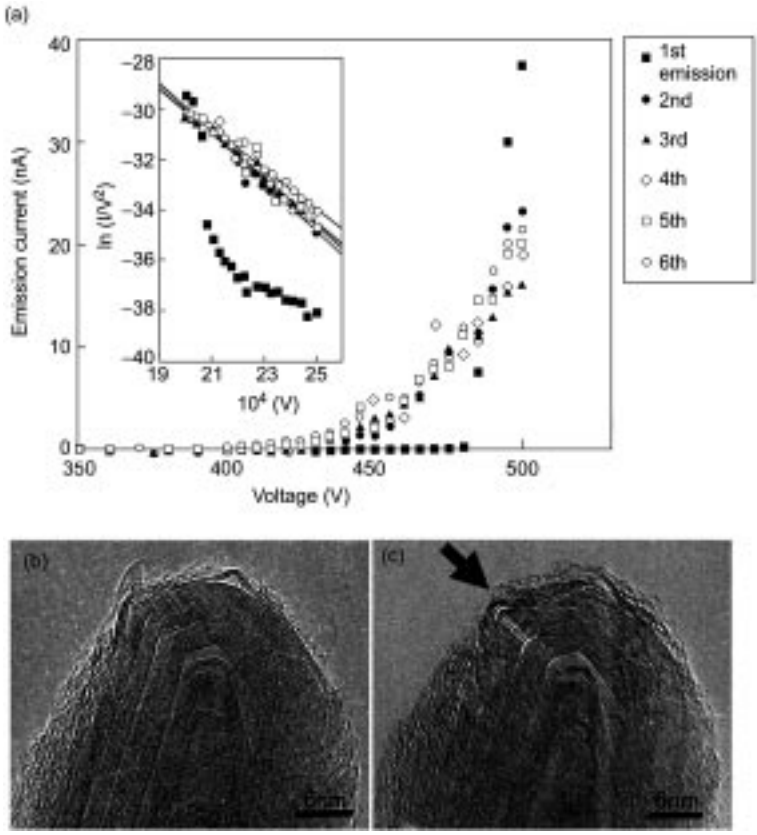

14.22 I-V characteristics of the CNT: (a) High-resolution TEM images of the CNT tip, (b) before field emission and (c) after field emission. A protrusion appears in the direction of the electric field, as indicated by the arrow in (c).

It is possible to number the individual CNTs during the TEM observations to identify the same CNT tip before and after the field emission. A typical tip structure of the closed CNT is shown before and after field emission in Fig. 14.22(b) and (c), respectively. The field emission causes a structural change of the CNT tip. The high-resolution TEM image revealed that the deformation of the CNT occurred at the local domain containing an isolated pentagonal carbon ring in the polyhedral cap and a protrusion was formed along the normal to the electric field, as indicated by the arrow in Fig. 14.22(c).

14.4.3 Dynamic TEM observation of the CNT tip during field emission

Dynamic observation of the CNT tip in an applied electric field was carried out by using a TEM equipped with a dual specimen holder system, as shown in Fig.

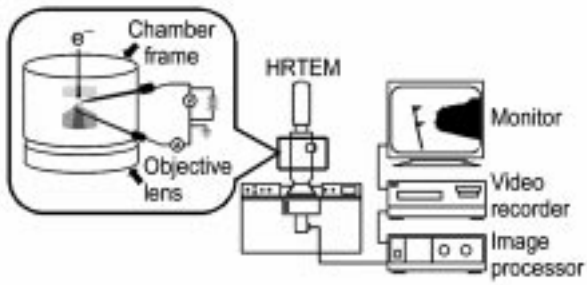

14.23 Schematic illustration of the in-situ TEM observation system.

14.23.[39,40] The tip of each specimen holder can be moved by the piezo driving device. The rod specimen with aligned CNTs was mounted on the tip of a specimen holder as a cathode. A gold-coated silicon cantilever for atomic force microscopy was fixed on the other tip as an anode. Both holders were inserted into the specimen chamber maintained at a pressure of 10^{-5} Pa. The TEM was operated with an accelerating voltage of 200 keV.

Figure 14.24 shows a series of the TEM images of the CNT tip in the applied electric field. The thick arrow in Fig. 14.24(a) indicates the anode direction. The distance between the tips is 30 nm and the applied bias is 200 V. During the observation, the emission current fluctuated widely by approximately 8–12 μA. The background current was 0.23–1.48 nA. At the applied bias (Fig. 14.24(b)–(f)), bending of the outer layers of the CNT tip was observed. This resulted in the formation of a nanoscale protrusion towards the anode direction, as shown in Fig. 14.24(f). Figure 14.24(b)–(f) also shows that the interlayer spacing of the CNT is wider than that of the original. The total observation time is approximately 270 s and structural damage is rarely observed in the CNT. In order to verify the deformation mechanism, the surface structure of the CNT tip should be observed on an atomic scale. The atomic configuration of the outermost surface can be observed by field ion microscopy (FIM).

For the FIM experiments, one of the composite specimens was fixed on a hairpin shaped tungsten filament (diameter 0.3 mm) with carbon binder, and it was introduced into an ultra high vacuum (UHV) chamber of 3×10^{-8} Pa. The detector composed of microchannel plates and a screen for the FIM was placed at a distance of 50 mm from an electron emitter. In order to clean the surface of the CNT tips, the composite specimen was heated to 1000 K in the UHV chamber. The experiments were carried out at the specimen temperature of 30 K.

The FIM experiments demonstrated that the reconstruction process of the honeycomb structure of the CNT tip began in an applied electric field.[38] The reconstruction process is very complicated. For example, during the reconstruction of the carbon atoms, three pentagonal carbon rings occur adjacent to each other.[38] The arrangement of the pentagonal carbon rings is inconsistent with the isolated pentagon rule which was empirically determined. The FIM

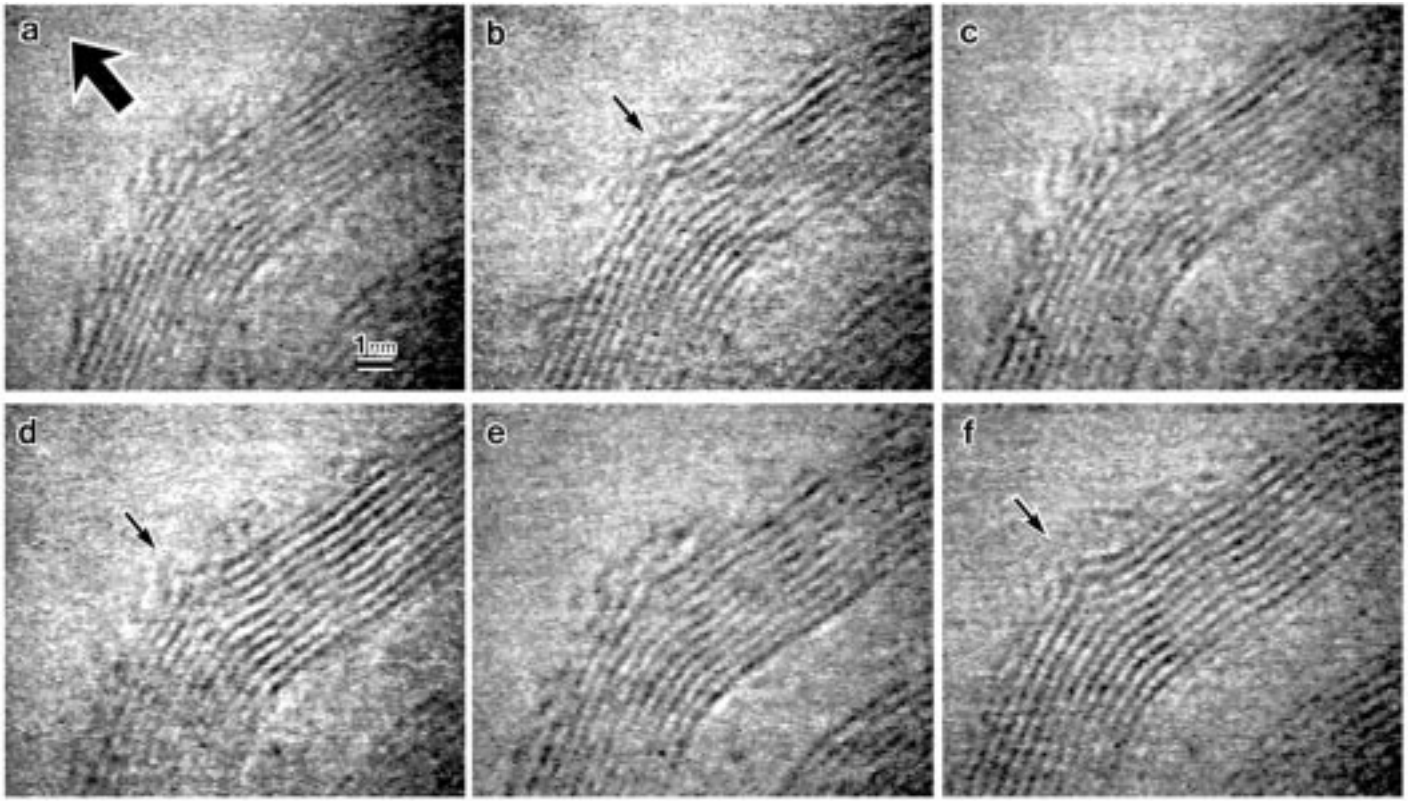

14.24 Series of high-resolution TEM images of a CNT tip at an applied bias of 200 V in the 30 nm gap. The thick arrow in (a) indicates the anode direction.

experiments indicate that the deformation process proceeds not only with the Stone-Wales transition[8,9,41] of the carbon atoms but also with the bonding state change mechanism (bonding state atoms similar to sp^2 to sp^3).[8,9,42] The formation mechanism of the nanoscale protrusion observed by the in-situ TEM can be explained on the basis of the reconstruction process. The deformation of the CNT tip might be due to the electrical attraction caused by the application of the bias voltage between the electrodes.

Observations of the carbon network by FIM enable us to identify the electron emission sites on the CNT tip. Figure 14.25(a) shows the FIM image of the CNT tip. This image shows some fragments of the honeycomb structure composed of hexagonal and pentagonal structures (Fig. 14.25(a) and (b)). In this case, it is possible to identify the emission site of the electrons by comparing the FIM image with the corresponding FEM image. Figure 14.25(b) shows the peculiar electron emission image of the cleaned CNT by FEM. This image can be classified into three patterns. The first pattern is a coalescence of six bright rings with five-fold symmetry (A′). The second pattern is of four bright rings with straight lines in the boundary regions between neighbouring rings (B′). The third pattern considers the other bright spots that correspond to either the edge species or adsorbates deposited on the CNT tip. These emission patterns (A′) and (B′) in Fig. 14.25(b) reflect the surface structure of the CNT observed by FIM. The FEM pattern (A′) in Fig. 14.25(b), which reflects the honeycomb structures, indicated a part of the CNT tip structure obtained by introducing a pentagonal carbon ring, as seen in the FIM pattern (A) in Fig. 14.25(a). This result indicates that the emission probability of electrons from a pentagonal carbon ring is low. The FEM pattern (B′) in Fig. 14.25(b) may be due to the interference of the coherent electron beams, which are emitted from the isolated bright areas that represent the protruding sites on the surface of the CNT tip. It has been predicted that the pentagonal carbon ring is an emission site of electrons. However, the electrons were emitted from the nanoscale protrusion formed by introducing a

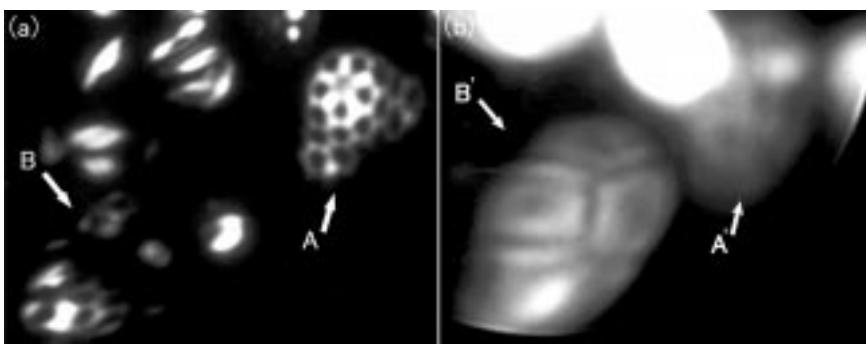

14.25 FIM image (a) and the corresponding FEM image (b) of the CNT tip. The tip voltages of FIM and FEM are 6.3 kV and −1.6 kV, respectively. The emission current detected in FEM is 6×10^{-7} A.

pentagonal carbon ring in the hexagonal carbon network, rather than from the ring itself. Pentagonal carbon rings play an important role in the formation of emission sites because they form nanoscale protrusions in the carbon network. The FEM image with interference fringes is not the image that originated from pentagonal carbon rings, but an interference image caused by coherent electron emissions from different sites in the CNT tip.

14.4.4 Influence exerted by an electric field on the CNT tip

The high electric field applied on the CNT tip influences the tip structure in different ways. Figure 14.26 shows a time sequence series of TEM images for the surface of a CNT tip during field emission. A single carbon strand gradually emerges from the carbon cluster that was deposited on the CNT tip. The carbon strand grows along the normal to the electric field, as indicated by the arrows in Fig. 14.26(b) and (c). The detected emission current was approximately 16 μA. The current density obtained from the specimen was approximately 200 mA/cm^2. In Fig. 14.26(c), there are three dark spot contrasts in the strand. The sequential dark spots became dimmer from the bottom towards the tip. The spots in the strand are located at a regular spacing of approximately 0.24 nm. These spots reflect the

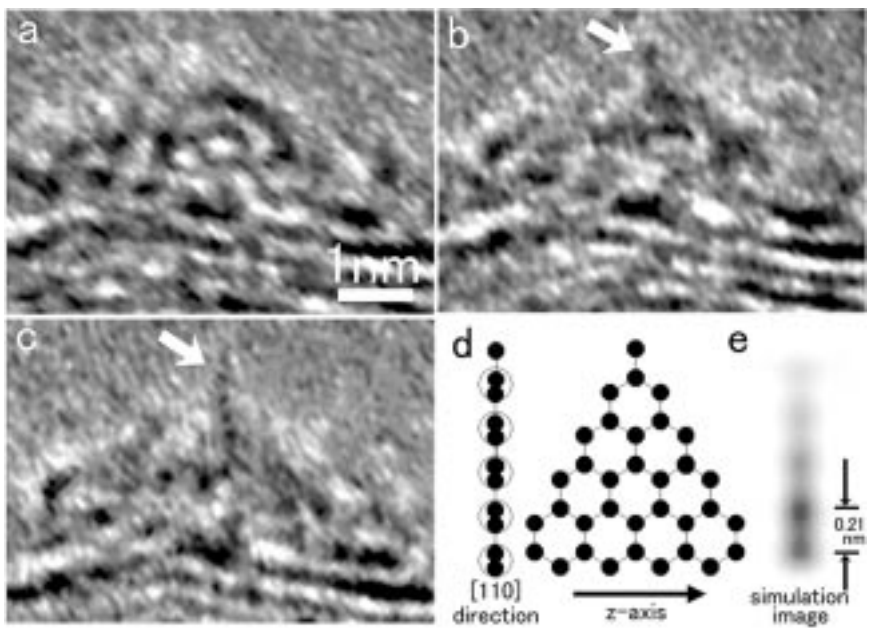

14.26 Series of high-resolution TEM images of the surface of a CNT tip at an applied bias of 200 V. The distance between the electrodes is 30 nm. These images were processed to highlight the carbon strand. The proposed structural model of the carbon strand and the multislice simulation image estimated from the model are shown in (d) and (e), respectively.

atomic configuration. However, the spacing between the spots is not in agreement with that of the atomic configuration of graphite. Simulations performed by the multislice method[43] are used for the structural analysis. The proposed structural model of the carbon strand and the multislice simulation image estimated from the model are shown in Fig. 14.26(d) and (e), respectively. The simulation image shown in Fig. 14.26(e) is similar to the observed one. The spot contrasts observed in the strand can be represented by the overlapped images of the nearest neighbouring atoms of a grapheme sheet observed from the armchair plane ([110] direction) rather than from a single atomic configuration. The decrease in the contrast of the individual spots is explained on the basis of a triangular structure with a varying number of carbon atoms stacked along the depth direction (z-axis), as shown in Fig. 14.26(d). By assuming that the proposed model is correct, the distance between the observed spot contrasts is increased by approximately 14% along the normal to the electric field. The atomic structure at the very tip of the carbon monolayer was barely visible due to its vibration. The formation of this carbon monolayer implies that the unravelling process of the CNTs, reported by Rinzler *et al.*,[26] will occur when the applied electric field is high. The lifetime of the carbon strand is extremely short. During the observation, it vibrated and then broke in a few minutes. The formation of the emission site by structural change has contributed to the excellent field emission characteristics of the CNT. However, the structural change observed in this experiment can be regarded as damage to the CNT that is caused by the interaction with the high electric field. Therefore, a detailed investigation is required for evaluating the lifetime as an electron source when a high electric field is applied in a narrow gap.

14.4.5 Summary

The in-situ TEM observations of the CNT tip in an applied electric field demonstrated that the field electron emission from the CNT is accompanied by a local structural change of the tip. The deformation mechanism can be explained not only by the Stone-Wales transition mechanism but also by the bonding state change mechanism. It has been predicted that the pentagonal carbon ring is an emission site of electrons. However, the electrons were emitted from the nanoscale protrusion formed by introducing a pentagonal carbon ring in the hexagonal carbon network, rather than from the pentagonal carbon ring itself. The pentagonal carbon rings play an important role in the formation of the emission sites because they form nanoscale protrusions in the carbon network. The FEM image with interference fringes is not the image that originated from pentagonal carbon rings, but an interference image caused by coherent electron emissions from different sites in the CNT tip. The composite specimen that has oriented structures of the CNTs shows excellent field emission characteristics. However, in order to use CNTs as electron emitters in field emission displays, further investigations on their lifetime are required.

14.5 Conclusions

Two types of composites were produced using novel carbons. C_{60} and CNT are expected to be among the most important materials in this century. Although there are several problems that should be solved in the future, the composite preparations described in this chapter may be one of the methods for using these novel carbons as engineering materials. Recently, the development of a CNT reinforced resin matrix composite has been advanced in the field of engineering. In order to use CNTs as fibre materials, it is important to evaluate the mechanical characteristics of individual CNTs. The development of the nanoscale evaluation technique in TEM is indispensable to the assembly of nanocomposite materials.

14.6 References

1. Iijima S, 'Helical microtubules of graphitic carbon', *Nature*, 1991 **354** 56–58.
2. Saito S and Oshiyama A, 'Cohesive mechanism and energy bands of solid C_{60}', *Phys Rev Lett*, 1991 **66**(20) 2637–2640.
3. Saito R, Fujita M, Dresselhaus G and Dresselhaus M S, 'Electronic structure of graphene tubules based on C_{60}', *Phys Rev B*, 1992 **46**(3/15) 1804–1811.
4. Overney G, Zhong W and Tomanek D, 'Structural rigidity and low frequency vibrational modes of long carbon tubules', *Z Phys D*, 1993 **27** 93–96.
5. Ajayan P M, Stephan O, Colliex C and Trauth D, 'Aligned carbon nanotube arrays formed by cutting a polymer resin nanotube composite', *Science*, 1994 **265** 1212–1214.
6. Treacy M M, Ebbesen T W and Gibson J M, 'Exceptionally high Young's modulus observed for individual carbon nanotubes', *Nature*, 1996 **381** 678–680.
7. Wong E W, Sheehan P E and Lieber C M, 'Nanobeam mechanics: elasticity, strength, and toughness of nanorods and nanotubes', *Science*, 1997 **277** 1971–1975.
8. Kuzumaki T, Hayashi T, Ichinose H, Miyazawa K, Ito K and Ishida Y, 'Fine structure of plastically deformed carbon nanotube', *J Jpn Inst Met*, 1996 **60**(1) 9–15.
9. Kuzumaki T, Hayashi T, Ichinose H, Miyazawa K, Ito K and Ishida Y, 'In situ observed deformation of carbon nanotubes', *Philos Mag A*, 1998 **77**(6) 1461–1469.
10. Kuzumaki T, Miyazawa K, Ichinose H and Ito K, 'Processing of carbon nanotube reinforced aluminum composite', *J Mater Res*, 1998 **13**(9) 2445–2449.
11. Kuzumaki T, Ujiie O, Ichinose H and Ito K, 'Mechanical characteristics and preparation of carbon nanotube fibre reinforced Ti composite', *Adv Eng Mater*, 2000 **2**(7) 416–418.
12. Katoh T, Suenaga K, Takayama Y, Ito K and Ishida Y, 'Plasticity and work hardenability of solid C_{60}', *J Jpn Inst Met*, 1993 **57**(9) 1101–1102.
13. Suenaga K, Tanaka M, Katoh T, Takayama Y, Ito K and Ishida Y, 'Mechanical properties of nanocrystalline C_{60}', *J Jpn Inst Met*, 1993 **57**(9) 1103–1104.
14. Regueiro M N, 'C_{60} under pressure', *Mod Phys Lett B*, 1992 **6**(19) 1153–1158.
15. Iwasa Y, Arima T, Fleming R M, Siegrist T, Zhou O, Haddon R C, Rothberg L J, Lyons K B, Carter Jr H L, Hebard A F, Tyeko R, Dabbagh G, Krajewski J J, Thomas G A and Yagi T, 'New phases of C_{60} synthesised at high pressure', *Science*, 1994 **264** 1570–1572.

16. Baskin I O, Rashchupkin V I, Gurov A F, Morevsky A P, Rybchenko O G, Kobelev N P, Soifer Y M and Ponyatovsky E G, 'A new phase transition in the T-P diagram of C_{60} fullerite', *J Phys Condens Matter*, 1994 **6** 7491–7498.
17. Kozlov M E and Yakushi K, 'Optical properties of high pressure phases of C_{60} fullerene', *J Phys Condens Matter*, 1995 **7** L209–L216.
18. Regueiro M N, Marques L, Hodeau J L, Bethoux O and Perroux M, 'Polymerised fullerite structures', *Phys Rev Lett*, 1995 **74**(2/9) 278–281.
19. Rao A M, Eklund P C, Hodeau J L, Marques L and Regueiro M N, 'Infrared and Raman studies of pressure-polymerised C_{60}s', *Phys Rev B*, 1997 **55**(7/15) 4766–4773.
20. Kuzumaki T, Hayashi T, Ichinose H, Miyazawa K, Ito K and Ishida Y, 'Structure and deformation behaviour of carbon nanotubes reinforced nanocrystalline C_{60} composite', *J Jpn Inst Met*, 1997 **61**(4) 319–325.
21. Kuzumaki T, Hayashi T, Ichinose H, Miyazawa K, Ito K and Ishida Y, 'Processing of ductile carbon nanotube/C_{60} composite', *Mater Trans JIM*, 1998 **39**(5) 574–577.
22. Kuzumaki T, Hayashi T, Ichinose H, Miyazawa K, Ito K and Ishida Y, 'Discussion on the mechanical behaviour of carbon nanotube/C_{60} composite based on observation of interfacial structure', *Mater Trans JIM*, 1998 **39**(5) 578–581.
23. Takahashi Y, Takada Y, Kotake S, Matsumuro A and Senoo M, 'Phototransformed C_{60} powder and film synthesised in toluene, benzene and carbon disulfide solvents', *J Ceram Soc Japan*, 1997 **105**(6) 544–547.
24. Kuzumaki T, Satsuki H, Hayashi T, Miyazawa K, Ichinose H and Ito K, 'Microstructure of C_{60}/Carbon nanotube composite sintered by ultra high pressure', *Tanso*, 1999 **190** 267–272.
25. Zabinsky S I, Rehr J J, Ankudinov A, Albers R C and Eller M J, 'Multiple-scattering calculations of x-ray absorption spectra', *Phys Rev B*, 1995 **52**(4/15) 2995–3009.
26. Rinzler A G, Hafner H H, Nikolaev P, Lou L, Kim S G, Tomanek D, Nordlander P, Colbert D T and Smalley R E, 'Unravelling nanotubes: field emission from an atomic wire', *Science*, 1995 **269** 1550–1553.
27. Heer W A De, Chatelain A and Ugate D, 'A carbon nanotube field emission electron source', *Science*, 1995 **270** 1179–1180.
28. Saito Y, Hamaguchi K, Hata K, Uchida K, Tasaka Y, Ikazaki F, Yumura M, Kasuya A and Nishina Y, 'Conical beams from open nanotubes', *Nature*, 1997 **389** 554–555.
29. Carroll D L, Redlich P, Ajayan P M, Charlier J C, Blase X, Vita A De and Car R, 'Electronic structure and localised states at carbon nanotube tips', *Phys Rev Lett*, 1997 **78**(14/7) 2811–2814.
30. Dean K A and Chalamala B R, 'Field emission microscopy of carbon nanotube caps', *J Appl Phys*, 1999 **85**(7) 3832–3836.
31. Bonard J M, Salvetat J P, Stockli T, Forro L and Chatelain A, 'Field emission from carbon nanotubes: perspectives for applications and clue to the emission mechanism', *Appl Phys A*, 1999 **69** 245–254.
32. Vita A De, Charlier J C, Blase X, Car R, 'Electronic structure at carbon nanotube tips', *Appl Phys A*, 1999 **68** 283–286.
33. Rao A M, Jacques D, Haddon R C, Zhu W, Bower C and Jin S, 'In situ grown carbon nanotube array with excellent field emission characteristics', *Appl Phys Lett*, 2000 **76**(25) 3813–3815.
34. Saito Y, Uemura S and Hamaguchi K, 'Cathode ray tube lighting elements with carbon nanotube field emitters', *Jpn J Appl Phys Part2 3B*, 1998 **37** L346–L348.

35. Wang Q H, Setlur A A, Lauerhaas J M, Dai J Y, Seeling E W and Chang R P H, 'A nanotube-based field emission flat panel display', *Appl Phys Lett*, 1998 **72**(22) 2912–2913.
36. Choi W B, Chung D S, Kang J H, Kim H Y, Jin Y W, Han I T, Lee Y H, Jung J E, Lee N S, Park G S and Kim J M, 'Fully sealed, high brightness carbon nanotube field emission display', *Appl Phys Lett*, 1999 **75**(20) 3129–3131.
37. Kuzumaki T, Takamura Y, Ichinose H and Horiike Y, 'Structural change at the carbon nanotube tip by field emission', *Appl Phys Lett*, 2001 **78**(23) 3699–3701.
38. Kuzumaki T, Horiike Y, Kizuka T, Kona T, Ohshima C and Mitsuda Y, 'The dynamic observation of the field emission site of electrons on a carbon nanotube tip', *Dia Rel Mater*, 2004 **13** 1907–1913.
39. Kizuka T, Ohmi H, Sumi T, Kumazawa K, Deguchi S, Naruse M, Fujisawa S, Sasaki S, Yabe A and Enomoto Y, 'Simultaneous observation of millisecond dynamics in atomistic structure, force and conductance on the basis of transmission electron microscopy', *Jpn J Appl Phys Part 2 2B*, 2001 **40** L170–L173.
40. Kuzumaki T, Sawada H, Ichinose H, Horiike Y and Kizuka T, 'Selective processing of individual carbon nanotubes using dual-nanomanipulator installed in transmission electron microscope', *Appl Phys Lett*, 2001 **79**(27) 4580–4582.
41. Stone A J and Wales D J, 'Theoretical studies of icosahedral C_{60} and some related species', *Chem Phys Lett*, 1986 **128**(5/6) 501–503.
42. Hiura H, Ebbesen T W, Fujita J, Tanigaki K and Takada T, 'Role of sp^3 defect structures in graphite and carbon nanotube', *Nature*, 1994 **367** 148–151.
43. Ishizuka K, 'Contrast transfer of crystal images in TEM', *Ultramicroscopy*, 1980 **5** 55–65.0

15

Filled polymer nanocomposites containing functionalized nanoparticles

O OK PARK, J H PARK and T-H KIM, Korea Advanced Institute of Science and Technology and Y T LIM, Korea Research Institute of Bioscience and Biotechnology, Korea

15.1 Introduction

The π-conjugated polymers with semi-conducting properties have recently attracted much attention due to their applicability in the field of optic and opto-electric devices such as light-emitting diodes and lasers. The light-emitting diodes based on conjugated polymers have attracted much attention because of their potential application to flat, large area displays, which can be operated at low driving voltage. However, the potential use of polymer-light-emitting diodes is ultimately limited by their low quantum efficiency as well as by their poor stability due to oxygen. In this chapter, some unique studies to improve the luminescent stability are introduced.

15.2 Organic and polymer materials for light-emitting diodes

Electroluminescence (EL), the generation of light (other than black-body radiation) from condensed matter by electrical excitation, has been investigated in organic molecular solids since the 1950s.[1] In particular, the work of Pope *et al.*[2] and Helfrich and Schneider[3] on single crystals of anthracene in the early 1960s initiated considerable efforts to creat light-emitting devices from organic molecular crystals. In spite of the principal demonstration of an operating organic electroluminescent display that even incorporated an encapsulation scheme similar to those used in present commercial display applications,[4] there were several drawbacks to the practical use of these early devices. Such drawbacks included insufficient current densities and light output, as well as instability. Other major obstacles included the high operating voltage, which was a consequence of the crystal thickness in the micrometer range, difficulties in reproducible crystal growth, and preparing stable and sufficiently well-injecting contacts to them. Nevertheless, these investigations have established the basic

and fundamental processes involved in organic injection-type EL, namely injection, transport, capture, and radiative recombination of oppositely charged carriers inside the organic materials (for a review see references 5 and 6).

Further progress towards applicable organic electroluminescent devices was made in the 1970s by the use of thin organic films prepared by means of vacuum vapor deposition or the Langmuir-Blodgett technique, instead of single crystals.[7–9] The reduction of the organic layer thickness to well below 1 μm allowed the realization of electronic fields comparable to those that were being applied to single crystals, but at a considerably lower voltage. In addition to the morphological instability of these polycrystalline films, fabricating pin-hole-free thin films from these materials was still a problem. These problems were overcome in the early 1980s by the use of morphologically stable amorphous films, as demonstrated by Partridge's work on films of polyvinylcarbazole doped with fluorescent dye molecules.[10]

The development of organic multi-layer structures considerably improved the efficiency of light-emission by achieving a better balance of the number of charge carriers of opposite signs and further lowered the operating voltage by reducing the mismatch of energy levels between the organic materials and the electrodes. The consequence of this development was well demonstrated by the organic light-emitting devices (OLEDs) of Tang and Van Slyke, which showed true potential for lighting and display applications.[11,12] These authors achieved astonishingly high light output, efficiency, and life-time at relatively low operating voltage. This was possible using hetero-layer structures, a few tens of nanometers thick and made of a hole conducting aromatic amine and an electron conducting aluminium chelate complex (Alq_3), sandwiched between indium-tin-oxide (ITO) and Mg:Ag-alloy electrodes. This breakthrough initiated great developments of new molecular materials and device structures, especially in Japan.[13–15] By the end of the 1990s, OLEDs have entered the stage of commercialization[16] and are considered promising candidates for the next generation of large area flat-panel displays.[17,18] Additionally, since the discovery of EL in conjugated polymers by the Cambridge group in the 1990s,[19] these materials have been widely examined and are going to be commercialized with equally as good prospects for display and lighting applications as the low molecular weight materials.[20,21]

Figure 15.1 shows a mechanism of electroluminescence. Organic/polymer EL devices have the structure which has an organic emitting layer between transparent anode like ITO and metal cathode with low work function (Ca, Li, Al:Li, Mg:Ag, etc.). Under the electric field, the electrons injected from the cathode and holes injected from the anode meet each other in the emitting layer. The excitons excited by this recombination energy of e^- and h^+ fall on the electronic ground state through radiative decay, and they generate luminescence, thermal energy, and vibrational energy.

The first polymer used for the fabrication of LEDs was poly(*p*-phenylene vinylene) (PPV). PPV is a conjugated polymer, that is, a polymer having

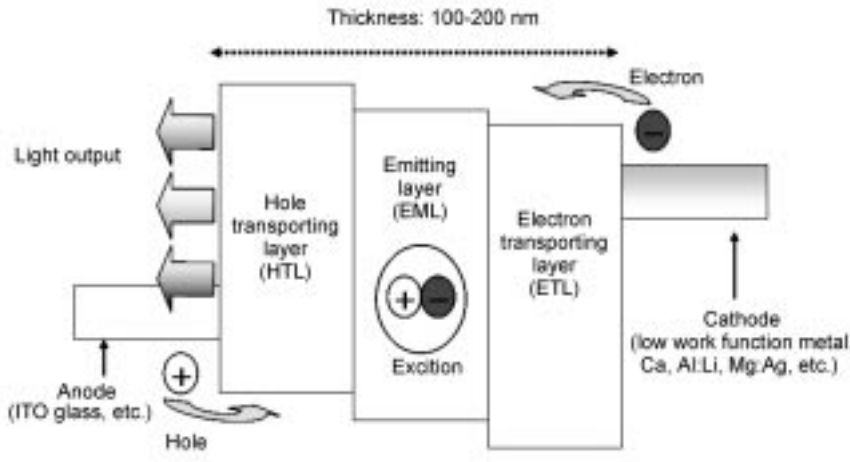

15.1 Mechanism of electroluminescence in organic/polymer EL device.

alternative single (σ) and double (π) bonds along its backbone. The carbon orbitals in these polymers are overlapped, leading to a delocalized π electron, which is able to move along the polymer backbone. The band structure of the conjugated polymer, which originates from the interaction of the π orbitals with the repeating units of the backbone, is similar to that of a classical semiconductor. The highest occupied band is called the valence band, while the lowest unoccupied band is called the conduction band, the difference in energy between these bands is called the band gap. The band gap energy is determined principally by the chemical structure of the material and to a certain extent by the delocalization of the π electrons, which is also called the effective conjugation length. In fact, the conjugation length of polymers depends on conformational randomness or chemical defects in the backbone. As it is not possible to control precisely the defect density, the conjugated length can not be adjusted to a specifically desired value. Instead, the use of conjugated oligomers with defined sequences and determined chain lengths enable precise control over the luminescence (color tuning). Depending on the colors emitted, the conjugated polymers can be arranged into three families: the poly(*p*-phenylene vinylene), the poly(*p*-phenylene), and the substituted poly(3-alkylthiophene), namely green, blue and red.

15.3 Luminescent polymer for device applications

In recent years, a second wave of interest in molecular electronics and organic compound-based devices began.[22–27] Polymer electronics, including the use of polymer nanocomposite-based devices provided a number of alternative approaches, such as the usage of adaptive circuits or neural network-based

processor architectures. Combined with a better understanding of the conductivity mechanism in conjugated polymers such as poly(*p*-phenylenevinylene) and poly(thiophenes), these developments have brought about renewed interest in low molecular weight organic and polymer-based optoelectronic, electronic, and photonic devices. Thus, we have seen the recent creation of various polymer-based devices, such as light emitting diodes,[23] photodiodes,[24,25] solar cells, gas sensors, field effect transistors,[26,27] all of which have been developed and intensively studied in research groups and R&D centers worldwide. Some of these devices are being produced commercially at the pilot scale.

Conducting polymers are novel, one-dimensional semiconductors, which are studied for their attractive electronic and optical properties.[22–27] The electronic properties of conducting polymers arise from electrons delocalized in π-bonds along the polymer backbone. This electron delocalization leads to stable and mobile charge carriers, as well as to uncharged excited species, i.e., polaron-excitons (excitons). An exciton in conducting polymers consists of a correlated electron-hole pair lightly bound to each other (with binding energies of a few tenths of an electron volt) and confined along the polymer backbone. The luminescent species in most conducting polymers is the spin zero singlet exciton. There is some controversy over the nature of the primary photoexcitations in conducting polymers, but at the absorption edge, it is

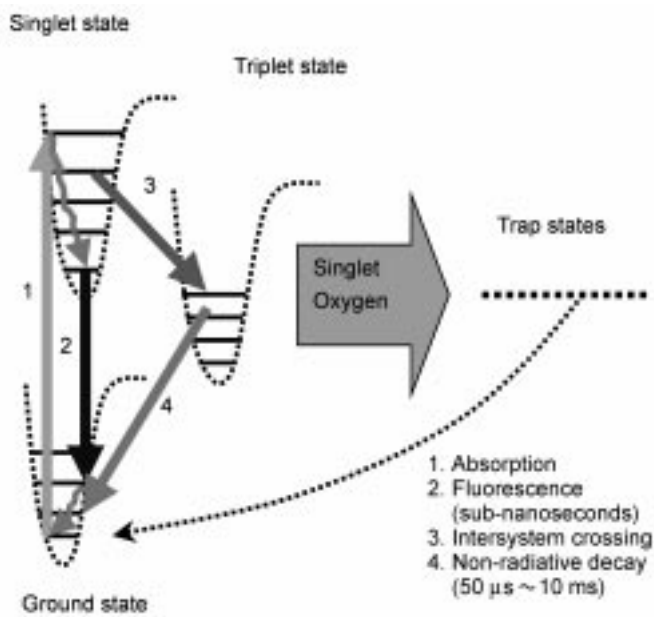

15.2 Photo-oxidation mechanism in luminescent conjugated polymers. Reprinted with permission from J.H. Park *et al., Chem. Mat.* **16**, 688 (2004).

considered likely that singlet excitons are preferentially excited. The singlet excitons may either decay radiatively with a sub-nanosecond lifetime or may undergo intersystem crossing to form spin 1 triplet excitons. The triplet exciton-ground state transition is dipole-forbidden, thus the triplet excitons are long-lived, exhibiting a non-radiative lifetime of 50 μs to 10 ms. These processes are shown in Fig. 15.2.[28] The charge carriers in conducting polymers consist of an electron and hole polarons. The polarons mean the charged particle (either an electron or hole) trapped on the polymer backbone by lattice relaxation caused by the particles Coulomb interaction with the delocalized π-electrons. The polarons move readily along the polymer backbone and hop between polymer chains. Electroluminescent devices based on conducting polymers work on the basis of electron and hole polaron injection and recombination into singlet and triplet excitons. For luminescent device purposes, one very attractive feature of conducting polymers is the sizable Stokes shift between the polymer absorption and emission. In general, this shift is on the order of 50 nm. This large Stokes shift is advantageous because the conducting polymer-based device exhibits almost no self-absorption of the emitted light.

15.4 Photo-oxidation of emitting polymers

The last decade has seen the development and refinement of many optoelectronic devices that rely on conducting polymers, such as LEDs,[23] photodiodes,[24,25] flat-panel displays, solar cells, and transistors.[26,27] In several cases, such devices are rapidly nearing commercialization. However, a significant obstacle to the commercial development of conducting polymer-based devices has been their high susceptibility to photo-oxidation under ambient conditions,[29,30] which degrades the device performance and limits device lifetime.

The most widely used method for improving conducting polymer-based device lifetime is encapsulation. Present encapsulation methods available are limited to low temperatures due to the degradation of the polymer active layer at temperatures approaching its melting point (generally less than 200ºC). Typical encapsulation methods for polymer-based devices include deposition of multiple organic or inorganic layers, which may be doped with oxygen scavengers,[31,32] or sandwiching the device between glass substrates bonded with epoxy,[33] or a combination of these two methods. Devices using a combination of these techniques have been demonstrated to have operating lifetimes in excess of 10,000 hours and storage lifetimes of at least two years, determined by accelerated testing conditions (elevated temperature and humidity).[34] However, these techniques are limited to devices on rigid substrates. One possible advantage of conducting polymer-based devices over inorganic devices is the ability to fabricate devices on flexible substrates, allowing for simple mass

production by reel-to-reel coating.[23] Successful encapsulation of flexible polymer devices has not yet been reported.

Another method of protecting conducting polymer films against photo-oxidation is the addition of a stabilizer material to block the action of oxygen. Several materials to prevent oxidation in polymers, such as polyethylene, have been studied in polythiophene derivatives.[34] The addition of 1-phenyldodecan-1-one(PDK) provided polythiophene derivatives with significant protection against photo-oxidation, but the additive was shown to protect the polymer by adsorbing UV light without transferring energy to the polymer.[35] This protection will be of no use in electroluminescent devices, which operate on the principle of electron-hole recombination, instead of photon absorption to form radiative species. Addition of C_{60} to polyphenylenevinylene derivatives has been shown to drastically reduce photo-oxidation of the polymer.[36] Unfortunately, C_{60} has the additional undesirable effect of efficiently quenching the luminescence of the polymer.[37]

A general picture of the photo-oxidation process in conducting polymers is presented in Fig. 15.2. Singlet oxygen reacts with the polymer and forms exciton traps. The result of the photo-oxidation process is that the polymer backbone is cut and exciton traps are formed on the chains.[38] Photo-oxidation of alkyl-substituted PPVs has been studied extensively,[29,39,40] and one possible reaction route is shown in Fig. 15.3.

Singlet oxygen formed via energy transfer from the polymer triplet exciton attacks the vinyl double bond to form a dioxetane, which then decomposes, resulting in decreased conjugation length and the formation of carbonyl species. The dioxetane may also react further with the polymer side groups, but this reaction also results in chain scission and chain termination with carbonyl

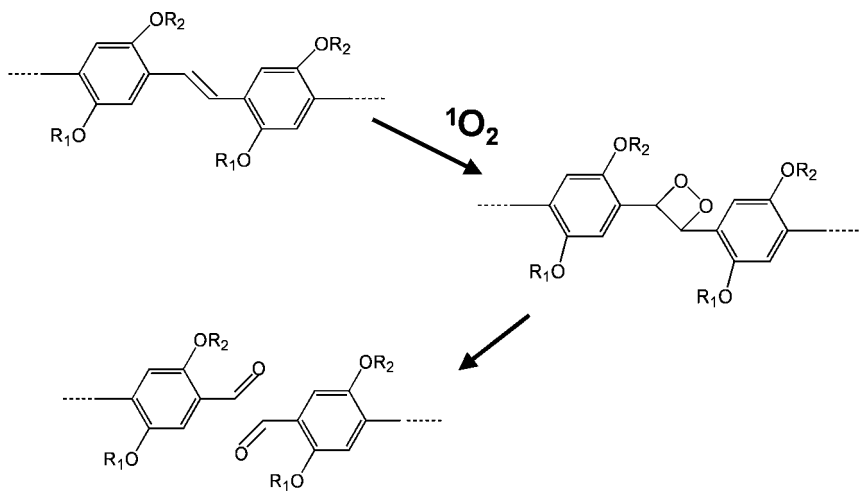

15.3 Photo-oxidation mechanism in PPV derivatives.

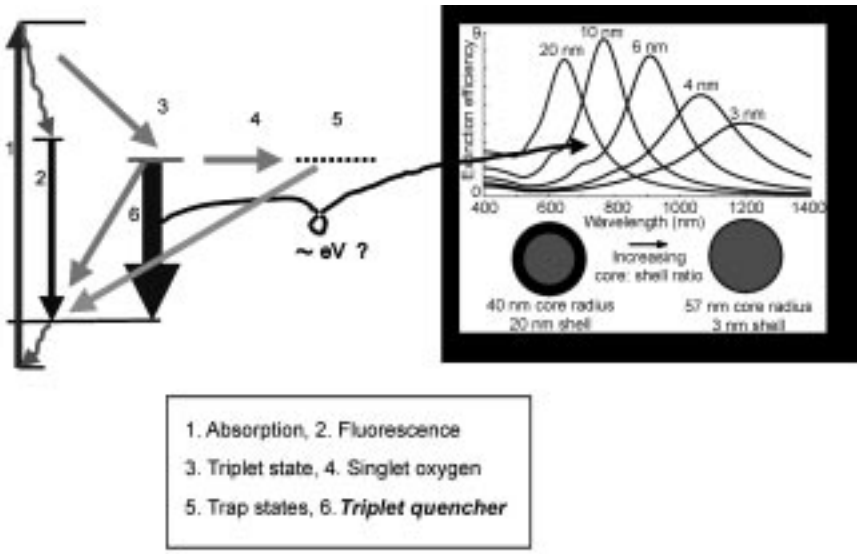

15.4 Proposed mechanism of impediment of photo-oxidation of luminescent conjugated polymers by doping triplet quencher. (Metal nanoshells whose plasmon resonance was specially designed to the triplet state of polymers were used as triplet quencher.)

groups. The carbonyl groups formed on the ends of polymer chains have been identified as efficient exciton quenchers in alkyl-substituted PPVs.[38] The strong electron affinity of the carbonyl groups leads to charge transfer between pristine polymer conjugation units and defect units, causing exciton dissociation. Since this leads to free charge generation, it is consistent with the observation of increased photoconductivity in photo-oxidized PPV.[39] The singlet excitons in PPV have a sub-nanosecond lifetime. Thus, the process of singlet oxygen formation by energy transfer from the polymer singlet excitons to oxygen is very inefficient. Experiments have shown that the alkyl-substituted PPVs triplet exciton transfers energy to oxygen efficiently.[41]

The proposed method for impeding this reaction is shown in Fig. 15.4. A triplet exciton quencher is added to the polymer film to compete with the formation of singlet oxygen, resulting in a reduction in the number of exciton traps formed. In the following section, we discuss a metal nanoshell, the optical resonance of which was specially designed for the triplet energy state of a polymer and which would be used as triplet quencher. During the photo-luminescence experiments, the triplet excitons are formed primarily by intersystem crossing from the singlet exciton state. Spin statistics indicate that the triplet excitons will be formed in a 3:1 ratio with the singlet excitons. Thus, the role of the triplet exciton in photo-oxidation is of primary importance to electroluminescent device operation and lifetime.

15.5 Nanoparticles approaches to enhance the lifetime of emitting polymers

15.5.1 Green emitting polymer/metal nanoshell nanocomposite

Poly(*p*-phenylenevinylene) (PPV) and its derivatives are versatile conjugated polymers that have been employed for polymer-based light-emitting devices,[42] lasers,[43] and photovoltaic cells.[44] Recently, a great deal of effort has been focused on improving the lifetimes of these devices. It has been found that the operating lifetimes of devices based on PPVs are sensitive to exposure to air.[45] One of the primary degradation mechanisms in polymer electroluminescent devices is photo-oxidation.[46] Photo-oxidation in many conjugated polymers begins with the formation of singlet oxygen via energy transfer from long-lived triplet excitons, resulting in chain scission and carbonyl defect formation on the polymer chain ends.[46] Since these carbonyl end-groups have lower ground and excited state energies relative to pristine chains, they can serve as exciton dissociation sites that trap electrons and produce mobile holes. Dissociation of the radiative singlet excitons at these sites results in quenched photo-luminescence (PL), while at low levels of oxidation, the production of mobile holes from the dissociation of excitons can also increase the photoconductivity of the polymer.[46] Therefore, a precise understanding of the effects of photo-oxidation in conjugated polymer films is a necessary step in the optimization of polymer-based materials and devices.

The utilization of nanoparticles in optoelectronic devices leads to the enhancement of optical, electrical properties, and stability.[47–52] In previous studies, it has been suggested that nanoparticles, such as, SiO_2 and TiO_2 can act as charge carrier promoters, or electro-optically active centers to influence the optical and electronic properties of PPV. Approaches to enhance stability of conjugated polymers by incorporating them with SiO_2[48] and metal nanoshells[30] have also been reported. Recently, our group synthesized a new type of gold-coated silica (SiO_2 @ Au) nanoparticles, by using a novel approach, which has proven to be convenient and versatile, as compared with conventional methods.[53]

Our group has prepared PPV nanocomposite films doped with SiO_2 @ Au nanoparticles prepared by the novel method and has characterized the PL properties of the films. The optical resonance of SiO_2 @ Au nanoparticles was specifically designed to interact with the triplet excitons of PPV. It has been observed that the rate of photo-oxidation in poly(*p*-phenylenevinylene) was drastically reduced by doping with SiO_2 @ Au nanoparticles, as expected.

Schematic diagrams for the synthetic schemes are illustrated in Fig. 15.5. To briefly summarize, silica nanoparticles were synthesized by the Stober-method and then coated with a Sn layer, which acts as a linker site for gold deposition. Gold layers were coated on the Sn-functionalized silica nanoparticles by reduction of $HAuCl_4$. Finally, the gold-coated silica nanoparticles were covered

15.5 Schematic diagram for the synthesis of gold-coated silica nanoparticles.

by another SiO_2 layer, which acts as a stabilizer for the composite particles. A PPV precursor (poly (xylylidene tetrahydrothiophenenium chloride)) was also prepared by well-known methods.[54] 1,4-Phenylenedimethylene-bis(tetramethylene sulfonium chloride) was prepared from 1,4-bis(chloromethyl) benzene and tetrahydrothiophene. The precursor of PPV was prepared from 1,4-phenylenedimethylene-bis(tetramethylene sulfonium chloride) and aqueous NaOH, following the published procedure.[54]

The SiO_2 @ Au nanoparticles were then dispersed in the PPV precursor solutions which were subsequently spin coated onto glass substrates. The experimental schemes are depicted in Fig. 15.6.[53] The substrates were held under vacuum at 180ºC for 5 h for the thermal conversion of the film. PL spectra were measured by exciting 410 nm monochromatic light. The PL decay of pristine PPV and PPV nanocomposite films was measured by exciting 310 nm light. While filtering the light through a UV cutting filter, the PL intensity was detected using an optical power meter connected to a photodiode with the function of time. There was no visible difference between the pristine PPV thin film and the PPV nanocomposite film.

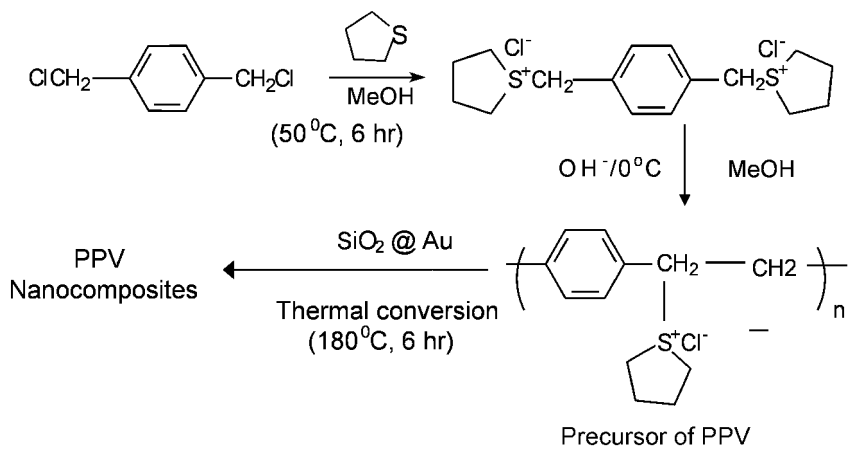

15.6 Experimental scheme for preparation of PPV nanocomposites doped with gold-coated silica nanoparticles. Reprinted with permission from Y.T. Lim *et al., Synth. Mat.* **128**, 133 (2002). Copyright © 2002 Elsevier.

Figure 15.4 illustrates the proposed mechanism for the impediment of photo-oxidation in PPV nanocomposites doped by SiO_2 @ Au nanoparticles. Because photo-oxidation of many PPV derivatives begins with formation of singlet oxygen via energy transfer from long-lived triplet excitons, triplet exciton energetics and dynamics play a primary role in the photo-oxidation process.[46] In photo-oxidation, reactive singlet oxygen undergoes 1,2-cycloaddition across the vinyl double bond to form a dioxetane, which in turn either cleaves to form two terminal aldehydes or produces a biradical, which reacts with the alkyl side-chains. The result is the formation of carbonyl groups at the end of the polymer chains. These carbonyl defects act as exciton traps, quenching the luminescence. Thus, the triplet excitons which play a primary role in the photo-oxidation process can be quenched by overlapping the energy level of the triplet state with the optical absorption of SiO_2 @ Au nanoparticles added.

Recently, optical properties of triplet excitons in PPV have been studied in detail.[55] Energy states in the triplet manifold in films of PPV have been investigated, using a multitude of optical spectroscopies, including photo-induced absorption, PL, optically detected magnetic resonances, and photo-generation action spectra. From the threshold energy for singlet fission, it was deduced that the lowest-lying, odd parity triplet excitonic state is located at 1.55 eV ($\lambda = 799.9$ nm) from the ground state, which is about 0.9 eV lower than the lowest-lying, odd-parity singlet state.

The TEM images and the absorption spectrum of SiO_2 @ Au nanoparticles are shown in Fig. 15.7.[53] The optical resonance of SiO_2 @ Au nanoparticles is located at a broad region of around 720–800 nm, which nearly overlaps with the triplet excitons in PPV. The diameter of composite nanoparticles is about 380 nm. The radius of silica core particles is about 170 nm, while the thickness of the gold shell is about 20 nm. The outer silica layer has a thickness of 20 nm.

Figure 15.8 shows the optical absorption and emission properties of PPV and SiO_2 @ Au nanoparticle doped PPV.[53] The optical absorption and PL spectra of the PPV polymer film after thermal conversion at various temperatures have been studied previously.[56] The optical and luminescent properties of our PPV agreed well with the previously reported results.[56] The relative height of the two features observed in each PL spectrum vary slightly between samples, but show no dependence on SiO_2 @ Au nanoparticle concentration, suggesting that the small height difference arises from minor variations in the local structure or film thickness of the polymer and polymer- SiO_2 @ Au nanoparticles composites.

The PL decay patterns for polymer nanocomposites films with two different SiO_2 @ Au nanoparticles are shown in Fig. 15.9. The rate of PL decay in PPV nanocomposites doped with SiO_2 @ Au nanoparticles was drastically reduced, as compared with that of the pristine PPV.[53] This suggests that the rate of luminescence-quenching by exciton trap formation is slowed considerably. The protection against photo-oxidation inherited by SiO_2 @ Au nanoparticles in PPV could be accomplished with an extremely low concentration, corresponding to

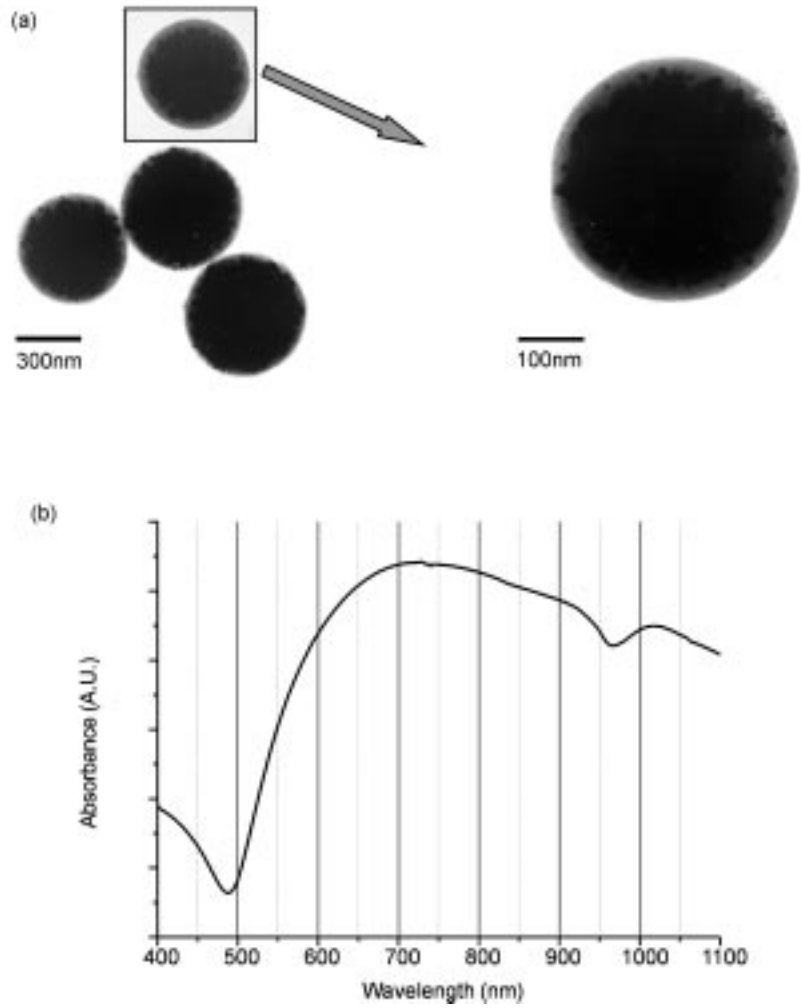

15.7 TEM images (a) and optical absorption spectra (b) of gold-coated silica nanoparticles ($D_{avg} = 340$ nm). Reprinted with permission from Y.T. Lim *et al., Synth. Mat.* **128**, 133 (2002). Copyright © 2002 Elsevier.

about 0.05% volume fraction. This concentration corresponds to about 1.6 μm separation between nanoshell particles in the film. It is noticeable that such a large separation between nanoshells yields a high level of protection against photo-oxidation.

One possible explanation for this enhanced energy transfer could be related to the nature of polymer excitons and the fact that the SiO_2 @ Au nanoparticles can exhibit greatly enhanced local field intensities. Since metal nanoparticle resonances have excitation lifetimes of only a few picoseconds, the donor-

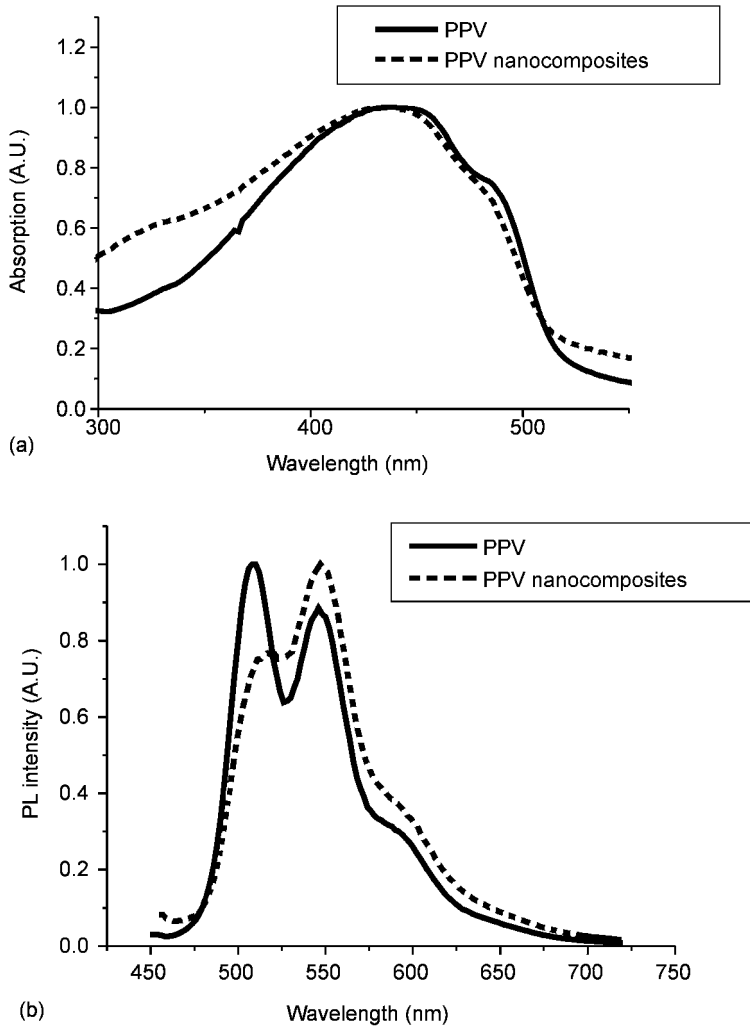

15.8 Optical absorption (a) and PL (b) spectra of pristine PPV and PPV nanocomposites (doped 0.05 vol.% gold-coated silica nanoparticles). Reprinted with permission from Y.T. Lim *et al., Synth. Mat.* **128**, 133 (2002). Copyright © 2002 Elsevier.

acceptor interaction between the comparatively long-lived excitons of the PPV and the nanoparticles will result in a strong quenching of the triplet excitation of the PPV, to which the SiO_2 @ Au nanoparticles resonance have been tuned. Furthermore, the excitons in the conjugated polymer are highly mobile along the polymer backbone and can hop between chains readily, finding the lowest-energy region of the film. It is possible that the SiO_2 @ Au nanoparticles dispersed in the polymer film will cause variations in the local energy environment of the triplet

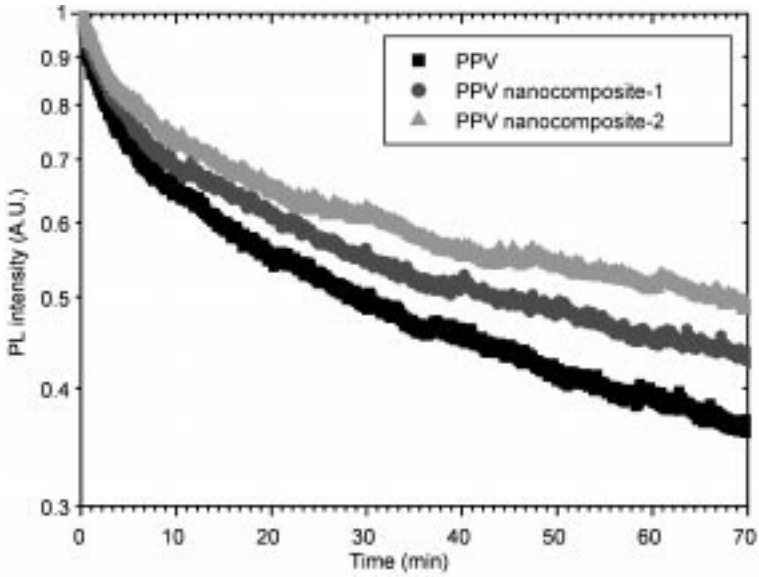

15.9 Retarded photo-oxidation in PPV nanocomposite films doped with gold-coated silica nanoparticles. (Nanocomposite-1 (0.05 vol.%), Nanocomposite-2 (0.1 vol.%). Reprinted with permission from Y.T. Lim *et al., Synth. Mat.* **128**, 133 (2002). Copyright © 2002 Elsevier.

excitons, attracting them to the SiO_2 @ Au nanoparticles, where the triplet exciton- SiO_2 @ Au nanoparticles interaction can take place easily.

Another experiment of time-resolved photo-induced absorption spectroscopy is necessary to characterize the dynamics of triplet-triplet absorption in detail. After the addition of SiO_2 @ Au nanoparticles into the PPV films, the dynamics of the triplet-triplet photo-induced absorption charateristic would be monitored. In addition, SiO_2 @ Au nanoparticles used in this work will not work directly in light-emitting diodes (LED), because typical conjugated polymer-based LED active regions are only 100 nm thick.

15.5.2 Blue emitting polymer/gold nanoparticle nanocomposites

Polyfluorenes have been investigated as a prospective blue emitting material for polymer light-emitting diodes. These materials display extremely high luminescence efficiencies with emission wavelengths primarily in the blue spectral region. However, for the commercialization of PLEDs, the long-term stability of the blue emitting polymers is a crucial factor because their high bandgap energy requires severe operating conditions.

The gold nanoparticles were synthesized according to the method reported earlier.[57] A 30 mM aqueous metal chloride solution ($HAuCl_4$) was added to a

25 mM solution of tetraoctylammonium bromide in toluene (80 mL). The transfer of the metal salt to the toluene phase can be clearly seen within a few seconds. A 0.4 M solution of freshly prepared $NaBH_4$ (25 mL) was added to the mixture while stirring, which caused an immediate reduction reaction. After 30 min, the two phases were separated and the toluene phase was subsequently washed with 0.1 M H_2SO_4, 0.1 M NaOH, and H_2O (three times), and then dried over anhydrous $NaSO_4$ to obtain the gold nanoparticles. The oxidative polymerization of fluorine, as well as 9-alkyl substituted derivatives has been reported.[58] We synthesized the emitting polymer material, PDOF, according to the reported synthesis scheme. PDOF was dissolved in chlorobenzene and the gold nanoparticles were then dispersed in this solution. The volume fraction of gold nanoparticles in PDOF was kept within $0–3 \times 10^{-5}$. Transmission electron microscopic (TEM) specimens were prepared by dropping the solution on a copper grid. Bright field images were obtained with a JEOL JEM-2010 TEM operating at 200 kV. PL spectra and PL decay characteristics of the pristine PDOF and the PDOF/gold nanocomposite films were measured using an ISS PC1 Photon Counting Spectrofluorometer while exciting the specimens at 380 nm using a dual grating monochromator (Spex 270M). The polymer light-emitting devices of the PDOF/gold nanocomposite films were fabricated as follows: The polymer films (80–100 nm thick) were obtained by spin-coating their solutions in monochlorobenzene on a PEDOT/PSS coated ITO glass anode. An aluminum cathode, 150 nm thick, was vacuum (5×10^{-6} torr) coated onto the emitting layers. Electroluminescence (EL) spectra were measured using the ISS PC1 Photon Counting Spectrofluorometer.

The TEM image and the UV absorption spectrum of the gold nanoparticles are shown in Fig. 15.10.[59] The optical absorption band of the gold nanoparticles with a diameter of 5–10 nm is located in a broad region, between 500 and 550 nm, which overlaps with the energy level of the triplet excitons in PDOF (539 nm).[60] Recently, silica core-gold shell nanoparticles, also known as 'gold nanoshells', have been used to reduce the rate of photo-oxidation in poly(*p*-phenyleneviyllene), poly[2-methoxy-5-(2′-ethylhexyloxy)-1,4-phenylene-vinylene] (MEH-PPV), and poly(3-octylthiophene) (P3OT).[49,57] In these studies, the size of the gold nanoshells was larger than 150 nm, and hence could not be applied to the PLED, because emitting layers of typical conjugated polymer-based LED are about 100 nm thick. General triplet energy transfer from the donor to dopant molecules proceeds by Dexter energy transfer or electron-hole capture at the guest molecule. The Dexter transfer mechanism involves mechanical tunneling of electrons between the host and guest, and is therefore a shorter-range process that requires the molecular separation of only a few Å. Electron-hole capture is favored by the overlap between the plasmon resonance of the metal nanoparticle and the polymer triplet state. Thus, the triplet excitons, which play a primary role in the photo-oxidation process, can be quenched by overlapping the energy level of the triplet state with the optical absorption of

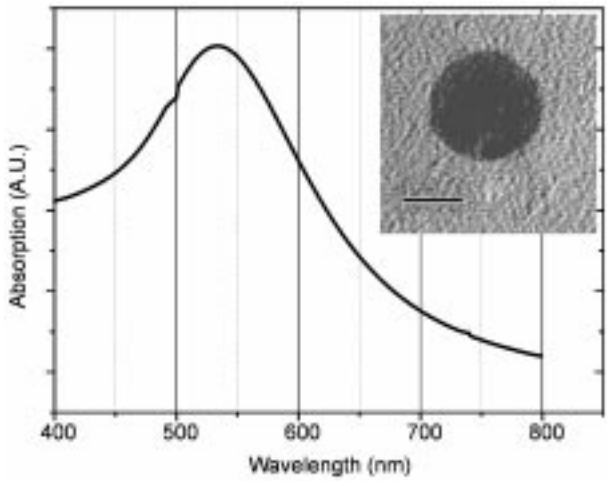

15.10 Optical absorption of gold nanoparticles dispersed in chlorobenzene solution. A TEM image of the gold nanoparticle is shown in the inset. Reprinted with permission from J.H. Park *et al., Rapid Commun.* **24**, 331 (2003).

metal nanoparticles and by increasing the contact area between the polymer and the metal nanoparticles.

The gold nanoparticles dispersed in the PDOF solution were spin cast on glass substrates. No visible differences between the pristine polymer films and the polymer nanocomposite films were observed. Figure 15.11 shows the optical absorption and emission properties of PDOF and the gold nanoparticle doped PDOF films. The relative heights and shapes of the absorption and PL spectra were nearly unchanged by the addition of gold nanoparticles in the pristine PDOF.[59] These observations suggest that the local structure and/or thickness of the composite films are perfectly identical. In addition, the PL peak wavelength was not affected by the interaction between the polymer and the gold nanoparticles. These are unique in that other polymer/nanoparticle composite systems showed small PL peak heights and shape differences between the pristine and the nanocomposite films. We surmise that the identical PL behaviors of all specimens originate from the very low volume fraction, as well as from the small size of the gold nanoparticles.

The PL decay of the PDOF/gold nanoparticle composite films with different nanoparticle volume fractions is shown in Fig. 15.12.[59] The rate of PL decay in the PDOF nanocomposite film was greatly reduced, as compared with that of the pristine PDOF. In general, excited chromophores can return to the ground state through a number of pathways involving both intermolecular and intramolecular interactions. While the system changes the state, both physical and chemical changes may occur. Two major chemical degradation processes, oxidation and cross-linking, can change the chemical structure of the original chromophore,

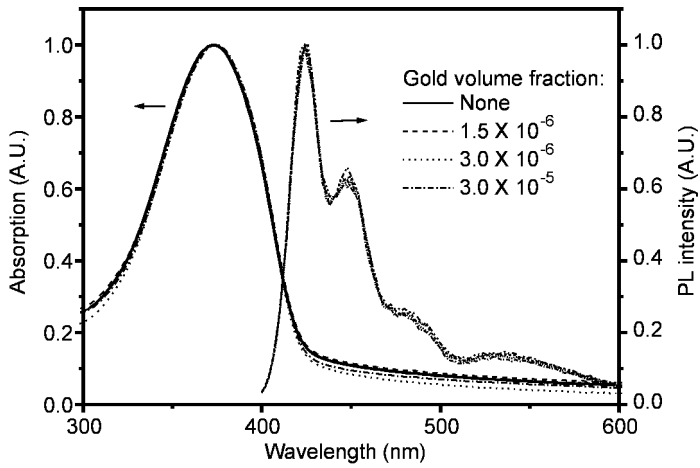

15.11 Optical absorption and PL spectra as a function of gold nanoparticles volume fraction. Reprinted with permission from J.H. Park *et al., Rapid Commun.* **24**, 331 (2003).

resulting in increased non-radiative relaxation rates. Regarding the chemical route, Bliznyuk *et al.*[61] reported that oxidation of a polymer leads to the formation of carbonyl-containing species, which quench fluorescence. Because photo-induced oxidation of conjugated polymers begins with the formation of singlet oxygen via the energy transfer from long-lived triplet excitons, the triplet

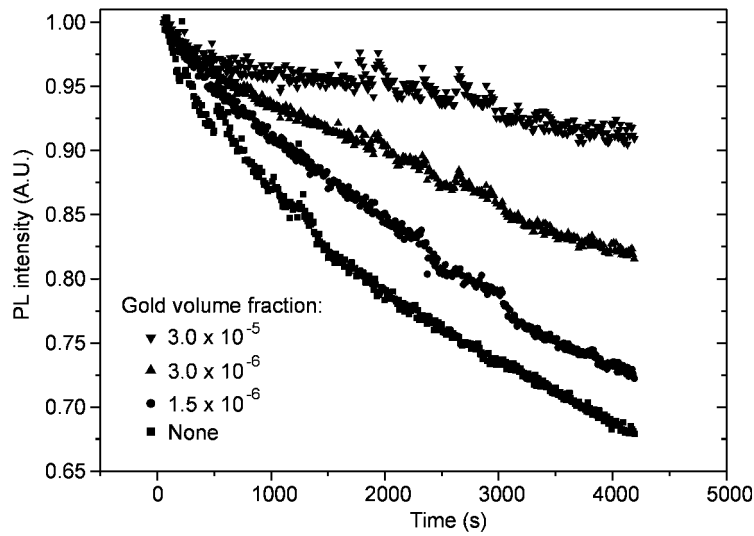

15.12 Retarded photo-oxidation in PDOF nanocomposite films with varying doped gold nanoparticles. Reprinted with permission from J.H. Park *et al., Rapid Commun.* **24**, 331 (2003).

exciton energetics and dynamics play a primary role in the photo-oxidation process. Thus, the triplet excitons can be quenched by overlapping their energy level with the optical absorption of the added gold nanoparticles. Although metal nanoparticle resonance has an excitation lifetime of only a few pico-seconds, the donor-acceptor interaction between the comparatively long-lived triplet excitons of PDOF and the nanoparticles will result in a strong quenching of the triplet state.

It is notable that the gold nanoparticle concentration in the nanocomposite film is about 30 times lower than that of previously reported polymer/gold nanoshell systems. This can be explained by the particle size effect. As the size of particles decreases and approaches the nanometer scale, the surface area of the particles increases dramatically, and the nanoparticles act as effective scavengers of the polymer triplet state. This behavior is very important with regard to the use of the polymer/nanoparticles nanocomposite film as the active layer of PLEDs. Due to the high conductivity of gold nanoparticles, the injected electrons from the cathode can be transported directly to the anode resulting in the diode breakdown. As the nanoparticle volume fraction in the polymer increases, the device stability will decrease.

Finally, it should also be noted that the previously reported polymer/metal nanoshell nanocomposite systems could not be applied to PLEDs, because the typical emitting layer thickness of PLEDs is about 100 nm. In contrast, our PDOF/gold nanoparticle nanocomposite film can be directly employed to PLED. To confirm our hypothesis a representative EL spectrum of PLED, using pristine PDOF and the PDOF/gold nanocomposite films as emitting layers is shown in Fig. 15.13.[59] The EL spectra of the composite films were slightly red shifted, but showed no dependence on gold particle concentration. The EL peak wavelength was not affected seriously by the interaction between the polymer and the gold nanoparticles. Due to the statistical ratio of 3:1 for the triplets and singlets formation under electroluminescence conditions, a much higher level of protection against the degradation of PDOF is expected. We are currently conducting a detailed study of the EL long-term stability.

Triplet energy transfer from donor to acceptor molecules generally proceeds via Dexter-type energy transfer or electron-hole capture by the acceptor molecules. The Dexter transfer mechanism involves the tunneling of electrons between the donor and the acceptor, and is therefore a short-range process that requires an intermolecular separation of only a few Ångstroms. Electron-hole capture is favored by overlap between the plasma resonance of the metal nano-particles and the polymer triplet state. Thus the triplet excitons that play a primary role in the oxidation of luminescent materials can be quenched as a result of the overlap of their energy levels with the optical absorption bands of metal nanoparticles. The excitation lifetimes of the metal nanoparticles and the host polymer are also important factors affecting energy transfer from the polymer to the metal nanoparticles. Gold nanoparticles of 5–10 nm size were

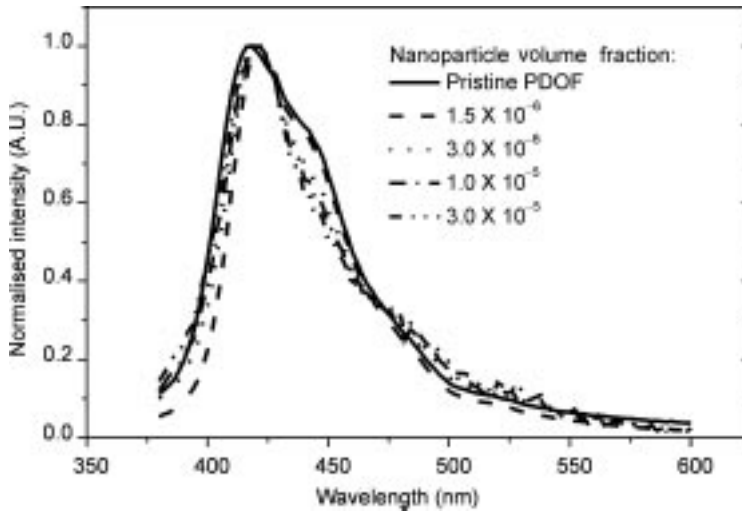

15.13 Normalized electroluminescence (EL) spectra of the PDOF/gold nanoparticle nanocomposite devices with different nanoparticle volume fractions. Reprinted with permission from J.H. Park *et al., Chem. Mat.* **16**, 688 (2004).

selected because their excitation states interact with the triplet exciton energy band of PDOF centered at ~530 nm. As the size of particles decreases and approaches the nanometer scale, the specific surface area of particles increases dramatically. Thus as the gold particle size decreases, the contact area between the polymer and the nanoparticles also increases and the nanoparticles become effective scavengers of the polymer triplet state. To investigate the dispersal of the gold nanoparticles within the nanocomposite film, morphological characterization of the PDOF/gold nanocomposite film with a volume fraction ($\approx 1 \times 10^{-3}$) was investigated by means of TEM as shown in Fig. 15.14. TEM revealed a uniform distribution of spherical shaped particles, 5–10 nm in size, throughout the bulk of the film.[28]

The normalized electroluminescence (EL) spectra of the PLEDs prepared using a pristine PDOF film and the PDOF/gold nanocomposite films are shown in Fig. 15.13. The EL spectral features of the PDOF PLED are virtually unaffected by the addition of gold nanoparticles to the luminescent polymer matrix. The stability of the devices was investigated under air atmosphere by recording their EL peak intensity as a function of time while applying a driving voltage of 10 V. The EL decay profiles of the nanocomposite devices with different gold nanoparticle concentrations were also investigated. The addition of gold nanoparticles to the PDOF PLED at a low volume fraction of 1.5×10^{-6} retards the EL intensity decay rate of the device. Since the resonance of the metal nanoparticles has an excitation lifetime of only a few picoseconds, their donor-acceptor interaction with the relatively long-lived triplet excitons of

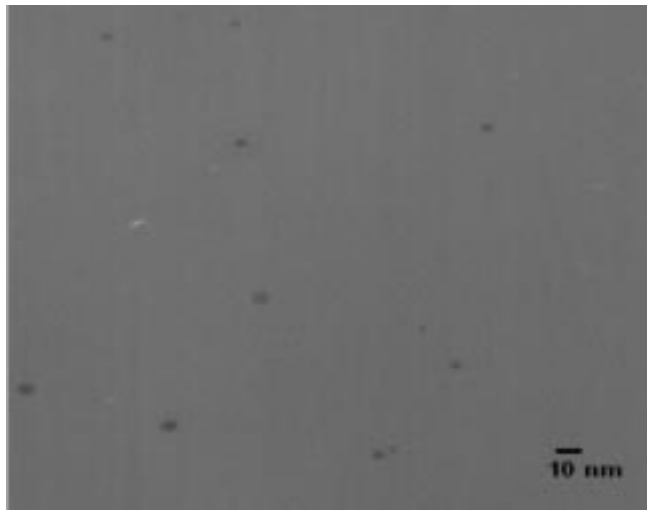

15.14 TEM image of the PDOF/gold nanoparticle nanocomposite film ($\approx 1 \times 10^{-3}$ volume fraction). Reprinted with permission from J.H. Park *et al., Chem. Mat.* **16**, 688 (2004).

PDOF effectively quenches the triplet state of PDOF. Accordingly, the performance of our devices has been improved significantly. We believe the device longevity can be improved more significantly if it is run in argon.

Recently, Bliznyuk *et al.*[61] reported on the degradation mechanisms of PLEDs based on blue-emitting polyfluorene polymers. In the presence of oxygen, they showed that the changes in fluorescence are accompanied by evidence for photo-oxidation. Chemical oxidation formed via energy transfer from the polymer triplet state attacks the polymer main chain, resulting in decreased conjugated length and the formation of carbonyl species. The carbonyl groups formed on the ends of polymer chains have been identified as efficient exciton quenchers in emitting polymers. The strong electron affinity of the carbonyl groups leads to charge transfer between the pristine polymer conjugation unit and defect units, causing exciton dissociation. The effects of electrical degradation on emission have been studied in failed polymer devices, after dissection. After electrically degraded devices in air were peeled apart, PL spectra were obtained. The data from Fig. 15.15 clearly show the effects of electrical degradation on PL emission characteristics.[28] The primary characteristic of the pristine PLED is a decreased exciton-to-excimer ratio, as compared to the PLED with a 1.0×10^{-5} gold volume fraction.

Chemical changes that occur during and after degradation were also monitored using FTIR spectroscopy. Figure 15.16 shows the IR transmission spectra of (1) a fresh PDOF film, (2) a film with a 1.0×10^{-5} gold volume fraction after electric degradation in air, and (3) the PDOF film after electric degradation in air.[28] The most obvious changes in the IR spectra of degraded

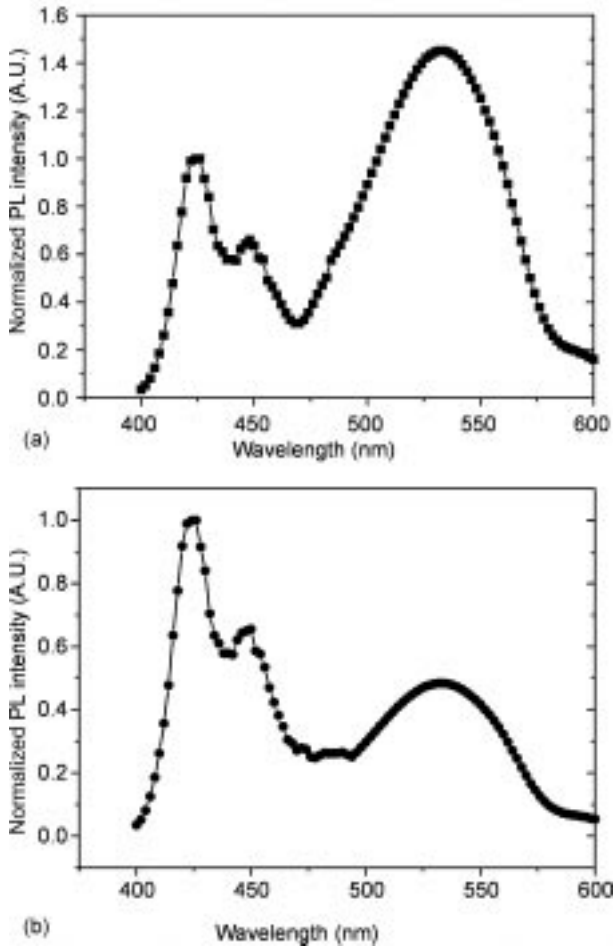

15.15 Photoluminescence (PL) spectra of the PDOF layer before and after electrical degradation of a working device: (a) pristine PDOF film; (b) PDOF/gold nanoparticle composite film. Reprinted with permission from J.H. Park *et al., Chem. Mat.* **16**, 688 (2004).

samples are observed between 1500 and 1800 cm^{-1} region, but only in the case of pristine PLEDs are the spectroscopic changes well pronounced.

In both the electrically degraded pristine PDOF film and the nanocomposite film, two new bands appeared around 1717 and 1606 cm^{-1}. The former band is consistent with carbonyl stretch of an aromatic ketone or ester, and the latter may be interpreted as a stretching mode of an asymmetrically substituted benzene ring.[19] The intensities of these two peaks may results in photo-oxidation. For the pristine PDOF sample, the intensities of these two peaks are more obvious and clear compared with those of the nanocomposite film.

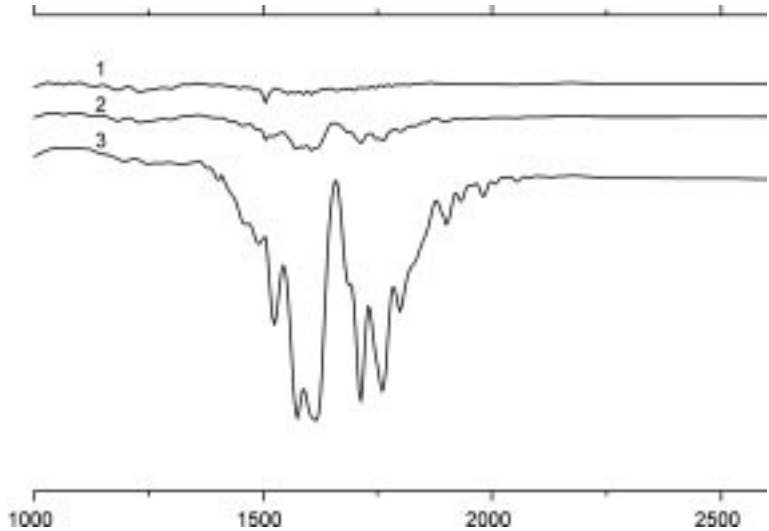

15.16 FTIR spectra of (1) a fresh PDOF film, (2) a PDOF/gold nanoparticle nanocomposite film after electric degradation in air after 10 min at 10 V and (3) a PDOF film after electric degradation in air after 10 min at 10 V. Reprinted with permission from J.H. Park *et al., Chem. Mat.* **16**, 688 (2004).

15.6 Conclusions and future trends

In this chapter, we have discussed both the design of inorganic nanoparticles for specified functional properties (optical and electrical) and the fabrication of fundamental polymer nanocomposites doped with those nanoparticles. By controlling a nanostructure with specified functionalities, the photo-stability can be drastically enhanced. Metal nanoparticles and nanoshell-type particles could be the best candidates, with applications in a variety of fields. These nanoparticles are ultra small particles, whose light-absorbing properties can be specifically designed for specific purposes in the visible and infrared regions of the spectrum. In addition, the composite nanoparticles can be used in various fields where the optical resonance properties of metal nanoshells are specifically designed for specific purposes. The particles can be made to selectively absorb or scatter light at virtually any wavelength, even at wavelengths for which no light-absorbing materials exist. In the present work, we presented only a few examples of applications that we strongly expect to be developed before long.

15.7 References

1. A. Bernanose, *J. Appl. Phys. Suppl.* **4**, S54 (1955).
2. M. Pope, H. Kallmann, P. Magnante, *J. Chem. Phys.* **38**, 2042 (1963).
3. W. Helfrich, W. G.. Schneider, *Phys. Rev. Lett.* **140**, 229 (1965).
4. D. F. Williams, M. Schadt, *Proc. IEEE Lett.* **58**, 476 (1970).

5. M. Pope, C. E. Swenberg, *Electronic Processes in Organic Crystals*, Clarendon Press, Oxford, 1982.
6. J. Kalinowski, *J. Phys. D: Appl. Phys.* **32**, R179 (1999).
7. N. Y. Vityuk, V. V. Mikho, *Sov. Phys. Semicond.* **6**, 1479 (1973).
8. P. S. Vincent, W. A. Barlow, R. A. Hann, G. G. Roberts, *Thin Solid Films* **94**, 476 (1982).
9. G. G. Roberts, M. Mcginnity, P. S. Vincett, W. A. Barlow, *Solid State Commun.* **32**, 683 (1979).
10. P. H. Partridge, *Polymer* **24**, 748 (1983).
11. C. W. Tang, S. A. Van Slyke, *Appl. Phys. Lett.* **51**, 913 (1987).
12. C. W. Tang, S. A. Van Slyke, *J. Appl. Phys.* **65**, 3610 (1989).
13. C. Adachi, S. Tokito, T. Tsutsui, S. Saito, *Jpn. J. Appl. Phys.* **27**, L269 (1988).
14. C. Adachi, S. Tokito, T. Tsutsui, S. Saito, *Jpn. J. Appl. Phys.* **27**, L713 (1988).
15. C. Adachi, T. Tsutsui, S. Saito, *Acta Polymerica* **170**, 215 (1990).
16. Pioneer Co. Japan. In November 1997 Pioneer Co. in Japan commercialized a monochrome 256 × 64 dot matrix OLED display for automotive applications.
17. H. Kubota, S. Miyaguchi, S. Ishizuka, T. Wakimoto, J. Funaki, Y. Fukuda, T. Watanabe, H. Ochi, T. Sakamoto, T. Miyake, M. Tsuchida, I. Ohshita, T. Tohma, *J. Lumin.* **87–89**, 56 (2000).
18. J. Kido, *Phys. World* **12**, 27 (1999).
19. J. H. Burroughes, D. D. C. Bradley, A. R. Brown, R. N. Marks, K. Mackay, R. H. Friends, P. L. Burn, A. B. Holmes, *Nature* **347**, 539 (1990).
20. J. R. Visser, *Philips J. Res.* **51**, 467 (1998).
21. R. H. Friend, J. Burroughes, T. Shimoda, *Phys. World* **12**, 35 (1999).
22. J. H. Burroughes, D. D. C.Bradley, A. R. Brown, R. N. Marks, K. Mackey, R. H. Friend, P. L. Burns, A. B. Holmes, *Nature* **347**, 539 (1990).
23. G. Gustafsson, Y. Cao, G. M.Treacy, F. Klavetter, N. Colaneri, A. J. Heeger, *Nature* **357**, 447 (1992).
24. G. Yu, J. Gao, J. C. Hummelen, F. Wudl, A. J. Heeger, *Science* **270**, 1789 (1995).
25. M. Granstrom, K. Petritsch, A. C. Arias, A. Lux, M. R. Andersson, R. H. Friend, *Nature* **395**, 257 (1998).
26. F. Granier, R. Hajlaoui, A. Yassar, P. Srivastava, *Science* **265**, 1684 (1994).
27. L. Torsi, A. Dodabalapur, L. J. Rothberg, A. W. P. Fung, H. E. Katz, *Science* **272**, 1462 (1996).
28. J. H. Park, Y. T. Lim, O. O. Park, J. K. Kim, J.-W. Yu, Y. C. Kim, *Chem. Mat.* **16**, 688 (2004).
29. B. H. Cumpston, K. F. Jensen, *Synth. Meta*. **73**, 195 (1995).
30. Y. Kaminorz, E. Smela, O. Inganas, L. Brehmer, *Adv. Mater*. **10**, 765 (1998).
31. S. Q. Shi, F. So, T. B. Harvey III, US Patent No. 5,811,177 (1998).
32. E. Haskal, S. Karg, J. R.Salem, J. C. Scott, US Patent No. 5,952,778 (1999).
33. C. Liedenbaum, Y. Croonen, P. van de Weijer, J. Vlegaar, H. Schoo, *Synth. Met.* **91**, 109 (1997).
34. N. Ljungqvist, T. Hjerrberg, *Macromolecules* **28**, 5993 (1995).
35. T. Caronna, M. Forte, M. Catellani, S. Meille, *Chem. Mater*. **9**, 991 (1997).
36. H. W. Sarkas, W. Kwan, S. R. Flom, C. D. Merritt, Z. H. Kafafi, *J. Phys. Chem*. **100**, 5169 (1996).
37. C. H. Lee, G. Yu, D. Moses, K. Pakbaz, C. Zhang, N. S. Saricific, A. J. Heeger, F. Wudl, *Phys. Rev. B*. **48**, 15425 (1993).

38. M. Yan, L. J. Rothberg, F. Papadimitrakopoulos, M. E. Galvin, T. M. Miller, *Phys. Rev. Lett*. **73**, 744 (1994).
39. H. Antoniadis, L. J. Rothberg, F. Papadimitrakopoulos, M. Yan, M. E. Galvin, M. A. Abkowitz, *Phys. Rev. B.* **50**, 14911 (1994).
40. R. D. Scurlock, B. J. Wang, P. R. Ogilby, J. R. Sheats, R. L. Clough, *J. Am. Chem. Soc*. **117**, 10194 (1995).
41. A. P. Monkman, H. D. Burrows, M. da G. Miguel, I. Hamblett, S. Navaratnam, *Chem. Phys. Lett*. **307**, 303 (1999).
42. A. Kraft, A. C. Grimsdale, A. B. Holmes, *Angew. Chem. Int. Ed*. **37**, 402 (1998).
43. M. A. Diaz-Garcia, H. Fumitomo, B. J. Schwartz, *Synth. Met*. **84**, 455 (1997).
44. Y. Cao, G. Yu, A. J. Heeger, *Adv. Mater*. **10**, 692 (1998).
45. B. H. Cumpston, K. F. Jensen, *Synth. Met*. **73**, 195 (1995).
46. R. D. Scurlock, B. J. Wang, P. R. Ogilby, J. R. Sheats, R. L. Clough, *J. Am. Chem. Soc*. **117**, 10194 (1995).
47. S. A. Carter, J. C. Scott, P. J. Brock, *Appl. Phys. Lett*. **71**, 1145 (1997).
48. W. P. Chang, W. T. Whang, *Polymer* **37**, 4229 (1996).
49. G. D. Hale, J. B. Jackson, O. E. Shmakova, T. R. Lee, N. J. Halas, *Appl. Phys. Lett***. 78**, 1502 (2001).
50. T.-W. Lee, J. Yoon, J.-J. Kim, O. O. Park, *Adv. Mater*. **13**, 211 (2001).
51. T.-W. Lee, O. O. Park, J.-J. Kim, J.-M. Hong, Y. C. Kim, *Chem. Mater*. **13**, 2217 (2001).
52. H.-C. Lee, T.-W. Lee, Y.T. Lim, O. O. Park, *Appl. Clay. Sci*. **21**, 287 (2002).
53. Y. T. Lim, T.-W. Lee, H.-C. Lee, O. O. Park, *Synth. Met*. **128**, 133 (2002).
54. J. Gmeiner, S. Karg, M. Meier, W. Riess, P. Strohriegel, M. Schwoerer, *Acta Polym*. **44**, 201 (1993).
55. R. Osterbacka, M. Wohlgenannt, D. Chinn, Z.V. Vardeny, *Phys. Rev. B* **60**, R11253 (1999).
56. M. Herold, J. Gmeiner, W. Riess, P. Strohriegel, *Synth. Met*. **76**, 109 (1996).
57. S. A. Carter, J. C. Scott, P. J. Brock, *Appl. Phys. Lett.* **71**, 1145 (1997).
58. A. P. Monkuan, H. D. Burrows, L. J. Hartwell, L. E. Horsburgh, I. Hamblett, S. Navaratnam, *Phys. Rev. Lett.* **86**, 1358 (2001).
59. J. H. Park, Y. T. Kim, O O. Park, Y. C. Kim, *Macromol. Rapid Commun.* **24**, 331 (2003).
60. F. Wang, Z. J. Chen, Q. H. Gong, K. W. Wu, X. S. Wang, B. W. Zhang, F. Q. Tang, Appl. Phys. Lett. **75**, 3243 (1999).
61. V. N. Bliznyk, S. A. Carter, J. C. Scott, G. Klarner, R. D. Miller, D. C. Miller, *Macromolecules* **32**, 361 (1999).

16

Polymer/calcium carbonate nanocomposites

X LU, Nanyang Technological University, Republic of Singapore and
T LIU, Institute of Advanced Materials, People's Republic of China

16.1 Introduction

Polymer nanocomposites (PNC) have received increasing attention in recent years. The research efforts in this area, as reflected by the number of articles, patents, or the amount of R&D funds, have been growing exponentially worldwide.[1] In contrast to conventional particulate-filled polymers, i.e. so-called micro-composites where the reinforcement is on the order of microns, PNC comprise discrete constituents of less than 100 nm in at least one dimension. PNC often exhibit dramatic improvements in performance at relatively low filler loadings, which provides value-added properties not present in a neat resin without sacrificing the resin's inherent processability or adding excessive weight.[1–2] Furthermore, with the dispersion of fillers at nanometer length scale, a level of filler-matrix interaction previously not achievable in conventional composite systems can now be attained. This often leads to interesting modifications to the polymer matrix, giving rise to new structures and new properties.

Among various nanofillers, two of the most extensively investigated particulates are layered silicates, i.e. clay, and carbon nanotubes, which are two- and one-dimensional elements in geometry, respectively, thus with large aspect ratio (usually 100). Recently increasing attention has also been paid to low aspect ratio, such as spherical or cubic-shaped, nanoparticles, in particular nano-calcium carbonate (nano-$CaCO_3$) due to its wide range of potential applications and low cost. Academic interest in this area has also arisen as PNC containing low aspect ratio nanoparticles are a critical bridge between the conventional micro-composites and the ones filled with high aspect ratio nanoparticles where, from the nanoparticle perspective, size is reduced and number density increased prior to the additional complexity of orientational correlations introduced by an extreme aspect ratio.[1]

This chapter provides a snapshot of the current status of the rapidly developing science and technology in the field of polymer/$CaCO_3$ nano-composites, which includes preparation and modification of nano-$CaCO_3$,

fabrication and characterization of the nanocomposites as well as their applications. The future research directions and challenges in the field are also addressed briefly.

16.2 Preparation and surface modification of nano-$CaCO_3$

16.2.1 Preparation of nano-$CaCO_3$

Various nanoparticle preparation methods, such as physical vapor deposition,[3] chemical vapor deposition,[4] reactive precipitation,[5] sol-gel,[6] microemulsion,[7] sonochemical processing[8] and supercritical chemical processing,[9] have been developed and reported in the literature. Among these methods, reactive precipitation is of high industrial interest because of its convenience in operation, low cost and suitability for massive production. The conventional precipitation process is, however, often carried out in a stirred tank or column reactor, and moreover the quality of the product is difficult to control and the morphology and size distribution of the nanoparticles usually change from one batch to another during production.

Recently, Chen *et al.* developed a novel technology, high-gravity reactive precipitation (HGRP), for synthesis of nanoparticles.[10] Using the HGRP approach, reactive precipitation takes place under high-gravity conditions. The experimental apparatus for HGRP is shown schematically in Fig. 16.1. A rotating packed-bed (RPB) reactor is used to generate acceleration higher than the gravitational acceleration on earth. The key part of the RPB is a packed rotator,[11] in which vigorous mixing and mass transfer occurs under a high stress

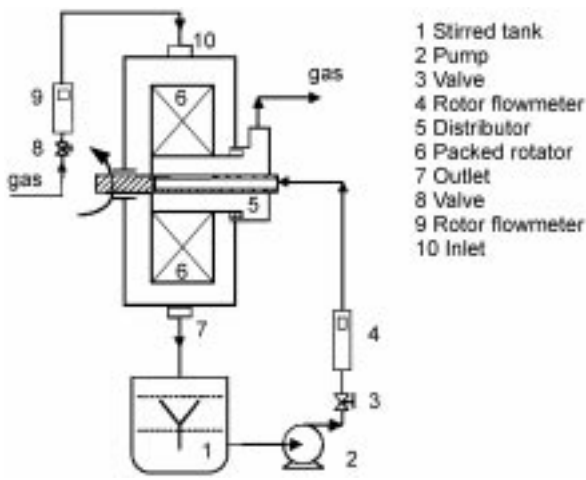

16.1 Schematic of experimental setup for HGRP. Reprinted with permission from ref. 10 (Figure 1). Copyright © (2000) American Chemical Society.

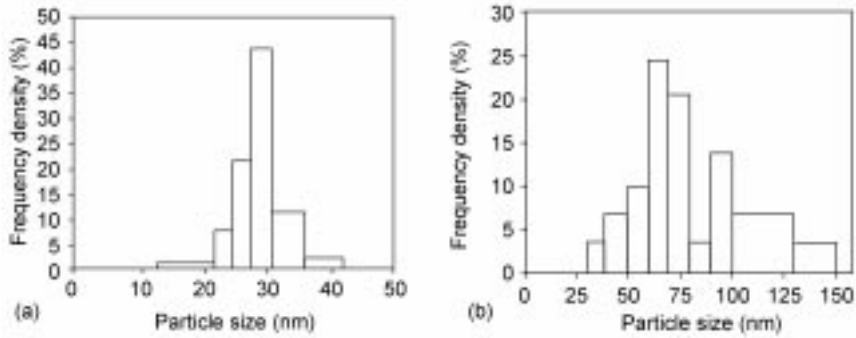

16.2 Particle size distributions of nano-$CaCO_3$ prepared by different methods: (a) by HGRP and (b) by conventional precipitation. Reprinted with permission from ref. 10 (Figure 9). Copyright © (2000) American Chemical Society.

field. This generates uniform concentration distribution at almost molecular level in the reactive precipitation process and hence yields nanoparticles with narrow size distribution. By means of this new approach, synthesis of $CaCO_3$, aluminum hydroxide, and strontium carbonate nanoparticles with narrow size distribution has been successfully achieved. A histogram of particle size distribution (PSD) of cubic nano-$CaCO_3$ prepared by HGRP is given in Fig. 16.2(a). Without any addition of crystal growth inhibitors, the mean size of $CaCO_3$ particles can be adjusted in the range of 15–40 nm by controlling the operation conditions, such as high-gravity level, fluid flow rate and reactant concentration. As a comparison, a histogram of PSD of nano-$CaCO_3$ prepared by conventional precipitation technology is shown in Fig. 16.2(b). It can be seen that the PSD of $CaCO_3$ synthesized by HGRP is much narrower and the mean particle size much smaller than that prepared by the conventional precipitation method.[10]

It is worth noting that this cost-effective HGRP technology has been commercialized in China[12] and Singapore[13] recently, which led to massive production of nano-$CaCO_3$ with narrow size distribution at relatively low cost and spurred more intensive research on polymer/$CaCO_3$ nanocomposites.[14-18]

16.2.2 Surface modification of nano-$CaCO_3$

There are generally two kinds of interactions existing in particulate-filled polymer composites.[19–20] On the one hand, a polymer matrix adheres to the surface of the particles forming an interphase with properties differing from those of the matrix;[21] on the other hand, the particles may also interact with each other creating aggregates.[22] Usually, homogeneous dispersion of nanoparticles in a polymer is very difficult to achieve due to the strong tendency of the ultra fine particles to agglomerate and the high melt viscosity of the matrix. Therefore, as with many other particulate-filled polymer systems, the two key

factors controlling the performance of a polymer/$CaCO_3$ nanocomposite are: (1) dispersion of nano-$CaCO_3$ in the matrix, and (2) the polymer-filler interface. Fine dispersion (without significant particle aggregation) and adequate interfacial adhesion are essential if high performance is to be achieved.

Surface treatment of fillers is a well-known way to modify the interfacial adhesion in polymer/$CaCO_3$ composites.[23] For instance, $CaCO_3$ particles are often modified by organic agents to provide a hydrophobic surface to increase the interfacial adhesion with hydrophobic polymers. Non-reactive treatment results in a decrease in the surface tension of fillers leading to a decrease in particle-particle and particle-polymer interactions. As a result, aggregation of the fillers decreases, homogeneity, surface quality and processability improve, but the yield stress and tensile strength of the composites decrease.[24] The non-reactive filler coatings include calcium and magnesium stearates, silicone oils, waxes, and ionomers.[25–27] Reactive coupling assumes the presence of reactive groups both on the surface of fillers and in polymer matrices.[24] Various reactive surface modifiers, such as alkylalkoxysilanes, alkylsiyl chlorides, dialkytitanates and stearic acid, have been used. $CaCO_3$ does not have active –OH groups on its surface which could react with silanes. Thermoplastics, especially apolar polyolefins, are also inactive since their polymer chains do not contain any reactive groups. Reactive coupling is thus not expected in such systems. However, studies by Demjen *et al.* showed that apparent reactive coupling of $CaCO_3$ to polypropylene (PP) has been achieved with the application of amino-functional silane coupling agents.[24] Detailed studies proved that amino-functional silane coupling agents adhered strongly to the surface of $CaCO_3$ and formed a polysiloxane layer probably due to the catalytic effect of the amino group in the polycondensation process. The silane coupling agents used successfully in their model reactions, i.e. surface modification of $CaCO_3$, are listed in Table 16.1.

Table 16.1 Silane coupling agents used in surface modification of $CaCO_3$. Reprinted from ref. 24, Copyright (1999), with permission from Elsevier

Abbr.	Formula	Grade	Producer
MPTMS	$CH_2{=}C(CH_3)\text{-}CO\text{-}O\text{-}CH_2\text{-}CH_2\text{-}CH_2\text{-}Si\text{-}(O\text{-}CH_3)_3$ (3-methacryloxypropyl)trimethoxysilane	GF31	Wacker
CVBS	$CH_2{=}CH\text{-}ph\text{-}CH_2\text{-}NH\text{-}(CH_2)_2\text{-}NH\text{-}(CH_2)_3\text{-}Si\text{-}(O\text{-}CH_3)_3{\cdot}HCl$ (ph = benzene ring) N-(4-vinylbenzyl)-N′-(3-trimethoxysilylpropyl-ethyl)enediamine, hydrochloride	Z6032	Dow Corning
AMPTES	$NH_2\text{-}CH_2\text{-}CH_2\text{-}CH_2\text{-}Si\text{-}(O\text{-}CH_2\text{-}CH_3)_3$ (3-aminopropyl)triethoxysilane	GF93	Wacker

For apolar polyolefin systems, an alternative approach is grafting, i.e. introducing polymer chains onto nano-$CaCO_3$ by irradiation grafting polymerization[28] or incorporating grafted polyolefins, such as maleic anhydride or acrylic acid grafted PP,[29] to obtain ternary-phase composites. In the case of grafting polymerization, owing to their low molecular weight, the monomers can easily penetrate into the agglomerated nanoparticles and react with the activated sites of the nanoparticles inside as well as outside the agglomerates.[28] Introducing a third component with good compatibility with nano-$CaCO_3$ can lead to encapsulation of the nanoparticles by the third component and hence a finer dispersion of the nanoparticles due to the reduced surface tension.[30] Clearly, the ternary phase can improve both the degree of nanoparticle dispersion and the interfacial interactions between nano-$CaCO_3$ and polymer matrices.

The significant influences of surface treatment on the morphology and properties of polymer/$CaCO_3$ nanocomposites have been clearly illustrated by the research work of Huang *et al.*[31] and Lorenzo *et al.*[32] In the first case, nano-$CaCO_3$ fillers were treated with stearic acid under different shear forces in a high and ultra-high speed mixer, respectively, and then melt-blended with PP.[31] Scanning electron microscopy (SEM) study showed that (a) micron-sized aggregates were formed in the PP matrix when using untreated nano-$CaCO_3$ due to high surface energy of the fillers (Fig. 16.3(a)); (b) the dispersion of nano-$CaCO_3$ was slightly improved when using nano-$CaCO_3$ surface-treated by stearic acid in the high speed (2000 rpm) mixer; (c) the degree of dispersion was greatly improved when using nano-$CaCO_3$ surface-treated in the ultra-high speed (6000 rpm) mixer (Fig. 16.3(b)). It can be concluded that:

1. higher shear force breaks up the agglomerates of nanoparticles more effectively during the surface treatment

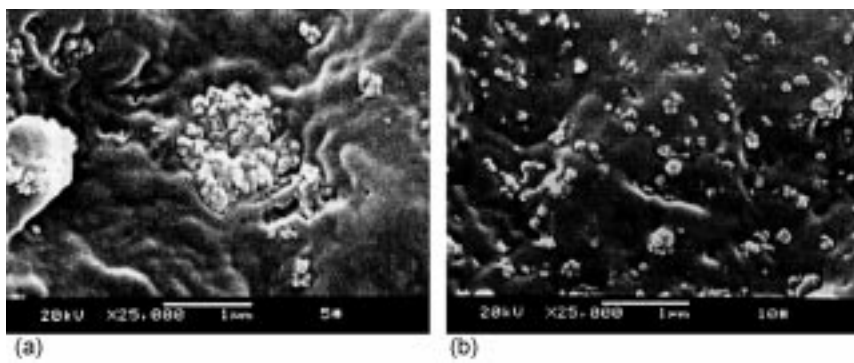

16.3 SEM images of PP/nano-$CaCO_3$ composites (content of $CaCO_3$ = 11.7 vol.%). (a) Nano-$CaCO_3$ was untreated. (b) Nano-$CaCO_3$ was treated with stearic acid in an ultra-high-speed mixer. Reprinted from ref. 31 (Figure 1), Copyright © (2002), with kind permission from Springer Science and Business Media and Professor Rui Huang, Sichuan University, China.

2. uniform surface coverage of nano-$CaCO_3$ by stearic acid decreases filler surface energy thus improving the nanoparticle dispersion in the matrix. As a consequence, the mechanical properties (tensile modulus, yield strength and notched Izod impact energy) of the PP nanocomposites prepared from treated nano-$CaCO_3$ are evidently superior to those from untreated nano-$CaCO_3$.

In the second case, Lorenzo *et al.* prepared poly(ethylene terephthalate) (PET)/$CaCO_3$ nanocomposites via in-situ polymerization, and the effects of surface treatment on the dispersion morphology and thermal behavior of the nanocomposites were studied.[32] For untreated nano-$CaCO_3$, a large number of very small discrete particles were observed. For the nanocomposites with stearic acid treated nano-$CaCO_3$ the discrete particles were still evident, but they were better welded to the PET matrix, suggesting that the stearic acid coating improves adhesion between the nano-$CaCO_3$ and the PET matrix. The improved compatibility between the phases is probably due to the hydrophobic characteristics of the treated nano-$CaCO_3$ imparted by the stearic acid coating.

16.3 Fabrication of polymer/$CaCO_3$ nanocomposites

Several methods, including in-situ polymerization, melt blending, sol-gel process and solution-casting, have been used to fabricate polymer/$CaCO_3$ nanocomposites. Each of these methods has its unique advantages and disadvantages.

16.3.1 In-situ polymerization

Using the in-situ polymerization approach, polymer nanocomposites are prepared by polymerizing the monomers or precursors in the presence of nanofillers. Usually, the nanoparticles are first dispersed into the monomers or precursors, and the mixture is then polymerized by adding the appropriate catalyst.[18,32–38] Particular attention is paid to this method because it permits one to synthesize nanocomposites with effectively tailored physical properties. The advantages of the in-situ polymerization technology with respect to the other methods are:[35]

- a direct and easier dispersion of the nanoparticles into the liquid monomers or precursors, avoiding agglomeration of the nanoparticles in the polymer matrix and improving the interfacial interactions between the two phases
- the possibility of using less expensive nanoparticles (e.g. $CaCO_3$ rather than silica particles) and conventional polymer processing technologies.

The in-situ polymerization method has been proved to be a successful approach for preparation of polymer/$CaCO_3$ nanocomposites with significantly enhanced properties.

Avella *et al.* successfully utilized the in-situ polymerization technology for preparation of poly(methyl methacrylate) (PMMA)/$CaCO_3$ nanocomposites.[35,36] To obtain the required homogeneous dispersion of the nanoparticles, the PMMA polymerization process has been modified and performed in two steps as follows. The acrylic monomer, in which the organic peroxide was previously dissolved, and the nano-$CaCO_3$ particles were added to a cylindrical reactor. The reaction was carried out under vigorous stirring at 100ºC until viscosity of the mixture reaches a critical value. In this step, pre-polymerization of the acrylic monomer in the presence of the nanoparticles occurred. It was observed that the time to the point of critical viscosity of the solution depended on the amount of nanoparticles. In the second step, the mixture was put into a mold and kept in an oven at 100ºC for 24 h to complete the polymerization process. As a result, the nanoparticles were fairly homogeneously dispersed in the PMMA matrix, even at relatively high contents of nanoparticles, with size of 40–70 nm.

Xi *et al.* prepared PMMA/$CaCO_3$ nanocomposites using reverse micro-emulsion approach.[38] Water in oil (w/o) microemulsion generally consists of small water droplets surrounded by a surfactant monolayer and dispersed in an oil-rich continuous phase. The particle size of the water droplets is less than 100 nm, allowing the controlled synthesis of inorganic nanoparticles. Hence, the water droplet is called a microreactor and has been used for chemical preparation of relatively monodispersed nanoparticles of various inorganic materials. Xi *et al.* took advantage of the good dispersion of such microreactors in an oily phase to modify nano-$CaCO_3$ with methyl methacrylate (MMA), rather than a non-reactive solvent, as the oil phase and to polymerize MMA in the presence of nano-$CaCO_3$ subsequently. The advantage of this approach is that the processes of modifying nano-$CaCO_3$ with organic agents and dispersing the modified nanoparticles into the precursors are combined together. The dynamic mechanical analysis (DMA) performed on the nanocomposites proved that an interface layer was formed around the nanoparticles. The motion of polymer chains in the interface layer was restricted because of the strong interactions between the nanoparticles and the matrix. The glass transition temperature of the interface layer was higher than that of the matrix because the mobility of the polymer chains was reduced, i.e. the nanoparticles functioned as crosslinkers in the interface layer.[38]

Although poly(vinyl chloride) (PVC) is a major commercial thermoplastic, its processability, thermal stability and mechanical properties are inferior to other commodity plastics such as polyethylene and PP. Incorporating inorganic fillers into PVC can improve these properties. The mechanical properties of these composites are strongly influenced by the filler aspect ratio. Polymer/clay nanocomposites are known to exhibit high strength, superior modulus, good heat distortion temperature, enhanced barrier, and flame retardant properties. Their low fracture toughness has, however, limited their applications.[39] To tackle this issue, Xie *et al.* prepared a series of PVC/$CaCO_3$ nanocomposites by in-situ

polymerization of vinyl chloride in the presence of $CaCO_3$ nanoparticles.[18] It was found that in the presence of 5 wt.% or less nano-$CaCO_3$ the nanoparticles could be uniformly distributed in the PVC matrix at nanometer-scale during the polymerization. At the optimum filler content of 5 wt.% the nanocomposite provided good thermal properties as well as the highest Young's modulus, tensile yield strength, elongation-at-break, and impact resistance.

16.3.2 Melt compounding

The melt compounding method has been extensively used to fabricate polymer nanocomposites[14–17,31,40–53] for several reasons. Firstly, it is environmentally benign due to the absence of organic solvents. Secondly, it is compatible with conventional industrial processes, such as extrusion, injection molding and other polymer processing techniques, thus can be easily commercialized. It is also a convenient and flexible process capable of producing a variety of formulations on a variety of product volume scales. Thirdly, the high-shear environment in an extruder or mixer may permit the incorporation of significantly higher loadings of nanoparticles in comparison with the nanoparticle loadings achievable by a commercial in-situ polymerization process. And finally, the melt compounding method may allow the use of polymers which are not suitable for in-situ polymerization.[2]

Nevertheless, direct melt-compounding of polymers with nanofillers achieved only limited success for most systems due to the high tendency of the nanoparticles to form larger aggregates during melt-blending, which diminishes the advantages of their small dimensions. In addition, polymer degradation upon melt compounding is sometimes severe, which cannot be overcome easily.[53] These limitations should be considered when using the melt compounding method to prepare nanoparticle-filled polymer composites. In addition to surface treatment, size and loading level of nanofillers, melt-processing conditions, such as processing temperature and time, shear force and configuration of the processing machines, can also be adjusted in order to achieve good dispersion of nanoparticles in polymer matrices.[31] Sometimes, appropriate compatibilizers are added to obtain ternary systems in order to improve the particle dispersion, and/or miscibility and adhesion between the nanofillers and the matrix.[16,44]

Chen *et al.* prepared PVC/nano-$CaCO_3$ and PVC/acrylonitrile-butadiene-styrene terpolymer (ABS)/nano-$CaCO_3$ composites by melt-mixing different concentrations of stearic acid modified nano-$CaCO_3$ with the matrices in a high-speed two-roll mixer at different processing temperatures.[40] TEM study revealed that the nano-$CaCO_3$ particles with size of 30–45 nm were dispersed uniformly at nanometer-scale in both PVC and the PVC/ABS blend. In particular a mono-dispersion of nano-$CaCO_3$ in the PVC matrix was observed at filler content of 10 phr. This is a rare example where nano-$CaCO_3$ can achieve truly mono-

dispersion at relatively high filler contents through melt-mixing. The mechanical properties of PVC have been significantly enhanced after the addition of 10–15 phr nano-$CaCO_3$ fillers.

To facilitate uniform dispersion of nanoparticles and avoid severe property deterioration caused by degradation, master-batch method, i.e. melt-blending nanoparticles with a resin at a relatively high filler content first and then compounding the product with the raw resin again to a low filler content, is often used in nanocomposite fabrication. The application of this method to achieve better dispersion of nano-$CaCO_3$ in a PP matrix has been reported by Ren *et al*.[48] The PP/nano-$CaCO_3$ composites were prepared through one-step and two-step melt compounding, respectively. The results showed that with the same filler loading the two-step compounding (master-batch method) led to predominantly nanometer-scale dispersion of the nano-$CaCO_3$ while the one-step extrusion resulted in agglomeration of the nano-$CaCO_3$.

16.3.3 Solution-casting

Solution-casting is rarely used for fabrication of nanocomposites. It is viable only if in-situ polymerization and melt compounding processes are unsuitable due to the nature of a polymer matrix. An example is that biodegradable poly(L-lactide) (PLLA) composite films containing nano- and micro-$CaCO_3$ particles were prepared by Fukuda *et al.* via solution-casting using methylene chloride as a solvent.[54] The $CaCO_3$ particles were first surface-treated by different agents to improve the compatibility of filler with the matrix. The treated $CaCO_3$ particles were then dispersed into a polymer/methylene chloride solution by ultrasonication. After that, the solution was cast on a Petri dish, followed by rapid solvent evaporation at room temperature. The solvent trapped in the resulting solid was extracted with methanol and dried in vacuum for a few days. Finally, the as-cast films were compression molded using a hot press to form the composite films. It was found that the composites exhibited higher weight loss rates than the pure PLLA film during enzymatic hydrolysis, which implies that the solution-casting has led to a good dispersion of the $CaCO_3$ particles, resulting in enormously large interfacial area susceptible to enzymatic hydrolysis.[54]

16.4 Characterization

16.4.1 Morphology and dispersion of nano-$CaCO_3$

As discussed in the previous sections, polymers filled with nano-$CaCO_3$ may exhibit superior properties over their counterparts filled with micro-$CaCO_3$ only if the nanometer-scale dimension of the dispersed phase is retained within the polymer matrices. Examination of morphology of polymer/$CaCO_3$ nano-

composites is, therefore, a critical step for understanding processing-morphology-property relations of the nanocomposites.

Transmission electron microscopy (TEM)

The nanometer-scale dispersion of $CaCO_3$ particles in polymer matrices is best investigated with TEM. A good example is TEM micrographs of melt-mixed PVC/nano-$CaCO_3$ and PVC/ABS/nano-$CaCO_3$ composites presented in ref. 40. The TEM micrographs show a mono-dispersion of nano-$CaCO_3$ in the PVC matrix as indicated by the regular shape and narrow size distribution of the nanoparticles. In contrast, at the same filler content, the nano-$CaCO_3$ particles in the PVC/ABS blend apparently have a wider size distribution and the shape of some larger particles appears to be irregular, which implies that these large particles are actually agglomerates. This work demonstrated the capability of TEM in determination of the degree of dispersion of nano-$CaCO_3$ in polymer matrices precisely.

TEM is also useful in identification of aggregation morphology of nano-$CaCO_3$ in polymer matrices. For example, Wang *et al.* presented TEM micrographs showing the formation of chain-like aggregates along the melt-flow direction in a injection-molded PP/high density polyethylene (HDPE)/nano-$CaCO_3$ composite sample.[52] With the aid of TEM, the effects of matrix,[40] filler content,[14,18,40,52] composite fabrication methods[48] on morphologies of various polymer/$CaCO_3$ nanocomposites have been studied.

Scanning electron microscopy (SEM)

Scanning electron microscopy (SEM) has been widely used to examine morphological features of polymer/$CaCO_3$ nanocomposites due to the simplicity of preparation of fractured surfaces compared to ultra-microtome sectioning required for preparation of TEM samples. While TEM provided unambiguous evidence for nanometer-scale dispersion of $CaCO_3$ particles, SEM is not particularly effective in this respect. It is mainly used in examining micron-scale agglomeration.

SEM is also a useful tool for evaluation of interfacial interactions. If severe agglomeration occurs, debonded agglomerates and holes may be observed on fractured surfaces of polymer/nano-$CaCO_3$ composites, which is a sign of extremely poor interfacial adhesion. When agglomerates are small and the majority of agglomerates are embedded in the matrix on the fractured surface, a sharp interface boundary also implies weak interfacial adhesion between the two phases. Sharp interfacial boundaries can be observed clearly under SEM even if a predominantly nanometer-scale dispersion of $CaCO_3$ is achieved,[31] and it is a distinctive morphological feature for most melt-compounded polymer/nano-$CaCO_3$ systems. In contrast, with adequate surface modification of nano-$CaCO_3$,

in-situ polymerization may yield not only a homogenous dispersion of the nanoparticles but also strong interfacial adhesion. For example, SEM studies showed that the nano-$CaCO_3$ particles in in-situ polymerized PET/nano-$CaCO_3$[32] and PMMA/nano-$CaCO_3$[35,38] were largely embedded in the matrices on the fractured surfaces without clear interfacial boundaries between the two phases.

Numerous SEM studies have been devoted to investigation of toughening mechanisms of polymer/nano-$CaCO_3$ composites, which will be discussed together with mechanical properties of the nanocomposites in section 16.4.4.

16.4.2 Thermal transitions and properties

Glass transition temperature (T_g)

The presence of rigid fillers in a polymer matrix generally leads to a slight increase of T_g with respect to the neat resin, usually only a few degrees, depending on the nature of the polymer matrix and the filler. In the case of nano-$CaCO_3$ filled polymers, the increase of T_g could be much more significant under some circumstances. Avella *et al.* reported T_g of in-situ polymerized PMMA/nano-$CaCO_3$ measured using differential scanning calorimetric (DSC).[35] The presence of nanoparticles shifted T_g to much higher values, as shown in Fig. 16.4. It was attributed to the strong interfacial interactions between the nano-$CaCO_3$ and the PMMA matrix, which hindered the motion of polymer chain segments. A significant increase of T_g with the addition of only 2 wt.% nano-$CaCO_3$ was also observed in in-situ polymerized PET/nano-$CaCO_3$.[32] The addition of untreated nano-$CaCO_3$ into PET led to a moderate increase of T_g (5ºC) while with the addition of stearic acid treated nano-$CaCO_3$ the T_g rose much more significantly (14ºC), which demonstrated the importance of

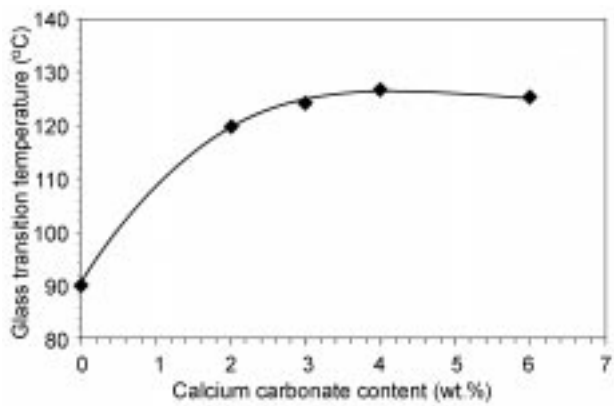

16.4 Glass transition temperature of in-situ polymerized PMMA/$CaCO_3$ nanocomposites as a function of filler content. Adopted from ref. 35 (Table 2).

interfacial interactions. The much higher T_g values were confirmed as not being caused by PET crystallinity change as in both cases the crystallinity was either reduced or unchanged.

As the effect of nano-$CaCO_3$ on T_g of the nanocomposites is strongly dependent on filler-matrix interactions, it is not surprising that it varies largely from system to system. In contrast to the aforementioned systems, there are also many polymer/nano-$CaCO_3$ systems where nano-$CaCO_3$ fillers only impose slight changes on T_g.[18,40,55,56] Chen *et al.* used DMA to measure T_g of PVC/nano-CO_3 and PVC/ABS/nano-$CaCO_3$ prepared by melt-mixing and observed only about 2ºC increase in T_g at filler contents of up to 15 phr despite the fact that excellent nanometer-scale dispersion was achieved for the two systems.[40] Xie *et al.* observed a slight increase of T_g from in-situ polymerized PVC/nano-$CaCO_3$ at filler concentrations up to 5 wt.%, while at 7.5 wt.% T_g was almost the same as that of the neat PVC due to agglomeration of the nano-fillers.[18] Kovačević *et al.* reported a moderate increase of T_g in poly(vinyl acetate) (PVAc)/nano-$CaCO_3$ prepared by emulsion blending.[56] A second tan δ peak was, however, also observed at about 60ºC above the T_g at a high filler loading of 24 wt.%, as shown in Fig. 16.5. The peak was assigned to the restricted motions of PVAc chains in the interface region due to the strong interactions between PVAc and the fillers. The appearance of two transitions was the result of the heterogeneously distributed regions of very different molecular mobilities. Similar behavior was also observed from a PMMA/$CaCO_3$ nanocomposite

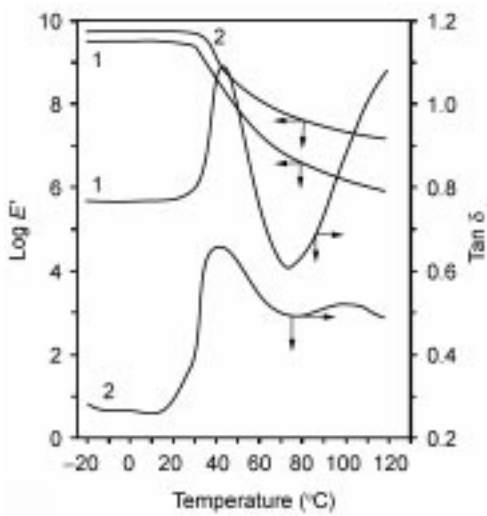

16.5 Change of storage modulus E′ (MPa) and tan δ with temperature for the PVAc/nano-$CaCO_3$ composites with filler loadings: (1) 12 vol.% and (2) 24 vol.%. Reprinted from ref. 56 (Figure 6), Copyright © (2002), with permission from Koninklgke Brill NV, Leiden, The Netherlands.

prepared by reverse microemulsion where the PMMA matrix had much lower T_g than the interfacial layer because a part of surfactants was dissolved in the matrix.[38]

Positron annihilation has been proven to be an effective tool to probe the interfacial characteristics of polymer nanocomposites. Zhang *et al.* used positron annihilation to study structures of melt-compounded HDPE/$CaCO_3$ nanocompositites in which nano-$CaCO_3$ fillers were treated with a coupling agent.[57] A rapid decrease of free-volume concentration with increasing nano-$CaCO_3$ weight fraction was observed. An interfacial layer between the nano-$CaCO_3$ fillers and HDPE was also detected, which verified that the interactions between the nano-$CaCO_3$ and HDPE matrix indeed restricted the chain segmental motion and reduced the mobilization of polyethylene chains.

Crystallization behaviors

In semicrystalline polymers, nano-$CaCO_3$ can also induce crystalline structural and morphological changes of the matrices, which may exert a great impact on mechanical properties of the nanocomposites. In this respect, the most extensively studied system is PP.

It is well known that isotactic polypropylene can simultaneously crystallize into three crystalline forms, namely α-, β- and γ-forms. Their relative amounts are essentially determined by crystallization conditions such as crystallization temperature, pressure and cooling rate. The α-phase crystallites are usually the predominant part in neat PP, while the β- and the γ-phase crystallites may develop substantially under some special circumstances, such as using β-phase nucleating agents or under high pressure.[58,59] The toughness of the β-phase PP is higher than that of the α-phase PP at temperatures both below and above glass transition temperature.[60] Several groups consistently reported that the addition of nano-$CaCO_3$ into PP could promote the formation of the β-phase PP crystallites,[14,17,48,61] which is an interesting comparison to a recent report that nano-clay could significantly inhibit the β-phase formation.[62] Zhang *et al.* measured β-form index (K value) of PP/$CaCO_3$ nanocomposites using wide angle X-ray scattering, as shown in Fig. 16.6, and found that the K value was significantly increased with the addition of nano-$CaCO_3$ into PP.[17] With the presence of polyoxyethylene nonyphenol as an interfacial modifier the increase of the K value was more prominent. Yang *et al.*, on the other hand, reported that nano-$CaCO_3$ whiskers (average size 100 nm) significantly promoted the β-phase formation while spindle-shaped submicro-$CaCO_3$ (average size 500 nm) promoted the β-phase formation very slightly.[61] These results imply that the formation of the β-phase is affected by both the surface area and the nature of the surface. More systematical and in-depth studies are required to clarify the mechanisms behind this.

Nano-$CaCO_3$ also have profound influence on crystallization temperature, crystallization rate, crystallinity and crystalline morphology of PP.[14,17,29,49,61] In

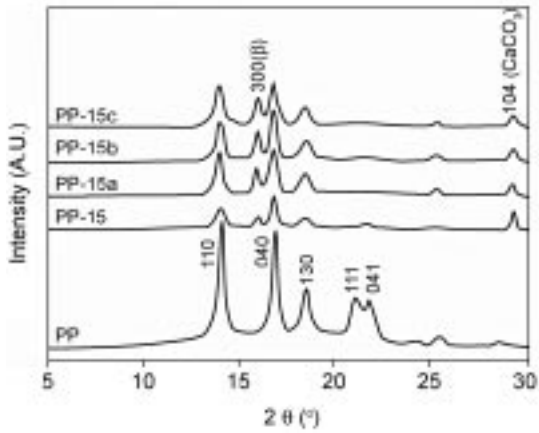

16.6 X-ray diffraction of neat PP and PP/nano-$CaCO_3$ composites. From bottom to top: neat PP; PP with 15 wt.% nano-$CaCO_3$; PP with 15 wt.% nano-$CaCO_3$ and 0.75 wt.% nonionic modifier; PP with 15 wt.% nano-$CaCO_3$ and 1.50 wt.% nonionic modifier; PP with 15 wt.% nano-$CaCO_3$ and 2.25 wt.% nonionic modifier. Reprinted from ref. 17 (Figure 4), Copyright © (2004), with permission from Elsevier.

general, nano-$CaCO_3$ fillers exhibit heterogeneous nucleation effect in PP as indicated by an increase in crystallization temperature in cooling processes and a decrease in spherulite size.[14,17,49] Well-dispersed nanoparticles can act as multi-nuclei leading to a huge number of very small spherulites,[14,17,49,63] which may have a positive effect on fracture toughness of the nanocomposites. The nucleating effect is dependent on filler content as the agglomeration occurring at high filler contents can weaken the effect.[49] For crystallinity and overall crystallization rate, the effects of nano-$CaCO_3$ are more complex. The nanoparticles may promote crystallization by acting as nucleating agents while they may also decrease the spherulite growth rate by hindering orderly packing of chain segments at late stages. The trend thus varies from system to system depending on the degree of the dispersion and the extent of the interfacial interactions.[14,17,29,49]

The synergistic effect of nano-$CaCO_3$ and an organic nucleating agent on crystallization behavior of PP copolymers has been studied by Zhu *et al*.[37] The nanocomposites were made by in-situ copolymerization of propylene with a low content of ethylene units in the presence of nano-$CaCO_3$ and an organic phosphate nucleating agent. The results of Avrami analysis showed a dramatic decrease in the half-life of crystallization and a significant increase of the overall crystallization rate in the presence of the organic nucleating agent, and the effects were further enhanced in the presence of both the organic nucleating agent and the nano-$CaCO_3$. Incorporation of the nano-$CaCO_3$ particles into the PP copolymer both formed much finer spherulites and increased the crystallinity, thus significantly augmenting the flexural modulus and impact strength as well as heat distortion temperatures.

Although most efforts in this area were devoted to PP/$CaCO_3$ nanocomposites, nucleating effect of nano-$CaCO_3$ was also detected in other systems. In our laboratory (Nanyang Technological University), two types of nano-$CaCO_3$ fillers treated with stearic acid and Portuguese gum rosin, respectively, were melt compounded with HDPE in the filler concentration range of 0 to 10 wt.%. With increasing the filler content both showed a slight increase in crystallization temperature upon cooling, while the influence of rosin treated nano-$CaCO_3$ was very weak probably due to the reactive nature of rosin. Crystallization behaviors of in-situ polymerized PET/nano-$CaCO_3$ has been studied by Lorenzo *et al*.[32] Without surface treatment, the nano-$CaCO_3$ fillers slightly retarded the crystallization of PET while nano-$CaCO_3$ particles coated with stearic acid were effective nucleating agents for PET.

Thermal stability

Thermogravimetric analyses (TGA) have confirmed the general enhancement of thermal stability of various polymer/$CaCO_3$ nanocomposites relative to the base polymers. Di Lorenzo *et al.* reported that the presence of 2 wt.% nano-$CaCO_3$ in PET raised the degradation temperature (temperature at 5% weight loss) of the material by about 15ºC.[32] Xie *et al.* reported a marginal increase of the degradation temperature of in-situ polymerized PVC/$CaCO_3$ nanocomposites with increasing filler loading.[18] It was proposed that the higher thermal degradation temperature may be related to the reduced long-range chain mobility in the nanocomposites[18] or modified polymer thermal degradation mechanism[32] due to polymer-filler interactions. Both hypotheses are subject to further experimental verification.

16.4.3 Thermal dynamic properties

Thermal dynamic properties of a few polymer/nano-$CaCO_3$ systems have been investigated using dynamic mechanical analysis (DMA). In general, the addition of nano-$CaCO_3$ fillers would lead to an increase of storage modulus (E′), albeit small, in a wide range of temperatures due to the reinforcement effect from the rigid nanoparticles. An example has been shown in Fig. 16.5, where the storage modulus of PVAc/nano-$CaCO_3$ increases with increasing the filler content.[57] Similar behavior was also observed for melt-mixed PVC/nano-$CaCO_3$ and PVC/ABS/nano-$CaCO_3$,[40] and in-situ polymerized PVC/nano-$CaCO_3$[18] systems.

16.4.4 Mechanical properties

Corporative stiffening and toughening effect in thermoplastics

It has long been known that micron-sized $CaCO_3$ can serve as reinforcing fillers to improve stiffness of thermoplastics, while the enhanced stiffness is usually

Table 16.2 Corporative stiffening and toughening effect of nano-$CaCO_3$ in common thermoplastics. Adopted from refs 18, 31 and 51

Matrix	Average filler diameter (nm)/ surface treatment	Change of mechanical properties with respect to the matrix at the filler content of 5 wt.%			Ref.
		Tensile modulus	Tensile yield strength	Notched impact strength	
PVC	44/stearic acid	~19% increase	No change	~70% increase (Charpy)	18
PP	70/stearic acid	~38% increase	~4% increase	~137% increase (Izod)	31
HDPE	*	~10% increase	~10% increase	~80% increase (Izod)	51

* not disclosed.

accompanied by a depression of toughness. In 1980s researchers discovered that if relatively high concentrations of sufficiently fine $CaCO_3$ particles are well dispersed in quasi-ductile polymer matrices, such as PP and HDPE, they may also play the role of toughening agents.[64,65] The findings spurred great interest on polymer/$CaCO_3$ nanocomposites. Through extensive research in the past few years, prominent toughening effect of nano-$CaCO_3$ in common thermoplastics has now been well established, although the mechanisms behind it are still subject to debate. Moreover, the corporative stiffening and toughening effect can be achieved by nano-$CaCO_3$ at fairly low filler contents, as exemplified in Table 16.2. This makes nano-$CaCO_3$ fillers a unique choice in the plastics industry.

Tensile behaviors of nano-$CaCO_3$ filled thermoplastics

Among tensile properties, modulus and yield strength have primary importance, which give information on the stiffness and the maximum allowable load without considerable plastic deformation. For polymer/$CaCO_3$ nanocomposites, in general, with increasing filler content, the tensile modulus increases, while the yield strength may increase or decrease depending, to a great extent, on the degree of dispersion and the interfacial adhesion between the matrix and the fillers.[14,17,18,66,67] An example is given in Fig. 16.7, in which the stearic acid modified nano-$CaCO_3$ fillers gave rise to better tensile properties, especially the yield strength, because they provided stronger interfacial adhesion than the untreated ones. The increase of Young's modulus with increasing nano-$CaCO_3$ content was attributed to the stiff nature of the fillers. Various classic theories have been used to simulate the quantitative relations between the tensile properties and the filler content for the nanocomposites,[14,17,18] but most experimental results indicated the limitation of the theories when applied to

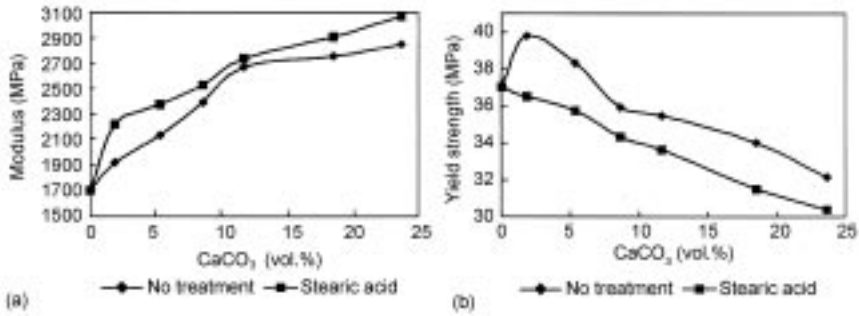

16.7 Tensile properties of PP/$CaCO_3$ nanocomposites as a function of filler content. (a) modulus; (b) yield strength; Reprinted from ref. 31 (Figure 2), Copyright © (2002), with permission from Springer Science and Business Media and Professor Rui Huang, Sichuan University, China.

nanocomposites.[14,18] For semi-crystalline matrices, it is believed that both the reinforcing effect and nanofiller-induced variation of crystallinity and crystalline morphology would affect tensile properties.

Toughening effect of nano-$CaCO_3$ and the mechanisms

Impact property of polymer/$CaCO_3$ nanocomposites has been extensively investigated.[14,17,18,31,40,46–53,67,68] In brittle or quasi-ductile matrices like PVC, PP and HDPE, in general as nano-$CaCO_3$ loading increases, the impact energy of the nanocomposites would increase until reaching a maximum, and then decrease continuously. An example is given in Fig. 16.8 where notched Izod impact energy of melt-compounded PP/$CaCO_3$ nanocomposites was plotted as a function of filler content.[31] The filler loading corresponding to the maximum impact strength and the extent of enhancement of the impact strength with respect to the neat resin vary from system to system, which depend primarily on the degree of dispersion of nano-$CaCO_3$ fillers and interfacial properties. In Fig. 16.8 the highest impact strength corresponds to the nano-$CaCO_3$ treated by stearic acid in an ultra high speed mixer because the fillers treated in this way were dispersed most uniformly in the matrix, as shown in Fig. 16.3(b).[31] In contrast, for the untreated fillers the impact strength was only marginally increased at very low filler contents. At high filler contents severe agglomeration caused the decrease of the impact strength.

The general idea behind using rigid fillers as toughening agent mimics the cavitation mechanism in rubber toughened thermoplastics.[64] The rigid particles act as stress concentrators because they have different elastic properties from that of the polymer matrices. Stress concentration causes building up of triaxial stress around the filler particles, which leads to debonding at the particle-polymer interface. The voids created by debonding alter the stress state in the polymer matrix surrounding the voids. This reduces the sensitivity towards

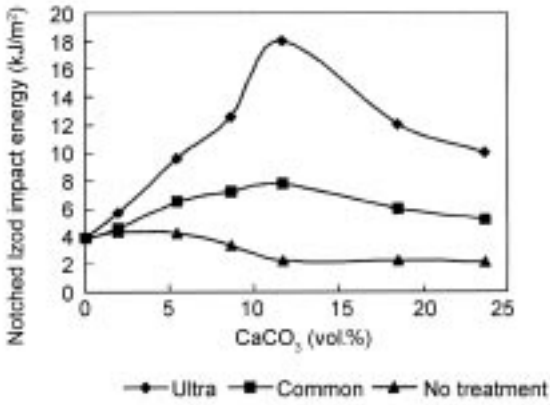

16.8 Impact energy of PP/$CaCO_3$ nanocomposites as a function of filler content. Reprinted from ref. 31 (Figure 3), Copyright © (2002), with permission from Springer Science and Business Media and Professor Rui Huang, Sichuan University, China.

crazing since the volume strain is released. The shear yielding mechanism thus becomes operative and the material is able to absorb large quantities of energy upon fracture. Moreover, the tip of the crack is blunted and the stress concentration is alleviated, resulting in slowing down of the propagation of cracks. Use of nanoparticles, on the one hand, would make the number of stress concentrators per volume much larger than that in micro-composites so that a larger number of voids can be created to induce shear yielding and hence absorb a greater amount of impact energy at fairly low filler loadings. On the other hand, it would ensure the voids that are created are small and do not act as initiation sites for the fracture process. A homogeneous dispersion of $CaCO_3$ particles in polymer matrices at nanometer-scale is, therefore, the key to the toughening effect, and a severe particle aggregation would alter the deformation mechanism and induce brittle failure.[67]

Successful toughening of rigid PVC with nan-$CaCO_3$ provided experimental evidence to the cavitation theory.[18,40] Xie *et al.* reported that the notched Charpy impact energy of an in-situ polymerized PVC/$CaCO_3$ nanocomposite with the filler content of 5 wt.% was 70% higher than that of the neat PVC. The corresponding impact-fractured surface of the nanocomposite was examined using SEM. Typical ductile characteristics, a rough fractured surface with a few elliptical voids around $CaCO_3$ particles due to interfacial debonding, were observed, as shown in Fig. 16.9.[18] Obviously, cavitation and the cavitation-trigged-matrix shear contributed to the energy-dissipation. While for the neat PVC, a surface typical of brittle failure was observed.

The cavitation mechanism presumably also works for nano-$CaCO_3$ filled PP and HDPE systems. Some evidence has been found through morphological

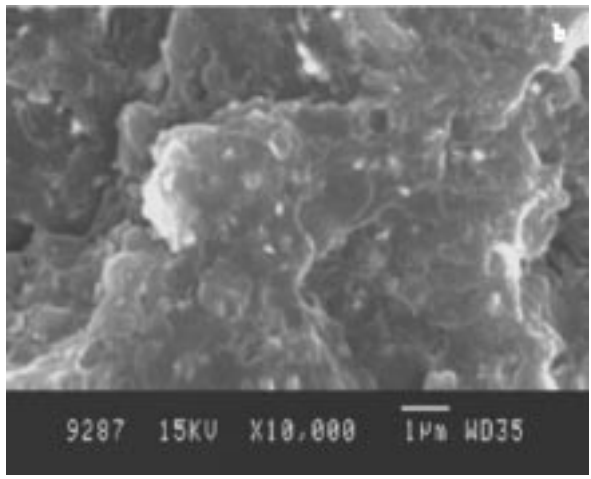

16.9 A SEM micrograph showing the surface of an impact-fractured PVC/$CaCO_3$ composite with 5.0 wt.% nano-$CaCO_3$. Reprinted from ref. 18 (Figure 12), Copyright © (2004), with permission from Elsevier.

studies.[14] It is, however, important to note that PP and HDPE are semi-crystalline polymers with relatively high crystallinity. Although the addition of nanofillers usually does not lead to a marked change in crystallinity, it does alter the crystalline morphology enormously, which includes increasing the number of spherulites per volume, reducing spherulite size, creating a large number of imperfection sites, and the possibility of formation of an interfacial layer with amorphous[14] or unique crystalline morphological features.[69] These factors have been accounted for when discussing the toughening effect of nano-$CaCO_3$ in PP and HDPE, but it is not clear to what extent they contribute to the impact energy absorption. The addition of nano-$CaCO_3$ into PP presents extra complexity as the fillers may also promote the β-form formation, as discussed earlier. There was indeed such an example that impact energy absorption of a PP/$CaCO_3$ nanocomposite was increased to about three times that of the neat PP but there were few signs of plastic deformation or debonding even in the region near the notch root.[17] Much further work is necessary to unfold the toughening mechanisms due to these rigid particles.

Blending of a thermoplastic with a rubber is an effective way to increase its toughness but one drawback of rubber toughening is the significant loss of both tensile strength and stiffness, especially at relatively high rubber concentrations. The mechanical properties of rubber toughened plastics are critically controlled by morphology of the blends, and may be severely deteriorated by coalescence of dispersed rubber domains at high rubber concentrations. Hrnjak-Murgiæ *et al.* reported that the addition of 5 wt.% nano-$CaCO_3$ into a rubber toughened styrene-acrylonitrile copolymer (SAN) caused significant improvement of compatibility between the two polymer phases, especially when the filler was

surface treated with sodium stearate.[30] As the extent of the surface modification increased, the rubber domain size decreased because interfacial tension was reduced. The impact strength, tensile strength and elongation at break were thus improved cooperatively. The work demonstrated that synergistic use of rubber and properly surface-treated nano-$CaCO_3$ may help fine control of the phase morphology of multiphase polymer blends and impark desirable mechanical properties of these materials.

Reinforcing effect of nano-$CaCO_3$ in rubbers

In addition to the stiffening and toughening effects of nano-$CaCO_3$ in plastics, its reinforcing effect in rubbers has also attracted great attention. Research showed that the addition of nano-$CaCO_3$ into rubbers provided them with higher tensile strength and elongation at break, better tear and abrasion resistance, greater flexibility and lower hardness in comparison with their counterparts filled with micro-$CaCO_3$ at the same loadings.[70] The improvements were attributed to the larger surface area of the nano-$CaCO_3$ fillers and their ability to form chain-like morphology in rubbers.

Nano-$CaCO_3$ alone as reinforcement cannot yield adequate mechanical properties, especially strengths, for most practical applications. It is usually used together with carbon black to achieve synergistic reinforcing effect. For example, when carbon black was used as reinforcement in styrene-butadiene rubber (SBR) alone, the strength of the rubber was greatly improved but elongation at break was relatively low and the hardness relatively high.[71] When nano-$CaCO_3$ and carbon black were used together, elongation at break was increased significantly and hardness reduced while the tensile and tear strengths only deteriorated slightly, as shown in Table 16.3.

The reinforcing effects of nano-$CaCO_3$ in various rubbers, which include natural rubber (NR) and butadiene rubber (BR),[70] SBR, SBR/NR and SBR/BR blends,[71] nitrile rubber[72] and ethylene-propylene-unconjugated diene ter-polymers (EPDM),[70] have been studied. Property improvements were found

Table 16.3 Mechanical properties of styrene-butadiene rubber (SBR) filled with nano-$CaCO_3$ (CC) and/or carbon black (CB). Adopted from ref. 71

Property	Filler content				
	0	25 phr CC	50 phr CC	50 phr CB	25 phr CC + 50 phr CB
Tensile strength (MPa)	1.51	1.75	3.05	20.67	17.94
Elongation at break (%)	251	256	387	389	478
Tear strength (kN/m)	6.71	11.85	18.26	35.73	34.60
Shore A hardness	45	50	54	70	63

in all systems but to fairly different extents, which depended not only on rubber type but also on formulations and processing conditions.

16.4.5 Rheology

Rheological properties of polymers are important for their processing. To characterize rheological behaviors of polymer/$CaCO_3$ nanocomposites usually their viscosities are measured as a function of shear rate and temperature using a capillary rheometer.

Xie *et al.* studied rheological behavior of in situ polymerized PVC/$CaCO_3$ nanocomposites.[18] It was found that at low filler loadings (< 2.5 wt.%) and very low shear rates (< 100 s^{-1}), apparent viscosity of the nanocomposites was slightly higher than that of the neat PVC, while when the filler contents were relatively high (up to 7.5 wt.%) or at shear rates of above 100 s^{-1}, apparent viscosities of the nanocomposites were lower than that of the neat PVC, as shown in Fig. 16.10. They proposed that the nanoparticles served as 'ball bearings' reducing the interlayer interaction of PVC melts and hence the viscosity. The bearing effect became more prominent at high filler loadings and shear rates. Liang studied rheological behavior of melt-compounded ABS/nano-$CaCO_3$ and found that when the filler content was smaller than 10 wt.% entry pressure drop was relatively small at low shear stress.[41] The results were also interpreted using the concept of bearing effect, it was claimed that the effect acted only at relatively low filler loadings (< 10 wt.%) and at higher filler loadings the particles inhibited the polymer chain motion and hence the flow

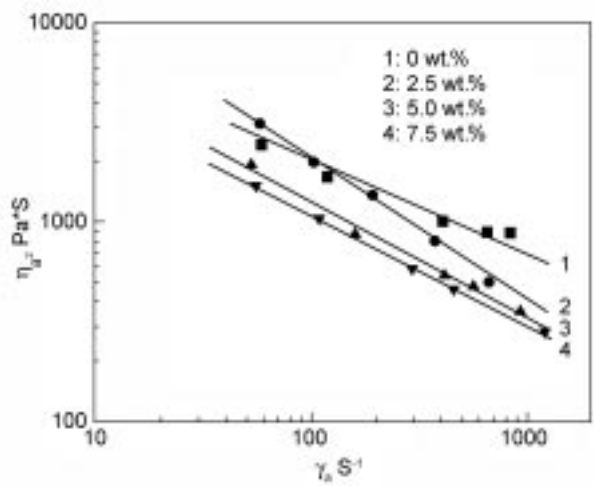

16.10 Rheological curves for neat PVC and PVC/nano-$CaCO_3$ composites at 175°C. Reprinted from ref. 18 (Figure 5), Copyright © (2004), with permission from Elsevier.

resistance increased. More experimental data from different systems need to be collected to confirm the 'ball bearing' effect of cubic nano-$CaCO_3$ in polymer melts.

Wang *et al.* studied shear viscosity of plasticized PVC filled with micro- and nano-$CaCO_3$, respectively, at room temperature using a rotational rheometer.[73] With the addition of nano-$CaCO_3$ the pastes were pseudoplastic with a yield point. They experienced significant shear thinning at a certain shear rate when the nano-$CaCO_3$ content was higher than 20 phr while the extent of shear thinning was much less in micro-$CaCO_3$ filled PVC pastes even at the filler contents of up to 50 phr. It was proposed that the presence of nano-$CaCO_3$ at high concentration has created a reversible gel-like structure. The relatively weak inter-particle interaction led to aggregation of modified nano-$CaCO_3$ particles at low shear rates while the aggregation could be destroyed at high shear rates which resulted in shear thinning. At high filler contents, thixotropy behavior of the nano-$CaCO_3$ filled pastes was also improved over that of micro-$CaCO_3$ filled ones.

16.4.6 Other properties

Abrasion resistance

It has been reported that the presence of nano-$CaCO_3$ strongly improved the abrasion resistance, as well as wear resistance, of PMMA.[36] The findings were attributed to the fact that the nanoparticles supported part of the applied load, thus the penetration into the polymer surface was reduced and only microploughing and/or microcutting phenomena could be generated. The wear behavior was significantly different from that of conventional micro-composites.

Weathering resistance

Most thermoplastics degrade rapidly when used outdoors because of photo-oxidation promoted by ultraviolet (UV) irradiation. A recent study on natural weathering of micro-$CaCO_3$ filled PP showed that the composites filled with surface treated $CaCO_3$ provided better retention of mechanical properties than those filled with untreated fillers, which demonstrated the importance of interfacial properties.[74] Weathering behaviors of nano-$CaCO_3$ filled polymers have not been reported, and a study on this topic would be useful for exploring applications of the nanocomposites.

16.5 Applications

Nano-$CaCO_3$ is widely used in plastics, rubbers, coatings/paints, papers, printing inks, cosmetics, pharmaceuticals and other synthetic or natural materials as

fillers or additives.[75] This section focuses on the applications of nano-$CaCO_3$ fillers in common thermoplastics and rubbers.

There are three main reasons for choosing nano-$CaCO_3$ as fillers in plastics:

- to improve mechanical properties, such as stiffness and toughness, of the materials
- to modify processing behaviors of the materials
- to reduce the cost of final products.

For example, nano-$CaCO_3$ filled PVC/chlorinated polyethylene (CPE) blends have been used for manufacturing window profiles where high stiffness and toughness, good flow property and low cost are essential.[68,76] Another example is that PVC pastes filled with nano-$CaCO_3$ have been used as car underbody paints because of the improved rheological properties.[73,76] Moreover, the corporative stiffening and toughening effect of nano-$CaCO_3$ in commodity thermoplastics like PP and HDPE may allow the nanocomposites to be used for products which are traditionally made of engineering thermoplastics. Significant cost reduction can, therefore, be achieved. Lightness is another interesting aspect of polymer/$CaCO_3$ nanocomposites. The nanocomposites can possess excellent mechanical properties at fairly low filler loadings which indeed barely exceed 10% in weight. On the contrary, their micro-$CaCO_3$ filled counterparts for appliance applications usually have loading levels ranging from 15 to 50% in weight leading inevitably to heavier products.

Polymer/$CaCO_3$ nanocomposites also exhibit enhanced optical clarity and reduced haze in comparison with conventional micro-$CaCO_3$ filled polymers, which encourages their usage for packaging and optical applications. As an example, PMMA/$CaCO_3$ nanocomposites with low filler contents can provide improvements of mechanical and thermal properties over neat PMMA without significant loss in clarity, and may be used in optical devices.[35]

Nano-$CaCO_3$ can be used as reinforcing fillers in rubbers as a partial replacement for carbon black or silica. It has been used together with carbon black or other ceramic fillers, such as TiO_2 and $MgCO_3$, for seals, oil-resistant rubber pipes, shoe components, bicycle tires, car tires, etc.[77] It is particularly suitable for use in light-colored rubber products.

16.6 Conclusions and future trends

Polymer/$CaCO_3$ nanocomposites have developed rapidly in the past few years. Cubic nano-$CaCO_3$ particles with narrow size distribution can now be produced on a massive scale at relatively low cost. Nanometer-scale dispersion of $CaCO_3$ particles in common polymer matrices has been successfully achieved via in-situ polymerization and/or melt-compounding with the aid of organic modification of filler surface. The nanocomposites fabricated possess a combination of good mechanical properties, processability and improved temperature resistance at

low filler loadings. Their performance clearly exceeds that of related micro-composites. One notable difference is the corporative toughening and stiffening effect of nano-$CaCO_3$. The technology has been developed to the point where they are ready be applied to commercial products.

Polymer/$CaCO_3$ nanocomposite technology is still advancing quickly. The areas for future progress are:

- *Preparation of nano-$CaCO_3$ particles*. In addition to preparation of cubic nano-$CaCO_3$, some efforts have been made to synthesize high aspect ratio nano-$CaCO_3$ particles.[13] Further studies with these high aspect ratio fillers should also be fruitful, particularly in building a bridge to other nanofiller systems to advance the fundamental understandings of nanocomposites. The high aspect ratio nano-$CaCO_3$ may also bring the nanocomposites unexpected behavior, much as cubic nano-$CaCO_3$ provided its own surprises.
- *Filler surface modification and nanocomposite fabrication*. Agglomeration of nano-$CaCO_3$ in the surface modification process has remained a major problem because of the enormous interfacial area of the nanoparticles. The uniform dispersion of nano-$CaCO_3$ in polymer precursors and melts, therefore, still presents a key challenge for the in-situ polymerization and melt compounding approaches. Carefully engineering and full understanding of interfacial properties are needed, and ultimately many perspectives will develop, dictated by the final applications of each specific system.
- *Characterization*. The studies completed so far leave several fundamental questions unanswered. The toughening mechanisms, especially the relative contributions of debonding, shear yielding and filler-induced crystallization variation to impact energy absorption, are still unclear. Progress in this area will require concerted efforts in both fracture mechanics and nanometer-scale structural characterization. Further rheological characterization is also demanded to understand the mechanism behind the 'ball bearing' effect of nano-$CaCO_3$. Data collection on environmental resistance and flame retardancy will be useful for defining the application areas of the nanocomposites.
- *Applications*. The extensive research work in the past few years has laid the ground for the transfer of polymer/$CaCO_3$ nanocomposites into production applications. A rapid growth in the use of the nanocomposites in commercial products, such as light-duty mechanical parts and small appliances, is therefore anticipated in the future.

16.7 References

1. Vaia R A, Wagner H D, 'Framework for nanocomposites', *Materials Today*, 2004 November 32–37.
2. Pinnavaia T J, Beall G W, *Polymer-Clay Nanocomposites*, Chichester, John Wiley & Sons, 2000.

3. Kruis F E, Fissan H, Peled A, 'Synthesis of nanoparticles in the gas phase for the electronic, optical, magnetic applications – a review', *J Aerosol Sci*, 1998 **29**(5–6) 511–535.
4. Hong L S, Lai H T, 'Pore structure modification of alumina support by SiC-Si3N4 nanoparticles prepared by the particle precipitation aided chemical vapor deposition', *Ind Eng Chem Res*, 1999 **38**(3) 950–957.
5. Jiang A Q, Li G H, Zhang L D, 'Dielectric study in nanocrystalline $Bi_4Ti_3O_{12}$ prepared by chemical coprecipitation', *J Appl Phys*, 1998 **83**(9) 4878–4883.
6. Chatterjee A, Chakravorty D, 'Electrical conductivity of sol-gel derived metal nanoparticles', *J Mater Sci*, 1992 **27**(15) 4115–4119.
7. Lopez Perez J A, Lopez Quintela M A, Mira J, 'Advances in the preparation of magnetic nanoparticles by the microemulsion method', *J Phys Chem B*, 1997 **101**(41), 8045–8057.
8. Mizukoshi Y, Okitsu Ki, Maeda Y, 'Sonochemical preparation of bimetallic nanoparticles of gold/palladium in aqueous solution', *J Phys Chem B*, 1997 **101**(36) 7033–7037.
9. Reverchon E, Della Porta G, Di Trolio A, 'Supercritical antisolvent precipitation of nanoparticles of superconductor precursors', *Ind Eng Chem Res*, 1998 **37**(3) 952–958.
10. Chen J F, Wang Y-H, Guo F, Wang X-M, Zheng C, 'Synthesis of nanoparticles with novel technology: high-gravity reactive precipitation', *Ind Eng Chem Res*, 2000 **39**(4) 948–954.
11. Mandal B M, 'Conducting polymer nanocomposites with extremely low percolation threshold', *Bull Mater Sci*, 1998 **21**(2) 161–165.
12. Guang Ping Nano Technology Group Ltd (Hong Kong) (http://www.gpnano.com/).
13. NanoMaterials Technology Pte Ltd (Singapore) (http://www.nanomt.com.sg).
14. Chan C-M, Wu J S, Li J X, Cheung Y-K, 'Polypropylene/calcium carbonate nanocomposites', *Polymer*, 2002 **43**(10) 2981–2992.
15. Wu D M, Meng Q Y, Liu Y, Ding Y M, Chen W H, Xu H, Ren D Y, '*In situ* bubble-stretching dispersion mechanism for additives in polymers', *J Polym Sci Part B Polym Phys*, 2003 **41**(10) 1051–1058.
16. Chen J F, Wang G Q, Zeng X F, Zhao H Y, Cao D P, Yun J, Tan C K, 'Toughening of polypropylene-ethylene copolymer with nanosized $CaCO_3$ and styrene-butadiene-styrene', *J Appl Polym Sci*, 2004 **94**(2) 796–802.
17. Zhang Q X, Yu Z Z, Xie X L, Mai Y-W, 'Crystallization and impact energy of polypropylene/$CaCO_3$ nanocomposites with nonionic modifier', *Polymer*, 2004 **45**(17) 5985–5994.
18. Xie X L, Liu Q X, Li R K Y, Zhou X P, Zhang Q X, Yu Z Z, Mai Y-W, 'Rheological and mechanical properties of PVC/$CaCO_3$ nanocomposites prepared by *in situ* polymerization', *Polymer*, 2004 **45**(19) 6665–6673.
19. Moczo J, Fekete E, Laszlo K, Pukanszky B, 'Aggregation of particulate fillers: factors, determination, properties', *Macromol Symp*, **2003** 194(1) 111–124.
20. Guillet A, 'Treatment of fillers with organofunctional silanes, technology and applications', *Macromol Symp*, **2003** 194(1) 63–74.
21. Yue C Y, Cheung W L, 'The morphology, character and strength of the interface in glass-fiber polypropylene composites', *J Mater Sci*, 1991 **26**(4) 870–880.
22. Rothon R, *Particulate-Filled Polymer Composites*, Harlow, Longman Sci. Technol., 1995.

23. Jones F R, *Interfacial Phenomena in Composite Materials*, London, Butterworths, 1989.
24. Demjen Z, Pukanszky B, Nagy J, 'Possible coupling reactions of functional silanes and polypropylene', *Polymer*, 1999 **40**(7) 1763–1773.
25. Akovali G, Akman M A, 'Mechanical properties of plasma surface-modified calcium carbonate-polypropylene composites', *Polym Int*, 1997 **42**(2) 195–202.
26. Demjen Z, Pukanszky B, Nagy J, 'Evaluation of interfacial interaction in polypropylene/surface treated $CaCO_3$ composites', *Composites A*, 1998 **29A**(3) 323–329.
27. Renger C J, Burrows S J, Shanks R A, 'Processing, crystallization, and dynamic mechanical analysis of high molar mass polysiloxane-modified PP/$CaCO_3$ composites', *J Appl Polym Sci*, 2001 **82**(12) 3091–3098.
28. Wu C L, Zhang M Q, Rong M Z, Friedrich K, 'Tensile performance improvement of low nanoparticles filled-polypropylene composites', *Compos Sci Technol*, 2002 **62**(10–11) 1327–1340.
29. Lin Z D, Huang Z Z, Zhang Y, Mai K C, Zeng H M, 'Crystallization and melting behavior of nano-$CaCO_3$/polypropylene composites modified by acrylic acid', *J Appl Polym Sci*, 2004 **91**(4) 2443–2453.
30. Hrnjak-Murgić Z, Jelčić Z, Kovačević V, Mlinac-Misak M, Jelencic J, 'Molecular and morphological characterization of immiscible SAN/EPDM blends filled by nano filler', *Macromol Mater Eng*, 2002 **287**(10) 684–692.
31. Wang G, Chen X Y, Huang R, Zhang L, 'Nano-$CaCO_3$/polypropylene composites made with ultra-high-speed mixer', *J Mater Sci Lett*, 2002 **21**(13) 985–986.
32. Di Lorenzo M L, Errico M E, Avella M, 'Thermal and morphological characterization of poly(ethylene terephthalate)/calcium carbonate nanocomposites', *J Mater Sci*, 2002 **37**(11) 2351–2358.
33. Usuki A, Kojima Y, Kowasumi M, Okada A, Fukushima Y, Kurauchi T, Kamigaito O, 'Synthesis of nylon 6-clay hybrid', *J Mater Res*, 1993 **8**(5) 1179–1184.
34. Ou Y C, Yang F, Chen J, 'Interfacial interaction and mechanical properties of nylon 6-potassium titanate composites prepared by in-situ polymerization', *J Appl Polym Sci*, 1997 **64**(12) 2317–2322.
35. Avella M, Errico M E, Martelli S, Martuscelli E, 'Preparation methodologies of polymer matrix nanocomposites', *Appl Organometal Chem*, 2001 **15**(5) 435–439.
36. Avella M, Errico M E, Martuscelli E, 'Novel PMMA/$CaCO_3$ nanocomposites abrasion resistant prepared by an *in situ* polymerization process', *Nano Lett*, 2001 **1**(4) 213–217.
37. Zhu W P, Zhang G P, Yu J Y, Dai G C, 'Crystallization behavior and mechanical properties of polypropylene copolymer by *in situ* copolymerization with a nucleating agent and/or nano-calcium carbonate', *J Appl Polym Sci*, 2004 **91**(1) 431–439.
38. Xi Q, Zhao C F, Yuan J Z, Cheng S Y, 'The effects of polymer-nanofiller interactions on the dynamical mechanical properties of PMMA/$CaCO_3$ composites prepared by microemulsion template', *J Appl Polym Sci*, 2004 **91**(5) 2739–2749.
39. Borchardt J K, 'PVC-calcium carbonate nanocomposites', *Materials Today*, 2004 November 26.
40. Chen N, Wan C Y, Zhang Y, Zhang Y X, 'Effect of nano-$CaCO_3$ on mechanical properties of PVC and PVC/Blendex blend', *Polym Test*, 2004 **23**(2) 169–174.
41. Liang J Z, 'Melt rheology of nanometer-calcium-carbonate-filled acrylonitrile-butadiene-styrene (ABS) copolymer composites during capillary extrusion', *Polym*

Int, 2002 **51**(12) 1473–1478.
42. Tang C Y, Liang J Z, 'A study of the melt flow behavior of ABS/$CaCO_3$ composites', *J Mater Process Technol*, 2003 **138**(1–3) 408–410.
43. Tang Y, Hu Y, Zhang R, Wang Z Z, Gui Z, Chen Z Y, Fan W C, 'Investigation into poly(propylene)/montmorillonite/calcium carbonate nanocomposites', *Macromol Mater Eng*, 2004 **289**(2) 191–197.
44. Su X Q, Hua Y Q, Qiao J L, Liu Y Q, Zhang X H, Gao J M, Song Z H, Huang F, Zhang M L, 'The relationship between microstructure and properties in PP/rubber powder/nano-$CaCO_3$ ternary blends', *Macromol Mater Eng*, 2004 **289**(3) 275–280.
45. Zeng X F, Chen J F, Wang G Q, 'Study on the toughened PVC blends with nano-$CaCO_3$ particles and elastic CPE particles', *Acta Polymeria Sinica*, 2002 **6** 738–741.
46. Ren X C, Bai L Y, Wang G H, 'Reinforcement and toughening of polypropylene composites by nanoparticle $CaCO_3$', *World of Chemistry* (in Chinese), 2000 **2** 83–87.
47. Xu W P, Huang R, Cai B H, Fan W Y, 'Nano-$CaCO_3$ filled HDPE composites', *China Plastics*, 1998 **12**(6) 30–34.
48. Ren X C, Bai L Y, Wang G H, Zhang B L, 'Study on reinforced polypropylene toughened by nano-$CaCO_3$ particles', *China Plastics*, 2000 **14**(1) 22–26.
49. Wang X, Huang R, 'Study on nano-$CaCO_3$ reinforced polypropylene', *China Plastics*, 1999 **13**(10) 22–25.
50. Luo Z F, Huang R, Lu A, Cai B H, Fan W Y, 'The influence of surface treatment on properties of HDPE/nano-$CaCO_3$ composites', *China Plastics*, 1999 **13**(1) 47–51.
51. Luo Z F, Huang R, Lu A, Cai B H, Fan W Y, 'Study on HDPE composites reinforced and toughened by nano-$CaCO_3$', *China Plastics*, 2000 **14**(8) 25–29.
52. Wang X, Huang R, Jin C H, Chen H T, Pu Y N, 'Study on PP/elastomer/nano-$CaCO_3$ composites', *China Plastics*, 2000 **14**(6) 34–38.
53. Hu S F, 'Nanometer $CaCO_3$ toughened and reinforced PVC', *China Plastics*, 1999 **13**(6) 25–28.
54. Fukuda N, Tsuji H, Ohnishi Y, 'Physical properties and enzymatic hydrolysis of poly(L-lactide)-$CaCO_3$ composites', *Polym Degrad Stabil*, 2002 **78**(1) 119–127.
55. Li X H, Tjong S C, Meng Y Z, Zhu Q, 'Fabrication and properties of poly(propylene carbonate)/calcium carbonate composites', *Journal of Polymer Science Part B: Polymer Physics*, 2003 **41** 1806–1813.
56. Kovačević V, Lučić S, Leskovac M, 'Morphology and failure in nanocomposites. Part I: structure and mechanical properties', *J Adhesion Sci Technol*, 2002 **16**(10) 1343–1365.
57. Zhang M, Fang P F, Zhang S P, Wang B, Wang S J, 'Study of structural characteristics of HDPE/$CaCO_3$ nanocomposites by positrons', *Radiation Physics & Chemistry*, 2003 **68** 565–567.
58. Li J X, Cheung W L, Jia D, 'A study on the heat of fusion of β-polypropylene ', *Polymer*, 1999 **40**, 1219–1222.
59. Chen H B, Karger-Kocsis J, Wu J S, Varga J, 'Fracture toughness of α- and β-phase polypropylene homopolymers and random- and block-copolymers ', *Polymer*, 2002 **43** 6505–6514.
60. Karger-Kocsis J, 'How does ''phase transformation toughening'' work in semicrystalline polymers?', *Polym Eng Sci*, 1996 **36** 203.
61. Yang J, Liu W, Chen G, Liu J, 'Influence of the size of ultrafine $CaCO_3$ powder on PP crystallization', *Acta Polymerica Sinica*, 2001 Issue **3** 383–386.

62. Wenge Z, Lu X, Toh C L, Zheng T H, He C, 'Effects of clay on polymorphism of polypropylene in polypropylene/clay nanocomposites', *Journal of Polymer Science Part B: Polymer Physics*, 2004 **42** 1810–1816.
63. Wan W, Chen L, Chua Y C, Lu X, 'Crystalline morphology and crystallization kinetics of poly(ethylene terephthalate)/clay nanocomposites', *J Appl Polym Sci*, 2004 **94**(4) 1381–1388.
64. Liang J-Z, 'Toughening and reinforcing in rigid inorganic particulate filled polypropylene: a review', *J Appl Polym Sci*, 2002 **83** 1547–1555.
65. Hoffmann H, Grellmann W, Zilvar V, In: *Polymer Composites*, Sedlacek B Ed., New York, Walter de Gruyter, 1986: 233.
66. Zhang M Q, Rong Z M, Pan S L, Friedrich K, 'Tensile properties of polypropylene filled with nano-scale calcium carbonate particles', *Advanced Composites Letters*, 2002 **11**(6) 293–298.
67. Zuiderduin W C J, Westzaan C, Huetink J, Gaymans, 'Toughening of polypropylene with calcium carbonate particles', *Polymer*, 2003 **44** 261–275.
68. Hu S, Yan H, Wang Y, 'Study of filling of PVC/CPE composite by nano-$CaCO_3$', *China Plastics Industry*, 2000 **28**(1) 14–15.
69. Bartczak Z, Argon AS, Cohen RE, Kowalewski T, 'The morphology and orientation of polyethylene in films of sub-micron thickness crystallized in contact with calcite and rubber substrates', *Polymer*, 1999 **40** 2367–2380.
70. Wu S-Y, Ma W-S, Ye P-F, 'Application of nano-calcium carbonate in the elastomers', *China Elastomerics*, 2003 **13**(1), 57–62.
71. Wu S-Y, Li H-Y, Ma W-S, 'Reinforcing effect of nanometer calcium carbonate on S-SBR compound', *China Rubber Industry*, 1999 **46**(8) 456–460.
72. Wu S-Y, Lian E-S, Ma W-S, Li X-J, Gou G-J, 'Study on nanon calcium carbonate-filled NBR', *China Rubber Industry*, 2000 **47**(5) 267–271.
73. Wang G Q, Wang Y H, Zou H K, Chen J F, 'Rheological and gelation properties of PVC paste filled with nanometer $CaCO_3$', *Plastics Science & Technology*, 2000 **139**(5) 15–17.
74. Leong W Y, Bakar A B, Ishak Z A M, Ariffin A, 'Characterization of talc/calcium carbonate filled polypropylene bybrid composites weatered in a natural environment', *Polymer Degradation & Stability*, 2004 **83** 411–422.
75. http://www.reade.com/Products/Nanomaterials/calcium_carbonate_nano.html
76. Chen J-F, 'Inorganic nanoparticles filled polymer nanocomposites', *China – EU Forum on Nano-Sized Technology* (http://www.863.org.cn/english/Forum/5.doc)
77. Wu S, Lian E, 'Characteristics of nano-calcium carbonate and its application', *China Rubber Industry*, 1999 **46**(3) 146–151.

17

Magnetic polymer nanocomposites

A MILLAN and F PALACIO, University of Zaragoza, Spain
and E SNOECK, V SERIN and P LECANTE,
CEMES-CNRS, France

17.1 Introduction

Magnetic polymer nanocomposites can be defined as materials composed of an inorganic magnetic component in the form of particles, fibers or lamellae with at least one dimension in the nanometer range (1–100 nm) embedded in an organic polymer or vice versa. The basic idea in a composite is to integrate several component materials and their properties in a single material. In magnetic polymer nanocomposites, organic-inorganic synergies add new properties that cannot be achieved in just organic or inorganic materials. The magnetic component has nanometer dimensions, therefore its magnetic properties can differ qualitatively from the bulk, and they vary with the particle size. The polymer brings high processability, and interesting mechanical, optical, and electrical properties. In addition the magnetic properties can be strongly affected by the polymer interphase, and the capacity of polymers for structuring can be used to control the interparticle magnetic interactions. Thus, magnetic nanocomposites open a great number of possibilities for the design of materials in terms of reducing functional space, improving magnetic performance, modulating magnetic properties, multi-functionalization, and the development of materials with unique properties. The realization of these expectations passes through a better understanding of the physics at the nanometer scale, the development of characterization techniques, and the design of low cost production methods. This last is probably the most important challenge, because the performance of magnetic nanocomposites is very dependent on a fine control of size, size dispersion, shape, interface, and organization of the component materials.[1]

The history of magnetic nanomaterials is relatively recent. The scientific and patent production in nanotechnology was relatively low before 1989. In six years the number of publications increased by three orders of magnitude and that of patents by two orders of magnitude.[2] It was then that the issue came to the forefront of government and industry research.[3–6] About a quarter of the total production corresponds to magnetic nanomaterials. This roaring growth comes

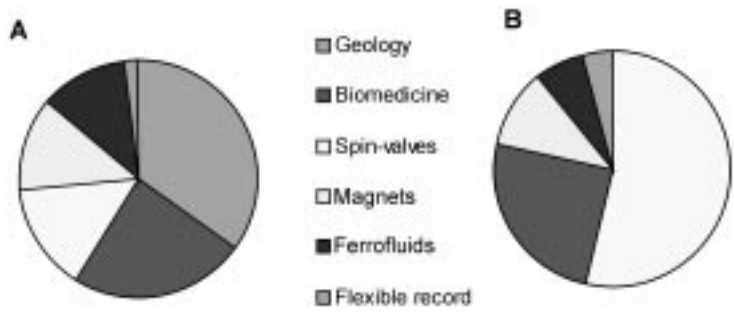

17.1 Comparison of (A) the number of publications in the years 1996–2002 and (B) the number of patents active in 2002 in different areas within magnetic nanomaterials.

as a result of the development of characterization techniques at this scale (SPM, SAXS, EELS, HRTEM, STEM, XMCD), the development of biomimetization synthetic methods,[7] the trend to reduce the size of devices, and the discovery of new nano-related phenomena[8] (superparamagnetism, ferro-antiferro bias-exchange, GMR, TMR, quantum tunnelling). A bibliometric study of publications in the period 1996–2002, and patents active in 2002 is shown in Fig. 17.1.

The polymer can play several roles in magnetic nanocomposites:

- as a template to control size, shape and organization
- as a coating protecting from the environment, an isolator, a separator or a compacting medium
- endowing the magnetic material with the mechanical properties and processability of the polymers
- as a functional component, adding its own optical, electrical or chemical properties, enhancing the properties of the magnetic component, or creating new properties by interaction with the magnetic component.

Polymers can also be useful as tools for moulding, templating, and structuring inorganic magnetic nanomaterials. Thus, the area of interest of magnetic nanocomposites extends to most of the fields in nanomagnetism. Patterned media for information storage, MRAM and magnetic sensor applications are often made through the intervention of polymers at intermediate stages, if not in the final product. In fact, magnetic nanocomposites are strong candidates for patterned media in ultrahigh density recording. Nevertheless, biomedicine is probably the area gathering the highest activity, actual realizations, and expectations in magnetic nanocomposites. The first application in this field was as contrast agents in magnetic resonance imaging[9] (MRI). Just as an example, the diagnosis of lymphatic metastasis has improved from 60% to 94% with the use of

nanoparticles. Nowadays, their interest extends onto many other areas:[10] drug targeting,[11] diagnostics,[11,12] immunoassays,[13] molecular biology,[14] DNA purification,[15] cell separation and purification, and hyperthermia therapy.[16] Other current applications of magnetic ferrofluids are: magnetic inks, sealing of rotating shafts, speakers, shock absorbing systems, magnetic sensors, etc. Their applications in radioelectronics, microelectromechanical systems (MEMS),[17] and advanced photo systems are under progress.[18] Magnetic refrigeration and X-Ray Switching are also of industrial interest. Moreover, polymer nanocomposites are used as intermediate materials in the fabrication of nano-organized inorganic magnetic materials, such as patterned media,[19,20] mesoporous magnetic ceramics,[21] magnetic hollow spheres.[22] Apart from their industrial value, they are very interesting in basic magnetism and other scientific fields, e.g. life science[23] and in earth and planetary sciences. Iron oxides in nature are usually in the form of nanoparticles. The study of their magnetic properties is an important tool to follow geological evolution. For instance, a relevant evidence of extra planetary life comes from the finding of magnetite nanoparticles in a Mars meteorite that are very similar to those produced by magnetotactic bacteria.[24] Magnetic studies are also evidences on the study of the evolution of sediments, sea floor, soils and rock formation. Iron oxide magnetic nanoparticles are also produced by animals that use them as orientation tools[25,26] (bacteria, eels, trout , pigeons, dauphins, sea turtles, etc). They are also employed for iron storage in mammalians and their formation can occasionally be related with diseases[27] (Alzheimer).

Magnetic polymer nanocomposites may present a large variety of forms. Within each of these forms, they are designed to yield an optimal performance for a certain application. Following the basic chain in materials research in an inductive direction, the performance of composites is related to their properties, which are determined by their composition and structure, which are leading to the development of methods for their preparation. Thus, in the next section of this chapter, the different types of magnetic nanocomposites will be presented accordingly with this scheme. Then, in further sections, each of the elements of the materials research chain will be revised, starting with an exposition of methods for the synthesis of magnetic nanocomposites, and following with a description of the basic techniques for the characterization of their structure, and their main physical properties. Finally, we will comment on the future trends in this field.

17.2 Classification of magnetic polymer nanocomposites

Magnetic polymer nanocomposites can be in the form of: powders and suspensions, fibers, films and multilayers, or tridimensional solids. In each of these forms, they can be used in a large number of applications accordingly with their properties. A scheme of this classification is shown in Fig. 17.2.

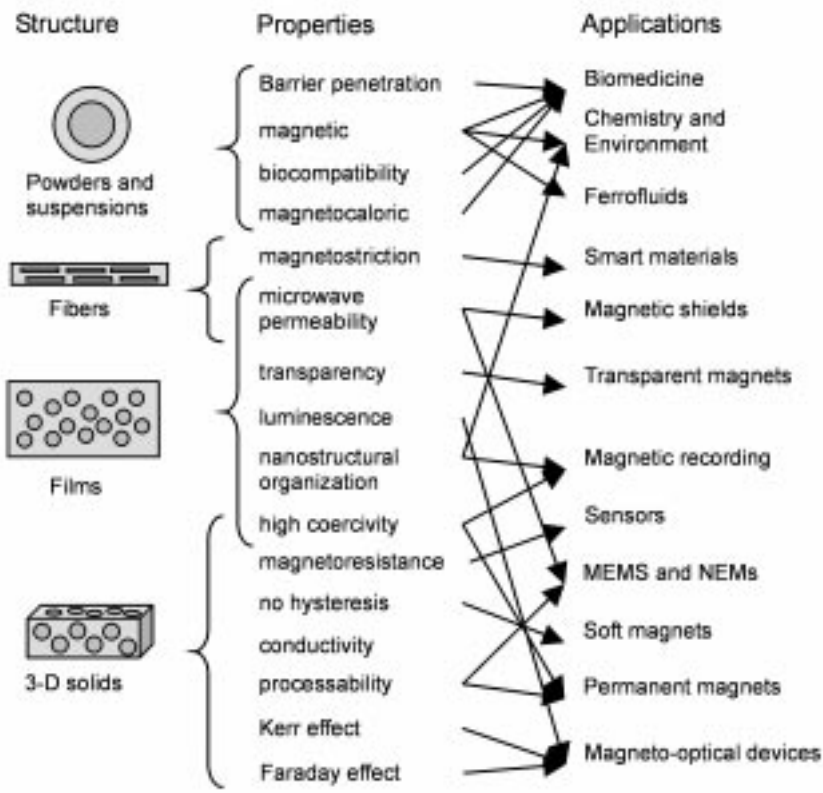

17.2 Classification of magnetic polymer nanocomposites.

17.2.1 Powders and suspensions

Biomedical applications

They are mostly based on the use of superparamagnetic nanoparticles. Their performance is related to two elemental magnetic properties:

1. a high magnetic moment that permits the *detection*, *separation*, and/or *direction* of biological entities attached to the particles; and
2. their *heating* power in an oscillating magnetic field that is useful for hyperthermia therapy.

Magnetic biomedical materials are typically composed of a magnetic core, a biocompatible shell, and one or more biologically active molecules (drug, antibody, enzyme, etc.) anchored to the surface. As detection agents, they are very useful in diagnosis. In combination with recently developed magnetic biosensors (10^{-13} mole/L), they have opened new frontiers in early detection of diseases,[12] and inmunoassays.[13,14,28] Their use in MRI permits the real time in

vivo visualisation of biological processes, such as cell tracking[29a] and DNA expression,[29b] with a resolution close to molecular level.[29c] They are currently used in the diagnosis of cancer, specially lymphatic and brain tumours.[30] As separation tools, they have been extensively used for cell sorting,[31] DNA separation,[15] and blood purification.[32] As targetable drug carriers they are used to retain drugs in areas of low blood irrigation, and to localize the drugs in the damage area in order to avoid side effects on the rest of the body. In hyperthermia, they can play two roles:

1. enhancing drug action or tissue regeneration by heating to temperatures below 41ºC;[30] and
2. cytolysis of cancer cells by heating to temperatures above 45ºC.[16]

The preferred magnetic component for biomaterials is maghemite (γ-Fe_2O_3), because it is highly biocompatible, and then ferrites. Other proposed compounds are metals (Co) and metal alloys (CoPd, CoNi and NiCoPd). Polymers suitable for the shell are: (a) natural polymers, such as carbohydrates, proteins, lipids, or oligonucleotides; or (b) artificial polymers, such as polyols (polyvinyl alcohol, PVA, polyethylenglycol, PEG), polysaccharides (dextran), polycarboxylic acids (polymethylmetacrylate, PMMA), polyamines, polyimines, polyvinylpyridine and polyethylene.

Ferrofluids[33]

Their performance is linked to a high magnetic moment and suitable rheological properties. Suspensions of polymer coated magnetic nanoparticles are or might be used in low temperature cooling, vacuum sealing, lubricants in rotating shafts, magnetic inks, printing systems,[34] stamps, shock absorbing systems, speakers, and other uses.[35] Magnetic components for these applications are usually magnetite, Fe or Co. The polymer shell can be made of polycations, amphyphile polymers, polyols, etc. The dispersing fluid is usually kerosene, water, oil, or a liquid metal (Hg, Ga alloys).

Magnetic nanoparticles in ferrofluids can incorporate chemically active agents in order to fix them or separate them from a solution. Ferrofluids of this type have been designed for environmental applications, catalysis,[36] ion recovery processes, etc. For instance, magnetite polymer poly(1-vinylimidazole) nanocomposites have been used for the selective separation/recovery of metal ions in water.[37]

17.2.2 Fibers

Polymer fibers filled with magnetic nanoparticles are magnetoactive and they show magnetostriction. Therefore, fabrics made with these fibers can be used in magnetic shielding (military and civil), and high strain actuators.[38] Examples of

this type of materials are:[39] fibers containing oriented magnetic particles of $Fe(CO)_5$ in low-density polyethylene (PE-LD), cellulosic fibers filled with ferrite nanoparticles, and fibers of spider silk coated with magnetite nanoparticles.

17.2.3 Films

Magnetooptical materials

Magnetic nanoparticles showing Faraday rotation effect, and/or Kerr effect can be of interest in the fabrication of switches and devices. Size dependant transmittance and Faraday rotation have been found in maghemite ferrofluids and ferrite films.[40] Multilayered assemblies of yttrium garnet nanoparticles show magnetization-induced second harmonic generation (Kerr effect).[41] In metal/PMMA nanocomposites, the main absorption band narrows and additional peaks appear when decreasing the particle size.[42]

Sensor applications[43]

Nanocomposites of magnetic particles in isolating polymer matrixes show tunnelling magnetoresistance (TMR),[44] and nanocomposites with a conductive polymer matrix exhibit giant magnetoresistance (GMR).[45] Iron-poly(p-xylylene) nanocomposites display a significant magnetoresistance (36%) at room temperature.[45] Nanocomposites of metals (Ni, Cu and FeNiCo) in polyimide show magnetoresistance also in ac current (magnetoimpedance). Important advantages of polymer nanocomposites are the elimination of undesired eddy-current losses, and the protection from oxidation.

Ultrahigh density recording media

It is generally assumed that the next generation of magnetic recording materials will consist of a highly ordered arrangement of ferromagnetic nanoparticles, each of them supporting a bit. Polymer nanocomposites are good candidates,[46] thanks to the extraordinary capability of polymers for templating and self-assembly. A magnetic nanocomposite film with a 5 nm grain size would provide a recording density as high as 10^{10} bit/cm^2. Magnetic compounds proposed for this application are cobalt ferrite,[47] maghemite,[48] magnetite,[49] metals[50], and metal alloys. The preferred one is FePt[51–54] because it has a high saturation magnetization and a high coercivity. The ordering can be achieved by self-assembly of nanoparticles coated with a surfactant,[51] or by 'in situ' growth of the particles in a block copolymer template.[47,49,50,54–56] Materials consisting of nanocomposite grains embedded in a second polymer have also been proposed for magnetic recording.[57] The performance of magnetic nanocomposites for magnetic recording can be improved by using elongated particles, with

enhanced shape anisotropy,[56] or ferro-antiferro core-shell particles (Co-CoO or Fe-FeO), that show a high magnetic stability thanks to exchange coupling between the two magnetic phases.[58–60]

Membranes and sensors

Ordered films of magnetite in cellulose can be used as magnetic membranes,[61] and assembled multilayers of clay, polymer polycations, and magnetite nanoparticles have been proposed as sensor arrays.[62]

17.2.4 Tridimensional solids

Polymer bonded magnets[63]

The role of the polymer in this type of materials is to compact the magnetic nanoparticles. Polymer-iron composites begin to replace laminated materials in selected electromagnetic applications due to their large possibilities for design and their corrosion resistance. Their application in MEMS and NEMS are specially interesting.[64] Nanocomposites of NdFeB in epoxy resins,[65,66] and earth alloys in polyimides[67] have shown a high performance for these applications. Magnetic nanocomposites are also employed in soft magnetic materials due to their extremely low hysteresis loss.

Materials with high microwave permeability

There is a strong demand of materials with a high permeability and a low power loss at high frequencies in order to improve the performance of electromagnetic devices such as small power converters, inductors and antennas in communications technology,[68] magnetic shielding,[69] and microwave absorbers for civil and military purposes.[69] The microwave properties of a magnetic material are determined by the ferromagnetic resonance. To obtain high microwave permeability, both the frequency and the amplitude of the resonance should be as high as possible.[69] Nanoparticles display a strong increase of the real and imaginary parts of the permeability, and a narrowing of magnetic resonance peak compared to composites made of micron-sized particles.[70] That explain the remarkable microwave absorption of metal nanocomposites in the 0.1–18 GHz frequency range.[71] Nanocomposites of ferrites or metals in epoxy resins have been proposed for ultra high frequency application, i.e. as inductive components in mobile communications.[72]

Piezoelectric materials

Polymer bonded nanocomposites with orientated nanoparticles show high magnetostrictive strain under relatively low magnetic field, and, additionally, a

high modulus of rupture.[63] That is the case with TbDyFe Terfenol-D polymer bonded magnets.[73]

Nanocomposites of iron oxide in a polystyrene resin have also been proposed as *magnetic refrigeration materials*,[74] and nanocomposites of magnetic nanoparticles in thermosetting or thermoplastic adhesive compound are available for *magnetic gluing*. Nanocomposite polymer gels show striking phenomena in response to impressed magnetic fields: giant deformational effects, high elasticity, anisotropic properties, temporary reinforcement and quick response to magnetic field.[75] Gels of this type have been prepared from hydroxypropyl cellulose and magnetite.[76]

Multifunctional materials

Multifunctional materials are basic ingredients in the design of modern sensors and devices. Some of the many possibilities of combination of magnetism with other property in a polymer nanocomposites are:

- *Conductive magnetic materials* are useful in the fabrication of sensors and devices.[77] They consist of magnetic nanoparticles in a conductive polymer matrix. A charge transfer can be established between the particle surface and the polymer, so that the material acts as a united electronic system.[78] Some proposed compositions are: magnetite-polyanyline,[78,79] maghemite-polypyrrole,[80] cobalt ferrite- polypyrrole,[81] and several metal-polymer combinations.[45]
- *Transparent magnetic materials*. Magnetic oxides are considerably more transparent to visible light as nanoparticles than in the bulk.[82] Thus, magnetic nanocomposites can be made with a reasonable transparency and a magnetization greater by more than an order of magnitude than those of the strongest transparent magnets.[83]
- *Luminescent magnetic materials*. They can be useful in combined detection and separation in bioanalytical assays. For instance, polymer coated γ-Fe_2O_3 cores and CdSe/ZnS shells with immobilized anticycline E antibodies have been used for the separation and observation of MCF-7 breast cancer cells.[84] Materials joining potentially tunable optical and magnetic properties have been proposed that are composed of three-dimensional binary superlattices of self-assembled γ-Fe_2O_3 and PbSe nanoparticles.[85]

17.3 Synthesis

It is apparent from previous sections that magnetic nanocomposites may adopt a large variety of compositions and structures. It is also clear that the performance of these materials is closely related to the dimensions of the magnetic component, the organization of the components, and the organic-inorganic synergies. Therefore, synthetic methods must be versatile, and they must

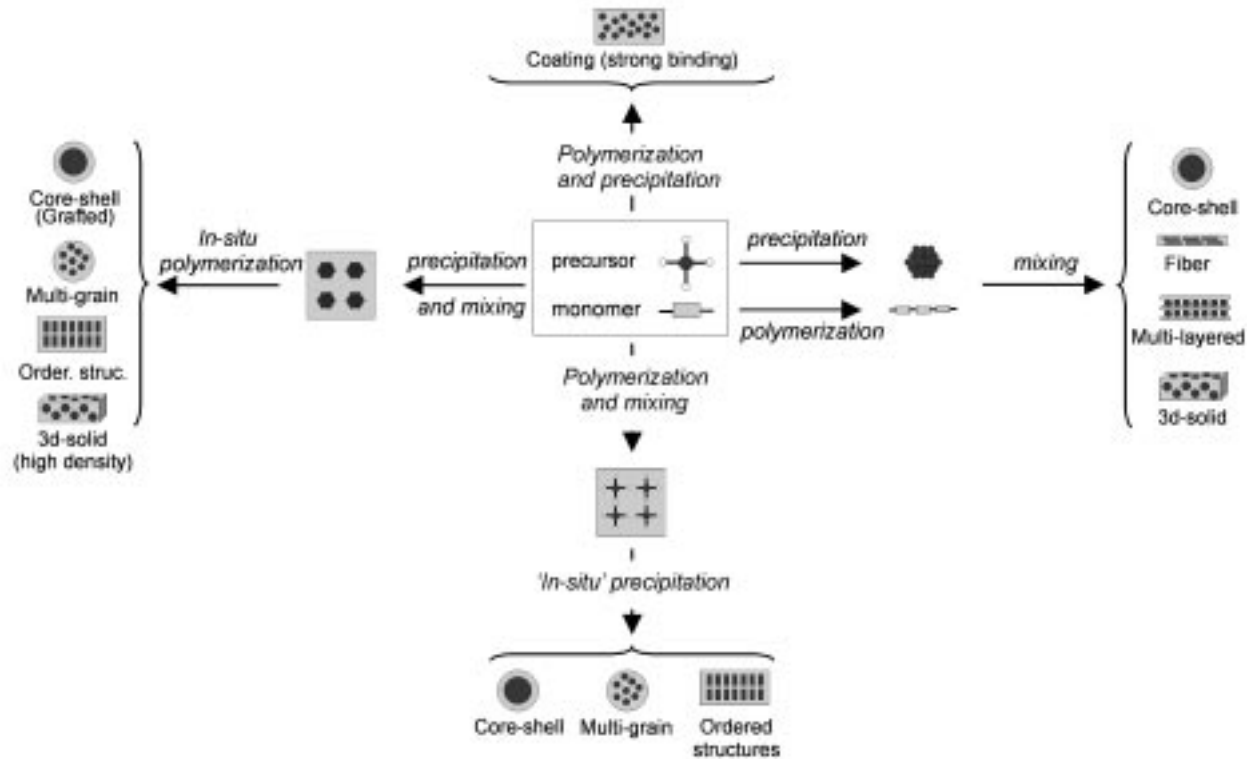

17.3 Synthetic routes for the preparation of magnetic polymer nanocomposites.

guarantee a fine control of particle size, particle size dispersion, particle-polymer interactions, and particle-polymer ordering. In a top-down approach, the starting point is a bulk material and it proceeds by mechanical attrition.[86] This procedure is energy consuming and yields high particle size dispersion, therefore its utility is quite limited. In a bottom-up approach, the starting materials for the synthesis of magnetic nanocomposites are a monomer and a molecular precursor of the magnetic component. The basic processes for making a magnetic nanocomposite are: polymerization of the monomer, formation of the magnetic component (precipitation), and mixing of the magnetic and polymer components. These processes can be carried out in several ways:

1. separated precipitation of the magnetic component and polymerization, and then mixing of the magnetic nanoparticles and the polymer;
2. precipitation of the magnetic component, mixing the magnetic nanoparticles with the monomer, and then in-situ polymerization;
3. polymerization, mixing of the precursor with the polymer, and then in-situ precipitation;
4. mixing monomer and precursor, and then simultaneous precipitation and polymerization.

Figure 17.3 schematically illustrates these four routes. In this section we will comment on the several steps included in these four routes for the synthesis of magnetic nanocomposites, and we will dedicate an extra subsection to methods for the fabrication of nanostructured composites.

17.3.1 Precipitation of the magnetic component

There are several stages in the process of precipitation: reaction of the precursor to generate the growth units, formation of stable nuclei, particle growth, and particle aggregation that must be avoided. As it has been pointed out above, the key question in this process is the control of particle size. Consequently, several procedures have been developed to achieve size control.

Reaction of the precursor

The choice of the precursor will depend on the reaction medium. High vacuum deposition methods use volatile organometallic precursors or ion, atom or molecule beams. Normal pressure vapor methods use similar volatile precursors, or sprayed metal salt solutions. Aqueous solution methods use water soluble salts, and organic solution methods use organometallic soluble compounds. Typical chemical reactions to generate the growth units are:

- *Hydrolysis of metal salts*. It is widely used to obtain magnetite nanoparticles.[86] This iron oxide phase is precipitated by addition of a base

to a solution of Fe(II) and Fe(III) salts in a 1:2 ratio, at a pH between 8 and 9.6. Magnetite oxidizes easily to maghemite, and therefore it is frequently used to obtain mixtures of both phases. A method to obtain pure magnetite is described by Schwertmann.[87] Ferrites are also prepared by hydrolysis of Fe(III) ions and metal divalent ions. Maghemite is not a direct product of iron salt hydrolysis. It must be obtained by transformation of other iron oxide phases.[87,88]

- *Hydrolysis of metal alkoxides*. It is used in the synthesis of garnets. A typical procedure to prepared yttrium garnet (YIG) nanoparticles[89] can be: mixing iron ethoxide and yttrium butoxide in a 5:3 molar ratio, and then hydrolyzing with an excess of water. It results in amorphous YIG nanoparticles that yield crystalline YIG after heating at 650–700ºC.
- *Decomposition of metal carbonyl compounds*. This is a very useful reaction for the preparation of metal and metal alloy nanoparticles in the vapor phase, or in organic solvents. Iron pentacarbonyl decomposes at temperatures above 170ºC.[51] Cobalt nanoparticles can also be prepared in a similar way. In the presence of a mild oxidant the final product of iron pentacarbonyl decomposition is maghemite.[48]
- *Redox reactions*. The chemical reduction of metal salts by sodium boron hydride is a common procedure in the preparation of metals and metal alloys. Nanoparticles of iron,[89] FeZrB,[90] FeCoB and FeCoB have been obtained from the corresponding sulphate salts, and NdFeB compounds from neodymium and iron chloride salts.[91] Cobalt nanoparticles have been prepared from cobalt acetate using 1,2 dodecanediol as a mild reducing agent.[92] FePt nanoparticles are produced by the decomposition of iron pentacarbonyl and the reduction of platinum tetrachloride complexes in an organic solvent.[51a] Redox reactions can also be produced by electrochemical methods,[93] or in the solid phase.[94,96]

Nucleation and growth

After the generation of growth units, the next step in precipitation is the formation of nuclei larger than the critical size for thermodynamic stability.[97] Above the threshold value for critical nuclei formation, the nucleation rate increases exponentially with the supersaturation, whereas the growth rate increases with a low power of the supersaturation.[98] Thus, the production of nanoparticles requires that:

- the size of critical nucleus is small (it depends on surface tension and temperature),
- the initial supersaturation is high enough to allow fast nucleation, and
- the supersaturation decreases very fast after nucleation in order to avoid extensive particle growth.

Different strategies have been followed based on the above requirements. In normal pressure vapor methods, the reaction is activated for a short time by either an arc discharge, a flame, a laser beam,[88] a plasma,[99] or a collision with a hot wall, etc. In solution, a high initial supersaturation is built up by abrupt addition of reactants or non-solvents, or by fast cooling. A rapid reaction can also be triggered by ultrasound, UV or gamma irradiation.[100,101]

Aggregation

Fine particles tend to aggregate in order to reduce their high surface energy.[102] Additives that adsorb on the particle surface can restrain aggregation by reducing the surface energy, or by steric hindrance. In the first mechanism, additives such as polyions (citrate, tartrate, etc.), create a double electric layer around the particle lowering the zeta potential. In the second mechanism, additives are surfactant amphiphilic molecules which form a hydrophobic layer around the particle preventing particle aggregation.

Control of particle size

In normal pressure vapor methods,[103,104] the average size and the size distribution can be controlled by tuning the gas flow, the concentration of reactants in the carrier gas, and the heating power. Laser methods yield size standard deviations around 10%. In solution methods, a certain control of particle size can be achieved by adjusting the kinetics of the reaction conditions. For example, in the Massart method the size can be varied with the strength of the precipitating base[105] (NH_3: 6 nm, CH_3NH_2: 10 nm, NaOH: 19 nm). However, aqueous precipitation usually yields a broad size distribution (in between 20% and 30%). A better size control can be attained in the presence of surfactants especially in organic solvents. Monodisperse nanoparticles of various metals (Fe, Co, Ni) and metal alloys (FePt, CoNi) are obtained in nonpolar organic solvents (decaline, diphenyl ether, octyl ether) by decomposition or redox reaction of precursors. The size of the particles can be varied with the reactant/surfactant ratio,[48,101] the charge of the surfactant hydrophilic head, or the length of the hydrophobic tail.[92] Fatty acids (oleic and stearic acids), bis(2-ethylhexyl)sulfosuccinate (AOT) and sodium dodecyl sulfonate (SDS) are commonly used as strong anionic surfactants. Trialkyl amines (tetramethylammonium, cetyldimethylethylammonium bromide (CTAB)), and trialkyl phosphines (tributylphosphine, trioctylphosphine) are employed as cationic surfactants. Non-ionic surfactants have also been used (octadecanetiol). Small polycarboxylic acids such as citrate and tartrate also show a certain size modulation effect in the precipitation of iron oxides.[106]

Another strategy for the control of particle size is to confine the reactants in flexible nanocages. In spraying techniques, the reactants are enclosed in liquid

drops, and the particle size can be tuned with the concentration and volume of the liquid drops.[88] In solution, the reverse micelle technique consists of enclosing solutions of the reactants in regions delimited by a surfactant wall surrounded by an immiscible solvent.[35,107] Block copolymers can be very effective as surfactants in reverse micelles. Another method, known as sonochemical cavitation,[108] consists of performing the reaction in nanobubles generated by ultrasound radiation, or a rapid pressurization of a sol-gel solution. Finally, a fine control of size and shape can also be attained by enclosing the precursors or the growth units in rigid nanocages, such as carbon nanotubes.[109]

The size distribution can be further narrowed by size-sorting procedures such as: centrifugation,[110] magnetic separation,[111] field-flow fractionation, size-exclusion chromatography,[112] and size-selective precipitation.[113]

17.3.2 Mixing of the polymer and the magnetic component

Films and bulky materials can be prepared by dispersing the magnetic component in a polymer solution or a polymer melt, and then evaporating, spin-casting,[60] or cooling. Core-shell structures can also be prepared from dispersions of particles and polymer in a common solvent. A key question is the binding of the polymer to the particle surface. Metal oxide nanoparticles have abundant surface charges that can bind to polyelectrolyte polymers by electrostatic forces. They can also form M–O bonds with alcohol groups in the polymer, M–N coordination bonds with N-base groups, or hydrogen bonds. Metal nanoparticles may need surface activation with suitable functional groups like –SH, –CN, –COOH, $–NH_2$ and silanes. The stability of the nanocomposite suspension can be reinforced by crosslinking of the polymer after coating.[114] Another procedure to produce stable suspensions employs bifunctional polymer layers.[115] A simple way to get polymer coated particles is to precipitate the dispersion by addition of a non-solvent, and then fast cooling.[116]

17.3.3 'In-situ' polymerization

The polymerization can be carried out in a dispersion of the particles in a monomer solution or in a monomer melt. Monomers are far less viscous and more soluble than polymers. Thus, this route is specially suited for the preparation of nanocomposites with a high density of particles, when the polymer is insoluble or when it does not melt. Polyimide-bonded magnets of rare earth alloys have been prepared in this way.[67] In order to enhance cohesion, the polymer can be grafted to the particle surface by irradiation polymerization.[117] High homogeneity is achieved by sonochemical polymerization.[118]

Polymerization in solution is the preferred route for the fabrication of core-shell particles. If the polymerization is carried in a micellar system, the shell thickness can be modulated.[119] This route facilitates a strong particle-polymer

binding by pre-activation of the particle surface with reactive residues, polymerization initiators, or the own monomer. In polypyrrole-maghemite composites, polymerization is activated by citrate ions adsorbed on the particles.[120] Nanocomposite microparticles containing several magnetic nanoparticles in the interior have also been prepared by in-situ polymerization.[121]

17.3.4 'In-situ' precipitation

This route is suitable for the preparation of films and bulky materials. It allows a controlled particle growth, a regular particle-polymer interphase, a uniform distribution of particles in the matrix, and even microstructural organization. Polymer and metal precursor can be mixed by:

- absorption of metal ions in ionic exchange resins or in polymer gels;
- dissolution of the precursor in a polymer melt, or a polymer solution;
- deposition of the precursor in a porous polymer by chemical, electrochemical, or vapor methods.

Then, particle growth is carried out by one of the procedures already described in section 17.3.1. The size and the shape of the particles can be modulated with the precursor/polymer ratio, the molecular weight of the polymer, and the relative chain length in block copolymers.

Iron oxide nanocomposites have been prepared by hydrolysis of iron salts in sulfonated polystyrene resins,[82] mesoporous sulfonated styrene-divinylbenzene copolymer,[122] acrylonitrile-methyl methacrylate-divinylbenzene copolymer,[55] cross-linked high amylose starch,[123] polyimides,[124,125] polyvinylpyridine,[126,127] polypyrrole,[69c] cellulosics.[39b] Nanocomposites of metals (Cr, Mo, W, Fe, Co, Ni) with a variable particle size (2–10 nm), have been prepared from solutions of metal precursors in a molten polymer (polyethylene, polypropylene, polytetrafluoroethylene, polyamide, polyarylate, polycarbonate, polystyrene, polyethers, polyphenyleneoxide, siloxane).[128] There are also many examples of in-situ precipitation of iron oxides in aqueous solution of polymers, such as dextran,[129] PVA,[129] polyethylene glycol,[79] etc. In this case, size dispersion and aggregation are frequent, but they can be minimized by using reverse micelles.[130]

'In-situ' precipitation takes full profit of the templating capacity of polymers and organic-inorganic hybrids, emulating biological processes.[131] In solution, dendrimers,[132] and natural proteins[133] may act as nanoreactors with variable shapes and sizes. In the solid state, block copolymers allow monodispersion and organization in magnetic nanocomposites. In polymer microgels, it is possible to obtain nanoparticles with a predetermined shape.[134] Some examples of polymer templating are: apoferritine yield monodisperse magnetite nanoparticles by precipitation of $NH_4Fe(SO_4)_2$n encapsulated in the interior;[135] magnetoliposomes are prepared from phospholipids vesicles in a similar way;[136] polycarbonate membranes are used as moulds for the fabrication of Co, Ni and

NiFe nanowires by electrodeposition,[137] and multilayers of alternating polycations and polyanions have been used for the fabrication of magnetite nanocapsules[138] and films.[139]

'In-situ' precipitation is also compatible with vapor deposition methods. Magnetic recording tapes are prepared by deposition of metal vapors of a polymer substrate.[140] Nanocomposites of Co[141] and FePt[142] have also been produced in this way. An original variant consist of high pressure sputtering on low-vapor-pressure liquids to obtain nanoparticle suspensions of high purity.[143]

17.3.5 Simultaneous precipitation and polymerization.

This can be performed by co-condensation of monomer and precursor vapors. The main advantages of this method are a high homogeneity and a strong polymer-particle binding. It is frequently used for nanocomposites of metals in polyamides, polyimides, polystyrene or Teflon.[144] Co-condensation at low temperature in combination with gamma or UV irradiation yield metal-polymer nanocomposites of variable particle size and high particle density.[145]

17.3.6 Nanostructured composites

This subject has already been treated in previous sections. However, owing to its relevance, it deserves a few words apart. Nanostructural ordering can be worked out[146] by means of the polymer (matrix confinement, programmed assembly by molecular recognition), the inorganic component (interparticle conjugation, shape directed assembly), a substrate (substrate engineering), or a magnetic field.

There is a large variety of strategies for the ordering of organic-inorganic composites in a laminar stacking.[147] Langmuir-Blodgett films,[148] sequential deposition of polyelectrolites,[136] and two-dimensional perovskites[149] are some of them. Layer by layer assembly is also useful for the preparation of core-shell multilayered nanoparticles.[150,151] However, the most versatile route for the fabrication of ordered magnetic nanostructures is based on the use of block copolymers. Diblock-copolymers of linear $(A)_n(B)_m$ chains form self-assembled structures in the solid state that can be maintained in a length scale of centimeters. The shape of the structures can be changed with the values on n and m from spheres to cylinders, gyroids, and lamellae. The selective dissolution of one of the blocks followed by crosslinking and selective degradation lead to a large variety of nanostructures: hairy nanospheres, shaved nanospheres, porous nanospheres, hollow nanospheres, nanospheres with crosslinked shells, crosslinked polymer brushes, nanofibers, and nanochannels in polymer thin films.[152] Block copolymers proposed for the fabrication of ordered magnetic nanocomposites are: aniline and formaldehyde,[54,153] poly(norbornene-dicarboxylic acid) and poly(norbornene),[47,154] poly(4-vinylpyridine) and vinylstyrene-4-vinylpyridine,[49]

poly(styrene-b-2-vinyl pyridine),[50a] acrylonitrile-methyl methacrylate-divinyl-benzene,[55] polystyrene-polymethylmethacrylate,[56] etc.

Structural orientation can be induced by a fixed magnetic field,[155] whereas alternating magnetic fields have been used to produce nanocomposites with rotationally free particles.[156]

It has been pointed out that nature is the master in the creation of nanostructures. Thus, why not using living organisms to produce high quality magnetic nanocomposites? There are several lines open in this direction:

- magnetotactic bacteria are manipulated genetically to produce magnetite-protein nanoparticles with different sizes and shapes;[157]
- viruses have been used to produce magnetic nanoparticles with a controlled size shape and organization.[158]

17.4 Characterization

Continuing with the chain in materials research, both the development of synthetic methods and structure-properties models of magnetic nanocomposites require an adequate structural characterization of the materials. It has been shown in sections 17.2 and 17.3 that magnetic nanocomposites are composed of magnetic particles, wires or layers, which are coated or imbedded in a polymer matrix. Thus, the specific characterization for magnetic nanocomposites must focus on the determination of particle size and shape, coating thickness, interparticle distance, and particle-polymer interphases, and magnetic structure, in the nanometer scale. To this concern, scanning probe microscopies and electron microscopy give direct information on nanostructure but they are restricted to a small volume of the material, and their application is limited. On the contrary, radiation scattering methods are indirect but non-invasive, sample preparation is easy, and they give useful information about particle size, coating layer thickness, and particle ordering. Moreover, electron energy loss spectroscopy yields local chemical information (interphases), and holography and neutron scattering give about local magnetic structure. In the following, we will present in more detail some of these methods.

17.4.1 Transmission electron microscopy

The transmission electron microscope (TEM) is a choice instrument for the characterization of materials and devices at the nanoscale. Nanoparticles shape, and distribution can easily been determined by conventional TEM while the atomic resolution in real space capability offers the possibility to resolve their structure. In addition to this high intrinsic spatial resolution, TEM offers a number of signals which can be exploited to obtain chemical and structural information concerning the specimen (see, for example, Wang, 2000[159]). Recent years have

seen considerable advances in the use of electron microscopy and new techniques have been developed thanks to improved methodology, instrumentation and data acquisition systems. Here we describe three such techniques for analysing structure, chemistry and magnetism at the near atomic scale in nanomaterials.

17.4.2 High-resolution electron microscopy

High-resolution electron microscopy (HREM) differs from conventional electron microscopy in that images are formed of the atomic lattice (see Fig. 17.4). It is beyond the limits of this review to explain how the images are formed. For the present purposes it is sufficient to know that the position of lattice fringes seen in the image is closely related to the atomic planes in the specimen. (For more ample details, see Spence, 2003[160]). It was realised early that intereticular distances can easily be measured as well as angles between crystallographic planes as observed in the HREM micrograph in Fig. 17.4. This can be done with sufficient accuracy on the power spectrum of the Fourier Transform (FT) of the HRTEM micrograph, measuring both the lattice spacing in the reciprocal space and angles between the corresponding reflections. Non-periodic nanostructures are, however, difficult to resolve since the HRTEM fringes contrasts are no more directly connected to lattice planes. Moreover slight tilts of the nano-object far from a low indices crystallographic direction will induce drastic changes in the contrast inducing wrong interpretation.[161] Therefore, the exact resolution of the structure of nanomaterials requires the use of HREM image simulations.[162] The accuracy of such a determination is obviously improved when combining TEM local imaging with averaging techniques, e.g. WAXS and EXAFS, the latter giving starting models for image simulations. As example, in Fig. 17.5(a) is a HRTEM micrograph of a 1.5 nm diameter Co nanoparticle which exhibits a low periodical contrast suggesting a periodic structure. In reality it corresponds to the non-periodic polytetrahedral

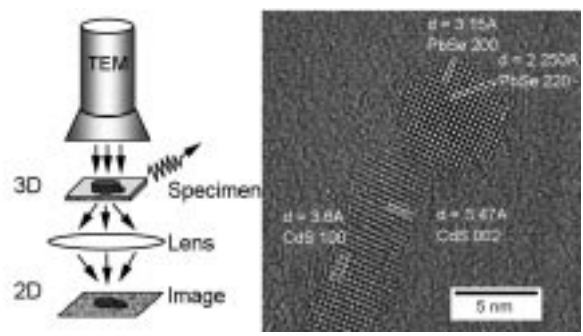

17.4 General scheme for transmission electron microscopy. HREM micrograph of one PbSe nanoparticle connected to a CdS rod (Unpublished E. Snoeck, 2004).

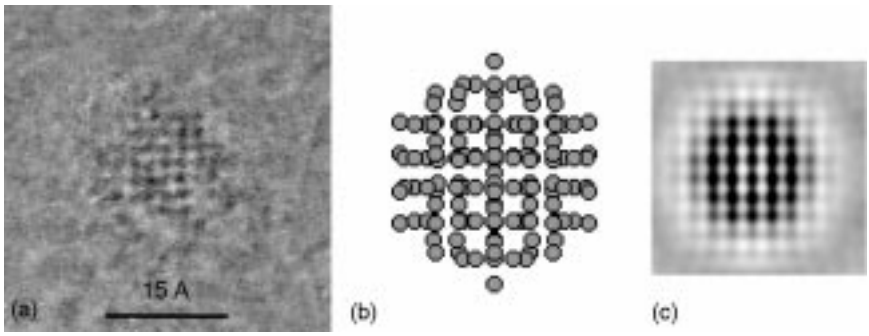

17.5 (a) HREM micrograph of a 1.5 nm diameter non-periodic polytetrahedral Co nanoparticle schematized in (b) with its corresponding HREM simulation in (c).

structure of Fig. 17.5(b) that has been deduced from WAXS experiments whose corresponding simulated image has been reported in[163] (Fig. 17.5(c)).

Further examples illustrating the necessity to combine local HREM experiments with averaging techniques are given by the study of iron oxide nanoparticles. Magnetite (Fe_3O_4) and Maghemite (Fe_2O_3) have similar lattice spacing that makes their differentiation difficult from the unique analyse of HREM contrast. The phase determination of the iron oxides nanoparticles in Fig. 17.6 is therefore not obvious. However, as will be discussed below, the EELS spectra of Fe_3O_4 and Fe_2O_3 is drastically different as well as their radial distribution

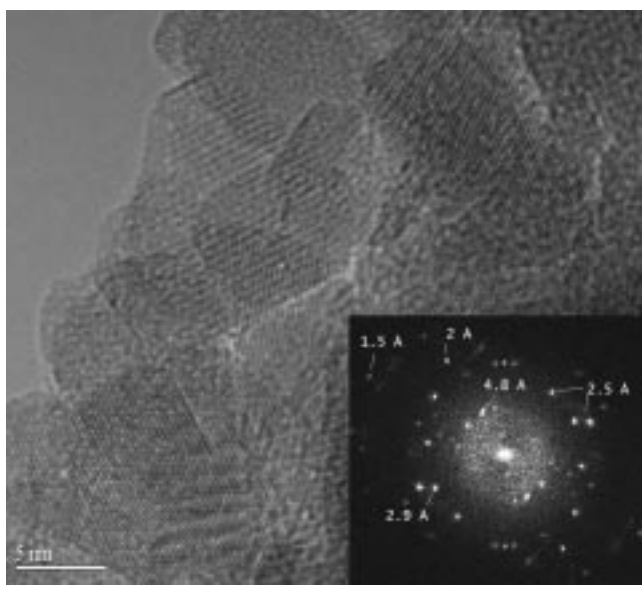

17.6 HREM micrograph of an assembly of maghemite nanoparticles with its Fourier Transform inset.

function (RDF) than can be achieved from WAXS or EXAFS experiments. Combination of these techniques allows the structure of these nanoparticles to be fully elucidated.

17.4.3 Electron energy loss spectroscopy

The combination of an electron microscope with a parallel electron energy loss spectrometer (PEELS) or imaging filter is well suited to the investigation of structural, chemical and electronic properties of individual nanostructures and interfaces. Major technical improvements have opened the field of image-spectra at sub-nanometric level and demonstrated its efficiency for mapping the composition of nano-objects (see Fig. 17.7), to the limit of single atom identification.[164] Furthermore, the detailed study of EELS fine structures enables the investigation of the unoccupied electron density of states, and therefore the local environment and bonding properties at specific atomic sites. As an example, Fig. 17.8 displays the O-K and Fe-L2,3 edges from different iron oxides.[165] Fine structure position and intensity give an indication of the nature of the oxide formed. Latest attempts in exploring the EELS signal have led to estimate local physical properties such as magnetic or electric ones.[165,166]

17.4.4 Mapping magnetic and electric fields

Off-axis electron holography in the transmission electron microscope can image magnetic fields at the nanometer scale. The high-energy electron beam is split in two coherent waves with the aid of a bi-prism, one passing through the specimen

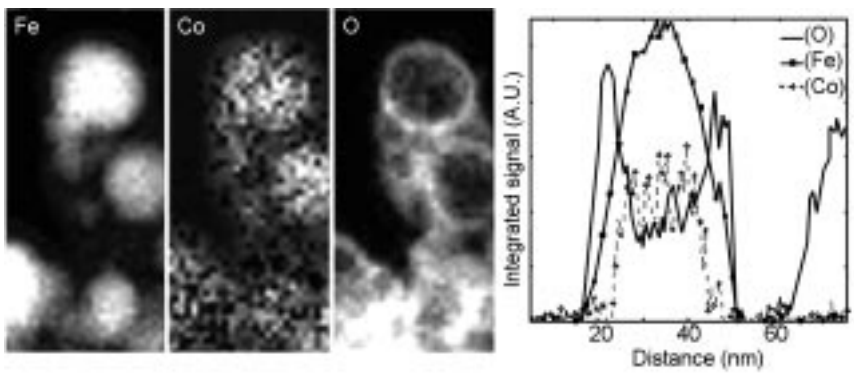

17.7 Images reconstructed from the Fe, Co and O EELS signals, imaging their distribution within Fe_xCo_{1-x} particles of 30 nm size embedded in silica matrix. They highlight the thin oxygen layer at the surface of the particle as well as the higher Fe content in the particle. At the right side is the elemental profile of Fe, Co and O along a diameter of a particle; vertical axis is proportional to atomic content. Experiments are done on a STEM VG HB 501 microscope.[165]

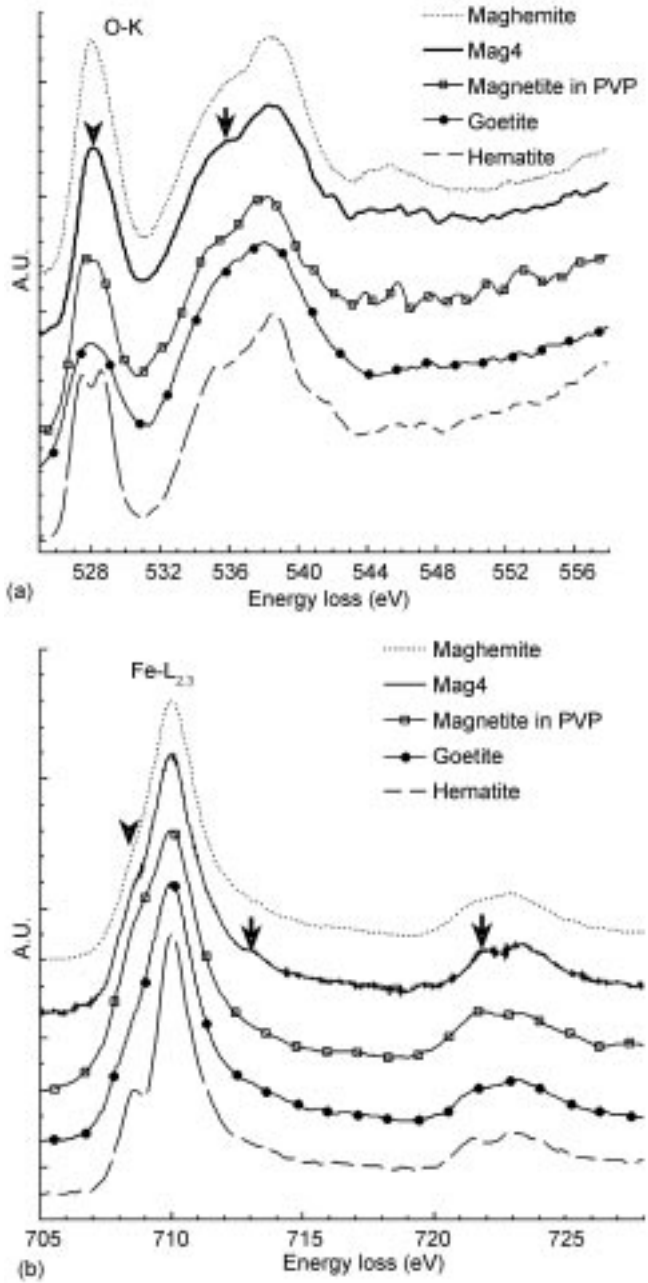

17.8 (a) O-K and (b) Fe-L2,3 edges at about 532 and 708 eV respectively, from different iron oxides compared to the ones from a sample called Mag4. The analysis of the fine structures in O-K and Fe-L2,3 (marked by arrows in the figure) allows identification of the presence of maghemite in sample Mag4.

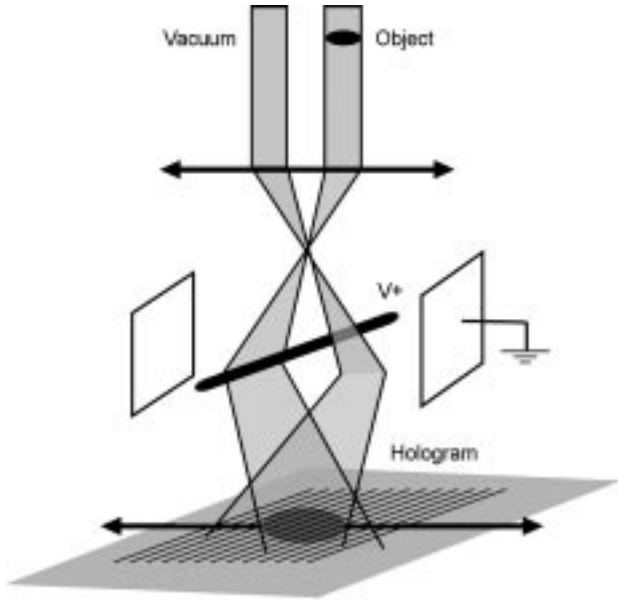

17.9 Principle of electron holography. A bi-prism deviates the part of the highly coherent electron wave which passes through the vacuum with that having interacted with the specimen. The resulting set of interference fringes contains the information concerning the phase of the electron wave.

and the other through the vacuum (see Fig. 17.9). Subsequent interference allows the amplitude and the phase shift of the high-energy electron to be recorded. The phase shift is sensitive to electric and in-plane magnetic fields in, and around, the sample. It is expressed by:

$$\Delta\phi = \frac{e}{\hbar}\oint (V.dt - A.ds). \tag{17.1}$$

The first term corresponds to the phase shift induced by the electrostatic potential and the second is due to the magnetic field. An important distinction with magnetic force microscopy (MFM) is that electron holography is fully quantitative giving the integrated field strength within particles and not restricted to just surface fields. The phase of the holographic fringes is measured from Fourier analyses selecting the fringe periodicity in the reciprocal space then extracting from the inverse Fourier transform the local phase and amplitude of the holographic fringes. Only specially equipped microscopes can, however, carry out holography experiments. Firstly, it is necessary to have a highly coherent electron source such as a field emission gun (FEG) which combines excellent temporal coherence ($\Delta E \sim 0.4$ eV) with high brightness. This explains why the original idea of Gabor[167] (1948) has only been exploited relatively recently (1990s). Holography also benefits from the development of slow-scan CCD cameras for quantitative image acquisition. Finally, the study of magnetic fields

at high spatial resolution has required the development of special lens called Lorentz lenses. This is because the traditional objective lenses affect the sample with intense magnetic fields, of the order of one tesla, thus saturating the magnetic structure of the sample with magnetization parallel to the electron beam axis, undetectable by electron holography. The advantage of the Lorentz lenses, although less powerful, is that the specimen is in field-free conditions. Resolutions of some few nanometers are nevertheless possible. A technical difficulty is that the phase depends on both the electric and magnetic fields in the sample. The phase will therefore depend strongly on the mean inner potential of the material, which is not necessarily of interest. Various schemes have been developed to remove this component, thus allowing the observation of magnetic fields[168] or electric fields within a device.[169] An example of the effect of the mean inner potential is shown in Fig. 17.10. In this case, the magnetic FeNi nanocrystal is magnetized out of the plane by the objective lens. The main component to the phase is therefore the mean inner potential of the material. The phase is then simply proportional to the thickness of the sample viewed in projection. Iso-phase contours clearly show the spherical nature of the particle.

An example of the measurement of magnetic fields in 4 nm thick Co nanowires is shown in Fig. 17.10. Here, the Co wire was magnetized in the observation plane with the objective lens switched off. A Lorentz lens was used to obtain high magnification. The components due to the mean inner potential and the magnetization of the Co were separated by reversing the magnetization in the wires thanks to the field of the objective lens. Figure 17.11 presents the results obtained by holography on one single Co nanowire and on crossing wires.[170] Figures 17.11(a) and 17.11(b) represent the phase shift due to the mean inner potential whose profiles along lines '1' and '2' are given in Figs 17.11(e) and 17.11(g) respectively. The phase shifts due to the magnetic induction of the

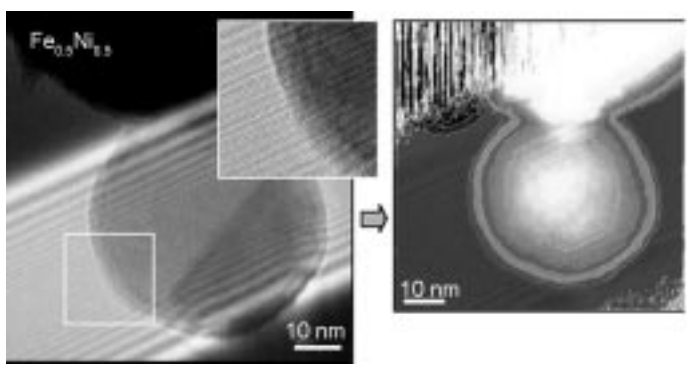

17.10 Mean inner potential measurements by electron holography. The phase of the holographic fringes (see the displacement of the fringes) is proportional to the mean inner potential and thickness of the specimen. The widely spaced fringes are from Fresnel effects from the edges of the bi-prism wire and can be removed by taking reference holograms in the absence of a specimen.

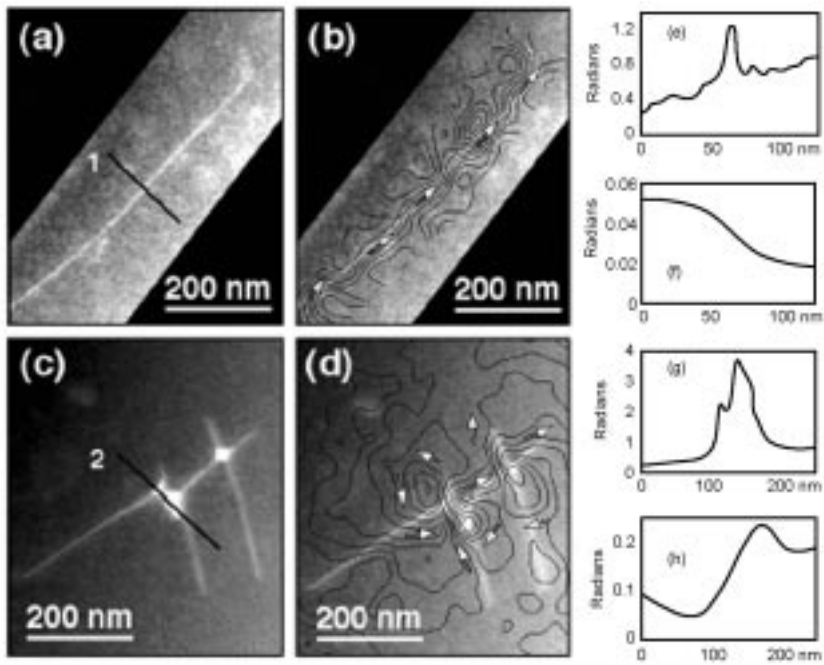

17.11 (a) MIP contribution to the phase shift for a single Co nanowire. (b) Contours ~ 0.005 radian spacing generated from the magnetic contribution to the phase shift for the nanowire, superimposed onto the MIP contribution. (c) As for (a) but for a multibranch nanowire, (d) as for (b) but for the multibranch nanowire with a 0.015 radian contour spacing. (e) and (f) line profiles obtained along line 1 from the MIP and magnetic contributions to the phase shift across the isolated nanowire, respectively. (g) and (h) as for (e) and (f) but for line 2 and the multibranch nanowire.[170]

two nanowires are reported in Figs. 17.11(c) and 17.11(d).

The phase shift due to the magnetic induction is about 10 times less than the one corresponding to the mean inner potential and its value across the wire (0.03 rad) corresponds to a nanowire fully magnetized along its axis with B = 1.7 tesla. The magnetization lies along the wire axis which is the Co-hcp 'c' axis (Fig. 17.11(b)) while it presents a peculiar vortex structure around the junction of the Co wires in Fig. 17.11(d).

17.4.5 XRD/WAXS

From the X-ray diffraction point of view, magnetic polymer nanocomposites can be considered as the mixture of a polymeric matrix and of a large set of randomly oriented very small crystals, thus their study does not introduce theoretical difficulties. However, when compared to the study of more usual crystallites of micrometric size, several practical drawbacks quickly appear:

- the intensity of a diffracted beam is directly related to the number of atoms included in the crystallites and only low count rates are obtained with that class of materials;
- according to the well known Scherrer relation, strong peak broadening is observed at the nanometric scale; for very small crystallite size, the peak to baseline ratio is so much reduced that nanometric powders can, wrongly, be perceived as amorphous;
- the scattering produced by the particles is, of course, mixed with the one generated by the polymeric matrix which can itself be more or less 'amorphous'.

These size-related difficulties can, and often do, combine with more common ones such as the reduced amount of powder available or the necessity to preserve the nanocomposite from oxygen or moisture exposure. They all point to specific measurement procedures providing the highest possible signal to background ratio. Slow measurements on powders sealed inside thin-walled glass capillaries have proved to be satisfactory in all respects. The size of the capillary should be adjusted to optimize the absorption and is of course composition dependant. Measurements of the matrix alone are mandatory and are combined with the nanocomposite ones taking into account all corrections in order to accurately extract the scattering pattern of the magnetic particles alone. The usual analysis in the reciprocal space can be performed, however, for a range of dimensions of some few nanometers, the Fourier transform approach is an efficient way to exploit the total wide angle X-ray scattering (WAXS). Data measurement up to large angles (typically 130º) using a short wavelength, i.e. molybdenum or silver radiation, reduces termination effects. The one-dimensional radial distribution function – RDF[171] obtained provides useful and easily readable information (see Fig. 17.12): the global shape and extent of the function envelope are related to the size and shape of the objects (the coherence length is not, however, a true size measurement since twinning or disorder also terminate the RDF); first peak(s) location is a direct measurement of bond-length in the material; finally, the complete set of distances is a signature of the order inside the objects and can immediately be compared with reference structures. Metallic nanoparticles (single metal or binary alloys) and nanowires have been successfully studied by this method which also applies to well-crystallized oxides.[172–173]

17.4.6 Small angle scattering

Small angle scattering of light, x-rays and neutrons are very useful techniques for the examination of structures. They are non-invasive and do not require much sample preparation. Therefore, they have been widely used for polymers, composites and biological materials. The length scale accessible by light scattering is hardly reaching the nanometer region. Although, multi-angle

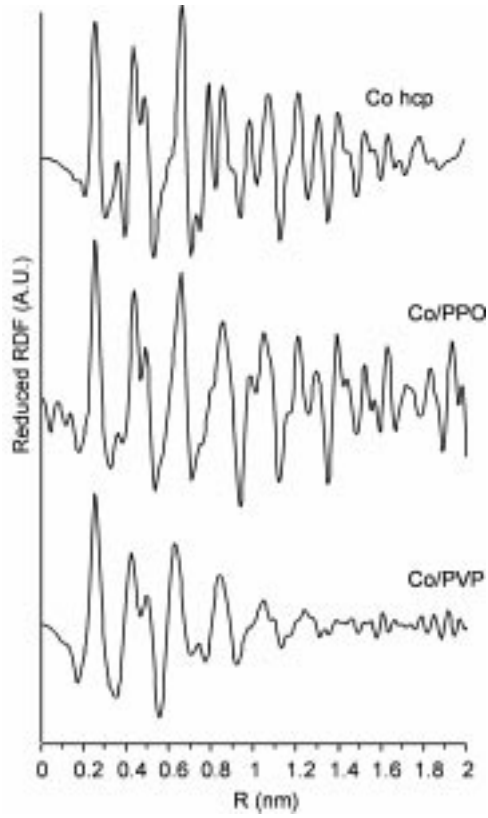

17.12 Cobalt magnetic nanocomposites – top curve: RDF computed from a spherical model with bulk cobalt hcp structure (320 atoms); middle: cobalt nanoparticles in polyphenyloxide (PPO), 4.2 nm in diameter (from HRTEM); bottom: cobalt nanoparticles in polyvinylpyrrolidone (PVP), 1.4 nm in diameter; for the bigger size, particles are structurally close to bulk metal whereas the very small size induces both a lower symmetry structure (polytetrahedral) and a strong increase of magnetization.[163]

dynamic light scattering is a useful tool for making rapid rough estimations of particle size in polymer, nanoparticle or nanocomposite suspensions. Small angle scattering of x-rays and neutrons is an excellent technique for the observation of structural features in the range from 1 nm to near 1 μm.[174] Compared with TEM and force microscopy, it has the advantages of easy sample preparation, rapid measurements, large areas of observation, and possibility of 'in-situ' observation of processes. SAXS technique consist of measuring the scattered intensity of an X-ray beam as a function of the scattering vector $q = (4\pi/\lambda \sin \theta)$, where λ is the wavelength of the radiation and θ is one half of the scattering angle. The scattered intensity in a nanocomposite can be expressed as:

$$I(q) = I_0 P(q) S(q) \tag{17.2}$$

where $P(q)$ corresponds to the Fourier Transform of the distance distribution function in a nanoparticle, $p(r)$, and $S(q)$ is a structure factor that is related to the distribution of interparticle distances $g(r)$. Therefore, intensity curves yield information about particle size and shape in monodisperse nanocomposites,[174] particle size distribution in polydisperse systems,[175] interparticle distances in dense nanocomposite solids and ferrofluids,[176] and shell thickness in ferrofluids.[177] Neutron scattering can also yield information about the magnetic structure and magnetic properties of nanoparticles,[178] specially when using polarised neutrons.[179] Figure 17.13 shows SAXS curves of pellets of PVP-iron

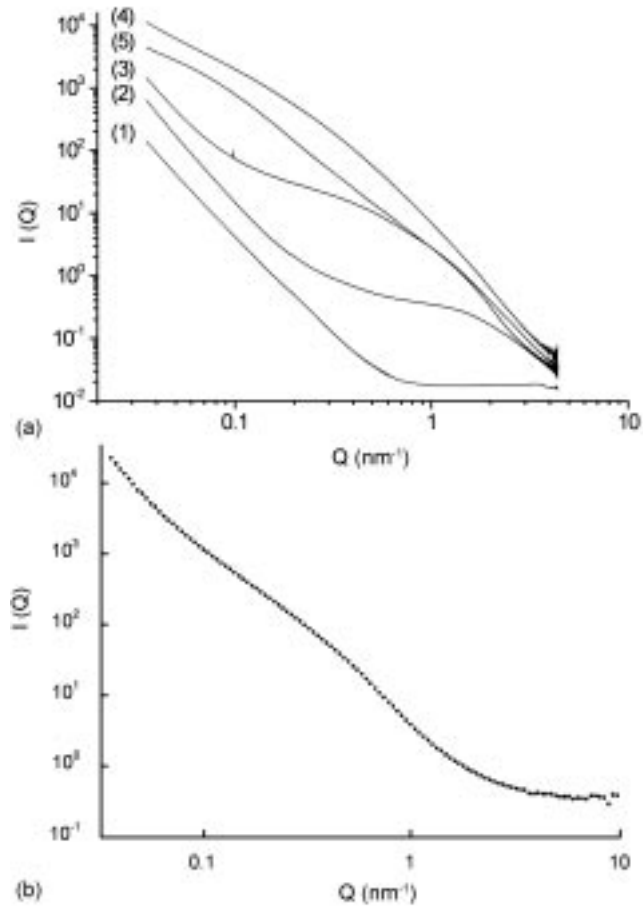

17.13 (a) SAXS log plot of PVP (1), maghemite-PVP nanocomposites containing spherical particles of different sizes (2–4), and goethite-PVP nanocomposite with rod-like particles. (b) SANS of the same sample as in curve (4) of (a).

oxide nanocomposite powdered samples. Three regions can be distinguished in these plots. The low q region corresponds to surface scattering from the polymer grains, and the high q region corresponds to surface scattering from the iron oxide nanoparticles. The curves in this regions are very closed to a Porod regime, thus, information about particle specific surface, particle volume and particle volume fraction can be derived from SAS general theorems.[180] The central region yields information about particle size distribution and interparticle distance. In curve (5), the central region is a straight line of slope near 2 that is typical of rod-like particles.

17.5 Magnetic properties

It has been stressed in previous sections: the need for a good control of particle size in the preparation and a fine characterization at the nanoscopic level. This is because, while magnetic properties of coarse grain materials are mainly dependent on composition and crystal structure, magnetic properties of nanoparticles are also very much dependent on size. Moreover, magnetic nanostructured materials show unique properties at certain sizes that are not found in bulk materials. First, particle sizes are similar or smaller to that of magnetic domains, something that affects the magnetization properties particularly the hysteresis cycle and coercive field. Second, finite-size and surface effects providing structural and magnetic disorder become increasingly influential as the size reduces. In sufficiently small magnetic particles, whether ferro or ferrimagnetic, the magnetization may be reversed by thermal agitation, a phenomenon that is known as superparamagnetism. Finally, very small particles of the size of some few nanometers at sufficiently low temperature can switch the direction of the magnetization through quantum tunnelling. Interaction between the polymeric matrix and the particles has the effect of introducing some further disorder at the particle surface, particularly in the presence of strong covalent bonds between the particle and the matrix. Moreover, in the case of conducting matrices, charge carriers may interact with the particle magnetic moment and conductivity may become field-dependent. In this section we will briefly describe these phenomena and will discuss recent results from the literature. Since the particles are considered to be well dispersed in the polymeric matrix we will assume they do not interact magnetically with each other.

17.5.1 Single domain particles

A material possessing net spontaneous magnetization generally consists of many domains. These are the consequence of the demagnetization field and the minimization of the free magnetic energy of the system. However, this is not the case for magnetic particles smaller than a critical diameter, below which the exchange forces may dominate and in spite of the presence of demagnetization

energy only one domain is energetically favored and the particle is uniformly magnetized.[181] The critical diameter for such 'single domain' particles can be estimated as $2J^{1/2}/M_S$, where J is the exchange constant and M_S the moment per unit volume.[182,183] Monodomain particles should behave as a paramagnetic gas following the Langevin equation. In practice, magnetization data can be fitted to Langevin behavior only when a distribution of magnetic moments is assumed.[184] Two important phenomena occur around the critical size for monodomain formation. As the grain size approaches this critical value, the coercive field, H_c, is roughly inversely proportional to the particle size.[185] Thus, optimal grain size for hard magnetic materials is around a few hundreds nanometers. However, below this size, H_c decreases very rapidly with the particle size.[185] Therefore, nanocrystalline alloys have a large potential as soft magnetic materials.

17.5.2 Finite-size and surface effects

As the particle size decreases finite-size and surface effects become increasingly important.[1,186] The lattice symmetry breaks at the surface resulting in large perturbations in the crystal field or in the electronic structure, differences in the magnetocrystalline anisotropy with respect to the core, spin disorder and magnetic frustration, particularly in ferrimagnets. Surface ions have incomplete coordination shells, which alters their moment orientation and results in a disorder spin configuration near the surface and a reduction in the magnetization as compared to bulk materials.[187] Then, in the case of either ferro- and ferrimagnetic particles, strong differences can be observed in the particle magnetization as compared to the bulk for the same isotherms.[188,189] An example of a decrease of the magnetization with decreasing particle size for maghemite nanoparticles is shown in Fig. 17.14(a). In the case of antiferromagnetic particles the appearing of net magnetization has also been observed associated to the 'uncompensated' moments and to spin casting effects due to the breaking of symmetry and differences in the magnetocrystalline anisotropy at the surface boundary.[190,191] In this case, the magnetization increases with the particle size (Fig 17.14(b)). Other phenomena related to finite-size and/or surface effects are a lowering of the Curie temperature, high closure fields in hysteresis loops and shifted loops after field cooling.[192]

17.5.3 Superparamagnetism

In sufficiently small ferro- or ferrimagnetic particles with an effective uniaxial anisotropy per unit volume K_a the relaxation of the magnetization will vary exponentially with the temperature following a Néel-Brown process[193,194] characterized by a relaxation time given by

$$\tau = \tau_0 e^{\epsilon/k_B T} \tag{17.3}$$

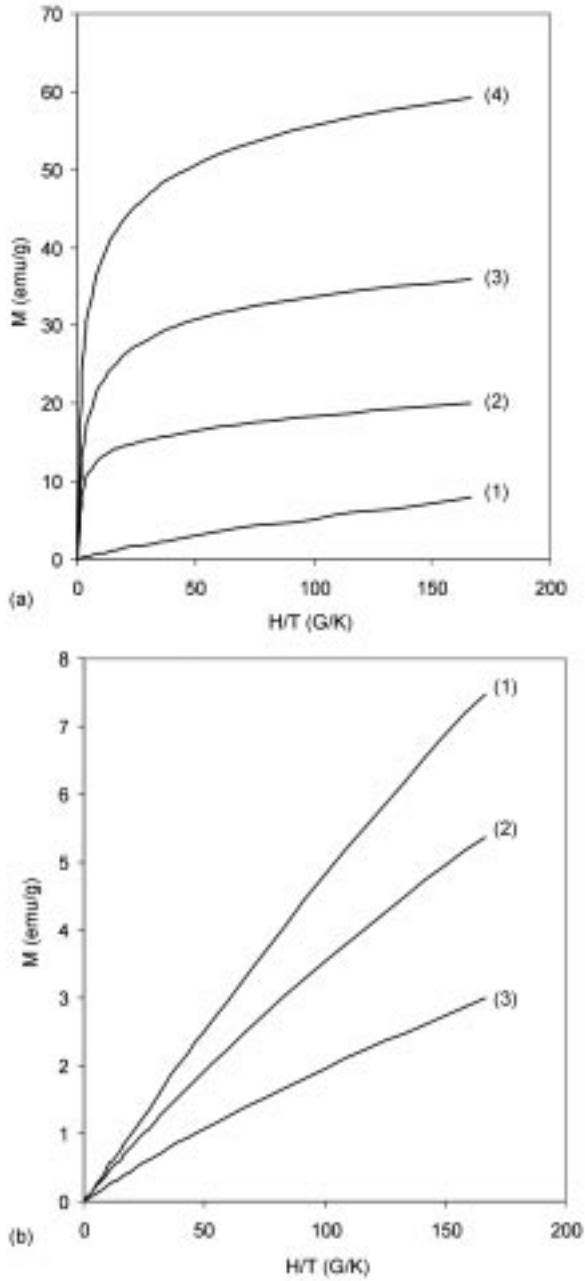

17.14 (a) Magnetization curves for maghemite-PVP samples containing particles with specific surface: 1.50 (1), 0.87 (2), 0.65 (3), 0.36 (4). (b) Magnetization curves for goethite-PVP samples containing particles with specific surface: 0.27 (1), 0.14 (2), 0.13 (3).

where τ_0 is a frequency factor, normally of the order of 10^{-9} to 10^{-13} s, E is the height of the energy barrier, which in a first approximation can be estimated to be proportional to the particle volume, V, and effective anisotropy, K_{eff},

$$E = K_{eff} V \tag{17.4}$$

and k_B is the Boltzmann constant. In noninteracting very fine particles the effective anisotropy is governed by surface anisotropy and shape anisotropy contributions whilst (core) magnetocrystalline anisotropy can be negligible.[195,196]

The existence of different particle sizes and shapes leads to a distribution of relaxation times, with an average value τ_{av}, that, in general, is also temperature dependent. The time τ is then the average time needed for a given kind of particle to reverse its magnetization after removing the external applied field. The practical consequence is that when the measuring time, τ_m, is greater than τ one observes a behavior similar to a paramagnet. However, for $\tau_m < \tau$ the complete reorientation of the magnetic moments of the cluster cannot take place during the measuring time. Thus, below a blocking temperature T_B, given by the condition $\tau_m(T_B) = \tau_m$, the system appears 'blocked' and its behavior is strongly dependent on τ_m. There is a number of techniques to experimentally observe superparamagnetism: magnetization, ac susceptibility, neutron scattering and Mössbauer spectroscopy. Each of these experimental techniques can provide information related to different relaxation rates since each has a different characteristic measuring time, which ranges from 10–100 s for dc magnetization measurements to 10^{-14}–10^{-12} s for neutron scattering experiments. Figure 17.15

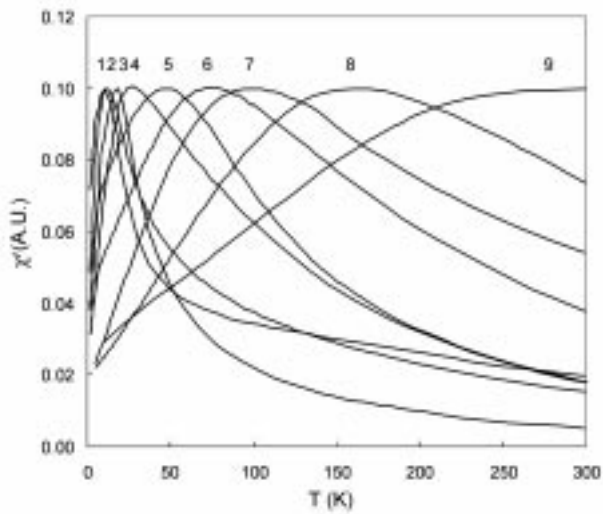

17.15 In-phase ac magnetic susceptibility of several maghemite-PVP samples with different particle sizes in a range from 4 nm (1) to 16 nm (9) (the curves are rescaled).

illustrates the variation of the blocking temperature with the particle size in maghemite-polyvinylpyridine nanocomposites. Superparamagnetic behavior sets a limit for the size of particles in magnetic recording. When the thermal energy, $k_B T$, is higher than the magnetic anisotropy energy, $K_{eff} V$, magnetization reversal can freely occur.

In the presence of an oscillating magnetic field, superparamagnetic nanoparticles can absorb energy by two resonance mechanisms:

1. Néel magnetic relaxation, and
2. ferromagnetic resonance (FMR).

The energy absorbed can be expressed as:[197]

$$E = \frac{\omega}{2\pi} \chi'' h^2 (1), \tag{17.5}$$

where ω is the frequency of the alternating field, χ'' is the out-of-phase susceptibility and h is the external field. Relaxation resonance occurs in the radiofrequency region (MHz), and FMR in the microwave region (GHz). The first is useful for hyperthermia therapy[16,30,198] and the second for microwave absorption.[69–72]

17.6 Future trends

There are two main areas of development for magnetic nanocomposites. One of them is dealing with applications in biomedicine, and the other with the development of methods for the fabrication of nano-organized structures and their applications in recording media, sensors and devices. These are very current in the main nanotechnology initiatives in the USA[199] and Europe.[200] In biomedicine, the usefulness of magnetic nanoparticles for imaging, separating, directing and heating is fully demonstrated. Looking to the future, there is a large number of biological processes to be followed, diseases to diagnose, drugs to deliver or localize, therapies to be improved by hyperthermia, substances and cells to be purified or separated, devices for microanalysis to be designed, for which magnetic nanoparticles can be used. However, the performance of available materials is far from being optimal. That would require joint expertise in: colloidal chemistry (monodisperse particles), organic-inorganic chemistry (stable shells appropriate for anchoring biological vectors), biochemistry (finding biological vectors), hematology and toxicology (biocompatibility assays), diseases (i.e. cancer), characterization and magnetism (structure-properties models), engineering (building magnetic instruments to generate and measure magnetic fields). Up to now, the research in this field has been somewhat fragmented. The future lies in the formation of multidisciplinary teams that can tackle the question with a global perspective. Several extensive programs have been launched in this direction.[199,200] Among them we can mention: the

BioMagnetICs program from the Defense Science Office oriented to the development of biosensors, magnetic base microanalysis devices, magnetically targeted therapeutics.[201] A number of companies are also fabricating and developing magnetic nanomaterials for biomedical applications.[201–203]

Concerning nanostructured magnetic nanocomposites, a large part of the research effort in this field is oriented to the control of particle size and organization by self-assembly, block copolymers, dendrimers or liquid crystals. These methods open the possibility of an easy fabrication of nanodevices at mild conditions and they have attracted the interest of the big companies in the field.[204] An illustrative example of research in this field can be found in the work of the magnetic materials group at NIST.[205]

Other uses, such as printing, magnetic shielding, microwave applications, etc., have the added difficulty of high manufacturing costs. Thus, another area for future developments is the design of low cost production methods for magnetic nanoparticles and films.

The list of companies dedicated to the manufacture of magnetic nanoparticles and nanocomposites is very extensive. Some of them are mentioned in ref. 206. More information about publications and developments in magnetic polymer nanocomposites can be found on the websites of 'magnetic microspheres',[207] and 'Nanoforum',[208] and in the books cited in refs 209–212.

17.7 References

1. Kodama R H, 'Magnetic nanoparticles', *J Magn Magn Mater*, 1999 **200** (1–3) 359–372.
2. Meyer M, Persson O and Power Y, 'Mapping excellence in nanotechnologies. Preparatory study'. European Comission, 2001. (http://europa.eu.int/comm/research/era/).
3. Institute for Prospective Technological Studies 'Emerging Thematic Priorities for European Research. Nanotechnology', 2000. (http://priorities.jrc.es).
4. Rocco M C, 'Vision for Nanotechnology R&D in the Next Decade', IWGN, National Science and Technology Council USA, 1999.
5. a) Torquato S, Hyun S, and Donev A, 'Multifunctional composites: optimizing microstructures for simultaneous transport of heat and electricity', *Phys Rev Lett*, 2002 **89** (26) 266601(1–4).
   b) Duan X F, Huang Y, Agarwal R and Lieber C M, 'Single-nanowire electrically driven lasers', *Nature* 2003 **421** 241–245.
6. IBM, 'The Giant Magnetoresistive Head: A giant leap for IBM Research', www.research.ibm.com/research/gmr.html.
7. a) Stephen Mann S, John Werbb J, Robert J P Williams R J P, *Biomineralization, Chemical and Biological Perspectives*, VCH, Weinheim, 1989.
   b) National Advisory Board, *Hierarchical Structures in Biology as a Guide for New Materials Technology*, National Academy Press, Washington DC, 1994.
8. a) Awschalom D D, McCord M A and Grinstein G, 'Observation of macroscopic spin phenomena in nanometer-scale magnets', *Phys Rev Lett*, 1990 **65** (6) 783–786.

b) Awschalom D D and Divincenzo D P, 'Complex dynamics of mesoscopic magnets', *Phys Today*, 1995 **48** (4) 43–48.
9. Weissleder R and Papisov M, 'Pharmaceutical iron oxides for MR imaging', *Rev Magn Reson Med*, 1992 **4** 1–20.
10. Moghimi S M, Hunter A C and Murray J C, 'Long-circulating and target-specific nanoparticles: theory to practice', *Pharmacol Rev*, 2001 **53** (2) 283–318.
11. Brigger I, Dubernet C and Couvreur P, 'Nanoparticles in cancer therapy and diagnosis', *Adv Drug DeliverRev*, 2002 **54** (5) 631–651.
12. Philips Research Press Release 24/06/2004, http://www.research.philips.com.
13. Lange J, Kötitz R, Haller A, Trahms L, Semmler W and Weitschies W, 'Magnetorelaxometry – a new binding specific detection method based on magnetic nanoparticles' *J Magn Magn Mater*, 2002 **252** (1–3) 381–383.
14. Bogoyevitch M A, Kendrick T S, Ng D C H and Barr R K, 'Taking the cell by stealth or storm? Protein Transduction Domains (PTDs) as versatile vectors for delivery', *DNA Cell Biol*, 2002 **21** (12) 879–894.
15. Uhlen M, 'Magnetic separation of DNA' *Nature* 1989 **340** (6236) 733–734.
16. Jordan A, Scholz R, Maier-Hauff K, Johannsen M, Wust P, Nadobny J, Schirra H, Schmidt H, Deger S and Loening S, 'Presentation of a new magnetic field therapy system for the treatment of human solid tumors with magnetic fluid hyperthermia', *J Magn Magn Mater*, 2001 **225** (1–2) 118–126.
17. Chin T S, 'Permanent magnet films for applications in microelectromechanical systems' *J Magn Magn Mater*, 2000 **209** (1–3) 75–79.
18. Advanced Magnetic Technologies and Consulting (http://amtc.org/Code/product_rd.htm).
19. Park M, Chaikin P M, Register R A, and Adamson D H, 'Large area dense nanoscale patterning of arbitrary surfaces', *Appl Phys Lett*, 2001 **79** (2) 257–259.
20. Park M, Harrison C, Chaikin P M, Register R A and Adamson D H, 'Block copolymer lithography: Periodic arrays of similar to 10(11) holes in 1 square centimeter', *Science*, 1997 **276** (5317) 1401–1404.
21. Sun Q H, Lam J W Y, Xu K T, Xu H Y, Cha J A K, Wong P C L, Wen G H, Zhang X X, Jing X B, Wang F S and Tang B Z, 'Nanocluster-containing mesoporous magnetoceramics from hyperbranched organometallic polymer precursors', *Chem Mater*, 2000 **12** (9) 2617–2624.
22. Caruso F, Spasova M, Susha A, Giersig M and Caruso R A, 'Magnetic nanocomposite particles and hollow spheres constructed by a sequential layering approach', *Chem Mater*, **2001** 13 (1) 109–116.
23. Safarik I and Safarikova M, 'Magnetic nanoparticles and biosciences', *Monatsh. Chem*, 2002 **133** 737–759.
24. Thomas-Keprta K L, Bazylinski D A, Kirschvink J L, Clemett S J, MacKay D S, Wentworth S J, Vali H, Gigson E K and Romanek C S, 'Elongated prismatic magnetite crystals in ALH84001 carbonate globules: Potential Martian magnetofossils', *Geochim, Cosmochim. Acta*, 2000 **64** (23) 4049–4081.
25. Lohmann K J and Lohmann C M F, 'Detection of magnetic field intensity by sea turtles', *Nature*, 1996 **380** (6569) 59–61.
26. Diebel C E, Proksch R, Green C R, Neilson P and Walker M M, 'Magnetite defines a magnetoreceptor', *Nature*, 2000 **406** (6793) 299–302.
27. Dobson J, 'Nanoscale biogenic iron oxides and neurodegenerative disease', *FEBS Lett*, 2001 **496** 1–5.

28. Grossman H L, Myers W R, Vreeland V J, Bruehl R, M. Alper M D, Bertozzi C R and Clarke J. 'Detection of bacteria in suspension by using a superconducting quantum interference device', *Proc Natl Acad Sci USA*, 2004 **101** (1) 129–134.
29. a) Bulte J W M, Douglas T, Witwer B, Zhang S, Strable E, Lewis B K, Zywicke H, Miller B, van Gelderen P, Moskowitz B M, Duncan I D and Frank J A, 'Magnetodendrimers allow endosomal magnetic labeling and in vivo tracking of stem cells', *Nat Biotech*, 2001 **19** (12) 1141–1147.
b) Weissleder R, Moore A, Mahmood U, Bhorade R, Benveniste H, Chiocca E A and Basilion J P, 'In vivo magnetic resonance imaging of transgene expression' *Nat Med*, 2000 **6** 351–354.
c) Weissleder R, 'Scaling down imaging: Molecular mapping of cancer in mice' *Nat Rev Cancer*, 2002 **2** (1) 11–18.
30. Häfeli U, Schütt W, Teller J and Zborowski M, *Scientific and Clinical Applications of Magnetic Carriers*, Plenum Press, New York, 1997.
31. Safark I and Safarkova M, 'Use of magnetic techniques for the isolation of cells', *J Chromatogr B*, 1999 **722** (1–2), 33–53.
32. Willard M A, Kurihara L K, Carpenter E E, Calvin S and Harris V G, 'Chemically prepared magnetic nanoparticles', *Int Mater Rev*, 2004 **49** (3–4) 125–170.
33. Berger P, Adelman N B, Beckman K J, Campbell D J, Ellis A B and Lisensky G C, 'Preparation and properties of an aqueous ferrofluid', *J Chem Educ*, 1999 **76** (7) 943–948.
34. Sen S, 'Nanoprinting with nanoparticles: Concept of a novel inkjet printer', *J Disper Sci Technol*, 2004 **25** (4) 523–528.
35. Sunderland K, Brunetti P, Spinu L, Fang J Y, Wang Z J and Lu W G, 'Synthesis of gamma-Fe2O3/polypyrrole nanocomposite materials', *Mater Lett*, 2004 **58** (25) 3136–3140.
36. Liao M H and Chen D H, 'Characteristics of magnetic nanoparticles-bound YADH in water/AOT/isooctane microemulsions', *J Mol Catal B-Enzym*, 2002 **18** (1–3) 81–87.
37. Takafuji M, Ide S, Ihara H and Xu Z H, 'Preparation of poly(1-vinylimidazole)-grafted magnetic nanoparticles and their application for removal of metal ions', *Chem Mater*, 2004 **16** (10) 1977–1983.
38. Farshad M and Benine A, 'Magnetoactive elastomer composites', *Polym Test*, 2004 **23** (3) 347–353.
39. a) Farshad M, Le Roux M and Clemens F, 'Magnetoactive polymer composite fibers and fabrics', *11th int conf composites/nano engineering*, Ed. Hui D, Hilton Head, August 8–14, 2004.
b) Raymond L, Revolt J F, Ryan D H and Marchessault R H, 'In-situ synthesis of ferrites in cellulosics', *Chem Mater*, 1994 **6** (2) 249–255.
c) Mayes E L, Vollrath F and Mann S 'Fabrication of magnetic spider silk and other silk-fiber composites using inorganic nanoparticles', *Adv Mater*, 1998 **10** (10).
40. Royer F, Jamon D, Rousseau J J, Cabuil V, Zins D, Roux H and Bovier C, 'Experimental investigation on gamma-Fe2O3 nanoparticles Faraday Rotation: particles size dependence', *Eur Phys J-Appl Phys*, 2003 **22** (2) 83–87.
41. Aktsipetrov O A, 'Nonlinear magneto-optics in magnetic nanoparticles' *Colloid Surface A*, 2002 **202** (2–3) 165–173.
42. a) Bamakov Y A, Scott B L, Golub V, Kelly L, Reddy V and Stokes K L, 'Spectral dependence of Faraday rotation in magnetite-polymer nanocomposites', *J Phys*

Chem Solid, 2004 **65** (5) 1005–1010.
b) Yamaguchi K, Sato T, Kato Y, Inoue M and Fujii T, 'Magnetic and magneto-optical properties of composite films of ferromagnetic ultrafine particles dispersed in polymethyl methacrylate', *Mater Sci Forum*, 1998 **287** (2) 483–486.
43. Lenssen K M H, *et al.*, 'Robust giant magnetoresistance sensors', *Sensors Actuators A*, 2000 **85** 1–8.
44. Varfolomeev A E, Godovskii D Y, Kapustin G A, Volkov A V and Moskvina M A, 'Giant negative magnetoresistance in a composite system based on Fe3O4 nanocrystals on a polymer matrix', *JETP Lett*, 1998 **67** 39–42.
45. Grigor'ev E I, Zav'yalov S A, Chvalun S N, 'The effect of a magnetic field on the conductivity of poly(p-xylylene) films containing iron and nickel nanoparticles', *Polym Sci Ser. A*, 2003 **45** (8) 780–784.
46. Frolov G I, 'Film carriers for super-high-density magnetic storage', *Tech Phys*, 2001 **46** (12) 1537–1544.
47. Ahmed S R, Ogale S B and Kofinas P, 'Magnetic properties and morphology of block copolymer templated ferrimagnetic CoFe2O4 nanoparticles', *IEEE Trans. Magn.*, 2003 **39** (5) 2198–2200.
48. Hyeon T, Lee S S, Park J, Chung Y, and Na H B, 'Synthesis of highly crystalline and monodisperse maghemite nanocrystallites without a size-selection process', *J Am Chem Soc*, 2001 **123** (51) 12798–12801.
49. Chen L, Yang W J, and Yang C Z, 'Preparation of nanoscale iron and Fe3O4 powders in a polymer matrix', *J Mater Sci*, 1997 **32** (13) 3571–3575.
50. a) Abes J I, Cohen R E and Ross C A, 'Block-copolymer-templated synthesis of iron, iron-cobalt, and cobalt-nickel alloy nanoparticles', *Mater Sci Eng C*, 2003 **23** (5) 641–650.
b) Ghanem M A, Bartlett P N, de Groot P and Zhukov A 'A double templated electrodeposition method for the fabrication of arrays of metal nanodots', *Electrochem Comm*, 2004 **6** (5) 447–453.
51. a) Sun S, Murray C B, Weller D, Folks L and Moser A, 'Monodisperse FePt nanoparticles and ferromagnetic nanocrystal superlattices', *Science* 2000 **287** (5460) 1989–1992.
b) Sun S H, Anders S, Hamann H F, Thiele J U, Baglin J E E, Thomson T, Fullerton E E, Murray C B and Terris B D, 'Polymer mediated self-assembly of magnetic nanoparticles', *J Am Chem Soc*, 2002 **124** (12) 2884–2885.
c) Anders S, Sunb S, Murray C B, Rettner C T, Best M E, Thomson T, Albrecht M, Thiele J U, Fullerton E E and Terris B D, 'Lithography and self-assembly for nanometer scale magnetism', *Microelectron Eng*, 2002 **61–62** 569–575.
52. Data Storage Systems Center, Carnegie Mellon University, (http://www.ece.cmu.edu/research/dssc/)
53. Seagate Corporation, http://www.seagate.com/
54. Vadera S R, Tuli A, Kumar N, Sharma B B, Gupta S R, Prakash C and Kishan P, 'Preparation and study of finely dispersed magnetic oxide in polymer matrix', *J Phys IV*, 1997 **7** (C1), 549–550.
55. Rabelo D, Lima E C D, Barbosa D P, Silva V J, Silva O, Azevedo R B, Silva L P, Lemos A P C and Morais P C, 'Investigation of magnetic nanoparticles in acrylonitrile-methyl methacrylate-divinylbenzene mesoporous template', *J Magn Magn Mater*, 2002 **252** 13–15.
56. Thurn-Albrecht T, Schotter J, Kastle G A, Emley N, Shibauchi T, Krusin-Elbaum

Guarini K, Black C T, Tuominen M T and Russell T P, 'Ultrahigh-density nanowire arrays grown in self-assembled diblock copolymer templates', *Science*, 2000 **290** (5499) 2126–2129.
57. Lopez D, Cendoya I, Mijangos C, Julia A, Ziolo R and Tejada J, 'Magnetic applications of polymer gels', *Macromol Simp*, 2001 **166** 173–178.
58. Skumryev V, Stoyanov S, Zhang Y, Hadjipanayis G, Givord D and Nogues J, 'Beating the superparamagnetic limit with exchange bias', *Nature*, 2003 **423** (6942) 850–853.
59. Berkowitz A E, and Takano K, 'Exchange anisotropy – a review', *J Magn Magn Mater*, 1999 **200** (1–3) 552–570.
60. Baker C, Shah S I and Hasanain S K, 'Magnetic behavior of iron and iron-oxide nanoparticle/polymer composites', *J Magn Magn Mater*, 2004 **280** (2–3) 412–418.
61. Sourty E, Ryan D H and Marchessault H, 'Characterization of magnetic membranes based on bacterial and man-made cellulose', *Cellulose*, 1998 **5** (1) 5–17.
62. Hua F, Cui T H and Lvov Y M, 'Ultrathin cantilevers based on polymer-ceramic nanocomposite assembled through layer-by-layer adsorption', *Nano Lett*, 2004 **4** (5) 823–825.
63. Fidler J, Schrefl T, Hoefinger S and Hajduga M, 'Recent developments in hard magnetic bulk materials', *J. Phys.: Condens. Matter*, 2004 **16** S455–S470.
64. Zahn M, 'Magnetic fluid and nanoparticle applications to nanotechnology', *J Nanopart Res*, 2001 **3** (1) 73–78.
65. Pawlowski B, Schwarzer S, Rahmig A and Töpfer J, 'NdFeB thick films prepared by tape casting', *J Magn Magn Mater*, 2003 **265** (3) 337–344.
66. Cho H J and Ahn C H, 'Microscale resin-bonded permanent magnets for magnetic micro-electro-mechanical systems applications', *J Appl Phys*, 2003 **93** (10) 8674–8676.
67. Yudin V E, Otaigbe J U, Bui T X, Svetlichnyi V M, 'Polyimide bonded magnets: Processing and properties', *J Appl Polym Sci*, 2003 **88** (14) 3151–3158.
68. Korenivski V, 'GHz magnetic film inductors', *J Magn Magn Mater*, 2000 **215** (SI) 800–806.
69. a) Lagarkov A N, Rozanov K N, Simonov A and Starostenko S N, 'Microwave permeability of magnetic films', forthcoming.
b) Rozanov, K N, 'Ultimate thickness to bandwidth ratio of radar absorbers', *IEEE Trans. Ant. Propagat.*, 2000 **48** 1230–1234.
c) Nguyen M T and Diaz A F, 'A novel method for the preparation of magnetic nanoparticles in a polypyrrole powder', *Adv Mater*, 1994 **6** (11) 858–860.
70. Brosseau C, Ben Youssef J, Talbot P and Konn A M, 'Electromagnetic and magnetic properties of multicomponent metal oxides heterostructures: Nanometer versus micrometer-sized particles', *J Appl Phys*, 2003 **93** (11) 9243–9256.
71. Fujieda T, Ikeda S, Suzuki S, Abe T and Aono Y, 'Microwave absorption properties of Fe-SiO_2 nanocomposite powder', *J Jpn I Met*, 2002 **66** (3) 135–138.
72. Brosseau C, Mallégo S, Quéffelec P and Youssef J B, 'Nonreciprocal electromagnetic properties of nanocomposites at microwave frequencies', *Phys Rev B*, 2004 **70** 092401-(1–4).
73. Kwon O Y, Kwon Y D, Kim D H, Kim J C and Lee Z H, 'Mechanical and magnetic properties of a novel polymer infiltrated directionally solidified RE-Fe giant magnetostrictive materials', *IEEE Trans. Magn.*, 2004 **40** (4) 2778–2780.
74. Malini K A, Anantharaman M R, Sindhu S, Chinnasamy C N, Ponpandian N,

Narayanasamy A, Balachandran M and Pillai V N S, 'Effect of cycling on the magnetization of ion exchanged magnetic nanocomposite based on polystyrene', *J Mater Sci*, 2001 **36** (4) 821–824.

75. Varga Z, Feher J, Filipcsei G, Zrinyi M, 'Smart nanocomposite polymer gels', *Macromol Symp*, 2003 **200** 93–100.
76. Chatterjee J, Haik Y, Chen C J, 'Biodegradable magnetic gel: synthesis and characterization', *Colloid Polym Sci*, 2003 **281** (9) 892–896.
77. Gangopadhyay R and De A, 'Conducting polymer nanocomposites: A brief overview', *Chem Mater*, 2000 **12** (3) 608–622.
78. Pokhodenko V D, Krylov V A, Kurys Y I and Posudievsky O Y, 'Nanosized effects in composites based on polyaniline and vanadium or iron oxides', *Phys Chem Chem Phys*, 1999 **1** (5) 905–908.
79. Deng J, Ding X, Zhang W, Peng Y, Wang J, Long X, Li P and Chan A S C, 'Magnetic and conducting Fe3O4cross-linked polyaniline nanoparticles with core–shell structure', *Polymer*, 2002 **43** (8) 2179–2184.
80. Sunderland K, Brunetti P, Spinu L, Fang J Y, Wang Z J and Lu W G, 'Synthesis of gamma-Fe_2O_3/polypyrrole nanocomposite materials', *Mater Lett*, 2004 **58** (25) 3136–3140.
81. Murillo N, Ochoteco E, Alesanco Y, Pomposo J A, Rodriguez J, Gonzalez J, del Val J J, Gonzalez J M, Britel M R, Varela-Feria F M and de Arellano-Lopez A R, '$CoFe_2O_4$-polypyrrole (PPy) nanocomposites: new multifunctional materials', *Nanotech*, 2004 **15** (4) S322–S327.
82. a) Ziolo R F, Giannelis E P, Weinstein B A, Ohoro M P, Ganguly B N, Mehrotra V, Russel M W and Huffman D R, 'Matris-Mediated synthesis of nanocrystalline gamma-Fe_2O_3 – A new optically transparent magnetic material', *Science*, 1992 **257** (5067) 219–223.
    b) Sohn B H and Cohen R E, 'Processible optically transparent block copolymer films containing superparamagnetic iron oxide nanoclusters', *Chem Mater* 1997 **9** (1) 264–269.
83. Vassiliou J K, Mehrotra V, Otto J W and Dollahon N R, 'Optical absorption tail and superparamagnetism of gamma-Fe2O3 nanoparticles in a polymer matrix', *Mater Sci Forum*, 1996 **225** 725–730.
84. Wang D S, He J B, Rosenzweig N and Rosenzweig Z, 'Superparamagnetic Fe_2O_3 Beads-CdSe/ZnS quantum dots core-shell nanocomposite particles for cell separation', *Nano Lett*, 2004 **4** (3) 409–413.
85. Redl F X, Cho K S, Murray C B, O'Brien C B, 'Three-dimensional binary superlattices of magnetic nanocrystals and semiconductor quantum dots', *Nature* 2003 **423** (6943) 968–971.
86. Massart R and Cabuil V, 'Synthese en milieu alkaline de magnetite colloidale: control de rendement et de la taille des particules', *J Chim Phys*, 1987 **84** (7–8) 967–973.
87. a) Nathani H, Gubbala S and Misra R D K, 'Magnetic behavior of nickel ferrite-polyethylene nanocomposites synthesized by mechanical milling process' *Mater Sci Eng B*, 2004 **111** (2–3) 95–100.
    b) Cornell R M and Schwertmann U, *The Iron Oxides*, VCH, Weinheim, 1996.
88. Morales M P, Pecharroman C, Gonzalez Carreño T and Serna C J, 'Structural chararacteristics of uniform γ-Fe_2O_3 particles with different axial (length/width) Ratios', *J Solid State Chem*, 1994 **108** 158.

89. a) S. Taketomi S, Kawasaki K, Ozaki Y, Yuasa S, Otani Y and Miyajima H, 'Characteristics of yttrium-iron-garnet ultrafine particles prepared by the alkoxide method', *J Am Ceram Soc*, 1994 **77** (7) 1787–1792.
b) Carpenter E E, 'Iron nanoparticles as potential magnetic carriers', *J Magn Magn Mater*, 2001 **225** 17–20.
90. a) Forster G D, Barquin L F, Pankhurst Q A and Parkin I P, 'Chemical reduction synthesis of fine particle FeZrB alloys under aerobic and anaerobic conditions' *J Non-Cryst Solids* 1999 **244** (1) 44–54.
b) Linderoth S, Mörup S and Bentzon M D, J. 'Influence of pH on the composition and structure of Fe-Co-B alloy particles prepared by borohydride reduction in aqueous solutions', *J Magn Magn Mater*, 1990 **83** (1–3) 457–459.
c) Mörup S, Sethi S A, Linderoth S, Koch C B and Bentzon M D. 'Chemically prepared amorphous Fe-Ni-B alloy particles', *J Mater Sci*, 1992 **27** (11) 3010–3013.
91. Dragieva I, Stoeva S, Stoimenov P, Pavlikianov E and Klabunde K, 'Complex formation in solutions for chemical synthesis of nanoscaled particles prepared by borohydride reduction process', *Nanostruct Mater*, 1999 **12** (1–4) 267–270.
92. Murray C B, Sun S, Gaschler Doyle H, Betley T A and Kagan C R, 'Colloidal synthesis of nanocrystals and nanocrystal superlattices', *IBM J Res Dev*, 2001 **45** 47–56.
93. Tanabe K and Tanaka C, Japan Patent JP2000336496 2000.
94. a) B.R.V. Narasimhan, S. Prabhakar, P. Manohar and F.D. Gnanam, 'Synthesis of gamma ferric oxide by direct thermal decomposition of ferrous carbonate', *Mater Lett*, 2002 **52** (4–5) 295–300.
b) Deb P, Biswas T, Sen D, Basumallick A and Mazumder S, 'Characteristics of Fe_2O_3 nanoparticles prepared by heat treatment of nonaqueous powder precipitate', *J Nanoparticle Res*, 2002 **4** 91–97.
c) Matutes-Aquino J, García-Casillas P, Ayala-Valenzuela O and García-García S, 'Study of iron oxides obtained by decomposition of an organic precursor', *Mater Lett*, 1999 **38** (3) 173–177.
95. Nishimura T and Asada I, Japan Patent JP11092148 1999.
96. Janot R and Guerard D, 'One-step synthesis of maghemite nanometric powders by ball-milling', *J Alloy Compd*, 2002 **333** (1–2) 302–307.
97. Chernov A A, 'Modern Crystallography III: Crystal Growth', *Springer Series in Solid-State Sciences*, Vol 36, Springer-Verlag, 1984.
98. Sohnel O and Garside J, *Precipitation: Basic Principles and Industrial Applications*, Butterworth-Heinemann, Oxford, 1992.
99. Bica I, 'Plasma device for magnetic nanoparticles production' *J Magn Magn Mater*, 1999 **201** (1–3) 45–48.
100. Khomutov G B, Obydenov A Y, Yakovenko S A, Soldatov E S, Trifonov A S, Khanin V V and Gubin S P, 'Synthesis of nanoparticles in Langmuir monolayer' *Mater Sci Eng C*, 1999 **8–9** 309–318.
101. Cao X, Koltypin Prozorov R, Y, Kataby G and Gedanken A, 'Preparation of amorphous Fe_2O_3 powder with different particle sizes', *J Mater Chem*, 1997 **7** (12) 2447–2451.
102. Myers D, *Surfaces, Interfaces and Colloids*, VCH Publishers Inc., Weinheim 1991.
103. Janzen C and Roth P, 'Formation and characteristics of Fe_2O_3 nano-particles in doped low pressure H-2/O-2/Ar flames' *Combust Flame*, 2001 **125** 1150–1161.

104. Veintemillas-Verdaguer S, Bomatí-Miguel O and Morales M P, 'Effect of the process conditions on the structural and magnetic properties of Fe_2O_3 nanoparticles produced by laser pyrolysis' *Scripta Materialia*, 2002 **47** 589–593.
105. Auzans E, Zins D, Blums E and Massart R, 'Synthesis and properties of Mn-Zn ferrite ferrofluids', *J Mater Sci*, 1999 **34** (6) 1253–1260.
106. Neveu S, Bee A, Robineau M and Talbot D, 'Size-selective chemical synthesis of tartrate stabilized cobalt ferrite ionic magnetic fluid', *J Colloid Interface Sci*, 2002 **255** (2) 293–298.
107. Pileni M P, 'Magnetic fluids: fabrication, magnetic properties, and organization of nanocrystals', *Adv Funct Mater*, 2001 **11** (5) 323–336.
108. Suslick K S, Choe S B, Cichowlas A A and Grinstaff M W, 'Sonochemical synthesis of amorphous iron', *Nature*, 1991 **353** (6343) 414–416.
109. Pradhan B K, Toba T, Kyotani T and Tomita A, 'Inclusion of crystalline iron-oxide nanoparticles in uniform carbon nanotubes prepared by a template carbonization method', *Chem Mater*, 1998 **10** (9) 2510–2515.
110. Sjögren C E, Johansson E, Nævestad A, Sontum P C, Briley-Sæbö K and Fahlvik A K, 'Crystal size and properties of superparamagnetic iron oxide (SPIO) particles', *Magn Reson Imag*, 1997 **15** (1) 55–67.
111. Rheinländer T, Kötitz R, Weitschies W and Semmler W, 'Magnetic fractionation of magnetic fluids', *J Magn Magn Mater*, 2000 **219** (2) 219–228.
112. Rheinländer T, Roessner D, Weitschies W and Semmler W, 'Comparison of size-selective techniques for the fractionation of magnetic fluids', *J Magn Magn Mater*, 2000 **214** 269–275.
113. a) Massart R, Dubois E, Cabuil V and Hasmonay E, 'Preparation and properties of monodisperse magnetic fluids', *J Magn Magn Mater*, 1995 **149** 1.
b) Chemseddine A and Weller H, 'Highly monodisperse quantum sized CdS particles by size selective precipitation', *Ber Bunsen-Ges Phys Chem*, 1993 **97** 636–637.
114. Grüttner C and Teller J, 'New types of silica-fortified magnetic nanoparticles as tools for molecular biology applications', *J Magn Magn Mater*, 1999 **194** (1–3) 8–15.
115. Moeser G D, Green W H, Laibinis P E, Linse P, Hatton T A, 'Structure of polymer-stabilized magnetic fluids: Small-angle neutron scattering and mean-field lattice modelling', *Langmuir*, 2004 **20** (13) 5223–5234.
116. Chatterjee J, Haik Y and Chen C J, 'Polyethylene magnetic nanoparticle: a new magnetic material for biomedical applications', *J Magn Magn Mater*, 2002 **246** (3) 382–391.
117. Rong M Z, Zhang M Q, Wang H B and Zeng H M, 'Surface modification of magnetic metal nanoparticles through irradiation graft polymerization', *Appl Surface Sci*, 2002 **200** (1–4) 76–93.
118. Kumar R V, Koltypin Y, Palchik O and Gedanken A, 'Preparation and characterization of nickel-polystyrene nanocomposite by ultrasound irradiation', *J Appl Polym Sci*, 2002 **86** (1) 160–165.
119. Csetneki I, Faix M K, Szilagyi A, Kovacs A L, Nemeth Z and Zrinyi M, 'Preparation of magnetic polystyrene latex via the miniemulsion polymerization technique', *J Polym Sci A*, 2004 **42** (19) 4802–4808.
120. Bidan G, Jarjayes O, Fruchart J M and Hannecart E, 'New nanocomposites based on tailor dressed magnetic nanoparticles in a polypyrrole matrix', *Adv Mater*, 1994

6 (2) 152–155.
121. Kommareddi N S, Tata M, John V T, McPherson G L, Herman M F, Lee Y S, O'Connor C J, Akkara J A and Kaplan D L, 'Synthesis of superparamagnetic polymer-ferrite composites using surfactant microstructures', *Chem Mater*, 1996 **8** (3) 801–809.
122. Rabelo D, Lima E C D, Reis A C, Nunes W C, Novak M A, Garg V K, Oliveira A C and Morais P C, 'Preparation of magnetite nanoparticles in mesoporous copolymer template', *Nano Lett* 2001 **1** (2) 105–108.
123. Veiga V, Ryan D H, Sourty E, Llanes F and Marchessault R H, 'Formation and characterization of superparamagnetic cross-linked high amylose starch', *Carbohyd Polym*, 2000 **42** (4) 353–357.
124. Castro C, Ramos J, Millan A, González-Calbet J and Palacio F, 'Production of magnetic nanoparticles in imine polymer matrixes', *Chem Mat*, 2000 **12** 3681–3688.
125. Millan A and Palacio F, 'Magnetic nanocomposites from N-base polymers', *Appl Organometal Chem*, 2001 **15** 1–5.
126. Ramos J, Millan A and Palacio F, 'Production of magnetic nanoparticles in a polyvinylpyridine matrix', *Polymer*, 2000 **41** 8461.
127. Millán A, Palacio F, Falqui A, Snoeck S and Serin V, 'Particle size and density control in magnetic polymer nanocomposites', *Mat Res Soc Symp Proc*, 2002 **733E** 1–6.
128. Gubin S P, 'Metalcontaining nano-particles within polymeric matrices: preparation, structure, and properties', *Colloid Surface A*, 2002 **202** (2–3) 155–163.
129. Pardoe H, Chua-anusorn W, St. Pierre T G and Jon Dobson J 'Structural and magnetic properties of nanoscale iron oxide particles synthesized in the presence of dextran or polyvinyl alcohol', *J Magn Magn Mater* 2001 **225** (1–2) 41–46.
130. a) Banerjee S, John V T, McPherson G L, O'Connor C J, Buisson Y S L, Akkara J A and Kaplan D L (1997), 'Polymer microsphere and polymer ferrite nanocomposite preparation by precipitation from water-in-oil microemulsions', *Colloid Polym Sci*, **275** (10), 930–937.
b) R18 Chatterjee J, Haik Y and Chen C J, 'Synthesis of polyethylene magnetic nanoparticles', *J Disper Sci Technol*, 2002 **23** (4) 563–568.
131. Bunker B C, Rieke P C, Tarasevich J, Campbell A A, Fryxell G E, Graff G L, Song L, Liu J, Virden J W and McVay G L, 'Ceramic thin-film formation on functionalized interfaces through biomimetic processing', *Science* 1994 **264** (5155) 48–55.
132. Strable E, Bulte J W M, Moskowitz B, Vivekanandan K, Allen M and Douglas T, 'Synthesis and characterization of soluble iron oxide-dendrimer composites', *Chem Mater*, 2001 **13** (6) 2201–2209.
133. Freedman D H, 'Exploiting the nanotechnology of life', *Science*, 1991 **254** (5036) 1308–1310.
134. Zhang J G, Xu S Q and Kumacheva E, 'Polymer microgels: Reactors for semiconductor, metal, and magnetic nanoparticles', *J Am Chem Soc*, 2004 **126** (25) 7908–7914.
135. Douglas T, Bulte J W M, Dickson D P E, Frankel R B, Pankhurst Q A, Moskowitz B M and Mann S, 'Inorganic-protein interactions in the synthesis of a ferromagnetic nanocomposite', *ACS Symp Ser*, 1995 **585** 19–28.
136. DeCuyper M and Joniau M, 'Magnetoliposomes – formation and structural characterization', *Eur Biophys J*, 1988 **15** (5) 311–319.

137. Chiriac H, Moga A E, Urse M and Ovari T A, 'Preparation and magnetic properties of electrodeposited magnetic nanowires', *Sensor Actuat A-Phys*, 2003 **106** (1–3) 348–351.
138. Sukhorukov G B, Donath E, Moya S, A. Susha S, Voigt A, Hartmann J, and Möhwald H, 'Microencapsulation by means of step-wise adsorption of poly-electrolytes', *J Microencapsul*, 2000 **17** (2) 177–185.
139. Dante S, Hou Z Z, Risbud S, Stroeve P, 'Nucleation of iron oxy-hydroxide nanoparticles by layer-by-layer polyionic assemblies', *Langmuir*, 1999 **15** (6) 2176–2182.
140. Kawana T, Onodera S and Samoto T, 'Advanced metal evaporated tape', *IEEE Trans Magn*, 1995 **31** (6) 2865–2870.
141. Hong J Kay E and Wang S X, 'Granular magnetic cobalt metal/polymer thin film system', *IEEE Trans Magn*, 1996 **32** (5) 4475–4477.
142. Nguyen L T, Lisfi A and Lodder J C, 'Effect of gas pressure on properties of FePt film sputtered on polymer substrate', *J Appl Phys*, 2004 **95** (11) 7492–7494.
143. Wagener M and Gunther B, 'Sputtering on liquids – a versatile process for the production of magnetic suspensions?', *J Magn Magn Mater*, 1999 **201** (1–3) 41–44.
144. Zaporojtchenko V, Zekonyte J, Biswas A and Faupel F, 'Controlled growth of nano-size metal clusters on polymers by using VPD method', *Surf Sci*, 2003 **532** (10) 300–305.
145. Trakhtenberg L I, Gerasimov G N, Aleksandrova L N and Potapov V K, 'Photo and radiation cryochemical synthesis of metal–polymer films: structure, sensor and catalytic properties', *Radiat Phys Chem*, 2002 **65** 479–485.
146. Mann S, Davis S A, Hall S R, Li M, Rhodes K H, Shenton W, Vaucher S and Zhang B J, 'Crystal tectonics: Chemical construction and self-organization beyond the unit cell', *J Chem Soc Dalton*, 2000 (21) 3753–3763.
147. Manne S and Aksay I A, 'Thin films and nanolaminates incorporating organic/inorganic interfaces', *Curr Opin Solid St M*, 1997 **2** 358–364.
148. Lee D K, Kang Y S, Lee C S and Stroeve P, 'Structure and characterization of nanocomposite Langmuir-Blodgett films of poly(maleic monoester)/Fe_3O_4 nanoparticle complexes', *J Phys Chem B*, 2002 **106** (29), 7267–7271.
149. Wortham E, Zorko A, Arcon D and Lappas A, 'Organic-inorganic perovskites for magnetic nanocomposites', *Physica B*, 2002 **318** (4) 387–391.
150. Zhu Y H, Yang X L, Li P L and Ying H, 'From layer-by-layer assembled core-shell particles to medical/biochemical diagnostics and drug delivery', *Prog Chem*, 2003 **15** (6) 512–517.
151. Caruso F, Susha A S, Giersig M and Mohwald H, 'Magnetic core-shell particles: Preparation of magnetite multilayers on polymer latex microspheres', *Adv Mater*, 1999 **11** (11) 950.
152. Liu G, 'Functional crosslinked nanostructures from block copolymers', *Mat Sci Eng C-Biomim*, 1999 **10** (1–2) 159–164.
153. Vadera S R, Mathur R, Parihar M and Kumar N, 'Direct synthesis of nanocomposite of gamma-Fe_2O_3 in the copolymer matrix of aniline-formaldehyde in presence of zinc ions', *Nanostruct Mater*, 1997 **8** (7) 889–898.
154. Ahmed S R, Ogale S B, Papaefthymiou G C, Ramesh R and Kofinas P, 'Magnetic properties of $CoFe_2O_4$ nanoparticles synthesized through a block copolymer nanoreactor route', *Appl Phys Lett*, 2002 **80** (9) 1616–1618.
155. Bizdoaca E L, Spasova M, Farle M, Hilgendorff M and Caruso F, 'Magnetically

directed self-assembly of submicron spheres with a Fe3O4 nanoparticle shell', *J Magn Magn Mater*, 2002 **240** (1–3) 44–46.
156. Tejada J, Zhang X X, Kroll E, Bohigas X and Ziolo R F, 'Solid containing rotationally free nanocrystalline gamma-Fe2O3: Material for a nanoscale magnetic compass?', *J Appl Phys*, 2000 **87** (11) 8008–8012.
157. Heyen U and Schüler D, 'Growth and magnetosome formation by microaerophilic Magnetospirillum strains in an oxygen-controlled fermentor', *Appl Microbiol Biotechnol*, 2003 **61** 536–544.
158. Flynn C E, Lee S W, Peelle B R and Belcher A M, 'Viruses as vehicles for growth, organization and assembly of materials', *Acta Mater*, 2003 **51** (19) 5867–5880.
159. Wang Z L, 'Transmission electron microscopy of shape-controlled nanocrystals and their assemblies', *J Phys Chem B*, 2000 **104** (6) 1153–1175.
160. Spence J C H, *High-resolution electron microscopy* (3rd edition), Oxford, Oxford University Press, 2003.
161. Malm J O and O'Keefe M A, 'Deceptive "lattice spacings" in high-resolution micrographs of metal nanoparticles' *Ultramicroscopy*, 1997 **68** (1) 13–23.
162. Stadelmann P A, 'EMS – a software package for electron diffraction analysis and HREM image simulation in materials science', *Ultramicroscopy*, 1987 **21** (2) 131–145.
163. Dassenoy F, Casanove M J, Lecante P, Verelst M, Snoeck E, Mosset A, Oud Ely T, Amiens C and Chaudret B, 'Experimental evidence of structural evolution in ultrafine cobalt particles stabilized in different polymers – From a polytetrahedral arrangement to the hexagonal structure', *J Chem Phys*, 2000 **112** (18) 8137–8145.
164. Suenaga K, Tencé M, Mory M, Colliex C, Kato C, Okazaki H, Shinohara T, Hirahara H, Bandow K, Ijima S, 'Element-selective single atom imaging', *Science*, 2000 **290** (5500) 2280.
165. Falqui A, Serin V, Calmels L, Snoeck E, Corrias A and Ennas G, 'EELS investigation of FeCo/SiO2 nanocomposites', *J Microsc-Oxford J*, 2003 **210** (1) 80–88.
166. Laffont L, Monthioux M and Serin V, 'Plasmon as a tool for in situ evaluation of physical properties for carbon materials', *Carbon*, 2002 **40** (5) 767–780.
167. Gabor D, 'A new microscopic principle', *Nature*, 1948 **161** (4098) 777–778.
168. Dunin-Borkowski R, McCartney M R, Smith D J and Parkin S S P, 'Towards quantitative electron holography of magnetic thin films using in situ magnetisation reversal', *Ultramicroscopy*, 1998 **74** (1–2) 61–73.
169. Rau W D, Schwander P, Baumann F H, Höppner W and Ourmazd A, 'Two-dimensional mapping of the electrostatic potential in transistors by electron holography', *Phys Rev Lett*, 1999 **82** (12) 2614–2617.
170. Snoeck E, Dunin-Borkowski R E, Dumestre F, Renaud P, Amiens C, Chaudret B and Zurcher P, 'Quantitative magnetization measurements on nanometer ferromagnetic cobalt wires using electron holography', *Appl Phys Lett*, 2003 **82** 88–90.
171. Warren B E, *X-ray Diffraction*, Addison-Wesley Publishing Company, Reading, MA, 1969.
172. Casanove M J, Lecante P, Snoeck E, Mosset A and Roucau C, 'HREM and WAXS study of the structure of metallic nanoparticles', *J. Phys. III France*, 1997 **7** 505–515.
173. Fromen M C, Lecante P, Casanove M J, Bayle Guillemaud P, Zitoun D, Amiens C

and Chaudret B, 'Structural study of bimetallic Co_xRh_{1-x} nanoparticles: Size and composition', *Phys Rev B*, 2004 **69** (23) 235416.

174. a) Guinier A and Fournet G, *Small-angle Scattering of X-rays*, Wiley, New York, 1955.
b) Glatter O and Kratky O, *Small-angle X-ray Scattering*, London, Academic Press, 1982.
c) Roe R-J, *Methods of X-ray and Neutron Scattering in Polymer Science*, Oxford University Press, New York, 2000.
175. a) Svergun D I 'Mathematical methods in small-angle scattering data analysis', *J Appl Cryst*, 1991 **24** 485–492.
b) Beaucage G, Kammler H K and Pratsinis S E, Particle size distribution from small-angle scattering using global scattering functions, *J Appl Cryst*, 2004 **37** 523–535.
c) Porod G, 'Die Röntgenkleinwinkelstreuung von dichtgepackten kolloiden Systemen. I. Teil,' *Kolloid Z*, 1951 **124** 83–114.
176 a) Riello P and Benedetti A, 'Small angle scattering of a polydisperse system of interacting hard spheres: An analytical solution', *J Chem Phys*, 1997 **106** (21) 8660–8663.
b) Laity P R, Taylor J E, Wong S S, Khunkamchoo P, Norris K, Cable M, Andrews G T, Johnson A F and Cameron R E, 'A review of small-angle scattering models for random segmented poly(ether-urethane) copolymers', *Polymer*, 2004 **45** 7273–7291.
177. Eberbeck D and Bläsing J, ' Investigation of particle size distribution and aggregate structure of various ferrofluids by small angle scattering experiments', *J Appl Cryst*, 1999 **32** 273–280.
178. a) Weissmüller J, Michels A, Barker J G, Wiedemann A, Erb U and Shull R D, 'Analysis of the small-angle neutron scattering of nanocrystalline ferromagnets using a micromagnetics model', *Phys Rev B*, 2001 **63** 214414(18).
b) Hellman F, Shapiro A L, Abarra E N, Robinson R A, Hjelm R P, Seeger P A, Rhyne J J and Suzuki J I, 'Long ferromagnetic correlation length in amorphous $TbFe_2$', *Phys Rev B*, 1999 **59** (17) 11408–11417.
179. Heinemann A and Wiedemann A, 'Benefits of polarized small-angle neutron scattering on magnetic nanometer scale structure modeling', *J Appl Cryst*, 2003 **36** 845–849.
180. Spalla O, Lyonnard S and Testard F, 'Analysis of the small-angle intensity scattered by a porous and granular medium', *J Appl Cryst*, 2003 **36** 338–347.
181. Frenkel J and Dorfman J, 'Spontaneous and induced magnetization in ferromagnetic bodies', *Nature*, 1930 **126** 274–275.
182. Frei E H, Shtrikman S and Treves D, 'Critical size and nucleation field of ideal ferromagnetic particles', *Phys Rev* 1957 **106** 446–455.
183. Zijlstra H, in *Ferromagnetic Materials*, ed. Wohlfarth E P, North-Holland, Amsterdam, 1982 **3** 37–105.
184. Elmore W C, 'The magnetization of ferromagnetic colloids', *Phys Rev*, 1938 **54** 1092–1095.
185. McHenry M E and Laughlin D E, 'Nano-scale materials for future magnetic applications', *Acta Mater*, 2000 **48** 223–238.
186. a) Dorman J L, Fiorani D and Tronc E, in *Advances in Chemical Physics*, ed. Prigogine I and Rice S A, Vol. 98, Wiley, New York, 1997.

b) Iglesias O and Labarta A, 'Finite-size and surface effects in maghemite nanoparticles: Monte Carlo simulations', *Phys. Rev. B*, 2001 **63** (18) 184416(11).
187. Kodama R H, Berkowitz A E, McNiff E J and Foner S, 'Surface spin disorder in $NiFe_2O_4$ nanoparticles' *Phys Rev Lett*, 1996 **77** (2) 394–397.
188. Respaud M, Broto J M, Rakoto H, Fert A R, Thomas L, Barbara B, Varelst M, Snoeck E, Lecante P, Mosset A, Osuna J, Ould Ely T, Amiens C and Chaudret B, 'Surface effects on the magnetic properties of ultrafine magnetic particles', *Phys. Rev B*, 1998 **57** (5) 2925–2935.
189. Kodama R H and Berkowitz A E, 'Atomic-scale magnetic modeling of oxide nanoparticles', *Phys. Rev. B* 1999 **59** (9) 6321–6336.
190. Pollard R J, Cardile C M, Lewis D G and Brown L J, 'Characterization of FeOOH polymorphs and ferrihydrite using low-temperature, applied-field, Mössbauer-Spectroscopy', *Clay Miner*, 1992 **27** (1) 57–71.
191. Coey J M D and Readman P W, 'New spin structure in an amorphous ferric gel', *Nature*, 1973 **246** (5434) 476–478.
192. Fiorani D ed., *Surface Effects in magnetic Nanoparticles*, Springer Berlin 2005.
193. Néel L, 'Theorie du trainage magnetique des ferromagnetiques en grains fins avec applications aux terres cuites', *Ann Geophys*, 1949 **5** 99–136.
194. a) Brown W F, 'Relaxational behavior of fine magnetic particles', *J Appl Phys*, 1959 **30** 130S–132S.
b) Brown W F, 'Thermal fluctuations of a single-domain particle', *Phys Rev* 1963 **130** 1677–1686.
195. Dormann J L, D'Orazio F, Lucari F, Tronc E, Prené P, Jolivet J P and Fiorani D, 'Thermal variation of the relaxation time of the magnetic moment of γ-Fe_2O_3 nanoparticles with interparticle interactions of various stregth', *Phys. Rev. B*, 1996 **53** (21) 14291–14297.
196. Dormann J L, D'Orazio F, Lucari F, Spinu L, Tronc E, Prené P, Jolivet J P and Fiorani D, 'Dynamical properties of gamma-Fe_2O_3 nanoparticles dispersed in a polymer', *Mater Sci Forum*, 1997 **235–238** 669–974.
197. Palacio F, Lazaro F J and van Duyneveld A J, ' Magnetic phenomena in molecular solids: A tutorial approach', *Mol Cryst Liq Cryst* 1989 **176** 289–306.
198. a) Hergt R, Hiergeist R, Hilger I, Kaiser W A, Lapatnikov Y, Margel S and Richter U, 'Maghemite nanoparticles with very high AC-losses for application in RF-magnetic hyperthermia', *J Magn Magn Mater*, 2004 **270** 345–357.
b) Jordan A, Scholz R, Wust P, Fähling H and Felix R, 'Magnetic fluid hiperthermia (MFH). Cancer treatment with AC magnetic field induced excitation of biocompatible superparamagnetic nanoparticles', *J Magn Magn Mater*, 1999 **201** 413–419.
c) Charité Hospital in Berlin, (http://www.germanyinfo.org/relaunch/info/publications/week/2003/030613/misc2.html).
d) Ito A, Matsuoka F, Honda H and Kobayashi T, 'Hyperthermia using magnetic nanoparticles in an experimental subcutaneous murine melanoma', *Cancer Immunol Immun*, 2004 **53** (1), 26–32.
e) Rosenweig R E, 'Heating magnetic fluid with alternating magnetic field', *J Magn Magn Mater*, 2002 **252** 370–374.
199. National Nanotechnology Inititative (http://www.nano.gov/).
200. European FP6 projects (http://www.cordis.lu/fp6).
201. *Bio-Magnetic Interfacing Concepts program*, Program Manager: Dr. Valerie

Browning, Defense Advanced Research Projects, USA (http://www.darpa.mil/dso/thrust/biosci/biomagn.htm).
202. Philips, http://www.research.philips.com.
203. Bayer, http://www.bayerdiag.com/index.cfm.
204. Some large companies with ongoing research on organized magnetic nanocomposites: IBM (www.research.ibm.com/), Seagate (www.seagate.com/), Xerox, (www.xeroxtechnology.com), Kodak (www.kodak.com/).
205. Materials Science and Engineering Laboratory, National Institute of Standards and Technology (http://www.metallurgy.nist.gov/).
206. Some suppliers of magnetic nanocomposite materials: Chemicell (www.chemicell.com/), Bio-Rad Laboratories (www.bio-rad.com/), Nanophase Technologies (www.nanophase.com/), Dynal Biotech (www.dynalbiotech.com/), Zyvex Corporation (http://www.zyvex.com), Advanced Magnetics Inc. (www.advancedmagnetics.com/), Reade Advanced Materials (http://www.reade.com/Products/Alloys/iron-platinum-alloy.html), NVE Corporation (http://www.nve.com/), Nanomat (http://www.nanomat.com/), Nanophase Technologies Corporation (http://www.nanophase.com/), Ferrotec (http://www.ferrotec.com/).
207. Magnetic microspheres, http://www.magneticmicrosphere.com/maglit.htm.
208. Nanoforum, http://www.nanoforum.org/.
209. Arshady R ed, *Microspheres, Microcapsules and Liposomes series*, Vol. 1-6, City Books , London , 1999, 2000, 2001, 2002, 2002, 2003.
210. Hadjipanayis G C and Prinz G A, *Science and Technology of Nanostructured Magnetic Materials*, New York, Plenum Press, 1991.
211. Ajayan M, Schadler L S and Braun P V, *Nanocomposite Science and Technology*, Weinheim, Wiley-VCH, 2003.
212. Schmid G ed, *Nanoparticles*, Weinheim, Wiley-VCH, 2004.

18

Phenolic resin/SiO_2 organic-inorganic hybrid nanocomposites

C-L CHIANG, Hung-Kuang University, Taiwan and
C-C M MA, National Tsing-Hua University, Taiwan

18.1 Introduction

The organic-inorganic hybrid materials are new types of composites which have attracted much interest in recent years. Of the several kinds of inorganic components, metal oxides such as silica,[1,2] alumina[3,4] and titania[5–8] are preferred in hybrid materials because they are readily prepared in-situ by the sol-gel process using the corresponding organic metal alkoxide. In particular, silicon alkoxide and silica are perhaps the most widely used for this purpose since the sol-gel reaction of silicon alkoxide is both mild and easily controlled. The fabricated materials possess the advantages of both organic polymers and inorganic ceramics. These materials are termed 'Ceramers' by Wilkes[9] or 'Ormosils' by Schmidt.[10] Several polymers have been investigated as the organic phase of the hybrids including, but not limited to, polyimides,[11,12] polybutadiene and polydimethylsiloxane.[13]

The sol-gel process[14–22] has provided promising opportunities for the preparation of a variety of organic-inorganic hybrid materials at the molecular level. The in-situ development of a three-dimensional cross-linked inorganic network structure using an organic precursor such as an alkoxide, $M(OR)_4$, can be carried out within the polymer matrix. The hydrolysis and condensation reactions involved in the process may proceed as follows:[23]

Hydrolysis

$$M(OR)_4 + H_2O \longrightarrow (RO)_3M{-}OH + ROH \qquad (18.1)$$

Condensation

$$\equiv M{-}OH + HO{-}M\equiv \longrightarrow \equiv M{-}O{-}M\equiv + H_2O \qquad (18.2)$$

and/or

$$\equiv M{-}OH + RO{-}M\equiv \longrightarrow \equiv M{-}O{-}M\equiv + ROH \qquad (18.3)$$

Net reaction

$M(OR)_4 \longrightarrow$ 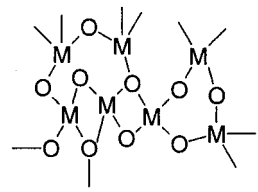 (18.4)

M = Si or Ti, etc.

The microstructure of the metal oxide obtained by using the sol-gel process is dependent on the hydrolysis and condensation reactions, which are largely controlled by the pH of the solution.[24–26] In the acid catalyzed reaction, the relative rate of the hydrolysis step is faster than the condensation step, thus resulting in more extended and less highly branched network structure. In the base-catalyzed reaction, the rate of condensation is faster than hydrolysis, thus resulting in highly condensed species, which may agglomerate into fine particles. Moreover, the sol-gel process is a very complex reaction involving many variables such as the type of alkoxide, pH value, the amount of water present, the type of cosolvent, and the temperature and drying method, for example.[27–30]

Phenolic resin is one of the common synthetic resins that have been used in a wide range of applications such as paints, adhesives, and composites. Phenolic resin is one of the thermoset class of polymers which has two types, namely resole type and novolac type, the formation of which depends on the synthetic method and catalyst used. Many attempts have been made to enhance the toughness[31–35] and thermal properties of phenolic resin. By the fundamental concept of hybrid materials preparation, the sol-gel method can be utilized to incorporate inorganic components into the phenolic resin and improve its properties. These systems have been studied by Haraguchi *et al.*[36,37] and Lin *et al.*[38,39]

It is well known that the sol-gel process is a useful technique for the preparation of organic-inorganic hybrid materials. In hybrid materials, the inorganic phase is formed within the organic polymer matrix by the sol-gel process. In a simple sol-gel process, hydrolysis and condensation reactions of inorganic alkoxides occur in a cosolvent containing water and are either acid or base-catalyzed at low temperature. The sol-gel process thus provides a method for the preparation of variety of organic-inorganic hybrid materials at the molecular level[40–47] for the in-situ development of a three-dimensional cross-linked inorganic network structure using an organic precursor such as alkoxy derivatives of metals such as Si or Ti for example. The most common precursor is tetraethoxysilane (TEOS) yielding a silica network.

Organic polymer matrix when combined with inorganic particles has been developed in past decades as a method for preparing organic-inorganic hybrid materials. These materials possess unique properties including improved physical, mechanical and thermal properties of the polymer systems. Material properties of physically mixed components depend on the concentration of the particle, its adhesion to polymer matrix, the uniformity of particle dispersion, etc. In the past

decade, a variety of elastomers, thermoplastics and thermosetting systems have been reinforced with inorganic fillers.[48–54] This in-situ formation of the organic-inorganic system becomes a new class of composites made by the sol-gel technique, frequently described as organic-inorganic hybrid materials. These new hybrid materials possess a controllable combination of the properties of both organic polymers and inorganic glasses. Due to the small size of the formed inorganic particles, usually in the order of nanometers, these hybrid materials are also called nanocomposites, thus often resulting in an optically transparent system.

In this study, two different coupling agents have been utilized to form the covalent bonding between organic and inorganic phases. The different coupling agents possess the different functional groups to react with the phenolic resin. Isocyanatopropyltriethoxysilane (IPTS) has the isocyante(NCO-) group to react with hydroxy(-OH) group. 3-Glycidoxypropyltrimethoxysilane (GPTS) uses the epoxy group to react with the hydroxy(-OH) group. We measured the feasibility of preparation to form the nanocomposites. This promoted the miscibility of hybrid ceramers. The inorganic components were dispersed uniformly in the organic matrix. The particle size was less than 100 nm, hence the formed products were nanocomposites. The inorganic components enhanced the thermal stability of polymer at high temperature. The nanocomposites will possess excellent flame retatardance and highly transparency. The properties imparted by the modification will increase the industrial uses for the polymer system. FTIR and ^{29}Si NMR were used to identify the structures of the hybrid ceramers. The thermal properties were investigated by thermogravimetric analysis (TGA) and differential scanning calorimeter (DSC). The flame retardance of hybrid ceramers was determined by limiting oxygen index (LOI) test and the UL-94 vertical test. Mechanical and thermal properties were also studied.

18.2 Experimental

18.2.1 Materials

Phenol and formaldehyde monomers are supplied by the Union Chemical Works Ltd, Taiwan. The novalac-type phenolic resin was synthesized in this laboratory. Hexamethylenetetramine (hexamine) was a purified industrial grade reagent obtained from Chu-Chung Resin Co., Taiwan. The concentrated sulfuric acid was obtained from the Osaka Chemical Co., Japan. Isocyanatopropyltriethoxysilane (IPTS) was purchased from United Chemical Technologies Inc., Bristol, PA, USA. 3-Glycidoxypropyltrimethoxysilane (GPTS) was purchased from Acros Organics Co., New Jersey, USA. Hexamethylene Tetramine (Hexa) was used as the curing agent, which was obtained from Acros Organics Co., New Jersey, USA. Tetraethoxysilane (TEOS) was also supplied from Acros Organics Co., Tetrahydrofuran (THF) was reagent grade supplied by Echo Chemical Co. Ltd., Taiwan.

18.2.2 Preparation of novolac phenolic resin

The novolac-type phenolic prepolymer was synthesized in a 1.0 L glass reactor equipped with a thermometer, reflux condenser, and stirrer. The reagents, 188 g phenol (2 mol) and 135 g formaldehyde (in 37 wt.% water solution, 1.67 mol), were fed into a flask reactor. The reaction was catalyzed by adding dilute sulfuric acid solution (2 g of sulfuric acid dissolved in 10 ml of water) and reacted at 100ºC for 7 hr in the reactor. The reaction was continued until the prepolymer with the desired viscosity (500–2000 cps at 25ºC) was obtained. At the end of the reaction, the calculated amount of NaOH (1.63g) was dispersed in 10 ml of water and added to neutralize the sulfuric acid catalyst and then stirred for an additional 30 min. The mixture was dehydrated under a pressure of 100 mm H_2O at 120–130ºC until the resin was clear.

18.2.3 Preparation of hybrid ceramers

IPTS was used as a coupling agent

Preparation of the hybrid ceramer involved the mixing of two solutions, A and B. Solution A consisted of modified phenolic resin and THF. The modified phenolic resin was synthesized as follows: 4 g 3-isocyanatopropyltriethoxysilane (equivalent weight 247 g) was added into 10 g phenolic resin (OH equivalent weight 90 g) at 60ºC, then it was stirred for 4 h until the characteristic peak of NCO group disappeared by FTIR spectra. Solution B contained H_2O/HCl/TEOS with a molar ratio 9:0.63:1. HCl was used as the catalyst for hydrolysis. DGEBA type epoxy (epoxy equivalent weight 180 g) was poured into the mixture of solutions A and B. DGEBA type epoxy was used as the curing agent for the modified phenolic resin. 3-Isocyanatopropyltriethoxysilane/phenolic resin/epoxy with the equivalent ratio was 0.3:1:1. The mixture was stirred until the solution became clear. The solution was cast to an aluminum dish to form a gel at room temperature. The wet gel was aged at room temperature for 48 h, then dried at 80ºC for 24 h. The samples were put in a vacuum oven at 150ºC for 24 h.

GPTS was used as a coupling agent

The preparation of the hybrid materials involved mixing with two solutions, A and B. Solution A was prepared as follows: 5 g of neat novolac type phenolic resin was dissolved in THF, the solid content was kept at 50%. Two grams of 3-Glycidoxypropyltrimethoxysilane (GPTS) was used as coupling agent to modify phenolic resin. GPTS was added slowly into the solution of phenolic resin and THF, the GPTS content was 10 phr (parts per hundred resin, it means the weight ratio of component to the main resin). Then, the mixture was stirred at 70ºC for 20–24 h. The modified-phenolic rein was obtained through the ring-opening

reaction of GPTS with hydroxyl groups in phenolic resin. This modified-phenolic resin/THF solution was called solution A.

Solution B composed of TEOS/H_2O/THF/HCl. In solution B, 1.25 g of TEOS was added to 1.25 g of THF solvent. The TEOS content was 20 wt.% (i.e, based on 100 parts of phenolic resin). The TEOS/H_2O molar ratio was 1:4, so 0.024 g of H_2O was added into the mixture. HCl was used as the catalyst for hydrolysis and its content was 0.03 wt.%. Then, the mixture was stirred at 25ºC for 30 min.

Hexamethylene tetramine was used as the curing agent, 0.6 g of hexamethylene tetramine was added into solution A. Then, solution A and solution B were mixed. The final solution was cast into aluminum dishes and aged at room temperature for 2–3 days. Then the samples were dried at the rate of 2ºC/h from 25ºC to 80ºC and then kept at 80ºC for 2 h. The samples were finally cured at 120ºC for 4 h, 180ºC for 2 h, and post-cured at 230ºC for 8 h.

18.2.4 Reaction scheme

IPTS used as coupling agent

Phenolic/silica hybrid ceramer was prepared as described in Fig. 18.1

GPTS used as coupling agent

Novolac type phenolic resin/SiO_2 hybrid ceramer was prepared as described in Figs 18.2 and 18.3.

18.2.5 Fourier transform infrared spectroscopy (FT-IR)

FTIR spectra of the hybrid ceramers were recorded between 4000–400 cm^{-1} on a Nicolet Avatar (USA) 320 FT-IR spectrometer. Thin films were prepared by the solution-casting method. A minimum of 32 scans was signal-averaged with a resolution of 2 cm^{-1} at the 4000–400 cm^{-1} range.

18.2.6 Solid state ^{29}Si nuclear magnetic resonance spectroscopy (^{29}Si NMR)

^{29}Si NMR was performed by a Bruker (Germany) DSX-400WB. The samples were treated at 180ºC for 2 h and then were ground into fine powder.

18.2.7 Thermogravimetric analysis (TGA)

Thermal degradation of phenolic hybrid nanocomposites was measured by a thermogravimetric analyzer (Du-Pont, model 951) from room temperature to

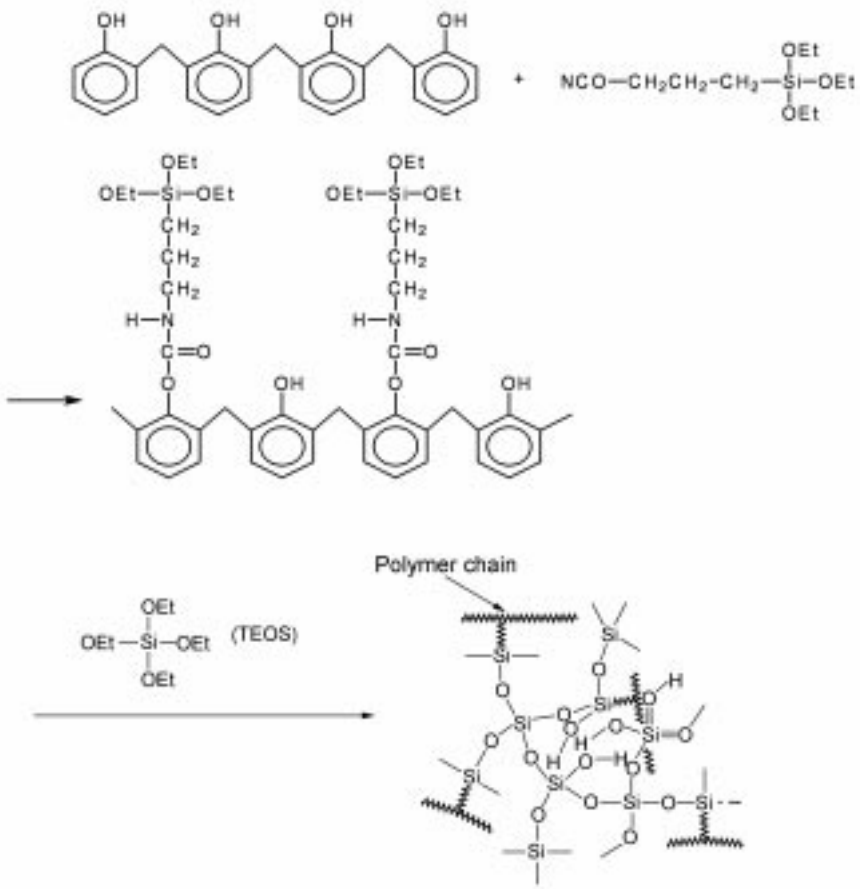
Polymer chain
(TEOS)

18.1

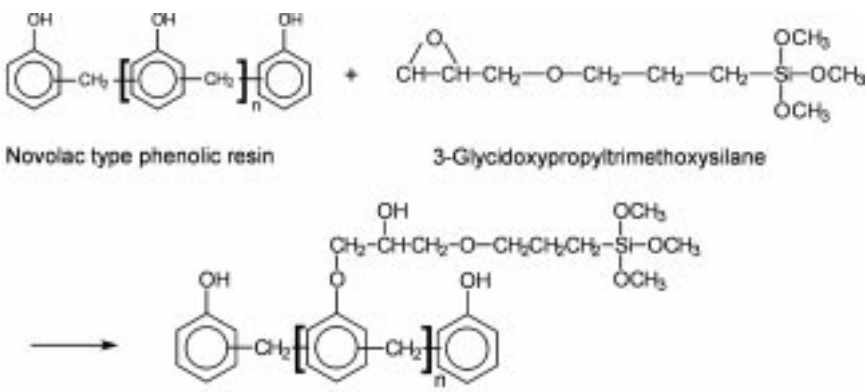
Novolac type phenolic resin
3-Glycidoxypropyltrimethoxysilane

18.2

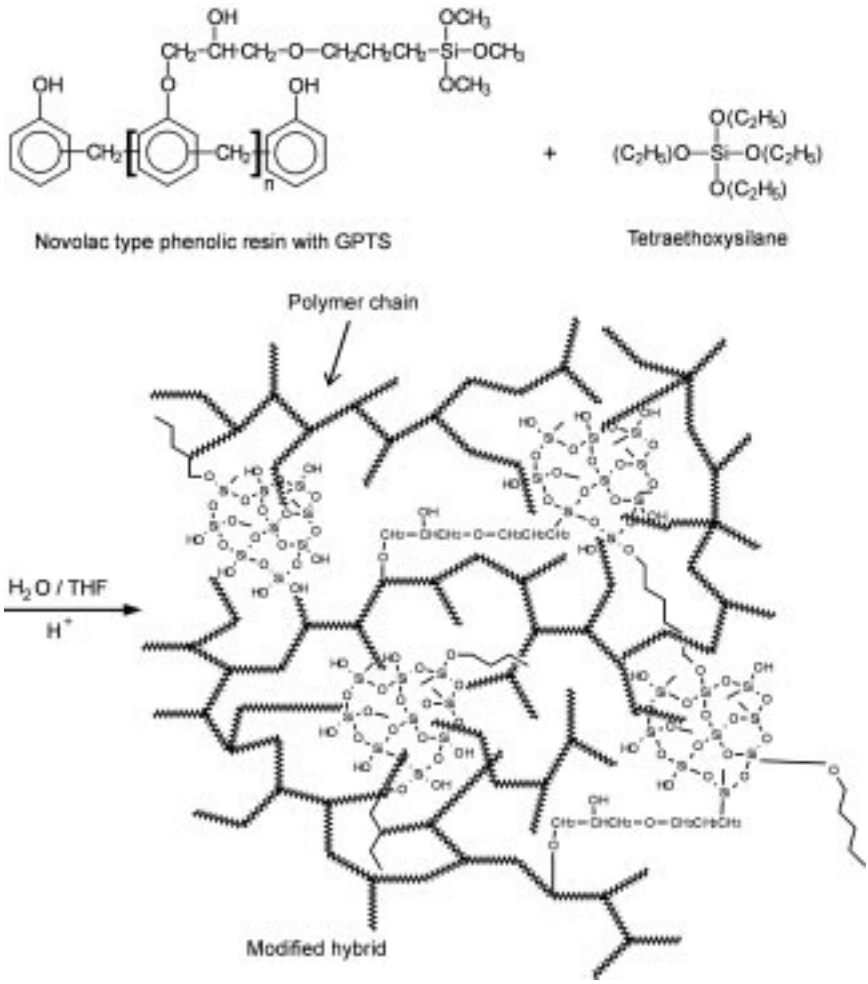

18.3

800ºC with a heating rate of 10ºC/min under a N_2 atmosphere. The measurements were conducted using 6–10 mg samples. Thermogravimetric curves were recorded.

18.2.8 Differential scanning calorimeter (DSC)

The glass transition temperatures (T_g) of the phenolic hybrid ceramers were measured by a differential scanning calorimeter (Du-Pont, model 10). The heating rate was 10ºC/min. The measurements were made with 3–4 mg sample on a DSC plate after the specimens were quickly cooled to room temperature following the first scan. Glass transition temperatures were determined at the

midpoint of the transition point of the heat capacity (Cp) changed, and the reproducibility of T_g value was estimated to be within 2ºC.

18.2.9 Limiting oxygen index (LOI) test

The LOI is defined as the minimum fraction of O_2 in a mixture of O_2 and N_2 that will just support flaming combustion. The LOI test was performed according to the testing procedure of ASTM D2836 Oxygen Index Method with a test specimen bar of 7–15 cm in length, 6.5 $\pm$ 0.5 mm in width, and 3.0 $\pm$ 0.5 mm in thickness. The sample bars were suspended vertically and ignited by a Bunsen burner. The flame was removed and the timer was started. The concentration of oxygen was raised if the specimen extinguished before burning 3 min or 5 cm. The oxygen content was adjusted until the limiting concentration was determined.

18.2.10 UL-94 vertical test

The UL-94 vertical test was performed according to the testing procedure of ASTM D 3801 with a test specimen bar of 127 mm in length, 12.7 mm in width and about 1.27 mm in thickness. Five sample bars suspended vertically over surgical cotton were ignited by a Bunsen burner. A flame was applied twice to the lower end of the specimen for 10 s. The class of UL-94 V-0 is achieved if each after-flame time does not exceed 10 s, and sum of the after-flame time for the five samples does not exceed 50 s. Meanwhile, for UL94 V-0, the surgical cotton below the specimen could not be ignited with the flaming drippings. The class of UL-94 V-1 is achieved if each after-flame time does not exceed 30 s, and sum of the after-flame time for the five samples does not exceed 250 s. Meanwhile, for UL-94 V-1, the surgical cotton below the specimen could not be ignited with the flaming drippings. If the surgical cotton below the specimen was ignited with the flaming drippings, the sample was assigned UL-94 V-2 class.

18.2.11 Morphological properties

The morphology of the fracture surface of the composite was examined using a scanning electron microscope (SEM) (JEOL JSM 840A, Japan) and a transmission electron microscopy (TEM) (Hitachi, H-7500, Japan). Samples were cut at room temperature with a diamond knife in an Ultracut Uct microtome (Leica Company, Austria).

18.2.12 Flexural strength test

Flexural tests were following the ASTM D790 method with a span-to-depth ratio of 40 and crosshead speed of 1.0 mm/min. The dimensions of samples were

60.0 × 13.0 × 3.0 mm (length × width × thickness). Six specimens were tested in each composition. All tests were performed at ambient temperature of 25 ± 2ºC.

18.2.13 Si mapping technology or energy dispersive X-ray spectroscopy (EDX)

The distribution of Si atoms in the hybrid ceramers were obtained from SEM EDX mapping (JEOL JSM 840A, Japan). The white points in the figures denote Si atoms. Semaphore image recording system operated at 15 kV. Analyses were performed directly in the SEM by the PGT Imix EDX microanalyser. The voltage for the energy dispersive analysis was 15 kV, and the time of X-ray collection 60 s.

18.3 Results when IPTS was used as a coupling agent

18.3.1 Characterization

Figure 18.4 shows the FT-IR spectra of the reaction between novalac phenolic and 3-isocyanatopropyltriethoxysilane. The figure displays the change of the characteristic peak of NCO group of 3-isocyanatopropyltriethoxysilane at

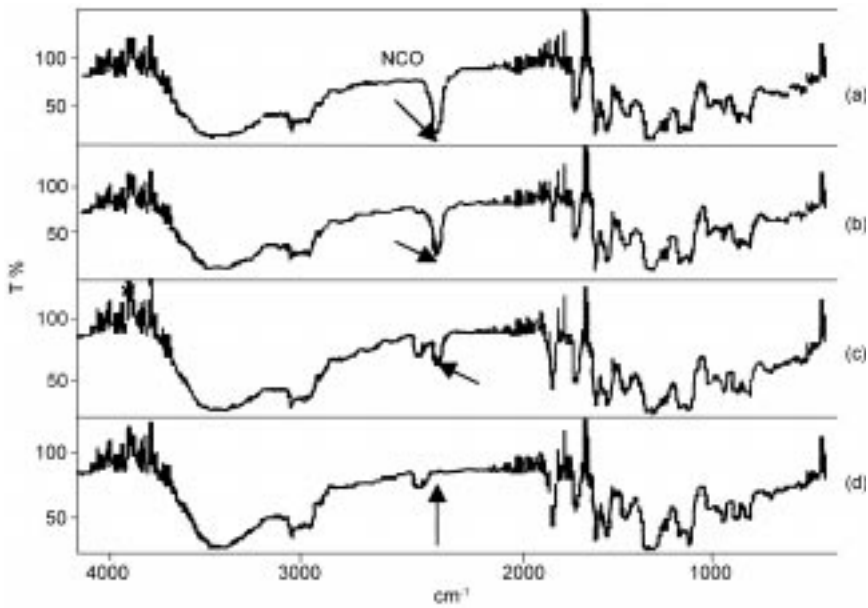

18.4 FT-IR spectra of the reaction between novalac phenolic resin and 3-isocyanatopropyltriethoxysilane, at various reaction times: (a) initial reaction (b) 4 h (c) 8 h (d) 12 h.

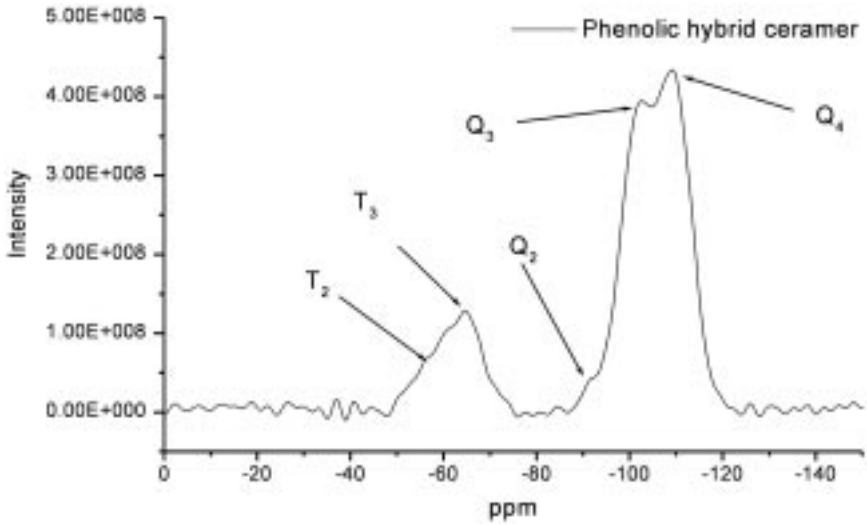

18.5 The curve of solid-state ^{29}Si NMR spectra of phenolic hybrid ceramer.

2270 cm^{-1}. As the reaction proceeded, the intensity of the NCO group decreased and finally disappeared. Results reveal that the novolac type phenolic resin had reacted with 3-isocyanatopropyltriethoxysilane at various times.

Figure 18.5 exhibits the curve of solid-state ^{29}Si NMR spectra of phenolic nanocomposite. Condensed siloxane species for TEOS in which a silicon atom through mono-, di, tri, tetra-substituted siloxane bonds were designated as Q^1, Q^2, Q^3, Q^4, respectively. The definition of Q^s is shown in Fig. 18.6. The chemical shifts −91, −101, −109 ppm of Q^2, Q^3, Q^4, respectively, were in good agreement with the literature.[55]

For 3-isocyanatopropyltriethoxysilanes with mono-, di-, tri-, tetra-substituted siloxane bonds were designated as T^1, T^2, T^3. The definition of T^s is shown in Fig. 18.7. The chemical shifts −56, −65 ppm of T^2, T^3, respectively, confirmed the values in the literature.[55] Results revealed that Q^4, Q^3, T^3 were the major environments, i.e., it formed network structure.

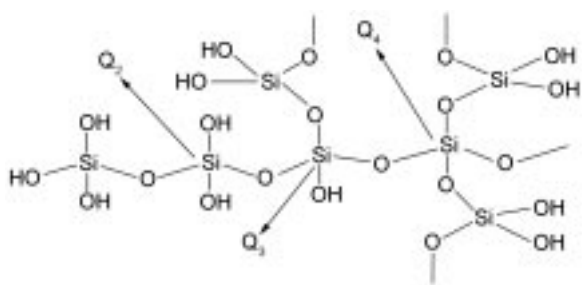

18.6

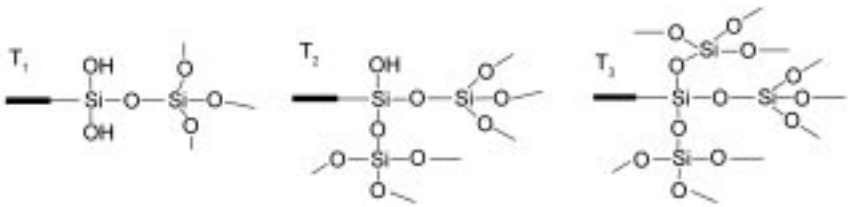

18.7

18.3.2 Thermal properties of hybrids

Figure 18.8 shows the TGA curves of the hybrids for different TEOS compositions from room temperature to 800ºC in the N_2 atmosphere. The char yields of the hybrids increased with increasing TEOS content. Increasing char formation can reduce the production of combustible gases, decreases the exothermic nature of the pyrolysis reaction and inhibits the thermal conductivity of the burning materials.[56] As the TEOS content increases, the rates of degradation will be slower. The inorganic components can retard the degradation of the hybrids. The char yield has been correlated to the flame retardance.[56] Therefore, through the condensed phase mechanism, the flame retardance of the hybrids is promoted. The inference will be discussed in the following LOI and UL-V test section. Figure 18.9 presents T_{d5} (the degradation temperature of 5% weight loss) of the hybrids for different TEOS contents. Table 18.1 shows T_{d5} of hybrid ceramer. When TEOS content was 20%, the T_{d5} of the hybrid is 290ºC. As the TEOS content increases to 80%, T_{d5} of the

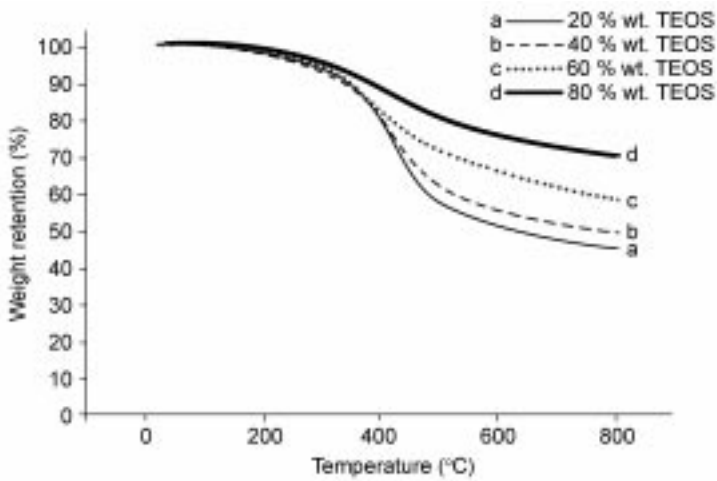

18.8 TGA curves of phenolic resin/silica hybrid ceramer with various TEOS contents.

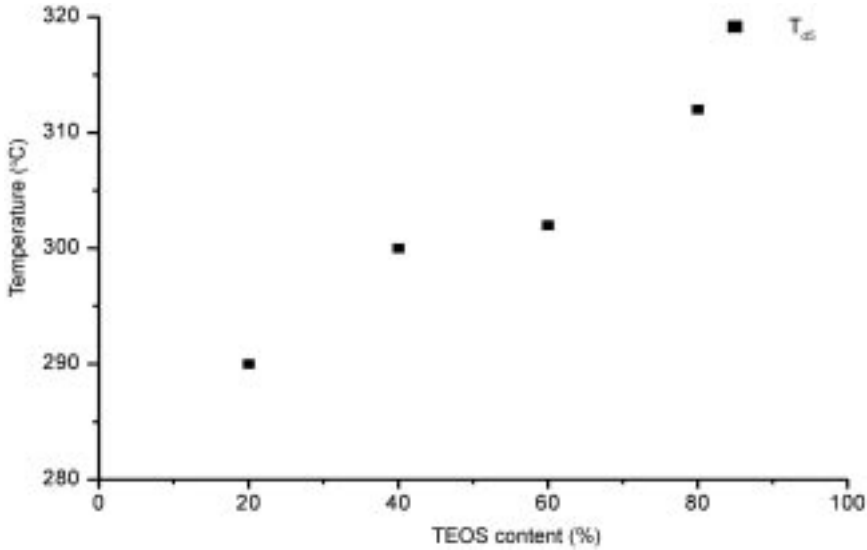

18.9 T_{d5} (the temperature of degradation at which the weight loss of material is 5%) of the hybrid with different TEOS contents.

hybrid raises to 312ºC. TEOS inorganic components enhance the heat stability of hybrids. Figures 18.10 and 18.11 show the isothermal degradation curves of phenolic/silica hybrids at different temperatures. From Fig. 18.10, it can be found that the hybrid containing 80% TEOS content at 200ºC is very stable, it still maintained 93 wt.% for 300 min. Even when it was kept at 800ºC for 300 min, the weight retention was 45%. The hybrid exhibited good heat resistance. Figure 18.11 possessed a similar trend as shown in Fig. 18.10.

Figure 18.12 presents the DSC thermograms of the phenolic/silica hybrid ceramers. From these curves, the glass transition temperature was not able to be clearly deduced. Table 18.1 summarizes the T_g of phenolic/silica hybrid ceramers. The T_g of the hybrid increased with the incorporation of inorganic

Table 18.1 Glass transition temperature (T_g) and 5% weight loss degradation temperature of the phenolic/silica hybrid ceramers

System wt.%TEOS	Glass transition temperature T_g (ºC)	5% weight loss degradation temperature T_{d5} (ºC)
20	140	290
40	152	300
60	—	302
80	—	312

—: not available.

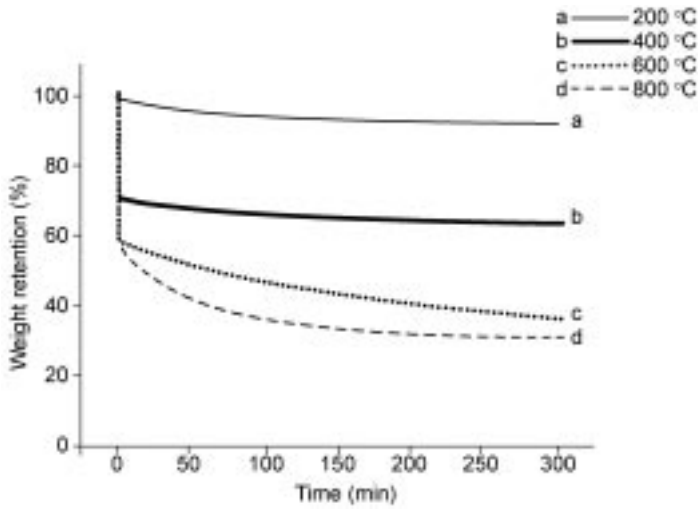

18.10 The isothermal degradation curves of phenolic/silica hybrid ceramer for 60 wt.% TEOS at different temperatures.

components. It revealed that the networks of inorganic components restricted the motion of the chains. This result confirmed the data of ^{29}Si NMR spectra for the phenolic/silica hybrid ceramers. The hybrid ceramers possess the structures of networks.

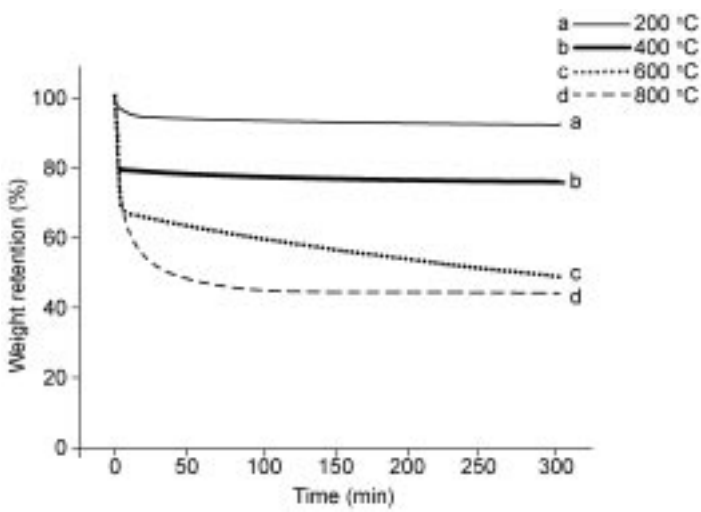

18.11 The isothermal degradation curves of phenolic/silica hybrid ceramer for 80 wt.% TEOS at different temperatures.

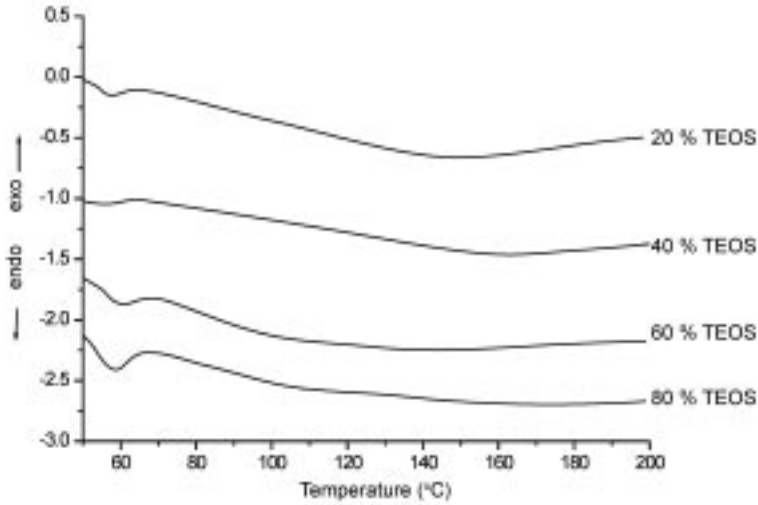

18.12 DSC thermograms of phenolic resin/silica hybrid ceramer.

18.3.3 Morphological properties

The compatibility of organic polymer and silica greatly affects the thermal, mechanical and optical properties of nanocomposites. The morphology of the fractured surfaces was observed by SEM, and the mapping technique was utilized to elucidate the distribution of silica and the separation of the microphase in the hybrid matrix. Figure 18.13 presents the SEM microphotograph of the nanocomposite. Figure 18.14 shows Si mapping of phenolic nanocomposite.

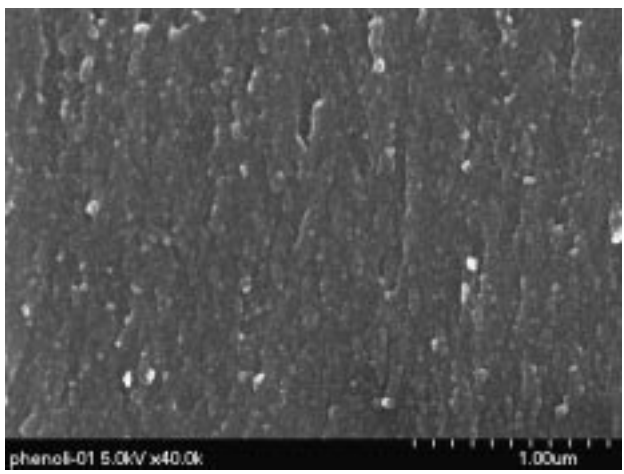

18.13 SEM of phenolic nanocomposite.

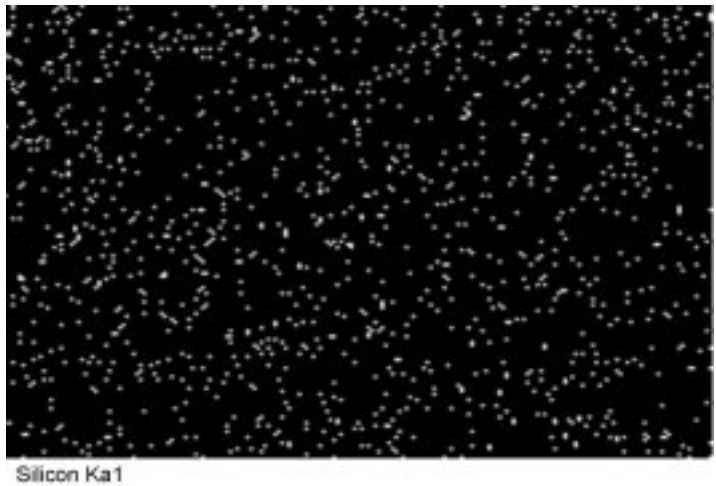

18.14 Si mapping of phenolic nanocomposite.

In the figure, the white dots represent the silicon atoms. The transmission electron microphotograph (TEM) of phenolic nanocomposite is shown as Fig. 18.15. The dark domains represent SiO_2 particles. According to SEM and TEM micrographs, the particles were uniformly dispersed throughout the polymer matrix with sizes below 100 nm. The phenomena showed the hybrids are nanocomposites. This result revealed that the nanocomposites exhibit good miscibility between organic and inorganic phases.

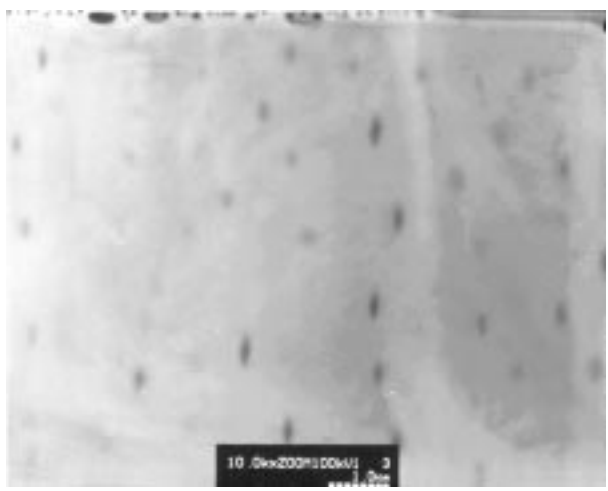

18.15 TEM of phenolic nanocomposite.

Table 18.2 The UL-94 and LOI test results of novolac type phenolic/TEOS hybrids

TEOS content (wt.%)	Flaming drops	Cotton ignited	UL-94 standard	LOI
Neat phenolic	N/A	N/A	94V-1	32
20	N/A	N/A	94V-0	35
40	N/A	N/A	94V-0	37
60	N/A	N/A	94V-0	40
80	N/A	N/A	94V-0	43

N/A: not available.

18.3.4 LOI and UL-94 test

The flame retardant properties of the obtained hybrids were examined by measuring the LOI of the hybrids. From Table 18.2, a significant increase in LOI was observed when TEOS was utilized in the phenolic resins. This indicates that incorporating silica shows a significant effect on promoting the flame retardance of phenolic resins. This result is coincident with the char yield data. Moreover, the UL-94 test was also applied to probe the flame retardance of the hybrids and to rank them into an industrial expression. The results of UL-94 test are also shown in Table 18.2. From this table, the neat phenolic resin may be classified into the UL-94 V-1. The hybrids containing 20 wt.% TEOS content can be classified as UL-94 V-0 grade. The phenolic hybrids with good flame retardancy (LOI: 32–44, UL94 V-0 grade) and excellent thermal stability (T_g is above 300ºC) are considered to be sufficient for applications as green flame retardant materials.

18.4 Results when GPTS was used as a coupling agent

18.4.1 Characterization

Figure 18.16 shows the FT-IR spectra of the reaction between novolac type phenolic resin and 3-glycidoxypropyltrimethoxysilane. The figure displays the change of the characteristic peak of epoxy group of 3-glycidoxypropyltrimethoxysilane at 914 cm^{-1}. Due to the ring-opening reaction of 3-glycidoxypropyltrimethoxysilane, the peak of 914 cm^{-1} disappeared and the bending red shift of C-H out of plane was moved to 889 cm^{-1}. Since the ring-opening reaction causes different hydroxyl group types, the characteristic peak of hydroxyl group at 3000–3600 cm^{-1} became broad. Results confirmed that the novolac type phenolic resin had reacted with the 3-glycidoxypropyltrimethoxysilane.

Figure 18.17 shows the solid-state ^{29}Si NMR spectra of the modified hybrid nanocomposite. Condensed siloxane species for TEOS, the silica network structure of the hybrid nanocomposite in which a silicon atom through mono-,

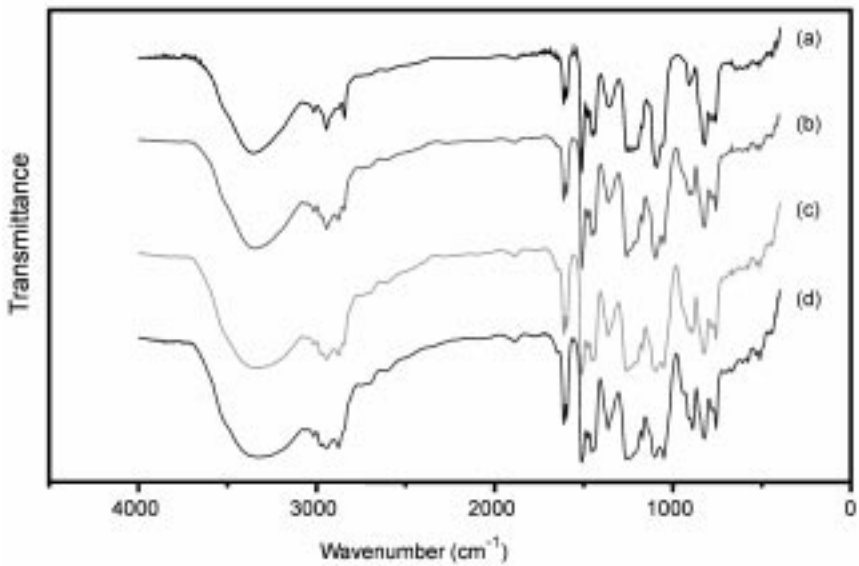

18.16 FT-IR spectrum of GPTS-Phenolic resin at different reaction times. (a) Initial, (b) $t = 6$ h, (c) $t = 20$ h, (d) final.

di, tri, tetra-substituted siloxane bonds were designated as Q^1, Q^2, Q^3, Q^4, respectively. The chemical shifts -91, -101, -110 ppm of Q^2, Q^3, Q^4, respectively, are in good agreement with the data in the literature.[55] For 3-glycidoxypropyltrimethoxysilane with mono-, di-, tri-, tetra-substituted siloxane bonds are designated as T^1, T^2, T^3. The chemical shifts -51, -58, -65 ppm of T^1, T^2, T^3, respectively, confirm the literature values.[55] Results reveal that Q^4, T^3 were the major microstructures in the modified hybrid nanocomposite, i.e., it formed network structure.

18.4.2 Morphological properties

In order to investigate the distribution of silica and micro-phase separation in the hybrid matrix, the morphology of the fractured surfaces was observed by SEM and a mapping technique. Figure 18.18 shows the SEM microphotographs of fractured surface of unmodified hybrid composite and modified hybrid nanocomposite. Figure 18.19 shows the mapping image of modified hybrid materials. As a coupling agent was added, the cluster of silica was decreased and the phase separation was improved. The cluster size of silica could be controlled to below 100 nm. This phenomenon exhibits the good miscibility which existed between organic (polymer) and inorganic (silica) phases. Figure 18.20 and Figure 18.21 were given by EDX spectroscopy. Figure 18.20 shows the Si-mapping image of the modified hybrid nanocomposite. The Si-mapping

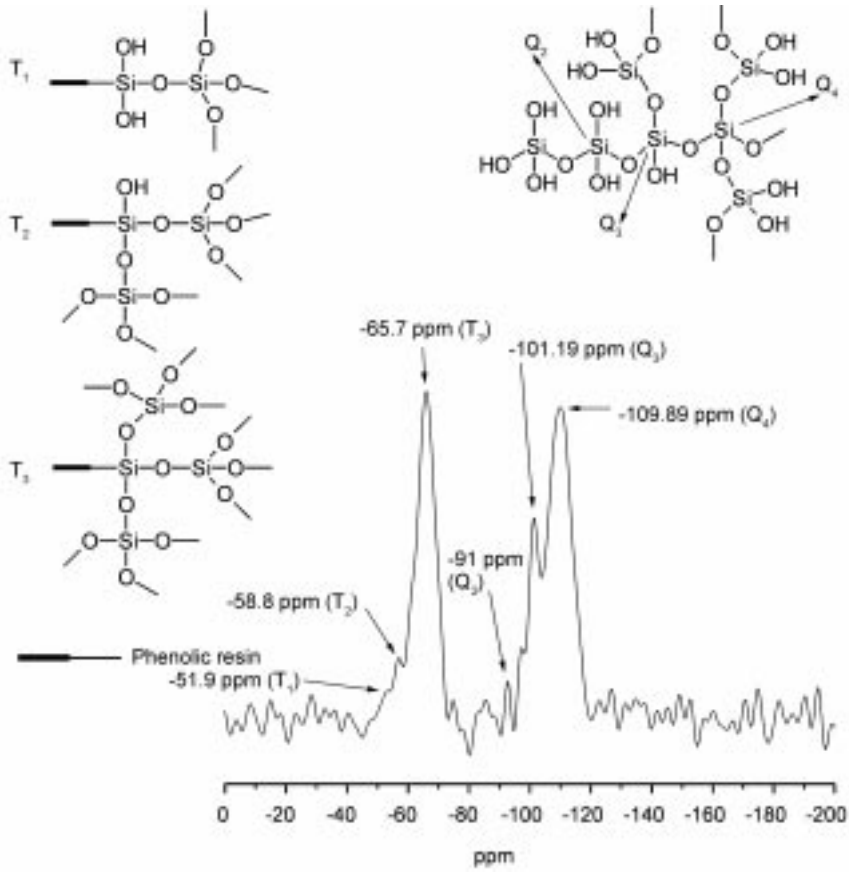

18.17 ^{29}Si-NMR spectra of GPTS-Phenolic resin/SiO_2 modified hybrid nanocomposite.

image confirms the silica particles were distributed uniformly in the modified hybrid nanocompsite. Therefore, when GPTS content is 10 phr, the modified hybrid materials were nanocomposites and showed good transparency similar to neat phenolic resin.

18.4.3 Thermal properties and flame retardance

Figure 18.21 shows the TGA curves of the hybrid composites with different coupling agent (GPTS) content. The TGA curves range from room temperature to 800ºC in the N_2 atmosphere. According to the TGA curves, the char yields of the hybrid materials increased with the increase of GPTS. As silica network was added, the degradation was slower. The inorganic components could retard the thermal degradation of the nanocomposite. Table 18.3 summarizes char yield, T_{d5} and T_{d10} (the temperature of degradation at which the weight loss is 5% and

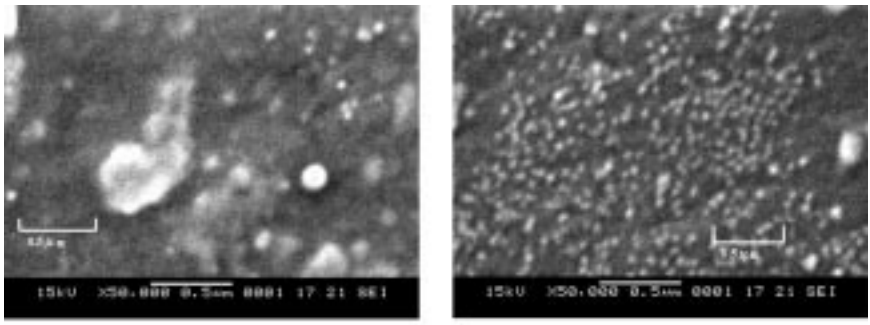

18.18 The SEM microphotographs of fractured surface of unmodified hybrid composite and modified hybrid nanocomposite.

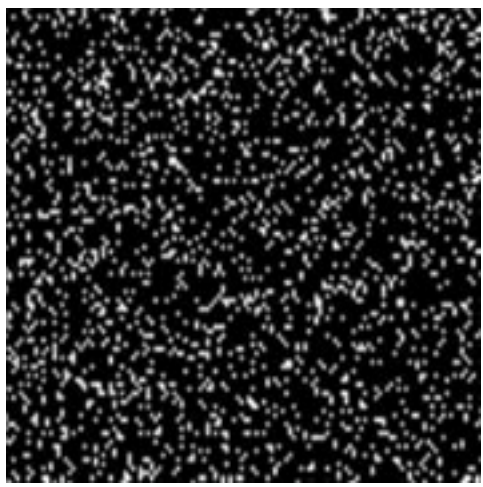

18.19 The Si-mapping image of modified hybrid nanocomposite.

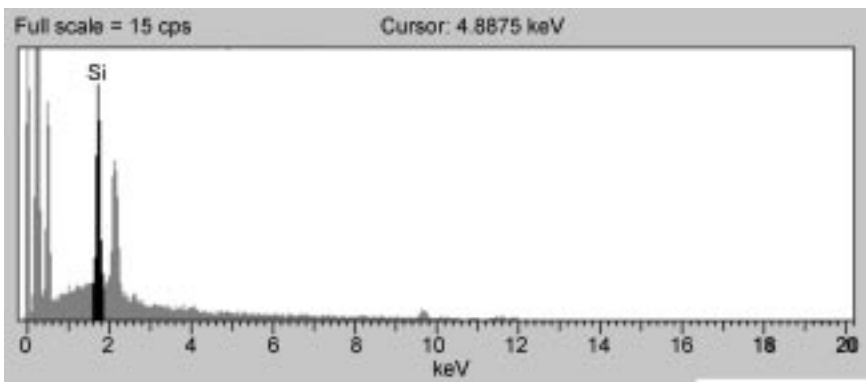

18.20 The EDX spectrum of modified hybrid nanocomposites.

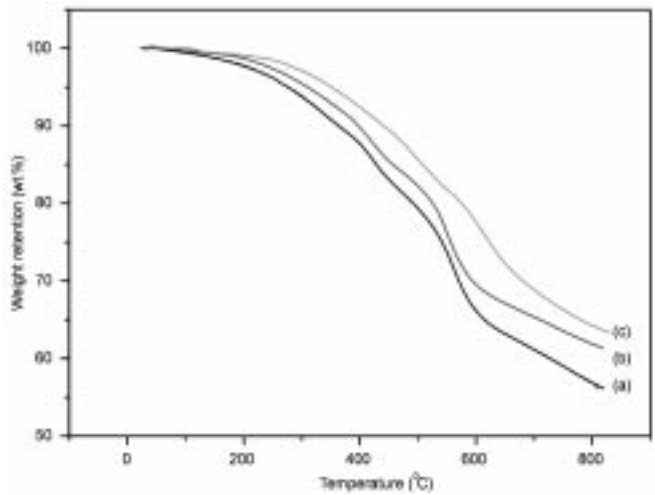

18.21 TGA curves of neat phenolic resin (a), unmodified hybrid composite (b) and modified hybrid nanocomposite (c).

10%) of the hybrids materials for different coupling agent (GPTS) contents. T_{d5} and T_{d10} of the neat novolac type phenolic resin were 281.8ºC and 365.3ºC, respectively. T_{d5} and T_{d10} of the hybrid material (GPTS content was 0 phr) were 315.1ºC and 401.1ºC. As GPTS content increased to 10 phr, T_{d5} and T_{d10} of the hybrid material raise to 350.8ºC and 439.9ºC, respectively. The char yield of the hybrid materials raised from 56.13 wt.% to 63.29 wt.%. The silica inorganic components enhanced the thermal stability of the hybrid materials.

The flame retardant properties of the hybrid composites were examined by measuring the Limiting Oxygen Index (LOI) and Underwriters Laboratory 94 (UL-94) of the hybrid composites. Table 18.4 illustrates a significant increase in LOI (from 33 to 37) was observed. This indicates that incorporating silica shows a significant effect on promoting the flame retardance of novolac type phenolic

Table 18.3 Comparison of the degradation temperature at 5%, 10% weight loss and the char yield of neat phenolic resin, unmodified hybrid composite and modified hybrid nanocomposite at N_2 atmosphere

Systems	Temperature of 5% weight loss (ºC)	Temperature of 10% weight loss (ºC)	Char yield (wt.%)
Neat phenolic resin	281.8	365.3	56.1
Unmodified hybrid composite	315.1	401.1	61.4
Modified hybrid nanocomposite	350.8	439.9	63.3

Table 18.4 The UL-94 and LOI test results of neat phenolic resin, unmodified hybrid composite and modified hybrid nanocomposite

Systems	Flaming drops	Cotton ignited	UL-94 standard	LOI
Neat phenolic resin	N/A	N/A	94V-1	33
Unmodified hybrid composite	N/A	N/A	94V-0	36
Modified hybrid nanocomposite	N/A	N/A	94V-0	37

N/A: not available.

resin. This result is coincident with the char yield data. The results of UL-94 test are also shown in Table 18.4. From this table, the neat phenolic resin may be classified into the 94V-1. The nanocomposite (GPTS content 10 phr) can be classified as 94V-0 grades. The hybrid phenolic nanocomposites of good flame retardance and excellent thermal stability are considered to be sufficient for applications as flame retardant materials.

18.4.4 Mechanical properties

The mechanical properties of the hybrid phenolic composites were examined by measuring the flexural mechanical properties. Figure 18.22 and Table 18.5

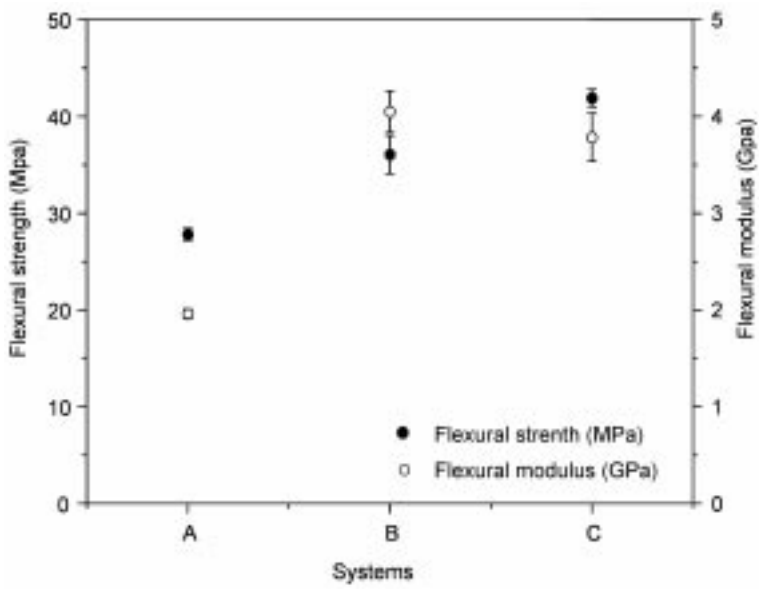

18.22 The flexural strength (•) and modulus (○) of neat phenolic resin (A), unmodified.

Table 18.5 Flexural strength and modulus of phenolic resin/SiO_2 hybrid systems with different TEOS contents

Systems	Flexural strength (MPa)	Flexural modulus (GPa)
Neat phenolic resin	27.8 ± 0.6	1.96 ± 0.05
Unmodified hybrid composite	36.1 ± 2.0	4.05 ± 0.21
Modified hybrid nanocomposite	41.9 ± 0.9	3.80 ± 0.25

show the flexural strength and modulus of neat phenolic resin and hybrid phenolic composites. The improvements in flexural mechanical properties of hybrid phenolic composites were affected by silica particle size and the compatibility between organic and inorganic phase. The flexural strength and modulus of the hybrid phenolic nanocomposite were 50% and 100% higher than that of the neat phenolic resin. The coupling agent, GPTS, reduces the serious phase separation from macro-phase to micro-phase and derives the fine silica particles in phenolic resin. Therefore, the results of flexural mechanical properties reveal that the hybrid phenolic nanocomposites containing fine silica particles (GPTS content 10 phr) have excellent properties, and incorporating the silica inorganic ingredients into the novolac type phenolic resin could enhance the flexural properties of the hybrid phenolic composites further.

18.5 Conclusions

Two novel phenolic/silica hybrid ceramers synthesized by the sol-gel process have been demonstrated. FTIR and ^{29}Si NMR was used to characterize the structure of the hybrids. Results revealed that Q^4, Q^3, T^3 was the major microstructure, thus it formed the network structure. The thermal properties were investigated by thermogravimetric analysis (TGA). The char yields of the hybrids increased with increasing TEOS contents. TEOS inorganic components enhanced the heat stability of hybrids. SEM microphotographs revealed that the silica particles were aggregated in the unmodified hybrid composite. The Si-mapping image confirms the silica particles were distributed uniformly in the modified hybrid nanocompsite. Both SEM and TEM micrographs reveal that the particles were uniformly dispersed throughout the polymer matrix with sizes below 100 nm. The phenomena showed that hybrids are nanocomposites. The nanocomposites showed good transparency close to that of the neat phenolic resin. LOI and UL-94 test results revealed that the hybrid ceramer possesses excellent flame retardance characteristics. Mechanical properties testing showed that the flexural strength and flexural modulus of silica-containing phenolic nanocomposites were improved.

18.6 References

1. M. W. Ellsworth and B. M. Novak, 'Mutually inorganic-organic networks, new routes into nonshrinking sol-gel composites materials', *J. Am. Chem. Soc.* 1991, 113, 2756.
2. B. M. Novak, 'Silicon oxide coating on anodized aluminium by the sol-gel process and its evaluation', *Adv. Mater.* 1993, 5, 422.
3. J. E. Mark and S. B. Wang, 'Reinforcement from alumina type fillers precipitated into an elastomer', *Polym. Bull.* 1988, 20, 443.
4. F. Suzuki, K. Onozato, and Y. Kurokawa, 'A formation of compatible poly (vinyl alcohol)/alumina gel composite and its properties', *J. Appl. Polym. Sci*. 1990, 39, 371.
5. S. B. Wang and J. E. Mark, 'Crystallinity of cellulose, as determined by CP/MAS NMR and XRD method', *Polym. Bull*. 1987, 17, 231.
6. S. J. Clarson and J. E. Mark, 'Reinforcement of elastomeric poly(methylphenylisiloxane by the in-situ precipitation of titania)', *Polym. Commun.* 1989, 30, 275.
7. F. Suzuki, K Onozato and Y Kurokawa, 'A formation of compatible poly (vinyl alcohol)/alumina gel composites and its properties', *J. Appl. Polym. Sci*. 1990, 39, 371.
8. M. Nandi, J. A. Conklin, L. Salvati Jr and A. Sen, 'Phosphonate modified titanium alkoxides: Intermediates in the sol-gel processing of novel titania/phosphonate inorganic-organic hybrids', *Chem. Mater*. 1991, 3, 201.
9. G. L. Wilkes, B. Orler and H. H. Huang, 'Ceramers: Hybrid materials incorporating polymeric/oligomeric species with inorganic glasses by a sol-gel process', *Polym. Bull.* 1985, 14, 557.
10. H. Schmidt, 'New type of non-crystalline solids between inorganic and organic materials', *J. Non-crystal. Solids* 1985, 73, 681.
11. A. Kioul and L. Mascia, 'Compatibility of polyimide-silicate ceramers induced by alkoxysilane silane coupling agents', *J. Non-crystal. Solids* 1994, 175, 169.
12. L. Mascia, Z. Zhang and S. J. Shaw, 'Carbon fibre composites based on polyimide/silica ceramers: aspects of structure-properties relationship', *Composites Part A* 1996, 27, 1211.
13. F. Surivet, T. M. Lam, J. P. Pascault and C. Mai, 'Organic-inorganic hybrid materials. 2. Compared structure of polydimethylsiloxane and hydrogenated polybutadiene based ceramers', *Macromol*. 1992, 25, 5742.
14. J. E. Mark, 'Novel reinforcement techniques for elastomers', *J. Appl. Polym. Sci. Appl. Polym. Symp*. 1992, 50, 273.
15. J. E. Mark, 'Physical properties of sol-gel coating', *J. Inorg. Organomet Polym.* 1993, 1, 431.
16. H. Schmidt, 'Transparent inorganic/organic copolymer by sol-gel process', *J. Sol-Gel Sci. Technol.* 1994, 1, 217.
17. S. C. Betrabet and G. L. Wilkes, *J. Inorg. Organomet Polym.* 1994, 4, 343
18. H. Schmidt, R. Kasemann, T. Burkhart, G. Wangner, E. Arpac and E. Geiter, *ASC Symp Ser on Hybrid Organic-Inorganic Composites* 1995, 585, 331.
19. Y. Osada, H. Okuzuki and J. P. Gong 'Electro-driven gel actuators', *Trends Polym. Sci.* 1995, 3, 61.
20. K. Gaw, H. Suzuki, M. Kakimoto and Y. Imai, 'Molecular design of sol-gel derived hybrid organic/inorganic nanocomposites', *J. Photopolym. Sci. Technol* 1995, 8, 307.

21. H. Kita, H. Saiki, K. Tanaka and K. Okamoto, 'The sol-gel process as a basic technology for nanoparticles dispersed inorganic-organic composites', *J Photopolym. Sci. Technol* 1995, 8, 315.
22. J. E. Mark, S. Wang and Z. Ahmad, 'Inorganic-organic composites, including some examples involing polyamides and polyimides', *Macromol Chem. Symp*. 1995, 98, 731.
23. M. I. Sarwar and Z. Ahmad, 'Interphase bonding in organic/inorganic hybrid materials using amino phenyl trimethoxy silane', *European Polymer Journal* 2000, 36, 89.
24. E. J. A. Pope and J. D. Mackenzie, 'Sol-gel processing of silica, II. The role of the catalyst', *Journal of Non-Crystalline Solids*, 1986, 87, 185.
25. J. C. Brinker, Keefer D. K., Schaefer W. D., Assink A. T., Kay D. B. and Ashley S. C., *J. Non-Cryst. Solids*, 1984, 63, 45.
26. E. J. A. Pope and J. D. Mackenzie, *J. Non-Cryst. Solids*, 1986, 87, 185.
27. G. Yi and M. Sayer, 'Sol-gel processing of complex oxide films', *Ceramic Bulletin*, 1991, 70, 7, 1173.
28. S. S. X. Chiaro, J. L. Zotin and A. C. Faro, 'Titania-alumina prepared by sol-gel method – Influence of pH and drying on textural and structural properties', *Studies in Surface Science and Catalysis*, 1998, 118, 633.
29. H. K. Liu and A. Parvizimajidi, 'Effect of particle additions on drying stresses and the green density of sol-gel-processed 3-dimensional ceramic-matrix composites', *Journal of the American Ceramic Society*, 1998, 81, 7, 1824.
30. S. Wallace and L. L. Hench, 'The processing and characterization of DCCA modified gel-derived silica', in *Better Ceramic through Chemistry*, MRS, 1984, 32, 47.
31. Her-Der Wu, Chen-Chi M. Ma and Char-Ming Lin, 'Processability and properities of phenoxy resin toughened phenolic resin composites', *Journal of Applied Polymer Science*, 1997, 63, 911.
32. Chen-Chi M. Ma, Hew-Der Wu, Yi-Feng Su, Ming-Shiu Lee and Yiu-Don Wu, 'Pultruded fiber reinforced novolac type phenolic composite processability, mechanical properties and flame resistance', *Composites: Part A: Applied Science and Manufacturing*, 1997, 9–10.
33. Chen-Chi M. Ma, Chih-Tsung Lee and Hew-Der Wu, 'Pultruded fiber reinforced poly(ethylene oxide) toughened novolac type phenolic resin: Mechanical properties, thermal stability, and flame retardance', International SAMPE Technical Conference Composites for Real World Proceedings of the 29th International SAMPE Technical Conference Oct 28–Nov 1, 1997, 29.
34. Chen-Chi M. Ma, Chih-Tsung Lee and Hew-Der Wu, 'Mechanical properties, thermal stability, and flame retardance of pultruded fiber-reinforced poly(ethylene oxide)-toughened Novolac-type phenolic resin', *Journal of Applied Polymer Science*, 1998, 69, 6.
35. Chen-Chi M. Ma, Han-Thing Tseng and Hew-Der Wu, 'Blocked diisocyanate polyester-toughened Novolac-type phenolic resin: Synthesis, characterization, and properties of composites', *Journal of Polymer Science, Part B: Polymer Physics*, 1998, 36,10.
36. K. Haraguchi, Y. Usami and Y. Ono, 'Preparation and characterization of hybrid materials composed of phenolic resin and silica', *J. Mater. Sci*., 1998, 33, 13, 337.
37. K. Haraguchi, Y. Usami, K. Yamamura and S. Matsumoto, 'Morphological

investigation of hybrid materials composed of phenolic resin and silica prepared by in-situ polymerization', *Polym*., 1998, 39, 25, 6243.
38. J. M. Lin, C. C. Ma, F. Y. Wang, H. D. Wu and S. C. Kuang, 'Thermal, mechanical, and morphological properties of resin/silica hybrid creamers', *J. Polym. Sci., Part B: Polym. Phy*., 2000, 38, 13, 1699.
39. J. M. Lin, C. C. M. Ma and W. C. Chang, 'Carbon/carbon composites derived from phenolic resin/silica hybrid creamers. Part I. Oxidation resistance and morphological properties', *J. Mater. Sci*., 36, 2001, 17, 4259.
40. J. E. Mark and S. J. Pan, 'Reinforcement of polydimethylsiloxane network by in-situ precipitation of silica: a new method for preparation of filled elastomers', *Macromol. Chem. Rapid Commun*., 1982, 3, 10, 681.
41. A. Usuki, Y. Kujima, M. Kawasumi, A. Okada, Y. Fukushima, T. Kurauchi and O. Kamigaito, 'Synthesis of nylon 6-clay hybrid'*, J. Mater. Res*., 1993, 8, 5, 1179.
42. J. E. Mark, 'Generate reinforcing particles in place', *Chemtech*, 1989, 19, 4, 230.
43. J. Wen, G. Lilkes, 'Abrasion resistant inorganic/inorganic coating materials prepared by the sol-gel method'*, J. Sol-gel Sci. Technol.,* 1995, 5, 2, 115.
44. R. Kasemann and H. Schmidt, 'Coatings for mechanical and chemical protection based on organic-inorganic sol-gel nanocomposites', *Nw J. Chem*., 1994, 18, 10, 1117.
45. Y. Wei, D. Yang and L. Tang, 'Synthesis, characterization, and properties of new polystyrene-SiO_2 hybrid sol-gel materials', *J. Mater. Res.,* 1993, 8, 1143.
46. S. Wang, Z. Ahmad, and J. E. Mark, 'A polyamide-silica composite prepared by the sol-gel process', *Polym. Bull.,* 1993, 31, 323.
47. Z. Ahmad, M. I. Sarwar and J. E. Mark, 'Dynamic-mechanical thermal analysis of aramid-silica hybrid composites prepared in a sol-gel process', *J. Appl. Polym. Sci.,* 1997, 63, 1345.
48. G. L. Wilkes, B. Orler and H. Huang, 'Ceramers: Hybrid materials incorporating polymeric/oligomeric species with inorganic glasses by a sol-gel process', *Polym. Bull*., 1985, 14, 557.
49. J. E. Mark, 'Ceramic reinforced polymers and polymer-modified ceramics,' *Polym. Eng. Sci*., 1996, 36, 2905.
50. T. Yamabe, 'Recent development of carbon nanotube', *Synthesis Metals*, 1995, 70, 1511.
51. V. Favier, G. R. Canova, S. C. Shivastava and J. Y. Cavaille, 'Mechanical percolation in cellulose whiskers nanocomposites', *Polym. Eng. Sci*., 1997, 37, 1732.
52. Y. Kojima, A. Usuki, M. Kawasumi, A. Okada, T. Kurauchi and O. Kamigaito, 'One-pot synthesis of nylon6-clay hybrid', J. *Polym. Sci Part A*, 1993, 31, 1755.
53. M. W. Ellsworth and B. M. Novak, 'Mutually interpenetrating inorganic-organic networks. New routes into nonshrinking sol-gel composite materials', *J. Am. Chem. Soc*., 1991, 113, 2756.
54. S. Wang, S. Adanur and B. Z. Jang, 'Mechanical and thermo-mechanical failure mechanism analysis of fiber/filler reinforced phenolic matrix composites', *Composites Part B*, 1997, 28B, 4, 215–231.
55. R. Joseph, S. Zhang and W. Ford, 'Structure and dynamics of a colloidal silica-poly (methyl methacrylate) composite by ^{13}C and ^{29}Si MAS NMR spectroscopy', *Macromolecules*, 1996, 29, 1305.
56. D. W. Van Krevelen, 'Some basic aspects of flame resistance of polymeric materials', *Polymer*, 1975, 16, 615.

19

Polymer/graphite nanocomposites

Y MENG, Sun Yat-Sen University, People's Republic of China

19.1 Introduction

Polymer materials are well known for exhibiting electrically insulating behavior. However, conductive fillers can be incorporated as a second phase into these polymer matrices, leading to an increase in the electrical conductivity of the resulting composites. The conducting properties of these composites are mainly varied as a function of the filler content. At a critical value (so-called percolation threshold in percolation theory[1]), a sharp transition of the conductivity of the composites occurs with a slight increase of filler content. The transition value varies for different conducting systems.[2] Moreover, the value is greatly affected by the properties of the fillers and the polymer matrices, processing methods, and dispersion of the fillers within matrices. For macro-composites, relatively large quantities of filler were required to reach the critical value.[3] High filler content generally leads to the high density and detrimental mechanical properties for a composite. In this regard, much effort has been devoted to produce composites with minimized critical filler concentration.[4]

Generally, nanocomposites exhibit a significant increase in the properties of polymer matrices, and even yield certain new properties that cannot be derived from macro-composites or counterparts.[5,6] The pioneer work of polymer/layered silicate nanocomposites was reported by Usuki *et al.*,[7] followed by series of reports on this topic.[8–9] Both intercalated and delaminated nanocomposites, where layered silicates were well dispersed within the polymers, resulted in the dramatic enhancement of mechanical, thermal, and barrier performance in comparison with conventional composites.[10]

Like layered silicates, natural flake graphite is also a layered material with good electrical conductivity in the range of about 10^4 S/m at room temperature. Because of the weak van der Waals forces between graphene layers, graphite intercalation compounds (GICs) can be prepared by intercalating various small compounds into graphene layers.[11] It is well known that expanded graphite (EG) can be formed when GICs are subjected to a thermal shock. During the process, the intercalants vaporize and tear the layers apart, leading to an expansion in the *c* direction and resulting in a puffed-up material or EG, with a very low

density.[11–12] The layered structures of parent graphite were maintained in the EG, whereas the volume expansion ratio of the resulting EG to GICs was typically as high as 200–300.[11] Consequently, polymer/graphite nanocomposites can be synthesized using EG via different intercalation methods, including in-situ polymerization,[13,14] melt polymer intercalation, exfoliation-adsorption, and direct solution or exfoliation-adsorption intercalation.[15]

The conducting polymer/graphite nanocomposites have attracted considerable attention and been extensively reported in recent years because of their potential applications in advanced technologies, for example, in antistatic coatings, electrochemical displays, sensors, catalysis, redox capacitors, electromagnetic shielding and in secondary batteries.[16,17] Due to their importance in both industry and academia, the features of natural graphite flake, GICs and EG, as well as the preparation, properties and applications of polymer/graphite nanocomposites are reviewed in this chapter.

19.2 Features of graphite

19.2.1 Features of natural graphite flakes

Natural graphite exists in three different types: graphite flakes, amorphous graphite and crystalline graphite. In general, graphite is found in nature in the form of natural graphite flakes (NGF) or powder of various particle sizes in purity greater than 99%. Graphite flake is naturally abundant and highly conductive.[11] As shown in Fig. 19.1, NGF are composed of graphite sheets, which are generally less than 100 nm in thickness.[18] The microstructure of the graphite sheets could be further described as the illustration in Fig. 19.2. Each sheet is further divided in aggregates of several graphite nanosheets,[19] which is 2–8 nm in thickness. The aggregate structures have a c-axis lattice constant ranging from 7 to 16 Å.[18–19] They also contain a number of graphene layers or carbon layers with a single carbon atom thickness. Those carbon layers have a

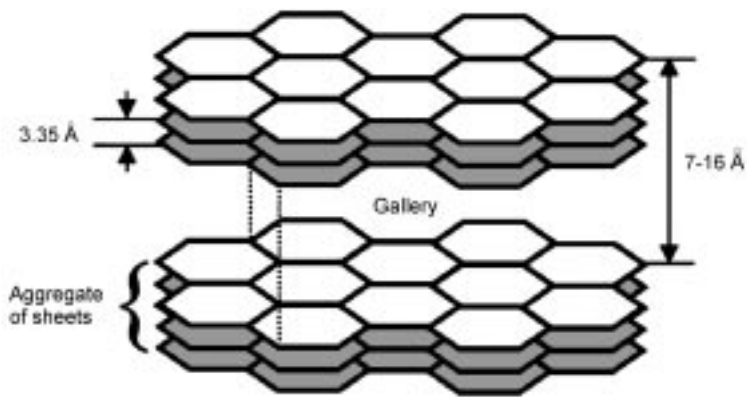

19.1 Schematic view of graphite layer structure.

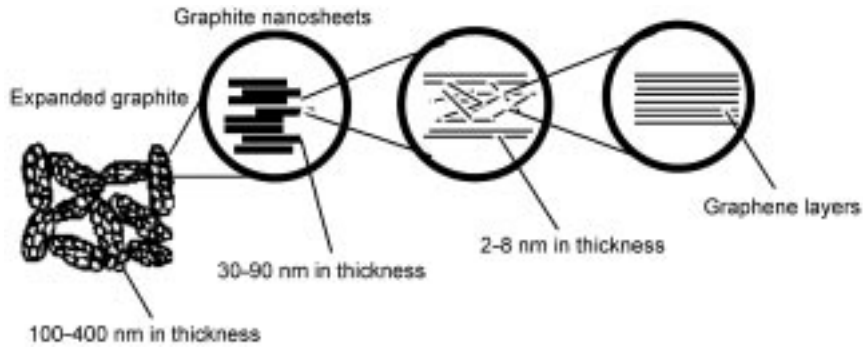

19.2 Illustrative model of the expanded graphite consisting of graphite nanosheets and graphene layers.

spacing of 3.35 Å as depicted in Figs 19.1 and 19.2.[19] Each carbon layer contains hexagonal arrays of carbon atoms hybridized in sp2 to form 1.42 Å sigma bonds with three nearest neighbors in the layer. Those covalent bonds between the carbons within a graphene layer are much stronger than those bondings between the graphene layers.[18] The delocalized π bonds, resulting from the sp2 hybridization, are responsible for the highly electrical conductivity of graphite. Moreover, the softness and lubricating nature of graphite arises from the weak bindings between the carbon layers that are joined together via weak van der Waals forces. Like other layered materials, such as montmorillonite and vermiculite, graphite is also a kind of layered material, the weak interplanar forces allow the possibility for certain atoms, molecules and ions to intercalate into the interplanar spaces of the graphite aggregates. The interplanar spacings, also called galleries, are thus increased.[20–25]

19.2.2 Formation of GIC

Unlike lamellar silicate solids,[11] whose exfoliation can be achieved by ion exchange reactions, the exfoliation of graphite cannot be afforded using the same approach as it does not bear any net charge. Nevertheless, owing to the weak van der Waals forces among graphene layers, some appropriate atoms or molecules, known as intercalating agents, can enter the graphite galleries by diffusion from the edge planes of graphite to form layered crystals. The resulting products composed of guest intercalants and host graphite layers are named graphite intercalation compounds (GICs) as mentioned in section 19.1.[12,13,26–31]

The graphite structure consists of carbon layers in an alternating stacking sequence. It has been reported that the lamellar graphite can be intercalated with alkali metals.[23,24,32] For example, potassium can insert into the graphite structure to give a number of compounds, called stages as shown in Fig. 19.3. The figure describes two different models for the formation of GICs. The stage is defined as the number of graphene layers between two intercalants. The first stage material, KC_8, has an orthorhombic orientation and the *d*-spacing of graphene layer

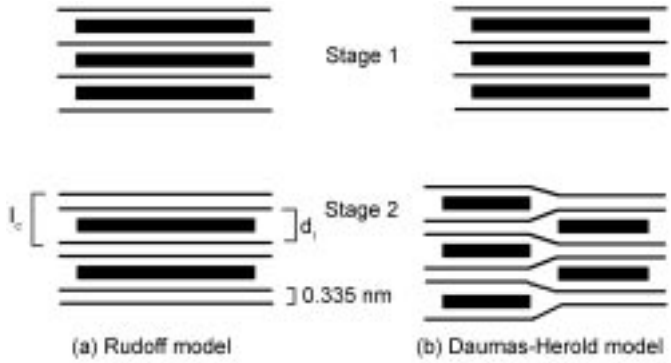

19.3 Scheme illustration of the stage structure of GICs. Black line: graphite layer; light black line: intercalated compound.

increases from 3.35 Å to 5.41 Å. The second stage, or KC_{24}, it shows a *d*-spacing of 8.72 Å. The stages *n* can be calculated from Equation (19.1):

$$n = (Ic - d_1)/C_0 + 1 \tag{19.1}$$

where $d_1 = d_i + C_0$, *Ic* is the repeat value of 001 peak in X-ray trace; d_1 is the thickness of intercalant; and C_0 is the spacing between graphene layers (3.35 Å).

Upon various intercalants being intercalated into the interlayers of graphite to produce GICs, the GICs can then carry out many reactions to yield expanded graphite or EG, that can be used as a layered filler to fabricate polymer/graphite nanocomposites. Therefore, the preparation of GICs is of great importance. The various synthesis methods of GICs include:

1. *Vapor phase transportation*.[33,34] Metal-GICs can be prepared using this method by heating alkali metal compounds, which pass through a separated tube to intercalate into the galleries of graphite. The temperature difference between heated graphite and metal is crucial to control the stages of resulting metal-GICs.
2. *Liquid intercalation, including molten liquid and solution liquid*.[35–41] The typical examples are the use of immersing graphite in molten metal chlorides or liquid bromine. The detailed procedure is given in the related literature.[35–41]
3. *Intercalation by electrochemical technology*.[42–49] The method can be used to intercalate organic acids such as concentrated sulfuric acid, nitric acid into the graphene layers. Also alkali metal and metal chlorides can be intercalated into the graphite using this way. The driving force for the intercalation is electricity flow. The stages of a GIC are generally controlled by the concentration of a solution liquid.[45]
4. *Co-intercalation and sequential intercalation approaches*. The atoms or molecules with relatively larger size such as Na, Cs or K find it difficult to

penetrate and enter the galleries of graphite because of the very small interlayer spacing. These atoms can enter the graphite galleries upon the formation of the alloy with other metals.[50] Similarly, small atoms such as H_2 also cannot intercalate into the graphite interlayer. However, by using both H_2 and potassium as co-intercalant, a stage 2 GIC can be produced via the formation of $C_{16}K_2H_{4/3}$.[51]

GICs have been reported to find wide applications as summarized in Table 19.1.[52–54] To prepare polymer/graphite nanocomposites, exfoliated or expanded graphite has to be used because high molecular weight polymers cannot diffuse into the extremely small galleries of pristine graphite. For the purpose of preparing EG, the easiest method is to rapidly heat a GIC and the most commonly used GIC is H_2SO_4-GIC. A typical preparation of the GIC derived from NGF and concentrated sulfuric acid is hence given as follows:[13] a mixture of

Table 19.1 Applications of GICs

Application	Comment
1. *Highly conductive materials*	
HNO_3, SbF_5, AsF_5, $CuCl_2$, $FeCl_3$, F_2, K-Bi, residual Br_2	Combinations between host graphite and intercalates
2. *Electrode materials in batteries*	
Primary battery	
$(CF)_n$, $(C_2F)_n$, graphite oxide, F_2, $CoCl_2$, TiF_4, etc	Efficiency enhancement of function of intercalates
Second battery	
H_2SO_4, $Ni(OH)_2$, $Mn(OH)_2$, HF	
Thermocell	Intercalation and deintercalation process
Br_2, HNO_3	
3. *Catalyzers for organic synthesis*	
Li, K, K-Hg, K-$FeCl_3$, SbF_5, Br_2, H_2SO_4, HNO_3, etc	Efficiency enhancement of function of intercalates
4. *Materials for storage and isotope-separation of hydrogen*	
K, Cs, Rb	Creation of functional space in intercalation compounds
5. *EMI shielding*	
Br_2-GIC-epoxy composite	Large skin depth
IBr-GIC-epoxy composite	
6. *Others*	
Exfoliation of graphite	Intercalation and deintercalation process
H_2SO_4, HNO_3, $FeCl_3$, K-THF, Na-THF	
Electrochromic	
Li-DMSO-GIC	
Photosensitizable	
$CuCl_2$–, $FeCl_3$–GIC	
Tribological	
$FeCl_3$–GIC	

concentrated sulfuric acid and hydrogen peroxide (H_2O_2-H_2SO_4 system) (1: 0.08, v/v) is mixed with NGF (80 mesh). The mixture is stirred at ambient temperature for about 1 h to allow H_2SO_4 to intercalate into intra-galleries of graphite. The resulting H_2SO_4-GIC is carefully washed and filtrated with deionized water until the pH value of the filtrate reached 6, and then dried at 100ºC for 24 h. The intercalation reaction between graphite and H_2SO_4 can be expressed as follows:

$$\text{n (graphite)} + \text{n } H_2SO_4 + 0.5 \text{ n [O]} \rightarrow \text{n (graphite}\cdot HSO_4) + 0.5 \text{ n } H_2O \quad (19.2)$$

where O is oxidant and (graphite·HSO_4) is GIC. The resulting GIC comprises graphene layers and intercalated layers stacked on top of one another in a periodic fashion. The stacking form can be of the form of –C–C–I–C– and –C–I–C–C–I–C–, where C is the graphene layer, and I is an intercalated layer. The number of carbon layers between each pair of intercalated layers is the stage number. The above structure, for example, shows a stage 2 intercalated graphite. The stage structure of intercalated graphite depends greatly upon the intercalation conditions. Generally, stage 2 to stage 5 GICs are obtained in case that conventional intercalation conditions are employed.

19.2.3 Preparation of expanded graphite

It has been well documented that when GICs are subjected to a thermal shock, the intercalants within graphite interlayers are led to a rapid volatilization. This can then tear the layers apart and lead to an expansion in the *c*-axis direction, perpendicular to the carbon layers of the GIC, resulting in a puffed-up material termed expanded graphite (EG), with a very low density.[11] The layered structures of parent graphite are maintained in the EG, whereas the volume expansion ratio, i.e. the ratio of the packing volume of EG to that of GICs, is typically as high as 200–300.[11]

Generally, the exfoliation of the expandable graphite or GICs is processed by heat-treatment at 900ºC or higher for a few seconds. Microwave irradiation was reported to be a new method to produce the exfoliated graphite.[55–58] The adoption of microwave irradiation heating results in a short reaction time compared with conventional heating, and ease workup after a reaction.[59,60] The exfoliated volume is proportional to the microwave irradiation time.[55] With 10 s of microwave irradiation, the intercalated graphite is expanded from a relative volume of 1 up to about 210 units. The expanded graphite appears a loose and porous vermicular material, and its structure is basically parallel layers, as shown in Fig. 19.4.

The XRD pattern of the H_2SO_4 intercalated graphite is shown as trace **b** in Fig. 19.5. Comparing with the natural graphite (trace **a** in Fig. 19.5), it is evident that the basal peak (0.335 nm) of natural graphite disappeared, indicating that the graphite was expanded completely.[60] The diffraction peaks in trace **b** of Fig.

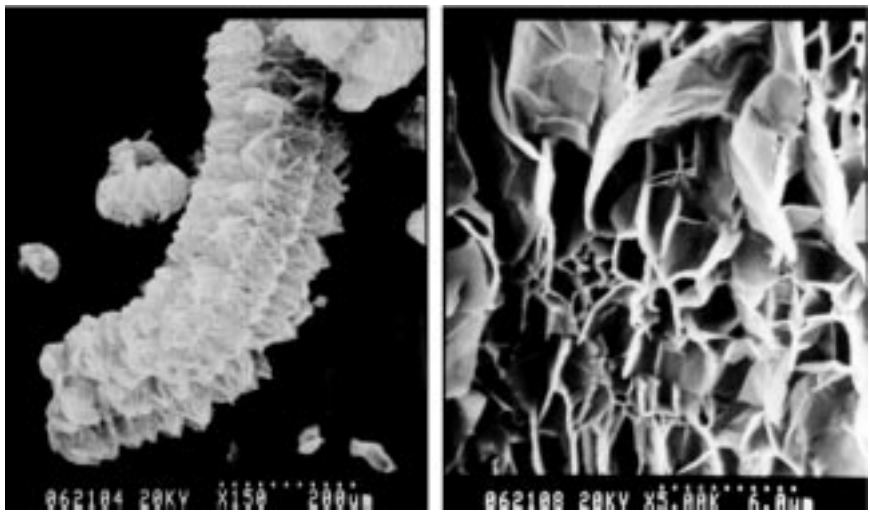

19.4 SEM micrographs of (a) wormlike EG of expansion ratio 100 at lower magnification, and (b) EG of expansion ratio 200 at higher magnification. (Adapted from ref. 58.)

19.5 are (5.5º, 001), (10.15º, 002), (25.26^0, 005), (30.31º, 006), (51.78º, 0010), (57.22º, 0011) in turn. All the diffraction peaks are indexed using the *c*-axis repeat distance I_c of 1.76 nm. The identity period in the *c* direction is one H_2SO_4 occupied graphene layer (0.755 nm) + three unoccupied graphene layers (3×0.335 nm) = 1.760 nm. These data demonstrate the formation of the

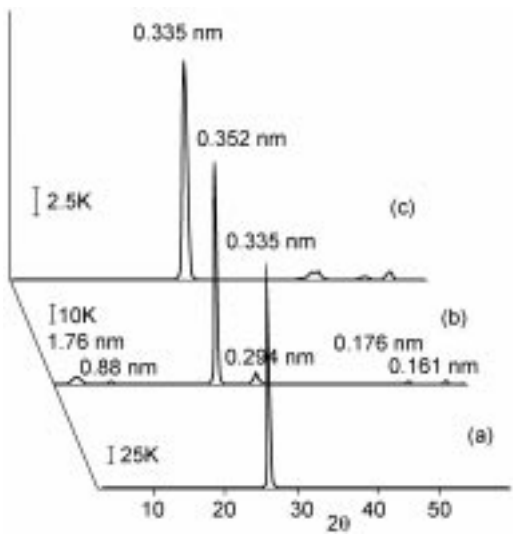

19.5 X-ray diffraction patterns: (a) original graphite; (b) H_2SO_4 intercalated graphite; and (c) expanded graphite. (Adapted from ref. 15.)

stage-4 intercalated graphite with a stacking sequence of —G–H_2SO_4–G–G–G–G–H_2SO_4–G–G–G— (G: graphite layer). Upon being heated at a certain temperature, the decomposition of the intercalating H_2SO_4 leads to the exfoliation of the expandable graphite, forming loose and porous layered structure though collapsed and deformed desultorily as shown in Fig. 19.4. The corresponding XRD pattern of the EG is shown in Fig. 19.5c. The diffraction peak appears the same as the natural graphite (Fig. 19.5a), indicating that the EG is composed of basic elements of a graphene layer of the original graphite.[61]

19.2.4 Synthesis of graphite nanosheets and graphite oxide

Exfoliated graphite consists of a large number of delaminated graphite nanosheets. The electrical conductivity is not obviously affected compared with the original graphite.[30,61] Ultrasonic irradiation has been widely applied in chemical reaction and engineering. When an ultrasonic wave passes through a liquid medium, the effect of ultrasonic cavitation can generate a very strong stirring environment. Therefore, ultrasound has been extensively used in dispersion, emulsifying, crushing, and activation of particles.[62] In this respect, the graphite worm can then be broken down to yield graphite nanosheets using ultrasonic irradiation technique. Figure 19.6 shows the SEM micrograph of the as-prepared graphite nanosheets. It can be seen clearly that the graphite worm is torn into sheets with thickness in nanoscale.

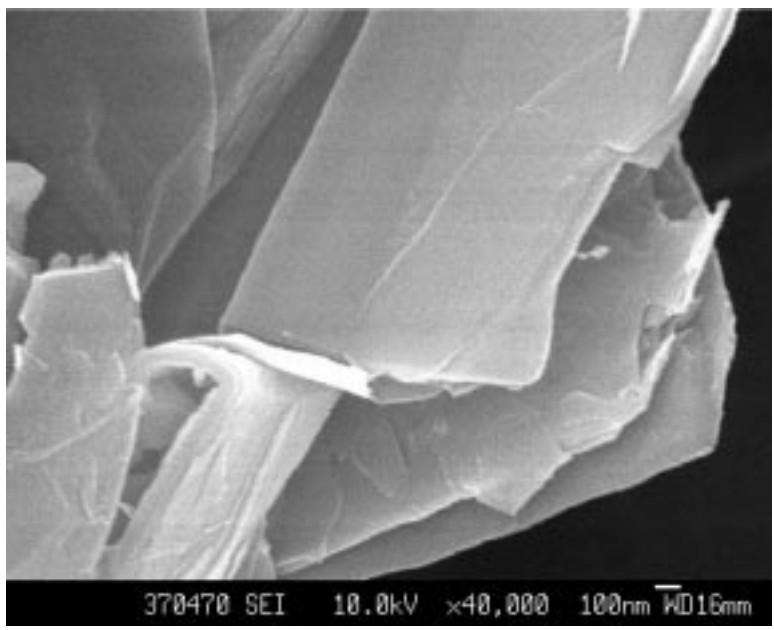

19.6 SEM micrograph of graphite nanosheets. (Adapted from ref. 58.)

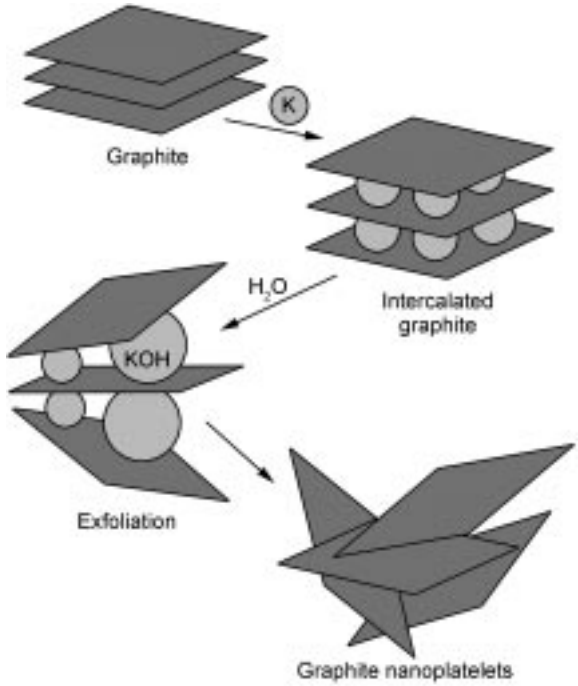

19.7 Simplified schematic of the intercalation/exfoliation process. Graphite is intercalated with potassium to form the first-stage intercalation graphite compound, KC_8, and then exfoliated in aqueous solvent to produce GNPs with 40 ± 15 layers thick. (Adapted from reference 112).

Graphite nanosheets can also be synthesized using known GIC chemistry.[63] A simplified schematic of the intercalation and exfoliation process is shown in Fig. 19.7. The first-stage intercalation compound, KC_8, is readily formed by heating graphite powder with potassium metal under vacuum at 200ºC. Powder X-ray diffraction confirms that only crystalline material present is KC_8. A *c*-axis expansion from 3.4 Å to 5.4 Å is calculated from the diffraction pattern, indicating an average stoichiometric distribution of potassium within the graphite galleries, rather than the idealized first-stage GIC depicted in Fig. 19.7. The involved reaction is given as follows:

$$KC_8 + CH_3CH_2OH \rightarrow 8C + KOCH_2CH_3 + \tfrac{1}{2}\,H_2 \qquad (19.3)$$

The resulting hydrogen gas evolution aids in separating the graphite sheets into nanosheets with a thickness of 40 ± 15 graphene layers.[64] It should be noted that individual graphene nanosheets are not obtained owing to incomplete exfoliation.

Unlike layered silicates, graphite does not undergo any ion exchange process,[20–24] but organophilic ammonium cations can intercalate the interlayers of graphite oxide (GO). GO is a well-known layer-structured compound

obtained by oxidation of graphite.[65,66] Each fundamental layer of GO has a dense two-dimensional carbonaceous skeleton, which is constructed of a larger number of sp3 carbons and a smaller number of sp2 carbons. GO ('oxidized-form') is reduced by heating,[13] or by reducing agents and so on, and becomes a graphite-like structure with turbostratic-tendency ('reduced-form'), which contains few or no oxygen and is electrically conductive. The resulted GO layers have been used as layered conducting fillers for polymer/graphite nanocomposites.[14,68] The preparation of graphite oxide involves the oxidation of graphite, using an oxidizer in the presence of nitric acid and both stage 1 and stage 2 materials have been formed.[65,66] Upon formation of graphite oxide, the layered structure of graphite is preserved, while the aromatic character is partially lost. The structure contains various amounts of hydroxyl groups, ether groups, double bonds, carboxyl, and ketone groups. The formula that has been suggested for graphite oxide is $C_7O_4H_2$ and it is known to be thermally unstable.[66,67,69] Graphite oxide is hydrophilic and readily adsorbs water or other polar liquids. Similar to layered silicates,[66] a one-dimensional swelling is observed as the lamellae move apart. In this case, the swelling of the graphite oxide allows for intercalation of various compounds such as alkyl ammonium salts and polymers.[13,65,67,70–77] When the bonds between the graphite layers (in the direction of *c*-axis) are broken up by strong oxidation, hydrophilic graphite oxide (GO) with lamellar structure is then generated. According to the amount of water absorbed in the GO layers, the interlayer spacing (d_L) (001 reflection in X-ray diffraction) varies from 6.1 to 11 Å. It readily disperses in NaOH solution (d_L = 12.3 Å in 0.05 N NaOH solution, $d_L = \propto$ in 0.01 N NaOH).[13] The intercalated GO can be used as the host of many kinds of nanocomposites and exhibits very rich intercalation chemistry.

19.3 Structures of polymer/graphite nanocomposites

Depending on the nature of the components used (natural graphite flakes, expandable graphite, expanded graphite, graphite oxide, graphite nanosheet, and polymer matrix) and the preparation method, three main types of composites may be obtained for a typical polymer/graphite system derived from the in-situ synthesis of graphite and monomer. As depicted in Fig. 19.8, when the polymer is unable to intercalate between the graphite sheets, a phase separated composite is obtained, whose properties stay in the same range as traditional macrocomposites. Beyond this classical family of composites, two types of polymer/graphite nanocomposites can be produced. Intercalated nanostructure, in which a single, and sometimes more than one, extended polymer chain is intercalated into the galleries of graphite layers resulting in a well ordered multilayer morphology built up with alternating polymeric and graphite layers. In case the graphite layers are completely and uniformly dispersed in a continuous polymer matrix, an exfoliated or delaminated nanostructure is yielded. It

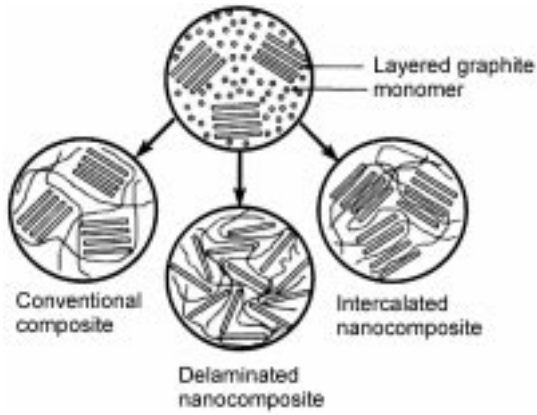

19.8 Possible structures for polymer/graphite composites.

should be noted, however, that the EG is a somewhat partially exfoliated graphite compared to polymer/clay nanocomposites, because the graphite layers interconnect with each other.[59,84] Only when the graphite sheets are fully exfoliated into polymer matrices can the resultant composites be called delaminated nanocomposites. It should be pointed out that the term 'delaminated' used in this context does not mean single graphene layer as it is used in polymer/clay nanocomposites, but refers to a separated graphite flake. In order to characterize above-mentioned nanostructures, two complementary techniques are used. XRD is used to identify intercalated nanostructures. In such nanocomposites, the repetitive nanoscale multilayer structure is well preserved, allowing the interlayer spacing to be determined. The intercalation of the polymer chains into a layered material usually increases the interlayer spacing, in comparison with the original spacing of the layered filler used, leading to a shift of the diffraction peak towards lower angle values. The angle and layer spacing values are related through the Bragg's relation, i.e., $\lambda = 2d \sin \theta$, where λ corresponds to the wavelength of the X-ray radiation used in the diffraction experiment, d the spacing between diffractional lattice planes and θ is the measured diffraction angle. For an exfoliated nanostructure, no diffraction peak is observable in the XRD diffractograms. This is because either the spacing between the filler layers exceeds 8 nm in the case of orderly exfoliated nanostructure, or the exfoliated layers are distributed disorderly. In the latter case, transmission electron microscopy (TEM) can be used to characterize the nanocomposite morphology.

19.4 Preparations of polymer/graphite nanocomposites

To prepare polymer/graphite nanocomposites, several strategies have been considered, including the three main processes as shown below:

- In-situ *intercalative and/or exfoliation polymerization*: In this process, the layered expanded graphite or exfoliated graphite nanosheets are swollen within the liquid monomer or a monomer solution, so that the polymer formation can then occur in between the intercalated graphite sheets or graphene layers. The polymerization can be initiated either by heating or radiation, by the diffusion of a suitable initiator or by an organic initiator inside the interlayer of graphite after the swelling step by the monomer. In spite of the different initiators used, varying polymerization processes can be adopted for the in-situ synthesis of polymer/graphite nanocomposites. The advantage of this technique is that a well-dispersed intercalated or exfoliated polymer/graphite nanocomposite is generally obtained. Under this process the nanocomposites are also prepared through emulsion polymerization where the expanded graphite is well dispersed in the aqueous phase.
- *Melt intercalative and/or exfoliation*: The layered expanded graphite or exfoliated graphite nanosheets are mixed with the polymer matrix in the molten state. Due to the neutral nature of graphite in chemistry, the chosen polymer can diffuse into the interlayer space or galleries of expanded graphite and yield either an intercalated or an exfoliated polymer/graphite nanocomposite. This methodology is solvent-free and cost-effective.
- *Exfoliation-adsorption*: The expanded graphite is broken down or exfoliated into graphite nanosheets and graphene layers (as illustrated in Fig. 19.2) using a solvent in which the polymer (or a prepolymer in the case of insoluble polymers such as polyimide) is soluble. In this case, the expanded graphite, due to the very weak forces that bond the graphene layers together can easily be dispersed in an adequate solvent. In the meantime, the dissolved polymer is adsorbed onto the delaminated graphite sheets. When the solvent is evaporated or the mixture precipitated out, the graphite sheets or graphene layers reassemble, sandwiching the polymer chains to form an ordered multilayer nanostructure or an exfoliated nanostructure in the best case. It should be noted that intensive stirring such as sonication is needed to break down the expanded graphite worm and help the polymer chains intercalate into graphite nanosheets or graphene layers to form a polymer/graphite nanocomposite.

19.4.1 In-situ intercalation and/or exfoliation polymerization

Polymerization initiated by alkali metal-GICs

Many interlamellar polymerization reactions were carried out and studied using alkali metal-GICs as initiators for the in-situ polymerization.[11,80,81] Although more than 100 kinds of GICs have been synthesized, only a few polymer/graphite nanocomposites have been reported because organic molecules are hard to be directly intercalated into the small spacings of graphite sheets. However,

organic polymerizable monomers can be cointercalated into some kinds of GICs or absorbed by some related graphite materials, thus the polymer/graphite nanocomposites can be synthesized via in-situ polymerization of the monomers. In this sense, a few hydrocarbons have been polymerized within the interlayer spacing of the graphite in GICs to produce polymer/graphite nanocomposites.[11,78] The above works have focused mainly on the polymerization mechanism and the characterization of the produced polymers, the reaction and reaction activity, and the effect on thermal stability. A typical example recently reported by Xiao *et al.* is that an in-situ polymerization of styrene in a ternary potassium-tetrahydrofuran-GIC (K-THF-GIC) solution system was performed to synthesize a polystyrene/graphite nanocomposite.[80] The mechanism for the polymerization initiated by K-THF-GIC was investigated and discussed in this paper. In order to perform an anion that can initiate the polymerization, some naphthalene (about 0.2 M) has to be added into the mixture of K-THF-GIC.[81–83] The reactions in the mixture can be presented as follows:

$$M + pTHF + \text{naphthalene} \longrightarrow M^{+}(THF)_p(\text{naphthalene})^{-} \tag{19.4}$$

$$M^{+}(THF)_p(\text{naphthalene})^{-} + nC \longrightarrow M^{+}(THF)_pC_n^{-} + \text{naphthalene} \tag{19.5}$$

The formed anion of $M^{+}(THF)_pC_n^{-}$ acts as the initiator for the polymerization of styrene. When styrene diffuses onto the surface of graphite sheets or enters the interlayer of graphite, the polymerization is initiated by accepting the anions from the complex of K-THF-GIC. The initiation and propagation steps can be depicted in Figure 19.9. TEM observation has showed the formation of polystyrene/graphite nanocomposite. The graphite sheets existed within the polystyrene matrix in a thickness smaller than 100 nm. Due to the interfacial interaction between graphite nanosheets and matrix, the nanocomposites exhibited higher glass transition temperature (T_g) and higher thermal stability when compared to neat polystyrene. The reported percolation threshold value of the electrically conductivity of the composites is less than 8.2 wt.%. However, it was shown that only part of styrene polymerized in some of the interlayer spacing of graphite, whereas most of polymerization took place on the surface of the graphite layers.

In-situ polycondensation approaches

Polyamide 6/graphite nanocomposites with markedly low percolation threshold value were recently prepared using an in-situ polycondensation approach.[18] Based on transmission electron microscopy (TEM) results, the thickness of EG filler incorporated in the polymer matrices was found to vary from 10 to 50 nm, and the aspect ratios (diameter to thickness) can be estimated as high as 100–300.[79] The graphite used by Pan *et al.*[18] is termed foliated graphite (FG). FG can

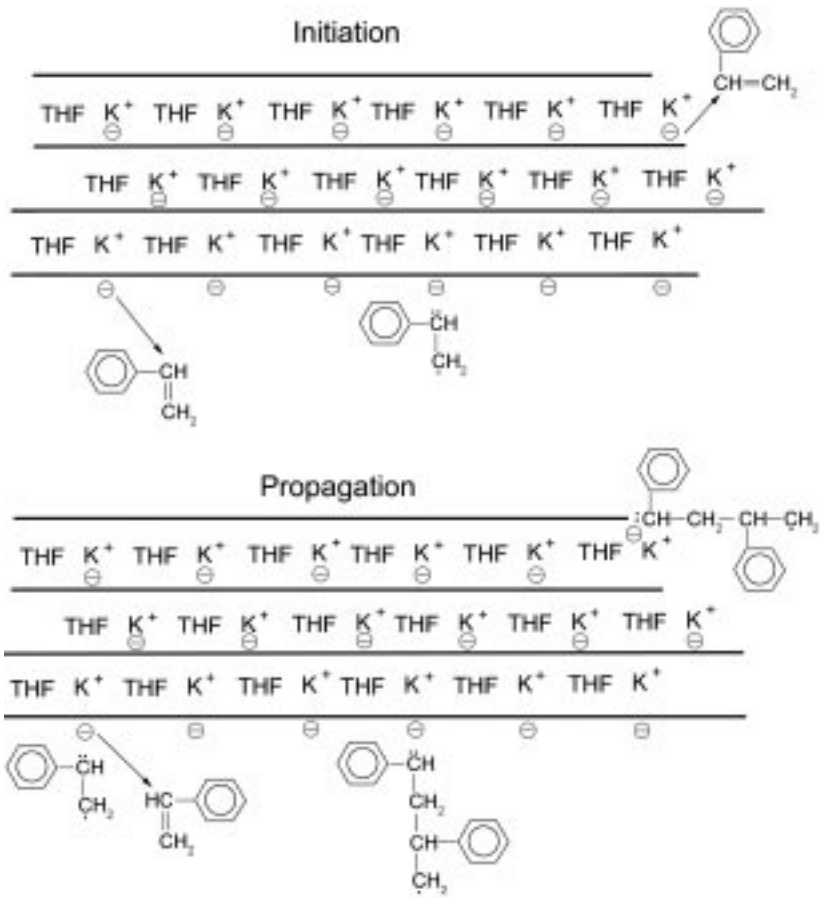

19.9 Reaction scheme for the polymerization of styrene initiated by K-THF-GIC.

be prepared by fragmentation of EG using ultrasonic irradiation as described elsewhere.[59,84–86] SEM showed that the as-made FG particles are roughly disk-shaped sheets with their thickness of the order of less than 100 nm. The size and size distribution of the FG nanosheets vary with respect to the ultrasonic irradiation timings.

The polyamide 6/graphite nanocomposites were prepared via anionic ring-opening polymerization.[79] First, the mixture of a given amount of ϵ-caprolactam and FG powder sealed in a tube was immersed in an ultrasonic bath at 110ºC for 25 min to disperse of the mixture. Then, a catalytic amount of sodium hydroxide was introduced into the mixture as activator, followed by vacuuming the system

at a limited pressure of 10^{-2} Pa to remove produced water during the reaction at 135ºC. Finally, after 30 min of reaction under ultrasonic irradiation, the vacuum was stopped and a catalytic amount of toluyl diisocyanate (TDI) was added into the mixture as chain initiator. After 2 min of stirring, the oil bath temperature was further increased to 155ºC, while the ultrasonic irradiation was maintained for 60 min. With the assistance of ultrasonic irradiation, the FG nanosheets were effectively dispersed in the polyamide 6 matrix. The nanocomposite exhibited a typical percolative transition of electrically conductivities at a FG content of as low as 0.74 vol.%.

To determine the percolation threshold value for a polymer insulator/conductive filler composite, several theoretical elaboration methods have been proposed, including percolation theory,[1,87–91] mean-field theory[92] and excluded volume theory.[79] Only the percolation theory is introduced in this review.

According to the percolation theory, the percolation threshold, ϕ_c, is the critical volume fraction, where an infinite continuous conducting cluster spanning across the sample is formed.[1] Due to the presence of a conducting or percolation path across the entire sample, a change from an insulator to a semiconductor occurs. Above the percolation threshold, the electrical conductivity is related to the content of conducting filler by a simple power law:

$$\sigma_m = \phi_h(\phi - \phi_c)^t \tag{19.6}$$

where σ_m is composite conductivity, ϕ_h conductivity of conductive filler, ϕ volume fraction of conductive filler, ϕ_c percolation threshold, and t critical exponent. Equation (19.6) is also used to describe the conductivity of continuum systems, such as metal–metal oxide and graphite–polymer mixtures. When the conductivity anisotropy is small, the experimental results are averaged to generate one single set of data, which are thereby fitted by means of Equation (19.6). Using the equation, Weng *et al.* have calculated the three parameter for the polyamide 6/graphite system.[79] The results are $\phi_c = 0.74$ vol.%; and $t = 2.32$, which correlates well with Equation (19.6) and the conductivities data above the percolation threshold. However, the critical exponent value derived is higher than the universal one, $t_{un} \approx 2$ in 3D, but still within the range reported in the literature for continuum systems.[31,88] Because this universal value is theoretically derived in the lattice models, it might not be true for real continuum systems.[89] The better result is observed for the low value of the percolation threshold of less than 0.75 vol.%. In the case of carbon black–filled polyamide 6 systems, a critical concentration of about 9.0 wt.% was reported for the composites prepared by compression molding,[91] whereas for melt blending of carbon black and polyamide 6, a value of as high as 27.0 vol.% is required for the critical transition.[3] Both of two systems are macrocomposites. Thus, it is clear that the nanocomposites containing FG nanosheets are more effective in increasing the electrical conductivity.

In-situ ring-opening polymerization approaches

Some polymeric materials such as polyimides or some conjugated polymers are infusible or insoluble in organic solvents. Therefore, the only possible route to produce nanocomposites with these types of polymers is to use soluble polymeric precursors that can be intercalated in the layered graphite and then thermally or chemically converted to the desired polymer. This method has been used successfully to fabricate polymer/graphite nanocomposites.[14,15,68] Meng *et al.* reported the preparation of exfoliated graphite by first synthesizing H_2SO_4-GIC in a H_2O_2-H_2SO4 mixture, followed by expansion under microwave irradiation. The structure of the expanded graphite could be described by the illustration in Fig. 19.2. Poly(arylene disulfide)/graphite nanocomposites were then fabricated by absorbing cyclic(arylene disulfide) oligomers into the pores of exfoliated graphite. Subsequently, the nanocomposite precursor was subjected to heat treatment to carry out the in-situ ring-opening polymerization (ROP) of the oligomers via free radical mechanism. The schematic illustration for the process is shown in Fig. 19.10. The as-prepared nanocomposite exhibited an exfoliated nanostructure as evidenced by TEM observation. The conducting network formed with the clear observation on the right-bottom corner as indicated. Compared with pure polymer, the electrical conductivity of the poly(arylene disulfide)/graphite nanocomposites was dramatically increased and had a value of about 10^{-3} S/cm for the nanocomposite containing 5 wt.% graphite. The nanocomposite exhibited a typical percolative transition of

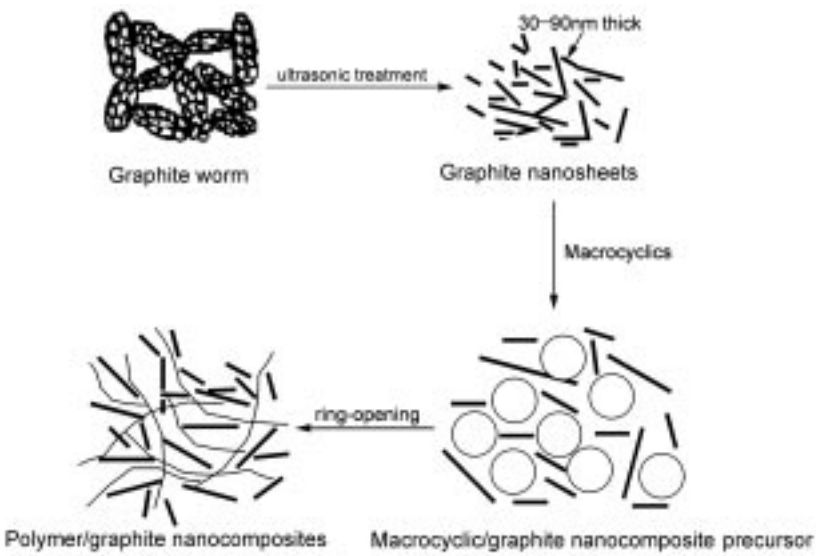

19.10 Schematic illustration of the formation of the poly(arylene disulfide)/graphite nanocomposites via in-situ ring-opening polymerization of macrocyclic oligomers. (Adapted from ref. 58.)

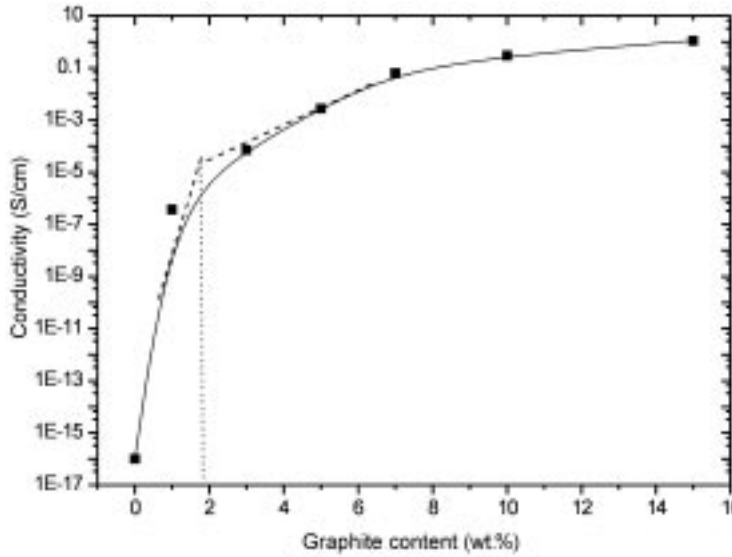

19.11 Electrical conductivity of poly(arylene disulfide)/graphite nanocomposites versus graphite nanosheet content.

electrically conductivities at a graphite content of less than 2.0 wt.% as shown in Fig. 19.11. The nanocomposites were reported to be used as high performance electrically conductive material.[93]

The unique advantage of using the macrocyclics to prepare polymer-based nanocomposite is the practicable application. This is due to the fact that these macrocyclic oligomers can instantly polymerize in the melt in the absence of any catalyst or initiator at a temperature as low as 150ºC, without liberation of any volatile by-products.[94–96] Therefore, they can be processed more easily compared with other polymerization processes.

Emulsion in-situ polymerization

This has been also studied in order to promote the intercalation of water insoluble polymers within layered silicates such as montmorillonite, which is widely used in the preparation of nanocomposites.[97–99] However, it is difficult to intercalate monomers or polymers into the interlayer spaces of graphene layer or carbon layer because carbon atoms on each graphene layer plane are tightly held by covalent bonds. Another hurdle is that graphite shows neither hydrophilic nor hydrophobic natures. Thus, graphite oxide (GO) needs to be synthesized by oxidation of natural graphite.[55,67] Since GO has larger *c*-axis spacing and polar groups, such as hydroxyl, ether and carboxylate groups, on its surface, intercalation of polymers into GO becomes possible.[19,72–74,100,101] For example, when the mixture of 1.0 g dried GO and 40 mL of methyl methacrylate (MMA)

was stirred at room temperature for 10 h, followed by adding 150 mL of distilled water and an emulsifier OP-10 (3 mL), and then mechanical stirring was continued for another 10 h. Then, a catalytic solution of potassium persulfate and anhydrous sodium sulfite was introduced into the emulsion system. The polymerization of MMA was carried out at 63–67ºC for 15 h to obtain a PMMA/graphite nanocomposite emulsion.[41,102] The oxidation of natural graphite by $KMnO_4$ in concentrated H_2SO_4 produced GO with hydroxyl, ether and carboxyl groups, and the interlayer spacing of GO in *c*-axis (*Ic*) increased to 9.1 Å because of the intercalation of H_2O. The intercalation of MMA and in-situ polymerization occurred during the emulsion polymerization of MMA in the presence of GO. Moreover, they found that during the emulsion polymerization, the grafting polymerization of a small amount of MMA took place. However, the TEM observation indicated that the spherical particles of GO are homogeneously distributed within the composites in nanoscale. The conductivity increased from 10^{-16} S cm^{-1} of pure PMMA to 10^{-4} S cm^{-1} of PMMA/intercalated GO composite at GO content of 8.0 wt.%.[102] The percolation threshold value is about 2 wt.% of GO.

19.4.2 Melt intercalative and/or exfoliation

It has been well documented that polymer/layered-inorganic and polymer/clay nanocomposites are being explored extensively due to their high promise for potential applications[6,7] and as model systems for nanoscopically confined polymers.[103–105] These polymer/inorganic nanocomposites can be prepared by in-situ polymerization, including solution, suspension, emulsion, and bulk polymerizations, as well as by melt blending and solution mixing. Both hydrophilic and hydrophobic natures of graphite favor the melt blending of graphite with the vast majority of polymer matrices, without surfactants being employed in order to promote interactions. However, the graphite sheets are not well dispersed as those by in-situ polymerization process. Generally, the preparation of nanocomposites by melt blending is performed either with a batch mixer or an extruder. Fawn *et al.* have successfully prepared polyamide 6/nanocomposites using a variety of graphites, including pristine graphite, expandable graphites and expanded graphite by melt blending.[106] Based on X-ray diffraction analyses and TEM observations, intercalated/exfoliated nanocomposite structure of polyamide 6/graphite was confirmed for the special treatments of graphite. Non-polar and low surface-energy polyolefins can also be used as the matrices for polymer/graphite composites. Gopakumar and Pagé reported that the preparations of polypropylene (PP)/graphite nanocomposites by melt-mixing PP with different levels of graphite.[107] Melt-mixing was achieved using a Gelimat, a high-speed thermo-kinetic mixer. The Gelimat system is specifically designed to handle difficult compounding and dispersion applications by completely mixing, heating and compounding products within a few minutes. The good dispersion of the

graphite in the PP matrix demonstrated that the Gelimat thermo-kinetic mixing was effective in producing PP/graphite-based nanocomposites.

Theoretical analysis for the intercalation of graphite sheets or layers is similar to that of layered silicates. The thermodynamics that drives the intercalation of a polymer inside expanded graphite while the polymer is in the molten state that is a lattice-based mean field theory by Vaia and Giannelis.[108] Generally, the outcome of polymer intercalation is determined by interplay of entropic and enthalpic factors. In fact, although the confinement of the polymer chains inside graphite galleries results in a decrease in the overall entropy of the polymer chains, this entropic penalty may be compensated by the increase in the gallery spacings of expanded graphite.

19.4.3 Exfoliation-adsorption intercalation/exfoliation

This technique can be used with both water-soluble and organic solvent-soluble polymers to produce intercalated/exfoliated nanocomposites based on grafted polypropylene (gPP)/graphite,[109] poly(methyl methacrylate) (PMMA)/graphite,[110,111] polyacrylonitrile/graphite,[112] poly(vinyl alcohol)/graphite[113] nanocomposites.

When polymeric aqueous solutions are added to dispersions of various graphites, including expanded graphite, graphite oxide and graphite nanosheets, the strong stirring and the neutral nature of graphite layers often trigger the reaggregation of the graphene layers as it occurs for polyacrylonitrile/graphite.[112] Generally, graphite nanosheets are obtained under strong ultrasonic stirring, consequently leading to the formation of nanocomposites containing graphite nanosheets. In particular, polymers intercalation using the so-called exfoliation-adsorption technique can also be performed in organic solvents because of the nature of graphite. PMMA has been successfully intercalated in expanded graphite by dispersion in chloroform,[110] increasing the intersheet spacing from 0.335 to about 1.76 nm. Some water-soluble polymers, such as poly(vinyl alcohol),[113] poly(acrylamide),[75] and poly(acrylic acid)[114] can be inserted into the GO lamella to form intercalated or exfoliated polymer/GO nanocomposites. Xu and coworkers[115] have investigated this technique in attempts to produce poly(vinyl alcohol)/graphite oxide nanocomposites in

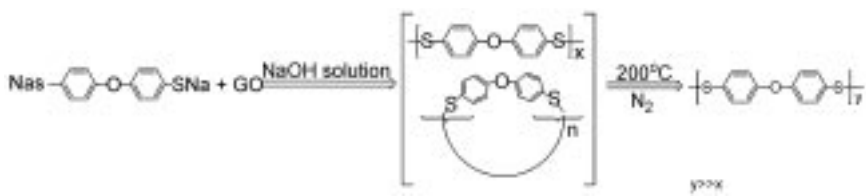

19.12 The possible reactions during the process of restoring graphene sheet structure upon thermal treatment. (Adapted from ref. 14.)

aqueous solution. These nanocomposites with graphite oxide have larger gallery spacing. High resolution microscopic image of the resulting poly(vinyl) alcohol/graphite oxide nanocomposite indicated that GO was fully exfoliated and the interlayer spacing of GO was larger than 5 nm.

Some polymeric materials such as polysufides, polydisulfides and polyimides have the particular property of being infusible and insoluble in organic solvents. Therefore, the only possible route to produce nanocomposites with those types of polymers consists of using soluble polymeric precursors that can be intercalated in the layered graphite and then thermally or chemically converted in the desired polymer. This has been successfully achieved by using the exfoliation-adsorption process. More recently, Du *et al.*[14] reported that the GO in polymer/GO nanocomposite can further restore graphene sheet structure upon thermal treatment. Therefore, it is possible to prepare polymer/graphite nanocomposite using the polymer/GO nanocomposite as a precursor. A schematic description is given in Fig. 19.12.

19.5 Properties

Similar to the layered silicates, layered graphite nanofillers with high aspect ratios (width-to-thickness) have been able to trigger a tremendous properties improvement in the polymers in which they are dispersed. Amongst those properties, an unexpectedly large increase in the electrical conductivity of polymer/graphite nanocomposite has drawn a lot of attention. Improved mechanical properties, thermal stability and fire retardancy through nanocomposite formation are other interesting properties displayed by nanocomposites. Those new materials have also been studied and applied for their superior gas barrier properties.

19.5.1 Electrically conducting properties

Electrically conducting polymers containing graphite have been studied extensively because of their potential applications in light emitting devices, batteries, electromagnetic shielding, anti-static and corrosion resistant coatings, and other functional applications.[116–120] Among the conducting polymeric composites, one main objective in design from both economical and processing viewpoints is to minimize the filler concentration. Natural graphite flakes possess good electrical conductivity (10^4 S/cm at ambient temperature) and low dielectric constant 3 at room temperature and at frequency of 1 Hz. Increase in electrical conductivity arising from the increase of filler content was observed for most conductive composites.[116] Generally, the introduction of very small amount of graphite (< 1.0 wt.%) into a polymer material leads to the transition from nonconductive with conductivity of about 10^{-16} S/cm to semi-conductive composite with conductivity of about 10^{-4} S/cm. However, too high concentration of the conductive filler could lead to the deterioration of mechanical

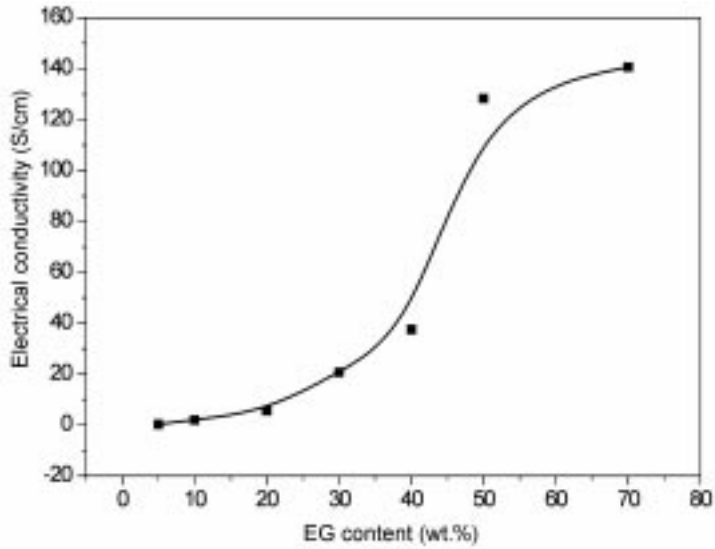

19.13 Electrical conductivity of poly(arylene disulfide)/EG nanocomposites with different content of EG. (Adapted from ref. 122.)

properties.[116] The conductive behavior can be explained by the percolation transition of the conductive network formation as discussed in previous section. In most cases, relatively large quantities of filler were needed to reach the critical percolation value, as the particle size is at micro- and millimeter scales. The transition in conductive particle containing polymers was greatly affected by the aggregation, structure, average size and size distribution of the dispersed graphites. Celzard *et al.*[31] first reported that the percolation threshold of epoxy/EG composite was only 1.3 vol.%. The EG filler was 100 nm in thickness on average under SEM examination. Recently, several authors reported that a markedly low volume fraction of EG was needed to satisfy the percolation threshold of conductivity in nylon 6/EG,[18] PS/EG composites[80] and EG containing styrene and methylmethacrylate copolymer[121] by in-situ polymerization. More recently, Meng's group has reported that the high electrical conductivity of poly(arylene disulfide)/graphite nanocomposite with a conductivity of greater than 100 S/cm can be prepared by incorporating about 40 wt.% EG.[122] Figure 19.13 shows the variation of electrical conductivity of the poly(arylene disulfide)/EG nanocomposites versus EG content. The electrical conductivity increased sharply with increasing EG content at EG content higher than 40 wt.%. The as-made highly conductive composite can be used as the material to fabricate the bipolar plates for proton exchange membrane fuel cells.

For the electrically conducting mechanism of polymer composites, two key questions are associated: (1) how to form the conducting paths and (2) how to conduct after the formation of the paths. Concerning the second question, there

are several theories, such as contact conducting, the tunneling effect, dielectric breakdown, and field emission. It is generally believed that conductibility depends on their combined effect that the microscopic migration of electrons might have several mechanisms. For the first question, there are, for example, the percolation theory,[123] the effective medium theory,[124] and the thermodynamic theory.[125] These theories all relate to the dispersed morphology and microstructure of conducting fillers in polymer matrices, which depend on geometrical, the nature of filler and polymer, formulation, preparation methods, and processing conditions. For the nanocomposites prepared by both solution intercalation and in-situ intercalative polymerization, the graphite particles with a large surface-to-volume ratio can abut or contact and then form a conducting path network at lower filler contents. Therefore, the percolation threshold values of the nanocomposites are remarkably low. As to the composites prepared by melt mixing, the graphite particles are broken up during processing and their sizes and the surface-to-volume ratios decreased drastically. Consequently, only at higher EG contents can they abut or contact and form the conducting paths.

19.5.2 Mechanical properties

Graphite consists of one-atom-thick layers of carbon. Upon separating the graphene layers through intercalation and exfoliation, thin nanoplatelets can be formed, which possess a high surface area and satisfy the high-aspect-ratio criterion needed for high-strength composites. The theoretical surface area of a graphene layer is 2630–2965 m^2/g.[126] In addition to its unique chemistry, graphite is also one of the strongest materials known per unit weight. The theoretical Young's modulus of an individual graphene layer is 1600 GPa.[127] Therefore, those unique characteristics make graphite nanosheets a potential reinforcement for high-strength composites.

Both tensile strength and Young's modulus have been shown to be strongly improved when polymer/graphite nanocomposites are yielded. Polyacrylonitrile/graphite nanocomposites show a drastic increase in both tensile strength and the Young's modulus at rather low filler content.[112] Actually, the material stiffness is substantially enhanced whatever the way of preparation: in-situ polymerization,[14,15] melt blending,[79,121] and exfoliation-adsorption method.[122] However, the elongation at break of polymer/graphite generally tends to decrease with the introduction of graphite fillers. It should be noted that because graphite sheet is fragile, it can be readily fractured during stirring and compounding with polymer.[111] To maintain its original structure of EG in the polymer matrices, careful procedures should be taken to avoid the fracture of EG sheets when mixing and compounding. Direct hot molding of the composites led to the deformation of EG and the orientation of graphite sheets.[122] Therefore, to obtain fully foliated graphite nanosheets, the fragmentation of EG by ultrasonic irradiation in the absence of grinding is recommended.

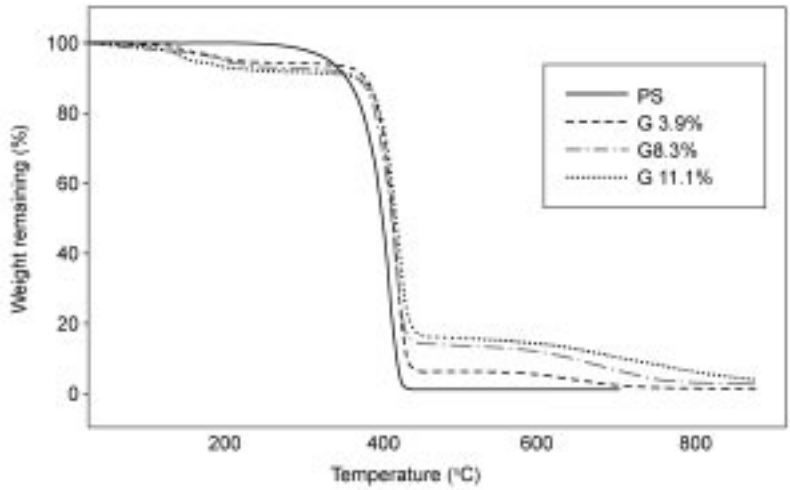

19.14 Weight loss versus temperature for neat polystyrene and polystyrene/graphite nanocomposite. (Adapted from ref. 80.)

19.5.3 Thermal stability

Another highly interesting property exhibited by polymer/graphite nanocomposites concerns not only their increased thermal stability but also their unique ability to promote flame retardancy at quite low filling level through the formation of insulating and incombustible char. Many research groups reported the thermal stability improvement in polymer/graphite nanocomposites.[14,15,58,78] Uhl and Wilkie[78] reported that the onset temperature of degradation for the polystyrene/graphite nanocomposites increases by about 50ºC compared to commercial polystyrene and similar results are obtained for maximum decomposition temperature. This is believed to result from the intercalation of polystyrene into the lamellae of graphite. A similar result was obtained by Xiao *et al.*[80] The typical weight loss curves are shown in Figure 19.14. The glass transition temperature of polystyrene/graphite nanocomposite is 5ºC higher than neat polystyrene. This is because when nanoscale fillers are finely dispersed in the matrix, the tremendous surface areas developed could contribute to polymer chain confinement effects that may lead to higher glass transition temperature.

19.6 Conclusions

The highly and efficiently improved electrical and mechanical properties at very low graphite content, together with the ease of manufacture through simple processes such as melt intercalation, in-situ polymerization, and exfoliation-adsorption or solution blending method make polymer/graphite nanocomposites a very promising new class of materials. These conducting materials are already

commercially available and applied in secondary batteries, anti-static, electromagnetic shielding, electrorheological fluids and other applications. The extremely low filler loading required to display unique properties enhancement makes the nanocomposites competitive with other conventional materials. Nevertheless, more in-depth understanding is needed for some of the critical factors such as mechanisms of intercalation/exfoliation of graphite in fabricating polymer/graphite nanocomposites, and the microstructure-property relationships.

19.7 Acknowledgements

The author wishes to acknowledge both the contributions of the figures adapted in this chapter, and my former and present students in my research group. Many of their names appear in the references.

19.8 References

1. Kirkpatrick S (1973), 'Percolation and conduction'. *Rev Mod Phys*, **45**, 574.
2. Das N C, Chaki T K, Khastgir D (2002), 'Effect of processing parameter, applied pressure and temperature on the electrical resistivity of rubber based conductive', *Carbon*, **40**, 807.
3. Miyasaka K, Waranabe K, Jojima E, Aida H, Sumita M, Ishikawa K (1982), 'Electrical conductivity of carbon-polymer composites as a function of carbon content', *J Mater Sci*, **17**, 1610.
4. Wycisk R, Pozniak R, Pasternak A (2002), 'Conductive polymer materials with low filler content', *J Electrostat*, **56**, 55.
5. Vaia R A, Price G, Ruth P N, Nguyen H T (1999), 'Lichtenhan, Polymer/layered silicate nanocomposites as high performance ablative materials', *J Appl Clay Sci*, **15**, 67.
6. Alexandre M, Dubois P (2000), 'Polymer-layered silicate nanocomposites: Preparation, properties and uses of a new class of materials', *Mater Sci Eng*, **28**, 1.
7. Usuki A, Kojima Y, Kawasumi M, Okada A, Fukushima Y, Kurauchi T, Kamigaito O (1993), 'Synthesis of nylon 6-clay hybrid', *J Mater Res*, **8**, 1179.
8. Vaia R A, Jandt K D, Kramer E J, Giannelis E P (1995), 'Kinetics of polymer melt intercalation', *Macromolecules*, **28**, 8080.
9. Manias E, Touny A, Wu L, Strawhecher K, Lu B, Chung T C (2001), 'Polypropylene/montmorillonite nanocomposites. Review of the synthetic routes and materials properties', *Chem Mater*, **13**, 3516.
10. Giannelis, E P (1996), 'Polymer layered silicate nanocomposites', *Adv Mater*, **8**, 29.
11. Chung D D L (1987), 'Exfoliation of graphite', *J Mater Sci*, **22**, 4190.
12. Shioyama H (2000), 'Interactions of two chemical species in the interlayer spacing of graphite', *Synth Met*, **114**, 1.
13. Du X S, Xiao M, Meng Y Z, Hay A S (2005), 'Direct synthesis of poly(arylene disulfide)/graphite nanosheet composites via the oxidation with graphite oxide', *Carbon*, **43**, 195–213.
14. Du X S, Xiao M, Meng Y Z, Hay A S (2004), 'New method to prepare poly(arylene disulfide)/graphite nanocomposite', *Synth Met*, **143(1)**, 129–132.

15. Du X S, Xiao M, Meng Y Z, Hay A S (2004), 'Facile synthesis of exfoliated and highly conductive poly(arylene disulfide)/graphite nanocomposites', *Polymers for Advanced Technologies*, **15(6)**, 320–323.
16. Malinauskas A (2001), 'Chemical deposition of conducting polymers', *Polymer*, **42**, 3959–3972.
17. Skotheim T A, Elsenbaumer R L, Reynolds J R (1998), *Handbook of Conducting Polymers*, New York, USA.
18. Pan Y X, Yu Z Z, Qu Y C, Hu H (2000), 'New process of fabricating electrically conducting nylon 6/graphite nanocomposites via intercalation polymerization', *J Polym Sci Part B: Polym Phys*, **38**, 1626.
19. Kotov N A, Dekany I, Fendler J H (1996), 'Ultrathin graphite oxide-polyelectrolyte composites prepared by self-assembly: transition between conductive and non-conductive states', *Adv Mater*, **8**, 637.
20. Lalancette J M, Roussel R (1976), 'Metals intercalated in graphite. I. The reactions of aromatic, olefinic, and acetylenic hydrocarbons with potassium-graphite intercalates', *Can J Chem*, **54**, 2110–2115.
21. Lalancette J M, Rollin R, Dumas P (1972), 'Metals intercalated in graphite. II. Reduction and oxidation', *Can J Chem*, **50**, 3058–3062.
22. Hennig G R (1959), 'Interstitial compounds of graphite', *Prog in Inorg Chem*, **1**, 125–205.
23. Rudorff W (1959), 'Graphite intercalation compounds', *Adv Inorg chem Radiochem*, **1**, 223–66.
24. Selig H, Ebert L B (1980), 'Graphite intercalation compounds', *Adv Inorg Chem Radiochem*, **23**, 281–327.
25. Inagaki K (1989), 'Application of graphite intecalation compounds', *J Mater Res*, **4(6)**, 1560–1568.
26. Dresselhaus M S, Kalish R (1992), *Ion Implantation in Diamond, Graphite and Related Materials*, Berlin: Springer.
27. Noel M, Santhanam R, (1998), 'Electrochemistry of graphite intercalation compounds', *J Power Sources*, **72**, 53.
28. Toyoda M, Inagaki M (2000), 'Heavy oil sorption by using exfoliated graphite new application of exfoliated graphite to protect heavy oil pollution', *Carbon*, **38**, 199–210.
29. Cao N, Shen W, Wen S, Liu Y (1996), 'Surface properties of expanded graphite', *Chem Bull*, **4**, 37–41.
30. Celzard A, Mareche J F, Furdin G, Puricelli S (2000), 'Electrical conductivity of anisotropic expanded graphite-based monoliths', *J Phys D: Appl Phys*, **33**, 3094–3101.
31. Celzard A, McRae E, Mareche J F, Furdin G, Dufort M, Deleuze C (1996), 'Composites based on micron-sized exfoliated graphite particles: electrical conduction, critical exponents and anisotropy', *J Phys Chem Solids*, **57**, 715–718.
32. Hennig G R (1959), 'Interstitial compounds of graphite', *Prog Inorg Chem*, **1**, 125.
33. Dresselhaust M S, Dresselhaust G (1981), 'Intercalation compounds of graphite', *Advances in Physics*, **30(2)**, 139–326.
34. Underhill C, Krapchev T, Dresselhaus M (1980), 'Synthesis and characterization of high stage alkali metal donor compounds', *Synth Metals*, **2**, 47–53.
35. Mittal J, Inagaki M (1998), 'Synthesis of stage-one $MoCl_5$-GIC in single phase', *Synth Met*, **92**, 87–89.

36. Mittal J, Inagaki M (1998), 'Formation of single-phase stage-1 $MoCl_5$-GIC in the presence of MoO_3', *Synth Met*, **95**, 23–28.
37. Mittal J, Inagaki M (1999), 'Effect of reaction of $MoCl_5$ with atmospheric water on its intercalation into graphite', *Solid State Ionics*, **121**, 183–188.
38. Inagaki M (1993), 'Formation and stability of new $FeCl_3$-graphite intercalation compounds' *Solid State Ionics*, **63–65**, 523–527.
39. Water J, Shioyama H (1999), 'Boron trichloride graphite intercalation compound studied by selected area electron diffraction and scanning tunneling microscopy', *J Phys Chem Solids*, **60**, 737–741.
40. Mizutani Y, Ihara E, Abe T (1996), 'Preparation of alkali metal graphite intercalation compounds in organic solvents', *J Phys Chem solids*, **57(6–8)**, 799–803.
41. Mizutani Y, Abe T, Ikeda K (1997), 'Graphite intercalation compounds prepared in solution of alkali metals in 2-methyletra hydrofuran and 2,5-dimethyltetrahydrofuran', *Carbon*, **35(1)**, 61–65.
42. Boehm H P, Helle W, Ruisinger B (1988), 'Graphite salt with perfluoro alkanesulfonic acid and alkanesulfonic acids', *Synth Met*, **23**, 395–400.
43. Ruisinger B, Boehm H P (1993), 'Intercalation of perfluorobutane sulfonic acid in graphite', *Carbon*, **31(7)**, 1131–1137.
44. Zhang Z, Lerner M M (1996), 'Preparation, characterization,and exfoliation of graphite perfleorooctanesulfonate', *Chem Mater*, **8**, 257–263.
45. Kang F, Leng Y, Zhang T (1998), 'Electrochemical synthesis and characterization of ferric chloride-graphite intercalation compounds in aqueous solution', *Carbon*, **36(4)**, 383–390.
46. Shioyama H, Crespin M, Seron A (1993), 'Electrochemical oxidation of graphite in anaqueous medium: Intercalation of $FeCl_4$', *Carbon*, **31(1)**, 223–226.
47. Frackowiak E, Tatsumi K, Shioyama H (1995), 'HOPG as a host for redox reactions with $FeCl_4$ in water medium', *Synth Met*, **73**, 27–32.
48. Kang F, Leng Y, Zhang T Y (1996), 'Electrochemical synthesis of graphite intercalation compounds in $ZnCl_2$ aqueous solutions', *Carbon*, **34 (7)**, 889–894.
49. Izumi I, Sato J, Iwashita, N (1995), 'Electrochemical intercalation of bromine into graphite in an aqueous electrolyte solution', *Synth Met*, **75(1)**, 75–77.
50. Billaud D, Herold A, Vogel F L (1980), 'The synthesis and resistivity of the ternary graphite-potassium-sodium compounds', *Mater Sci Engng*, **45**, 55–59.
51. Lagrange P, Herold A (1978), 'Chimisorption de L'hydrogene par les composes d'insertion graphite-potassium', *Carbon*, **16**, 235.
52. Gaier J R, Hardebeck W C, Bunch J R T (1998), 'Effect of intercalation in graphite epoxy composites on shielding of high energy radiation', *J Mater Res*, **13(8)**, 2297–2301.
53. Iwashita N, Izumi I, Hamada Y (1998), 'Photosensitization of graphite intercalation compounds with metal chlorides', *Carbon*, **36(11)**, 1700–1703.
54. Jun T, Qunji X (1997), 'Tribological properties of $FeCl_3$-graphite intercalation compound rubbed film on steel', *Carbon*, **35(3)**, 370–373.
55. Xiao M, Du X S, Meng Y Z, Gong K C (2004), 'The influence of thermal treatment conditions on the structures and electrical conductivities of graphite oxide', *New Carbon Materials*, **19(2)**, 92–96.
56. Mallon K H, Ray W H (1998), 'Enhancement of solid-state polymerization with microwave energy', *J Appl Polym Sci*, **69**, 1203–1212.

57. Lu J M, Zhu X L, Zhu J, Yu J (1997), 'Microwave radiation solid-state copolymerization in binary maleic anhydride-dibenzyl maleate systems', *J Appl Polym Sci*, **66**, 129–133.
58. Du X S, Xiao M, Meng Y Z, Hay A S (2004), 'Synthesis and characterization of poly(4,4'-oxybis(benzene) disulfide)/graphite nanosheet composites via in-situ ring-opening polymerization of macrocyclic oligomers', *Polymer*, **45(19)**, 6713–6718.
59. Chen G H, Wu D J, Weng W G, He B, Wu C L (2003), 'Exfoliation of graphite flake and its nanocomposites [14]', *Carbon,* 41, 619.
60. Chen G H, Wu D J, Weng W G, He B, Yan W L (2001), 'Preparation of polystyrene-graphite conducting nanocomposites via intercalation polymerization', *Polymer International*, **50**, 980–985.
61. Xia H S, Wang Q (2002), 'Ultrasonic irradiation: a novel approach to prepare conductive polyaniline/nanocrystalline titanium oxide composites', *Chem Mater*, **14**, 2158–2165.
62. Xiao M, Feng B, Gong K C (2002), 'Preparation and performance of shape stabilized phase change thermal storage materials with high thermal conductivity', *Energy Conversion and Management*, **43**, 103–108.
63. Bartlett N, McQuillan B W (1982), *Intercalation Chemistry* (Eds Whittingham M S and Jacobson A J), Academic, New York, Ch 2.
64. Viculis L M, Mack J J, Kaner R B (2003), 'A chemical route to carbon nanoscrolls', *Science*, **299**, 1361.
65. Nakajima T, Yoshiaki M (1994), 'Formation process and structure of graphite oxide', *Carbon*, **32**, 469–75.
66. Dekany I, Kruger-Grasser R, Weiss A (1998), 'Selective liquid sorption properties of hydrophobized graphite oxide nanostructures', *Colloid Polym Sci*, **76**, 570–576.
67. Lerf A, He H, Forster M, Klinowski J (1998), 'Structure of graphite oxide revisited', *J Phys Chem B*, **102**, 4477–4482.
68. Du X S, Xiao M, Meng Y Z (2004), 'Synthesis and characterization of polyaniline/graphite conducting nanocomposites', *J Polym Sci Part B Polym Phy*, **42**, 1972–1978.
69. He H, Riedl T, Lerf A, Klinowski J (1996), 'Solid-state NMR studies of the structure of graphite oxide', *J Phys Chem*, **100**, 19954–19958.
70. Patrick H N, Warr G G, Manne S, Aksay I A (1997), 'Self-assembly structures of nonionic surfactants at graphite/solution interfaces', Langmuir, **13**, 4349–4356.
71. Matsuo Y, Niwa T, Sugie Y (1999), 'Preparation and characterization of cationic surfactant-intercalated graphite oxide', *Carbon*, **37**, 897–901.
72. Matsuo Y, Tahara K, Sugie Y (1997), 'Structure and thermal properties of poly(ethylene oxide)-intercalated graphite oxide', *Carbon*, **35**, 113–120.
73. Matsuo Y, Tahara K, Sugie Y (1996), 'Synthesis of poly(ethylene oxide)-intercalated graphite oxide', *Carbon*, **34**, 672–674.
74. Matsuo Y, Hatase K, Sugie Y (1998), 'Preparation and characterization of poly(vinyl alcolol)-and $Cu(OH)_2$-poly(vinyl alcolol)-intercalated graphite oxides', *Chem Mater*, **10**, 2266–2269.
75. Xu J, Hu Y, Song L, Wang Q, Fan W (2001), 'Preparation and characterization of polyacrylamide-intercalated graphite oxide', *Mater Res Bull*, **36**, 1833–1836.
76. Liu P G, Xiao P, Xiao M, Gong K C (2000), 'Synthesis of poly(vinyl acetate)-intercalated graphite oxide by an in situ intercalative polymerization', *Chin J Polym Sci*, **18**, 413–418.

77. Hirata M, Gotou T, Horiuchi S, Fujiwara M, Ohba M (2004), 'Thin-film particles of graphite oxide 1: high-yield synthesis and flexibility of the particles', *Carbon*, **42**, 2929–2937.
78. Uhl F M, Wilkie C A (2002), 'Polystyrene/graphite nanocomposites: Effect on thermal stability', *Polym Degrad Stab*, **76**, 111.
79. Weng W G, Chen G H, Wu D J, Chen X F, Lu J R, Wang P P (2004), 'Fabrication and characterization of nylon 6/foliated graphite electrically conducting nanocomposite', *J Polym Sci Part B: Polym Phy*, **42**, 2844–2856.
80. Xiao M, Sun L, Liu J, Li Y, Gong K C (2002), 'Synthesis and properties of polystyrene/graphite nanocomposites', *Polymer*, **43**, 2245.
81. Beguin F, Setton R, Hamwi A (1979), 'The reversible intercalation of tetrahydrofuran in some graphite-alkali metal lamellar compounds', *Mater Sci Eng*, **40**, 167–173.
82. Tanaike O, Inagaki M (1997), 'Ternary intercalation compounds of carbon materials having low graphitization degree with alkali metals', *Carbon*, **35(6)**, 831–836.
83. Inagaki M, Tanaike O (1995), 'Host effect on the formation of sodium-tetrahydrofuran-graphite intercalation compound', *Synth Met*, **73**, 77–81.
84. Chen G H, Wu C L, Weng W G, Wu D J, Yan W L (2003), 'Preparation of polystyrene/graphite nanosheet composite', *Polymer*, **44**, 1781.
85. Weng W G, Chen G H, Wu D J, Wu C L (2004), 'Preparation and characterization of graphite nanosheets from ultrasonic powdering technique', *Carbon*, **42**, 753.
86. Yoda N, Miyake A (1960), 'Polymerization of 2-piperidone by alkali metal and certain acyl compounds', *J Polym Sci*, **43**, 117.
87. Mclachlan D S, Blaszkiewicz M, Newnham R E (1990), 'Electrical resistivity of composites', *J Am Ceram Soc*, **73**, 2187.
88. Stauffer D, Aharony A (1991), *Introduction to Percolation Theory*, Taylor & Francis: London.
89. Wu J, McLachlan D S (1997), 'Percolation exponents and thresholds obtained from the nearly ideal continuum percolation system graphite-boron nitride', *Phys Rev* B **56**, 1236.
90. Kang S, Chung D (2003), 'Improvement of frictional properties and abrasive wear resistance of nylon/graphite composite by oil impregnation', *Wear*, **254**, 103.
91. Pinto G, Gonzalez C L, Martin A (1999), 'Polymer composites prepared by compression molding of a mixture of carbon black and nylon 6 powder', *Polymer Composites*, **20**, 804.
92. Helsing J, Helte A (1991), 'Effective conductivity of aggregates of anisotropic grains', *J Appl Phys*, **69**, 3583.
93. Song L N, Du X S, Xiao M, Meng Y Z (2005), 'Short carbon fiber reinforced aromatic polydisulfide derived from cyclic(4,4′-oxybisbenzene) via ring-opening polymerization', *Polymers for Advanced Technologies*, **16(4)**, 323–327.
94. Liang Z A, Meng Y Z, Li L, Hay A S (2004), 'Novel synthesis of macrocyclic aromatic disulfide oligomers by cyclo-depolymerization of aromatic disulfide polymers', *Macromolecules*, **37(16)**, 5837–5840.
95. Meng Y Z, Tjong S C, Hay A S (2001) 'Synthesis of cocyclic(arylene disulfide) oligomers and their adhesion properties as heating-melt adhesive', *Polymer*, **42(12)**, 5215–5224.
96. Chen K, Liang Z A, Meng Y Z, Hay A S (2004), 'Ring opening polymerization of

macrocyclic(aromatic disulfide) oligomers derived from 4,4′-oxybis(benzenethiol)', *Polymer*, **45(6)**, 1787–1795.
97. Okamoto M, Mirita S, Taguchi H, Kim H J, Kotaka T, and Tateyama H (2000), 'Synthesis and structure of smectic clay/poly(methyl methacrylate) and clay/polystyrene nanocomposites via in situ intercalative polymerization', *Polymer*, **41**, 3887.
98. Pu X and Qutubuddin S (2001), 'Polymerclay nanocomposites: exfoliation of organophilic montmorillonite nanolayers in polystyrene', *Polymer*, **42**, 807.
99. Park C I, Park O O, Lim J G, and Kim H J (2001), 'The fabrication of syndiotactic polystyrene/organophilic clay nanocomposites and their properties', *Polymer*, **42**, 7465.
100. Liu P G, Gong K C, Xiao P, and Xiao M (2000), 'Preparation and characterization of poly(vinyl acetate)-intercalated graphite oxide nanocomposite', *J Mater Chem*, **10**, 933.
101. Du X S, Xiao M, Meng Y Z (2004), 'Facial synthesis of highly conductive polyaniline/graphite conductive nanocomposite', *European Polymer J*, **40(7)**, 1489–1493.
102. Wang W P, Pan C Y (2004), 'Preparation and characterization of poly(methyl methacrylate)-intercalated graphite oxide/poly(methyl methacrylate) nanocomposite', *Polym Eng Sci,* **44(12)**, 2335.
103. Krishnamoorti R, Vaia R A, Giannelis E P (1996), 'Structure and dynamics of polymer-layered silicate nanocomposites', *Chem Mater*, **8**, 1728–1734.
104. Cho J W, Paul D R (2001), 'Nylon 6 nanocomposites by melt compounding', *Polymer*, **42**, 1083–1094.
105. Tjong S C, Meng Y Z, Hay A S (2002), 'Novel preparation and properties of polypropylene-vermiculite nanocomposites', *Chemistry of Materials*, **14**, 44–51.
106. Fawn M U, Yao Q, Hiroyoshi N, Manias E, Wilkie C A (2005), 'Expandable graphite/polyamide 6 nanocomposites', *Polymer Degradation and Stability*, **89**, 70–84.
107. Gopakumar T G, Pagé D J Y S (2004), 'Polypropylene/graphite nanocomposites by thermo-kinetic mixing', *Polym Eng Sci*, **44**, 1162–1169.
108. Vaia R A, Giannelis E P (1997), 'Lattice of polymer melt intercalation in organically-modified layered silicates', *Macromolecules*, **30**, 7990–7999.
109. Chen X M, Chen J W, Huang W Y (2002), 'Novel electrically conductive polypropylene/graphite nanocomposites', *Mater Sci Lett*, **21**, 213.
110. Zheng W, Wong S C, Sue H J (2002), 'Transport behavior of PMMA/expanded graphite nanocomposites', *Polymer*, **73**, 6767.
111. Zheng W, Wong S C (2003), 'Electrical conductivity and dielectric properties of PMMA/expanded graphite composites', *Compos Sci Technol*, **63**, 225.
112. Mack J J, Viculis L M, Ali A, Luoh R, Yang G L, Hahn H T, Ko F K, Kaner R B (2005), 'Graphite nanoplatelet reinforcement of electrospun polyacrylonitrile nanofibers', *Adv. Mater*, **17**, 77–78.
113. J Y Xu, Y Hu, L Song, Q G Wang, W C Fan, G X Liao, Z Y Chen (2001), 'Thermal analysis of poly(vinyl alcohol)/graphite oxide intercalated composites', *Polym. Degrad. Stab*, **73**, 29.
114. J Y Xu, Y Hu, L Song, Q G Wang, W C Fan (2002), 'Structure of poly(acrylic acid)-intercalated graphite oxide', *Carbon*, **40**, 2964.
115. Xu J Y, Hu Y, Song L, Wang Q A, Fan W C, Chen Z Y (2002), 'Preparation and

characterization of poly(vinyl acohol)/graphite oxide nanocomposite', *Carbon*, **40**, 445–467.
116. Sichel E K (1982), *Carbon Black-polymer Composites*, New York, Marcel Dekker.
117. Ishigure Y, Iijima S, Ito H, Ota T, Unuma H, Takahashi M, Hikichi Y, Suzuki H (1999), 'Electrical and elastic properties of conductor-polymer composites', *J. Mater Sci*, **34**, 2979–85.
118. Flandin L, Bidan G, Brechet Y, Cavaille J Y (2000), 'New nanocomposite materials made of an insulating matrix and conducting fillers: processing and properties', *Polym Compos*, **21**, 165–174.
119. Ray S S, Biswas M (2000), 'Water-dispersible conducting nanocomposites of polyaniline and poly(N-vinylcarbazole) with nanodimensional zirconium dioxide', *Synth Met*, **108**, 231–236.
120. Quivy A, Deltour R, Jansen A G M, Wyder P (1989), 'Transport phenomena in polyer-graphite composite materials', *Phys Rev B*, **39**, 1026–1029.
121. Chen G H, Wu D J, Weng W G, Yan W L (2001), 'Preparation of polymer/graphite conducting nanocomposite by intercalation polymerization', *J Appl Polym Sci*, **82**, 2506–2513.
122. Song L N, Xiao M, Li X H, Meng Y Z (2005), 'Short carbon fiber reinforced electrically conductive aromatic polydisulfide/expanded graphite nanocomposites', *Mater Chem Phy*, in press.
123. Zhang C, Yi X, Yui H, Asai S, Sumita M (1998), 'Morphology and electrical properties of short carbon fiber-filled polymer blends: high-density polyethylene/poly(methyl methacrylate)', *J Appl Polym Sci*, **69**, 1813.
124. Weber M, Kamal M R (1997), 'Microstructure and volume resistivity of composites of isotactic polypropylene reinforced with electrically conductive fibers', *Polym Compos* **18**, 711.
125. Lux F (1993), 'Models proposed to explain the electrical conductivity of mixtures made of conductive and insulating materials', *J Mater Sci*, **28**, 285.
126. Chae H K, Siberio-Perez D Y, Kim J, Go Y, Eddaoudi M, Matzger A J, O'Keeffe M, Yaghi O M (2004), 'A route to high surface area, porosity and inclusion of large molecules in crystals', *Nature*, **427**, 523.
127. Schadler L S, Giannaris S C, Ajayan P M (1998), 'Load transfer in carbon nanotube epoxy composites', *Appl Phys Lett*, **73**, 3842.

20

Wear resisting polymer nanocomposites: preparation and properties

M Q ZHANG and M Z RONG, Zhongshan University, People's Republic of China and K FRIEDRICH, Institute for Composite Materials (IVW), Germany

20.1 Introduction

Polymeric nanocomposites have been an area of intense industrial and academic research for the past 20 years. No matter the measure – articles, patents, or R&D funding – efforts in this aspect have been growing exponentially worldwide over the last ten years. The composites represent a radical alternative to conventional filled polymers or polymer blends – a staple of the modern plastics industry.[1] In contrast to conventional composites, where the reinforcement is in the order of microns, polymer nanocomposites are exemplified by discrete constituents on a nanometer scale. The value of polymer nanocomposites technology is not solely based on the mechanical enhancement of the neat resin nor the direct replacement of current filler or blend technology. Rather, its importance comes from providing value-added properties not present in the neat resin, without sacrificing the resin's inherent processability and mechanical properties, and without adding excessive weight.[2] Traditionally, blend or composite attempts at 'multifunctional' materials impose a trade-off between desired performance, mechanical properties, cost, and processability. However, over and over again, improved properties as compared to the pure polymers or conventional particulate composites are reported for polymer nanocomposites containing substantially less filler (typically 1–5 vol.%) and thus enabling greater retention of the inherent processability of the neat resin.[3]

Polymer and polymer composites are used increasingly often as engineering materials for technical applications in which tribological properties are of considerable importance. Fillers (e.g., glass, carbon, asbestos, oxides and textile fibers) are incorporated within many polymers to improve their tribological performance.[4] The reduction in wear is due mainly to preferential load support of the reinforcement components, by which the contribution of abrasive mechanisms to the wear of the materials is highly suppressed. Besides, the solid lubricant particles transfer fairly readily to a metal counterface, leading to the formation of a strengthened transfer film. Finally, some fillers are used to improve the poor thermal conductivity possessed by polymers, thereby facilitat-

ing dissipation of frictional heat. However, the composites filled with the micron particles usually need quite a large amount of filler to attain an evident improvement of wear resistance. Yamaguchi found that the wear rates of unsaturated polyesters and epoxy resins filled with different proportions of SiO_2 decreased significantly only at a high loading of 40 wt.%.[5] In this case, some inherent defects are inevitable. For example, disintegration of the fillers and detached particles were frequently observed to be torn out of both the phenolic and epoxy resin composites when an indentor moved over the systems, resulting in sharp fluctuations in the measured coefficient of friction.[6] Furthermore, the high loading of fillers is also detrimental to the processability of polymer, especially for the thermosetting polymer used as coating. Considering the disadvantages imparted by micro-fillers, utilization of nanoparticles or nanofibers would be an optimum alternative way.

Since the predominant feature of nano-sized building blocks lies in their ultra-fine dimension, a large fraction of the filler atoms can reside at the interface and lead to a strong interfacial interaction if the nano-fillers are well dispersed. As a result, the nanocomposites coupled with a great number of interfaces could be expected to provide unusual tribological performance. In comparison with the widely used micrometer particulates, nanoparticles are believed to have the following advantages:[7,8]

- the mechanical behavior of the bulk materials can be emulated while the abrasiveness of the hard microparticles decreases remarkably owing to a reduction in their angularity
- the transferred film can be strengthened as the nanoparticles would have the capability of interacting well with wear debris
- the material removal of nanocomposites would be much milder than that of conventional composites because the fillers have similar size as the segments of the surrounding polymer chains.

The effectiveness of replacement of microcomposites with nanocomposites has been verified in many laboratories. Rong *et al.* compared the effects of micro-TiO_2 (44 μm) and nano-TiO_2 (10 nm) particles on the wear resistance of epoxy.[8] Their results indicate that the TiO_2 nanoparticles can remarkably reduce the wear rate of epoxy, while the micron-TiO_2 particles cannot. A similar conclusion was made by Ng *et al.* in an earlier report.[9] In the work by Yu and co-workers,[10] who studied the tribological behavior of micrometer copper particle- and nanometer copper particle-filled polyoxymethylene (POM) composites, the wear of micro-Cu/POM is characterized by scuffing and adhesion, while that of nano-Cu/POM by plastic deformation and hence decreased wear loss. Xue and Wang found that nanometer SiC is able to lower the wear of polyetheretherketone (PEEK) more greatly than micron SiC.[11] A thin, uniform and tenacious transfer film was formed on the counterpart surface in the case of carbon steel ring/nano-SiC filled composite block.

Because nano-sized fillers can bring special functionality to polymers, not available in microcomposites, nanocomposites have become an important member in the family of wear resisting and friction reducing materials. It is a topic having both theoretical and practical significance. As a qualified candidate for tribological application, polymer nanocomposites must simultaneously balance four interdependent areas: constituent selection, cost-effective processing, fabrication, and performance. A complete understanding of these areas and their interdependencies is still in its infancy, and ultimately many perspectives will develop, dictated by the final application of the specific composite materials. This chapter is focused on the state of the art in the area of wear resistant nanocomposites consisting of inorganic nano-sized fillers and (thermoplastic and thermosetting) polymers, with particular interests in the filler surface pre-treatment technique and its effect on the tribological performance improvement.

20.2 Surface treatment

It is well-known that the tiny particles are easy to agglomerate due to their large specific surface area. Moreover, the hydrophilic nanoparticles and the hydrophobic polymer are not compatible in nature. Consequently, the so-called nanocomposites sometimes contain a number of loosened clusters of nano-fillers, where the polymer binder is impoverished. This may make properties of nanoparticle-filled composites even worse than conventional microcomposites. Extensive material loss would thus occur due to disintegration and crumbling of the particle agglomerates under tribological conditions.[12] It is therefore necessary to break down these nanoparticle agglomerates in order to produce nanostructured composites. In this context, control and/or manipulation of surface properties of nano-fillers are critical, which can be achieved by coating the individual fillers with a second modifier or a polymer layer.

In general, surface modification of inorganic fillers can be carried out by utilizing physical or chemical interactions between the fillers and the modifiers. The resultant bonding is often a mixture of secondary and chemical bonds.[13] There is no evident difference between the treatments of micro-particles and nanoparticles, except that it is quite difficult for the surface modifiers to penetrate into the tightly bonded nanoparticle agglomerates, especially in the case of physical treatments such as surfactant treatment and polymer encapsulation.

20.2.1 Physical methods

Physical treatment (through covering the filler with a low molecular weight surfactant or a high molecular weight polymer) usually results in secondary forces (like van der Waals, hydrogen and electrostatic forces) between the

particles and modifier. A surfactant contains one or more polar groups and a long aliphatic chain. The principle of surfactant treatment is the preferential adsorption of the polar group of the surfactant onto the high energy surface of the fillers by electrostatic interaction. Ionic bonds can also be formed under certain circumstances. A typical example can be cited regarding the surface treatment of $CaCO_3$ with stearic acid,[14] which is necessary when producing nano-$CaCO_3$. Stearic acid or its ammonium salt can be added directly during the precipitation step of $CaCO_3$. It is proved that ionic bonds were established between the surfactant molecules and the filler surface. Hence a reduced surface energy resulted from the shield made of C18 alkyl chains on the filler surface. Alkyl dihydrogenphosphate, containing functional groups such as olefine, chloro, methacryloxy and mercapto, is another kind of effective surface modifiers for calcium carbonate fillers.[15] It was shown that alkyl dihydrogenphosphate molecules can react with $CaCO_3$ resulting in a dibasic calcium salt of phosphate. The products are deposited on $CaCO_3$ and provide the surface of $CaCO_3$ with a certain hydrophobicity, as evinced by the good dispersibility in mineral oil.[16] Relatively larger groups in the phosphates (like octyl dihydrogenphosphate, 3,7-dimethyl-6-octenyl dihydrogenphosphate, etc.) help to enhance the conversion of the agent due to a lower hydrophilicity. Besides, a treatment with alkyl dihydrogenphosphates always results in an increase in the surface area of the treated particles. This can be ascribed to the surface erosion and/or to the calcium salt formation.

Another technique of physical treatment lies in encapsulating inorganic fine particles with preformed polymers or in-situ formed polymers. In the former case, a macromolecular dispersant, hyperdispersant, has been successfully used.[17] Similar to surfactants, polymeric dispersants consist of two major components. One is a functional group, like –OH, $–NH_2$, $–NR^{3+}$, –COOH, $–COO^-$, $–SO_3H$, $–SO^{3-}$ and $–PO_4^{2-}$, which helps anchoring of the dispersants to the particles surface through hydroxyl and electrostatic bonds. The other is a solvable macromolecular chain, like polyolefine, polyester, polyacrylate and polyether, which is appropriate to be dispersed in different media of low to high polarity. Compared to traditional surfactants, hyperdispersants have the following advantages:

- they are anchored to the particles' surface more strongly than surfactants, and hence can hardly be desorbed
- the long polymeric chains can prevent the re-agglomeration of the particles more effectively
- their specific molecular structures characterized by an A-B or B-A-B block copolymer type, ensure the efficiency of particle isolation and avoid bridging between particles through an identical solvable chain.

When treating nanoparticles, however, it should be noted that hyperdispersants can only encapsulate nanoparticle agglomerates and can hardly diffuse into the agglomerates due to their long molecular feature.

Relatively, encapsulation with in-situ formed polymers may result in more uniform coverage. In the presence of nanoparticles, the polymer can be formed by either solution or emulsion polymerization. Yoshinaga and co-workers utilized radical polymerization of vinyl monomers to produce SiO_2/polymer composites.[18] Since the surface of silica colloid particles possesses negative charges on the electric double layer, the initiator 2,2′-azobis (2-amidinopropane) dihydrochloride can be concentrated and resulted in free radicals on the silica surface. It was found that the solvent used during solution polymerization is an important factor influencing the percentage of the attached polymer. A solvent with lower miscibility to the polymer should facilitate the attachment of the macromolecular chains to the particles. Du *et al.*[19] demonstrated that when a seed emulsion polymerization was carried out in the presence of nanoparticles, a core-shell structure can be obtained, in which the inorganic particles stayed in the middle layer while the polymer was located at the inner and outer layers. For the system containing Fe_2O_3 nanoparticles (3–5 nm) and styrene/acrylic acid/butyl acrylate (St/AA/BA) latex particles, for example, the size of the resultant composite microspheres is 80 nm.

Nanoparticles covered by a polymer layer can also be obtained during the manufacture of nanoparticles. For instance, nanocrystalline titania coated with poly(methacrylic acid) (PMAA) was prepared by microwave-induced plasma.[20] Such an in-situ treatment is characterized by high effectiveness and homogeneity. Transmission electron microscopy (TEM) observation showed that the titania particles were 10–25 nm in diameter, with a 7 nm thick PMAA layer.

20.2.2 Chemical methods

In comparison with the physical methods, the effect of surface modification based on chemical interaction is more significant, as the latter provides stronger interaction between modifiers and nanoparticles. Besides, a fine adjustment of interfacial interaction in the composites with chemically pretreated nanoparticles can be completed by introducing modifiers containing reactive groups onto nanoparticles, which helps to construct chemical bonding between the fillers and the matrix.

Among the available chemical methods, coupling agent treatment is the most popular and the easiest to be applied. A variety of coupling agents, such as silane, titanate, zirconate, etc., has been used to improve the adhesion between inorganic fillers and organic matrices. Extensive information on reaction mechanisms and effects of coupling agents is available for micro-fillers, but fewer for nanoparticles. It is clear that in the case of trifunctional silane, a three-dimensional siloxane multilayer forms on the solid surface, which remains even after an extensive washing in boiling water.[21] However, only a portion of the functional groups in grafted silanes can interact with the particle surface or with

other functional groups of the reactant due to a relatively low concentration of surface hydroxyls (1–2 OH/nm^2). As a result, a fraction of functional groups remains, and these residual groups can influence the properties of both the covering material and the polymer matrix. The whole process is dependent on the synthesis and treatment conditions.

Gunko *et al*.[22] studied the features of fumed silica coverage with silanes from both experimental and theoretical aspects. It was found that a modification by means of methacryloyloxymethylenemethyl diethoxysilane (MMDES), 3-methacryloyloxypropyltrimethoxysilane (MAPTMS) and 3-aminopropyltriethoxysilane (APTES) strongly changed the ξ(pH) potential. The quantity and the structure of the modifiers controlled the particle size distribution in an aqueous suspension. MMDES gave better results in comparison to its mixture with APTES or to pure MAPTMS, when considering the reduction in particle (agglomerate) size of modified silica at a modifier concentration of over 0.05–0.2 mmol/g. Depending on the pretreatment conditions, the attached silanes can reduce the hydrophilic properties of silica to different extents.

Grafting macromolecules onto inorganic particles has some advantages over the modification by low molecular surfactants or coupling agents. The polymer-grafted particles can possess desired properties through a proper selection of the species of the grafting monomers and the grafting conditions, so that the interfacial characteristics between the treated nanoparticles and the matrix can be tailored when manufacturing nanocomposites. Besides, the fragile nanoparticle agglomerates become stronger because they turn into a nanocomposite microstructure comprising the nanoparticles and the grafted, homopolymerized polymer. A series of works has been done in this field of growing interest for purposes of improving the dispersibility of the nanoparticles in solvents and their compatibility with polymers. Mostly, the grafting polymerization was conducted via two routes:

1. monomers are polymerized from active compounds (initiators or comonomers) covalently attached to the inorganic surface, and
2. ready-made polymers with reactive end-groups react with the functional groups on the particles. The latter benefits the control of the molecular weight of the grafting polymer.

So far, many grafting techniques, such as chemical grafting, irradiation grafting and mechanical grafting, have been applied to modify nanoparticles. Besides, various kinds of initiation or polymerization processes, including radical, anionic and cationic polymerizations, were also undertaken in the grafting investigations. Here, only a few examples will be presented to illuminate grafting procedure.

Espiard and Guyot[23] studied grafting onto silica nanoparticles using radical processes in an emulsion. The particle surface was first covered with silane coupling agent containing a polymerizable group, i.e. methacryloxypropyltrimethoxysilane (MPTMS). Then the modified silica was engaged in the emulsion polymerization of ethyl acrylate. It was proved that a part of the

polymer could be covalently grafted onto the nano-silica only if the latter has been functionalized. Tsubokawa and co-workers systematically investigated the grafting of various polymers onto ultrafine silica and carbon black by polymerization starting from the initiating groups previously introduced onto the surfaces.[24–29] They have conducted anionic, cationic and radical graft polymerization of various monomers initiated by potassium carboxylate, acylium or benzylium perchlorate, and peroxyester or azo groups already introduced onto ultrafine silica, respectively.

Graft polymerization onto nanoparticles can also be realized by γ-irradiation, which is superior to chemical graft process in improving graft homogeneity, controlling pollution and simplifying procedure. Under the high energy radiation, the surfaces of the nanoparticles outside and inside the agglomerates are equally activated. Therefore, the low molecular weight monomers are allowed to react with the activated sites of the nanoparticles throughout the agglomerates.[12] The interstitial volume inside the nanoparticle agglomerates will be partly filled with grafting macromolecular chains, and the agglomerated nanoparticles will be separated further (Figs 20.1 and 20.2).

Fukano and Kageyama published a series of works on irradiation-induced graft polymerization of styrene and methyl methacrylate absorbed on several kinds of nanoparticles, including silica gel, white carbon, zeolite and activated alumina.[31–38] They found that the amount of grafted polymer varies with the type of the inorganic substrate, with the maximum of about 30%. In the case of substrates that are chemically identical, the amount of the grafted polymer is proportional to the surface area of the particles. In the case of substrates having the same surface area, inorganic substances that contain aluminum as a component element are grafted more easily than those consisting of SiO_2 alone.

To increase the degree of grafting, Fukano and Kageyama conducted the polymerization under high vacuum ($<10^{-4}$ Hg). Actually, this is less convenient for industrial application. Therefore, Rong *et al.* developed another method in which the strict irradiation grafting conditions usually required in the case of

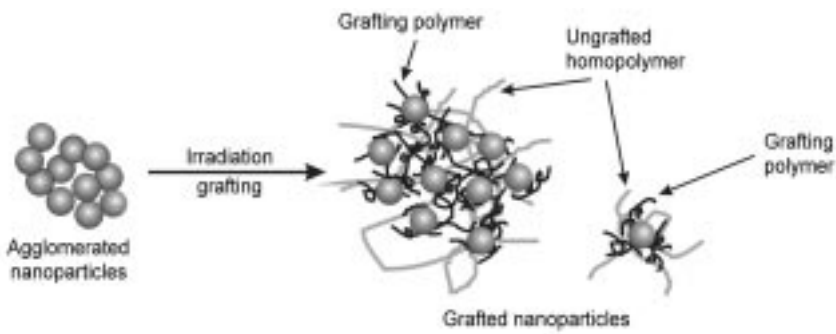

20.1 Schematic drawing of the possible structures of nanoparticle agglomerates before and after graft polymerization treatment.

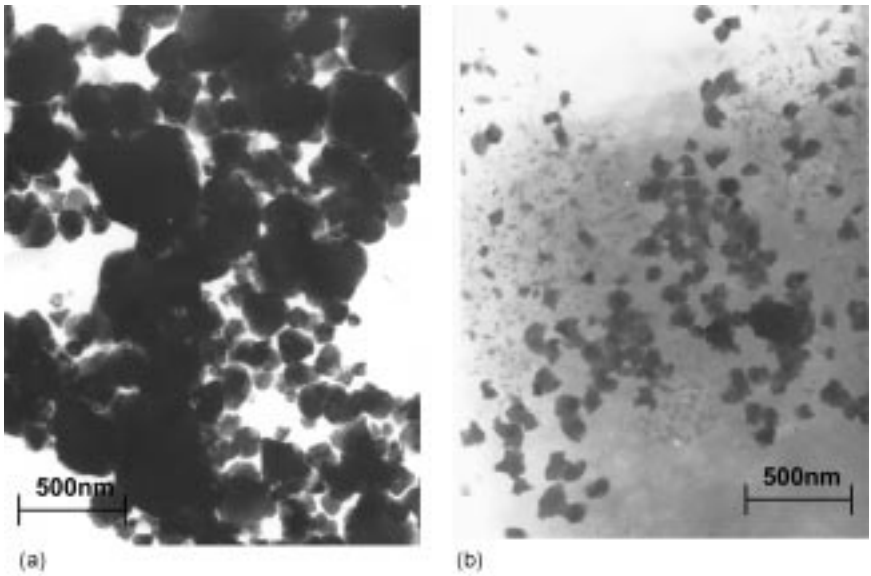

20.2 TEM photos of (a) untreated nano-SiC and (b) polyglycidyl methacrylate (PGMA) grafted nano-SiC[30] (reprinted from *J. Polym. Sci. Polym. Chem.*, vol. 42, Y. Luo *et al.*, Surface grafting onto SiC nanoparticles with glycidyl methacrylate in emulsion, p. 3842, 2004, with permission from John Wiley & Sons, Inc.).

conventional particles, such as high vacuum and purification of monomers, are no longer necessary.[39] The key issue might be the removal of the absorbed water before irradiation. Various polymers were grafted on the surface of silica nanoparticles by this method (Table 20.1). The molecular weights (M_n and M_w)

Table 20.1 Grafting details of nano-SiO_2 grafted with different polymers (irradiation dose = 10 Mrad; weight ratio of monomer/SiO_2 = 20/100; all the systems used acetone as solvent when they were irradiated, except for methyl acrylic acid/SiO_2 system with ethanol as solvent).[39] (Reprinted from *Polymer*, vol. 42, M. Z. Rong *et al.*, Structure-property relationships of irradiation grafted nano-inorganic particle filled polypropylene composites, p. 167, 2001, with permission from Elsevier)

Grafting polymers	PS[a]	PBA[b]	PVA[c]	PEA[d]	PMMA[e]	PMA[f]
Percent grafting[g] (%)	3.64	3.32	2.82	1.73	1.85	2.16
Homopolymer fraction[h] (%)	16.3	15.4	13.7	12.3	15.5	15.4

[a] PS = polystyrene
[b] PBA = polybutyl acrylate
[c] PVA = polyvinyl acetate
[d] PEA = polyethyl acrylate
[e] PMMA = polymethyl methacrylate
[f] PMA = polymethyl acrylate
[g] Percent grafting = weight of grafting polymer/weight of SiO_2
[h] Homopolymer fraction = weight of homopolymer/weight of SiO_2.

Table 20.2 Molecular weights and their distributions of grafting PS and homopolymerized PS in the system of nano-SiO_2 grafted with PS (irradiation dose = 10 Mrad).[39] (Reprinted from *Polymer*, vol. 42, M. Z. Rong *et al.*, Structure-property relationships of irradiation grafted nano-inorganic particle filled polypropylene composites, p. 167, 2001, with permission from Elsevier)

Irradiation conditions	Materials	M_w ($\times 10^4$)	M_n ($\times 10^4$)	M_w/M_n
Without solvent	Grafting PS	3.5	1.7	2.1
	Homopolymerized PS	7.3	4.3	1.7
With solvent	Grafting PS	5.3	2.2	2.4
	Homopolymerized PS	2.1	6.3	3.3

of both the grafted and the homopolymerized polystyrene obtained by irradiation are shown in Table 20.2. The higher M_n of the homopolymer, relative to the grafted polymer, could be ascribed to the stronger motional ability of nanoparticles compared to conventional particles, which made the chain termination between the two radicals easier. They also found that different silica nanoparticles exhibit different reactivities under irradiation. Precipitated nano-silica performs better than fumed nano-silica.[40,41] Another interesting result is that some metallic nanoparticles (i.e. iron, nickel and cobalt) can be grafted with polymers under irradiation even though these particles contain few hydroxyl groups.[42] It means that either the surface hydroxyl groups or the structural defects are capable of acting as the reactive sites. Nevertheless, the double bonds introduced to the surface of particles by silane are helpful for yielding higher grafting percentage.[43]

20.3 Composites manufacturing

20.3.1 Thermoplastics

By examining the documented processing methods for making wear resistant polymer nanocomposites, it is known that the widely used compounding techniques for preparation of conventionally filled polymers (characterized by a direct mixing of the components) are still playing the leading role. They can be classified as melt mixing, solution mixing, suspension mixing, polymerization filling, etc.

Melt mixing is most commonly used in thermoplastics-based composites. Hé blended the powdered ultra high molecular weight polyethylene (UHMWPE, 50 μm) with Al_2O_3 nanoparticles (20–30 nm), followed by hot compression molding.[44] Such a simple technique has been employed by other groups to produce their nanocomposites specimens, like nano-Al_2O_3 (33 nm)/polyphenylene sulfide (PPS, <150 μm)[7] and nano-Cu (10 nm)/POM (1.9 mm).[10] Sawyer *et al.* mixed PTFE powder (20 μm) with Al_2O_3 nanoparticles (38 nm)

through a jet mill.[45] The jet mill apparatus was not used to mill or reduce the size of any of the constituents; rather, it was used to break apart agglomeration of the individual constituents. Bhimaraj *et al.* also used a batch melt mixer for melt mixing poly(ethylene terephthalate) (PET) pellets with Al_2O_3 nanoparticles (38 nm) at 260ºC under an inert atmosphere.[46]

For improving the phase homogenization prior to hot pressing, some researchers prepared suspensions containing nanoparticles firstly. The typical procedures have been described in a series of works on PEEK composites by Xue *et al*.[11,47–54] That is, the polymer powder (100 μm) was fully mixed with the nanoparticles (SiC (<100 nm), ZrO_2 (10 nm), Si_3N_4 ($\leq$50 nm) and SiO_2 ($\leq$100 nm)) in alcohol by ultrasonic agitation for about 15min. Then the mixture was dried at 110ºC to get rid of the alcohol and moisture. Finally, the composites sheets were molded by compression at 340ºC. Comparatively, this method was accepted more widely than the former one based on dry mixing. For example, SiO_2 (20nm)/polyphthalazine ether sulfone ketone (PPESK, 40 μm),[55] TiO_2 (40 nm)/PPESK (40 μm),[56] carbon nanotube (diameter = 20–30 nm, length – several micra)/PTFE (20–100 μm),[57] ZnO (50 nm)/polytetrafluoroethylene (PTFE, 20–100 μm),[58] Al_2O_3 (60–70 nm)/polyamide 1010 (PA1010, <175 μm)[59] and Fe_2O_3 (40–50 nm)/PA1010 (<175 μm)[59] were all prepared similarly, except that the solvent of the suspension was changed from alcohol to acetone.

Surface pre-treatment of the nano-fillers before melt mixing was done in a few labs. Lai and co-workers[60] put the attapulgite powder (width = 10–25 nm) into hydrochloric acid solution for 4 h under reflux. The treated precipitates were collected and washed to pH = 7.0 by deionized water, finally the treated attapulgite was ground into less than 75 nm after drying at 105ºC in vacuum. Eventually, the treated attapulgite particles were mechanically mixed with PTFE powder, and molded into blocks by compression molding under a pressure of 50 MPa for 5min. Ge *et al.* added the surfactant triethanolamine into the suspension consisting of nylon powder, acetone and TiO_2 or SiO_2 nanoparticles.[61] The microstructural observation indicated that the nanocomposites exhibit relatively uniform distribution of the fillers at the content of 20 wt.%.

When preparing thermoplastic nanocomposites coating, solution mixing has to be the main measure. The development of low friction carbon nanofiber reinforced polymeric composite coatings on alumina/aluminum substrates by Chen *et al.* can be cited here as an example.[62] They prepared the nanofiber (diameters = 100–250 nm)/polymer (poly(arylene ether phosphine oxide)), or polycarbonate (PC) or PMMA solution using chloroform as the solvent at room temperature. The solution mixture was continuously stirred for 1 h, and then subjected to an ultrasonic bath mixing until the liquid system became a fine dispersion of dark solution. Nanofiber/polymer thin film was spin-coated by placing the solution mixture onto a substrate that was then spun at 1000 rpm. After solvent evaporation, a thin film was obtained on the substrate. A similar route can also be seen in making nano-Ni (50 nm)/polyurethane (PU) composite

coating.[63] The work by Lee and Lim[64] is an exception; they dispersed nano-diamonds (5–10 nm) in distilled water and then mixed the fillers with PTFE suspension. The slurry of PTFE with nano-diamonds was sprayed on aluminum substrate.

To overcome the limitations of conventional techniques for polymer nanocomposites manufacturing, such as the use of high working temperature for melt mixing and solvents for solution mixing, thermal spray seems to be a viable solution.[65,66] During a thermal spray process, materials, in powder, wire or rod form, are heated, accelerated and propelled by a high temperature jet through a confining nozzle towards a surface. The individual molten or softened droplets impact, spread, cool and solidify to form continuous coatings. Materials heating, quenching, consolidation and post-treatment are thus combined in a single step. The important benefits of using a thermal spray process for making polymer nanocomposites include:

- powdered polymers are heated only to a temperature at which the particles are viscous enough to spread due to the high kinetic energy
- good dispersion of nanoparticles is achieved by the high velocity
- processing without use of a volatile solvent.

Accordingly, Schadler *et al.* employed a high-velocity oxy-fuel (HVOF) system to thermally spray SiO_2 (7 and 12 nm)/nylon 11 nanocomposite coatings.[65,67,68]

Polymerization filling (i.e. monomers polymerized in the presence of fillers) is an effective approach to ensure intimate contact between the fillers and the matrix. Cai *et al.* synthesized carbon nanotube/polyimide (PI),[69] nano-Al_2O_3/PI[70] and nano-SiO_2/PI[71] composites in this way. The poly(amic acid) solution (PAA) was obtained by adding an equimolar amount of diphenylether-3,3′,4,4′-tetracarboxylic dianhydride to a solution of 4,4′-oxydianiline/N-methyl-2-pyrrolidone (NMP). The homogeneous suspensions of nano-fillers/NMP with different filler proportions were added into PAA solution under vigorous agitating. The homogeneous suspension of nano-filler/PAA/NMP was precipitated by introduction of triethylamine and pyridine. After drying to allow thermal imidization, nano-filler/PI powders were hot compressed into specimens. For producing abrasion resistant nanocomposites, Avella *et al.* prepared stearic acid pre-treated $CaCO_3$ (40 nm)/PMMA systems by in-situ polymerization using free-radical initiator dicumyl peroxide (DCP).[72]

20.3.2 Thermosets

Besides thermoplastic nanocomposites, polymerization filling was also used in preparing thermosetting composites. Che *et al.* added nanoparticles (TiO_2, Al_2O_3, SiO_2) into the reaction systems in which phenolic resin was being synthesized.[73] As the particles changed the crosslinking microstructure, the nanocomposites were greatly toughened. On the other hand, solution mixing

plays the dominant role in producing epoxy and bismaleimide-based nanocomposites.[74]

In the case of epoxy-based nanocomposites, the authors of the current chapter proposed the following manufacturing approaches.[12,75–81] The mechanically mixed nanoparticles/epoxy blends were heated to 130ºC and the curing agent 4, 4′-diamino-diphenylsulfone (DDS) was added with stirring for 10 min. Finally, the mixture was filled into a mold and placed in vacuum for 50 min to get rid of air bubbles. For curing the composites, the procedures listed below were followed step by step: 3 h at 100ºC, 2 h at 140ºC, 2 h at 180ºC and 2 h at 200ºC. To uniformly disperse nanoparticles into liquid epoxy resin, utilization of certain intense mixing apparatus, like ultrasonicator or stirring under vacuum, proved to be beneficial.

Additionally, the curing kinetics of epoxy nanocomposites was carefully characterized. It is generally agreed that the reaction mechanism for the addition of amine to epoxy takes into account the phenomenon of catalysis by hydrogen bond donors. The mechanism of this catalytic effect is via hydrogen bonding of the hydroxyl group to the oxygen of the glycidyl ether in the transition state. Therefore, as hydrogen bond donors (hydroxyl groups exist on the surface of particles), inorganic nanoparticles should promote the curing reaction of epoxy resin. This was demonstrated by the differential scanning calorimetry (DSC) measurement for nano-Al_2O_3/epoxy and nano-Si_3N_4/epoxy systems. At a given heating rate, the peak exothermic temperatures of nano-Al_2O_3/epoxy and nano-Si_3N_4/epoxy systems shift towards low temperature regime as filler loading is raised (Figs 20.3(a) and (b)). However, the opposite phenomena were observed for nano-SiC/epoxy system, offering some insight into the special reaction mechanism for the nanoparticles/epoxy blend.

To quantify the above effects, the Kissinger equation,[82] Crane equation[83] and Arrhenius equation are used to analyze reactive kinetics, and the corresponding results are listed in Table 20.3. The activation energy of curing reaction of nano-Al_2O_3/epoxy decreases with increasing filler content and the rate constant is greatly increased. Nano-Si_3N_4 composites also exhibit similar dependence, but not as significant as the former system. These coincide with the results illustrated in Fig. 20.3. For nano-SiC/epoxy composites, however, the changes in both E and K are marginal and the value of E becomes higher at higher filler loading. Clearly, nano-Al_2O_3 and nano-Si_3N_4 accelerate the curing of epoxy, while nano-SiC decelerates the reaction.

Basically, due to the strong interaction between the nanoparticles and the epoxy resin resulting from the specific surface feature of nanoparticles, the curing reaction kinetics of the nanocomposites might be different from neat epoxy resin. The above-observed accelerating effect results from the hydroxyl groups on the nanoparticles' surfaces (donors of hydrogen bonding). The more the surface hydroxyl groups, the higher the activity of the particles. Since nano-Al_2O_3 particles possess a much higher amount of hydroxyl groups than nano-

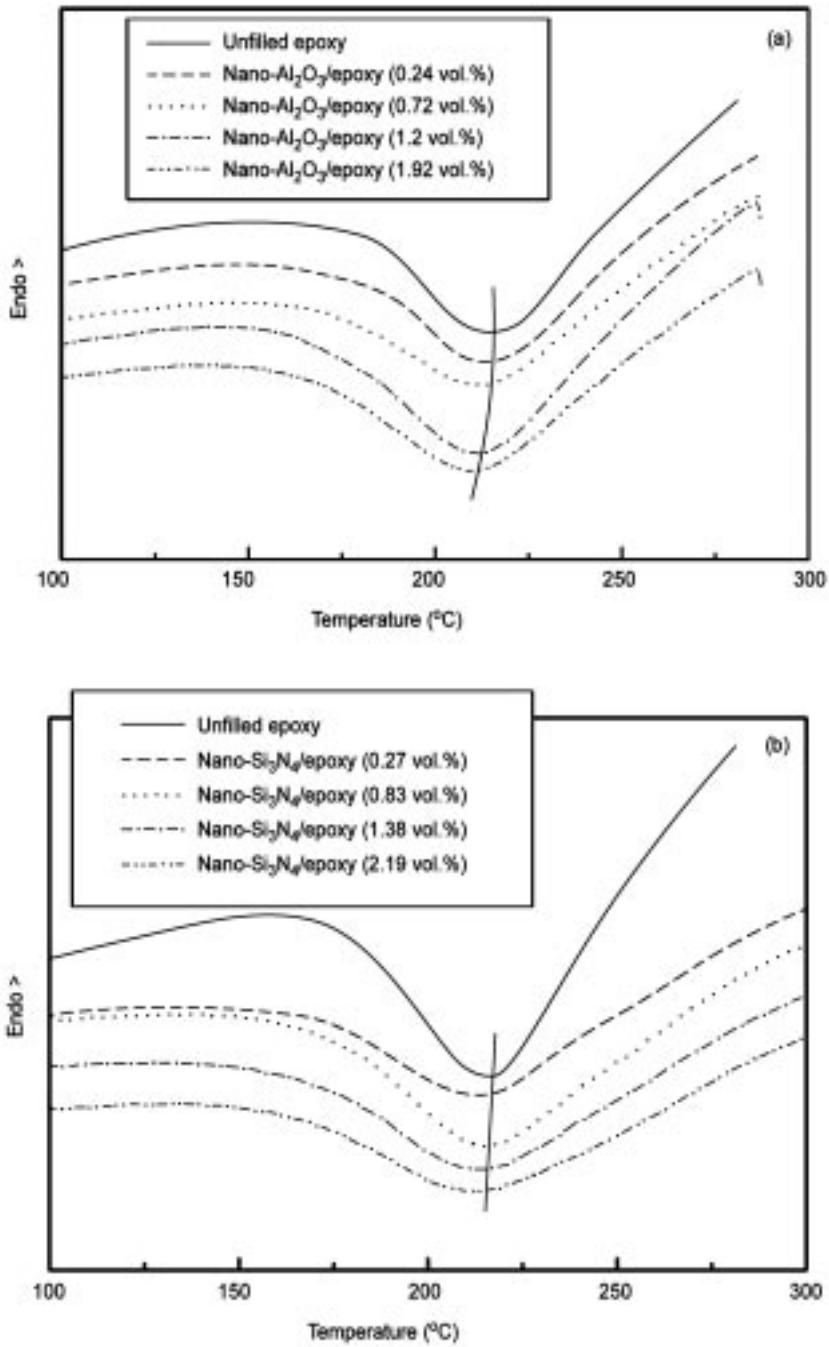

20.3 DSC scans of nonisothermal curing processes of (a) nano-Al_2O_3/epoxy, (b) nano-Si_3N_4/epoxy, and (c) nano-SiC/epoxy composites at a heating rate of 7.5°C/min.

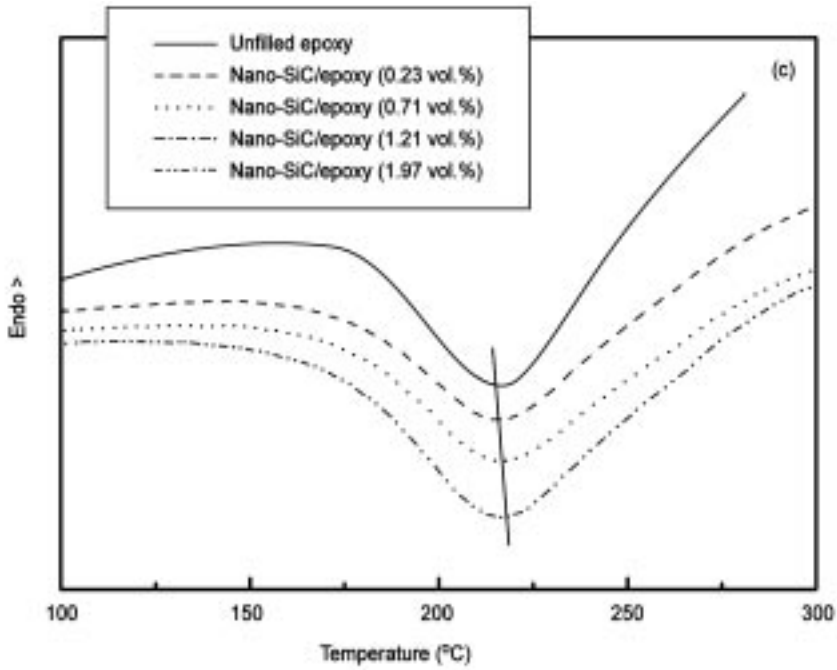

20.3 Continued

Table 20.3 Activation energy, *E*, pre-exponential factor, *A*, reaction order, *n*, and rate constant, *K*, of curing reaction of different nanoparticles/epoxy composites

Composites	Nanoparticles (vol.%)	*E* (kJ/mol)	*n*	*K* (s^{-1})
Epoxy	0	62.1	0.89	7.0×10^{-4}
Nano-Al_2O_3/epoxy	0.24	62.4	0.93	8.5×10^{-4}
	0.72	67.9	0.93	5.0×10^{-2}
	1.20	58.8	0.91	6.3×10^{-2}
	1.92	53.8	0.90	5.1×10^{-2}
Nano-Si_3N_4/epoxy	0.27	67.1	0.91	4.4×10^{-3}
	0.83	65.0	0.90	2.0×10^{-3}
	1.38	57.7	0.88	2.1×10^{-3}
	2.19	50.7	0.93	2.1×10^{-3}
Nano-SiC/epoxy	0.23	55.6	0.89	8.0×10^{-4}
	0.71	65.0	0.90	7.1×10^{-4}
	1.21	57.8	0.89	7.4×10^{-4}
	1.97	68.0	0.91	6.6×10^{-4}

* *K* represents the rate constant of curing at 180°C.

SiC,[40,42] it is reasonable to understand the evident acceleration perceived in the nano-Al_2O_3/epoxy system. On the other hand, the incorporation of the nanoparticles must raise the viscosity of the composite system (before curing) and/or the strong interaction between the nanoparticles and the matrix polymer would hinder the molecular motion of epoxy, which disfavors the curing of epoxy. Therefore, the effect exerted by the nanoparticles is a competition between the two opposite factors. In the case of nano-Al_2O_3 and nano-Si_3N_4 particles, the effect of acceleration is measured because of the higher amount of their surface hydroxyl groups. For nano-SiC, the hindrance effect plays the leading role as a result of the fewer surface hydroxyl groups. From Table 20.3, it is known that the curing reaction orders of the three composites are almost the same, suggesting that the nanoparticles did not change the curing mechanism of epoxy.

It has been stated previously that the treatment of nanoparticles in terms of graft polymerization would significantly change the surface characteristics and separate the agglomerated fillers. When these pre-grafted nanoparticles are compounded with a thermosetting polymer, the former will keep their more stationary suspension state due to the interaction between the grafting polymer and the matrix. After curing of the mixture, filler/matrix adhesion would be substantially enhanced by the entanglement and/or the chemical bonding between the grafting polymer and the matrix polymer.

To look into the influence of graft treatment of nanoparticles on composites manufacturing, polyacrylamide grafted nano-SiO_2 particles (SiO_2-g-PAAM) filled epoxy has been evaluated.[12,78] PAAM is selected because the active hydrogen atoms of amide of PAAM might react with epoxy groups during curing and form three-dimensional networks throughout the composites, so that the nanoparticles can be covalently connected with the matrix and take effect. Similarly, when the particles are incorporated into epoxy, the curing kinetics of the resin are changed significantly (Fig. 20.4). Evidently, the unmodified silica nanoparticles hinder the curing reaction to a certain extent and lead to a shift of the temperature dependence of conversion towards higher temperature. In contrast, the addition of grafted silica nanoparticles accelerates curing of epoxy, probably due to the catalytic effect of the active hydrogen atoms in amide of PAAM. This behavior is indicative of an improved processability of the system in practice. Figure 20.5 illustrates Arrhenius plots of rate constant ln$K$ of the materials as a function of the reciprocal temperature. The results demonstrate that SiO_2/epoxy has almost the same rate constant as epoxy. For SiO_2-g-PAAM/epoxy, the rate constant is higher than that of the former two systems at a temperature below 205ºC, but it becomes lower when the temperature exceeds 205ºC. That is, the appearance of the active hydrogen atoms in amide of PAAM grafted nanosilica favors the curing reaction. Since hydrogen bond formation and dissociation in a polymer are thermally reversible, a large portion of hydrogen bonds has to be dissociated at elevated temperature. As a result, diffusion control plays the leading role in SiO_2-g-PAAM/epoxy composites at a temperature higher than 205ºC.

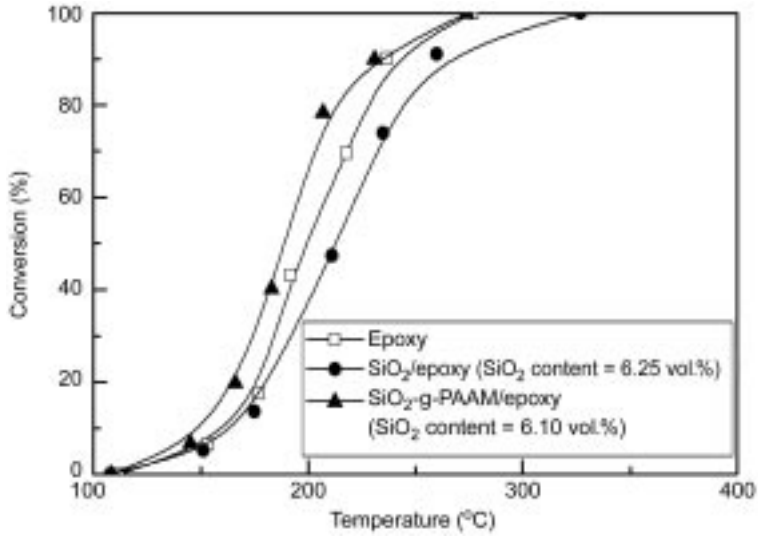

20.4 Nonisothermal curing behavior of epoxy and its composites at a heating rate of 2°C/min[12] (reprinted from *Macromol. Mater. Eng.*, vol. 287, M. Q. Zhang *et al.*, Improvement of the tribological performance of epoxy by the addition of irradiation grafted nano-inorganic particles, p. 111, 2002, with permission from John Wiley & Sons, Inc.).

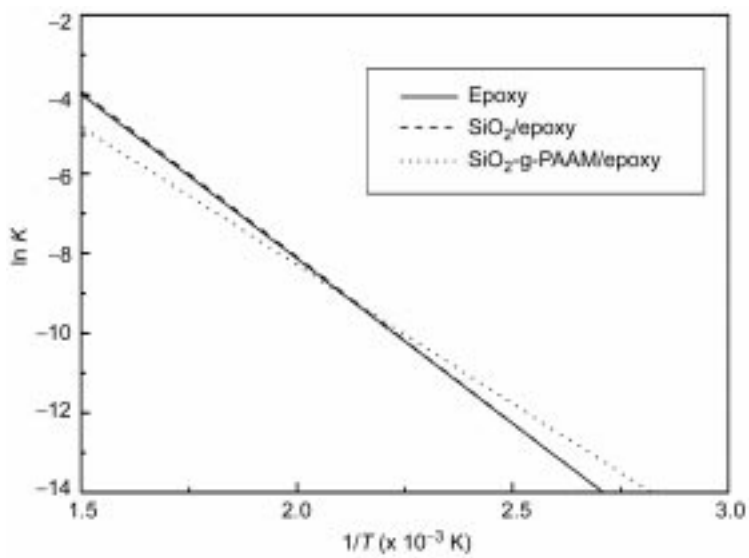

20.5 Temperature dependence of rate constant characterizing curing processes of epoxy and its composites at 2.17 vol.% nanosilica content[79] (reprinted from *Wear*, vol. 253, M. Q. Zhang *et al.*, Effect of particle surface treatment on the tribological performance of epoxy based nanocomposites, p. 1086, 2002, with permission from Elsevier).

For purposes of revealing details of the reaction between the grafted PAAM on the nanoparticles and epoxy, a model system consisting of PAAM homopolymer and epoxy (1/2 by weight) excluding other curing agents was thermally treated following the same curing sequence as that applied for producing the composites. Visual inspection indicated that the blends of PAAM and epoxy became consolidated after curing and the resultant product can only be swollen by acetone instead of dissolve in the solvent. In addition, comparison of the infrared spectra of the materials can also yield interesting information. As illustrated by the spectrum of PAAM in Fig. 20.6, the C=O peak at 1665 cm^{-1} and the NH_2 peak at 1616 cm^{-1} correspond to the primary amide. In the case of PAAM/epoxy blends, however, the spectrum profile has been changed as a result of transformation of partial primary amide groups and band overlap due to the incorporation of epoxy. The carbonyl peak shifts to lower wavenumber, 1656 cm^{-1}, implying that carbonyl groups obtain more electrons compared with that of primary amide. This phenomenon may result from the change of primary amine to secondary amine, because methylene groups are usually considered as electronic donor groups than hydrogen groups. It can thus be concluded from the above visual observation and spectral analyses that PAAM is able to take part in

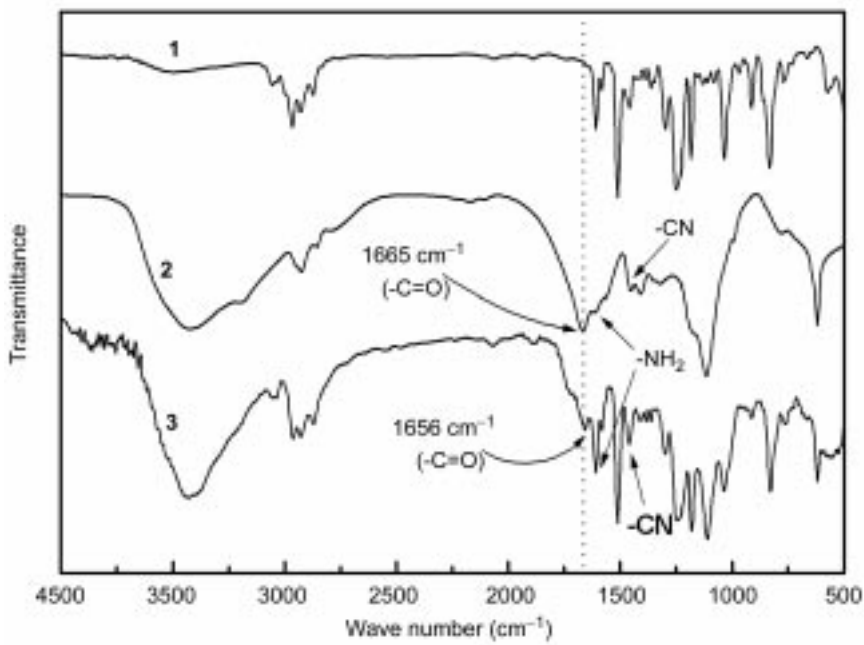

20.6 FTIR spectra of (1) epoxy without any curing agent, (2) PAAM, and (3) cured blends of PAAM and epoxy (1/2 w/w)[12] (reprinted from *Macromol. Mater. Eng.*, vol. 287, M. Q. Zhang *et al.*, Improvement of the tribological performance of epoxy by the addition of irradiation grafted nano-inorganic particles, p. 111, 2002, with permission from John Wiley & Sons, Inc.).

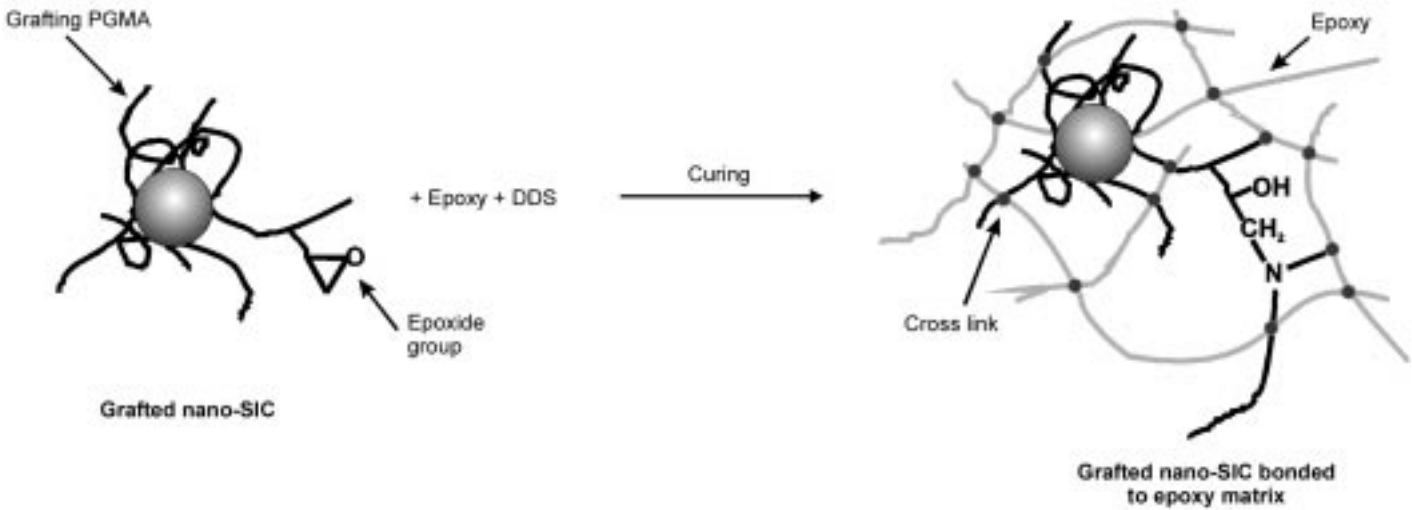

20.7 Schematic drawing of PGMA grafted nano-SiC chemically bonded with epoxy resin through the reaction between the epoxide group and curing agent.

the curing reaction of epoxy. Such a chemical bonding between the PAAM chains grafted onto the nanoparticles and surrounding epoxy networks would certainly enhance the filler/matrix adhesion in the composites.

From the above discussion, it is clear that a fine adjustment of interfacial interaction in the polymer nanocomposites with chemically pretreated nanoparticles can be achieved by introducing modifiers containing reactive groups onto nanoparticles, which helps to construct chemical bonding between the fillers and the matrix. So far, however, there are few reports using this approach for nanocomposites manufacturing. To further bring the positive effect of grafting polymer, in one of our works, polyglycidyl methacrylate (PGMA) was adhered to silane (γ-methacryloxypropyl trimethoxy silane) pre-treated SiC nanoparticles through emulsifier-free emulsion graft polymerization.[30] It is hoped that the epoxide groups on PGMA would take part in the curing reaction of epoxy forming a structure of nano-SiC-PGMA-epoxy (Fig. 20.7). As a result, the epoxy composites filled with PGMA grafted nano-SiC particles (SiC-g-PGMA), which are covalently connected to the matrix, would possess performance superior to those with the untreated versions.

20.4 Wear performance and mechanisms

Recent progress indicated that polymer-based nanocomposites acquired mechanical properties much higher than the usual systems at a rather low filler loading.[39,84–87] Although there are relatively few reports concerning the effect of nanoparticles on the tribological behavior of the composites, some scientists have made pilot investigations of nanoparticle/thermoplastics and nanoparticle/thermosetting composites. Table 20.4 summarizes the representative results published by various groups in the world in recent years. It is seen that wear rate of polymers can be significantly reduced by the addition of the nanoparticles. For both thermoplastic and thermosetting nanocomposites, the greatest decrement lies in three orders of magnitude and the lowest wear rate is about 1×10^{-6} mm^3/Nm. In contrast, however, the reduction in frictional coefficient is not attractive enough. In some cases, the values of the nanocomposites are even higher than those of the neat matrices. Therefore, much more efforts have to be made to understand the mechanisms and to further improve the performance.

20.4.1 Effects of size and content of the nano-fillers

It is generally believed that the nanocomposites with finer fillers would gain more remarkable properties improvement. Although one can hardly figure out a general size dependence of wear rate or frictional coefficient from Table 20.4, the results of comparisons carried out with given polymer species are still meaningful. Wang *et al.* measured the friction and wear properties of PEEK composites filled with ZrO_2 nanoparticles with different sizes (10, 15, 50, 86 and

Table 20.4 Friction and wear properties of nano-fillers incorporated polymeric composites reported in the literature

Matrix polymer	Nano-filler	Surface treatment	Lowest wear rate[a] (10^{-6} mm^3/Nm)	Filler loading corresponding to the lowest wear rate	Lowest frictional coefficient[a]	Filler loading corresponding to the lowest frictional coefficient	Ref.
Thermoplastics							
PTFE	ZnO (50 nm)	—	13.0 (1.2×10^{-2})	15 vol.%	0.19 (0.94)	12.5 vol.%	58
PTFE	Al_2O_3 (38 nm)	—	1.2 (1.9×10^{-3})	20 wt.%	0.18 (1.20)	12 wt.%	45
PTFE	Attapulgite (width = 10–25 nm, length ‹ 75 μm)	HCl treated	3.6 (5.8×10^{-3})	5 wt.%	0.21 (0.95)	5 wt.%	60
PTFE	Carbon nanotube (diameter = 20–30nm, length = several micra)	—	2.5 (3.4×10^{-3})	20 vol.%	0.17 (0.84)	30 vol.%	57
UHMWPE	Al_2O_3 (20–30 nm)	—	258 (0.70)	10 wt.%	0.32 (0.94)	5 wt.%	44
PA1010	Fe_2O_3 (40–50 nm)	—	8.6 (0.31)	10 wt.%	0.42 (0.76)	20 wt.%	59
PA1010	Al_2O_3 (60–70 nm)	—	18.9 (0.68)	20 wt.%	0.76 (1.38)	20 wt.%	59
PET	Al_2O_3 (38 nm)	—	9.5 (0.55)	2 wt.%	0.30 (0.91)	2 wt.%	46
PI	Carbon nanotube (diameter = 10–50 nm)	—	9.7 (0.17)	8 wt.%	0.28 (0.76)	5 wt.%	69
PU	Ni (50 nm)	—	25 (0.2)	9 wt.%	0.30 (0.71)	9 wt.%	63
PEEK	SiC (< 100 nm)	—	3.3 (0.45)	2.5 wt.%	0.20 (0.54)	20 wt.%	11
PEEK	ZrO_2 (10 nm)	—	4.0 (0.54)	7.5 wt.%	0.29 (0.78)	15 wt.%	48
PEEK	Si_3N_4 ($\leq$50 nm)	—	1.1 (0.15)	7.5 wt.%	0.23 (0.62)	15 wt.%	49
PEEK	SiO_2 ($\leq$100 nm)	—	2.2 (0.30)	7.5 wt.%	0.21 (0.57)	15 wt.%	50
PPESK	TiO_2 (40 nm)	—	5.1 (6.7×10^{-2})	1.7 vol.%	0.44 (0.80)	0.94 vol.%	56
PPESK	SiO_2 (20 nm)	—	3.0 (3.3×10^{-2})	14.5 vol.%	0.21 (0.34)	14.5 wt.%	55
PPS	γ-Al_2O_3 (33 nm)	—	10.4 (0.70)	2 vol.%	0.39 (0.88)	10 vol.%	7
PPS	CuO (16–32 nm)	—	2.5 (0.16)	2 vol.%	0.47 (0.96)	4 vol.%	85

Table 20.4 Continued

Matrix polymer	Nano-filler	Surface treatment	Lowest wear rate[a] (10^{-6} mm^3/Nm)	Filler loading corresponding to the lowest wear rate	Lowest frictional coefficient[a]	Filler loading corresponding to the lowest frictional coefficient	Ref.
Thermosets							
BMI	Si_3N_4 (20–50 nm)	—	1.9 (0.28)	1.5 wt.%	0.24 (0.67)	2.0 wt.%	74
Phenolic resin	TiO_2 (50 nm)	Surfactant treated	2.2 (0.18)	5 wt.%	0.43 (1.05)	5 wt.%	73
Epoxy	ZnO (20 nm)	Silane treated	71.4 (0.29)	10 wt.%	0.48 (0.81)	4 wt.%	84
Epoxy	Si_3N_4 (<20 nm)	—	1.9 (5.1×10^{-2})	0.83 vol.%	0.35 (0.61)	1.38 vol.%	78
Epoxy	γ-Al_2O_3 (3.8 nm)	—	6.7 (0.18)	1.2 vol.%	0.50 (0.86)	0.48 vol.%	76
Epoxy	γ-Al_2O_3 (3.8 nm)	PAAM grafted	1.6 (4.3×10^{-2})	0.24 vol.%	0.35 (0.61)	0.24 vol.%	76
Epoxy	Al_2O_3 (10.4 nm)	—	7.8 (3.3×10^{-2})	1.23 vol.%	0.49 (0.90)	0.74 vol.%	81
Epoxy	Al_2O_3 (10.4 nm)	PS grafted	1.6 (6.9×10^{-3})	0.48 vol.%	0.46 (0.85)	1.47 vol.%	81
Epoxy	SiC (61 nm)	—	2.3 (0.55)	0.40 vol.%	0.90 (0.80)	0.20 vol.%	80
Epoxy	SiC (61 nm)	PAAM grafted	1.1 (0.27)	0.20vol.%	0.74 (0.66)	0.20 vol.%	80
Epoxy	SiO_2 (9 nm)	—	23.5 (0.11)	6.25 vol.%	0.41 (0.71)	6.25 vol.%	12
Epoxy	SiO_2 (9 nm)	PAAM grafted	11.0 (5.3×10^{-2})	2.17 vol.%	0.37 (0.64)	2.17 vol.%	12
Epoxy	Al_2O_3 (13 nm)	—	3.8 (0.66)	2.0 vol.%	—	—	86
Epoxy	TiO_2 (200–400 nm)	—	14.0 (0.35)	5.0 vol.%	—	—	87

[a]The numerals in the brackets stand for the normalized properties of the composites relative to the unfilled matrices.

100 nm), respectively.[48] In the case of a fixed filler content of 7.5 wt.%, all these nanoparticles were able to reduce the friction of PEEK, but the frictional coefficient increases slightly with increasing the particulate size, although it is still lower than that of pure PEEK. The wear rate of the filled PEEK decreases gradually with a decrease in the size of nano-ZrO_2, and a drastic reduction was found when the particles are smaller than 15 nm. The abated scuffing between the transfer film and the composite surface accounts for the improvement. For the particles larger than 50 nm, the wear rate gradually increases with a rise in ZrO_2 size and is higher than that of pure PEEK because of the appearance of a discontinuous thick transfer film poorly adhered to the substrate. It means there might be a critical particle size. Only the nanoparticles with size below the critical value can effectively improve the wear resistance of the composites.

Xing and Li[88] prepared two groups of uniformly sized silica particles (120 and 510 nm in diameter, respectively), which were then used as model fillers in epoxy composites. The sliding wear tests manifest that the filler with smaller size is more effective in the improvement of the wear resistance of the composites. The mechanism was attributed to the fact that the number of the filler particles per unit volume for the composite with 120 nm silica particles is greater than that of the composite with the 510 nm silica particles. As the fillers were uniformly sized spherical particles, the greater the number of the particles on the worn surface, the larger the contact area between the particles and the wear pin, and hence the better the wear resistance offered by the silica particles. The same conclusion was also made by Tang *et al.* in their experiments studying the wear loss of epoxy filled with α-Al_2O_3 (200 nm) and γ-Al_2O_3 (30–60 nm), respectively.[89]

With respect to the influence of filler content, it can be concluded that there is often an optimum filler loading corresponding to the lowest wear rate of the nanocomposites. Such a U-shaped dependence of wear rate on nano-filler concentration has been found in many reports, like the systematic investigations on PEEK composites filled with a series of inorganic nanoparticles.[11,47–54] Nevertheless, the filler content dependence of frictional coefficient usually does not follow this rule. The frictional coefficient often decreases (or increases) slightly with increasing filler content and at times even varies irregularly with filler content.

The addition of low loading nanoparticles into polymers would greatly change the wear mode, for example, from severe wear of unfilled epoxy dominated by fatigue-delamination mechanism to mild polishing in nano-Si_3N_4 filled version as a result of improved surface hardness.[77] When the particles content is so high that severe agglomeration of the particles takes place due to the significantly increased viscosity as confirmed by positron annihilation life time spectroscopy (PALS),[84] the composites would be easily damaged under repeated frictional stress.[80] Therefore, the lowest wear rate of the nanocomposites only appears within a narrow range of filler content. Wang *et al.*

found that too high content of nanometer ZrO_2 in PEEK led to abrasive wear during the friction process and the counterpart steel ring was subsequently abraded severely.[51] The abrasive wear caused by the hard wear debris enhanced the wear rate of the composite block. With an increasing of nanometer ZrO_2 content, the dominant wear mechanism had to change from melting adhesive transfer wear to slight transfer wear, and finally to abrasive wear.

For the friction reducing manner, it is known that the detached nanoparticles might act as tiny rolling balls at the counterface, providing the effect of solid lubricating.[8] In case the nanoparticles still had certain angularity, the corresponding lubricating effect would be weaker or even three-body abrasive wear occurs. In accordance with the increased amount of material loss, the large wear debris detached from the worn surface would also result in abrasion that increases the frictional coefficient of the system.

Since the transient surface temperature at rubbing surface is always rather high, frictional coefficient of the composites might be correlated to their viscoelasticity. Fig. 20.8 plots frictional coefficient of nano-Si_3N_4/epoxy as a function of the area under the α-transition peak determined from the tan δ–temperature spectrum.[78] It is obvious that the relationship follows exponential growth with decreasing filler fraction, which is analogous to Arrhenius equation implying that the frictional process is closely related to thermally activated motion of the molecular segments of epoxy. Since frictional coefficient increases with a rise in damping of the composites, the ability of the materials to

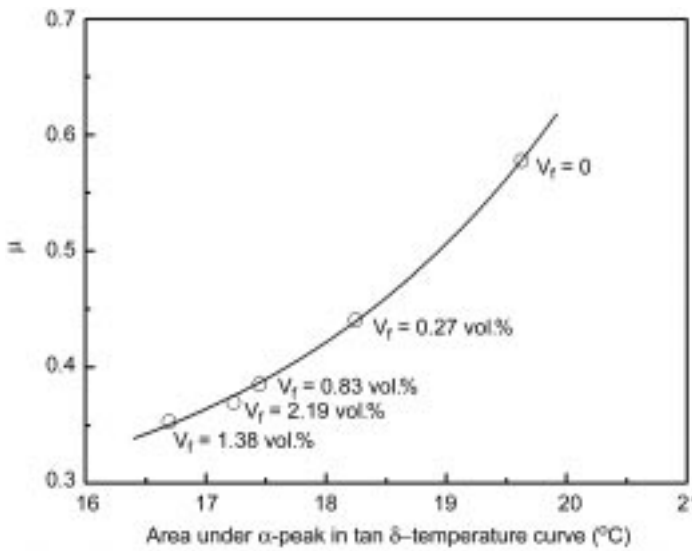

20.8 Frictional coefficient, μ, versus area under the α-transition peak in tan δ–temperature curve[78] (reprinted from *Wear*, vol. 254, G. Shi *et al.*, Friction and wear of low nanometer Si_3N_4 filled epoxy composites, p. 784, 2003, with permission from Elsevier).

transform mechanical energy into heat contributes to the frictional behavior. In other words, the stiffer the composites, the lower the frictional coefficient, so that the stick-and-slip phenomenon can be prevented with a rise in the nano-filler loading.[90]

20.4.2 Tribochemistry

Owing to the fine dimension and high surface area, inorganic nanoparticles possess much higher chemical activity than their micron versions. Under the circumstances of friction, tribochemical reactions tend to take place in the contacts between nanocomposites and counterparts, in favor of modifying the transfer film and/or increasing the bonding strength of transfer film to the counterparts. Shi *et al.* examined the elements on the steel counterpart surface before and after the wear tests against nano-Al_2O_3/epoxy composites with X-ray energy distribution spectroscopy (EDS).[76] Having been rubbed with epoxy, sulfur appears on the surface of the steel ring, implying the transfer from epoxy to the counterface. When the specimen was changed into nano-Al_2O_3/epoxy composites, both sulfur and aluminum can be detected. It thus proves substances transfer across the frictional surfaces. In the case of nano-SiC/PEEK composites,[47] Wang *et al.* revealed that some proportion of nanometer SiC was oxidized into SiO_2 during the rubbing process, existing in the transfer film and the wear trace of the block. As nano-SiO_2 in PEEK is very effective in decreasing friction and wear, it may partly explain why nano-SiC/PEEK system exhibits decreased frictional coefficient and wear rate.

For nano-Si_3N_4/epoxy sliding against steel ring, formation of SiO_2 on the worn surface of the composites pin was also confirmed by X-ray photoelectron spectra (XPS).[78] It represents a tribochemical way of wear in which material is removed molecule by molecule, instead of the classic removal of fragments by fracture.[91,92] In addition, the tribofilm of SiO_2 protects the specimens and the steel counterpart, providing friction-reducing ability.[93] On the other hand, besides the reactions between the Fe atoms from the metal counterface and the S atoms from epoxy and Si_3N_4, the Fe atoms can also be oxidized, forming FeO and Fe_3O_4. Kong *et al.* reported on the effect of surface oxide layers on wear behavior.[94] FeO or Fe_3O_4 layers show a significant reduction in friction and wear, while Fe_2O_3 layer promotes the wear. Therefore, the decrease in frictional coefficient and wear rate of epoxy with the addition of Si_3N_4 nanoparticles can be partly attributed to the appearance of FeO and Fe_3O_4 on the counterfaces.[95] To conclude the tribochemical reactions of epoxy and its nano-Si_3N_4 composites, and those between the materials and the counterface metal Fe, Fig. 20.9 presents a summary of the above discussion, which might help to understand the role of the nanocomposites operating under sliding wear conditions.

Schwartz and Bahadur measured the bond strength between the transfer film and the counterface, and correlated it to the wear rate of nano-Al_2O_3/PPS

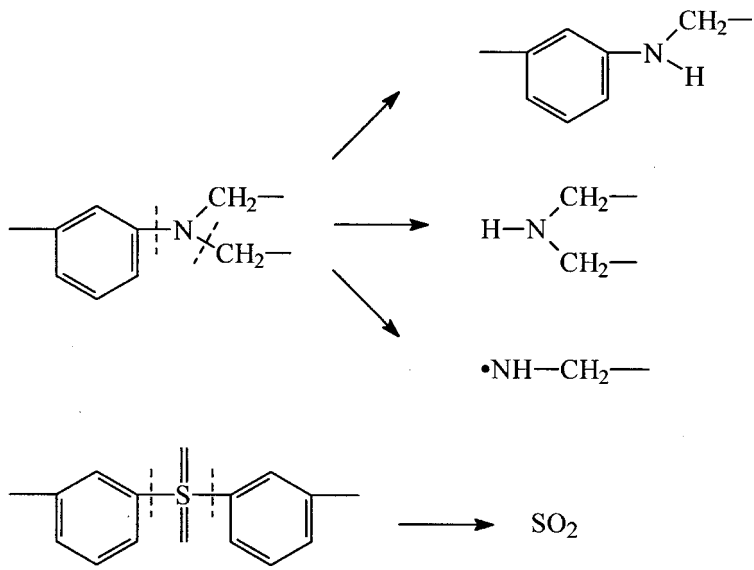

$$O_2 + \bullet NH{-}CH_2{-} \rightarrow ON{-}CH_2{-}$$

$$SO_2 + Fe + O_2 \rightarrow FeSO_4$$

$$Fe + H_2O + O_2 \rightarrow Fe_3O_4$$

$$Fe + O_2 + H_2O \rightarrow FeO$$

$$Fe + S \rightarrow FeS$$

$$Si_3N_4 + O_2 + H_2O \rightarrow SiO_2$$

$$Si_3N_4 + Fe + H_2O + O_2 \rightarrow Fe_2SiO_4$$

20.9 Tribochemical reactions occurring at the rubbing interface between nono-Si_3N_4/epoxy nanocomposite and iron counterpart.

composites.[7] With the addition of 2 vol.% alumina nanoparticles to PPS, the bond strength of the transfer film to the steel counterface increases and correspondingly the wear rate decreases. When the bond strength of the transfer film for the counterface is very low, there is no reduction in wear in this case. A recent report by Bahadur and Sunkara further proved the importance of adhesion of transfer film to the counterface in the case of PPS nanocomposites. [96]

It is worth noting that tribochemical reactions are not bound to result in positive effects on tribological performance. When PTFE powder and nano-SiC particles were jointly incorporated into PEEK,[52] for instance, the friction reduction and wear resistance capacities of the nanocomposites became worse. The reason for this was the chemical reaction between the nanometer SiC and PTFE during the sliding friction process. The formation of SiF_x by consuming a certain amount of nano-SiC and PTFE deteriorated the property of transfer film. Only when the content of PTFE was high enough, the ternary composites nano-SiC/PTFE/PEEK exhibit lower frictional coefficient than the binary ones PTFE/PEEK.

20.4.3 Effect of surface treatment of the nano-fillers

Although the importance of filler surface treatment in nanocomposites has been well recognized, only a few works have been published on this aspect of tribological application up to now, as exemplified by the statistics in Table 20.4. In most cases, the nanoparticles were compounded with polymers without any treatment. Due to the strong agglomeration tendency of nanoparticles, the probability of intimate filler/matrix contacts might be greatly reduced and the extraordinary effects of the nanoparticles cannot be fully brought into play as a result. Nevertheless, the published results concerning the treated nanoparticles composites are quite encouraging. Bauer and co-workers modified nano-sized silica and alumina particles with silanes to produce functionalized nano-fillers in transparent UV/EB curable acrylates.[97–101] In radiation (UV, EB) induced polymerization reactions, these modified nanoparticles form covalent crosslinks to acrylate substrates, thus efficiently modifying their viscoelastic properties. The transparent nanopowder composites can be used as scratch and abrasion resistant coatings.

Systematic research has been carried out by Shi *et al.* to evaluate the sliding wear behavior of epoxy containing nano-Al_2O_3 particles with different pretreatments.[76] In their work the treatments are classified into two categories. The first one deals with the use of amino-silane coupling agent. The functional group ethoxyl of the coupling agent reacts with hydroxyl groups on the filler surface, while the amino groups can react with epoxy groups. The other is graft polymerization onto the nanoparticles with the monomers of acrylamide, styrene and ethyl acrylate, respectively. It has been proven that the amide groups of polyacrylamide take part in the curing of epoxy resin (Fig. 20.6).[12] The encapsulation of nano-Al_2O_3 with polystyrene or polyethyl acrylate is believed to be able to greatly increase the hydrophobicity of the particles and hence the compatibility with the polymer matrix.

As shown by Fig. 20.10, the high wear rate of unfilled epoxy due to the three-dimensional crosslinking network is greatly decreased by adding nano-Al_2O_3 particles, especially when treated nano-Al_2O_3 is incorporated. Besides, the

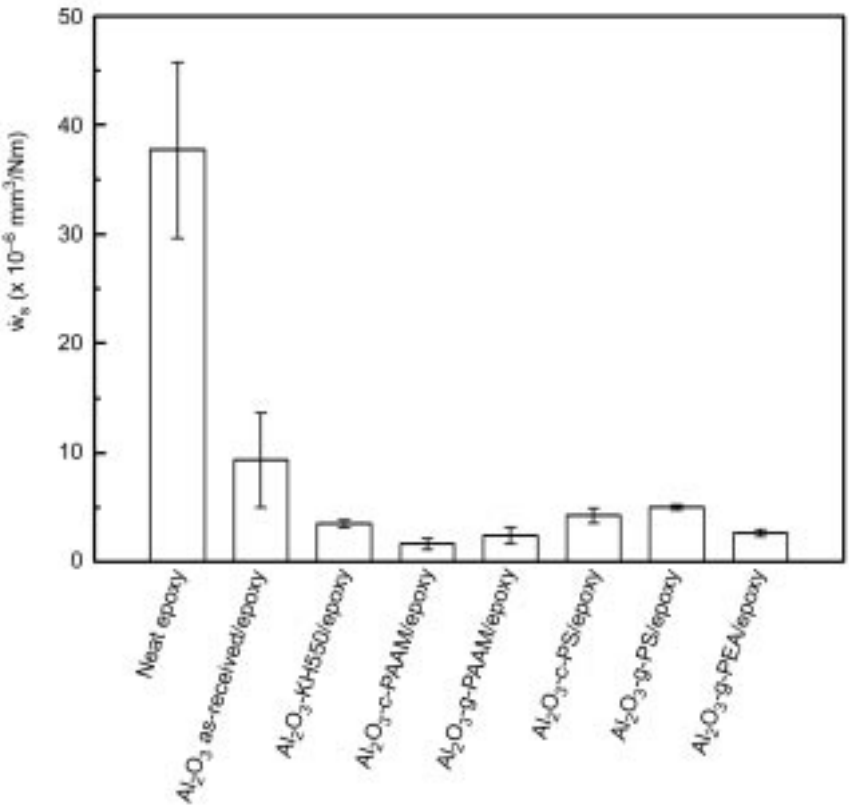

20.10 Specific wear rate, $\dot{w}_s$, of nano-Al_2O_3/epoxy composites at a volume fraction of nano-Al_2O_3 of 0.24vol%.[76] The identifications of the modified particles are described as follows. Al_2O_3-KH550 means the nanosized alumina particles have been treated by KH550 silane. Al_2O_3-c-PAAM and Al_2O_3-c-PS denote that the particles are grafted by polyacrylamide and polystyrene without removing the homopolymers generated during the graft polymerization. Having experienced extraction with proper solvents, the grafted nanoparticles are symbolized by Al_2O_3-g-PAAM, Al_2O_3-g-PS and Al_2O_3-g-PEA, respectively, meaning the particles are accompanied only with the unextractable grafting polymers. (Reprinted from *Wear*, vol. 256, G. Shi *et al.*, Sliding wear behavior of epoxy containing nano-Al_2O_3 particles with different pretreatments, p. 1072, 2004, with permission from Elsevier.)

nanoparticles also reduce frictional coefficient of epoxy (Fig. 20.11), and the composites with treated nanoparticles have lower frictional coefficients. For example, the frictional coefficient of Al_2O_3-c-PAAM/epoxy is 0.35 which amounts to 61% of the value of unfilled epoxy and 69% of the value of untreated nano-Al_2O_3/epoxy. Meanwhile, the specific wear rate of Al_2O_3-c-PAAM/epoxy is decreased by 97% and 88% respectively, as compared with the values of unfilled epoxy and untreated nano-Al_2O_3/epoxy.

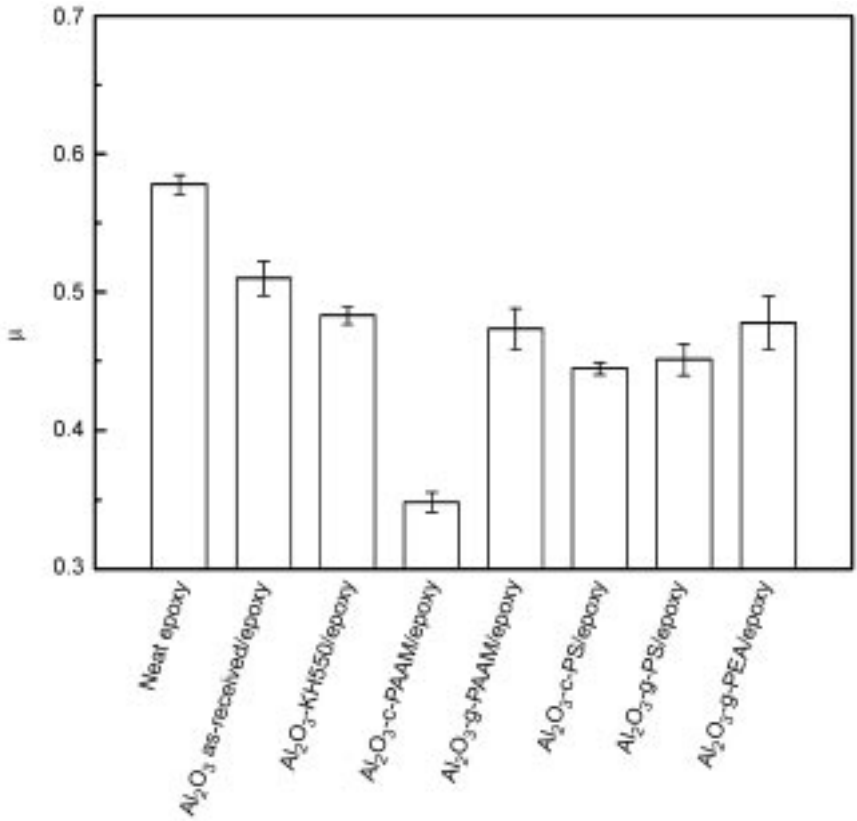

20.11 Frictional coefficient, μ, of nano-Al_2O_3/epoxy composites at a volume fraction of nano-Al_2O_3 of 0.24 vol.%.[76] The composites' codes are the same as those explained in Fig. 20.10. (Reprinted from *Wear*, vol. 256, G. Shi *et al.*, Sliding wear behavior of epoxy containing nano-Al_2O_3 particles with different pretreatments, p. 1072, 2004, with permission from Elsevier.)

The difference in improving the friction reducing and wear resisting ability of epoxy between the composites with untreated and treated nano-alumina should result mainly from the filler/filler adhesion strength. The untreated nanoparticles have to present themselves in the composites in the form of agglomerates because of the hydrophilic nature of the particles and the limited dispersion force during blending with epoxy. Inside the nanoparticle agglomerates, the particles are bound only by hydrogen bonds and van der Waals bonds. When the composites with the untreated nanoparticles are subjected to wearing, damage induced by localized shear stress concentration at the loosened nanoparticle agglomerates would occur on a large scale and produce bigger blocks of wear debris. For the composites with enhanced interaction inside and outside the treated nanoparticle agglomerates, the resistance to periodic frictional stress is

greatly increased. Detachment of nanoparticles and the small amount of the surrounding matrix plays the leading role in material removal due to wear. The detached nanoparticles might also act as solid lubricants. These account for the low wear rates and frictional coefficients of the composites.

Figure 20.12 illustrates morphologies of the worn pins' surfaces. Severe damage characterized by the disintegration of the top layer was observed in unfilled epoxy (Fig. 20.12(a)). The material removal takes the form of larger blocks, which might be captured between the steel counterface and the test pin, and abrade the specimen surface leading to even more substantial material loss. In the case of filled composites, the appearances are completely different and become rather smooth. Although the ploughing grooves are still visible on the composites with untreated nano-Al_2O_3 (Fig. 20.12(b)), the groove depths are quite shallow on the composites with treated nano-Al_2O_3 (Fig. 20.12(c–e)) or simply invisible (Fig. 20.12(f)). It suggests that polishing predominates the wear processes of the latter composites.

Lu *et al.* studied thermal stability of frictional surface layer and wear debris of epoxy nanocomposites in relation to the mechanism of tribological performance improvement.[102] It was concluded that the fatigue-delamination effect responsible for the sliding wear of epoxy is accelerated by the surface structural deterioration induced by the rather high friction temperature. The unfilled epoxy is thus characterized by poor tribological performance. When nano-silica is added, the flash temperature is reduced, resulting in less significant fatigue driven surface failure and improved wear resistance of SiO_2/epoxy composites. In the case of SiO_2-g-PAAM/epoxy, the covalent bonding between the grafting polymers on the nanoparticles and the matrix greatly increases the composites integrity. The reduced amount and size of wear debris weaken the abrasive effect of the wear debris as the third-body in the contact area.[103] This in turn lowers the frictional temperature to a much greater extent, and the fatigue-induced material removal of the composites consequently becomes even less than SiO_2/epoxy.

20.5 Conclusions and future trends

By surveying the nanocomposites prepared so far, wear resisting polymer nanocomposites can be regarded as a successful example that brings the so-called 'nano-effect' into full play. At a filler loading of less than 1%, the wear rate of the matrix was lowered by over thousands of times (Table 20.4). Similar enhancement due to the addition of small amounts of fillers is impossible to perceive in microcomposites. The developments in this aspect have broadened the application possibility of particulate composites and solved the dilemma arising from the contradiction between tribological performance improvement and processability deterioration, as often observed in microparticles filled composites.

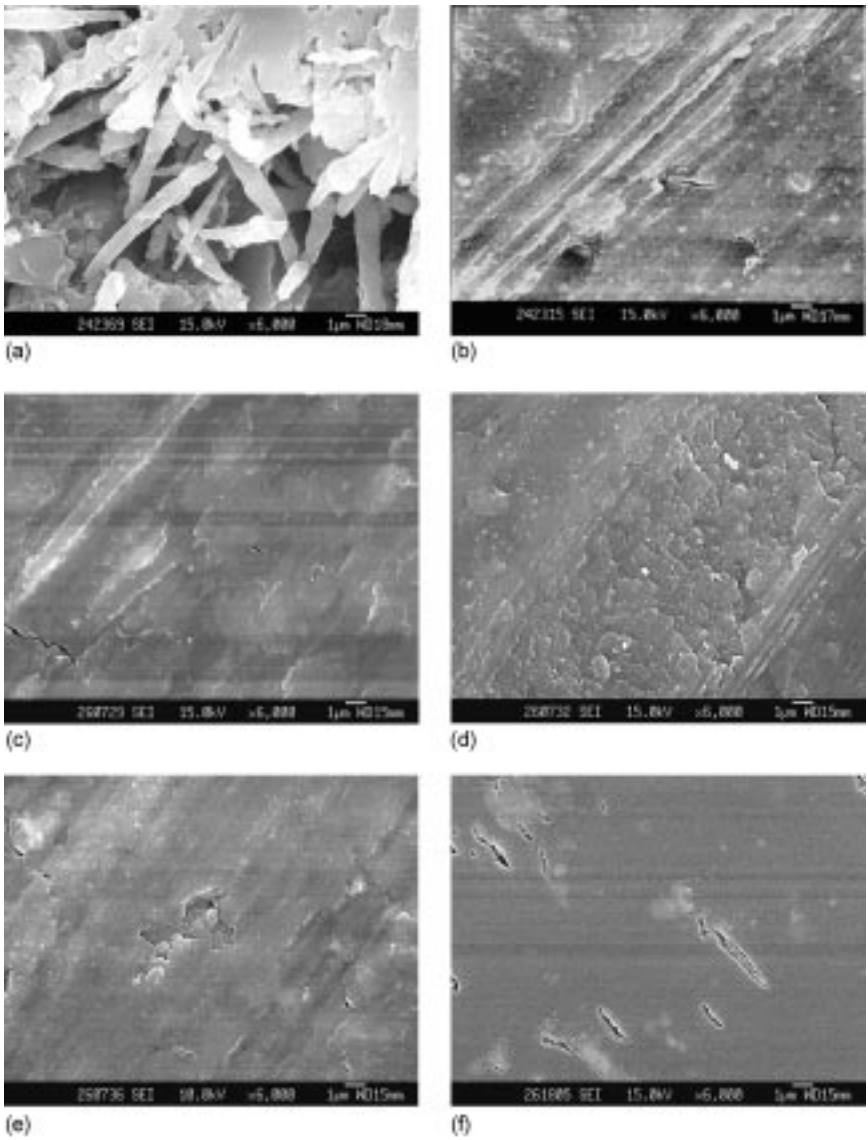

20.12 Scanning electron microscopic photos of the worn surfaces of (a) unfilled epoxy and its composites filled with (b) untreated nano-Al_2O_3, (c) Al_2O_3-KH550, (d) Al_2O_3-g-PAAM, (e) Al_2O_3-g-PS, and (f) Al_2O_3-g-PEA at a volume fraction of nano-Al_2O_3 of 0.24 vol.%.[76] The composites' codes are the same as those explained in Fig. 20.10. (Reprinted from *Wear*, vol. 256, G. Shi *et al.*, Sliding wear behavior of epoxy containing nano-Al_2O_3 particles with different pretreatments, p. 1072, 2004, with permission from Elsevier.)

Transparent wear resisting nanocomposite coatings represent a typical application, which take the advantages of low angularity, colorlessness and anti-abrasion of the nanoparticles (Al_2O_3, SiO_2, etc.) and are adaptable for the surfaces of plastics, metals, woods and glass to increase the end-products' service life and even the aesthetic values.[99,104] Moreover, when coating a surface with polyelectrolyte multilayers composed of polyallylamine hydrochloride (PAH) and polyacrylic acid (PAA) in which silver nanoparticles or multiwall carbon nanotubes are incorporated, reduced coefficient of friction as well as substrate wear prevention can be achieved.[105] Self-lubricating composites with hybrid fillers, like nano- and micro-sized inorganic particulates,[86,87] inorganic nanoparticles and PTFE powders,[52,106] inorganic nanoparticles and glass fabric,[107] short carbon fibre, graphite, PTFE powder and inorganic nanoparticles,[108,109] have combined the positive effects of the components and are capable of operating under much severer circumstances than the composites with only one type of nanoparticles.

Further research ought to concentrate on the investigation of wear mechanism (that is still an open question) and application-oriented innovation of composites manufacturing (including formulation, surface treatment of nanoparticles and processing). Much finer manipulation on molecular basis might make revolutionary breakthroughs.

20.6 Acknowledgements

The financial support by the Volkswagen-Stiftung, Federal Republic of Germany (Grant: I/76645), for the cooperation between the German and Chinese institutes on this subject is gratefully acknowledged. Further thanks are due to the National Natural Science Foundation of China (Grant: 50273047), the Team Project of the Natural Science Foundation of Guangdong, China (Grant: 20003038), the Key Program of the Science and Technology Department of Guangdong, China (Grant: 2003C50107, 2004A10702001) and the project of Guangdong Economic & Trade Commission, China (Grant: 20040112).

20.7 References

1. Fischer H, 'Polymer nanocomposites: from fundamental research to specific applications', *Mater Sci Eng* 2003 **C23** 763–72.
2. Huang Z M, Zhang Y Z, Kotaki M and Ramakrishna S, 'A review on polymer nanofibers by electrospinning and their applications in nanocomposites', *Compos Sci Technol* 2003 **63** 2223–53.
3. Rong M Z, Zhang M Q, Pan S L and Friedrich K, 'Interfacial effects in polypropylene-silica nanocomposites', *J Appl Polym Sci* 2004 **92** 1771–81.
4. Briscoe B J, 'The tribology of composite materials: a preface', in Friedrich K, *Advance in Composite Tribology*, Amsterdam, Elsevier, 1993, 3.
5. Yamaguchi Y, 'Improvement of lubricity', in Yamaguchi Y, *Tribology of Plastic*

Materials, Tribology Series, vol.16, Amsterdam, Elsevier, 1990, 143–202.
6. Bely V A, Sviridenok A I, Petrokovets M I and Savkin V G, *Friction and Wear in Polymer-Based Materials*, Oxford, Pergamon Press Ltd, 1982.
7. Schwartz C J and Bahadur S, 'Studies on the tribological behavior and transfer film-counterface bond strength for polyphenylene sulfide filled with nanoscale alumina particles', *Wear* 2000 **237** 261–73.
8. Rong M Z, Zhang M Q, Liu H, Zeng H M, Wetzel B and Friedrich K, 'Microstructure and tribological behavior of polymeric nanocomposites', *Ind Lubr Tribol* 2001 **53**(2) 72–7.
9. Ng C B, Schadler and Siegel R W, 'Synthesis and mechanical properties of TiO_2-epoxy nanocomposites', *Nanostruct Mater* 1999 **12** 507–10.
10. Yu L, Yang S, Wang H and Xue Q, 'An investigation of the friction and wear behaviors of micrometer copper particle- and nanometer copper particle-filled polyoxymethylene composites', *J Appl Polym Sci* 2000 **19** 2404–10.
11. Xue Q and Wang Q, 'Wear mechanisms of polyetheretherketone composites filled with various kinds of SiC', *Wear* 1997 **213** 54–8.
12. Zhang M Q, Rong M Z, Yu S L, Wetzel B and Friedrich K, 'Improvement of the tribological performance of epoxy by the addition of irradiation grafted nano-inorganic particles', *Macromol Mater Eng* 2002 **287**(2) 111–15.
13. Plueddemann E P, *Silane Coupling Agents*, New York, Plenum Press, 1982.
14. Fekete E, Pukanszky B, Toth A. and Bertoti I, 'Surface modification and characterization of particulate mineral fillers', *J Colloid Interf Sci* 1990 **135** 200–8.
15. Nakatsuka T, Kawasaki H and Itadani K, 'Phosphate coupling agents for calcium carbonate filler', *J Appl Polym Sci* 1982 **27** 259–69.
16. Papirer E, Schultz J and Turchi C, 'Surface properties of a calcium carbonate filled treated with stearic acid', *Eur Polym J* 1984 **20** 1155–8.
17. Li H, Hyperdispersant, *Plastics* 1999 **28**(2) 25–8 (in Chinese).
18. Yoshinaga K, Yokoyama T, Sugawa Y, Krakawa H, Enomoto N, Nishida H and Komatsu M, 'Preparation of monodispersed polymer-modified silica particles by radical polymerization using silica colloid and introduction of functional groups on the composite surface', *Polym Bull* 1992 **28** 663–8.
19. Du H, Liu Z Q, Liu F Q, Li T J, Tang X Y, Xu W Q and Wu Y, 'The characterization of polymer microspheres composited with Fe_2O_3 in nano-scale', *Chem J Chinese U* 1997 **18**(9) 1565–7 (in Chinese).
20. Liu H B, 'Microwave-induced plasma synthesis of organically encapsulated TiO_2 nanoparticles', *Chem Commun* 1997 **(10)** 44–46 (in Chinese).
21. Jancar J, 'Impact behavior of polypropylene, its blends and composites', in Karian H G, *Handbook of Polypropylene and Polypropylene Composites*, New York, Marcel Dekker, 1999, 367–381.
22. Gunko V M, Voronin E F, Pakhlov E M, Zarko V I, Turov V V, Guzenko N V, Leboda R and Chibowski E, 'Features of fumed silica coverage with silanes having three or two groups reacting with the surface', *Colloid Surf A* 2000 **166** 187–201.
23. Espiard Ph and Guyot A, 'Poly (ethyl acrylate) latexes encapsulating nanoparticles of silica: 2. Grafting process onto silica', *Polymer* 1995 **36** 4391–5.
24. Tsubokawa N, Kogure A and Sone Y, 'Grafting of polyesters from ultrafine inorganic particles: copolymerization of epoxides with cyclic acid anhydrides initiated by COOK groups introduced onto the surface', *J Polym Sci Polym Chem* 1990 **28** 1923–33.

25. Tsubokawa N, Ishida H and Hashimoto K, 'Effect of initiating groups introduced onto ultrafine silica on the molecular weight polystyrene grafted onto the surface', *Polym Bull* 1993 **31** 457–64.
26. Tsubokawa N and Ishida H, 'Graft polymerization of methyl methacrylate from silica initiated by peroxide groups introduced onto the surface', *J Polym Sci Polym Chem* 1992 **30** 2241–6.
27. Hayashi S, Takeuchi Y, Eguchi M, Iida T and Tsubokawa N, 'Graft polymer of vinyl monomers initiated by peroxycarbonate groups introduced onto silica surface by Michael addition', *J Polym Sci Polym Chem* 1999 **71** 1491–7.
28. Tsubokawa N, Kogure A, Maruyama K, Sone Y and Shimomura M, 'Graft polymerization of vinyl monomers from inorganic ultrafine particles initiated by Azo groups introduced onto the surface', *Polym J* 1990 **22** 827–33.
29. Tsubokawa N, Shirai Y, Tsuchida H and Handa S, 'Photografting of vinyl polymers onto ultrafine inorganic particles: photopolymerization of vinyl monomers initiated by Azo groups introduced onto these surface', *J Polym Sci Polym Chem* 1994 **32** 2327–32.
30. Luo Y, Rong M Z, Zhang M Q, Friedrich K, 'Surface grafting onto SiC nanoparticles with glycidyl methacrylate in emulsion', *J Polym Sci Polym Chem* 2004 **42** 3842–52.
31. Fukano K and Kageyama E, 'Study on radiation-induced polymerization of vinyl monomers adsorbed on inorganic substances. I. Radiation-induced polymerization of styrene adsorbed on several inorganic substances', *J Polym Sci Polym Chem* 1975 **13** 1309–24.
32. Fukano K and Kageyama E, 'Study on radiation-induced polymerization of vinyl monomers adsorbed on inorganic substances. II. Radiation-induced polymerization of methyl methacrylate adsorbed on several inorganic substances', *J Polym Sci Polym Chem* 1975 **13** 1325–38.
33. Fukano K and Kageyama E, 'Study of radiation-induced polymerization of vinyl monomers adsorbed on inorganic substances. VII. Effect of pretreatment temperature of silica gel on styrene-silica gel system', *J Polym Sci Polym Chem* 1976 **14** 1743–51.
34. Fukano K and Kageyama E, 'Study of radiation-induced polymerization of vinyl monomers adsorbed on inorganic substances. X. Influences of H_2O on the styrene-silica gel system', *J Polym Sci Polym Chem* 1977 **15** 65–72.
35. Fukano K and Kageyama E, 'Study of radiation-induced polymerization of vinyl monomers adsorbed on inorganic substances. IX. Preirradiation polymerization of styrene-silica gel system', *J Polym Sci Polym Chem* 1976 **14** 2193–205.
36. Fukano K and Kageyama E, 'Study of radiation-induced polymerization of vinyl monomers adsorbed on inorganic substances. VIII. Polymerization of styrene and methyl methacrylate adsorbed on aerosil', *J Polym Sci Polym Chem* 1976 **14** 2183–92.
37. Fukano K and Kageyama E, 'Study of radiation-induced polymerization of vinyl monomers adsorbed on inorganic substances. IV. Dose rate and temperature dependences in the styrene-silica gel system', *J Polym Sci Polym Chem* 1976 **14** 23–36.
38. Fukano K and Kageyama E, 'Radiation-induced polymerization of vinyl monomers adsorbed on inorganic substances. VI. Temperature dependence and effects of additives on methyl methacrylate-silica gel system', *J Polym Sci Polym Chem* 1976 **14** 1031–41.

39. Rong M Z, Zhang M Q, Zheng Y X, Zeng H M, Walter R and Friedrich K, 'Structure-property relationships of irradiation grafted nano-inorganic particle filled polypropylene composites', *Polymer* 2001 **42** 167–83.
40. Wu C L, Zhang M Q, Rong M Z and Friedrich K, 'Tensile performance improvement of low nanoparticles filled-polypropylene composites' *Compos Sci Technol* 2002 **62**(10–11) 1327–40.
41. Wu C L, Zhang M Q, Rong M Z and Friedrich K, 'Silica nanoparticles filled polypropylene: effects of particle surface treatment, matrix ductility and particle species on mechanical performance of the composites' *Compos Sci Technol* 2005 **65** 635–45.
42. Rong M Z, Zhang M Q, Wang H B and Zeng H M, 'Surface modification of magnetic metal nanoparticles and its influence on the performance of polymer composites', *J Polym Sci Polym Phys* 2003 **41**(10) 1070–84.
43. Ma C G, Rong M Z and Zhang M Q, 'Irradiation initiated grafting of poly(butyl acrylate) onto nano-sized calcium carbonate particles', *Chin Chem Lett* 2005 **16**(3) 409–12.
44. Hé C X, 'Friction and wear properties of ultra-high-molecular-weight-polyethylene and its composites filled with nanocrystalline Al_2O_3', *Tribology*, 2002 **22**(1) 32–5. (in Chinese).
45. Sawyer W G, Freudenberg K D, Bhimaraj P and Schadler L S, 'A study on the friction and wear behavior of PTFE filled with alumina nanoparticles', *Wear* 2003 **254** 573–80.
46. Bhimaraj P, Burris D L, Action J, Sawyer W G, Toney C G, Siegel R W and Schadler L S, 'Effect of matrix morphology on the wear and friction behavior of alumina nanoparticle/poly(ethylene) terephthalate composites', *Wear* 2005 **258** 1437–43.
47. Wang Q, Xu J, Shen W and Q Xue, 'The effect of nanometer SiC filler on the tribological behavior of PEEK', *Wear* 1997 **209** 316–21.
48. Wang Q, Xue Q, Liu H, Shen W and Xu J, 'The effect of particle size of nanometer ZrO_2 on the tribolological behavior of PEEK', *Wear* 1996 **198** 216–19.
49. Wang Q, Xu J, Shen W and Liu W, 'An investigation of the friction and wear properties of nanometer Si_3N_4-filled PEEK', *Wear* 1996 **196** 82–6.
50. Wang Q, Xue Q and Shen W, 'The friction and wear properties of nanometre SiO_2-filled polyetheretherketone', *Tribol Int* 1997 **30** 193–7.
51. Wang Q, Xue Q, Shen W and Zhang J, 'The friction and wear properties of nanometer ZrO_2-filled polyetheretherketone', *J Appl Polym Sci* 1998 **69** 135–41.
52. Wang Q, Xue Q, Liu W and Chen J, 'The friction and wear characteristics of nanometer SiC and polytetrafluoroethylene-filled polyetheretherketone', *Wear* 2000 **243** 140–6.
53. Wang Q, Xue Q, Liu W and Chen J, 'Effect of nanometer SiC filler on the tribological behavior of PEEK under distilled water lubrication', *J Appl Polym Sci* 2000 **78** 609–14.
54. Wang Q, Xue Q, Liu W and Chen J, 'Tribological characteristics of nanometer Si_3N_4 filled polyetheretherketone under distilled water lubrication', *J Appl Polym Sci* 2001 **79** 1394–400.
55. Shao X, Tian J, Liu W, Xue Q and Ma C, 'Tribological properties of SiO_2 nanoparticle filled-phthalazine ether sulfone/phthalazine ether ketone (50/50 mol %) copolymer composites', *J Appl Polym Sci* 2002 **85** 2136–44.

56. Shao X, Tian J, Liu W M, Ma C L and Xue Q J, 'Friction and wear properties of nanometer TiO_2 particle-filled poly(phthalazine ether sulfone ketone) composites', *Polym Mater Sci Eng* 2003 **19**(3) 208–11 (in Chinese).
57. Chen W X, Li F, Han G, Xia J B, Wang L Y, Tu J P and Xu Z D, 'Tribological behavior of carbon-nanotube-filled PTFE composites', *Tribol Lett* 2003 **15**(3) 275–8.
58. Li F, Hu K, Li J and Zhao B, 'The friction and wear of nanometer ZnO filled polytetrafluoroethylene', *Wear* 2002 **249** 877–82.
59. Ge S R, Zhang D K, Li L and Liu J L, 'Tribological behaviors of polyamide 1010 composites filled with nanoscale Al_2O_3 and Fe_2O_3particulates', *Tribology* 2004 **24**(1) 25–8 (in Chinese).
60. Lai S-Q, Li T-S, Liu X-J and Lv R-G, 'A Study on the friction and wear behavior of PTFE filled with acid treated nano-attapulgite', *Macromol Mater Eng* 2004 **289** 916–22.
61. Ge S R, Zhang D K, Li L and Liu J L, 'Tribological behavior of nano-TiO_2 and nano-SiO_2 filled nylon composites', *Tribology* 2004 **24**(2) 152–5 (in Chinese).
62. Chen M Y, Baib Z, Tan S C and Unroe M R, 'Friction and wear scar analysis of carbon nanofiber-reinforced polymeric composite coatings on alumina/aluminum composite', *Wear* 2002 **252** 624–34.
63. Ye Y P, Zhang Y S, Sun X J and Zhou H D, 'Preparation and tribological behavior of Ni/polyurethane nanocomposite coatings', *Tribology* 2003 **23**(2) 104–7 (in Chinese).
64. Lee J-Y and Lim D-S, 'Tribological behavior of PTFE film with nanodiamond', *Surf Coat Technol* 2004 **188–189** 534–8.
65. Schadler L S, Laul K O, Smith R W and Petrovicova E, 'Microstructure and mechanical properties of thermally sprayed silica/nylon nanocomposites', *J Therm Spray Tech* 1997 **6**(4) 475–85.
66. Mateus C, Costil S, Bolot R and Coddet C, 'Ceramic/fluoropolymer composite coatings by thermal spraying – a modification of surface properties', *Surf Coat Technol* 2005 **191** 108–18.
67. Petrovicova E, Knight R, Schadler L S and Twardowski T E, 'Nylon 11/silica nanocomposite coatings applied by the HVOF process. I. Microstructure and morphology', *J Appl Polym Sci* 2000 **77** 1684–99.
68. Petrovicova E, Knight R, Schadler L S and Twardowski T E, 'Nylon 11/silica nanocomposite coatings applied by the HVOF process. II. Mechanical and barrier properties', *J Appl Polym Sci* 2000 **78** 2272–89.
69. Cai H, Yan F and Xue Q, 'Investigation of tribological properties of polyimide/carbon nanotube nanocomposites', *Mater Sci Eng* 2004 **A364** 94–100.
70. Cai H, Yan F, Xue Q and Liu W, 'Investigation of tribological properties of Al_2O_3-polyimide nanocomposites', *Polym Test* 2003 **22** 875–82.
71. Cai H, Yan F and Xue Q, 'Tribological behavior and SEM investigation of the polyimide/SiO_2 nanocomposites', *J Chin Electr Microscopy Soc* 2003 **22**(5) 420–5 (in Chinese).
72. Avella M, Errico M E and Martuscelli E, Novel PMMA/$CaCO_3$ nanocomposites abrasion resistant prepared by an in situ polymerization process, *Nano Lett* 2001 **1** 213–17.
73. Che J, Song Y, Xiao Y, Lu Y and Wang X, 'Nano-TiO_2 modified phenolic resin and its application in frictional material', *Non-metallic Mines* 2001 **24**(3) 50–2 (in Chinese).

74. Yan H X, Ning R C, Ma X Y and Zhang Q Y, 'Friction and wear behavior of nanometer Si_3N_4-filled bismaleimide composites', *Tribology*, 2001 **21**(6) 452–5 (in Chinese).
75. Rong M Z, Zhang M Q, Shi G, Ji Q L, Wetzel B and Friedrich K, 'Graft polymerization onto inorganic nanoparticles and its effect on tribological performance improvement of polymer composites', *Tribol Int* 2003 **36** 697–707.
76. Shi G, Zhang M Q, Rong M Z, Wetzel B and Friedrich K, 'Sliding wear behavior of epoxy containing nano-Al_2O_3 particles with different pretreatments', *Wear* 2004 **256** 1072–81.
77. Shi G, Zhang M Q, Rong M Z and Friedrich K, 'Tribological behavior of nanometer Al_2O_3 filled epoxy resin composites', *Tribology* 2003 **23**(3) 211–15 (in Chinese).
78. Shi G, Zhang M Q, Rong M Z, Wetzel B and Friedrich K, 'Friction and wear of low nanometer Si_3N_4 filled epoxy composites', *Wear* 2003 **254** 784–96.
79. Zhang M Q, Rong M Z, Yu S L, Wetzel B and Friedrich K, 'Effect of particle surface treatment on the tribological performance of epoxy based nanocomposites', *Wear* 2002 **253** 1086–93.
80. Ji Q L, Zhang M Q, Rong M Z, Wetzel B and Friedrich K, 'Tribological properties of nanosized silicon carbide filled epoxy composites', *Acta Mater Compos Sin* 2004 **21**(6) 14–20 (in Chinese).
81. Ji Q L, Zhang M Q, Rong M Z, Wetzel B and Friedrich K, 'Tribological properties of surface modified nano-alumina/epoxy composites', *J Mater Sci* 2004 **39** 6487–93.
82. Kissinger H E, 'Reaction kinetics in differential thermal analysis', *Anal Chem* 1957 **29** 1702–6.
83. Crane L W, Dynes P J and Kaelble D H, 'Analysis of curing kinetics in polymer composites', *J Polym Sci Polym Lett Ed* 1973 **11** 533–40.
84. Hu Y H, Gao H, Yan F Y, Liu W M and Qi C Z, 'Tribological and mechanical properties of nano ZnO-filled epoxy resin composites', *Tribology* 2003 **23**(3) 216–20 (in Chinese).
85. Cho M H and Bahadur S, 'Study of the tribological synergistic effects in nano CuO-filled and fiber-reinforced polyphenylene sulfide composites', *Wear* 2005 **258** 835–45.
86. Wetzel B, Haupert F and Zhang M Q, 'Epoxy nanocomposites with high mechanical and tribological performance', *Compos Sci Technol* 2003 **63** 2055–67.
87. Wetzel B, Haupert F, Friedrich K, Zhang M Q and Rong M Z, 'Impact and wear resistance of polymer nanocomposites at low filler content', *Polym Eng Sci* 2002 **42**(9) 1919–27.
88. Xing X S and Li R K Y, 'Wear behavior of epoxy matrix composites filled with uniform sized sub-micron spherical silica particles', *Wear* 2004 **256** 21–6.
89. Tang G, Wang Z, Ma Q and Zhao D, 'Study on improving wear resistance of epoxy resin filled with nanometer alumina', *Thermoset Resin* 2002 **17**(1) 4–8 (in Chinese).
90. Shimbo M, Ochi M and Ohoyama N, 'Frictional behavior of cured epoxide resins', *Wear* 1983 **91** 89–101.
91. Tomizawa H and Fischer T E, 'Friction and wear of silicon nitride and silicon carbide in water: hydrodynamic lubrication at low sliding speed obtained by tribochemical wear', *ASLE Trans* 1987 **30**(1) 41–6.

92. Fischer T E and Tomizawa H, 'Interaction of tribochemistry and nicrofracture in the friction and wear of silicon nitride', *Wear* 1985 **105** 29–45.
93. Gao Y-M, Fang L, Su J-Y andXu X-W, 'An investigation on component and formation of tribochemical film in Si_3N_4-white iron sliding pair lubricated with distilled water', *Tribol Int* 1997 **30** 693–700.
94. Kong H, Yoon E-S and Kwon O K, 'Self-formation of protective oxide films at dry sliding mild steel surfaces under a medium vacuum', *Wear* 1995 **181–183** 325–33.
95. Nakamura M, Hirao K, Yamauchi Y and Kanzaki S, 'Tribological behaviour of unidirectionally aligned silicon nitride against steel', *Wear* 2002 **252** 484–90.
96. Bahadur S and Sunkara C, 'Effect of transfer film structure, composition and bonding on the tribological behavior of polyphenylene sulfide filled with nano particles of TiO_2, ZnO, CuO and SiC', *Wear* 2005 **258** 1411–21.
97. Bauer F, Ernst H, Decker U, Findeisen M, Glasel H J, Langguth H, Hartmann E, Mehnert R and Peuker C, 'Preparation of scratch and abrasion resistant polymeric nanocomposites by monomer grafting onto nanoparticles, 1 – FTIR and multinuclear NMR spectroscopy to the characterization of methacryl grafting', *Macromol Chem Phys* 2000 **201**(18) 2654–9.
98. Glasel H J, Bauer F, Ernst H, Findeisen M, Hartmann E, Langguth H, Mehnert R and Schubert R, 'Preparation of scratch and abrasion resistant polymeric nanocomposites by monomer grafting onto nanoparticles, 2 – Characterization of radiation-cured polymeric nanocomposites', *Macromol Chem Phys* 2000 **201**(18) 2765–70.
99. Bauer F, Sauerland V, Glasel HJ, Ernst H, Findeisen M, Hartmann E, Langguth H, Marquardt B and Mehnert R, 'Preparation of scratch and abrasion resistant polymeric nanocomposites by monomer grafting onto nanoparticles, 3 – Effect of filler particles and grafting agents', *Macromol Mater Eng* 2002 **287**(8) 546–52.
100. Bauer F, Sauerland V, Ernst H, Glasel HA, Naumov S and Mehnert R, 'Preparation of scratch- and abrasion-resistant polymeric nanocomposites by monomer grafting onto nanoparticles, 4 – Application of MALDI-TOF mass spectrometry to the characterization of surface modified nanoparticles', *Macromol Chem Phys* 2003 **204**(3) 375–83.
101. Bauer F, Ernst H, Hirsch D, Naumov S, Pelzing M, Sauerland V and Mehnert R, 'Preparation of scratch and abrasion resistant polymeric nanocomposites by monomer grafting onto nanoparticles, 5(a) – Application of mass spectroscopy and atomic force microscopy to the characterization of silane-modified silica surface', *Macromol Chem Phys* 2004 **205**(12) 1587–93.
102. Lu J, Zhang M Q, Rong M Z, Yu S L, Wetzel B and Friedrich K, 'Thermal stability of frictional surface layer and wear debris of epoxy nanocomposites in relation to the mechanism of tribological performance improvement', *J Mater Sci Lett* 2004 **39** 3817–20.
103. Godet M, 'The third body approach: a mechanical view of wear', *Wear* 1984 **100** 437–52.
104. Gong Q, Cao H and Zhao S, 'Development of nano-scale Al_2O_3 filled transparent and anti-abrasion compound paint', *Mod Paint Finish* 2004 **(2)** 2–7 (in Chinese).
105. Pavoor P V, Gearing B P, E G Russell, Bellare A and Cohen R E, 'Engineering the friction-and-wear behavior of polyelectrolyte multilayer nanoassemblies through block copolymer surface capping, metallic nanoparticles, and multiwall carbon nanotubes', *J Appl Polym Sci* 2004 **92** 439–48.

106. Peng X, Ma H, Zeng Q and Lei Y, 'Tribological behavior of inorganic nano-particulates and polytetrafluoroethylene filled polyetheretherketone composites', *Tribology* 2004 **24**(3) 240–43 (in Chinese).
107. Su F, Zhang Z, Jiang W and Wang K, 'Study on the friction and wear properties of glass cloth composites filled with various nano- and micro-particles', *Tribology* 2004 **24**(5) 406–10 (in Chinese).
108. Zhang Z, Breidt C, Chang L, Haupert F and Friedrich K, 'Enhancement of the wear resistance of epoxy: short carbon fibre, graphite, PTFE and nano-TiO_2', *Compos Part A – Appl S* 2004 **35**(12) 1385–92.
109. Chang L, Zhang Z, Breidt C and Friedrich K, 'Tribological properties of epoxy nanocomposites – I. Enhancement of the wear resistance by nano-TiO_2 particles', *Wear* 2005 **258**(1–4) 141–148.

Index